Monwabisi: a hydrodynamic study of the hazardous cell circulation and potential related solutions to a safer bathing facility

by
Stephan Kistner

Thesis presented in fulfilment of the requirements for the degree of Master of Engineering in the Faculty of Civil Engineering at Stellenbosch University

Supervisor: Dr André K. Theron

December 2016

DECLARATION

By submitting this thesis electronically, I declare that the entirety of the work contained therein is my own, original work, that I am the sole author thereof (save to the extent explicitly otherwise stated), that reproduction and publication thereof by Stellenbosch University will not infringe any third party rights and that I have not previously in its entirety or in part submitted it for obtaining any qualification.

Date: December 2016

ABSTRACT

The objective of this thesis is to investigate the hazardous hydrodynamic circulation pattern at Monwabisi (False Bay, South Africa) and potential solutions to a safer bathing facility, by means of a complex hydrodynamic numerical model.

A hazardous circulation cell exists at Monwabisi which is caused by a spur extending off an adjacent tidal pool. The partial wave-sheltering of the spur produces a wave setup gradient in the bay which facilitates a strong anti-clockwise circulation. The wave-sheltering creates a false perception of safety as the spur forces the current in a strong and concentrated flow in a seaward direction. This strong current, often referred to as a rip current, has been linked to several rescues and drownings. Removal of the structure was not considered an option as it protects the tidal pool against wave overtopping and scouring as well as holds a beach which did not exist pre-construction. The CSIR (1997) showed by means of a physical model study that the hazardous circulation could be reduced to a great extent by means of structural interventions. However, no structural changes have been implemented since the publication of their report.

This study reinvestigates the CSIR's proposed solutions by means of a 2D Boussinesq type numerical wave model. The numerical model aimed to replicate the CSIR's physical model setup conditions, to simulate the resultant circulation patterns and current velocities, and comparing the results to the measurements of the CSIR's physical model.

An initial baseline simulation was set-up to simulate the cell circulation present at Monwabisi. The simulation showed excellent agreement to the prototype conditions in terms of the observed and reported physical processes and the hazardous counter-clockwise current circulation.

The numerical simulation of the CSIR's proposed solutions followed. An in-depth analysis of the numerical model's results demonstrated the effectiveness of groynes in reducing the current velocity of the cell circulation. Various other options were tested, but proved to be less successful. The groynes physically divided the beach, thereby producing a wave-sheltered bay removed from the feeder currents originating from high wave energy section of the bay. The optimal solution was a T-shaped groyne structure placed perpendicularly to the incoming waves. The flanges of the T-groyne reduced the incoming wave energy even further, whilst also separating the newly created sheltered and high wave energy bays, thus reducing circulation intermixing between the two. The T-groyne reduced the strong velocity along the spur significantly and also resulted in the most quiescent bay of all the tested options.

The results of the numerical model were also compared to the CSIR's physical simulation model results. The majority of the simulations showed good agreement in terms of the measured velocities and the general circulation patterns. Both models indicated that the T-groyne is the most effective solution, especially in terms of reducing the current along the spur. The Boussinesq Wave model proved to be a reliable and useful tool in simulating the complex hydrodynamic system at Monwabisi and has great potential for similar studies in the future.

SAMEVATTING

Die doel van hierdie tesis is om die sirkulasiepatroon by Monwabisi (Valsbaai, Suid-Afrika) en potensiële oplossings vir 'n veiliger swemfasiliteit te ondersoek aan die hand van 'n komplekse hidrodinamiese numeriese model.

Die gevaarlike sirkulasie by Monwabisi word veroorsaak deur 'n golfbreker-uitsteeksel vanaf 'n aangrensende getypoel. Die gedeeltelike beskerming teen die inkomende golwe produseer 'n golf opstuwing gradiënt in die baai wat 'n sterk anti-kloksgewyse sirkulasie veroorsaak. Die beskerming teen golwe skep 'n vals persepsie van veiligheid, aangesien die golfbreker uitsteeksel hier die stroom in 'n sterk en gekonsentreerde vloei in 'n seewaartse rigting dwing. Dié stroom word dikwels na verwys as 'n sleurstroom, en is gekoppel aan verskeie redding- en verdrinkingsgevalle. Die verwydering van die struktuur word nie oorweeg nie, aangesien dit die getypoel teen golfoorstroming asook die strand teen erosie beskerm. Die WNNR (1997) het deur middel van 'n fisiese modelstudie geïllustreer dat die gevaarlike sirkulasiepatroon tot 'n groot mate verminder kan word deur strukturele ingryping. Sedert die publikasie van die verslag is egter nog geen fisiese veranderinge aangebring nie.

Hierdie studie herevalueer die WNNR se voorgestelde oplossings deur middel van 'n 2D *Boussinesq* golf-tipe numeriese model. Die numeriese model was daarop gemik om die fisiese model opstelling van die WNNR na te boots, die gevolglike sirkulasiepatrone en stroomsnelhede te simuleer, en dié te vergelyk met die praktiese metings van die WNNR.

'n Aanvanklike basislyn-simulasie is opgestel om die huidige sirkulasiepatroon by Monwabisi na te boots. Die simulasie het uitstekende ooreenkomste met die prototipe se waargenome en gerapporteerde fisiese prosesse, asook die gevaarlike anti-kloksgewyse sirkulasie getoon.

Daarna het die numeriese simulasie van die WNNR se voorgestelde oplossings gevolg. 'n Diepgaande ontleding van resultate van die numeriese model het aangetoon dat strandhoofde die sirkulasie se stroomsnelheid effektief verminder. Verkeie ander opsies was ook getoets, maar het minder sukses getoon. Die strandhoofde verdeel die strand fisies, en skep dus 'n golfbeskutte baai wat ook verwyder is van die sterk strome wat opgewek word deur hoë golfenergie. Die optimale oplossing was 'n T-vormige strandhoof struktuur loodreg georiënteer teenoor die inkomende golwe. Die flense van die T-strandhoof verminder die inkomende golfenergie nog verder, terwyl dit ook die beskutte en hoë-golfenergie-baaie verder van mekaar skei en sodoende sirkulasievermenging tussen die twee verminder. Die T-strandhoof het die sterk snelheid langs die golfbreker-uitsteeksel aansienlik verminder en het ook die kalmste baai van al die getoetste opsies gelewer.

Die resultate van die numeriese model is ook vergelyk met dié van die WNNR se fisiese model. Die simulasies het algeheel 'n goeie ooreenkoms getoon in terme van die stroomsnelhede en die algemene sirkulasiepatrone. Beide modelle het getoon dat die T-strandhoof die mees doeltreffende oplossing is, veral om die stroomsnelheid langs die golfbreker-uitsteeksel te verminder.

ACKNOWLEDGEMENTS

I would like to thank the Council for Scientific and Industrial Research (CSIR) for providing me research data, without which this study would not have been possible. I am also thankful to the South African Navy Hydrographic Office (SANHO), Lifesaving South Africa (LSA), United States Lifesaving Association (LSA) and the Department of Rural Development and Land Reform (DRDLR) for providing me research material essential to this study.

I would like to acknowledge Mr Stephen Luger for taking interest in this study and providing his time and expertise to assist with the numerical model. I would also like to thank Mr Marius Rossouw and Mr Gert Jacobs for their valuable input and assistance on the Boussinesq wave model.

I wish to express my sincere gratitude to my supervisor, Dr André Theron, for his support, guidance and motivation.

Many thanks to my family and friends, to Jim, Brandon, Will and especially to Yasmin for the motivation and support throughout this project.

Lastly, I would like to thank Mr Geoff Toms for sharing his passion of the ocean and introducing me to the field of Coastal Engineering.

CONTENTS

LIST OF FIGURES

LIST OF TABLES

LIST OF APPENDICES

NOMENCLATURE

LIST OF ABBREVIATIONS

C	Chézy friction coefficient
C_{sponge}	Sponge layer coefficient
C_r	Courant number
c	Wave celerity
c_g	Group wave celerity
d	Water depth
E	Wave energy density
$\mathcal{F}_C$	Comparison factor for the CSIR-MBWS rating system
f	Velocity conversion factor
g	Gravitational acceleration constant
H_{m0}	Significant wave height
H_s	Wave height of a regular wave series
$\bar{H}'_S$	Average absolute wave height change
k	Wave number
L	Wave length
M	Manning M coefficient
M_T	Mass transport
$\mathcal{M}$	Momentum flux
n	Ratio of group wave celerity to individual phase celerity
p	Fluid pressure
S_{xx}, S_{yy}, S_{xy}	Wave radiation stresses
$\mathcal{S}_D$	Swimming danger factor
T	Wave period
T_p	Peak wave period
U_r	Relative current velocity ratio from the MBWS numerical model
U_f	Factorised current velocity ratio from the MBWS numerical model
$\bar{U}_{Ar}$	Relative weighted area average velocity
u	Horizontal component of particle orbital velocity
u, u_{PA30}	Current velocity (absolute) from the MBWS numerical model
$\bar{u}'_S$	Average absolute velocity change
$\bar{u}_A$	Area velocity distribution weighted average
V_f	Factorised current velocity ratio from the CSIR's physical model
v	Current velocity (absolute) from the CSIR's physical model
α_P	Porosity coefficient
α_r	Reflection coefficient
η	Wave amplitude
η_{RMS}	Root mean square value of a wave amplitude series
θ	Wave direction
ρ	Fluid density
σ	Standard deviation of the surface elevation

List of Abbreviations

CD	Chart Datum
CoCT	City of Cape Town
CSIR	Council for Scientific and Industrial Research
DHI	Danish Hydraulic Institute
DRDLR	Department of Rural Development and Land Reform
LSA	Lifesaving Association (South Africa)
MBWS	Monwabisi Boussinesq Wave Simulation
MSL	Mean Sea Level
NSRI	National Sea Rescue Institute
PA30	30 m peak average
RNLI	Royal National Lifeboat Institution
SANHO	South African Navy Hydrographic Office
SLSNZ	Surf Life Saving New Zealand
USLA	United States Lifesaving Association
WL	Water Level

1 INTRODUCTION

Monwabisi is a very popular beach resort situated in False Bay, South Africa. The resort is located on a naturally rocky-sandy coastline, which is not safe or comfortable for bathers. Because of this, a tidal pool was built in 1987 and later a spur extension, completed in 1997, was built to trap sediment to allow for the accretion of a beach and to reduce wave action into the tidal pool. The beach attracts many beach goers, but at the same time, the addition of the spur allows for a strong cell circulation to develop in the embayment.

This danger is made worse with the wave sheltered area creating an illusion of security. Closer to the spur, the beach is more sheltered against incoming waves. This creates a false perception of safe water, as currents are not easily spotted by the untrained eye. Near the head of the spur the beach profile steepens. The sudden increase in depth and strong current present a very hazardous combination. To date, several drownings and need for rescues at Monwabisi have been attributed to the strong currents caused by the spur. The spur and the cell circulation have been a topic of controversy ever since.

Relatively soon after the completion of the spur, the CSIR (1997) conducted a physical model study to solve the problem of the cell circulation, whilst retaining the beach. The report showed strong evidence that the hazardous circulation could be reduced to a great extent by means of structural interventions, but at the date of publishing this thesis– almost 20 years later - no such modifications have been implemented.

Therefore, in this study a complex hydrodynamic numerical model was used to investigate the solutions proposed by the CSIR from another perspective. The results of this model were analysed qualitatively and quantitatively and compared to the results of the CSIR's numerical model.

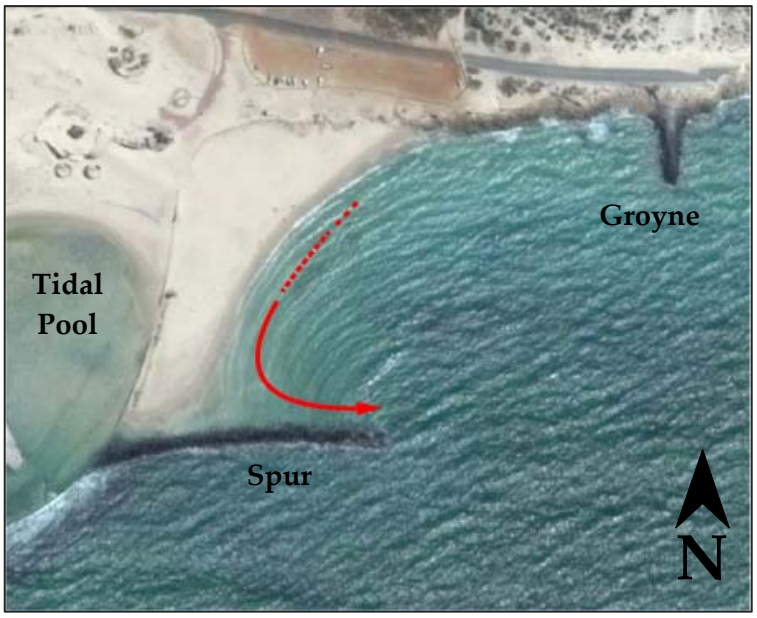

Figure 1-1: Visualisation of the hazardous circulation cell present at Monwabisi, False Bay (Google Earth, 2014).

1.1 LIMITATIONS OF THIS STUDY

This study exclusively used a two-dimensional Boussinesq type wave model to study the hydrodynamics at Monwabisi. The Boussinesq wave model resolves wave-induced currents by means of phase-averaged, depth-integrated formulations, which implies that the currents are limited to time-averaged, depth-uniform flow on a 2D-horizontal grid. The Boussinesq equations are computer intensive and require relatively small time-steps, which limits the numerical model to relatively short term simulations.

The numerical model set-up was based on the CSIR's physical model study of 1997. Identical structural, bathymetric, wave and tidal conditions were used in the numerical model for comparative purposes. The numerical model simulations only tested the proposed solutions and environmental conditions as simulated by the CSIR. Only the CSIR's wave configuration options were tested. The wave generation equipment of the time was limited to long-crested, regular waves only. The beach profile response to structural placements was only accounted for in a limited amount of simulations and was based on estimated profiles from the CSIR. The numerical model did not include any further sediment transport related effects.

There was not enough data for the calibration of the current velocities. The velocities were therefore expressed as change relative to the simulation of the present situation at Monwabisi.

This study focussed on the current-related performance of the proposed solutions. Wave action was also considered in this report, but only as an extension to the qualitative study of the circulation process. This study did not focus on the cost of the structures or social and environmental aspects.

1.2 CHAPTER LAYOUT

This thesis commences with an overview of the objectives of this study (Chapter 2). It is followed by a brief chapter outlining the methodology for the numerical model investigation (Chapter 3).

Chapter 4 includes a literature study, which discusses the nearshore circulation process and the related hazard.

Chapter 5 discusses the hazardous circulation present at Monwabisi and the CSIR's (1997) physical model study on the mitigation of the hazard.

Chapter 6 provides detail on the numerical model used in this study. Chapters 7 and 8 and follow with the detailed results analysis and comparison to the CSIR's physical model study respectively.

The conclusions of this study is set out in Chapter 9, followed by recommendations for further studies in Chapter 10.

2 OBJECTIVES

The main objective of this study was to investigate the present hazardous cell circulation at Monwabisi beach (False Bay, South Africa) and to study the effectiveness of proposed solutions by means of a numerical model. The secondary objective was to investigate whether this complex hydrodynamic system can be successfully simulated by means of a numerical 2D Boussinesq type wave model.

To meet the above objectives this study focusses on current formation and velocities presently occurring at the beach, as well as the influence of structures proposed by the CSIR (1997) that could potentially diffuse the hazardous cell circulation. This study makes use of the *MIKE 21 Boussinesq Wave* numerical model to simulate the hydrodynamic process of the present condition as well as the proposed structural changes to the beach. The results of the numerical model will be compared to the physical model results of the CSIR to evaluate the differences and agreements between the two studies. The numerical study will also be discussed in further depth to discuss details not covered by the CSIR report.

The results of the numerical model could further emphasize the necessity of a structural modification to Monwabisi beach to provide safer conditions for the bathers.

3 METHODOLOGY

This study first examined the existing situation at Monwabisi with an in-depth investigation of the CSIR's 1997 report. A two-dimensional Boussinesq wave model, referred to as the *Monwabisi Boussinesq Wave Simulation* (MBWS) numerical model, was then set up with the *MIKE 21 BW Boussinesq Wave* suite. The bathymetry, structures, wave conditions and tide levels used in the numerical model were mostly based on the same configurations as used in the CSIR's physical model for comparative purposes.

A total of 24 simulations were run to test a variety of structural changes, wave conditions and water levels. To provide a baseline for comparison, an additional 11 simulations were run to simulate the existing layout at Monwabisi for a variety of wave and tide combinations. Each of the 35 simulations was based on a combination of the following:

- 16 structurally modified beach layouts and present layout
- 7 tide levels (-0.3 m MSL to +0.9 m MSL)
- 6 wave heights (H_s = 1.0 m to H_s =1.8 m)
- 2 wave periods (12 s & 8 s)

The main output parameters for of interest for the hydrodynamic study were

- Current velocities
- Circulation patterns (horizontal 2D)

Where required, some additional parameters were considered in special cases, which included the surface elevation (wave height), average wave height distribution and wave energy density flux. With the lack of prototype velocity measurements, the measurements of the numerical model were reported as percentage values to indicate relative change, rather than an unguaranteed absolute velocity.

The first simulation, **MB610**, was based on the existing situation at Monwabisi. This was used to verify the model, as well as to improve understanding of the present current circulation process. The mitigating solutions proposed by the CSIR were subsequently simulated and analysed by means of visual and statistical analysis to gain a qualitative and quantitative overview on how the proposed structures would influence the circulation at Monwabisi. To aid the qualitative measuring process, some velocity measuring methods were defined for specific use in this study.

The circulation pattern and current velocities of the numerical model were then compared to the results of the CSIR's physical model to compare the similarities between the two models and to explain any discrepancies.

4 LITERATURE STUDY

The literature review focuses on the nearshore circulation, especially with regard to cell circulations in the horizontal plane. The mechanisms contributing to the origin of the current-generation will be discussed, as well as other external factors that influence the currents. The currents will also be discussed in the context of the potential hazard to people and possible measures to reduce or mitigate the problem.

4.1 NEARSHORE CURRENTS

4.1.1 Introduction to nearshore circulation

Shepard and Inman (1951) attributed nearshore circulation to an interrelated system of two nearshore current types. The first, the *coastal currents*, are currents flowing in a longshore direction outside of the surf zone. These currents are usually tidal currents, wind-driven currents or pressure-gradient-induced currents. The second type, the *nearshore system*, may exist either in conjunction with coastal currents or as a system on its own, confined to the surf zone. This study will focus on the *nearshore system*.

Wind-generated waves originating from deep water will propagate into shallow water, undergoing processes of refraction, shoaling and breaking. The breaking waves dissipate their energy in the surf zone, transferring energy to currents. This may include non-uniform longshore currents, rip currents and cross-shore flows (Battjes *et al.*, 1990; Shepard & Inman, 1951). This wave-current energy transfer process has been theorised with the concept of *radiation stresses* by Longuet-Higgins and Stewart (1963). The wave-current interaction is a very important topic throughout this study, and will therefore be discussed in greater detail in the sub-sections that follow.

4.1.2 Mass transport

Waves propagating to the shore bring a small mean amount of water in the direction of propagation. Dean and Dalrymple (2004) described the phase-averaged shoreward transportation of water, the *mass transport.* Equation 4.1, below, formulates the phase-averaged non-linear mass transport, M_T:

$$M_T = \int_{-d}^{\eta} \overline{\rho u \cdot dz} \tag{4.1}$$

where

- ρ = fluid density
- u = horizontal particle oscillation velocity based on *Airy wave theory*
- η = surface elevation
- z = vertical axis used in the depth-integration
- $-d$ = bed elevation
- The overbar denotes phase-averaging

An interesting characteristic of this integral is that the depth-integrated mass transport at the still water level yields a null value, while the depth-integrated mass transport to the surface

elevation results in a positive mass transport. The shoreward mass transport is carried between the crest and trough level of the wave, and is larger than the backward transport below the trough level. The forward mass transport is therefore proportional to the size of the wave (Dean & Dalrymple, 2004).

The law of mass conservation requires that the wave-induced mass transport must undergo a return flow because there cannot be a net shoreward flow. The induced return flow is referred to as undertow. Undertow is thus a two-dimensional cross flow of water in the vertical plane. A small mass flux of water is brought shoreward between the crest and trough level of the waves, and returned as a seaward current near the bottom. Undertow also significantly contributes to suspended sediment and bedload flow seaward (Hansen & Svendsen, 1984; Battjes *et al.*, 1990; Dean & Dalrymple, 2004; Reeve *et al.*, 2004).

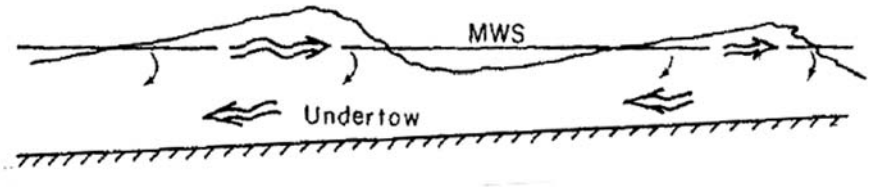

Figure 4-1: Schematization of undertow: a two-dimensional cross-flow process. (Hansen and Svendsen, 1984)

4.1.3 Momentum flux

In ocean engineering, momentum flux is described as the product of the mean mass transport and group velocity. The horizontal momentum flux is defined as the transfer of momentum through the vertical plane. Newton's 2nd law dictates that any change of magnitude or direction to the momentum will generate forces (Dean & Dalrymple, 2004; Buchard *et al.*, 2015). Following on equation 4.1, the momentum flux, $\mathcal{M}$, in horizontal x direction could be described by:

$$\mathcal{M} = \int_{-d}^{\eta} \overline{\rho u^2 \cdot dz} \tag{4.2}$$

4.1.4 Radiation stress

Longuet-Higgins and Stewart (1963) formulated the theory of radiation stresses. By adding a depth-integrated pressure component to the momentum flux, the excess momentum flux due to the presence of a wave can be formulated. It is therefore the sum of the pressure force acting on a vertical plane normal to the flow direction and the transfer of momentum through the vertical plane, minus the depth-integrated hydrostatic pressure over still-water depth.

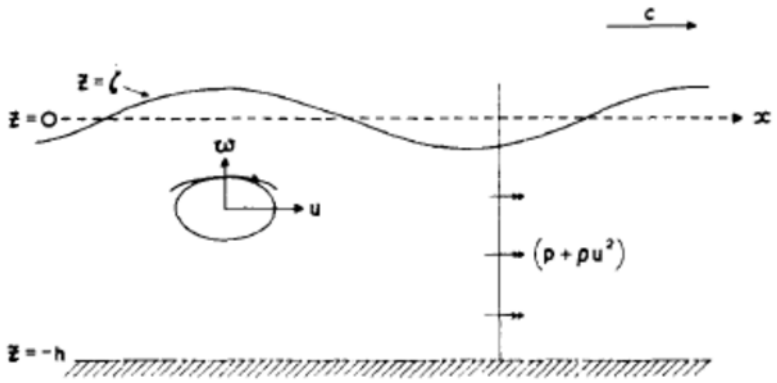

Figure 4-2: Momentum flux in a progressive wave (Longuet-Higgins & Stewart. 1963)

4.1.4.1 One-dimensional radiation stress

For unidirectional wave propagation parallel to an x-coordinate direction (shoreward), the radiation stress tensor in the x-direction along the x-plane is therefore defined as:

$$S_{xx} = \int_{-d}^{\eta} \overline{(p + \rho u^2) \cdot dz} - \int_{-d}^{0} \rho g \cdot dz \tag{4.3}$$

where

- S_{xx} = radiation stress tensor in the x-direction on the x-plane
- p = fluid pressure
- The overbar denotes phase-averaging

By integration and the principles of *Airy wave theory*, equation 4.3 becomes:

$$S_{xx} = \frac{\rho g \eta^2}{2}\left(\frac{1}{2} + \frac{2kD}{\sinh(kD)}\right) = E\left[2n - \frac{1}{2}\right] \tag{4.4}$$

$$c_g = n \cdot c \tag{4.5}$$

$$E = \frac{1}{4} \cdot \rho g a^2 \tag{4.6}$$

where

- E = total wave energy density
- k = wave number
- g = gravitational acceleration constant
- n = ratio of group wave celerity to individual phase celerity
- c_g = group wave celerity
- c = individual wave celerity

For a unidirectional wave traveling parallel to the x-axis, a y-directed momentum flux, S_{yy}, also exist, and is defined by:

$$S_{yy} = \frac{\rho g \eta^2}{2}\left(\frac{2kD}{\sinh(kD)}\right) = E\left[n - \frac{1}{2}\right] \tag{4.7}$$

From equation 4.4 and equation 4.7 it can be seen that when an external force is applied, the radiation stress and wave energy both change as a function of the water depth, or by Newton's 2nd law.

4.1.4.2 Two-dimensional radiation stresses

In the case of two-directional flow two principal stresses and a shear stress component act on the horizontal plane (see Figure 4-3). Waves travelling at an angle of θ relative to the x axis (on-offshore axis) would have the following radiation stresses:

$$S_{xx} = E\left[n(\cos^2\theta + 1) - \frac{1}{2}\right] \tag{4.8}$$

$$S_{yy} = E\left[n(\sin^2\theta + 1) - \frac{1}{2}\right] \tag{4.9}$$

$$S_{xy} = S_{yx} = \frac{E \cdot n \cdot \sin 2\theta}{2} \tag{4.10}$$

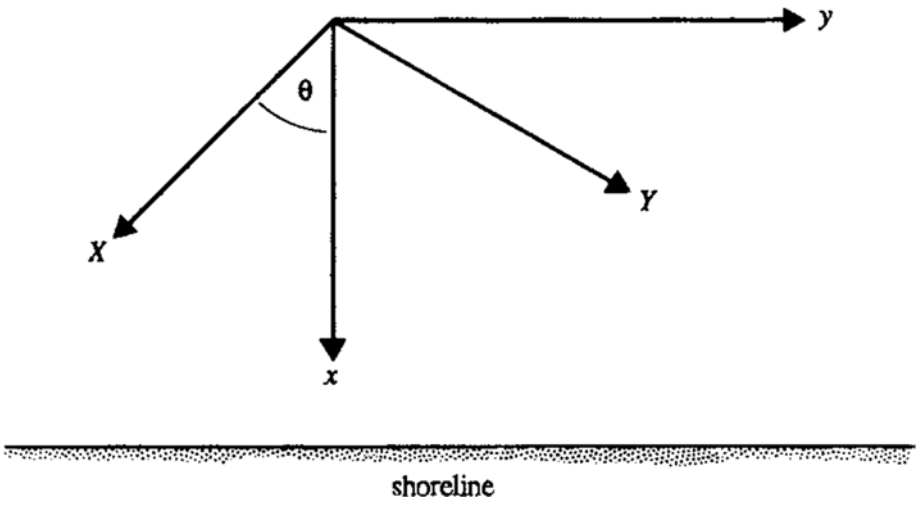

Figure 4-3: Cartesian coordinate system used for reference of radiation stress tensors in the horizontal plane (Reeve et al.*, 2004)*

4.1.5 Radiation stress and wave decay

In the surf zone, waves break causing a dissipation of wave energy. The law of conservation of energy requires that the dissipation of wave energy need balanced by counteracting forces.

4.1.5.1 Cross shore component

The onshore-directed momentum flux, S_{xx}, peaks at point of breaking, decreasing towards the shoreline and eventually reaching zero at the point of maximum wave run-up. This

momentum flux gradient is balanced by an increase of mean water level, $\bar{\eta}$, above the mean sea level. This slope is commonly referred to as the wave setup (Dean & Dalrymple, 2004).

4.1.5.2 Alongshore-component

If waves propagate oblique to the shoreline, the rapid decay of wave heights due to wave breaking causes a variation in the radiation shear stress component, S_{xy}. In an infinitely long, uniform shoreline the water-level slope cannot exist on the oblique S_{xy}.axis, as it will result in infinite or negative water depths in the surf zone. The water-level slope in the on-offshore axis only provides partial dissipation. Additional counteracting forces are therefore required to balance the shear component in the longshore axis (Dean & Dalrymple, 2004; Reeve *et al.*, 2004).

The waves exert a thrust force on the water, driving an alongshore current. The bottom stress generated by the current subsequently balances the gradients of the radiation stress terms. The result is a wave-current interaction in the form of an exchange of energy between the wave's energy and mean flow. The longshore current system plays an important role in the nearshore circulation system (Longuet-Higgins & Stewart, 1962; Longuet-Higgins, 1970; Gourlay, 1982; Dean & Dalrymple, 2004).

Longuet-Higgins and Stewart (1964) also noted the effect of long-waves: the energy exchange between wave and currents is proportional to the wave celerity, as seen in equations 4.4 and 4.5. For this reason long waves traveling at lower phase velocities can result in relatively large radiation stresses and therefore stronger currents.

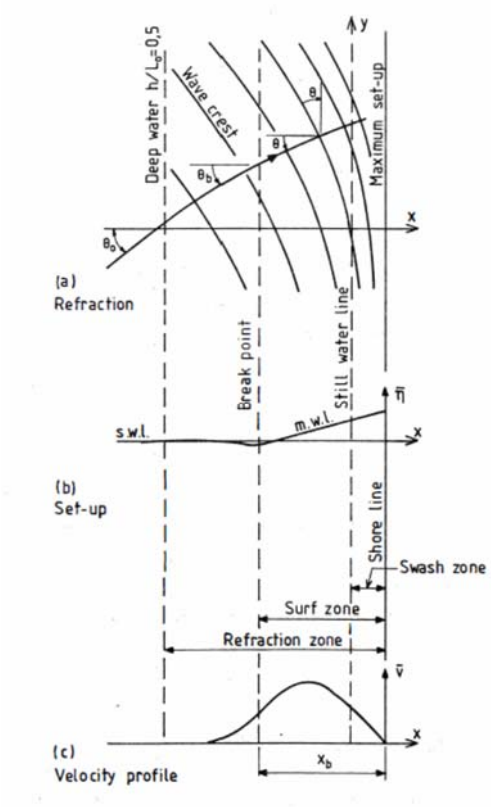

Figure 4-4: Schematic process of oblique waves generating alongshore currents. The cross-shore counteracting forces are shown by the increase of M.W.L., whereas the alongshore forces are counteracted by the bed shear stress from the alongshore mean velocity (Gourlay. 1982)

4.1.6 Horizontal circulation

Longshore currents are an integral component in nearshore circulation cells. Topographical, bathymetrical, structural or wave-current influences can force the longshore current in an on-offshore direction. In a generalised situation the conservation of energy necessitates a return flow to complete a cell circulation. The process of vortex stretching leads to a stronger and concentrated current in the offshore direction, and, conversely, the onshore flow is characterised by a broader and weaker current (Battjes *et al.*, 1990).

The feature engendering the offshore flow – sometimes referred to as a *rip current* – is discussed in the sections that follow. Clear definitions of a rip current exist, but when investigating strong circulation cells, literature differs on using the term rip current to describe strong flow patterns. The driving mechanisms and influences of well-defined rip currents are in many cases also applicable to strong circulation currents which are not necessarily termed rip-currents. The use of the term rip current, however, loses priority over the cause and effect which it entails.

4.1.7 General definition of a rip current

Rip currents return water from breaking waves in the form of a concentrated flow of water in the seaward direction past the breaker zone. They form part of cell circulations – a local current circulation within the surf zone. Rip currents typically span the whole water column, but past the breaker zone the flow is more confined near the surface (Haller & Dalrymple, 2003; Reeve *et al.*, 2004).

Rip currents can often be found along long straight beaches, but can also be found under piers, jetties, groynes, breakwaters, in the middle of embayments and at breaks in sandbars. The average velocity of a rip current is in the range of 0.3- 0.5 m/s, but can exceed 2 m/s – enough to put unsuspecting bathers at risk of drowning (Dean & Dalrymple, 2004; McMahan *et al.*, 2005).

4.1.8 General components of a rip current

Rip currents consist of three components: “feeders”, “neck” and “head”. Feeders refer to longshore currents, the driving force of rip currents. Water flows parallel to the shore before it is forced – or fed - seaward towards the neck of the rip current. Water primarily enters the neck through the feeder currents, but some water also enters the current laterally further seaward. The neck is the main component of a rip current, where the current is the strongest. Here the current is characterised by a narrow and intense flow. In the breaker zone, waves momentarily slow the current, resulting in a pulsating flow pattern. Past the breaker zone, the current weakens and spreads, forming the head. The general spreading is seaward, but also considerably lateral. The lateral flow often returns shoreward with incoming waves in the form of a broad and weak current, completing the circulation cell (Shepard *et al.*, 1941; Battjes *et al.*, 1990; Haller, 1999).

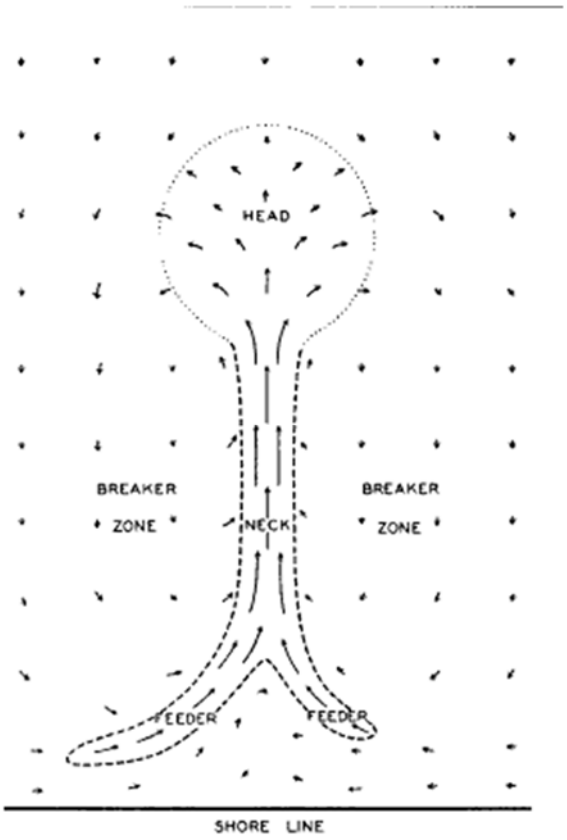

Figure 4-5: Flow pattern and components of a common rip current (Shepard et al.*, 1941)*

4.1.9 Velocity of a rip current

The velocity of the rip-current is subject to variability based on the wave climate and physical environment. It is therefore difficult to establish a transition point to distinguish non-rip currents from rip currents.

RIPEX experiments conducted by McMahan *et al*. (2005), showed average rip current velocities to be in the magnitude of 0.3 m/s. In storm conditions (where H_{m0} > 3.0 m) the 1-hourly average velocities reached 1.0 m/s and 1-minute average velocities reached 2.0 m/s. MacMahan *et al*. (2006) observed the hourly mean velocities of rip currents at various sites, which are tabulated below.

Table 4-1: Hourly mean and hourly maximum rip current velocities measured at different sites (MacMahan et al. 2006)

Location	u_{mean} [m/s]	u_{max} [m/s]	H_{m0} [m]	T_p [s]
Skallingen, NED	0.3	1.7	0.8	8
Palm Beach, AUS	0.4	2	0.75	10
Muriwai, NZL	0.65	2	1.5	14
Moreton Island, AUS	0.4	1	0.5	10
Torrey Pines, CA, USA	0.2	1	0.5	12
Monterey, CA, USA	0.3	2	1.5	12
SeaGrove, FL, USA	0.35	1.25	0.5	8

MacMahan *et al.* (2006) suggested that the notion expressed in previous literature of rip current magnitudes in the order of 1.0 m/s velocities represented larger events, as studies were more prone to study rip currents where the effect was more prominent.

4.1.10 Factors influencing rip current magnitude and direction

There are four major influences affecting the magnitude and/or direction of rip currents: wave height (and period), tide-level, incident-wave direction and coastal configuration. The latter two factors (especially coastal configuration) are more susceptible to variability along a shoreline and are therefore the main factors of variation in rip currents between different beaches. All of these factors combined make it very difficult to predict accurately where rip currents will form (McKenzie, 1958).

4.1.10.1 Wave height

Early research by Shepard *et al.* (1941), Shepard (1950) and Shepard and Inman (1951) has shown that rip current velocities increase with larger waves (Figure 4-6). This was concluded by observing the relatively instantaneous change in current rip current strength in response to wave height variations. This ties in with the discussion of -wave height relation to mass transport discussed in section(s) § 4.1.2 through to § 4.1.5.

Shepard (1950) related the increase in velocity to the increase in wave setup from larger waves. This was before the theorisation by Longuet-Higgins and Stewart (1963), who related the increase in longshore current velocity to radiation stresses.

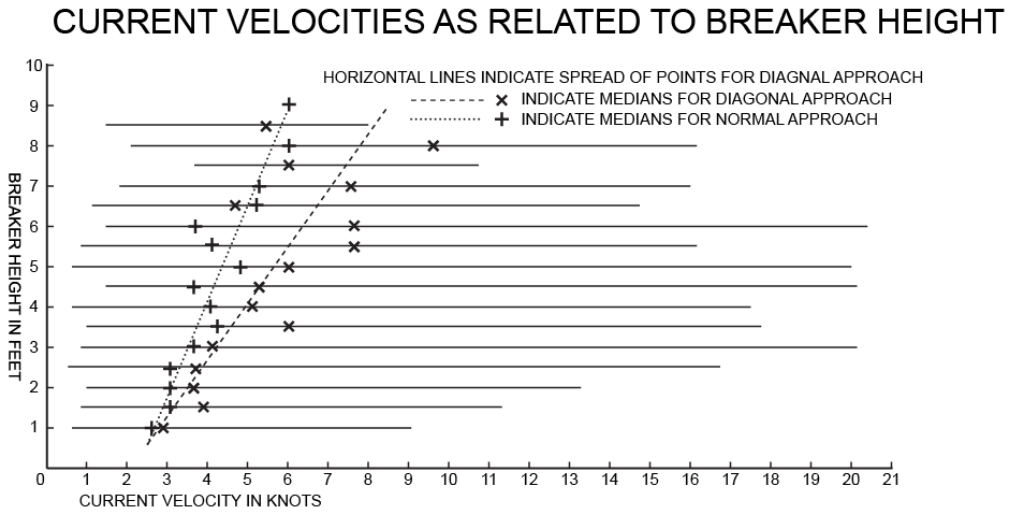

Figure 4-6: Current velocities related to breaker height (Shepard, 1950)

McKenzie (1958) described the characteristics of the rip currents in relation to wave heights: during very low wave conditions numerous miniature rip currents are formed. These small rips are typically induced by the concentrations of swash in the hollows of beach cusps. As the wave conditions increase, the volume of shoreward water flow increases as well. The rip currents accordingly increase in size and velocity, but reduce in quantities. As the rip currents increase in size and velocity, other rip currents eventually diminish. The newer, stronger currents may move laterally in the longshore direction and also change in direction.

McKenzie (1958) also noted the relationship between wave heights, sediment balance and current velocities: smaller waves with shorter wave periods typically result in an increase of sand accumulation on the beach. This allows the formation of smaller, more distinct channels which have a lower flow capacity than the broad rip channels typically associated with larger waves and longer wave periods.

4.1.10.2 Tidal influence

The tidal influence of rip currents is often misunderstood. Some sources incorrectly refer to rip currents as "rip tides", but there is, in fact, very little influence of tidal currents on rip currents due to tidal change (McMahan *et al.*; 2005; Tarbuck *et al.*, 2011). The tide level, on the other hand, does have an indirect influence: as the water level drops, the water flow concentrates into current channels, resulting in stronger rips (McKenzie, 1958).

In more recent studies by MacMahan *et al*. (2005 & 2006), the tide-current relationship was confirmed by a field study (See Figure 4-7). It is interesting to note that during this field study, the rip currents were almost non-existent at high tides. The authors further noted the increasing danger of rip currents at low spring tides – current velocities will increase until the water depth of the rip channel becomes too shallow to allow flow.

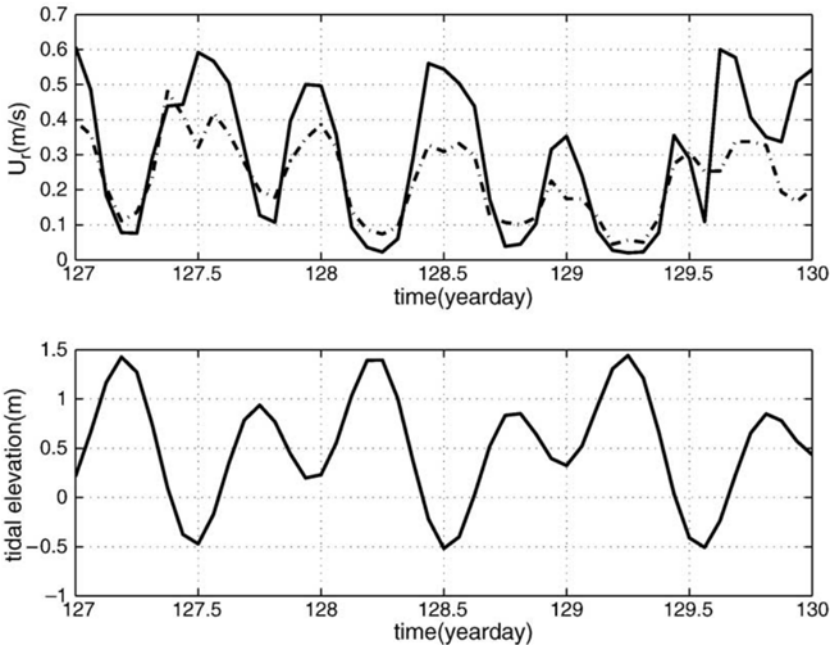

Figure 4-7: Rip-current velocity recordings of two adjacent rip channels (top) based on 90-minute averages, U_r, compared to tidal elevations (bottom) (MacMahan et al.*, 2005)*

4.1.10.3 Incident wave direction

The incident wave direction influences rip currents in two ways. The primary influence is the direct influence of the incident wave direction on the direction and magnitude of the rip current. The secondary influence is indirect and related to the wave size and frequency range associated with a specific wave direction.

Extensive site-based research by Shepard (1950) showed that rip currents may respond to the incident wave angle. A large amount of site observations has shown that rip currents were generally orientated against incoming waves. It was noted, however, that this may not be the general rule as other factors, such as the bathymetry, may also influence the current direction.

That said, in almost 90% of the field observations by Shepard (1950) the current directions predictably responded to the incident wave angle. Shepard (1950) further reported that the wave angle also influenced the velocity of the currents. Incident waves with an angle oblique to the shore tend to result in higher current velocities compared to normally-incident waves for the same breaker heights, as shown in Figure 4-6.

Incident-waves have a specific range of average wave heights and wave periods associated with the directional spreading (for example contrasting wind and swell waves). Different incident wave angles will typically result in different wave height configurations. As discussed earlier in § 4.1.10.1, the current velocity will proportional change to the wave height.

4.1.10.4 Coastal configuration

The coastal configuration has a direct effect on the wave energy. Variations in the local bathymetry and topography lead to the refraction and diffraction of waves, causing concentration of wave energy in some areas and dispersion of energy in others (Shepard & Inman, 1951). The process of refraction further influences the incident wave direction which was discussed in § 4.1.10.3.

4.1.11 Conditions facilitating rip currents and horizontal circulation

Dalrymple (1978) owed the presence of rip currents to two types of mechanisms: *wave-interaction* and *structural-interaction*. The *wave-interaction* mechanism explains the presence of rip currents for normally incident waves or planar beaches whereas the *structural-interaction* mechanism relates rip currents to non-planar beaches with structural features or where irregularities in the bathymetry or topography exist.

4.1.11.1 Wave interaction mechanisms

4.1.11.1.1 Longshore variation of wave heights

Rip currents and subsequent cell circulations can exist in long straight beaches with normal or near-normal wave incidence. This is possible where a spatially-periodic variation of wave height is present in the longshore direction. Offshore flow occurs in areas of lower wave energy and onshore flow oppositely occurs with larger waves (Battjes *et al.*, 1990). Spatially periodic longshore variation of wave heights can occur through *edge waves* or *intersecting wave trains* (Dalrymple, 1978).

Edge waves (sometimes referred to as "trapped waves") are waves propagating in the longshore direction. They are waves "trapped" between the breaker line and shoreline due to reflection and refraction processes. Edge waves can either be progressive (moving nodes and anti-nodes) or standing (stationary nodes and anti-nodes). A notable characteristic of edge waves is an increase of wave heights and orbital velocities closer to the shoreline (Aagard, 2007).

When two different incident wave trains with similar frequencies intersect the super positioning of the two sets causes a standing longshore variation in wave height. In the case of slightly varying frequencies the longshore variation will be progressive. In such cases the rip current system will move along the shore (Dean & Dalrymple, 2004)

4.1.11.1.2 Wave-current interaction

When a wave crosses a current field at an oblique angle wave refraction will occur (Figure 4-8), akin to the process of bathymetric refraction (Reeve *et al.*, 2004.).

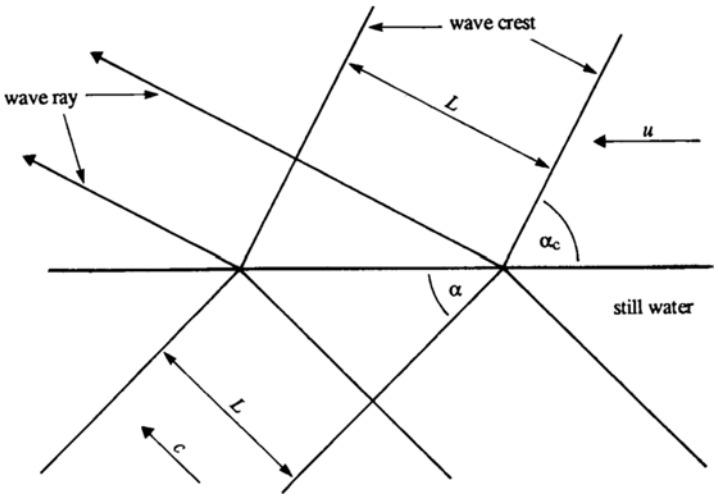

Figure 4-8: Wave-current refraction illustration by Reeve et al. *(2004)*

Dalrymple (1978) explained that in the case of a planar beach with normally-incident long-crested waves and longshore-uniform setup no circulation patterns will necessarily develop. Alternatively, considering a similar case with a pre-existing rip current, the wave-current interaction will cause the incident waves to slow down to where the wave and currents intersect, therefore causing wave refraction towards the current. The oblique waves cause a longshore current which feeds back into the rip current, thereby creating a strong flow. This results in a self-reinforcing interaction between waves and currents.

4.1.11.2 Structural interaction mechanisms

4.1.11.2.1 Sand bars

In the case of offshore sand bars with rip channels, wave setup on the shoreward side of the bar is found to be higher than on the seaward side. This causes a mean pressure head on the shore side of the bars (as shown in Figure 4-9). Under these conditions water will be forced through the channels, causing a concentrated, high velocity flow in the form of a rip current (Dalrymple, 1978; Zyserman *et al.*, 1990; Engle *et al.*, 2002).

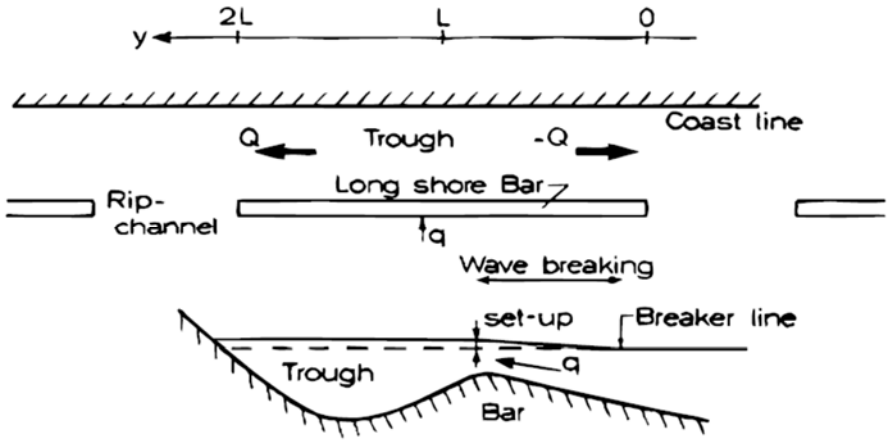

Figure 4-9: Higher pressure head due to wave setup causes rip currents through rip channels. (Fredsøe & Deigaard, 1992:369)

4.1.11.2.2 Refraction and diffraction around structures

Structures, including piers, jetties, groynes and breakwaters, will refract and diffract incoming waves. This forces the flow fields into enclosed areas such as embayments or topographic boundaries. The structural or topographical constraints will interrupt the flow direction, forcing the current alongside the structure in an offshore or onshore direction. The offshore flow is characterised by an intense, narrow current due to vortex stretching. In a generalised situation the conservation of energy requires a return flow to complete a cell circulation (Battjes *et al.*, 1990). The US Army Coastal Engineering Research (1984) discussed three mechanisms in which cell circulations may develop in the presence of structural or topographical boundaries.

4.1.11.2.2.1 First mechanism

The first mechanism is a simple case where a longshore current is restricted by a groyne and forced in a seaward direction (as illustrated in Figure 4-10).

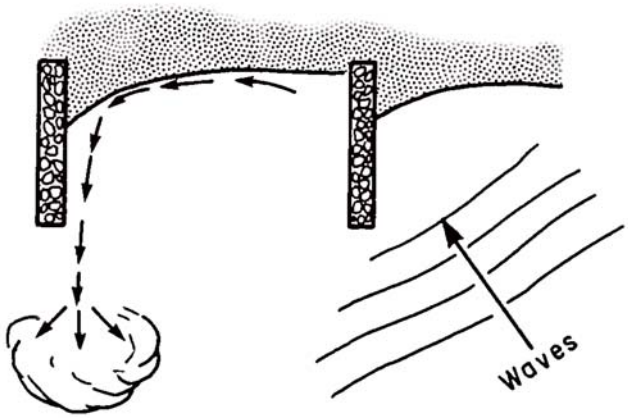

Figure 4-10: 1st mechanism of current-groyne interaction: groynes deflecting currents. (US Army Coastal Engineering Research, 1984)

4.1.11.2.2.2 Second mechanism

The second mechanism is caused by a variation in wave setup. When waves approach the shoreline at an angle, the groyne will partially protect the beach from wave energy, thus creating a wave setup gradient, which results a circulation cell. The seaward flow will exit where the wave setup is the smallest – thus the lee of the protecting groyne. The current will then join the shoreward flow, corresponding to the area of higher wave setup, completing the circulation cell (see Figure 4-11).

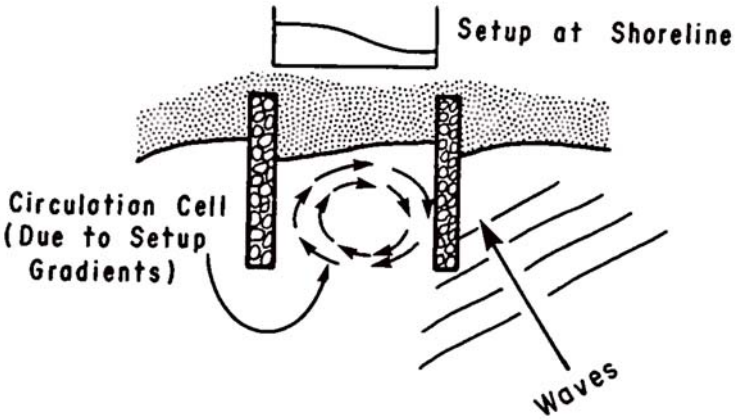

Figure 4-11: 2nd mechanism of current-groyne interaction: wave gradient causing circulation cell. (US Army Coastal Engineering Research, 1984)

4.1.11.2.2.3 Third mechanism

The third mechanism is caused by waves approaching the beach at a normal angle. Wave-groyne interaction will dissipate the wave energy closer to the structures creating a symmetrical wave setup gradient. Similar to the abovementioned 2nd mechanism, the wave setup gradient will result in cell circulation. In this case two symmetrical circulation cells may develop. The seaward flow will exit where the setup is smallest (along the two groynes) and the shoreward flow will enter through the centre of the groyne compartment where the wave setup is the highest. The two completed circulation cells will thus act like two interacting gears (see Figure 4-12).

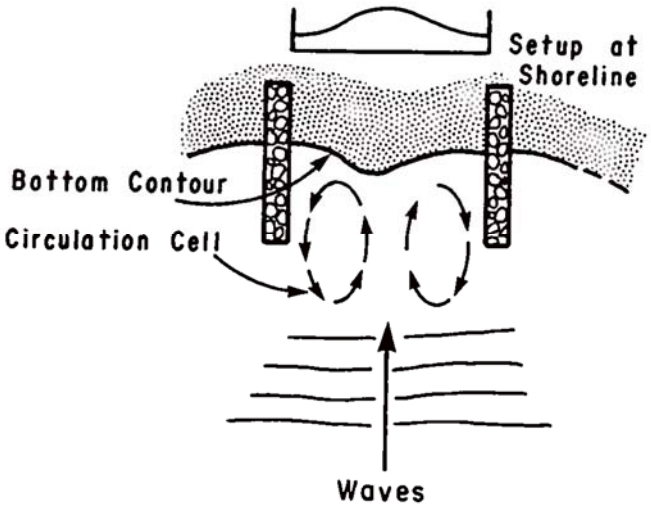

Figure 4-12: 3rd mechanism of current-groyne interaction: symmetrical wave gradient causing a two-part circulation cell. (US Army Coastal Engineering Research, 1984)

4.2 HAZARD TO HUMANS

Rip currents and circulation cells present a significant threat to swimmers. Unwary bathers can easily be caught in a rip current and transported to deeper water offshore. Such cases often lead to inexperienced swimmers attempting to swim against the current, causing exhaustion and ultimately end in drowning. Rip current incidents are a global problem and account for the majority of beach-related drownings and rescues. Other hazards such as large incoming waves, rocks, shark attacks, etc. also present a hazard to humans, but the thesis will only focus on current-related hazards.

4.2.1 International sea rescue statistics

The United States Lifesaving Association (USLA) reported on rip-current-related beach rescues in the United States. Between 2010 and 2012 there were a total of 201 480 beach rescues of which 108 164 (53.7%) were rip current related. The remaining 46.3% could be attributed to "other" causes (12.3%) and rescues where the cause was not reported (34%). Thus, considering the known causes only, rip currents contributed to 81.4% of the beach rescues (Brighton *et al.*, 2013; USLA, 2014).

The Royal National Lifeboat Institution (RNLI) reported that in the United Kingdom, 66.6% of all beach rescues were rip current related (2006 and 2011). Note that this is only related to rescues where RNLI lifeguards were present (RNLI, 2011; Woodward *et al.*, 2013).

Surf Life Saving New Zealand (SLSNZ) reported that the annual average rip-current-related rescues amounted to 49.4% of the total sea rescues for the years 2004 to 2011 (Brighton *et al.*, 2013).

Brighton *et al*. (2013) also studied rip-current-related rescues in New South Wales, Australia. They estimated the annual average rip-current-related rescues to be 57.4 % of all major surf rescues (between 2004 and 2011). They also reported that rip-current-related drownings to amounted to 44% of all beach-related drownings.

The variation in the figures is due to the limited data available on rip current incidents. Rip current incidents are often estimated from incomplete data sets where the cause of incident was not documented. Furthermore, the vast majority of rescues go unreported since treatment is unnecessary (Brighton *et al.*, 2013). Although the information on rip-current-related incidents is limited, the general consensus is that rip currents are the leading contributor to sea-rescues and drownings.

4.2.2 South African sea rescue statistics

Sea rescue statistics on rip current drownings are very limited for South Africa. The National Sea Rescue Institute (NSRI) is a charity organisation responsible for water-life saving across South Africa. For the summer-season of 2013/2014 and 2014/2015, the NSRI released statistics on the amount of fatal water incidents, as shown in Table 4-2.

In the summer season of 2013/2014, the NSRI reported 31 drownings. Of these, 42% were rip current related, one of which happened at Monwabisi (refer to § 5.2.5.2). In the 2014/2015 summer season, 29% of the 31 drownings were reported as rip current related. This adds up to about 36% on average for the two summer seasons (NSRI, 2015b).

Table 4-2: Drowning Statistics for the South African summer seasons, 2013/2014 and 2014/2015

Summer-season (December to January)	Drownings			
	Adults	Children	Total	Rip-current related
2013 / 2014	20	11	31	13 (42%)
2014 / 2015	12	19	31	9 (29%)
Total	32	30	62	22 (36%)

It should be noted that these statistics only reflect distress calls where the NSRI was involved. Another lifesaving association, Lifesaving South Africa (LSA), also operates along the South African Coast. Between 2011 and 2014, there was a total of 204 drownings at LSA-patrolled beaches – an average of 51 beach drownings per year. It should be noted that these figures can overlap with the NSRI data where the NSRI assisted the LSA. The LSA-provided data did not specify the cause of drowning (LSA, 2015b).

Drowning statistics, however, do not fully reflect the overall number of rescues operated and the cause of rescues for South Africa.

4.3 REDUCING OR MITIGATING THE HAZARD

There are two main safety responses to reduce or mitigate the hazard of rip currents: passive and active solutions. Passive solutions create safer conditions without eliminating the problem itself. Active solutions create safer beaches by changing the physical environment with the aim of reducing or mitigating the rip current.

4.3.1.1 Passive solutions

Passive solutions create safer conditions on the beach, but have little to no effect on the rip current dynamics. One of the advantages of passive solutions is that it can be more cost effective than the structural changes required for active solutions. The two main methods of passive solutions are to inform the public and/or to apply minor structural changes.

4.3.1.1.1 Informing the public

Hatfield *et al.* (2012) and Brander *et al.* (2011) explained that a campaign to inform the public about rip currents could make a significant impact. By using posters, postcards and brochures, the public could be informed on how to avoid the potential dangers of a rip current. This includes informing the public on how to identify a rip current, how to swim away from a rip current, how to respond when caught in a rip current and the intention not to swim at unpatrolled beaches.

4.3.1.1.2 Active research

Active research on rip currents can aid to predict rip current conditions to keep the public informed on safe bathing conditions (University of Delaware, 2009). The University of Delaware's Centre for Applied Coastal Research has been researching rip currents over the past 35 years. Together with the National Weather Service and beach patrols, they started the *Delaware Atlantic Rip Current Project*. The project aims at predicting rip current actions by using wind, wave and tidal data as well as rip current rescue information. In doing so, the public can stay informed on the formation of rip currents based on the weather conditions (Carey *et al.*, 2005).

4.3.1.1.3 Lifesavers

Lifesaving organisations have saved lives at sea for almost two centuries. Britain was the first nation to start a lifesaving association in 1824, followed by Denmark (1848), Sweden (1856), France (1865), Germany (1885), Turkey (1868), Russia (1872), United States (1877), Italy (1879), Spain (1880) and South Africa (1911) (Dear & Kemp, 2006; LSA, 2015a). Areas supervised by lifesavers are usually marked with flags and are confined to limited, safer regions on a shoreline.

4.3.1.1.4 Minor structural changes or additions

Minor and/or temporary structures can be placed in or near the rip current to prevent people from being caught in a rip or assist those caught in the rip.

4.3.1.1.4.1 Safety rope / buoy

Floating safety ropes can be spanned across rip currents. Miniature buoys are attached along the rope to assist with flotation and visibility. One or both ends can be attached to safe exit point. One of the major advantages of safety ropes with buoys is that it can be spanned across a relatively broad area, creating a wide safety barrier. A person caught in a rip can catch onto the rope and pull him-/herself out of the rip towards safety. Additionally, floating safety ropes can keep boats away from the bathing area.

4.3.1.1.4.2 Rip Buoy

The Rip Buoy, developed by Rip Buoy Holdings Ltd, is an example of a flotation device that can be placed in a rip current. The Rip Buoy is moored to be permanently secured in a rip current. Persons caught in a rip can hold onto the Rip Buoy where they can wait for further rescue. The Rip Buoy can accommodate three people on board and an additional 15 people in the water via lifelines. A wireless SOS transmitter on board can then be used to signal rescue services (Rip Buoy, 2014).

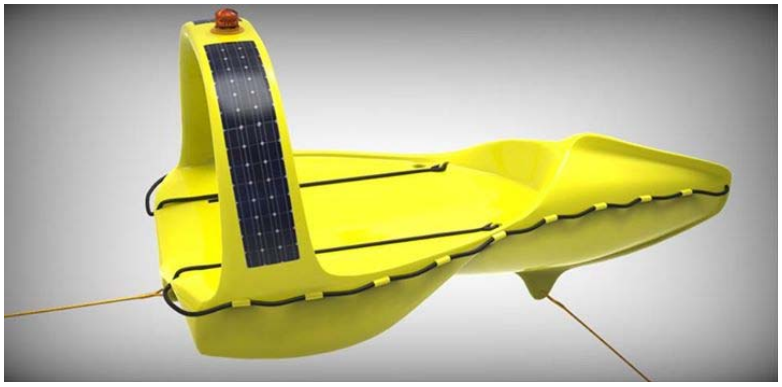

Figure 4-13: Example of a Rip-Buoy (Rip Buoy, 2014)

4.3.1.1.4.3 Stream Indicator Buoy

A Danish company, Alfa Kinetic, has developed a "stream indicator buoy" capable of indicating the direction and magnitude of a current in real time. This special buoy makes use of an arrow to indicate the presence of a rip current. When anchored in water with a current, the buoy will stay in place, but will start rotating and tilt in the direction of the flow (see Figure 4-14). The rotational speed and angle of tilting is directly proportional to the velocity of the current.

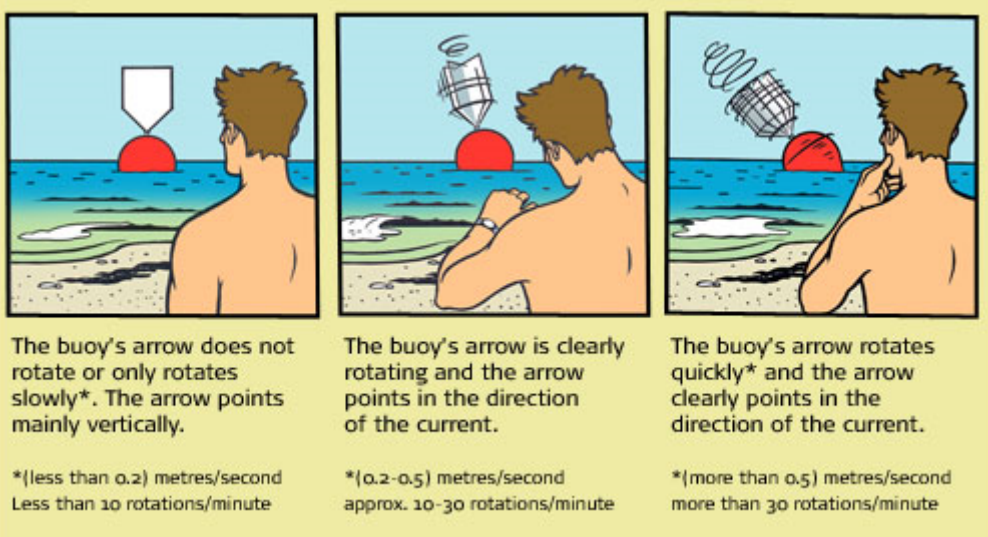

Figure 4-14: Alfa Kinetic developed a buoy to indicate the direction and magnitude of a current in real time (Alfa Kinetic, 2008).

The real-time insight of the stream indicator buoy can thus improve beach safety and reduce the risk of drownings. This requires the public to be educated on how to interpret stream indicator buoy.

4.3.1.2 Active solutions – Engineering the problem

To date, not a lot of research on rip-current-reducing structures has been published. Short and Hogan (1994) explained that the lack of focus on rip-current-preventing structures could be attributed to several factors. Coastal projects mainly focus on major hazards such as cyclones, flooding and erosion, whereas rip currents are viewed as a minor hazard. Recent focus in coastal engineering projects have shifted towards reducing adverse environmental impact. In many cases lifeguards are seen as the most cost-effective method of providing safer bathing conditions, reducing the need for costly structural changes. The safety aspect of environmental coastal hazards often gets ignored.

The unique bathymetry and wave climate that every scenario present, make it difficult to provide a universal solution. Thus, every scenario requires a unique approach based on the local topography and wave climate.

4.3.1.2.1.1 Case Study: Songdo Beach (Busan, Korea)

Hur *et al.* (2014) presented a study of two submerged breakwaters at Songdo Beach, Busan, Korea (see Figure 4-15). The two breakwaters were constructed to reduce incoming wave energy. Consequently, the waves breaking on the shore side resulted in a pressure head, forcing a strong rip current through the inlet. This relates to the mechanism mentioned in § 4.1.11.2.1.

Figure 4-15: Two submerged breakwaters are visible at Songdo Beach, Busan, Korea. Breaking waves cause a mean pressure gradient on the shore side, resulting in a rip current through the inlet. Google Images (2015)

Hur *et al.* (2014) examined – by means of numerical modelling - three different methods to reduce the rip current: increasing surface roughness by placing gravel in the opening, adding a smaller submerged structure on the shore-side of the opening, and installing a drainage channel through the breakwater. The results, with reference to Figure 4-15, were as follows:

Table 4-3: Comparison of current velocity reduction by different tested methods (Hur et al.*, 2014).*

Method	**Velocity reduction**		
	Inlet-entrance (*Point A*)	**Middle of inlet (*Point B*)**	**Inlet-Exit (*Point C*)**
Large gravel at inlet bottom	41.8%	6.4%	9.5%
Submerged structure	26.1%	6.5%	10.7%
Drainage channel	47.4%	12.8%	15.6%

From Table 4-3 can be seen that the drainage channel proved to be the most successful in reducing the current velocities. The biggest difference in flow velocity was made at the approach of inlet, reducing the flow rate by 47.4%. Interestingly, the gravel also led to a significant reduction in the approach velocity by reducing the flow velocity by 41.8%. In the middle of the inlet, where the velocity was at its maximum, the reduction effect was the least effective, with a maximum reduction of 12.8% by the drainage channel.

From this study it could be concluded that structural changes can have had a significant effect on the rip current. The change in the peak velocity was relatively small, but the approach velocity (or feeder current) was greatly reduced – which means less of a chance to be dragged

into the rip current. This provides a safer condition for swimmers, but, subjectively, not safe enough yet.

4.3.1.2.1.2 Monwabisi, False Bay, South Africa

The CSIR (1997) did a physical model study to investigate possible structural changes to reduce rip currents at Monwabisi, False Bay, South Africa. This study forms an integral part of this thesis, and is therefore discussed in its own section in Chapter 5.

4.4 CONCLUSION

Nearshore circulation and driving of wave-induced currents have been topics of ocean research for many decades. By considering the vertical plane as depth-averaged, the circulation process can be simplified to horizontal plane.

The concept of radiation stresses by Longuet-Higgins and Stewart (1963) is a widely accepted formulation to describe the process of wave-induced currents. The formulation expands on the previously accepted notion of wave-setup-induced currents. The concept of radiation stresses provides a logical simplification of depth-averaged velocities in the horizontal plane.

The wave induced currents lead to a mean longshore flow which can be deflected in an offshore direction by wave or structural interaction. The term *rip current* is commonly used to describe concentrated, strong currents in the offshore direction, but the definition varies across literature. A broader and weaker seaward return flow is associated with rip currents, which complete the circulation process. There are many mechanisms facilitating and influencing the development of rip currents. These include structural features or wave-current interaction. Rip currents, together with nearshore circulation form part of a complex hydrodynamic system, but through years of interest and research, the nearshore circulation is well understood.

Rip currents pose a great risk to bathers. Unsuspecting bathers can easily be caught in a rip current and transported to deeper water offshore. Attempts to swim against the current can be perilous and can lead to exhaustion, which ultimately end in drowning. Rip current incidents are a global problem and account for the majority of beach related drownings and rescues.

No single solution exists to eliminate this hazard, but the problem could be addressed by means of *passive* or *active* solutions. *Passive* solutions attempt to mitigate the hazard without any effect on the current itself. This relies on solving the issue on a social level, but the root of the problem always remains. *Active* solutions include engineering solutions that would ultimately diffuse or reduce the dangerous currents through structural intervention. The costs involved in active solutions dissuade the use of such measures. It is therefore no surprise that case studies of *active* solutions are very sparse.

5 PRESENT SITUATION AT MONWABISI

5.1 SOUTH AFRICAN TIDAL POOLS AND BEACH SAFETY

South Africa's warm and sunny weather, combined with an attractive coast, attracts many people to the shore for recreational activities. The peak season coincides with the warmer summer holiday season of December/January with most beach goers accessing the beach to relax, swim or walk (Prochazka & Kruger, 2010).

The South African coastline, however, does not come without its hazards. Shark attacks, strong currents, wave action and rocky outcrops on sandy shores can make the beach a very hostile environment. Tidal pools can provide safe and comfortable bathing conditions, and can sometimes be the only safe option in the vicinity (Bosman & Scholtz, 1982).

In the early 1950s, after a fairly large number of shark attack incidents, numerous tidal pools were constructed along the KwaZulu-Natal coast in South Africa (Bosman & Scholtz, 1982). Before 1980, no formal design criteria were available for tidal pools. Tidal pools were initially built between openings in rocky outcrops. Throughout the years of development, water circulation and sediment control became more important design factors (Kraus, 1996).

In 1980, the CSIR launched a project to formalise the design of tidal pools. This included a study of existing pools and recommendations on design factors pertaining to sand entry, shape, water quality management, safety and maintenance of the tidal pool. Presently, about 80 tidal pools exist along the South African coastline, of which 50 can be found in the Western and Eastern Cape, and 30 in KwaZulu-Natal (Bosman & Scholtz, 1982).

5.2 MONWABISI TIDAL POOL

5.2.1 A brief history

5.2.1.1 Introduction

In 1986 the Monwabisi resort was established in False Bay, South Africa (Figure 5-1). The resort was built in the late apartheid-era as a recreational facility to the local population. The tidal pool was finished in 1987 to provide safe bathing conditions to the resort as the beach was known to be very rocky and dangerous for swimming. A spur and groyne was constructed in 1997 to protect the tidal pool against wave excessive overtopping – which caused an uneven and dangerous pool bottom – and to trap sediment adjacent to the pool, resulting in a built-up beach. The sediment-rich beach significantly reduced the rocky hazards, but conversely allowed for a dangerous current circulation to develop (Theron & Schoonees, 2007; Bezuidenhout, 2011; Thompson, 2013; CoCT, 2015).

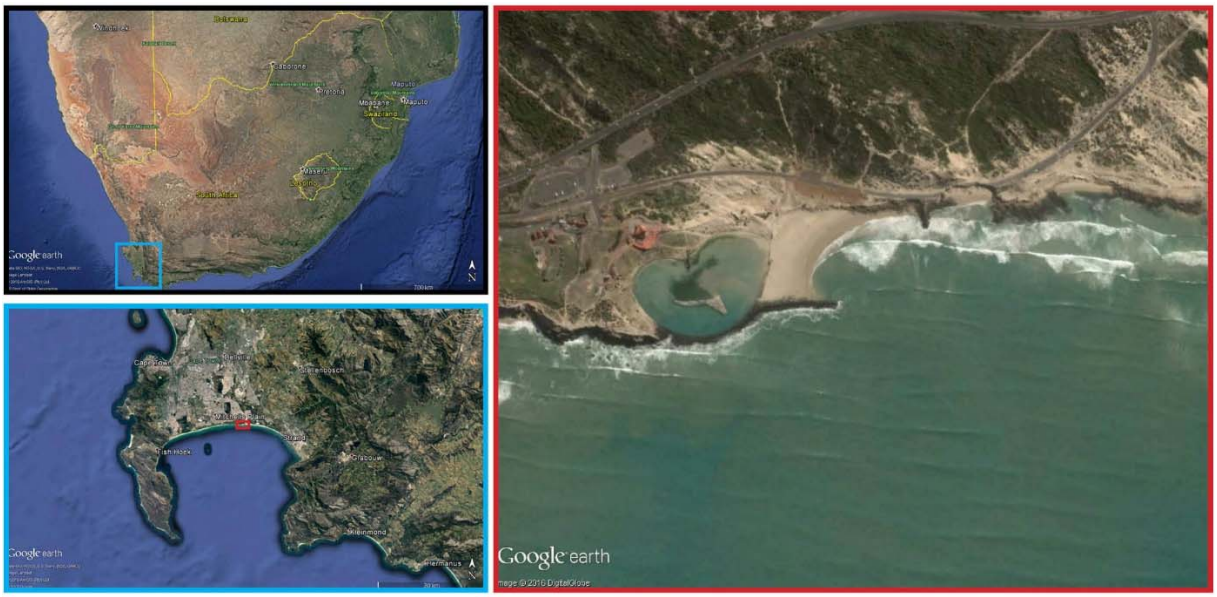

Figure 5-1: Geographical location of Monwabisi, False Bay

5.2.2 Pre-construction conditions

The beach at Monwabisi was mainly sandy-rocky and confined by rocky outcrops to the west and limestone and calcrete cliffs to the east. This was very unfavourable and dangerous to potential bathers. The rocky characteristic of the pre-developed beach is shown in the aerial photos below (Figure 5-2 & Figure 5-3) provided by the *Department of Rural Development and Land Reform* (DRDLR, 1945).

Figure 5-2: Aerial photograph of Monwabisi beach and its surroundings before any formal developments (DRDLR, 1945)

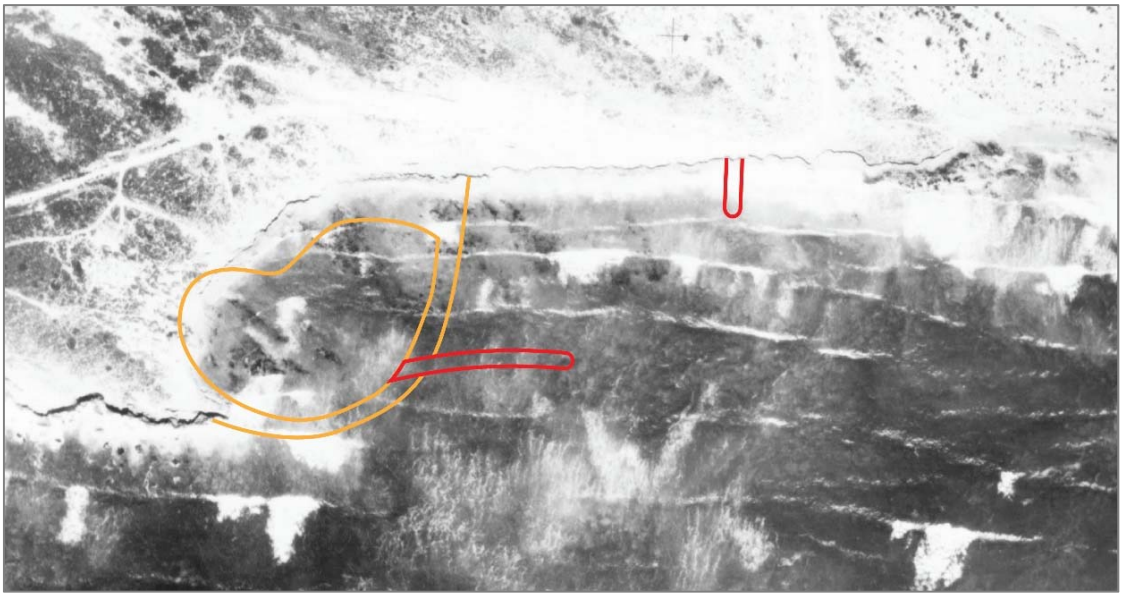

Figure 5-3: Close-up aerial photograph of Monwabisi beach and its surroundings before any formal developments. The orange outlines indicate the position of the present tidal pool and the red outlines indicate the position of the spur and groyne (DRDLR, 1945)

The close up aerial photo (Figure 5-3) from DRDLR (1945) shows the underwater rocky features of Monwabisi beach before any formal development had taken place. These rocks caused unpleasant and unsafe swimming conditions to any potential bathers. The construction of the tidal pool (marked orange) and later the construction of the spur (marked red) were intended to solve the problem and create a pleasant and safe swimming environment.

5.2.3 Construction of Monwabisi Resort and the tidal pool

Monwabisi means "bringing joy" or "the one who makes us happy" in Xhosa. The resort served as a recreational facility mainly for the local population from the nearby settlement of Khayelitsha. In 1987 the Monwabisi tidal pool was constructed (Figure 5-4) to provide safe bathing conditions to the resort as the beach was too dangerous for swimming (Theron & Schoonees, 2007; Bezuidenhout, 2011; Thompson, 2013; CoCT, 2015).

Figure 5-4: Monwabisi beach and tidal pool, 10 May 1990. (CSIR, 1990)

Soon after construction it was realised that the bathing conditions in the pool were not safe. The tidal pool was exposed to excessive wave overtopping, causing current action within the tidal pool with an uneven pool bottom due to scouring. The bathing beach adjacent to the pool remained dangerous due to the exposed rocky outcrops (Figure 5-5), thus failing to provide any safe bathing alternative (Theron & Schoonees, 2007).

Figure 5-5: Archive photos from the CSIR showing limited beach capacity and exposure to rocks. (CSIR. 1989)

5.2.4 Further construction for a safer beach

To address the dangers of the tidal pool and beach, a spur was built parallel to the shoreline. Construction of the spur commenced September 1996 and was completed February 1997. The 170 m-long spur was attached to the tidal pool, extending towards the east. The spur was built about 175 m southward of the shoreline, at a water depth of about 3 m. Additionally, a 60 m-long groyne was constructed about 350 m east from the pool. The construction of the spur and groyne interrupted the local littoral process, causing sediment build-up in the area enclosed by the structures.

Figure 5-6: Present state of Monwabisi tidal pool and beach, with spur and groyne. (Google Earth, 2014)

Three years after the commencement of the construction, the sediment transport reached equilibrium with a total accretion volume of about 32 000 m^3, of which 5 000 m^3 of sand was artificially placed between September 1996 and January 1997. The equilibrium state was evident by the formation of a stable beach adjacent to the east of the pool. This new beach

provided protection against both excessive wave overtopping to the tidal pool as well as covering of the rock protrusions adjacent to the pool, making the apparent bathing conditions safer (Theron & Schoonees, 2007).

Monwabisi resort underwent upgrades in 2013 as part of the City of Cape Town's redevelopment plan for local resorts. As of February 2014, the other amenities at Monwabisi Resort include 26 chalets with ablution facilities, car parking, picnic areas with braai facilities for day visitors, electrified caravanning and camping sites and a conference facility that can accommodate up to 100 people (CoCT, 2014; News24, 2014).

5.2.5 Adverse effect of construction

Construction of the spur and accretion of the new beach, however, had an adverse effect: the formation of a strong circulation current within the enclosed bathing area.

5.2.5.1 Process of the circulation current

The present circulation system at Monwabisi is very similar to the wave-structure interaction discussed in § 4.1.11.2.2.2. Figure 5-7, below, illustrates the mechanisms facilitating the hazardous circulation: The incoming waves (1) approach from a generally-southern direction. The spur partially protects the bay, causing waves to (2) diffract around the spur, which results in a wave-setup gradient (3).This in turn creates an anti-clockwise circulation cell (4). The exit current is where the waves are the smallest: along the sheltered side of the spur.

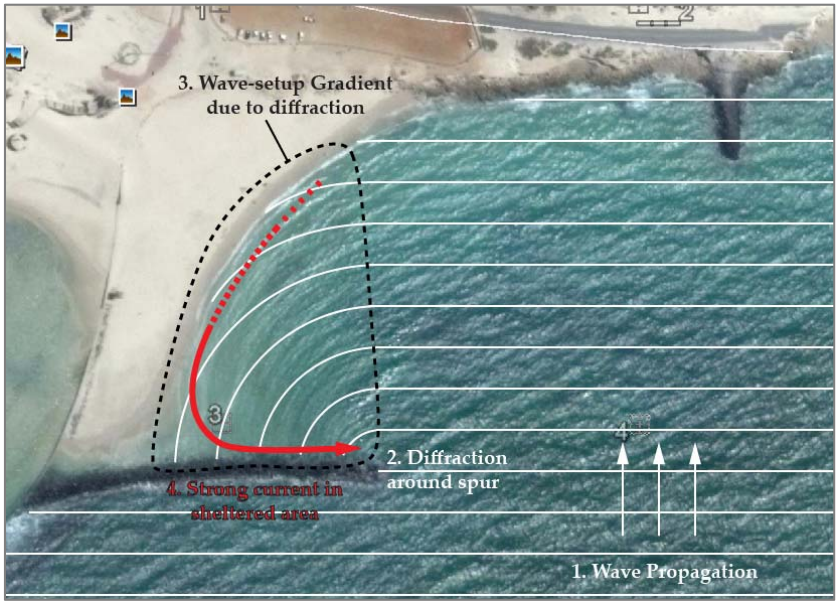

Figure 5-7: Simplified process causing circulation current at Monwabisi. Underlay: Google Images (2014).

Closer to the head of the spur, the beach profile steepens and the water depth rapidly increases. The sudden depth increase in combination with a strong current can cause a person to lose hold of the sea bottom and be dragged sea-ward with the current. Panic in combination with insufficient swimming skills ultimately can lead to drowning (CSIR. 1997).

5.2.5.2 *Current statistics on drownings at Monwabisi*

Forty-three people have reportedly drowned within five years after construction of the Monwabisi beach resort. The construction of the spur at Monwabisi has been controversial (Bamford, 1999).

There are various accounts of rescues and drownings at Monwabisi. The National Sea Rescue Institute (NSRI) and News24 reported on some of these cases between 2011 and 2016. Table 5-1 summarises the reported incidents.

Table 5-1: Summary of reported rescue and drowning incidents at Monwabisi between 2011 and 2016

Date			Rescues	Drowned	Cause / Activity
Year	**Month**	**Day**			
2011	September	11	-	1	Angler
2011	September	25	-	1	Angler
2012	January	8	-	1	Surf (current possible)
2012	August	17	-	1	Angler
2013	May	1	-	2	Pool
2013	November	24	-	1	Surf (current possible)
2013	December	1	6	1	Current
2015	January	1	-	1	Unknown
2016	July	10	-	1	Unknown

Between 2011 and 2016 there were a total of 16 Monwabisi-related incidents reported in the media. In seven of these cases strong current action was involved, resulting in one drowning and another 6 lives being saved. In two other drownings the strong current could have been the cause, but it was not clearly specified. The rest of the reported drownings were related to angling activities, tidal pool incidents or other undocumented causes (News24, 2012a; News24, 2012b; News24, 2014; NSRI, 2013; NSRI, 2015a; NSRI, 2016).

It is important to note that media reports mostly include cases of drowning. Incidents related to successful rescue or assists are not widely reported since it is a more common occurrence and less newsworthy.

Signage has been put in place to warn bathers about the danger of rip currents, but it was noted that the signs only illustrate a generalised case of rip currents and does not inform the public on the hazardous circulation specific to Monwabisi. Figure 5-8 below shows one of the signs at Monwabisi.

Figure 5-8: Signage visible at Monwabisi warning bathers about rip currents and providing information on general beach safety.

A lot of speculation implied that the ill planning and design were to be blamed for the drownings at Monwabisi, but social factors including alcohol and drug use, beach overpopulation and lack of basic swimming skills also contributed to the drownings (Weaver, 1999). Regardless, the presence of the strong currents at Monwabisi presents a hazardous situation, putting bathers at fatal risk.

5.3 ADDRESSING THE STRONG CURRENTS: CSIR REPORT OF 1997

5.3.1 Introduction to the CSIR report

In early 1997, the Cape Metropolitan Council requested an investigation of the existing tidal pool situation and subsequent recommendations to be made to once again satisfy the original goal of providing safer bathing conditions. The investigation, which was jointly carried out by CSIR and Entech Engineering Consultants, involved a site investigation combined with a physical model study of the present situation. The physical model was used to replicate the prototype conditions at Monwabisi and to study possible structural solutions (as showed in Appendix B) to reduce the hazardous circulation. The CSIR published the findings in a report in August 1997.

The numerical model investigation in this study was largely based on this report. The aim of the numerical model was to gain an in-depth understanding of the hydrodynamics and to analyse and compare the results to the CSIR's physical model. The structural configurations of the numerical model, bathymetry, wave and tide conditions were replicated from the CSIR's physical model study. The discussion of the CSIR report that follows therefore serves the dual purpose of providing an overview on the CSIR's physical model study, as well as providing background on the tested configurations for the numerical model presented in this thesis.

5.3.1.1 Dangerous environmental conditions

One of the major issues associated with the hazardous circulation was a strong current in the lee of the spur. The close proximity to the spur meant that this area was sheltered well against incoming waves. This created a false sense of safe bathing conditions to the untrained eye, as

the strong current is not easily spotted by unwary bathers. This, in combination with other physical environmental conditions such as deep water, strong currents, energetic waves and sudden increase in water depth, clearly present a hazardous condition. The CSIR (1997) report acknowledged that social issues also contributed towards drownings, but these were outside the scope of the study.

5.3.1.2 Proposed solutions

The CSIR (1997) report mainly focussed on the current velocity reduction by means of structural solutions. Proposed solutions included keeping the bathers away from the hazardous area, creating a flatter bottom slope, reducing the current and changing the wave climate. The CSIR conducted a physical model that focussed on testing these proposed solutions. Sixteen different layout schemes were designed and tested, which could be categorised as one of the following:

A. Groynes extending from the beach
B. Modification to the spur (gap/sills, extension/reduction)
C. Detached breakwater
D. Current-reducing or deflecting structure
E. Combination of the above

Based on the success (and failures) of the initial tests (A to E), the CSIR designed a more refined solution, which was also tested in the physical model:

F. T-groyne extending from the beach

The above-mentioned structural solutions are illustrated in Appendix B. Larger offshore-type structures (e.g. submerged breakwaters) were not considered in the report as they were considered to be too costly. The ambient conditions used for the model setup is set out in § 5.3.2 and a summary of the results from the CSIR's (1997) study follow in § 5.3.3.

5.3.2 Ambient conditions

5.3.2.1 Bathymetry

5.3.2.1.1 Survey data

The bathymetry for the model was created as a hybrid map consisting of a combination of various survey data. Outside of the embayment, enclosed by the spur and groyne, "older" survey data predating the construction of the spur was used. Inside the embayment a "new" topographic survey was conducted for the 1997 report to reflect the bathymetric changes induced by the structures.

The offshore bathymetry mainly consisted of a survey conducted on 22 August 1994 for a previous study. For the area closer to the embayment and seaward from the spur, finer survey data was used from a survey dating 31 March 1994 - also conducted for a previous study. The older data was considered acceptable as the spur and groyne would not have significantly influenced the bathymetry outside of the embayment.

Inside the embayment a topographic survey was conducted on 8 April 1997 – relatively shortly after the spur construction completion in February 1997. This was to create a more realistic representation of the bathymetric influence of the spur and groyne on the beach. A

similar survey was conducted on 30 January 1997 for preliminary testing. It was found that the beach configuration did not significantly change between the two profiles, indicating that the sediment balance was already close to equilibrium. This notion was further supported in a later sediment transport-based study by Theron and Schoonees (2007).

Figure 5-9: Bathymetry data as used in the Boussinesq wave model. The bathymetry is a composition of various survey data from the CSIR, dating between 1983 and 1997.

5.3.2.1.2 Further modification of the bathymetry

It would be expected that any structural modification would affect the local beach configuration to some extent. Most of the simulation configurations used the bathymetry of the original survey without any re-profiling in response to the structural modification. The beach profile was only adjusted in the models where re-profiling was considered a necessity. This included models where new current entry or exit points were created (gap through the spur), as well as the more-detailed analysis of the refined T-groyne models in Group F.

5.3.2.2 Wave conditions

The CSIR (1997) tested only long-crested regular waves. The chosen wave height, period and angle were based on exceedance criteria from long-term (20-year) on-site wave recordings.

5.3.2.2.1 Wave height (H_s)

The wave heights were chosen to achieve a good balance between reasonable occurrences and fairly energetic wave height. The wave heights were also varied according to the tidal levels – preventing too large waves that would break away from the embayment, expending the wave energy before reaching the structures. The wave heights ranged between 1.0 m and 1.8 m, depending on the tide level.

5.3.2.2.2 Wave period (T_P)

The most common wave period in this region is about 12 seconds, which was used for all of the waves, with the exception of one simulation (8 seconds).

5.3.2.2.3 Wave angle (θ)

The most commonly occurring angle (58% occurrence) was from +188° clockwise from the north, in other words, waves propagating towards a direction of +8° clockwise from the north. This angle was used throughout all of the configurations with no directional spreading.

5.3.2.3 Tide/water levels (WL)

The closest tide gauge is in Simon's Town, approximately 25 km from Monwabisi. The table below provides tide levels from SANHO. The tide levels are defined relative to the *Chart Datum* (which is equal to the Lowest Astronomical Tide). Alternatively, the tide levels are also defined relative to the *Mean Sea Level* – which is used as reference throughout this study.

Table 5-2: Tidal levels for Simons Town (SANHO, 2016)

Tide Level	Relative to CD=LAT	Relative to MSL
Highest Astronomical Tide (HAT)	2.09m	+ 1.29m
Mean High Water Spring (MHWS)	1.79m	+ 0.99m
Mean High Water Neap (MHWN)	1.29m	+ 0.49m
Mean Level (ML)	1.0m	+ 0.2m
Mean Sea Level (MSL)	0.8m	0
Mean Low Water Neap (MLWN)	0.73m	- 0.07m
Mean Low Water Spring (MLWS)	0.24m	- 0.56m
Lowest Astronomical Tide (LAT)	0.0m	- 0.80m

The tidal levels used in the physical model ranged between -0.1 m MSL and +0.9 m MSL. It was important to test a variety of tide levels, but also keeping the occurrence realistic.

5.3.2.4 Sediment Transport

Longshore direction and estimated transport rates were not included in the CSIR report. It was noted that the sediment equilibrium would be influenced by the addition or modification of structures, but the extent of the influence was outside the scope of the report.

5.3.2.5 CSIR model calibration

The CSIR model calibration was very limited. This included visual observations (wave runup and overtopping), photographs and limited current measurements by means of timing of dye movements. The limited current measurements were not sufficient to calibrate the measurement of the model, and the velocities were subsequently reported as relative (percentage) values.

5.3.2.6 Summary of tested models

The summary of the proposed solutions is set out below in Table 5-3. This table can also be found in Appendix F for quick reference throughout this study.

Table 5-3: Summary of proposed solutions

ID	Grouping	Short Description	WL [m MSL]	H_s [m]	T_p [s]	θ [deg]
MB610	N/A	*Baseline test*	0.7	1.5	12	8
MT001	A.1	*Short groyne opposite spur head.*	0.7	1.5	12	8
MT002	A.2	*Long groyne opposite spur head.*	0.7	1.5	12	8
MT003	A.3	*Long groyne away from spur head*	0.7	1.5	12	8
MT004	A.4	*Dog-legged groyne opposite spur head*	0.7	1.5	12	8
MT005	B.1	*Dog-legged spur off spur head (landward)*	0.7	1.5	12	8
MT006	B.2	*Spur off spur head (seaward)*	0.7	1.5	12	8
MT007	A.5	*Dog-legged groyne off present beach*	0.7	1.5	12	8
MT008	B.3	*Lowered end of Spur*	0.4	1.4	12	8
MT009	B.4	*Gap through spur (west section)*	0.7	1.5	12	8
MT010	C.1	*Detached breakwater in bay*	0.4	1.4	12	8
MT011	D.1	*Raised bed level at spur head*	0.7	1.5	12	8
MT012	E.1	*Gap in spur section (west) & groyne off beach*	0.3	1.3	12	8
MT013	E.1	*Gap in spur section (west) & groyne off beach*	-0.3	1.3	12	8
MT014	E.2	*Lowered spur section (east) & groyne off beach*	0.3	1.3	12	8
MT015	E.2	*Lowered spur section (east) & groyne off beach*	-0.3	1.3	12	8
MT016	F.1	*T-groyne off beach*	0.45	1.4	12	8
MT017	F.1	*T-groyne off beach*	0.9	1.4	12	8
MT018	F.1	*T-groyne off beach*	0.9	1.8	12	8
MT019	F.1	*T-groyne off beach*	-0.1	1	12	8
MT020	F.1	*T-groyne off beach*	-0.1	1.4	12	8
MT021	F.1	*T-groyne off beach*	0.4	1.1	12	8
MT022	F.1	*T-groyne off beach*	0.4	1.4	8	8
MT023	F.2	*T-groyne off beach (built-up beach)*	0.4	1.4	12	8
MT024	F.3	*T-groyne off beach (denuded beach)*	0.4	1.4	12	8

A unique sequential identification (ID) (**MT001**, **MT002**, etc.) was assigned to each model. This identification reference is used throughout the remainder of this study. The prefix "**MB**-" denotes baseline models, which include all the simulations of the present situation at Monwabisi (without any form of modification). The prefix "**MT**-" denotes tested solutions, which include all the proposed structural modifications to the current beach.

5.3.3 Performance of tests and measurements taken

This section provides a brief overview of the performance of the CSIR's (1997) physical model tests. The individual results are illustrated in Appendix E in conjunction with the numerical model results in Chapter 7.

The performance of the tests is divided into two sections: initial test results and T-groyne results. The initial tests results include – as the name suggests – the results of the first batch of proposed solutions (Groups A to E) that were tested in the physical model. Based on the

results of the initial tests, the CSIR refined a final proposed solution: a T-Groyne off the beach (Group F). The significance and success of the results of the T-groyne warrant a dedicated section.

The performance benchmark was primarily based on the reduction of current velocity along the spur. The velocities were provided as percentage values relative to the baseline condition, i.e. the current velocity measured along the spur with no structural modifications to the beach, as modelled by the CSIR.

Only a limited amount of velocity measurements were taken in areas of importance. The velocities were reported with visual aid of the related current patterns in the form of a simplified illustration as shown below:

Figure 5-10: Simplified circulation pattern (left) from the CSIR's (1997) physical model, compared to prototype condition (right) (Google Images, 2014)

The current velocities were measured by means of floats placed in the physical model, measuring the distance travelled by the float in a given time. Multiple measurements were taken for the same spot to produce an average velocity and peak velocity. The wave action was considered in the results, but only as part of the descriptive analysis (no illustrative or photographic material are available).

5.3.3.1 Summary of initial tests

The summary of the initial tests follows the categorisation set out in § 5.3.1.2 as set out below:

A. Groynes extending from the beach
B. Modification to the spur (gap/sills, extension/reduction)
C. Detached breakwater
D. Current-reducing or deflecting structure
E. Combination of the above

5.3.3.1.1 Group A: Groynes extending from the beach

By placing a groyne on the beach, the strong current along the spur was reduced. The length and position of the groyne had a significant influence on the extent of velocity reduction. In some cases the groyne caused the strong current to move further away (landward) from the spur. The most successful solution was a *dog-legged groyne off the beach* (**MT007**), which reduced average velocity along the spur to 65% of the baseline velocity.

5.3.3.1.2 Group B: Modification to the spur (gap/sills, extension/reduction)

The modifications to the spur did not produce successful solutions. The modifications included extensions to the spur, partially lowering sections of the spur and creating a full gap

in the spur. The extensions to the spur increased the velocity relative to the baseline value. The lowered crest marginally increased the average velocity. The gap in the spur somewhat reduced the dangerous velocity along the spur, only to create new potentially dangerous circulation cells.

5.3.3.1.3 Group C: Detached breakwater

Only a single case of a detached breakwater off the beach was tested. The breakwater increased the wave energy into the bay, subsequently resulting in a velocity along the spur that was stronger than the baseline velocity. Additionally, a circulation pattern around the breakwater developed.

5.3.3.1.4 Group D: Current-reducing or deflecting structure

Only a single case of a current-reducing modification was tested. By raising the bed level at the head of the spur, the current along the spur was somewhat reduced, but a strong circulation cell was still present in the bay.

5.3.3.1.5 Group E: Combination of Groups A to D

The Group E models included combinations of a groyne off the beach and a gap or lowered section in the spur. None of the tests had apparent positive results. The addition of the groyne caused the circulation cell to move outward, allowing for stronger currents off the head of the spur.

5.3.3.1.6 Summary

A total of 15 preliminary models were tested. Seven of the tests allowed for reduction of the current along the spur (or close to the spur), the others caused an increase of current velocities. Only one of the tests resulted in a significant reduction worth considering: the *dog legged groyne off the beach* (**MT007**). It should also be noted that the preliminary tests did not include a bathymetry that reflects the beach equilibrium profile response to the modification. Based on the results of the preliminary tests, the CSIR designed an "optimised solution" – a T-groyne extending off the beach – which was used for further testing in the physical model.

5.3.3.2 Optimised solution: T-groyne

5.3.3.2.1 Layout of the T-groyne

The CSIR concluded that enclosing the beach yielded the best result in decreasing the exit velocity along the spur. The T-groyne was therefore an optimisation based on the results from Group A. The position of the T-groyne was roughly located to the position of the groyne in **MT002**: the head-centre of the "T" was placed just eastward of **MT002's** groyne with the "T" angled perpendicular to the incoming wave direction. The flanges of the T-groyne head created a smaller bay opening relative to **MT002**.

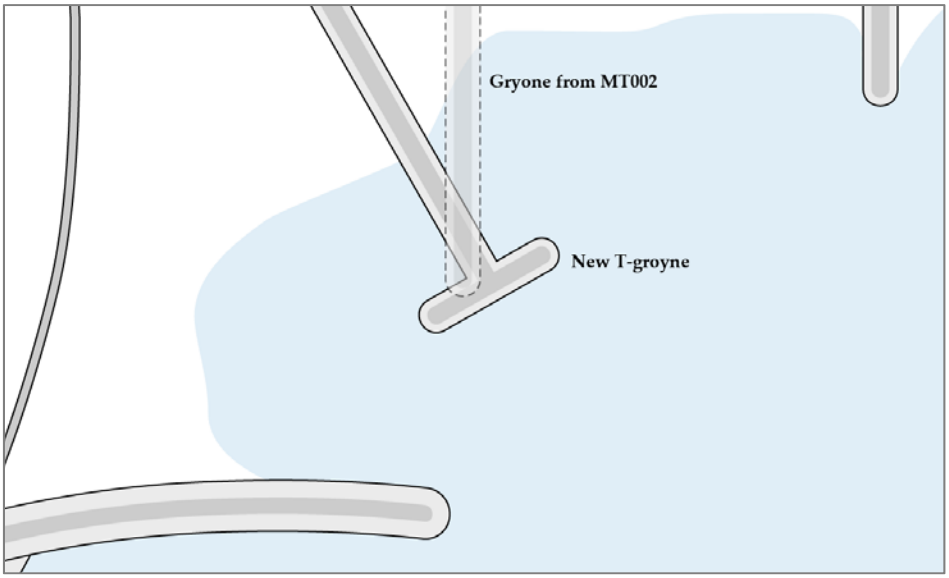

Figure 5-11: Comparison of the T-groyne position relative to the groyne from MT002

Unlike the preliminary tests, the bathymetry was re-profiled to match the expected beach configuration from the T-groyne. A beach equilibrium study would have been ideal, but was never executed due to time and budget constraints. The new beach configuration was therefore estimated from on-site observations and experience.

A total of nine T-groyne models were used to test a variety of wave, tidal and bathymetric conditions. The position and layout of the structure remained the same throughout all of the models. In seven of the models, the wave and tidal conditions were varied. The remaining two models were used to test alternative beach equilibrium profiles.

5.3.3.2.2 Performance of the T-groyne models

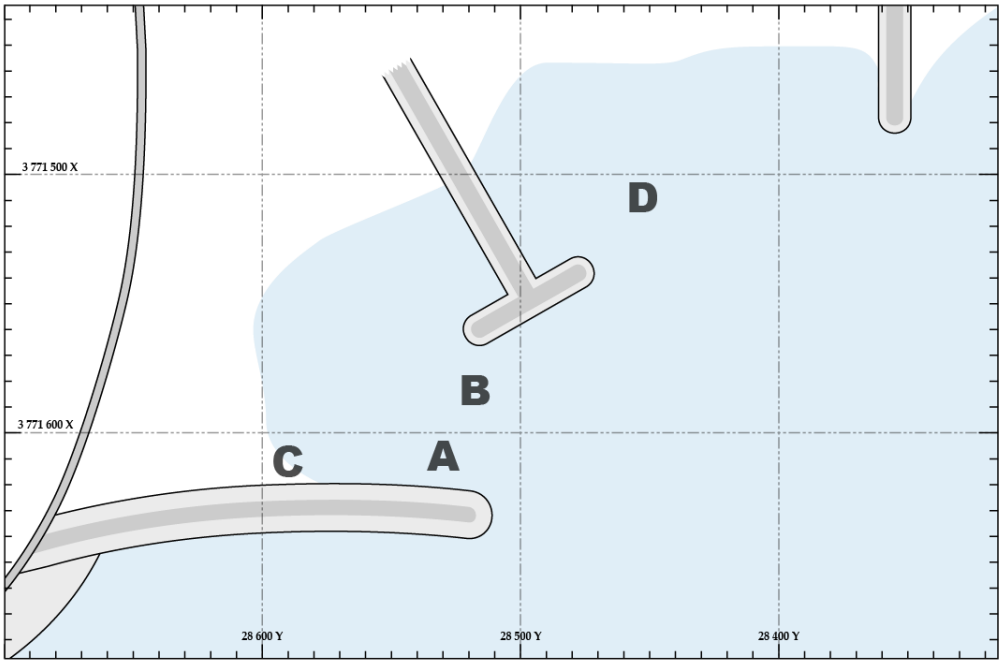

Figure 5-12: T-groyne model layout with identified key areas

In seven out of nine of the T-groyne tests conducted by the CSIR, the flow along the spur (Figure 5-12-A) was below the measuring capability of their instruments. The remaining case (**MT024**) still had very low current velocities compared to original recording, with a peak recorded velocity of 23% relative to the baseline measurement.

In some cases, an exit current developed between the spur and the flanges of the T-groyne (Figure 5-12-B). The average velocity ranged between 30% and 52% of the baseline velocity. A maximum peak velocity of 71% was recorded. These currents were usually situated in the deeper water just outside the bay and exposed to incoming waves, would deter bathers.

In the high tide tests, overtopping occurred along the spur (Figure 5-12-C), causing large velocities: average values ranging between 84% – 114% with a peak velocity measurement of 121%. It should be noted that these velocities were measured in a relatively shallow area, with the energy quickly dissipating in deeper water. The overtopping action and large waves may furthermore intimidate bathers from accessing this area.

One of the adverse effects of the T-groyne was a cell circulation forming in the eastern bay (Figure 5-12-D) between the T-groyne and existing-groyne. Depending on wave and tide conditions, the circulation moved landward and seaward with varying current velocities and circulation sizes. In one occurrence, a rip current formed off the head of the T-groyne, with the peak velocity measured at 150% of the baseline current. This occurrence was very rare and noted to be cyclic. The possible causes were not investigated in detail, and could have been due to long waves caused by boundary effects. Since this area is very exposed to incoming wave action, it presents a visually obvious "danger" area, which helps to deter bathers.

5.3.3.2.3 Conclusion and recommendation by the CSIR

All nine of the T-groyne models proved to drastically reduce the strong current along the spur under a variety of tide and wave conditions. It was a clear improvement on the preliminary models. Any potentially dangerous currents present were associated with visible, dangerous wave action, which should discourage any bathers from using these areas.

5.4 SUMMARY

Monwabisi beach is a very popular recreational destination. Since the completion of the spur in 1997, the beach facilitated the development of a dangerous circulation cell: the spur results in a wave-setup gradient which causes a strong anti-clockwise current in the embayment. Several drownings have been reported which were believed to have been caused by the spur-induced current. This problem has been a topic of controversy ever since.

The CSIR (1997) demonstrated by means of a physical model that a structural solution could reduce the current significantly, while still protecting the tidal pool and maintaining an accessible beach. A variety of proposed layout schemes were tested, but the T-groyne models showed excellent performance across a variety of wave and tidal conditions.

The CSIR consequently recommended that a T-groyne should be considered as a structural solution for safer beach at Monwabisi. They also noted that a structural solution alone would not be sufficient and should be combined with other physical measures, such as marked swimming areas with controlled access, lifeguards and warning signs. They recommended further testing and structural optimisation of the T-groyne model. It should be noted that

dynamic effects, such as scouring and further accretion or erosion, were not included in the physical model.

At the time of the publication of this thesis, almost twenty years have passed since the CSIR's report was published, but no structural changes have been made to Monwabisi beach to reduce any hazardous currents.

The physical model configurations from the CSIR's (1997) report will be re-investigated in this thesis by means of a numerical model. The structural configurations, bathymetry configurations, wave and tide conditions will all be replicated accordingly. In the chapters that follow the setup of the numerical model will be discussed (Chapter 6), along with the - analysis of the results (Chapter 7) and comparison to the CSIR model (Chapter 8).

6 BOUSSINESQ-TYPE WAVE NUMERICAL MODEL SET-UP

6.1 INTRODUCTION

The primary purpose of this study was to investigate proposed structural modifications to make Monwabisi beach a safer bathing area by reducing current velocities. The secondary objective was to investigate whether this complex hydrodynamic system could be successfully simulated by means of a numerical 2D Boussinesq type wave model. The proposed structural modifications were based on the CSIR's (1997) physical model study. For easier referencing, these Boussinesq wave simulations from this study are referred to as the ***M**onwabisi **B**oussinesq **W**ave **S**imulation* (hereafter MBWS).

6.1.1 Brief scope of the simulation analysis

The primary component of interest was the wave-induced currents – to investigate the performance of the proposed solutions as a function of the change of velocities across the various test cases. This also involved visually analysing the current patterns. A secondary component of interest was the propagation of incoming waves – referred to as 'surface elevation' component in modelling terminology.

The results of the numerical simulation were processed, analysed and presented in two sections: The MBWS-results analysis (Chapter 7) and the comparison to the CSIR's (1997) physical model (Chapter 8). The purpose of the chapter on the MBWS analysis was to study the data independently of the CSIR's results. This included examination of components that were not available in the CSIR's report. The section on the CSIR-MBWS comparison has a dual purpose: to serve as a form of calibration for the baseline model and to investigate the validity of the numerical (MBWS) and physical (CSIR) models.

6.1.2 Advantages of using a 2D Boussinesq type wave model

Numerical modelling can be used to simulate real-world cases of nearshore circulation. The Boussinesq wave model is known for its ability to predict the depth-averaged hydrodynamics in the surf zone relatively well with the inclusion of wave breaking in the model (Madsen *et al.* 1997).

MIKE 21 Boussinesq Wave is a wave resolving model designed by DHI, which solves Boussinesq-type equations by means of a flux-formulation. *MIKE 21 BW Boussinesq Wave* includes "enhanced" Boussinesq-type equations based on the formulations by Madsen *et al*. (1991) and Madsen and Sørensen (1992). These include frequency dispersion in the model, which allows for more accurate simulation of waves propagating from deeper water to shallower water.

Wave breaking and associated wave-driven currents are included with the surface roller concept, which approximates the roller thickness as a separate bulk of water propagating with the waves. The wave-induced currents are resolved with the inclusion of additional convective momentum terms (radiation stresses) associated with the surface rollers. *MIKE 21 BW Boussinesq Wave* can also include wave runup by means of the moving shoreline function, which treats solid beach as a depth-variable permeable beach with a very small porosity (Sørensen *et al*., 1998; DHI, 2014).

The main drawback to the Boussinesq-type model is the simulation time required. Relatively small-time step intervals are used to resolve the waves, especially with the inclusion of wave-breaking, thus limiting the models to shorter term simulations.

6.1.3 Motivation for application of a 2D Boussinesq Wave model

The wave-resolving ability of 2D Boussinesq wave model is one of the major motivations for its application. The 2D Boussinesq wave models combine the visual elements of a physical model with the quantitative features of a numerical model.

For the specific case study of Monwabisi the simulation required, amongst other things, two main modelling elements (which were not available in all nearshore model types): wave-induced currents with wave-current interaction and wave diffraction.

The wave-induced currents is self-explanatory: the purpose of this study was to investigate the cell circulation at Monwabisi. The wave resolving inclusion of wave diffraction was also very important to simulate the noticeable wave diffraction effects caused by the spur.

DHI's *MIKE 21 Boussinesq Wave* was chosen for this study as it is a reputable Boussinesq-wave-type-model and is well documented in terms user guidance. It is acknowledged that alternative modelling suites exist, but the readily availability of *MIKE 21 Boussinesq Wave* was another motivation for its use.

6.2 LIST OF TESTED SCENARIOS FOR THE MBWS MODEL

6.2.1 Proposed solution simulations

All beach modifications tested in the CSIR (1997) report were also tested in the MBWS model. Each of the tests was set up by following the process set out in § 6.3. The modifications tested for the MBWS are illustrated in Appendix B and the brief description list is set out in Table 6-1 on the next page. This table can also be found in Appendix G for quick reference throughout this study.

6.2.2 Baseline simulations

Several extra "baseline" tests were also set up for the MBWS detailed analysis (Chapter 7). The baseline simulations were used to investigate the relative change of velocity for a given wave and tide combination. This differs from the CSIR's comparison to only one baseline condition (**MB610**), as it isolates the effect of the structural change, whereas the CSIR's comparison provided a generalised performance indicator. A brief description list is set out in Table 6-2 on the next page. This table can also be found in Appendix G for quick reference.

To clarify the connection between the baseline models and the modified beach models a flowchart was drawn. The flowchart also relates the water/tide level and wave height to each test. The flowchart is shown in Figure 6-1 on page 6-4. The gold highlighted-tests indicate T-groyne models and the green highlighted-test is the single baseline configuration as used in the CSIR report.

Table 6-1: Summary of proposed solution simulations

ID	Grouping	Short Description	WL [m MSL]	H_s [m]	T_p [s]	θ [deg]
MT001	A.1	*Short groyne opposite spur head.*	0.7	1.5	12	8
MT002	A.2	*Long groyne opposite spur head.*	0.7	1.5	12	8
MT003	A.3	*Long groyne away from spur head*	0.7	1.5	12	8
MT004	A.4	*Dog-legged groyne opposite spur head*	0.7	1.5	12	8
MT005	B.1	*Dog-legged spur off spur head (landward)*	0.7	1.5	12	8
MT006	B.2	*Spur off spur head (seaward)*	0.7	1.5	12	8
MT007	A.5	*Dog-legged groyne off present beach*	0.7	1.5	12	8
MT008	B.3	*Lowered end of spur*	0.4	1.4	12	8
MT009	B.4	*Gap through spur (west section)*	0.7	1.5	12	8
MT010	C.1	*Detached breakwater in bay*	0.4	1.4	12	8
MT011	D.1	*Raised bed level at spur head*	0.7	1.5	12	8
MT012	E.1	*Gap in spur section (west) & groyne off beach*	0.3	1.3	12	8
MT013	E.1	*Gap in spur section (west) & groyne off beach*	-0.3	1.3	12	8
MT014	E.2	*Lowered spur section (east) & groyne off beach*	0.3	1.3	12	8
MT015	E.2	*Lowered spur section (east) & groyne off beach*	-0.3	1.3	12	8
MT016	F.1	*T-groyne off beach*	0.45	1.4	12	8
MT017	F.1	*T-groyne off beach*	0.9	1.4	12	8
MT018	F.1	*T-groyne off beach*	0.9	1.8	12	8
MT019	F.1	*T-groyne off beach*	-0.1	1	12	8
MT020	F.1	*T-groyne off beach*	-0.1	1.4	12	8
MT021	F.1	*T-groyne off beach*	0.4	1.1	12	8
MT022	F.1	*T-groyne off beach*	0.4	1.4	8	8
MT023	F.2	*T-groyne off beach (built-up beach)*	0.4	1.4	12	8
MT024	F.3	*T-groyne off beach (denuded beach)*	0.4	1.4	12	8

Table 6-2: Summary of baseline models

ID	Grouping	Short Description	WL [m MSL]	H_s [m]	T_p [s]	θ [deg]
MB110	N/A	*Baseline test*	-0.3	1.3	12	8
MB210	N/A	*Baseline test*	-0.1	1	12	8
MB220	N/A	*Baseline test*	-0.1	1.4	12	8
MB310	N/A	*Baseline test*	0.3	1.3	12	8
MB410	N/A	*Baseline test*	0.4	1.1	12	8
MB420	N/A	*Baseline test*	0.4	1.4	12	8
MB430	N/A	*Baseline test*	0.4	1.1	8	8
MB510	N/A	*Baseline test*	0.45	1.4	12	8
MB610	N/A	*Baseline test*	0.7	1.5	12	8
MB710	N/A	*Baseline test*	0.9	1.4	12	8
MB720	N/A	*Baseline test*	0.9	1.8	12	8

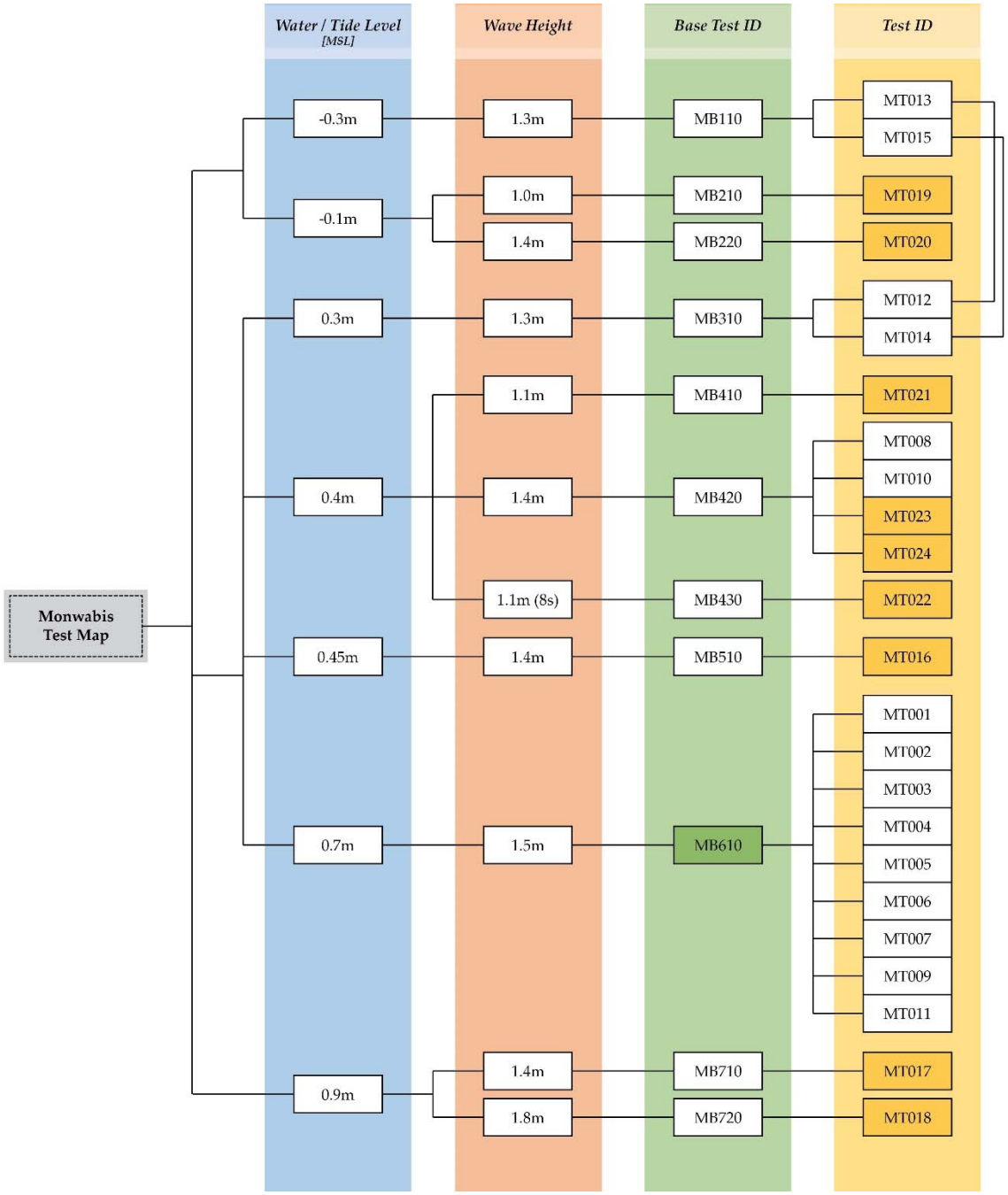

Figure 6-1: Flow chart indicating the different tested conditions (water/tide levels and wave heights) and the baseline's relation to the proposed solutions and tested conditions.

Note from Figure 6-1 that three different tide levels were tested within a relatively close range of 15 cm. It is not clear why the CSIR (1997) chose such close intervals, but it might have been related to the precision of filling and emptying of the physical model basin to adjust tide levels. Higher tide levels were generally tested as the CSIR (1997) suggested that more wave energy, and thus stronger currents, would exist under these conditions. This viewpoint differs from the literature in § 4.1.10.2, which described stronger currents at lower tide levels. The literature specifically referred to rip currents with concentrated flow through current channels. This is not fully applicable to Monwabisi as the cell circulation is unrelated to typical rip currents and channel-concentrated flow.

6.3 SETUP OF THE BOUSSINESQ WAVE MODEL

This section includes the process that was followed for the setup of the *MIKE21 Boussinesq Wave* model. It will only provide a generalised overview of the process that was followed to set up each model.

The *MIKE21 Boussinesq Wave* model requires an extensive list of input parameters and data. The input requirements vary depending on the desired outcome, with some optional parameters included for more advanced modelling cases (such as wave runup). The list of requirements is set out below. Each item will be discussed in the sub-sections that follow.

- Module selection
- Bathymetry
- Type of equation
- Numerical parameters
- Simulation period
- Bathymetric parameters
- Surface elevation
- Internal wave generation
- Bottom friction
- Eddy viscosity
- Filtering
- Wave breaking
- Moving shoreline
- Porosity
- Sponge Layer

The majority of the input data used in the *MIKE21 Boussinesq Wave* model was based on the CSIR's (1997) report as discussed in § 5.3.2. The sub-section that follows will elaborate on how the input data was used in terms of the *MIKE21 Boussinesq Wave* model.

A general rule to the model setup was to keep the attention to detail within embayment, in other words, the accuracy of input data was of more importance at the embayment. The area outside of the embayment was expected to influence the hydrodynamics inside the embayment, but only to a limited extent. Thus, a good balance was required to create an accurate simulation, but not to expend time on elements that would not significantly influence the hydrodynamics.

6.3.1 Setup parameters

The setup process as discussed below outlines each parameter compartmentally as required for the *MIKE21 Boussinesq Wave* model. The actual setup process was much more unstructured, and would have been too complex to document as such.

6.3.1.1 Module Selection

The module selection is used to choose between one-dimensional and two-dimensional modelling. The focus of this study was to investigate two-dimensional flow patterns, thus two-dimensional simulation was the clear choice.

6.3.1.2 Bathymetry

A hybrid bathymetric map was setup similar to the CSIR's physical model as explained in § 5.3.2.1. This process required converting bathymetric survey data (hard copies) to a final *MIKE 21 Boussinesq Wave*-ready bathymetry file. This process arguably was the most important part of the setup as it defined the physical domain for the simulation, as well as any structural elements. The process was also the most time consuming, with a relatively long

process from input to output. The fully-detailed explanation of the bathymetry setup is set out in Appendix C.1.

6.3.1.2.1 Available Survey Data

The majority of the bathymetry-input data was based on old survey data predating- and including the year 1997. The survey data was mainly sourced from the CSIR's (1997) report with some additional satellite imagery from *Google Earth* for topographical features. The readily available survey data from the CSIR was convenient and also meant that the bathymetry would be consistent between the MBWS and CSIR models. It was also mentioned in in § 5.3.2.1 that the survey data was representative of the beach equilibrium profile, and thus any newer surveys would only reflect seasonal variability as no major physical modifications have been made to the beach since 1997. Table 6-3 below lists the survey data as used in the MBWS model.

Table 6-3: Collection of various survey data as used in the MBWS model

Source	Survey Date	Description
CSIR	22/8/1994	Detailed depth on offshore side of spur
CSIR	8/4/1997	Detailed bathymetry of the embayment
CSIR	11/1983 - 12/1983	Depth readings outside of embayment
CSIR	14/01/1997	Elevation measurements along the spur
CSIR	25/04/1994	Beach topography outside of the embayment
Google Earth	*Varied*	Beach topography outside of the embayment

It should be noted that the survey data from the 1997 CSIR report were recorded in the Cape / Lo19 projection format which uses a Cartesian coordinate system, plotting the coordinates along an X and Y axis with the distance units in meters (1:1 scale). With the survey data already in Cartesian-distance format, no conversion of coordinate system was necessary. The Cape / Lo19 projection format has also been used for reference in this study.

The survey data from the CSIR (1997) report was only available in hard-copy format and had to be scanned, digitized and interpolated to be used in the *MIKE 21 Boussinesq Wave* environment.

6.3.1.2.2 Defining the bathymetry dimensions

The spatial domain of the model's bathymetry is confined to a finite area between the simulation boundaries. Logically this should include the area of interest (the embayment in this case), but also sufficient surrounding coverage to account for any potential hydrodynamic interaction between the areas. A minimum water depth also needed to be defined for model stability to avoid artificial dissipation of the wave energy (Madsen & Sørensen, 1992).

A 1 600 m x 1 310 m bathymetry size was chosen with grid cell size of 2 m x 2 m and a minimum water depth of 0.5 m. These specifications provided a good balance between model stability, resolution of detail and simulation time. Figure 6-2 below illustrates the model boundaries and Figure 6-3 illustrates the grid bathymetry file of the specified domain.

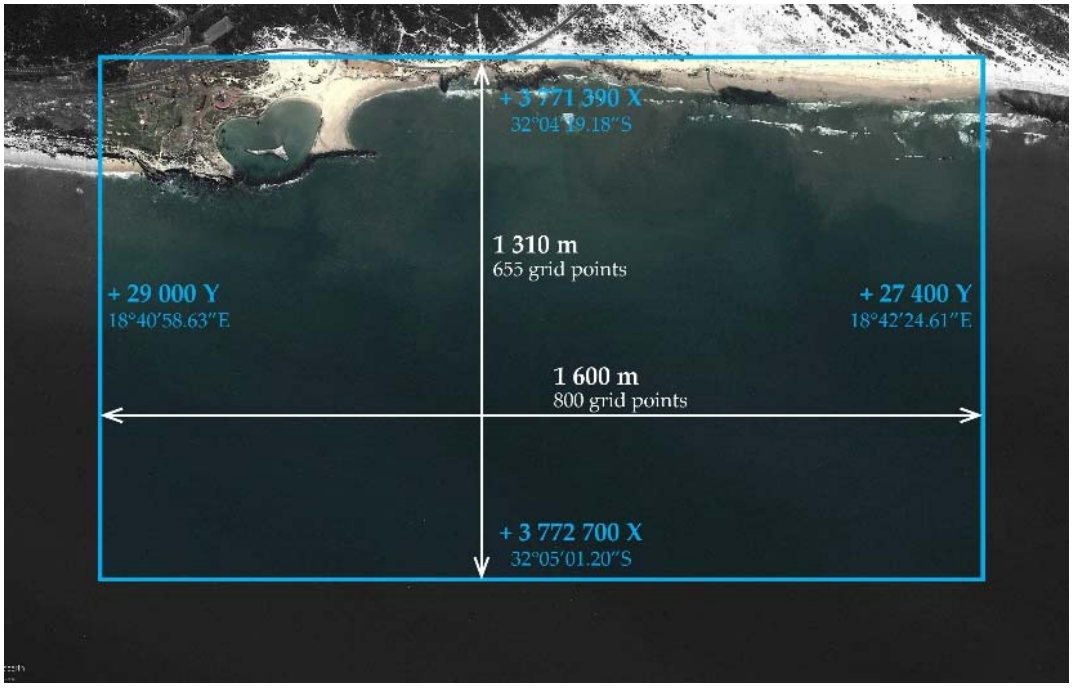

Figure 6-2: Visual representation of the modelling domain. Satellite image obtained from Google Earth (2014)

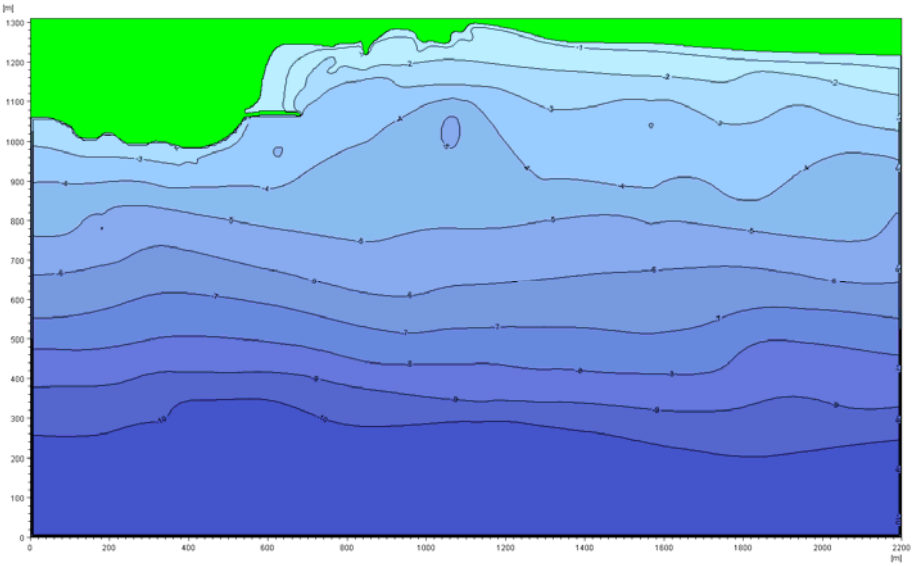

Figure 6-3: Visualisation of final bathymetry file as used for the MB610 baseline test (+0.7m MSL).

6.3.1.2.3 Additional adjustments to the bathymetry grid file

6.3.1.2.3.1 Definition of structures in terms of the bathymetry

MIKE 21 Boussinesq Wave makes it possible to model structural features by simplifying the characteristics of the structure to a two-dimensional footprint with reflective properties. It is possible to include 3D structures (specification of structure height) in *MIKE 21 Boussinesq Wave*, but the setup process is complex and only necessitated in specialist cases such as wave overtopping studies. Only two simulations from the CSIR's (1997) study showed evidence of wave overtopping on the existing spur. Furthermore, these overtopping-currents only occurred momentarily and generally had little influence on the circulation process. The

overall influence of the overtopping was therefore too trivial to justify the inclusion of crest heights.

Any structural features, including the spur, groyne and proposed structural solutions were integrated in the MBWS bathymetry grid. The slope of the structure was to some extent accounted for by the definition of the porosity coefficient, as discussed in § 6.3.1.15.

6.3.1.2.3.2 Bathymetry re-profiling

Sediment transport was not accounted for in the MBWS model as it was accepted that the beach was in equilibrium state. For most of the cases the structural modifications were applied to the same static bathymetry, thus ignoring any potential beach profile changes due to the addition of the structure. The beach profile was only adjusted in the models where re-profiling was considered a necessity. This included models where new current entry or exit points were created (gap through the spur) as well as the more refined T-groyne models. The re-profiling was done in accordance with the CSIR's (1997) test cases; the re-profiled bathymetries for the MBWS layout schemes corresponded to the re-profiled bathymetries of the CSIR's layout schemes. Table 6-4 below lists the layout schemes with required special modifications.

Table 6-4: Special modifications to layout schemes

Appendix Reference	Description	Special Modifications
App. B.B.3	*Lowered End of Spur*	• Structural modification
App. B.B.4	*Gap through spur (west section)*	• Bathymetry re-profiling
App. B.D.1	*Raised bed level at spur head.*	• Bathymetry re-profiling
App. B.E.1	*Gap in spur section (west) & groyne off beach*	• Bathymetry re-profiling
App. B.E.3	*Lowered spur section (east) & groyne off beach*	• Bathymetry re-profiling • Structural modification
App. B.F.1	*T-Groyne (standard)*	• Bathymetry re-profiling
App. B.F.2	*T-Groyne (built-up beach)*	• Bathymetry re-profiling
App. B.F.3	*T-Groyne (denuded beach)*	• Bathymetry re-profiling

6.3.1.2.3.3 Structural modifications

Two of the proposed beach modifications required special structural changes to the existing spur. Both of these cases were related to a lowered crest elevation of the spur (but not a complete gap). These cases differ from the other structural modifications in their relative modelling complexity. The lowered sections in the spurs effectively meant that the wave overtopping had to be modelled. *MIKE 21 Boussinesq Wave* is capable of including overtopping effects, but it is an intricate setup process which requires extensive calibration data. To model overtopping is a study on its own, and it was therefore decided that it was outside the scope of this study. The lowered spur crest simulations were still included in the MBWS study, but the results were not expected to be reliable.

6.3.1.2.4 Bathymetry layout

Figure 6-3 illustrates a complete grid bathymetry layout, as used for the specific baseline simulation of **MB610**.

6.3.1.3 Type of equation

The equation type refers to the selection between Classical and Enhanced Boussinesq equations. The Enhanced equations differs from the Classical equations by the addition of a dispersion factor, B. This factor improves the linear dispersion characteristics with regard to phase celerity and group velocities for waves propagating from deeper water to shallower water (Madsen & Sørensen, 1992). The dispersion factor can be specified in the *MIKE 21 Boussinesq Wave* model, and the value recommended by Madsen & Sørensen (1992) is $B = 0.0667$ (or $B = {}^{1}/_{15}$).

For accurate modelling and numerical stability in the simulation of wave breaking, it was decided to use the Enhanced Boussinesq equations, as recommended by DHI (2014) and Madsen & Sørensen (1992).

6.3.1.4 Numerical Parameters

The numerical parameter section was used to define the space discretisation for the convective terms.

6.3.1.4.1 Space discretisation of the convective terms

MIKE 21 Boussinesq Wave offers four different space discretisation schemes to solve the convective terms by means of finite difference techniques. The space discretisation scheme refers to the numerical integration algorithm used to solve the convective variables on a space-staggered rectangular grid. The discretisation schemes are:

- Central differencing with side-feeding
- Central differencing with simple upwinding at steep gradients and near land
- Central upwinding with simple upwinding at steep gradients and near land
- Simple upwinding differencing.

The latter three schemes are recommended for high spatial resolution grids (1 m to 2 m). All four schemes were tested for the MBWS, but only the *Simple upwinding differencing* scheme resulted in a stable simulation. *Simple upwinding differencing* was therefore chosen as the space discretisation scheme across all tests. The figure below shows a surface elevation time series plot extracted from a simulation using a *central differencing with side-feeding* discretisation scheme.

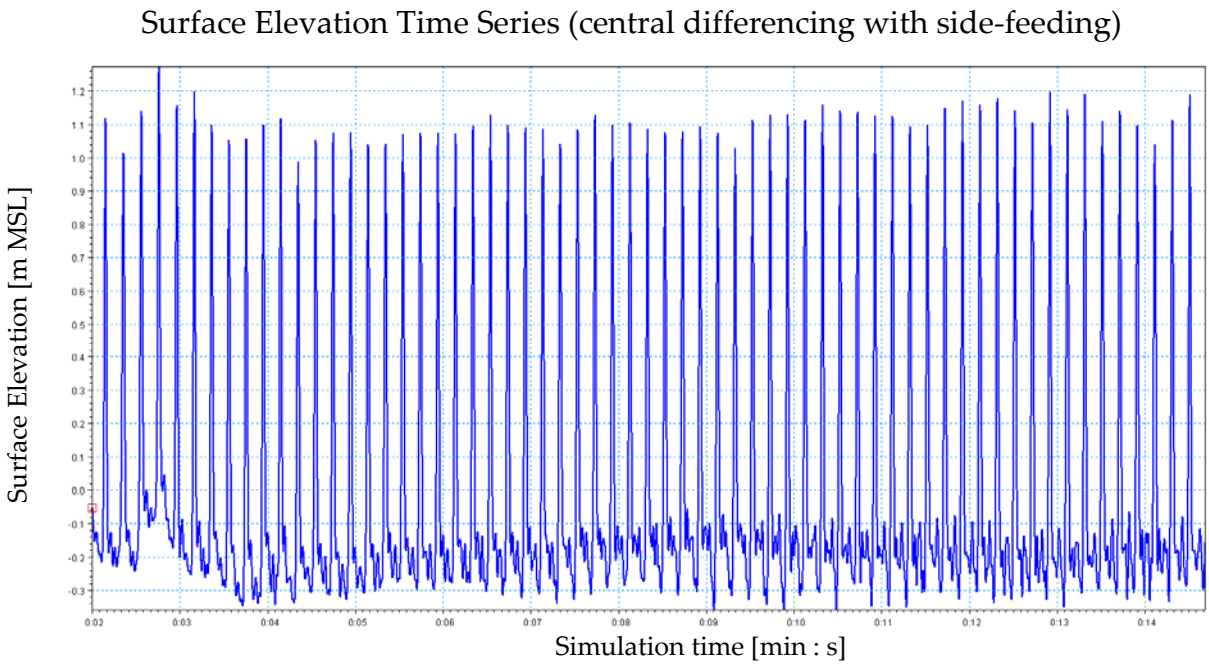

Figure 6-4: Example of a surface elevation time series for a simulation with a "central differencing with side-feeding space" discretisation scheme. The surface elevation never reached stability or regular wave form.

6.3.1.4.2 Time extrapolation factor

A time extrapolation factor is used obtain the correct time centering for the Boussinesq terms in the enhanced equations. The ideal time extrapolation factor is 1 which results in the correct time centering, but requires a fine resolution of the wave period. Lower factors can be used where such a fine resolution is not possible, but the result is artificial dissipation of the wave energy where the waves are propagating oblique to the grid. With lower resolutions, a time-extrapolation factor of 1 can lead to model instability in the form of a high-frequency noise. The compromise is therefore to keep the time-extrapolation high enough (without causing model instabilities), and wave resolution fine enough without requiring too lengthy simulation time (Madsen & Sørensen, 1992; DHI, 2014).

A time extrapolation factor of 0.95 (with a spatial resolution of 2 m and a time-step of 0.05 s) resulted in a stable numerical simulation for the MBWS model. The factor of 0.95 is satisfactory as it results in a stable simulation without too much artificial dissipation. Higher time extrapolation values resulted in model instabilities. Deciding on these parameter values, however, was mainly a heuristic process involving many simulation re-run attempts before settling on the final value.

6.3.1.5 Simulation period

The simulation period is used to define the two main time parameters: the duration of the simulation and the calculation intervals or time step intervals.

6.3.1.5.1 Time steps

The time step interval is determined by the balance between modelling stability and computational time. With regard to numerical stability (discussed in § 6.3.1.4), it was decided to use a time step interval of 0.05 s. This equates to 240 time steps for a 12-second- wave. This

is well above the recommendation by Madsen and Sørensen (1992) to use 24 to 30 time steps per wave length. The time step interval was also satisfactory in terms of the *Courant Number*, as explained in § 6.3.1.5.3.

6.3.1.5.2 Duration of the simulation period

The duration of the simulation was defined as the number of time steps. The duration of the simulation can be divided into two parts. The first part (warm up period) is the duration it takes for the simulation to reach equilibrium. Only once the simulation has reached equilibrium, the recording of the output files could be started. This is especially important with regard to the phase-averaged output, as the warm up period would adversely affect the averaged values with irregularities.

A time-series evaluation of the surface elevation within the bathymetry was used to visually determine when the model reached equilibrium state. The figure below shows the surface elevation recording taken within the embayment. It can be seen that the waves only reached stability after about 10 000 to 11 000 time steps (roughly 8 to 9 minutes of simulation time). For extra caution the recording of the data was only started from the 12 000th time step (10 minute mark).

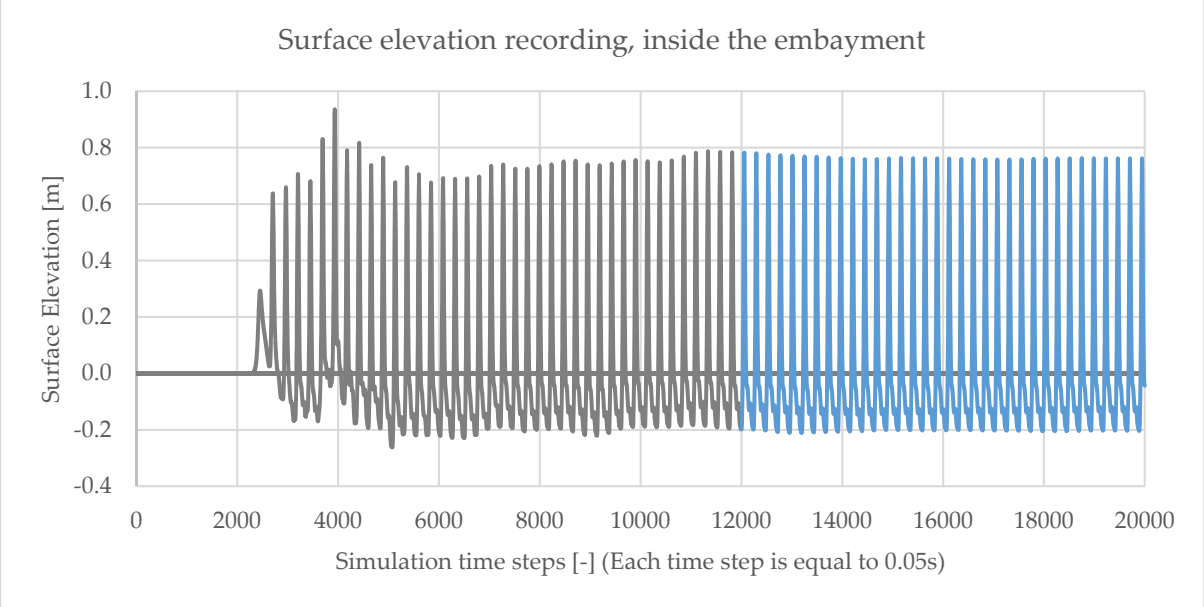

Figure 6-5: Surface elevation time-series at a fixed point in the embayment, just off the spur. The grey area indicates instability whereas the blue area indicates a stable model.

The total simulation period was set to 16 minutes 40 seconds. With the recordings starting at the 10-minute mark, this left 6 minutes 40 seconds of recording time, equal to about 33 wave lengths (for a 12 s wave period). For regular waves, this seemed to be sufficient. The time-dependent stability of the model was further tested in the sensitivity analysis (§ 6.7.3.4).

6.3.1.5.3 Courant number

The Courant number is used in numerical simulations to determine if waves can be resolved accurately. It relates the wave speed, to the user-specified time steps and spatial resolution. The Courant number is defined as:

$$Cr = c \cdot \frac{\Delta t}{\Delta x} \tag{6.1}$$

where

- C_r = Courant number
- c = wave celerity
- Δt = time step, as specified by the user
- Δx = spatial resolution (grid size) as specified by the user.

To ensure numerical stability, the time step and spatial resolution should be specified in such a way that the Courant number is below 1. For the MBWS models, the grid spacing of 2 m, time step of 0.05 s and a maximum depth of 0.5 m resulted in a maximum courant number of 0.238 – well below 1.

6.3.1.6 Bathymetric parameters

Bathymetric parameters can be used to distinguish the land-water boundary and to adjust the water level. This assumes that the boundaries are static. For the case of MBWS, the different tide levels had a significant effect on the land-water boundaries, especially at the beach of interest. The land-water boundaries were therefore adjusted by hand in the bathymetry setup process.

6.3.1.7 Boundary data

The boundary data specification is only used where there are no user-defined boundaries. In such cases the model boundaries reflect the wave energy back into the domain. For the purpose of the MBWS model, the boundaries are needed to absorb the wave energy exiting the domain, therefore user-defined boundaries in the form of sponge layers were used, which are discussed in § 6.3.1.16.

6.3.1.8 Surface elevation

The surface elevation adjustments are only used in special cases, such as landslide-generated waves, tsunami waves or other type of transient wave phenomena (DHI, 2014). This was not applicable to the MBWS model.

6.3.1.9 Internal wave generation

Internal wave generation refers to the method of wave generation for the *MIKE21 Boussinesq Wave* model. Waves are generated along a specified generation line placed in front of an absorbing sponge layer. This layer prevents wave reflection and is a means of allowing wave energy to "exit" the domain. Figure 6-6 below illustrates the position of the wave generation line relative to the absorbing sponge layers and model domain.

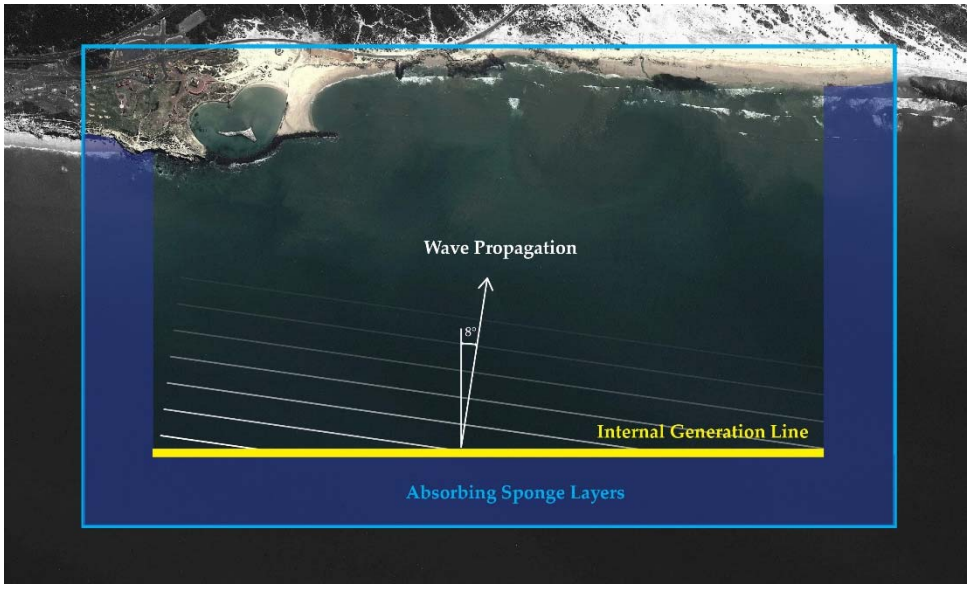

Figure 6-6: Visual representation of internal wave generation line and absorbing sponge layers.

Wave generation data are specified by the flux density and slope of the surface elevation along the wave generation line. The *MIKE 21* suite includes a tool to generate the flux density and surface elevation characteristics based on the wave height, wave period and water depth (for regular waves). Other additional features include directional parameters with directional spreading as an option. For the MBWS model, only regular waves were tested with a constant incident wave angle (+188˚ clockwise from the north) - per the CSIR's (1997) physical model. The list of tested wave conditions is listed in Table 6-5.

Table 6-5: Variety of wave conditions as used in the MBWS models.

Tide Level [m MSL]	H_s [m]	T_p [s]
-0.3	1.3	12
-0.1	1	12
-0.1	1.4	12
0.3	1.3	12
0.4	1.1	12
0.4	1.4	12
0.4	1.1	8
0.45	1.4	12
0.7	1.5	12
0.9	1.4	12
0.9	1.8	12

6.3.1.10 Bottom friction

Bottom friction can be specified as constant value or as a spatially varying value (defining coefficient for each grid cell). *MIKE21* accepts two formulations of the bottom friction, the Manning "M" or Chézy "C" number.

There was no field data available to motivate the use of a spatially-varying bottom friction map, thus a constant friction factor was used. The constant was based on a combination of research by Ghani *et al.* (2007), Chow (1959) and recommendations by DHI (1994). It was decided to use a Manning bottom friction number of $M = 32\, m^{1/3}/s$. The influence of the variation of the bottom friction factor was further tested as discussed in the Sensitivity Analysis section (§ 6.7.3.1).

6.3.1.11 Eddy viscosity

In *MIKE 21 Boussinesq Wave*, wave-current interaction is simulated by balancing the radiation stresses with the bottom friction and mixing processes in the breaking zone. The mixing processes are usually solved by the calculation of the eddy viscosity. In *MIKE 21 Boussinesq Wave*, the mixing process is solved by convective terms that represents a form of viscous shear. Thus, by default *MIKE 21 Boussinesq Wave* implements a form of eddy viscosity simulation in the convective terms. In some special cases the convective terms do not sufficiently resolve the wave-current interaction. The additional option eddy viscosity modelling in *MIKE21* is to simulate the effects of wave-current interaction where the sub-grid effects in the current field are not resolved by the convective terms. This requires extensive calibration and is only necessary for studies focusing on the eddy viscosity effects (DHI, 2014). This option was therefore not included in the MBWS study.

6.3.1.12 Filtering

Filtering may be required to reduce high noise frequencies for model stability. It works by means of a low pass filter to reduce high frequency wave energy. In most cases this is applied to the moving shoreline where instabilities may exist due to uprush and downrush. In some cases it is also required for wave breaking. For this study, no high frequency noise occurred in the surf zone, and thus no filtering was required.

6.3.1.13 Wave breaking

6.3.1.13.1 Description

The inclusion of wave breaking is important to the simulation of wave-induced currents as the energy dissipation of breaking waves results in wave-induced currents. Wave breaking was therefore included in the MBWS model.

MIKE 21 Boussinesq Wave can simulate wave breaking by means of the surface roller concept. Wave breaking occurs if the surface slope exceeds a specified angle. Once wave breaking has initiated, a surface roller forms that is represented by a separate bulk entity of water propagating with the wave celerity. The surface roller is resolved by an additional convective momentum term originating from the depth-integrated horizontal velocity. These additional convective terms relate directly to the radiation stress theory as discussed in the literature study (§ 4.1.4), and are used to resolve the wave-current interaction (Schäffer *et al.*, 1993; DHI, 2014).

6.3.1.13.2 Wave breaking parameters

Most of the wave breaking parameters were based on recommended values by Schäffer *et al.* (1993). The *type of roller celerity* determines whether the surface roller propagates in the direction of the wave (Type 3) or in a fixed pre-determined angle (Type 1). The latter option requires a specified wave direction. This model required multi-directional wave breaking

(due to prominent wave diffraction and refraction within the surf zone), therefore a *Type 3 roller celerity type* was used.

The *half-time for cut-off* roller defines the transition period for breaking waves, defined as $T_P/10$ (Schäffer *et al.*, 1993) or $T_P/5$ (DHI, 2014). For 12-second waves this should be in the region of 1.2 to 1.4 seconds. Only after completion of the simulations and processing of the results of all the MBWS simulations was it discovered that the parameter was equal to the pre-set value of 0.4 seconds. The influence of this modelling error was therefore tested in the sensitivity analysis and it was fortunately discovered to have only a very marginal influence on the velocity measurements. The influence is further discussed in § 6.7.3.2. Schäffer *et al.* (1993) also noted that the Boussinesq model is not too sensitive to this parameter, though it may be important to the surface elevation modelling of the wave decay, especially in 1D wave breaking models.

Table 6-6: Wave breaking parameters

Parameter	Value	Source
Roller form factor	1.5	Schäffer *et al.* (1993).
Type of roller celerity	Type 3	Angle-dependent
Roller celerity factor	1.3	Schäffer *et al.* (1993).
Initial breaking angle	20	Schäffer *et al.* (1993).
Final breaking angle	10	Schäffer *et al.* (1993).
Half-time for cut-off roller	0.4	Default
Wave direction	N/A	Angle-dependent

6.3.1.14 Moving shoreline

The incorporation of the moving shoreline is for the simulation of the uprush and down rush of waves on a beach. The numerical modelling of a moving shoreline is a difficult task that also requires extensive calibration data. Furthermore, the moving shoreline parameters are not spatially varying and are generalised across the whole domain. The parameters can only be calibrated to a specific slope, and are not ideal for conditions where the beach slope varies significantly. In addition to all of this, there is no clear literature guidance on the combination of porosity layers and moving shorelines within a single model – which would have been required for the MBWS simulation. Finally, the focus of this study was on wave-current interaction and it was therefore decided not to include a moving shoreline in the MBWS model.

6.3.1.15 Porosity

Porosity layers are used to simulate the wave-land or wave-structure interaction. Without porosity layers, waves will simply reflect off the land. Porosity layers provide a form of wave absorption to prevent this reflection. They differ from sponge layers as they allow for a defined amount of partial wave reflection. This feature is used to simulate the partial reflection properties of various structures and sloping beaches. A more complete explanation of the porosity theory and setup is set out in Appendix C.2.

The porosity-formulations are based on Madsen's (1983) *Vertical Wall absorption* theory. Linear waves reflect a defined amount off a vertical-faced wall with a homogenous porous structure. The reflection amount is quantified by a reflection coefficient, α_r, ranging between $\alpha_r = 0$ (full

absorption) and $\alpha_r = 1$ (full reflection). The reflection coefficient is a function of the porosity coefficient, α_p, width of the porous absorber, water depth in front of structure, wave period and incoming wave height.

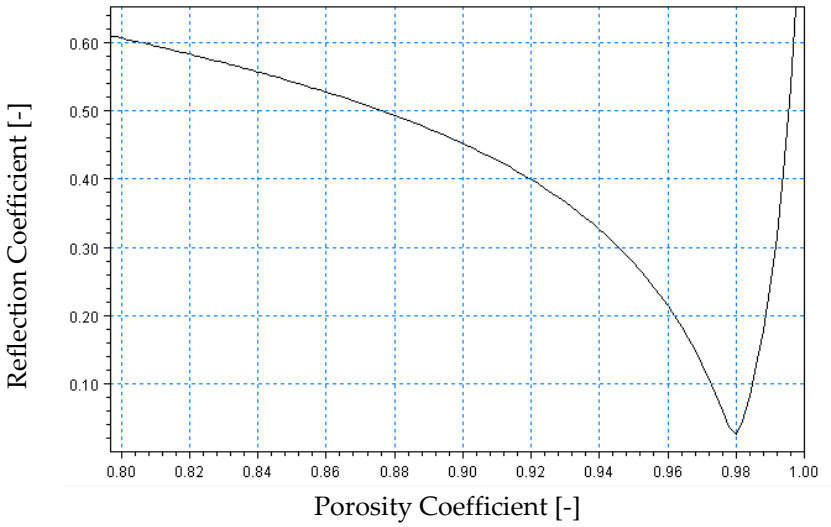

Figure 6-7: Theorised reflection-porosity coefficient ratio for 2 m wave height, 12 s wave period, 2 m depth, 16 m layer width

Figure 6-7 above illustrates a typical porosity-reflection coefficient curve. This curve will vary depending on the on the nearby bathymetry (water depth in front of structure) as well as incoming wave configuration. Specifying the reflection coefficient at each water-land interaction point in the bathymetry grid can quickly lead to an unrealistically long and tedious exercise which only results a theoretical reflection amount.

Highly accurate wave reflection was not a critical aspect in the MBWS model as the priority of the study remained accurate modelling of the wave-current interaction. The aim of the porosity scheme was therefore to keep reflection low, albeit in accordance to the structure reflection coefficients as defined by Thomson *et al.* (1996). It was decided to define only four unique groups of porosity coefficients. The porosity parameters (coefficient and layer width) remained constant throughout all of the simulations. The parameters are set out below in Table 6-7. The influence of the porosity scheme on the current velocities is further discussed in the Sensitivity Analysis section (§ 6.7.3.3).

Table 6-7: Summary of reflection coefficients used in MBWS model

Description	Porosity Coefficient	Layer Width [m]
West of Spur	0.925	12
Spur	0.925	16
Beach, groyne and eastern shore	0.940	8
Additional structure in bay	0.930	10

6.3.1.16 Sponge

Sponge layers are used to fully absorb wave energy that "exits" the domain of the model. Without sponge layers, the wave energy will be fully reflected at the boundaries. The Sponge layer setup is based on the techniques presented by Larsen and Dancy (1983): waves are generated inside the model boundaries and sponge layers are placed at the open boundaries to absorb "exiting" wave energy.

6.3.1.16.1 Estimating the longest wave:

It is recommended that the sponge layer should at least be as wide as the longest wave length (DHI, 2014). Considering a maximum depth of 12 m (extra tolerances) and a maximum wave period of 12 seconds, the maximum wave length was estimated from the transitional wave length equation:

$$L = \frac{g \cdot T^2}{2 \cdot \pi} \cdot \tanh\left(\frac{2 \cdot \pi \cdot d}{L}\right) \tag{6.2}$$

$$\therefore L = \frac{g \cdot 12^2}{2 \cdot \pi} \cdot \tanh\left(\frac{2 \cdot \pi \cdot 12}{L}\right) = 122.9\ m$$

To allow for extra tolerances, a sponge layer of 150 m (or 75 grid cells) was adequate.

6.3.1.16.2 Sponge layer coefficients

The sponge layer is defined by the equation:

$$C_{sponge} = a^{r^{i-1}} \tag{6.3}$$

where

- C_{sponge} = sponge layer coefficient at point i along the grid
- a = base value
- r = power value
- i = the grid number along the sponge layer

The base value and power value are dependent on the width (number of grid cells) of the sponge layer, and are set out in Table 6-8:

Table 6-8: Recommended values for sponge layer coefficients (DHI, 2014)

Sponge layer width (no. grid cells)	a	r
10	5	0.5
20	7	0.7
50	10	0.85
100	10	0.92
200	10	0.95

For a sponge layer width of 75 grid cells, the coefficients were $a = 10$ and $r = 0.90$. The *MIKE 21* suite has a built-in sponge layer generator, requiring the input of the spatial coordinates and the coefficients as set out above. The same input data was used for all the tests and the sponge layers were generated accordingly.

6.3.2 Summary of input items

Table 6-9 below summarises the setup parameters as used for the MBWS models.

Table 6-9: Summary of setup parameters for the MBWS models

MODULE SELECTION		
Module	2D Boussinesq Wave Module	
BATHYMETRY		
Boundaries		
Latitude boundaries	+ 29 000 Y / 18°40'58.63"E	+ 27 400 Y / 18°40'58.63"E
Longitude boundaries	+ 3 771 390 X / 32°04'19.18"S	+ 3 772 700 X / 32°05'01.20"S
Grid dimensions		
Cell size	2x2m	
Width	1 600 m (800 cells)	
Height	1 310 m (655 cells)	
Extra		
Minimum water depth	0.5 m	
TYPE OF EQUATION		
Deep water terms	Included	
Dispersion factor	0.0667 (default)	
NUMERICAL PARAMETERS		
Space discretisation of the convective terms	Simple upwind differencing	
Time-extrapolation factor	0.95	
SIMULATION PERIOD		
Number of time steps	20 001 (16 min 40 s)	
Time step interval	0.05 s	
Max courant no:	0.238 (calculated by MIKE21)	
BATHYMETRIC PARAMETERS		
Cell value representing land	10 m	
Increment bathymetry with	N/A	
SURFACE ELEVATION		
Surface elevation adjustment	N/A	

INTERNAL WAVE GENERATION		
Wave properties		
Wave type	Regular / Monochromatic	
Wave height	*Varying by test*	
Wave period	12 s	
Wave direction type	Unidirectional	
Wave angle	+8 deg	
Wave generation line		
Starting point	*+28 924 Y*	*+3 772 624 X*
End point	*+27 476 Y*	*+3 772 624 X*
Depth	*varying by simulation*	

BOTTOM FRICTION	
Bottom friction specification	Constant
Manning "*M*" number	32 $m^{1/3}/s$

EDDY VISCOSITY	
Inclusion of sub-grid eddy viscosity calculations?	Excluded

FILTERING	
Inclusion low-pass filter?	Excluded

WAVE BREAKING	
Roller form factor	1.5 (default)
Type of roller celerity	Type 1
Roller celerity factor	1.3 (default)
Initial breaking angle	20 (default)
Final breaking angle	10 (default)
Half-time cut-off roller	0.4 (default)

MOVING SHORELINE	
Inclusion low moving shoreline	Excluded

POROSITY	
Porosity Coefficient	*Spatially varying, defined for each testing condition*

SPONGE	
Sponge layer width	150 m / 75 grid points
"a" - coefficient	10
"r" - coefficient	0.90

6.4 SPECIFICATION OF OUTPUT RESULTS

A big advantage of numerical modelling was the amount of data that could be extracted from the results. However, there were two main limitations: time constraints and physical hardware limitations. The former determined how much of the data could be processed and interpreted according to the needs of the author. The hardware limitations included computational power (Computational Process Unit - or *CPU*) and storage space (Hard disk drive). More data would have taken more time to simulate, required more storage space and required more time for post-processing. It was therefore imperative to identify the scope and parameters of interest *before* running the simulations.

The output results were specified by a spatial domain (two-dimensional, one-dimensional or zero-dimensional/time series) over specified time intervals.

The primary focus of this study was on wave-current interaction and the parameters of interest were chosen accordingly:

- Wave-induced velocity (depth-integrated)
- Current circulation pattern (horizontal 2D)

Some secondary parameters were also recorded for supplementary information:

- Surface elevation – including instantaneous wave height and wave height distribution
- Roller thickness - as defined by Sørensen *et al*. (2004)
- Wave energy flux (depth-integrated)

The parameters of surface elevation, roller thickness and wave energy flux, can be specified both as deterministic- and phased-averaged output. Because wave-induced current velocities are only available as a time-mean, phase-averaged output, the *MIKE 21 Boussinesq Wave* is not ideal for the investigation of time-dependent developments (for example moving or oscillating circulation patterns, occasional rip currents, etc.).

The *MIKE21 Boussinesq Wave* suite provided two types of output data: deterministic and phase-averaged parameters. *Deterministic* parameters are instantaneous output data available for each specified time step. *Phase-averaged* results are temporal averaged values for a specified time interval. A *phase-averaged* output is especially important in functions where $\Delta t \to 0$ would result in null values, such as the wave-induced current formulations. A more detailed explanation of the deterministic and phase-averaged terms are provided in Appendix C.3.

Recording of the output values could only start after the model reached stability, otherwise the measurements would be compromised by abnormal values. It was mentioned in § 6.3.1.5.2, "Duration of the simulation period", that the model was stable enough to start recording from the 12 000th time step (10 minute mark). The deterministic results were recorded between time steps 12 000 and 20 000 to provide a time-series output. For the phase-averaged output the same duration (time steps 12 000 to 20 000) was used to provide a single, time-independent averaged output.

6.5 PROCESSING OF THE RESULTS

The simulation-generated output data needed to be post-processed before meaningful data could be extracted. The output files were native to the *MIKE 21* environment, meaning most of the post processing was done within the *MIKE 21* suite.

The requirement for the data extraction was dependent on the two methods of results analysis: visual and statistical. Although the visual and statistical analysis are discussed as two separate processes, they were co-dependent.

6.5.1 Visual requirements

Visual cues play a significant role in the qualitative analysis of the output results, providing an overview of the holistic process of the wave and current interaction with the bathymetry and structures. To create a clear view of this process, the following was required:

- **Average current velocity and direction**: identification of strong current flows as well as circulation pattern formations.
- **Surface elevation "snapshot"**: analysis of the wave propagation - useful for analysing wave-reflection, diffraction and refraction.

The average current velocity output is a good indicator of *what* is happening, but it is also important to know *why* the current velocity is happening. An additional two visual parameters were therefore specified as output items as supplementary data to the current flow information:

- Wave height distribution
- Wave energy density flux

The data extraction for the visual analysis was relatively straight forward. Most of the output data was ready for visualisation without extensive post-processing. The *MIKE 21* suite includes a *Plot Composer* and *Result Viewer* - both dedicated to visualise two-dimensional data and to produce graphical output in a generally accessible format.

6.5.2 Statistical measurements

The statistical requirements necessitated additional post-processing to extract the relevant information from the data. There were two main statistical components measured for the study:

- Current velocity vectors at peak points
- Area distribution of the current velocities

Wave heights were also required for a few selected tests. It should be noted that the statistical information mainly originated from the same output data as the visual analysis, with the main difference being the post-processing required. All velocity recordings were time-mean (phase-averaged) velocities. A maximum velocity in this context is therefore the maximum velocity of average values. Since regular waves were used to result in a stable model, it can be assumed that the average (or time-mean) velocity is uniform over time.

6.5.2.1 *Measurement of the current velocity vectors at peak points*

This thesis primarily focussed on the stronger and more prominent currents. This meant that these currents had to be measured in a consistent matter to allow for reliably statistical comparison.

Absolute maximum velocities typically occurred at a single grid cell (2m x 2m). Reporting these values would not be realistic, as they are not representative of the whole current. Furthermore, a current is a phenomenon happening over a distance, and not just a single point. A measurement along the distance of the current would be a better indicator of the current's strength. On the other hand, determining the start and end point of the *whole current* was also problematic – as the transition between irrelevant flow rate and definite current flow is a relative concept.

For this reason it was decided to use a *30 m peak average velocity* – simply denoted as u_{PA30}. It is defined as the average velocity across a 30 m length, measured along a locally identified peak. The area of measurement should therefore be aligned to include the maximum possible average as such (see Figure 6-8), while still keeping true to the flow direction and 30 m constraint.

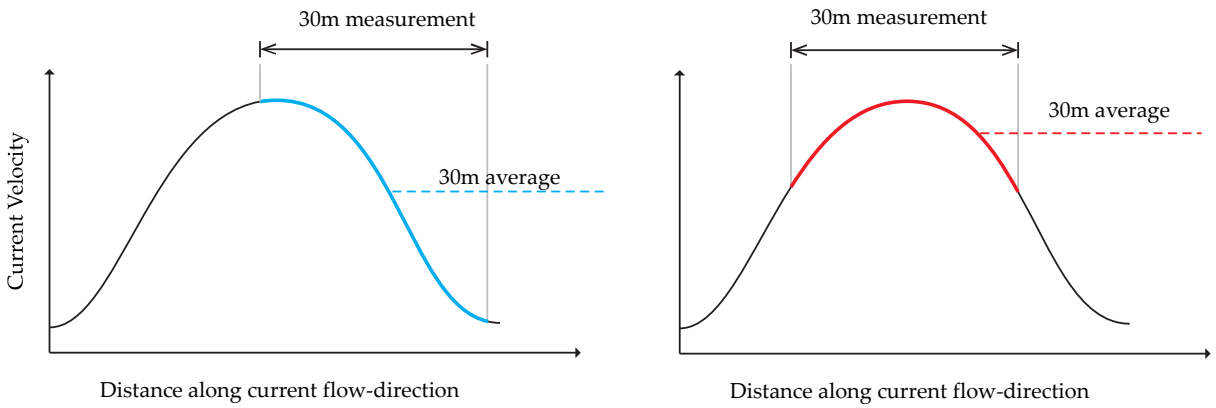

Figure 6-8: Simplified example of 30m peak average velocity measurement: the red curve shows a more efficient measurement, resulting in a more representative value of the current

It was more or less arbitrarily decided that 30 m was a good balance of length, not being too long or too short, limiting excessive low or high values respectively. The CSIR report's (1997) method of measuring was also taken into account for comparability purposes. The velocity measurement by means of recording distance travelled by floats over time suggests that the recording distance could not have been too small (also taking the 1:75 scale of the CSIR's physical model into consideration). A width of 6m was used (3 cells) to allow for oblique measurements on the spatial grid.

To conduct the u_{PA30} velocity measurements, the corresponding grid cells needed to be selected from the simulation output file. For currents aligned along the grid it was simple task: simply selecting a 30 m x 6 m (= 180 m²) area (or 15 x 3 = 45 cells). Most currents curved and flowed oblique to the grid, which made the selection process less simple. In such cases a 30 m-length had to curve along the flow current. To improve consistency across all measurements, the cell count for the measured area was checked to be close to 45. Since this process is not entirely an exact process, the rigidity of the measurements were tested in the sensitivity analysis (§ 6.7.3.5)

6.5.2.2 *Measurement of the area-velocity statistics*

The velocity distribution over a defined *designated swimming area* was studied as an indicator of the danger. The *designated swimming area* was defined as a safe and sheltered zone which could be demarcated with the proposed structural configuration and confined to a depth range of 0 m to 2 m. In the majority of the cases the structural modification physically divided the beach into two distinct areas: a safer, sheltered area and a relatively unsafe, wave-exposed area – as shown in Figure 6-9 below.

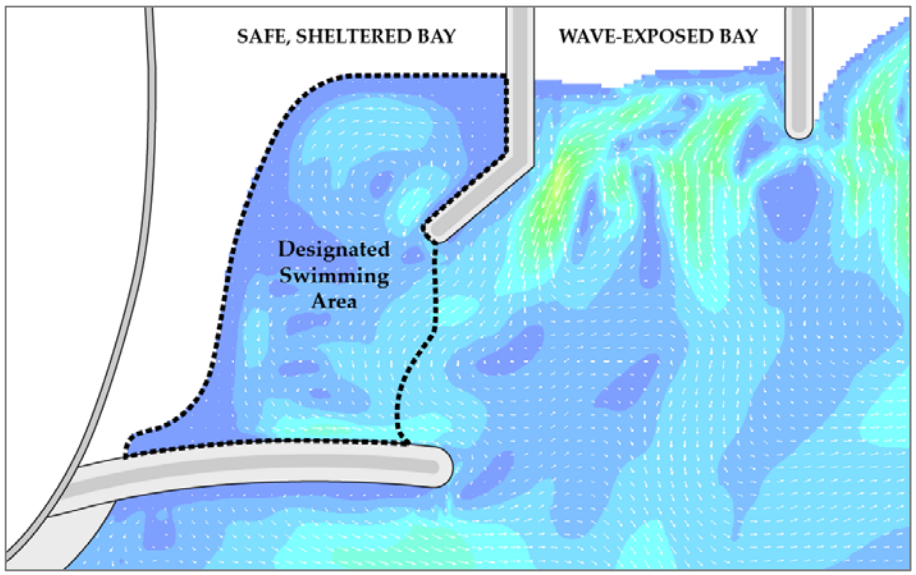

*Figure 6-9: Example of the designated swimming area. The area is physically demarcated by the addition of a dog-legged groyne (**MT004**) and confined to a depth range of 0m to 2m*

In the cases (including the baseline tests) where the beach was not separated into two distinguishable areas, the whole beach spanning from the existing spur to the existing groyne was considered as the *designated swimming area*. These cases therefore included the high energy area within the embayment that was the most exposed to incoming wave action. This undoubtedly created a "safer" bias towards the tests that physically separated the beach. This bias was considered acceptable as the focus of the study was to create a safer environment, which was the end result of these "biased" cases. The *designated swimming area* boundaries are illustrated for each simulation in Appendix D.

The area velocity-distribution is derived from the velocity occurrences, and is expressed as an exceedance distribution. The probability of the velocity exceedance in the *exceedance distribution* was expressed as percentage by convention.

6.6 CALIBRATION & VERIFICATION

It was mentioned previously that the calibration of the CSIR's physical model was very limited (§ 5.3.2.5), focussing more on the visual hydrodynamic processes observed, including wave runup, overtopping and the general circulation pattern present at the beach. The observations were not conclusive enough to verify the physical model's current velocities against prototype velocities. For reliability reasons the velocities were therefore presented in the CSIR report (1997) as relative (percentage) values only.

The current velocities were the key parameter to the hydrodynamic study. As with the CSIR's physical model study, no prototype velocity measurements were available for calibration. The accuracy of the model therefore heavily relied on the correct use of the setup input parameters.

The CSIR's (1997) report only used relative (percentage) velocities, which meant that the velocities of the MBWS model could not be calibrated against the CSIR's model. The CSIR did, however, provide limited wave height measurements, but they were not sufficient for calibration purposes. Thus, with the lack of quantitative calibration material, the calibration relied more on the qualitative material available:

- CSIR (1997) report
- Satellite imagery of the area
- General literature on current velocities

The calibration was mostly executed by means of a process of trial-and-error involving many simulation re-runs. These re-runs were not documented as the results of the "uncalibrated" models were discarded. Only the results of the final qualitatively "calibrated" models were saved, as they were used for analysis in this study. This section will therefore mainly focus on the visual verification of the baseline model.

6.6.1 CSIR Report Comparison

The CSIR's (1997) visualised results of their baseline model were mainly used to verify the circulation pattern present at Monwabisi. The description of the circulation process was used as supplementary information to support to verification. The results below show the original MBWS results output (Figure 6-10) compared to the CSIR's visualised results (Figure 6-11).

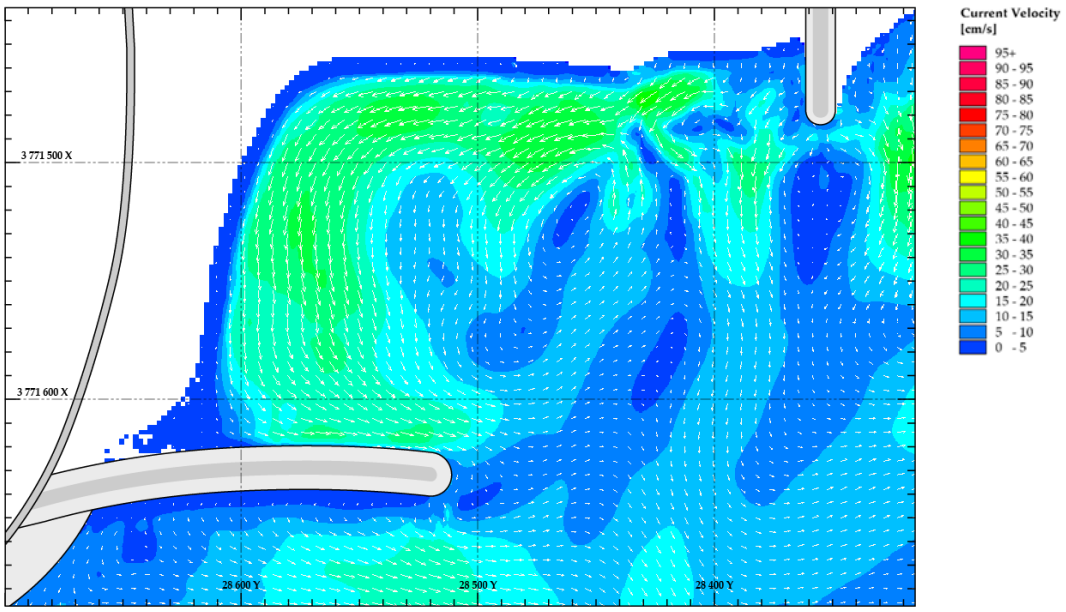

*Figure 6-10: MBWS results of the current velocity and direction for the baseline simulation (**MB610**)*

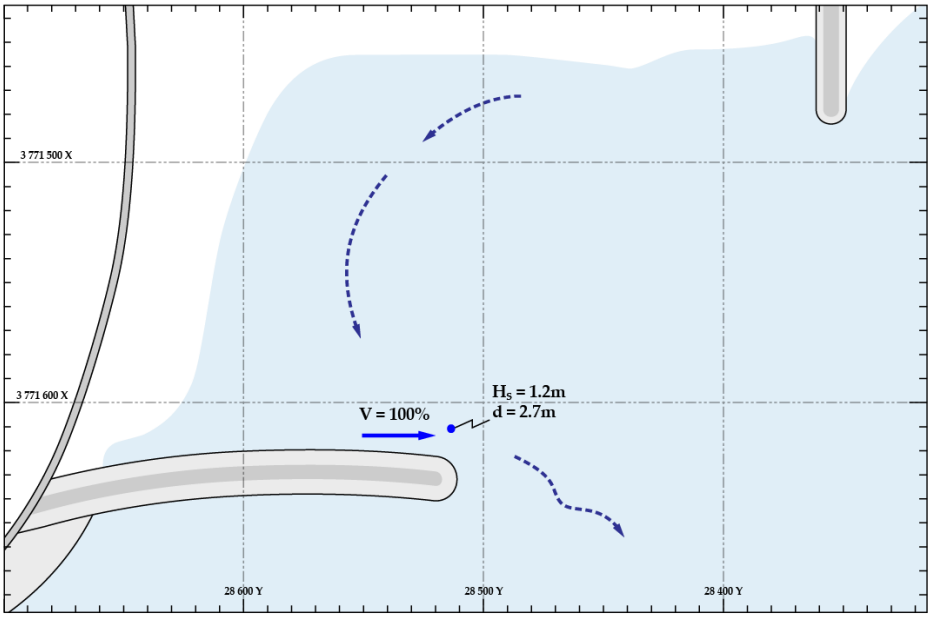

*Figure 6-11: CSIR's visualised results for the baseline simulation (**MB610**)*

6.6.1.1 Current circulation pattern

The circulation pattern in the MBWS model showed good agreement to CSIR's model, with a prominent, counter-clockwise circulation in the sheltered area behind the spur. This also agreed to the description of a strong circulation with a prominent current along the spur, whereafter the current diffuses into deeper water. Other secondary flow patterns were also visible in the MBWS model, but the CSIR only reported on velocities and circulations that were important to the study. Note that the CSIR reported a velocity of 100% along the spur, as this was the (V_{MB610}) velocity used as reference to all of the other models.

6.6.1.2 Wave height

The CSIR included a limited number of wave height measurements from their physical models. As discussed in the literature study, the current velocity is proportional to the wave height, which implies that it is important to calibrate the wave height.

From the baseline simulation **MB610**, it was found that the MBWS simulation's wave height at point "**a**" (Figure 6-12) was 20% smaller than the CSIR's reported simulation wave height of 1.2 m. The coordinates of the wave-measurement area were derived from a coarse gridded map. It is therefore very possible that there was an offset between the CSIR and MBWS point of measurement. Figure 6-12 on the next page shows the point of measurement, "**a**".

The spur provides partial wave sheltering at this point, resulting in a steep wave distribution gradient. An offset of just 10 m can result in a measured wave height of 1.2 m for the MBWS model. Furthermore, scaling effects from the physical model (the CSIR's physical model was built on a 1:75 scale) could also contribute to differences in wave height measurements. The information on the CSIR's wave height measurement was therefore insufficient for calibration purposes.

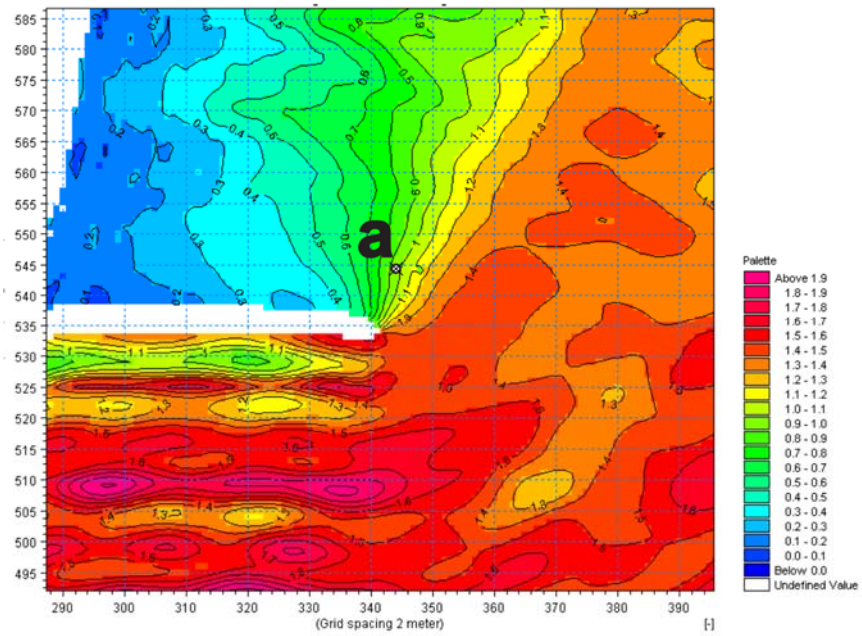

*Figure 6-12: Wave height distribution for the MBWS baseline (**MB610**) model close to the spur.*

6.6.2 General literature on current velocities

In the absence of absolute velocity measurements, a literature survey was done to obtain a rough verification of the expected velocities. The u_{PA30} velocities as measured in the MBWS model were not extremely strong, ranging between 25.2 cm/s and 32.1 cm/s, but were comparable to the site- and RIPEX measurements of average rip current velocities from McMahan *et al.* (2005 & 2006) (Refer to Table 4-1).

6.6.3 Satellite Imagery

Satellite imagery (acquired from *Google Earth*) was used to roughly validate the bathymetry and the associated wave-interactions (shoaling, wave breaking, wave diffraction and wave refraction). Snapshots of the surface elevation from the MBSW model were compared to suitable satellite imagery sourced from *Google Earth*. This was not an exact study as the aim was to see if the surface elevation of the MBWS would roughly reproduce the prototype conditions. The tested wave conditions and tidal conditions were in some cases adjusted to extreme conditions beyond the scope of the conditions tested in the proposed solutions. Only long-crested wave conditions were investigated.

Figure 6-13, below, shows a typical wave-bathymetry interaction occurring at Monwabisi. Two areas have been highlighted as red-dashed zones where the effects of shoaling and wave breaking are very apparent. The leftmost area shows a sort of diagonal shoaling pattern extending to the south-east. The rightmost area clearly shows that the wave shoaling and breaking is not consistent along the shore. The two areas are divided by a temporary "flat zone" where the effects of shoaling seem to temporary decay. This "flat zone" is a consistent effect that could be observed across various satellite images (not shown here), including historic imagery pre-dating the construction of the tidal pool. The consistency and broad-width of this "flat zone" meant that it was unlikely to be current-related, but more likely to be related to bathymetric effects

.

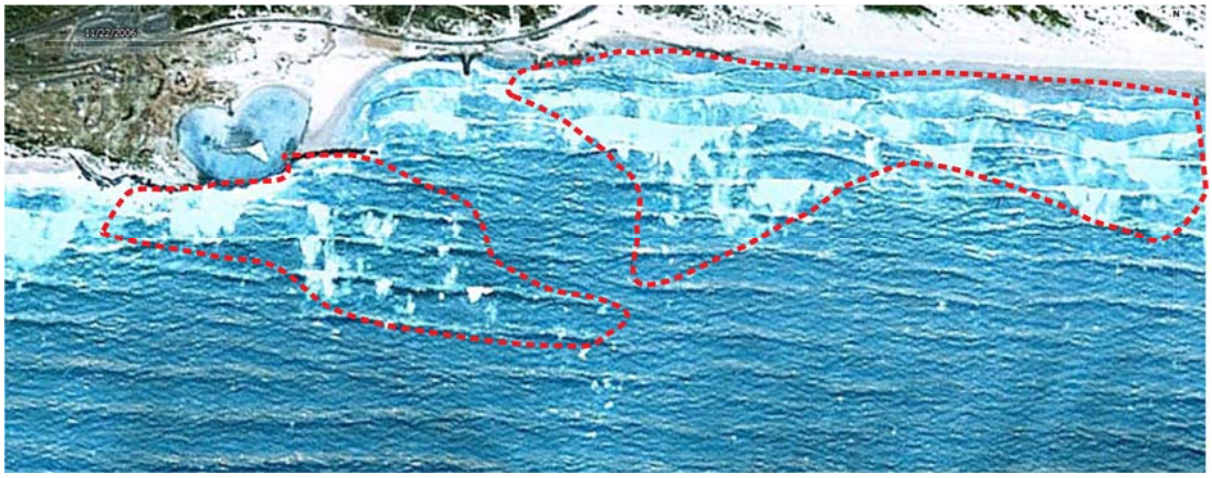

Figure 6-13: Wave shoaling and breaking at Monwabisi. Two distinct zones are separated by a visible "flat zone" Google Earth (2009).

Figure 6-14 shows the comparison of a *Google Earth* satellite image (2013) to the MBWS model with H_s = 3.2 m, T_p = 12 s, Wave angle = 8° N, Tide level = +0.1 m MSL. The two distinguishable zones of wave shoaling and breaking, divided by the "flat zone" were visible in the MBWS simulation. The shape and diagonal orientation of the leftmost zone were also consistent between the MBSW model and prototype conditions. The predicted wave transformation processes from the Boussinesq model thus satisfactorily replicated the observed processes from the satellite imagery.

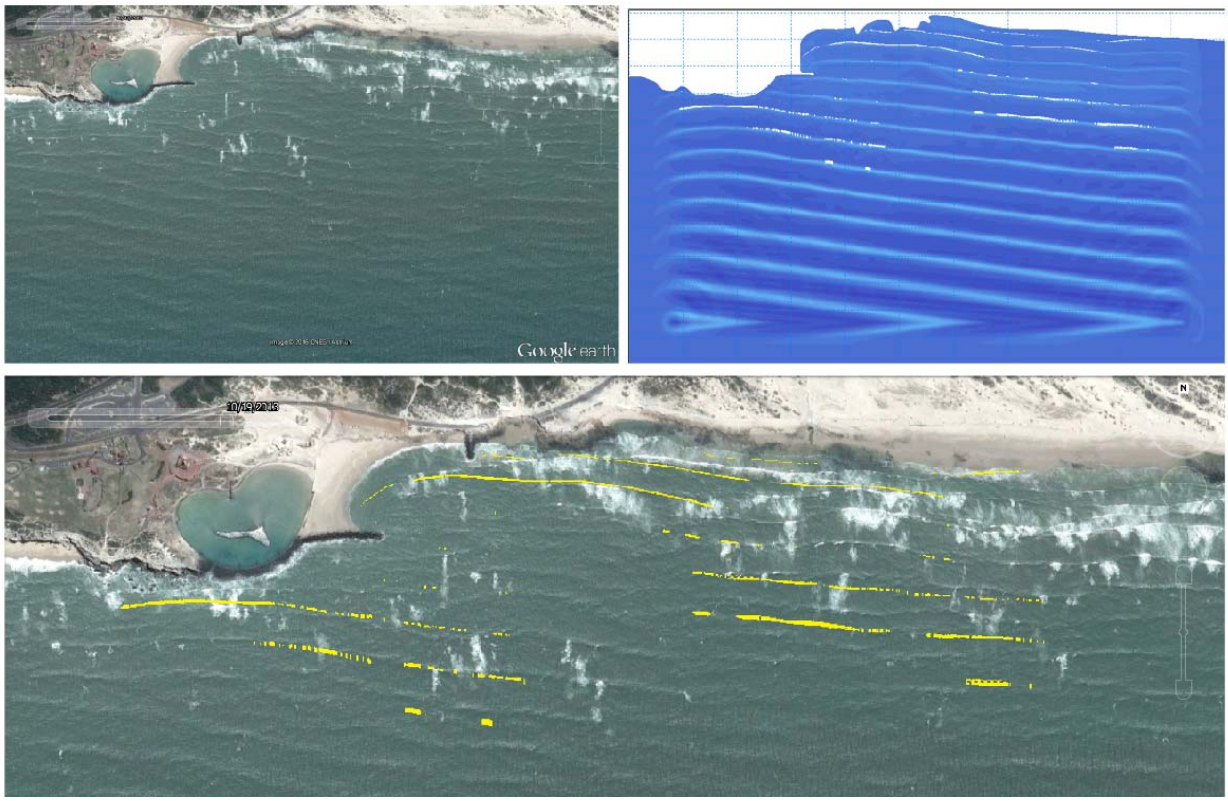

Figure 6-14: Top left: Satellite Image from Google Earth (2013). Top Right: MBWS surface elevation with breaking waves. Bottom: The breakers from the MBWS overlaid on the satellite image – in yellow for clear distinction.

Figure 6-15, below, shows the comparison of diffraction effects inside on a smaller scale inside the embayment. It can be seen that the wave diffraction effects were modelled with good accuracy. Note the difference to the shoreline – possibly due to seasonal changes in the bathymetry.

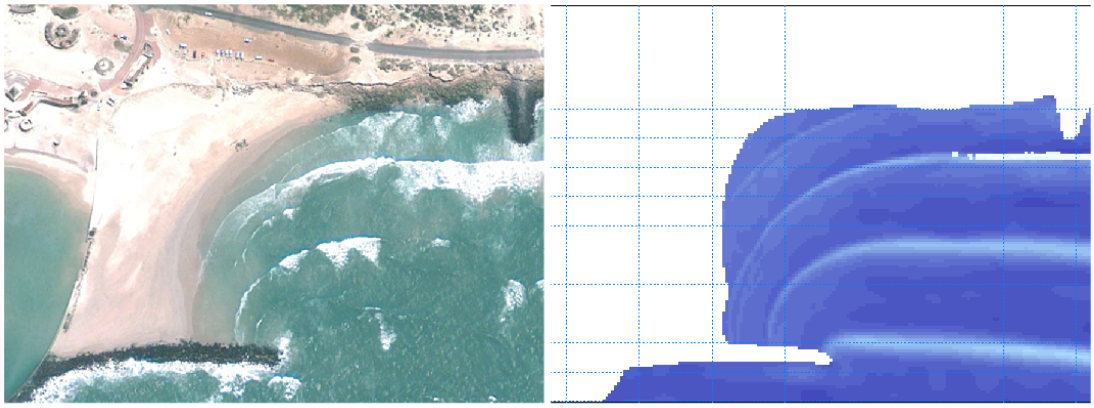

Figure 6-15: Diffraction-effect comparison in the embayment.
Left: Google Earth satellite image from 5 December 2010. Right: MBWS model at +0.3 m MSL, H_s = 1.4 m, Tp = 12 s.

Some discrepancies were also visible. These may have been due to wave-condition differences, bathymetric differences or model-boundary effects. These differences were not drastic and it was decided that the model's overall comparison to the satellite imagery was satisfactory.

6.7 SENSITIVITY ANALYSIS

6.7.1 Introduction

The sensitivity analysis was primarily concerned with *MIKE 21 Boussinesq Wave* setup parameters where there were uncertainties or possible accuracy issues regarding the input values. The parameters of interest included:

- Friction factor (Manning M value) [**MS01**]
- Wave breaking parameter: half-time cut off roller [**MS02**]
- Porosity coefficients [**MS03**]
- Simulation duration [**MS04**]
- Rigidity of measurements [**MS05**]

Note that the last parameter is not an input parameter but an output parameter. The measurements of the u_{PA30} velocities were not an exact process, and were consequently also tested for sensitivity. There were other possible parameters to test as well, but time constraints allowed for only a limited amount sensitivity simulation runs.

The "**MS01**", "**MS02**", etc. refer to the identification labelling of each sensitivity parameter test, and are used for reference throughout this section.

6.7.2 Measurement of sensitivity

The original baseline model of **MB610** (as used in the CSIR's physical model study) was used for the sensitivity analysis. For each sensitivity parameter of interest a couple of models were

run with adjusted values. The results of the sensitivity studies were compared to the original values (as used in this study) to quantify the sensitivity of the parameters. The sensitivity analysis focussed on the change of velocities and wave heights

The sensitivity analysis mainly examined the influence of the abovementioned parameters on the current velocities. The analysis only studied the velocities from a quantitative point of view, and did not regard any possible changes to the circulation pattern. It was nonetheless found that the circulation pattern remained fairly consistent throughout all of the sensitivity models.

The consistent circulation pattern made it possible to identify four velocity peaks that were present in each simulation, as shown by the velocity vectors "H", "I", "J" & "K" in Figure 6-16. For each of the sensitivity models the u_{PA30} velocity was measured in their respective areas, and then tabulated for the sensitivity analysis. The velocities are denoted: $u_{(H)}, u_{(I)}, u_{(J)}$ and $u_{(K)}$, but note that all of these velocities were in fact measured as u_{PA30} velocities. The influence of the sensitivity parameters on the wave heights was also quantitatively studied by measuring and tabulating the wave heights at the fixed points "a" and "b" in in Figure 6-16.

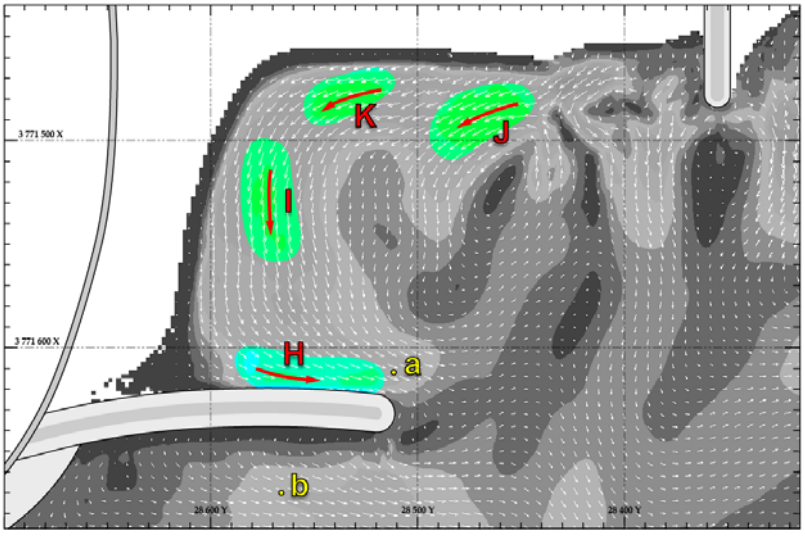

Figure 6-16: Key velocity areas and wave height measuring points. The highlighted areas at the velocity vectors indicate that the velocity vector position varied marginally between the different sensitivity tests.

The average absolute change for each sensitivity were tabulated to summarise the influence on all of the measured points. The average parameters are defined as:

- $\bar{H}'_S$ = average absolute wave height change [%]
- $\bar{u}'_S$ = average absolute velocity change [%]

For a full description of the average absolute change parameters, refer to Appendix C.4. The results of the sensitivity analysis is summarised in Appendix F.3.

6.7.3 Sensitivity parameters

6.7.3.1 Friction Coefficient (MS01)

A Manning M friction factor of 32 $m^{1/3}/s$ was used. The Manning M factor was varied between 80% and 200% of the original value for the sensitivity analysis. In addition, the influence of using a Chézy C value was also tested. The average velocity changes (average change of all four key areas) are tabulated below. The individual absolute velocities is shown in the graph below.

Table 6-10: Sensitivity analysis results for bottom friction factor variation

Test	Sensitivity Parameter		Average Change	
	Value	Adjustment [%]	$\bar{u}'_S$	$\bar{H}'_S$
MB610	M = 32	-	-	
MS01-1	M = 38.4	+20%	21%	1.2%
MS01-2	M = 25.6	-20%	24%	2.0%
MS01-3	M = 64	+100%	79%	1.4%
MS01-4	C = 32	-	7%	2.6%

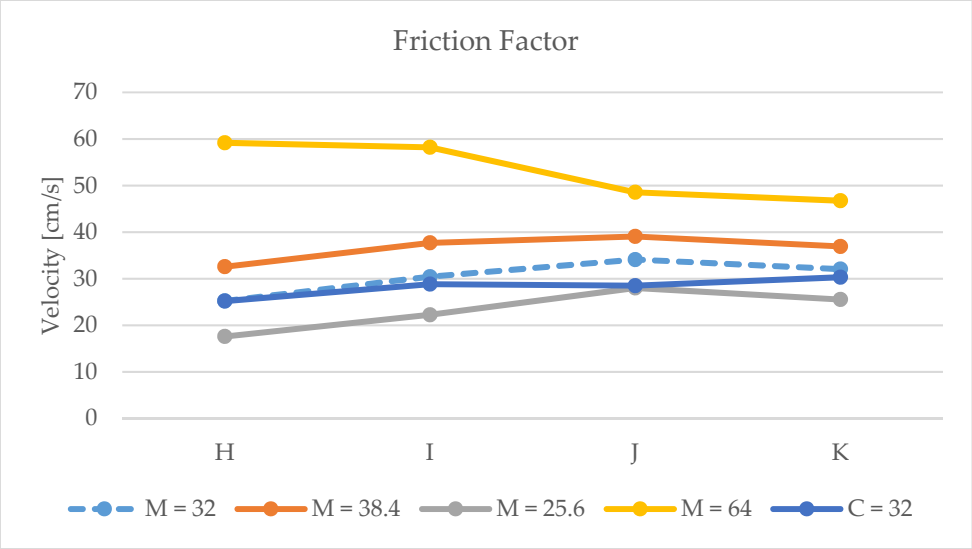

Figure 6-17: Comparison of velocities for the sensitivity analysis on the bottom friction factor

The table and graph both show that the bottom friction factor had a substantial effect. This is understandable as the bed shear stress is directly related to the wave-induced currents, as discussed in the literature study (§ 4.1.4).

In the two cases where the Manning M value was varied by ±20% (orange and grey line), all the velocities changed linearly to the Manning adjustment. For the extreme case, where the Manning M value was increased by +100%, the velocities $\boldsymbol{u}_{(H)}$ and $\boldsymbol{u}_{(I)}$ increased dramatically (+134.7% and +91.3% respectively), while the velocities $\boldsymbol{u}_{(J)}$ and $\boldsymbol{u}_{(K)}$ increased less dramatically (+42.3% and +45.8% respectively).

For the case of the Chézy coefficient ($C = 32\ m^{1/2}/s$) the velocities were fairly similar to the Manning value of the same absolute value. This can be explained by the ratio between the Chézy and Manning coefficient;

$$M = \frac{C}{d^{\frac{1}{6}}} \tag{6.6}$$

where

- d = water depth

For a Chézy coefficient of $C = 32\ m^{1/2}/s$, and depth range of 0.5 m to 2.0 m (all velocities in the embayment were measured within this depth range), the corresponding Manning coefficients would be $M = 35.9\ m^{1/3}/s$ and $M = 28.5\ m^{1/3}/s$, which explains the similarity to a Manning coefficient of $M = 32\ m^{1/3}/s$.

The wave heights did not change significantly (refer to Appendix F.3).

6.7.3.2 Wave breaking: half-time cut off roller (MS02)

The wave breaking parameters were mostly defined by literature values from Schäffer *et al.* (1993) and DHI (2014). Schäffer *et al.* (1993) noted that the Boussinesq model is not extremely sensitive to wave breaking parameters, but it is still important for the surface elevation modelling of the wave decay. The adjustment of the wave breaking parameters is typically adjusted heuristically to calibrate the simulated surface elevation to a prototype recording.

However, as mentioned in § 6.3.1.13, a *half-time cut off roller (HTCR)* parameter of 0.4 s was used inadvertently instead of 1.2 s (Schäffer *et al.*, 1993) or 2.4 s (DHI, 2014). The more "correct" parameters were tested in the sensitivity analysis to see if the incorrect value of HTCR = 0.4 s would have had any adverse effects. The results are tabulated and graphed (refer to Figure 6-18) below:

Table 6-11: Sensitivity analysis results for half-time cut off roller variation

Test	Sensitivity Parameter		Average Change	
	Value	Adjustment [%]	$\bar{u}'_S$	$\bar{H}'_S$
MB610	HTCR = 0.4s	-	-	
MS02-1	HTCR = 1.2s	+200%	1.7%	0.1%
MS02-2	HTCR = 2.4s	+500%	2.6%	0.2%

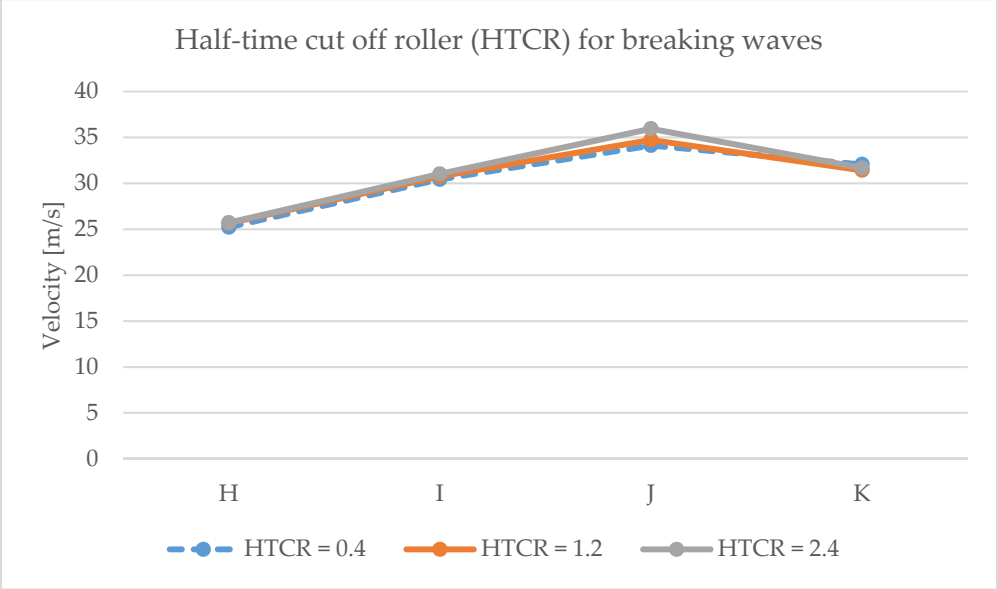

Figure 6-18: Comparison of velocities for the sensitivity analysis on half-time cut off roller for breaking waves

There is some visible, but arguably negligible, change. The $\boldsymbol{u}_{(H)}$, $\boldsymbol{u}_{(I)}$ and $\boldsymbol{u}_{(J)}$ velocities increased slightly, proportionally to the sensitivity adjustment, whereas the $\boldsymbol{u}_{(K)}$ velocity decreased slightly. The difference in increase/decrease might be related to spatially-based wave decay effects that were affected by the breaking wave half time cut off roller.

The wave heights were barely influenced (refer to Appendix F.3).

6.7.3.3 Porosity Coefficient (MS03)

The porosity coefficient sensitivity study investigated how the variation of the porosity coefficient influenced the velocities, rather than the reflection properties of the structures per se. There were four groups of porosity coefficients (refer to Table 6-7), each with its own coefficient and layer width corresponding to a certain depth and wave exposure range. Since these curves will vary at each point along the porosity layer, the group sensitivity study was conducted as a collective.

The four groups were adjusted simultaneously by adjusting the coefficients with the same percentage-factor. From Figure 6-7 (page 6-16), it can be seen that relatively minor changes to the porosity coefficient can influence the reflection coefficient quite significantly. Extreme adjustments, as tested in the friction sensitivity analysis, were not necessary, as it was known that the reflection coefficient should be kept in the lower bounds. The adjustments and results are tabulated below:

Table 6-12: Sensitivity analysis results for porosity coefficient variation

Test	Sensitivity Parameter		Average Change	
	Value	Adjustment [%]	$\bar{u}'_S$	$\bar{H}'_S$
MB610	$\propto_p = 100\%$	-	-	
MS03-1	$\propto_p = 102\%$	+2%	1.7%	0.8%
MS03-2	$\propto_p = 98\%$	-2%	0.5%	0.4%
MS03-3	$\propto_p = 96\%$	-4%	0.5%	0.8%

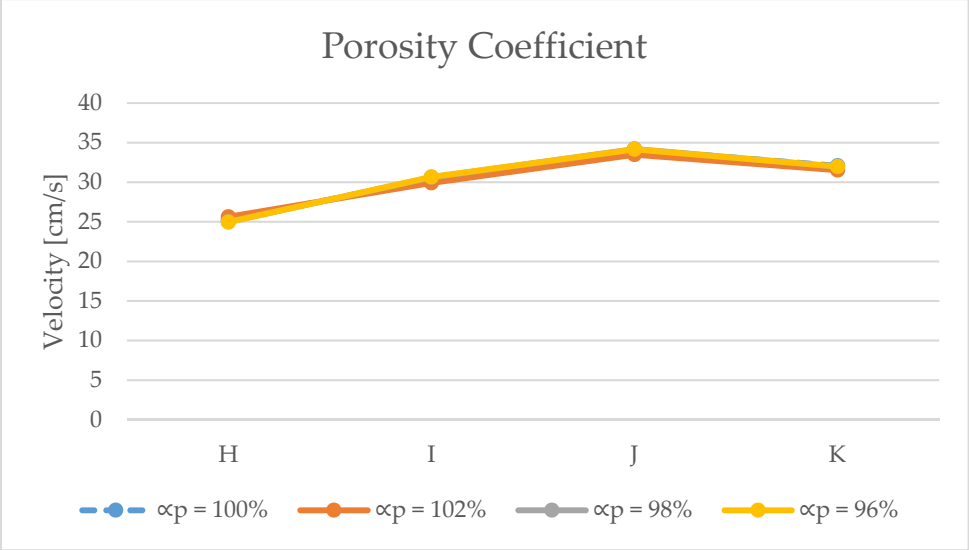

Figure 6-19: Comparison of velocities for the sensitivity analysis on porosity coefficient

The results clearly show that the adjustments to the porosity coefficients did not significantly influence the velocities. It is not known to what extent the adjustments actually influenced the reflection coefficient itself, but based on Figure 6-7 (page 6-16), the reflection coefficients were expected to vary slightly more than the porosity coefficients. A more thorough sensitivity study is possible, but would be beyond to the scope of this study. It can therefore be concluded that low-key setup of the porosity layer was sufficient in terms of velocity generation.

The wave heights were barely influenced (refer to Appendix F.3).

6.7.3.4 Simulation-duration (stabilisation) (MS04)

It was shown in § 6.3.1.5.2 that the surface elevation time-series and cumulative phase-averaged velocity indicated that the model reached stability from the 12 000th time step (10 minutes). The simulation was run for another 8 000 time steps to record the cumulative phase-averaged values as they reached uniformity by the end of the simulation. The sensitivity study of the simulation duration explored the stability of the model and the associated effects by increasing the simulation duration.

For the sensitivity study, the simulation duration was adjusted (longer run) as well as the recording period for the cumulative-series phase-averaged velocities. The results are tabulated and graphed below.

Table 6-13: Sensitivity analysis results for simulation duration adjustment

Test	Sensitivity Parameter		Average Change	
	Parameter	Value	$\bar{u}'_s$	$\bar{H}'_s$
MB610	Recording length	s = 12 000 → 20 000	-	-
MS04-1	Recording length	s = 20 000 → 40 000	6.9%	0.6%

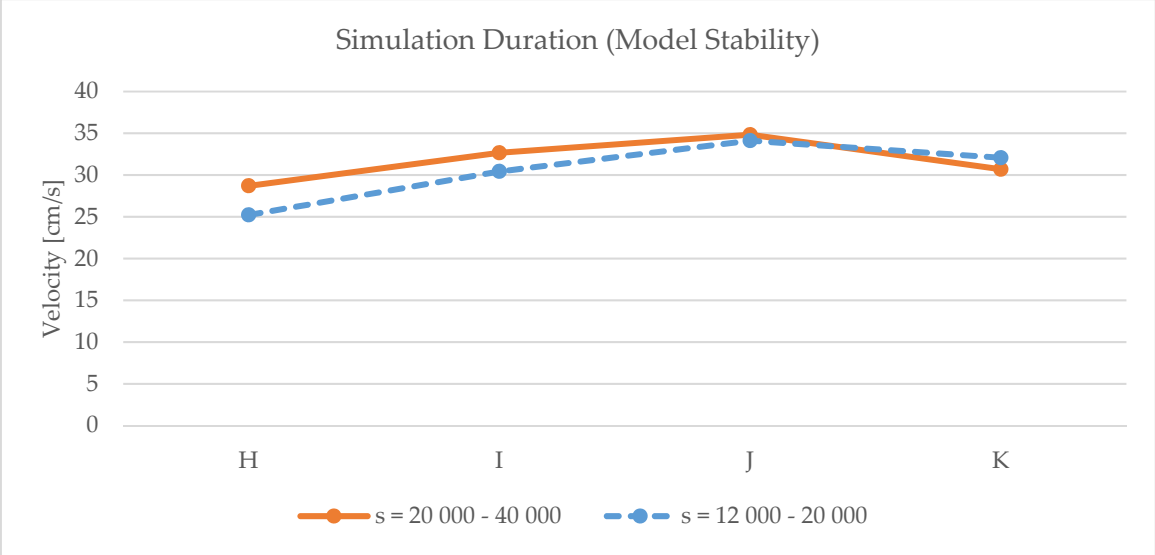

Figure 6-20: Comparison of velocities for the sensitivity analysis on the simulation duration

The maximum velocity change was +14% (Δu_H) and the absolute average velocity change for all the velocities ($\overline{u}'_S$) was 7% - both values were higher than expected. The velocities for the adjusted simulation period also did not follow the same trend as the baseline velocities. These effects were not expected, and thus prompted an investigation to the root cause.

A sub-series phase-averaged velocity curve was recorded at a single point inside the embayment in an attempt to identify the cause of the deviations. The sub-series intervals were synchronised to the wave period (12 seconds) to disregard any intra-phase fluctuations. The results of the sub-series phase-averaged recordings from time step 0 to 40 000 are shown in Figure 6-21 and Figure 6-22.

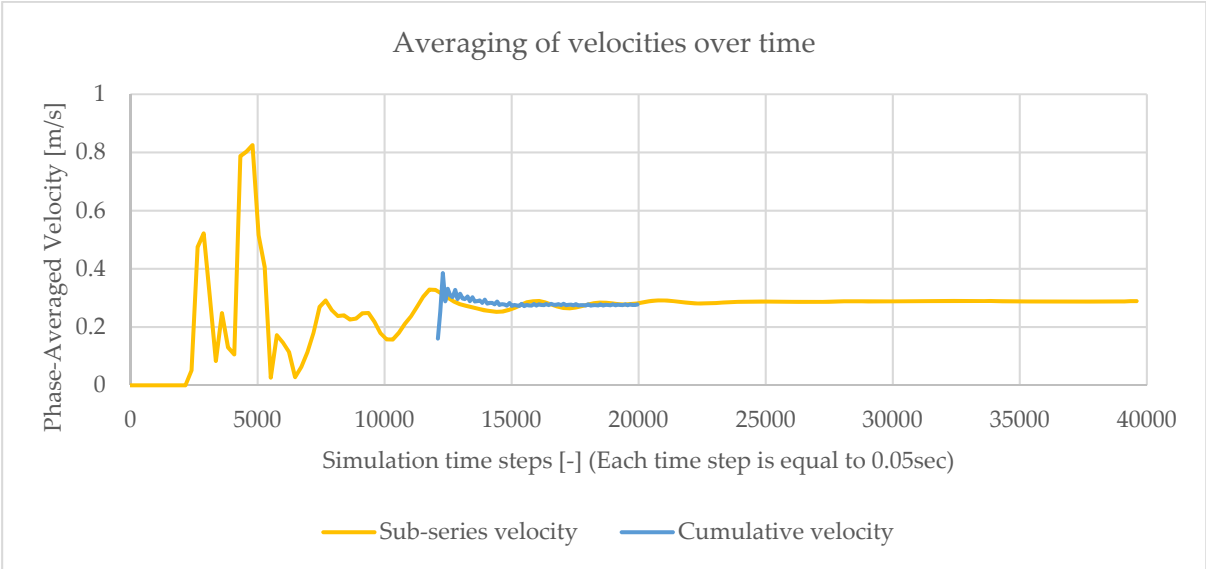

*Figure 6-21: Comparison of sub-series phase-averaged velocity measurement (**MS04-1**: time steps 0 to 40 000) and cumulative phase averaged velocity (**MB610**: time steps: 12 000 to 20 000)*

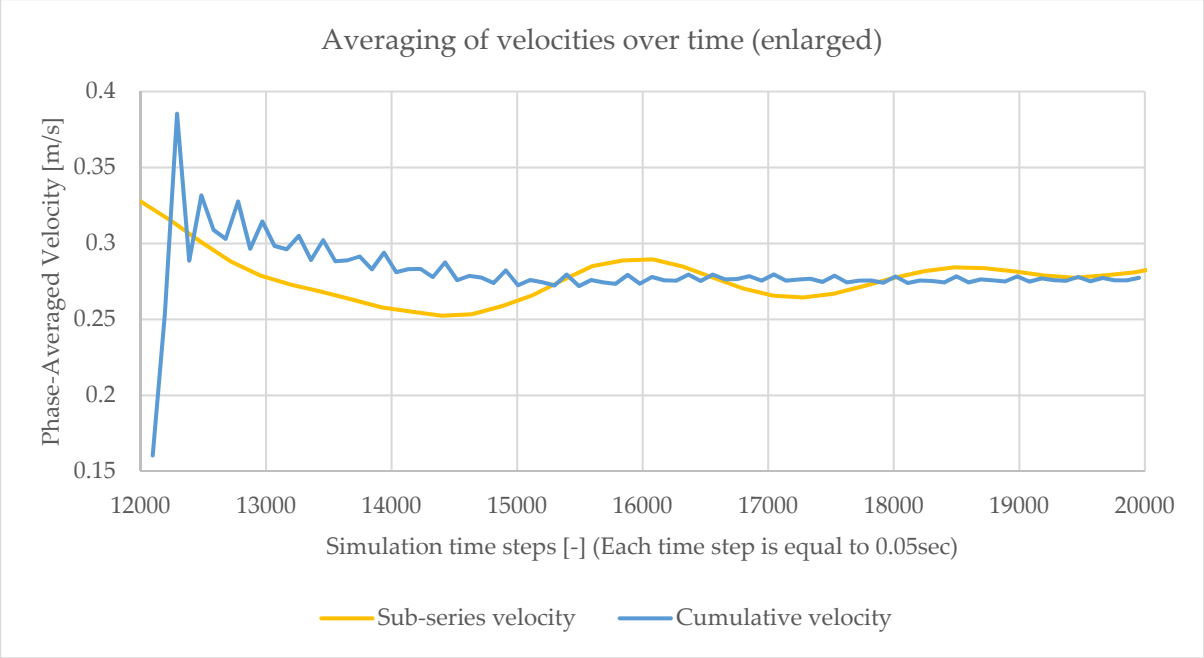

*Figure 6-22: Comparison of sub-series phase-averaged velocity measurement (**MS04-1**: time steps 0 to 40 000) and cumulative phase averaged velocity (**MB610**: time steps 12 000 to 20 000), enlarged*

The sub-series phase-averaged time series graph shows fluctuation of the wave-induced currents for each wave length at the point of measurement. The cumulative phase-averaged velocities between time steps 12 000 and 20 000 are overlaid in Figure 6-21 & Figure 6-22 to provide insight of how the cumulative function is related to the sub-series function.

Between time steps 12 000 and 20 000, the sub-series phase-averaged velocity (yellow line) still fluctuated, with velocities ranging between 25.2 cm/s. and 32.8 cm/s. The fluctuations were periodic and wave-like, which indicates a highly probable influence of long waves caused by boundary effects. The wave-like fluctuations allowed the cumulative phase-averaged velocities to prematurely converge – as illustrated in Figure 6-22. As the fluctuations diffused over the extended time, the sub-series average seemed to slightly increase from time step 20 000 to 40 000, allowing for the 14% deviation at $\boldsymbol{u}_{(\boldsymbol{H})}$ seen in Figure 6-20. This long wave influence is in good agreement with the theory of Longuet-Higgins and Stuart (1964) of long-waves considerably contributing to the wave-current interaction.

Note that this explanation explicitly focussed on $\boldsymbol{u}_{(\boldsymbol{H})}$, whereas the other velocity areas showed less deviation, but the same principle should still be true. This long wave effect was only discovered after the completion of all the models.

The individual wave heights remained about the same height, not affected by the extended simulation time or long wave effects.

6.7.3.5 Velocity Measurement Rigidity (MS05)

The *30 m peak average velocity* measurements are not an exact process, and relied on the author's ability to measure all velocities consistently by following the process as set out in § 6.5.2.1. It is therefore highly probably that inconsistencies may have occurred, which necessitated the sensitivity study of the rigidity of the *30 m peak average velocity* measurements.

The test for rigidity of measurements involved re-measuring the *30 m peak average velocities* at the same key areas, but at different intervals. To reduce the bias of memory (or familiarity associated to measuring the same areas), the re-measurements were done at intervals of more than 24-hours apart. The velocity magnitude colour palettes were also modified to further reduce any memory-bias.

Table 6-14: Sensitivity analysis results for velocity measurement rigidity test

Measurement Iteration	u_{PA30} velocities [cm/s]			
	$u_{(H)}$	$u_{(I)}$	$u_{(J)}$	$u_{(K)}$
MB610	25.2	30.4	34.1	32.1
MS05-1	24.7	30.4	34.2	32.0
MS05-2	24.7	30.4	34.2	32.0
MS05-3	24.7	30.4	34.2	32.1

The tabulated measurements clearly illustrate a good consistency in the measurement process. The largest deviation was encountered at $u_{(H)}$ with a deviation of 2.2%, which was acceptable. There may arguably still be a memory bias which could have resulted in a smaller deviation, but it has been attempted to reduce the bias as much as possible to provide the best sensitivity results.

The wave heights were not applicable to the velocity measurement rigidity analysis.

6.8 SUMMARY OF THE MODEL SETUP

6.8.1 Setup of models

A two-dimensional Boussinesq-type wave model was chosen for this study for its ability to predict the surf zone hydrodynamics. In the context of the hydrodynamic study of Monwabisi, the main advantages of a Boussinesq wave model was to resolve wave-induced currents by the inclusion of additional convective terms associated with the breaking waves. *MIKE 21 Boussinesq Wave* by DHI was chosen for the hydrodynamic modelling of Monwabisi.

The Monwabisi Boussinesq Wave Simulation (MBWS) model was based on the physical model of the CSIR's 1997 study. The majority of the input data were therefore sourced from the CSIR's report. The simulation configurations were set up to the exact same specifications to allow for comparison between the two models.

6.8.2 Simulation output parameters

The primary output parameters of interest were the depth-integrated wave-induced velocity and the associated horizontal current circulation pattern. Secondary parameters of interest included wave height (or surface elevation), wave height distribution, roller thickness and depth integrated wave energy flux.

For this specific study two statistical means of measurement were defined, namely 30 m peak average velocities (u_{PA30}) and *designated swimming area*-based velocity distribution. The u_{PA30} velocities were used to measure peak velocity vectors for statistical performance comparison. The area-velocity distribution was based on the *designated swimming area*: a safe and sheltered area which could be demarcated with a structure and confined to a depth range of 0 m to 2 m.

The area-velocity distribution could be used to plot exceedance distributions for the statistical comparison of larger areas of velocity distribution.

6.8.3 Calibration and verification

The limited results from the CSIR's (1997) report and lack of prototype measurements meant that the calibration of the MBWS model was very limited. The accuracy of the model therefore relied heavily on the correct use of the setup input parameters to result in a stable model that resembled the prototype conditions. The study consequently focussed more on the qualitative verification of the MBWS models.

The initial baseline MBWS simulation did show satisfactory agreement to the available data. The hazardous circulation cell in the embayment was present, with a prominent current along the spur - as described in the in the report of the CSIR (1997). The surface elevation of the MBWS simulation also matched the satellite imagery of the area reasonably well, indicating that the MBWS model was fairly representative of the prototype conditions in terms of the bathymetry and the associated wave effects of shoaling, breaking, refraction and diffraction. Some differences were visible, but the overall resemblance was satisfactory.

Although the numerical model showed good qualitative accuracy, there was no absolute indication on the reliability of current velocities from the MBWS model. The MBWS current velocities compared well to measurements reported by McMahan *et al*. (2005 & 2006), but this was only a rough indication of the order of magnitude. For this reason it was decided to use *relative velocities* (ratio of one velocity to relative to another) throughout the study, by assuming that the ratio between the velocities would remain linear.

6.8.4 Sensitivity analysis

A sensitivity analysis was required to study the influence of parameters where there were uncertainties or possible accuracy issues regarding the input values. The sensitive analysis only focussed on the quantitative influence on the current velocities and wave heights.

It was found that the friction coefficient had a rather drastic influence. This implied that for accuracy purposes, the Boussinesq model required a specifically defined friction coefficient. Since no velocity calibration data were available, the MBWS model relied on literature values. For this study this was acceptable, but the friction coefficient may require more attention if velocity calibration becomes available for future studies.

The investigation of an increased simulation duration, led to the discovery of long-wave effects, likely to be caused by boundary effects. As the model "warmed up" these boundary effects slowly dissipated by absorption through the sponge and porosity layers. The recording period used in the MBWS model overlapped with the last remaining energy of the long waves which was not visible in initial observations from the surface elevation, but were revealed in the sub-series phase averaged velocity analysis. The adverse influence of this long wave effect was only discovered after the simulation and analysis of all MBWS simulations, but the extent of the influence was considered to be inconsequential in the context of this study.

The wave-breaking half-time cut off parameter, porosity coefficient and the measurement rigidity of the *30 m peak average velocities* (u_{PA30}) were also tested in the sensitivity analysis, but were found to have only marginal influences on the current velocities. In all of the

sensitivity tests the wave heights remained mostly unchanged in comparison to the current velocities.

6.8.5 Conclusion on the numerical model setup

A numerical model is only as accurate as time allows it to be. The accuracy of a model could perhaps be portrayed by a logarithmic graph as a function of time: the initial setup sees a rapid development of model accuracy, but as more time is spent on improving the model, the accuracy improves at an ever-decreasing rate. A 100% accurate model is thus an elusive goal, and a decision should ultimately be made when the model is sufficiently accurate. In terms of this study, there will always be potential for improvement of the MBWS model, but taking time-constraints into account, it was decided that the MBWS model performed with sufficient accuracy for the purposes of this study.

7 SIMULATION RESULTS AND IN-DEPTH ANALYSIS

7.1 INTRODUCTION

The Monwabisi Boussinesq Wave Simulation analysis chapter will provide a qualitative and quantitative review of the performance of all of the proposed solutions by means of a visual and statistical analysis. The results of the simulation were generated as described in § 6.4. Appendix D contains the detailed results and Appendix F summarises all the measured velocities of the simulations discussed in this chapter.

7.1.1 Scope of the analysis

The visual analysis will mainly focus on the current circulation patterns by examining the 2D-horizontal flow patterns. The visual analysis will also refer to the wave-height (instantaneous or average) and wave energy density flux where necessary. The purpose of the visual analysis is to qualitatively analyse how the proposed structural solutions influence the hydrodynamics of the embayment and to clarify why certain solutions perform better than others.

The statistical analysis will only focus on the current velocities by examining the relevant peak velocities as well as area velocity distributions. The purpose of the statistical analysis is to provide a quantifiable and objective indicator of the performance of the proposed structures.

7.1.2 Velocity measurement and presentation

This chapter refers to two types of velocity recordings: *absolute* and *relative*. *Absolute velocities* refer to the normal convention of a velocity magnitude as a distance-over-time unit (m/s or cm/s). *Relative velocities* refer to a simple ratio of one velocity relative to another multiplied by 100, and are therefore expressed as a percentage.

It was already mentioned that no prototype data were available to calibrate the *absolute velocities* from the MBWS model (refer to § 6.6), which meant that the absolute velocities will not necessarily be accurate. *Relative velocities* offer a solution by comparing the performance of the proposed solutions as a relative change of velocity, which disregards the concern of reliability associated with absolute velocities. The *relative velocities* were also formulated in such a way that they provide a better quantitative indication of the performance of proposed structure compared to the *absolute* velocities.

7.1.2.1 Absolute measurements

The *absolute velocities* were not omitted from this study, as they still have relevance to this study. Firstly, the absolute velocities provide an overview of the original output results from the MBWS model, which cannot necessarily be derived from the relative velocities. The absolute velocities also allow for potential future studies that may further require the original measurements. Lastly, the absolute velocities were further used for the empirical study of the influence of environmental conditions on the current velocities.

In this chapter, the absolute velocities are used to express localised current peaks as well as area-velocity distribution. The current peaks are expressed as *30 m peak average* velocities (as described in § 6.5.2.1) and the area-velocity distribution is expressed as an exceedance curve (as described in § 6.5.2.2).

7.1.2.2 Relative measurements

7.1.2.2.1 Definition of the relative velocity

The relative velocities were used to benchmark the performance of the proposed structural solutions relative to the present beach configuration (or *baseline* configuration). In essence, the relative velocities compare the velocity differences between a proposed structural solution and the present beach configuration for the same tide and wave configuration. In doing so, the relative velocity isolates the influence of the proposed structural solution itself, which makes it possible to compare the performance of all the different structures regardless of the tide and wave configuration.

The baseline simulation related to the proposed solution simulation with the same tide and wave configuration is referred to as a *relative baseline*. Figure 6-1 on page 6-4 illustrates the connection between the proposed solution simulations and their relative baseline simulations. The relative velocity can therefore be formulated as:

$$U_r = {}^{u_{(T)}}/_{u_{(RB)}} \tag{7.1}$$

where

- $U_{r(i)}$ = relative baseline velocity at point i, expressed as %
- $u_{(T_i)}$ = Absolute velocity from the proposed solution at point i, in m/s
- $u_{(RB_i)}$ = Absolute velocity from the relative baseline at point i, in m/s

From this formulation it follows that for relative velocities below 100% ($U_r < 100\%$) indicates a weaker current relative to the baseline conditions (improvement). Relative velocities above 100% ($U_r > 100\%$) indicate a stronger current relative to the baseline conditions (worsening).

7.1.2.2.2 Velocity class system

The proposed solutions usually altered the circulation patterns significantly, which meant that it was not always a simple task to select two comparable velocities between the proposed solution and the relative baseline. It was consequently decided to make use of a *velocity class system:* by identifying certain similarities between the model flow patterns, the velocities could be categorized as belonging to a certain class. The velocity class system was based on the following consistencies found in most of the models:

Class 1 (C1): A strong flow along the spur, or alternatively, a prominent exit flow from the *sheltered bay**. Class 1 currents are the most dangerous currents, which could lead to drowning. They are therefore also the most important velocity class in the context of this study.

Class 2 (C2): A secondary strong current in the *sheltered bay**. Class 2 currents do not necessarily lead to an exit flow, but can still be potentially dangerous.

Class 3 (C3): Strong current in the exposed bay or outside of the sheltered area. Class 3 currents are typically stronger than Class 1 and 2 currents, but they occur in high wave energy areas where bathers are less likely to access the beach due to the visible danger.

**The "sheltered bay" refers to the wave-protected area behind the spur. It differs from the "designated swimming area" (§ 6.5.2.2) as the sheltered bay always excludes the wave-exposed area adjacent to the existing groyne.*

The purpose of this categorisation was to identify the velocities which can be compared to others for the U_r velocity. From this categorisation system *Class 1* velocities could be compared to *Class 1* only. The same follows for *Class 2* and *Class 3*. For a single simulation it is possible for more than one velocity to meet the same class criteria, and in such cases the strongest velocity was chosen. Thus, for each simulation a maximum of three velocities were identified (one in each class) for the relative velocity comparison. Some simulations were limited to two classes where a third velocity was not identified or measured at all. Figure 7-1 below illustrates the class system in the context of the baseline simulations (left) and one of the T-groyne simulations (right).

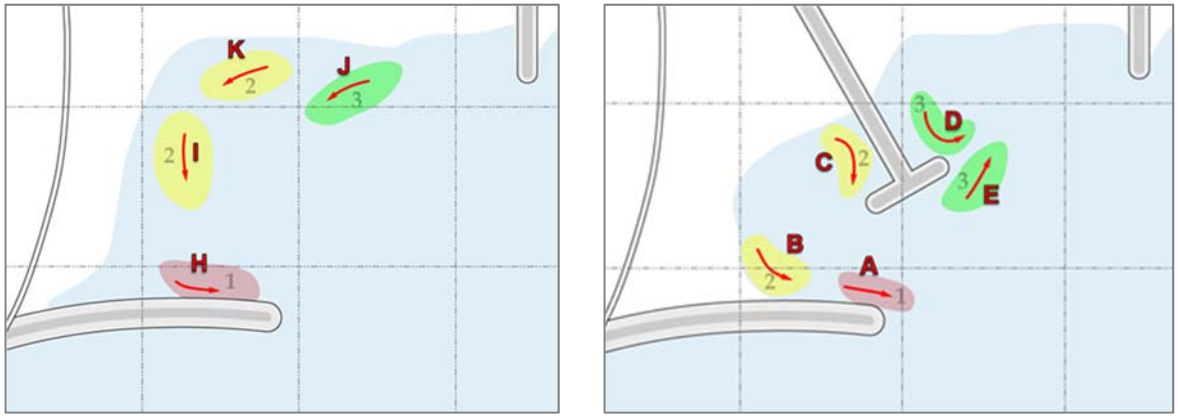

Figure 7-1: Illustration of the velocity class system as used in the baseline simulations (left) and proposed solution simulations (right). Class 1 (red) velocities could be compared with each other. Similarly, Class 2 (yellow) and Class 3 (green)

7.1.2.2.3 Definition of the exceedance difference curve

The exceedance curves from the baseline simulations could be used to compare the improvement or deterioration relative to the existing situation at Monwabisi, similar to the relative velocities. The difference curve is simply calculated by determining the difference between the relative baseline exceedance curve and the exceedance curve of the proposed solution:

$$D(i) = E_{R.B.}(i) - E_T(i) \tag{7.2}$$

where

- $D(i)$ = exceedance difference curve as function of i
- $E_T(i)$ = Exceedance curve for proposed solution scenario
- $E_{R.B.}(i)$ = Exceedance curve for relative baseline
- i = velocity exceedance interval, $i = 0, 5, 10, \ldots$ [cm/s]

Figure 7-2 depicts the relation between an exceedance curve and exceedance difference curve with a visual example from the d*og-legged spur off spur head* (**MT005**). From this formulation it follows that a positive difference (or decrease of exceedance value) ($D(i) > 0\%$) indicates an improvement and a negative difference (or increase of exceedance value) ($D(i) < 0\%$) indicates a deterioration relative to the baseline. The concept is slightly different from the relative velocities, as the difference curve is still a function of the absolute velocities.

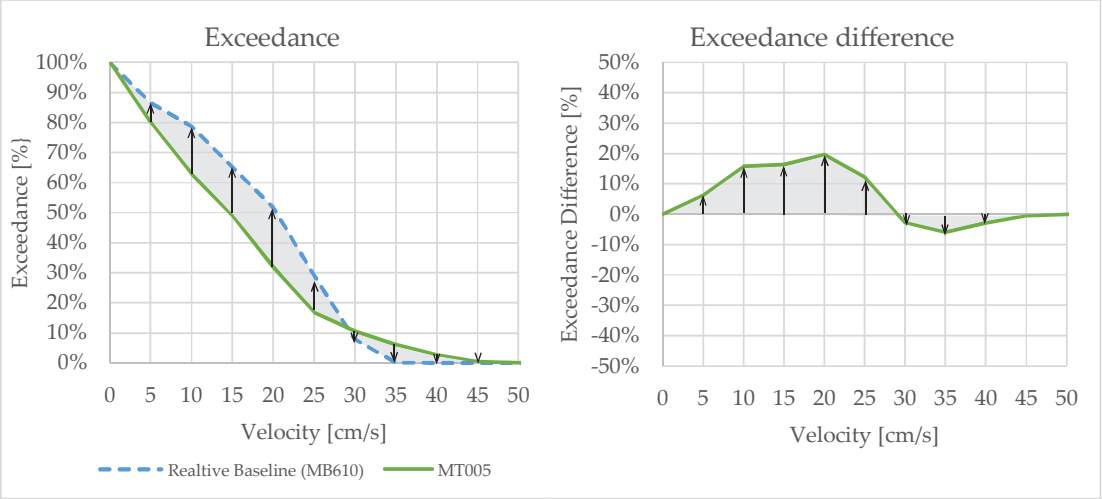

Figure 7-2: Illustrative example of a exceedance difference curve.

7.1.3 Layout of this chapter

This chapter will first discuss the results of the baseline simulations (§ 7.2) to better understand the complex hydrodynamic system which facilitates the hazardous circulation. The baseline configurations will also be analysed to examine the influence of the environmental conditions on the current velocities. The proposed solution analysis (§ 7.3) will follow for an in-depth analysis on the relative performance of the various configurations. § 7.4 will discuss the *Swimming Danger Factor* as a single quantitative measurement of the beach hazard. The chapter will be concluded by an overall summary in § 7.5.

7.2 Baseline Simulations Analysis

All of the baseline simulations used the same bathymetric setup, but with varying water levels and wave conditions. The different baseline simulations and their setup conditions are described in Table 7-1 below.

Table 7-1: Wave and tide conditions for the different baseline tests

Test ID	Setup Conditions		
	WL [m MSL]	H_s [m]	T_p [s]
MB110	-0.3	1.3	12
MB210	-0.1	1	12
MB220	+0.1	1.4	12
MB310	+0.3	1.3	12
MB410	+0.4	1.1	12
MB420	+0.4	1.4	12
MB430	+0.4	1.1	8

Test ID	Setup Conditions		
	WL [m MSL]	H_s [m]	T_p [s]
MB510	+0.45	1.4	12
MB610	+0.7	1.5	12
MB710	+0.9	1.4	12
MB720	+0.9	1.8	12

7.2.1 Visual observations

A general anti-clockwise circulation pattern was consistently visible in all of the baseline simulations. The components of a rip current – as defined in the literature study (§ 4.1.8) – could be applied to this scenario. The breaking waves in the embayment allow for the

development of a longshore current. This longshore current is the driving force of the rip current, and can therefore be classified as the "feeder" currents. As the spur deflects the current to deeper water, the flow along the structure becomes narrow and intense, akin to the "neck" of a rip current. At the tip off the spur, past the breaking waves, there is no confinement anymore and the current weakens and spreads, forming the "head" of the rip current.

About halfway between the groyne and tidal pool a secondary, breakoff current was present, forming a smaller anti-clockwise current within the embayment. Figure 7-3 illustrates the primary and secondary current. The circulation was at its strongest at the split point (Figure 7-3, Point X), rapidly dissipating velocity as the current progressed seaward.

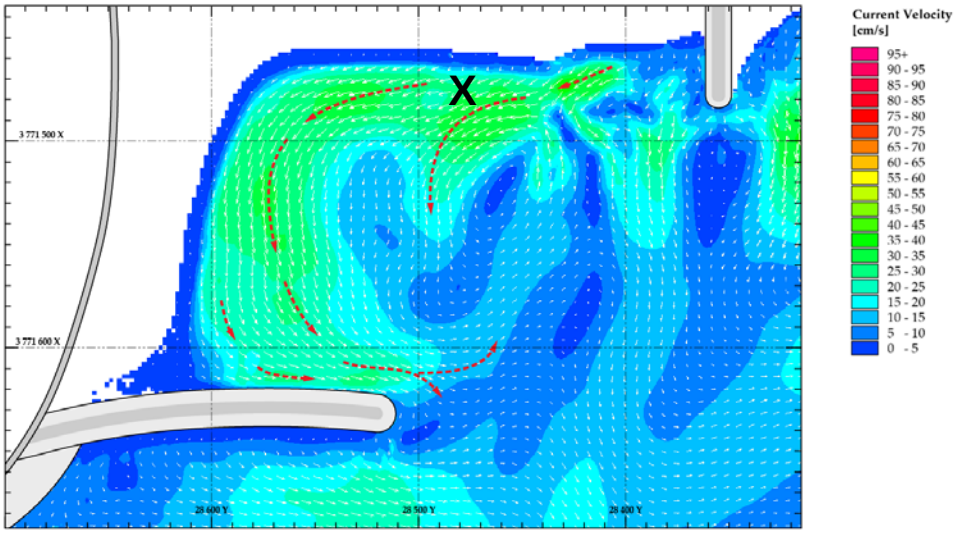

*Figure 7-3: General circulation pattern present in all baseline simulations. (**MB610**: H_s = 1.5 m, T_p = 12 s, WL = +0.7 m MSL)*

This circulation pattern could be explained by analysing the relationship between bathymetry, current velocities and wave energy density flux. The two images below shows the bathymetry (contours relative to 0 MSL) and the current velocity (left) and wave energy flux (right) overlays for a regular wave height of H_s = 1.5m with T_p = 12s. Flux is measured as the time-averaged depth-integrated flux density [$m^3/s/m$]

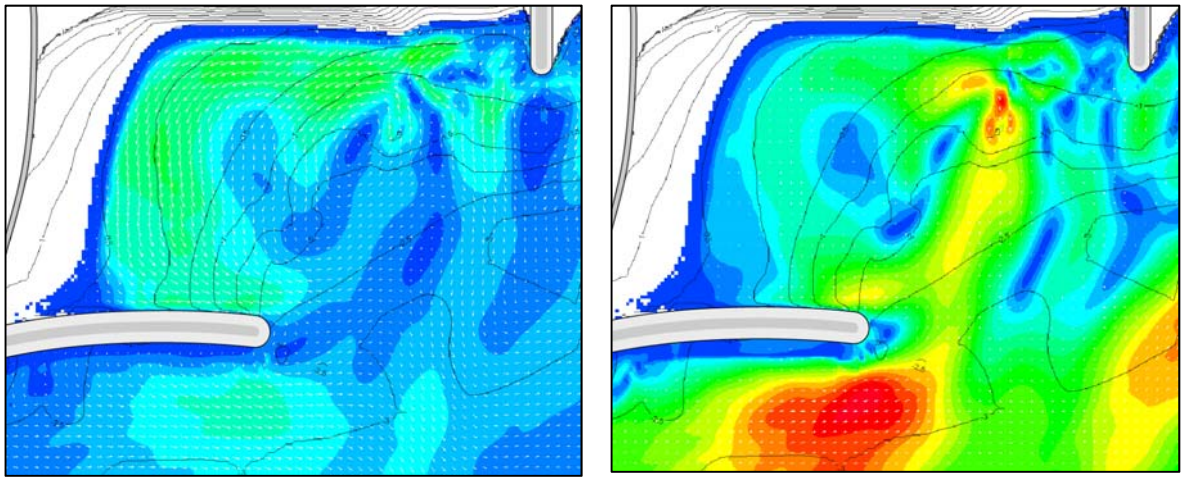

*Figure 7-4: The average velocity (left) compared to the average wave energy density flux (right) (**MB610**: H_s = 1.5 m, T_p = 12 s, WL = +0.7 m MSL)*

It is clearly visible that there is a wave flux energy concentration at the "splitting point" mentioned above. A strong possibility for this localised concentration of energy is the direct exposure to incoming wave energy combined with a steep bathymetric gradient. The energy flux is largely concentrated along the bathymetry contour in a direction corresponding to the flow of the smaller secondary circulation cell. The larger primary circulation pattern is associated with a reduced wave flux energy, but over a shallower depth (< 0.5m) the energy is concentrated to a relatively high velocity circulation.

Although the majority of the high velocity currents is found in shallow areas, this still presents a danger to younger bathers. The critical area is closer to the spur, where the mean current is concentrated away from the shore and the bathymetry suddenly increases in depth at the head of the spur. The lack of high-wave energy here creates an illusion of safety. The wave energy is visualised in Figure 7-5 below.

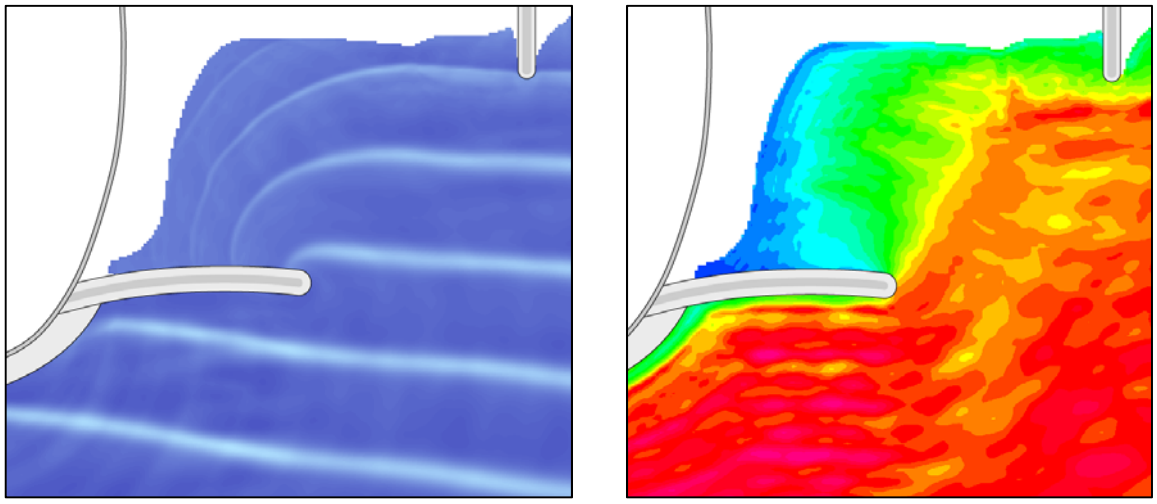

*Figure 7-5: Time snapshot of surface elevation (left), compared to average wave height distribution (**MB610**: H_s = 1.5 m, T_p = 12 s, WL = +0.7 m MSL)*

Also evident from the flux pattern (Figure 7-4, right) is high concentration of flux energy off the spur head. By tracing the flux vector-paths it is apparent that there's a broad flux of energy moving roughly southward along the beach. This broad flow pattern "collides' with the spur, which forces the flow out of the bay. As this energy flux is forced outward, the flux pattern narrows in a concentrated funnel-like flow, along the spur – ultimately resulting in a highly concentrated peak energy flux evident at the spur head (see Figure 7-6, below). Past this point, the energy quickly dissipates as the water gets deeper with no bathymetric feature or structure present to significantly influence the energy flux. The wave-induced velocity is depth-averaged and therefore the highest velocity does not necessarily coincide with highest energy flux.

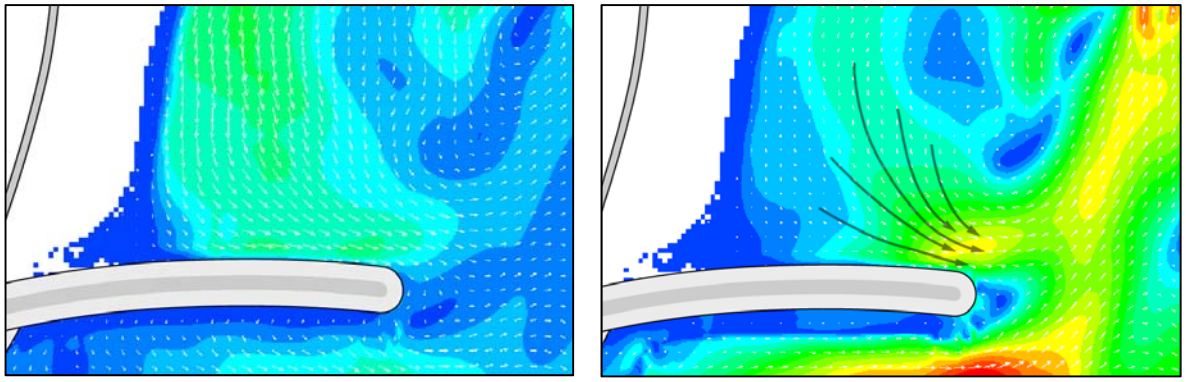

Figure 7-6: The average velocity (left) compared to the average wave energy density flux (right) at the spur
*(**MB610**: H_s = 1.5 m, T_p = 12 s, WL = +0.7 m MSL)*

7.2.2 Statistical analysis: summary of baseline conditions

7.2.2.1 Measurement of velocities

The consistent circulation pattern made it possible to identify four velocity peaks occurring in the same vicinity for each baseline simulation. These consistent velocity peaks were identified by "H", "I", "J" and "K" as shown in Figure 7-7. For each of the baseline simulations, these velocities were measured as 30 m peak averave velocities (u_{PA30}, § 6.5.2.1), but for simplicity denoted as: $u_{(H)}, u_{(I)}, u_{(J)}$ and $u_{(K)}$. Note that both $u_{(I)}$ and $u_{(K)}$ were classified as Class 2 velocities, due the partial wave sheltering from the spur. For each simulation, the stronger of the two was chosen for comparison purposes as only one Class 2 velocity can be used.

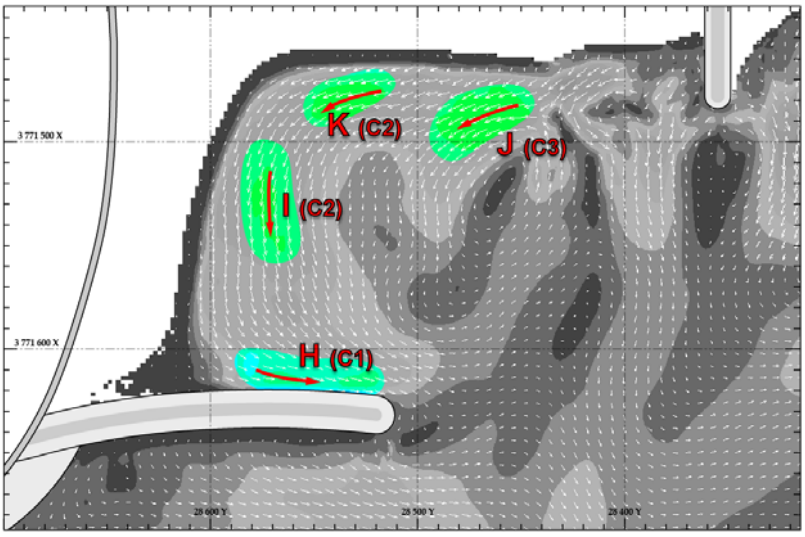

Figure 7-7: Velocity peak areas which occurred consistently across the baseline simulations.

In addition, the area velocity distribution were also measured for the baseline simulations. The *designated swimming area* spanned the whole beach (see Figure 7-8) - confined between the existing spur and groyne, as there were no physical structures to divide the beach. The *designated swimming area* for each baseline simulation is presented in Appendix D.2.

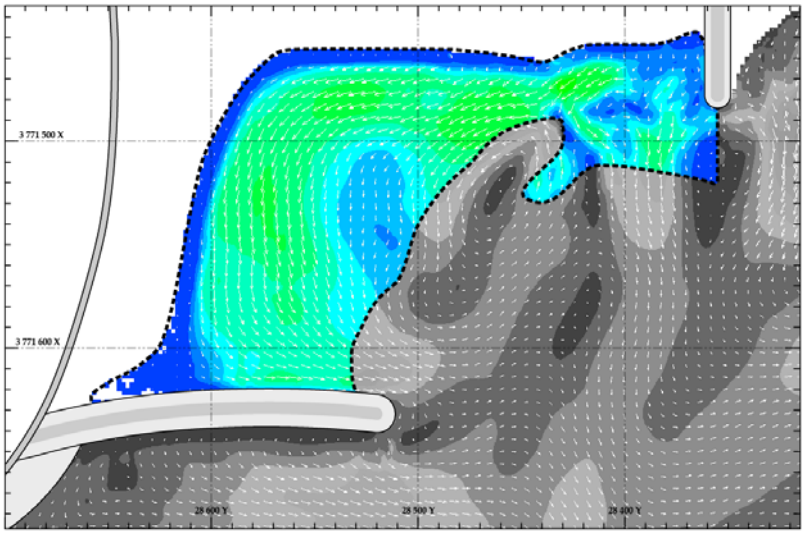

Figure 7-8: Example of designated swimming area for the baseline test of MB610. The area is confined between the depths of 0 m and 2 m for a tide level of +0.7 m MSL.

7.2.2.2 *Summary of measured velocities*

Figure 7-9 and Figure 7-10 below summarises the velocity measurements for the peak velocities (organised by *velocity class system*) and area-velocity distribution (based on *designated swimming area*) respectively. These are the measurements that are used for the relative baseline comparison.

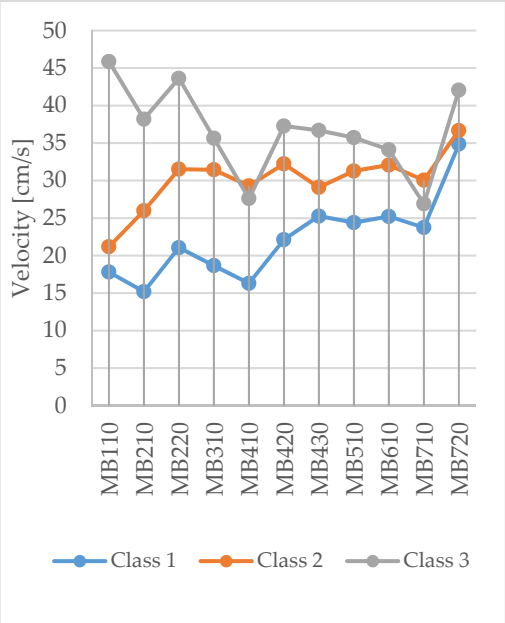

Figure 7-9: Absolute (u) velocities for the baseline configurations

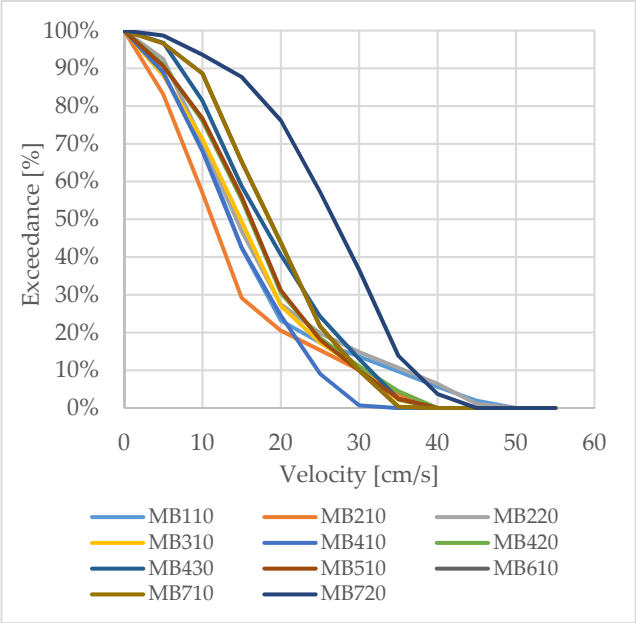

Figure 7-10: Designated swimming area (whole beach) exceedance curves for the baseline configurations

It can be seen that there is considerable variation between the different configurations. These variations are caused by wave and tide configurations only, and thus clearly illustrate the importance of comparing each proposed solution to a baseline scenario with the same wave and tide configuration.

7.2.3 Statistical analysis: influence of variable environmental conditions

A total of 11 baseline configurations were tested, of which some shared a common setup parameter (tide level, wave height or wave period). These common parameters were used to compare the influence of the specific *environmental variable*. The number of common parameters was limited however, which meant that the analysis was somewhat restricted. The baseline configurations and absolute velocity measurements (u) are listed below in Table 7-2. Note that the absolute velocities are used without the velocity class system.

Table 7-2: Summary of baseline U_{PA30} velocities, measured at the consistent current peaks

Test #	Setup Conditions			Velocity [cm/s]			
	WL [m MSL]	H_s [m]	T_p [s]	$u_{(H)}$	$u_{(I)}$	$u_{(J)}$	$u_{(K)}$
MB110	-0.3	1.3	12	17.8	21.2	45.9	18.6
MB210	-0.1	1	12	15.2	26.0	38.2	21.9
MB220	-0.1	1.4	12	21.1	31.5	43.6	24.7
MB310	0.3	1.3	12	18.7	31.4	35.7	30.1
MB410	0.4	1.1	12	16.3	26.5	27.6	29.3
MB420	0.4	1.4	12	22.1	30.9	37.3	32.2
MB430	0.4	1.1	8	25.3	28.8	36.7	29.1
MB510	0.45	1.4	12	24.4	30.2	35.7	31.3
MB610	0.7	1.5	12	25.2	30.4	34.1	32.1
MB710	0.9	1.4	12	23.7	30.0	26.9	29.2
MB720	0.9	1.8	12	34.9	36.7	42.0	34.3

7.2.3.1 *Influence of water/tide Level*

The graphs below show the variation of the peak velocities and velocity distribution for all baseline simulations with H_s = 1.4 m.

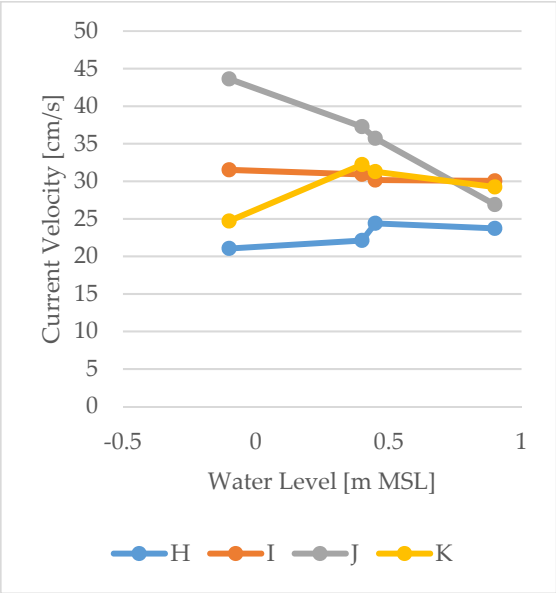

Figure 7-11:Influence of water/tide level on current velocities for a constant wave height of Hs =1.4 m

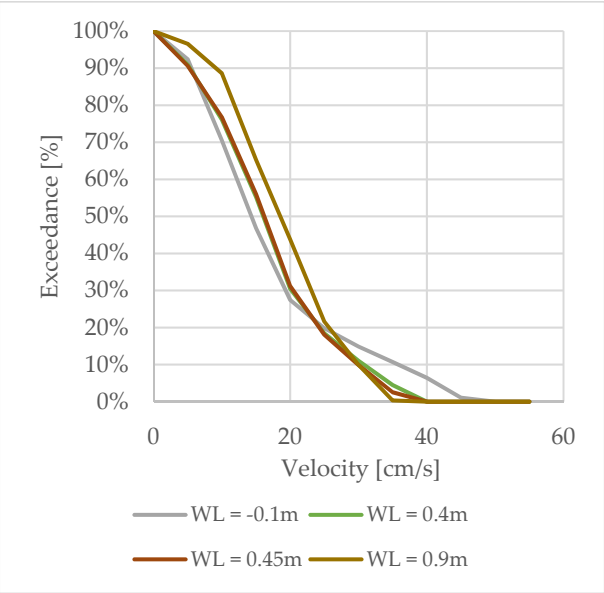

Figure 7-12:Influence of water/tide level on current velocity distribution for a constant wave height of Hs =1.4 m

All the velocities responded quite differently to the change of water level. $\boldsymbol{u}_{(H)}$. and $\boldsymbol{u}_{(I)}$. remained relatively constant, only showing a slight change corresponding to the water level. $\boldsymbol{u}_{(J)}$. showed a strong linear decline with increasing water levels. This may be a result of an "increase" of the beach size, allowing the wave energy to spread more. $\boldsymbol{u}_{(K)}$. initially increased with the lower water levels, but stabilized from +0.4 m MSL.

A stronger trend was observed from the exceedance curves in Figure 7-12. The exceedance curves were spaced relative to each other in accordance to their water level. At a velocity of 25 cm/s, the exceedance curves inverted their order. This suggests that the lower tide levels generally have more calm (lower velocity) areas, but their peak velocities are also stronger. The higher tide levels therefore have a higher average velocity, but with less contrast between the lower and higher velocities.

There is also a noticeable kink in the peak velocity graph (Figure 7-11) between the water levels +0.4 m and +0.45 m MSL, especially for $\boldsymbol{u}_{(H)}$. This was not expected as the water levels were relatively close. The probable cause may be measuring-inconsistency between the two simulations. This difference was not noticeable in the exceedance curves from Figure 7-12.

7.2.3.2 Influence of Wave Height

There were three baseline combination pairs with constant water levels and varying wave heights. The water level differed for the three pairs, which meant that they had to be compared separately.

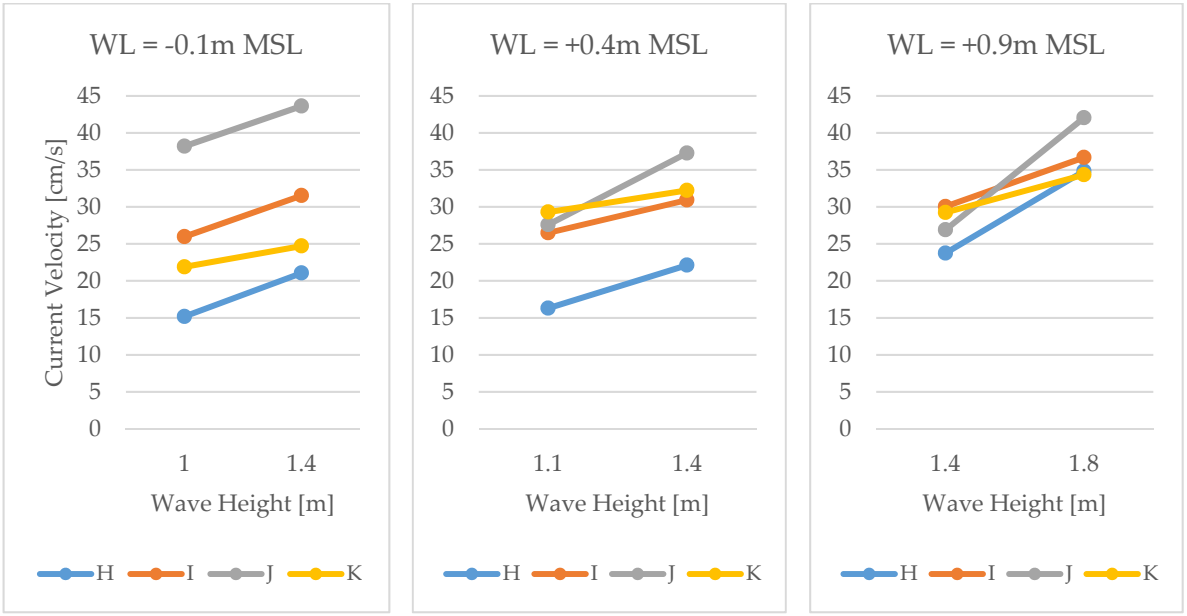

Figure 7-13: Influence of wave height on current velocities

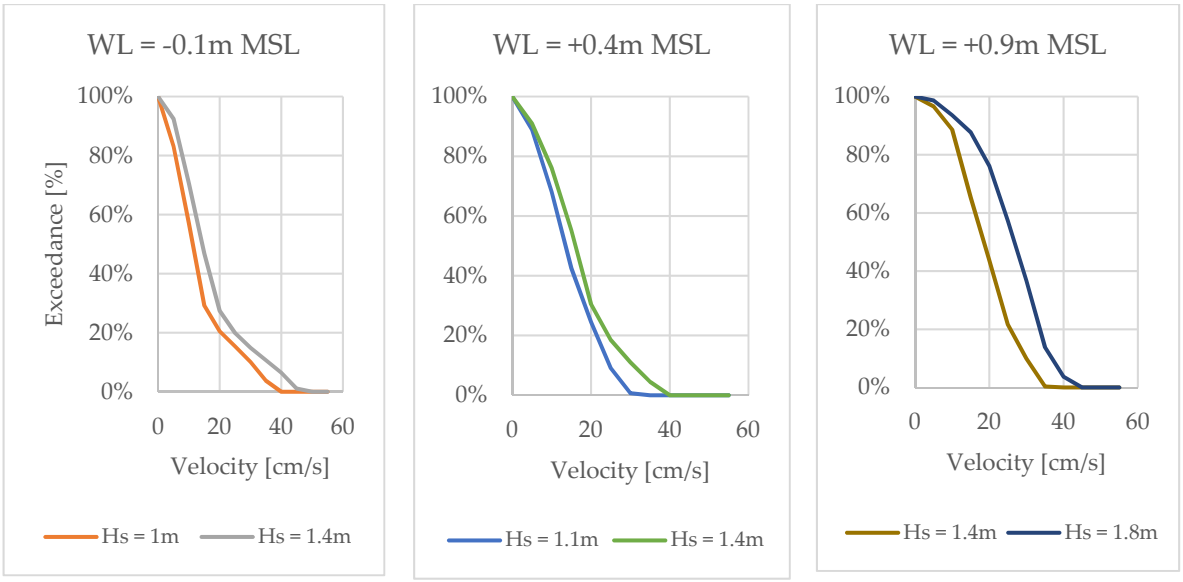

Figure 7-14: Influence of wave height on current velocity distribution

In all three test combinations the trend was clear: the velocities increased with bigger wave heights. This trend agrees well with the radiation stress theory which relates the momentum flux of the wave proportionally to the wave height. Interestingly $\boldsymbol{u}_{(J)}$ showed the most significant increase in velocity at tide levels +0.4 m MSL and +0.9 m MSL, probably due the direct exposure to incoming waves. The trend was also very clear in the exceedance curves, but seemingly more prominent for the larger waves (H_s = 1.4 m compared to H_s = 1.8 m).

7.2.3.3 Influence of wave period

Most of the baseline tests used a 12-second wave period. An 8-second wave period was tested in only one of the baseline simulations, which meant that limited insight could be gained on the influence of wave period on current velocities.

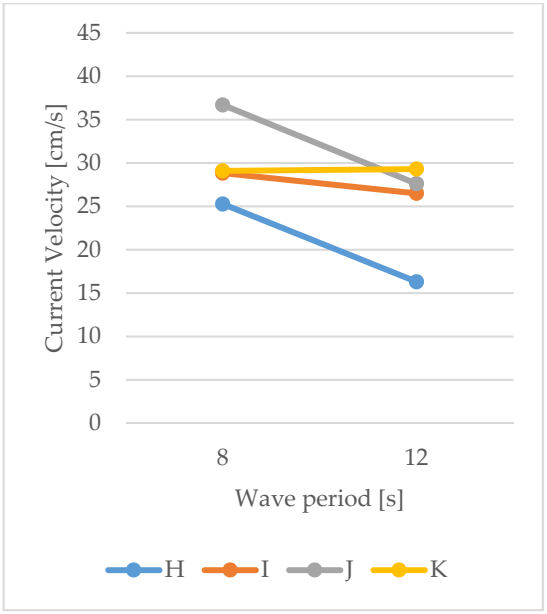

Figure 7-15:Influence of wave period on current velocities for a constant wave height of Hs =1.4 m and water level of +0.4 m MSL

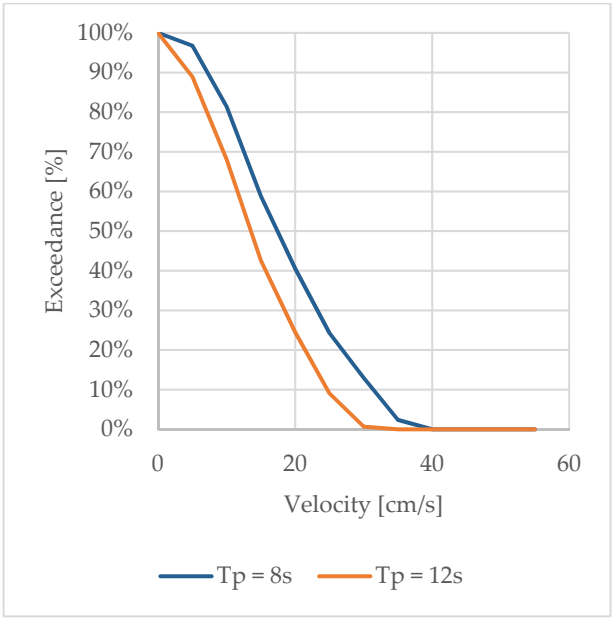

Figure 7-16: Influence of wave period on current velocity distribution for a constant wave height of Hs =1.4 m and water level of +0.4 m

A clear trend was visible in both Figure 7-15 and Figure 7-16: as the wave period increased the current energy decreased. The change was the most prominent for the velocities $\boldsymbol{u}_{(H)}$ and $\boldsymbol{u}_{(J)}$, corresponding to the most wave-sheltered and most wave-exposed areas respectively. $\boldsymbol{u}_{(K)}$ seemed to react oppositely, by increasing slightly with longer wave periods. The results suggest that the shorter waves result in stronger currents, perhaps due to the more frequent wave energy dissipation. However, the total range and amount of wave period-related simulations were too limited to make strong conclusions.

7.3 PROPOSED SOLUTION SIMULATION ANALYSIS

This section will discuss the performance of the proposed solutions by visually and statistically analysing the results of the MBWS simulations. The simulation analysis will be discussed in the respective groups, as set out below.

A. Groynes extending from the beach
B. Modification to the spur
C. Detached breakwater
D. Current-reducing or reflecting structure
E. Combination of the above (A to D)
F. T-groyne off the beach

The full results is set out in Appendix D (individual results) and Appendix F.1 (summary).

7.3.1 Group A: Groynes extending from the northern shoreline or tidal pool

Group A included groynes placed on the beach. The groynes varied in lengths, placement and angles relative to the beach.

Table 7-3: Simulation conditions for Group A

ID	Short Description	Setup Conditions			
		WL [m MSL]	H_s [m]	T_p [s]	Angle [deg]
MT001	*Short groyne opposite spur head.*	0.7	1.5	12	8
MT002	*Long groyne opposite spur head.*	0.7	1.5	12	8
MT003	*Long groyne away from spur head*	0.7	1.5	12	8
MT004	*Dog-legged groyne opposite spur head*	0.7	1.5	12	8
MT007	*Dog-legged groyne off present beach*	0.7	1.5	12	8

7.3.1.1 Visual observations

The groynes reduced the hazard of the current circulation cell by physically separating the bay into two areas: a calm, sheltered area and an energetic, wave-exposed area. The groyne significantly reduced the incoming waves (mostly spur-diffracted waves) in the sheltered area, thus reducing the energy to generate wave-induced currents. In the wave-exposed area a strong circulation was still present, confined between the new groyne and existing groyne. This generalised pattern is illustrated in Figure 7-17 below.

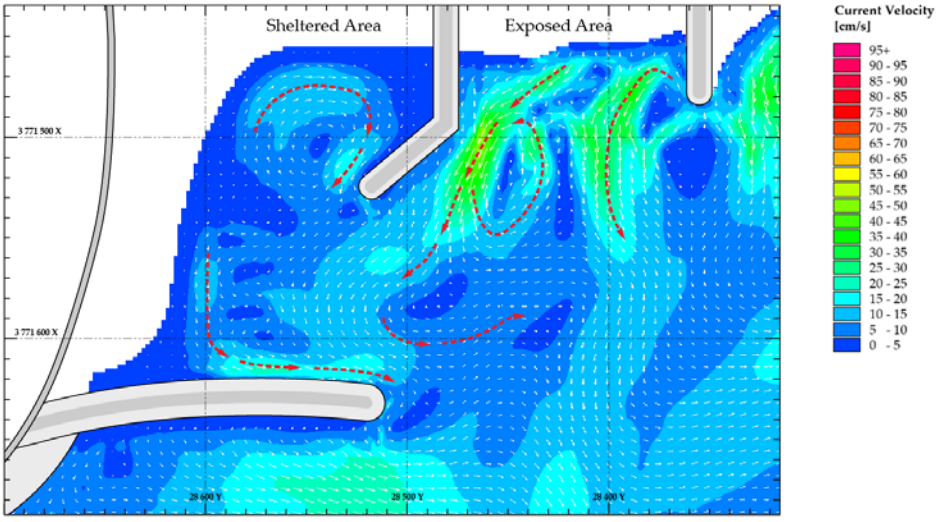

*Figure 7-17: Typical circulation pattern comparison of the sheltered and exposed areas. (**MT004**: H_s = 1.5 m, T_p = 12 s, WL = +0.7 m MSL)*

The sheltered area was only partially protected against incoming waves, which meant that weak circulation cells still developed. It was also noticed that circulation patterns from the sheltered and exposed areas were somewhat intermixed, which allowed the circulation current originating from the exposed area to strengthen the exit current from the sheltered bay to a certain degree. This pattern was the most prominent for the scenario of the *dog-legged groyne opposite spur head* (**MT004**), and is clearly visible in Figure 7-17 above.

7.3.1.2 Statistical Analysis

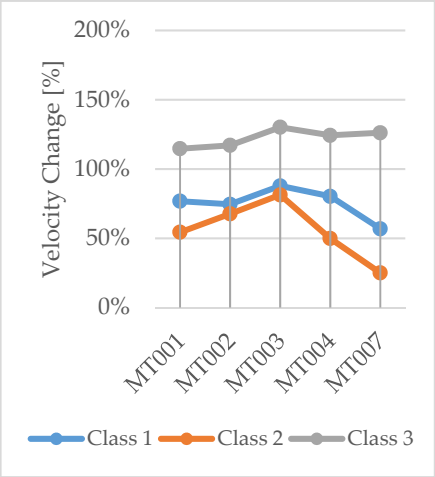

Figure 7-18: Baseline relative (U_r) velocities for Group A

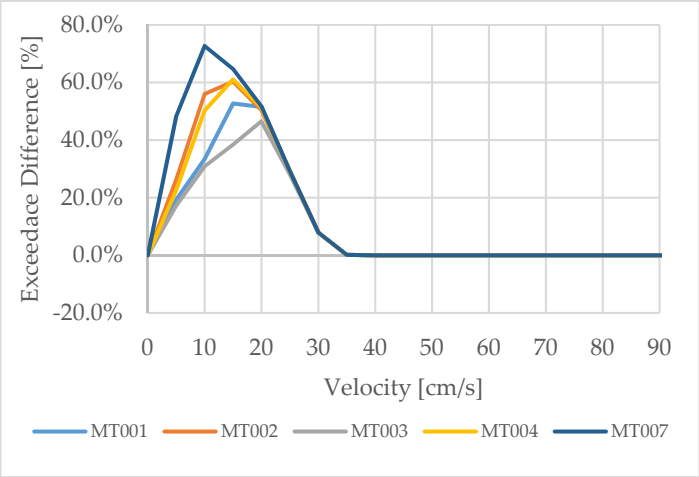

Figure 7-19: Designated swimming area exceedance difference curves for Group A

The quantitative results of Group A were relatively consistent. The *Class 1* and *Class 2* velocities were reduced by a fair amount for all of the Group A simulations. The *dog-legged groyne* (**MT007**) showed the most promising results with the velocity along the spur reduced to $\boldsymbol{U_{r(C1)} = 57\%}$, and the secondary velocity reduced considerably to $\boldsymbol{U_{r(C2)} = 25\%}$,

The designated swimming areas for the groyne configurations were noticeably calm. The *dog-legged groyne* (**MT007**) again showed the most promising results with the highest positive change to the exceedance curve.

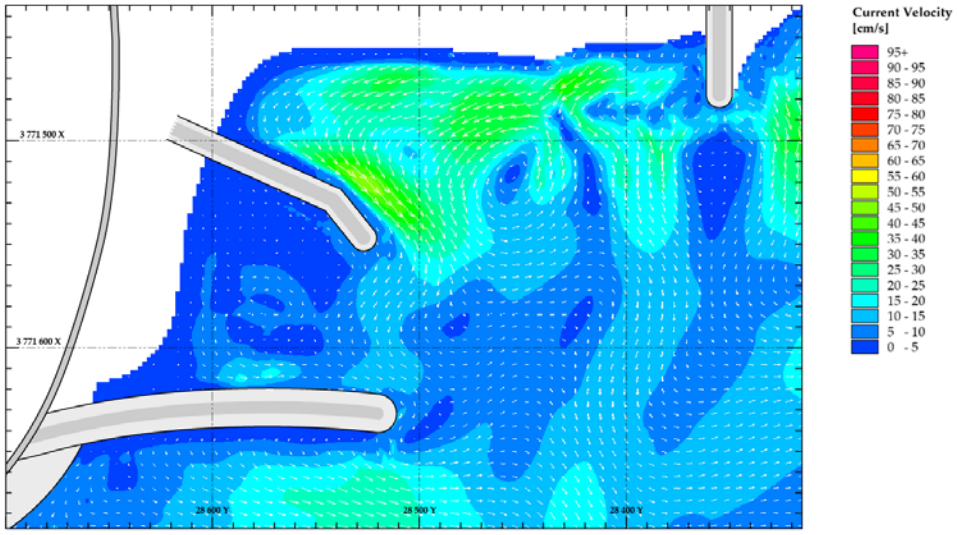

*Figure 7-20: Current circulation pattern from **MT007**, the most successful configuration from Group A*

7.3.2 Group B: Modification to the spur

Group B included modifications to the spur by the addition of extensions to the spur, reducing the crest height or creating a complete gap through the spur.

Table 7-4: Simulation conditions for Group B

ID	Short Description	Setup Conditions			
		WL [m MSL]	H_s [m]	T_p [s]	Angle [deg]
MT005	*Dog-legged spur off spur head (landward)*	0.7	1.5	12	8
MT006	*Spur off spur head (seaward)*	0.7	1.5	12	8
MT008	*Lowered end of spur*	0.4	1.4	12	8
MT009	*Gap through spur (west section)*	0.7	1.5	12	8

7.3.2.1 Visual observations

7.3.2.1.1 Extensions to the spur

Modifications to the spur had mostly adverse effects. The extensions to the spur (**MT005** & **MT006**) caused the velocity along the spur to increase even further, resulting in an overall stronger and more coherent circulation in the bay. The extensions to the spur only marginally reduced the incoming wave energy which meant that the longshore current in the bay was not significantly affected. The lee of the spur was more sheltered against diffracted waves, allowing the velocity along the spur to increase, with less resistance from incoming waves. This is illustrated in Figure 7-21.

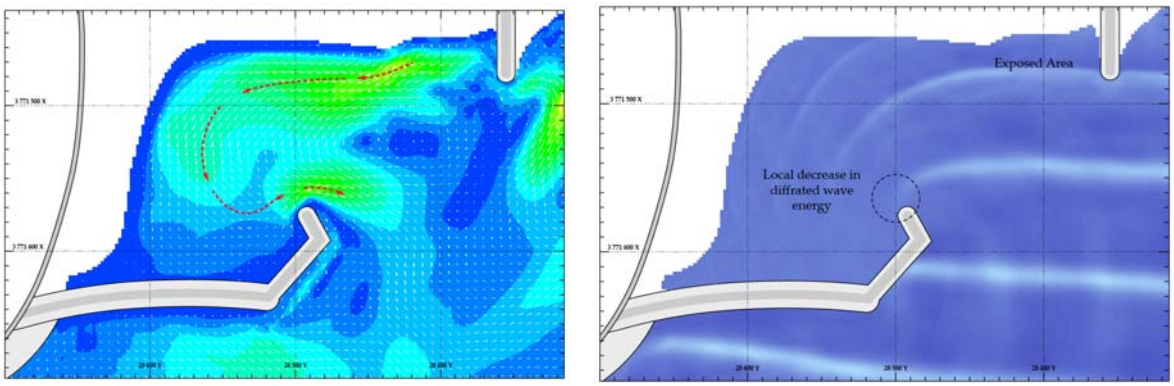

Figure 7-21 Comparison of circulation pattern (left) and incoming waves (right) for the spur-extension scenario
*(**MT006**: H_s = 1.5 m, T_p = 12 s, WL = +0.7 m MSL)*

7.3.2.1.2 Lowered end of spur

The *lowered spur head* (**MT008**) did not simulate successfully. This was the first of the "wave overtopping models". The lowered crest did not effectively simulate the wave overtopping, which allowed for an excessive amount of wave energy to enter the bay. The excessive wave energy reversed the current direction into a very strong, clockwise circulation (Figure 7-22). This extreme result was attributed to a model setup error. The extremes could have been reduced by artificially dampening the overtopping energy by means of a friction or porosity coefficient. To correctly model overtopping is a difficult task which relies on experience and extensive calibration data, and could very well be a study of its own. This complexity was considered outside the scope of this study.

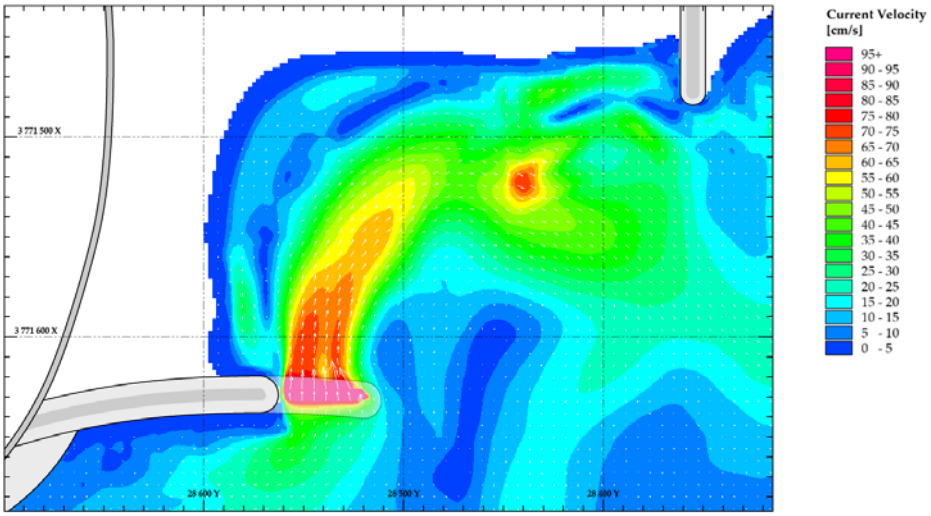

Figure 7-22: The extreme current circulation pattern from lowered-spur crest simulation
*(**MT008**: H_s = 1.4 m, T_p = 12 s, WL = +0.4 m MSL)*

7.3.2.1.3 Gap through the spur

The opening in the spur (**MT009**) diffused the flow along the spur, but did not resolve the hazardous circulation. The longshore current was still obstructed by the spur, but was split in two directions: the one current flowing southbound exiting the bay through the hole, and the other current forced into deeper water in an easterly direction. The strongest exit current

occurred at the concentrated exit point through the hole through the spur, but was somewhat weaker than the original current due to the direct exposure of incoming waves.

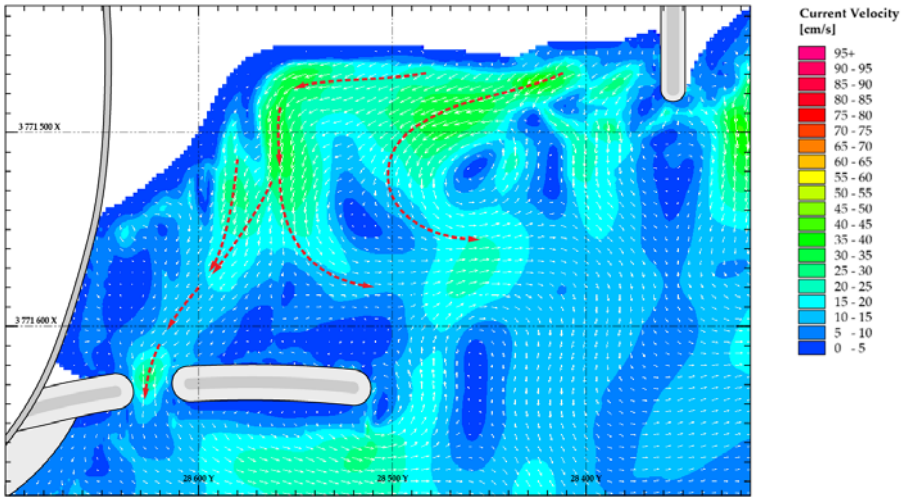

*Figure 7-23: Circulation pattern for the gap-through-spur simulation (**MT009**: H_s = 1.5 m, T_p = 12 s, WL = +0.7 m MSL)*

7.3.2.2 *Statistical Analysis*

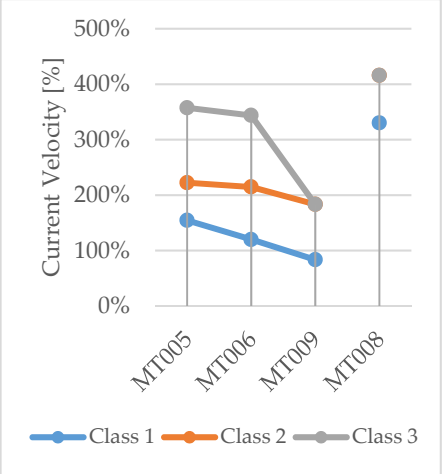

Figure 7-24: Baseline relative (U_r) velocities for Group B

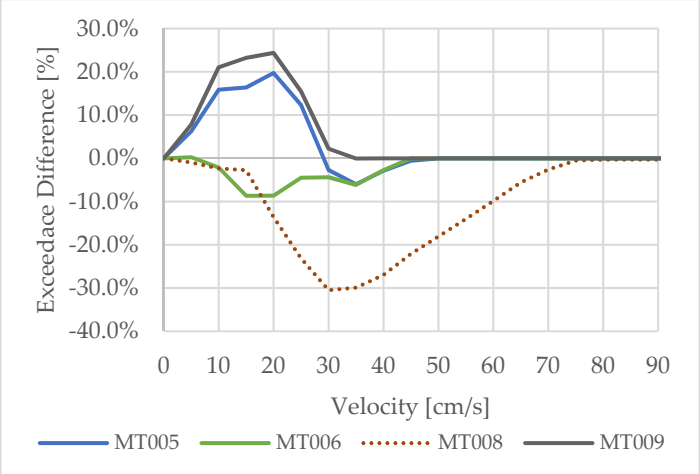

Figure 7-25: Designated swimming area exceedance difference curves for Group B

The results of Group B were not very promising. The *spur-extension* configurations (**MT005** and **MT006**) resulted in a noticeable increase for all of the relative baseline velocities ($\boldsymbol{U_r}$) of *Class 1*, *Class 2* and *Class 3*. The *landward extension to the spur* (**MT005**) created a sheltered area (see Figure 7-21), which is also statistically evident by the positive increase of the area-velocity distribution relative to the baseline. This contrast between the velocity at the spur and the area-velocity distribution is particularly dangerous to bathers as the sheltered designated swimming area may provide a false impression of safety. The *gap-through-the-spur* configuration (**MT009**) only slightly reduced exit velocity to $\boldsymbol{U_{r(C1)}}$ **= 84%.** The designated swimming area were also somewhat safer relative to the baseline condition.

*Note the extremely high velocities for the lowered spur crest (**MT008**) were most likely due to unsuccessful modelling of wave overtopping action.*

7.3.3 Group C: detached breakwater

There was only one configuration for Group C: a detached breakwater placed inside the bay, roughly aligned parallel to the incoming waves.

Table 7-5: Simulation conditions for Group C

ID	Short Description	Setup Conditions			
		WL [m MSL]	H_s [m]	T_p [s]	Angle [deg]
MT010	*Detached breakwater in bay*	0.4	1.4	12	8

7.3.3.1 Visual observations

Overall the detached breakwater worsened the hydrodynamics. The smaller circulation cell was "compressed" by the breakwater, resulting in a stronger, concentrated circulation pattern (Point A in Figure 7-26, left).

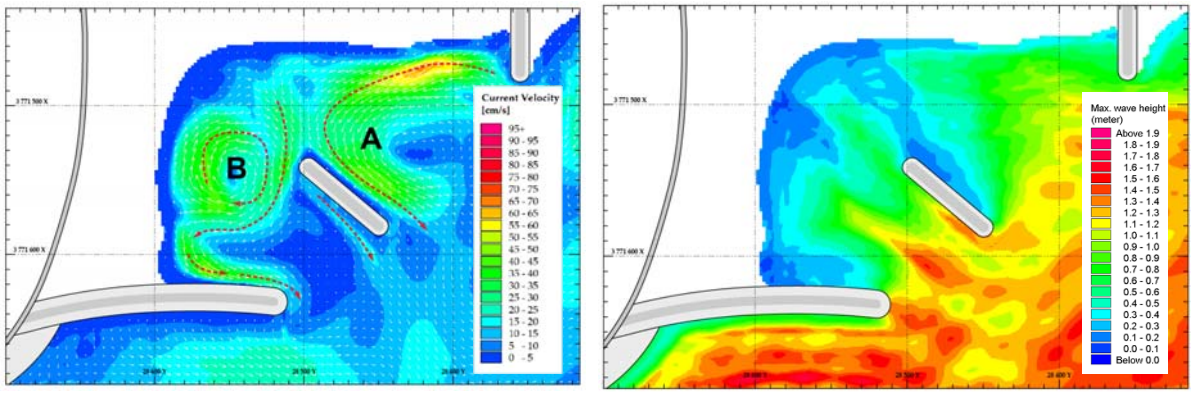

Figure 7-26: Circulation pattern compared to the wave height distribution for the detached breakwater simulation.
*(**MT010**: H_s = 1.4 m, T_p = 12 s, WL = +0.4 m MSL)*

The waves entering the bay between the spur and detached breakwater were reflected in the direction of the beach, thus increasing the wave energy and consequently the longshore current velocity. A small, albeit strong clockwise circulation pattern developed in this area (Point B in Figure 7-26, left), driven by the reflected wave energy and partially by the circulation pattern from the exposed area. The increase in wave energy also strengthened the current along the spur.

7.3.3.2 *Statistical analysis*

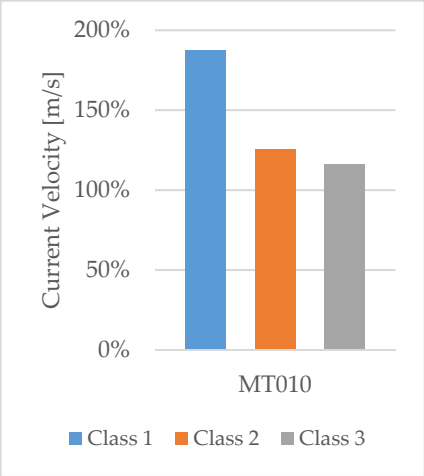

Figure 7-27: Baseline relative (U_r) velocities for Group C

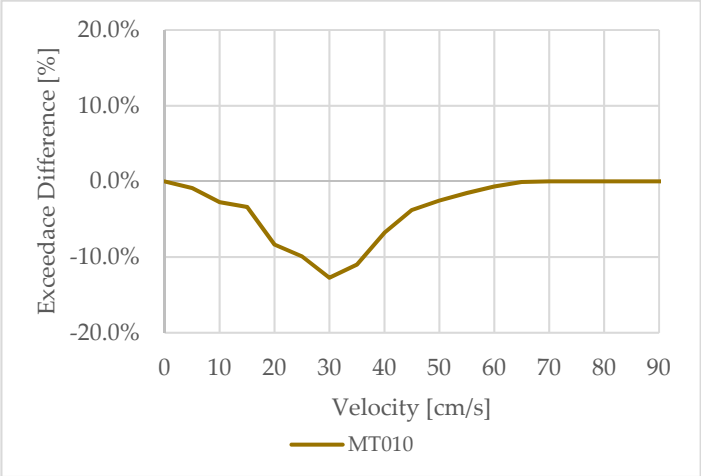

Figure 7-28: Designated swimming area exceedance difference curve for Group C

The increase in wave energy resulted in a significant increase of current velocities. The velocity along the spur (Class 1) was almost doubled, with a relative velocity of $\boldsymbol{U_{r(C1)} = 187\%}$. The secondary peak current (Class 2) in the bay was also relatively high, with an increased velocity of $\boldsymbol{U_{r(C2)} = 125\%}$. The exceedance difference curve (Figure 7-28) also clearly showed an overall increase of current energy in the swimming bay, indicating more dangerous swimming conditions relative to the present situation.

7.3.4 Group D: current deflecting structures

There was only one configuration for Group D: a locally raised bed level inside the embayment, at the head of the spur. The bed level was raised to -0.5m MSL.

Table 7-6: Simulation conditions for Group D

ID	Short Description	Setup Conditions			
		WL [m MSL]	H_s [m]	T_p [s]	Angle [deg]
MT011	*Raised bed level at spur head*	0.7	1.5	12	8

7.3.4.1 *Visual Observations*

The raised bathymetry deflected the current away from the spur in a northern direction. Initially, the deflection process appeared similar to the simulation of the *landward spur-extension* (**MT005**). Further inspection revealed that the primary cause was breaking waves on the raised bed level area. The relatively low water level induced wave breaking (visible by the white in Figure 7-29-left below). The localised dissipation of energy led to wave-induced currents off the raised bed level. The direction of the new current was probably influenced by the pre-existing circulation pattern which forced and strengthened the new current in a northerly direction.

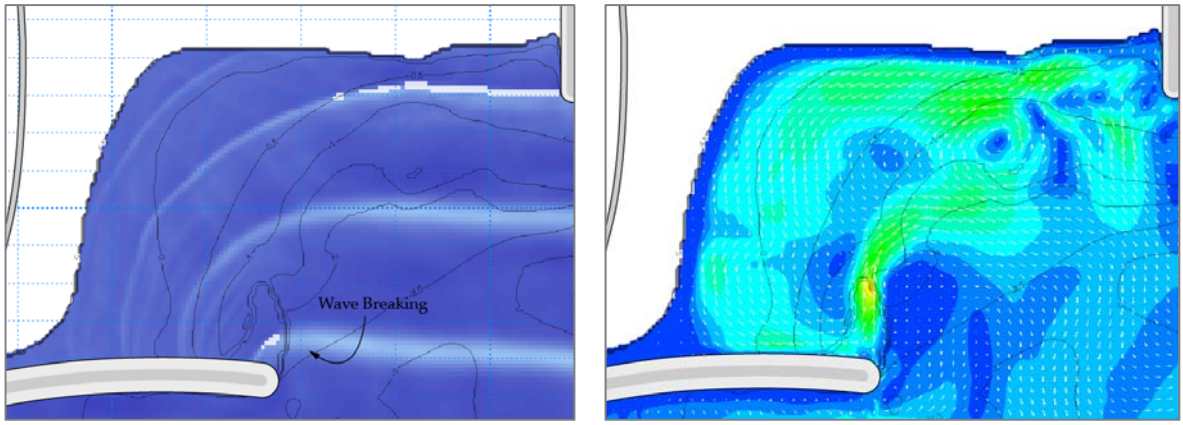

Figure 7-29: Comparison of wave breaking on the raised bathymetry plane (left) to the circulation pattern (right)
*(**MT011**: H_s = 1.5 m, T_p = 12 s, WL = +0.7 m MSL)*

7.3.4.2 *Statistical analysis*

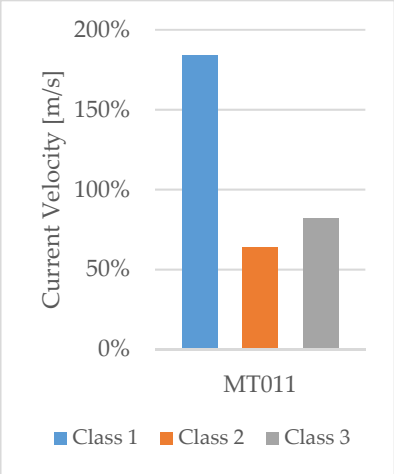

Figure 7-30: Baseline relative (U_r) velocities for Group D

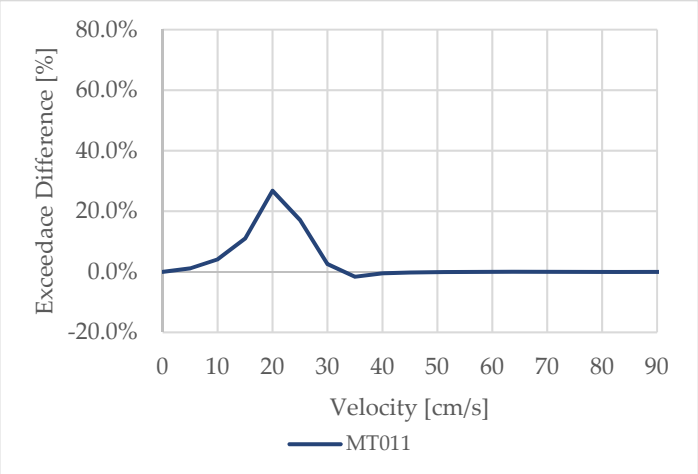

Figure 7-31: Designated swimming area exceedance difference curve for Group D

The wave breaking on the *raised bed level* caused the velocity off the spur (*Class 1*) to almost double ($\boldsymbol{U_{r(C1)}}$ **= 184**%). Interestingly, in the rest of the swimming area, the peak velocities were reduced (Class 2 velocity to $\boldsymbol{U_{r(C2)}}$ **= 64**%) and the designated swimming area, was calmer relative to the baseline conditions. This dangerous contrast between the calm bay and strong current off the spur presents a false impression of safety, similar to the *landward extension to the spur* (**MT005**).

7.3.5 Group E: structural combination of Groups A to D

The structural combinations for Group E included the addition of a groyne off the beach, with a modification to the spur (lowered crest or complete gap).

Table 7-7: Simulation conditions for Group E

ID	Short Description	Setup Conditions			
		WL [m MSL]	H_s [m]	T_p [s]	Angle [deg]
MT012	*Gap through spur (west section) with groyne off beach*	0.3	1.3	12	8
MT013	*Gap through spur (west section) with groyne off beach*	-0.3	1.3	12	8
MT014	*Lowered section in spur (east) with groyne off beach*	0.3	1.3	12	8
MT015	*Lowered section in spur (east) with groyne off beach*	-0.3	1.3	12	8

7.3.5.1 Visual observations

7.3.5.1.1 Gap through spur (west section) with groyne off beach

For the higher tide level, the addition of the new groyne extending from the beach confined the large circulation pattern between the two groynes. This groyne reduced the exit current through the gap in the spur to a larger extent than in the preceding *gap-through-spur* simulation (**MT009**). For the lower tide level, the groyne had less of an effect, which allowed the circulation to strengthen the current along the beach and past the head of the spur.

Interestingly, in the high tide condition a small circulation pattern developed near the head of the detached spur (Figure 7-32, left). During low tides this circulation disappeared, with a strong current flowing past the head of the spur (Figure 7-32, right). This small clockwise pattern may have been influenced by the cusp in the lee of the spur, combined with the wave energy entering through the spur-gap. Note that the bathymetry appear to be different between the two tides, but this apparent effect was only caused by the emerging sand bank in the lee of the detached-spur section.

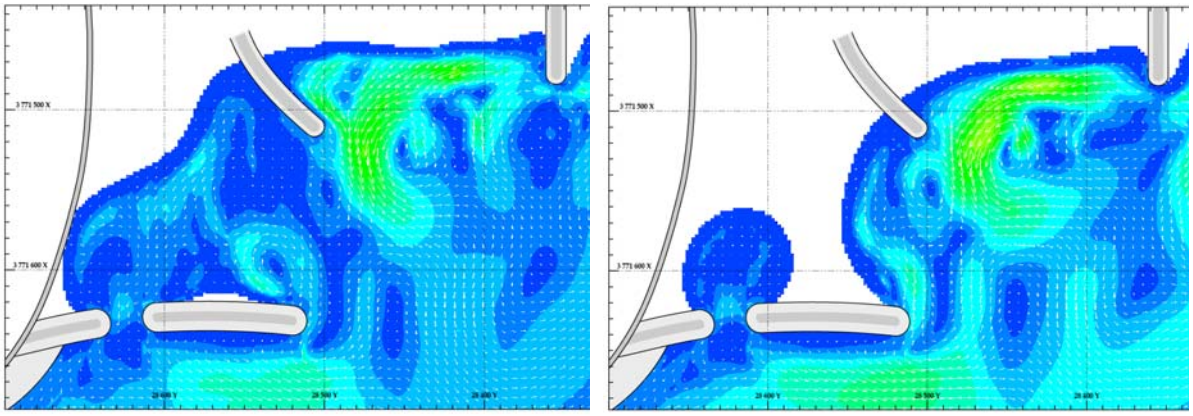

*Figure 7-32: Comparison of circulation patterns for the higher tide (**MT012**, left) and lower tide (**MT013**, right)*

7.3.5.1.2 Lowered section in spur (east) with groyne off beach

Similar to the *lowered spur head* (**MT008**), the l*owered section in spur (east) with groyne off beach* (**MT014** and **MT015**) did not simulate successfully probably due to setup error, and the results were therefore also unreliable. The results of **MT014** and **MT015** are therefore not sufficient for an analysis, but the results are presented in Appendix D.

7.3.5.2 *Statistical analysis*

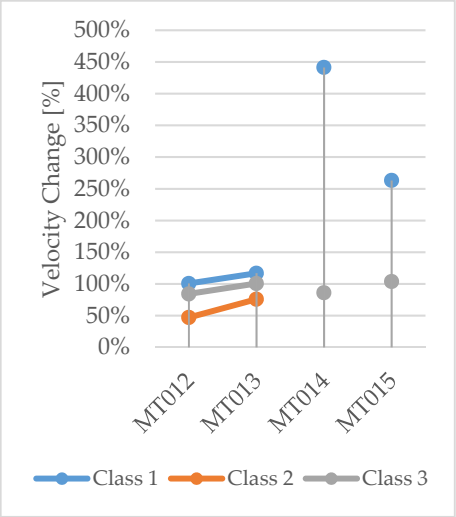

Figure 7-33: Baseline relative (U_r) velocities for Group E

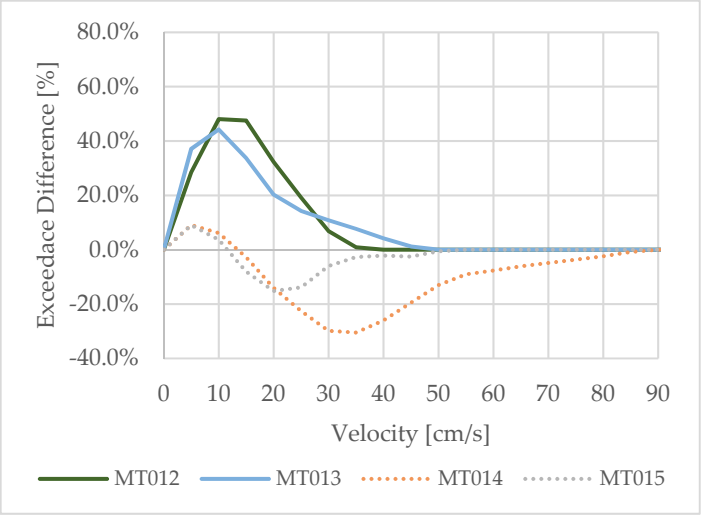

Figure 7-34: Designated swimming area exceedance difference curve for Group E

The combination of a *gap in spur section with a groyne off beach* (**MT012** and **MT013**) was unsuccessful in reducing the dangerous exit velocity (*Class 1*), with an average increased relative baseline velocity of $\boldsymbol{U_{r(C1)} = 117\%}$. The rest of the bay appeared to be safer, with reduced Class 2 velocities ($\boldsymbol{U_{r(C2)} = 62\%}$) and a significantly calmer designated swimming area. The contrast between the calmer bay and strong exit velocities once again presented the danger of false safety, similar to **MT005** and **MT011**, but with less of a contrast between the velocities.

*Note the extremely high velocities for the lowered spur crest configurations (**MT014** & **MT015**) are believed to be due to the unsuccessful modelling of wave overtopping action.*

7.3.6 Group F: T-groyne structures

Group F included only T-shaped groyne structures. The tested wave and tidal conditions are more emphasised for the T-groyne models, as the same structural modification and layout were used in each simulation run. The additional configurations provide more insight on how the T-groyne performed under a variety of environmental conditions.

Table 7-8: Simulation conditions for Group F

ID	Short Description	Setup Conditions			
		WL [m MSL]	H_s [m]	T_P [s]	Angle [deg]
MT016	*T-groyne off beach*	0.45	1.4	12	8
MT017	*T-groyne off beach*	0.9	1.4	12	8
MT018	*T-groyne off beach*	0.9	1.8	12	8
MT019	*T-groyne off beach*	-0.1	1	12	8
MT020	*T-groyne off beach*	-0.1	1.4	12	8
MT021	*T-groyne off beach*	0.4	1.1	12	8
MT022	*T-groyne off beach*	0.4	1.4	8	8
MT023	*T-groyne off beach (built-up beach)*	0.4	1.4	12	8
MT024	*T-groyne off beach (denuded beach)*	0.4	1.4	12	8

7.3.6.1 Visual observations

All of the T-groyne models performed consistently, with similar current patterns identifiable across all nine of the T-groyne tests. The T-groyne divided the bay into two sections, an exposed bay (north-east) and a sheltered bay (south-west), very similar to the Group A simulations.

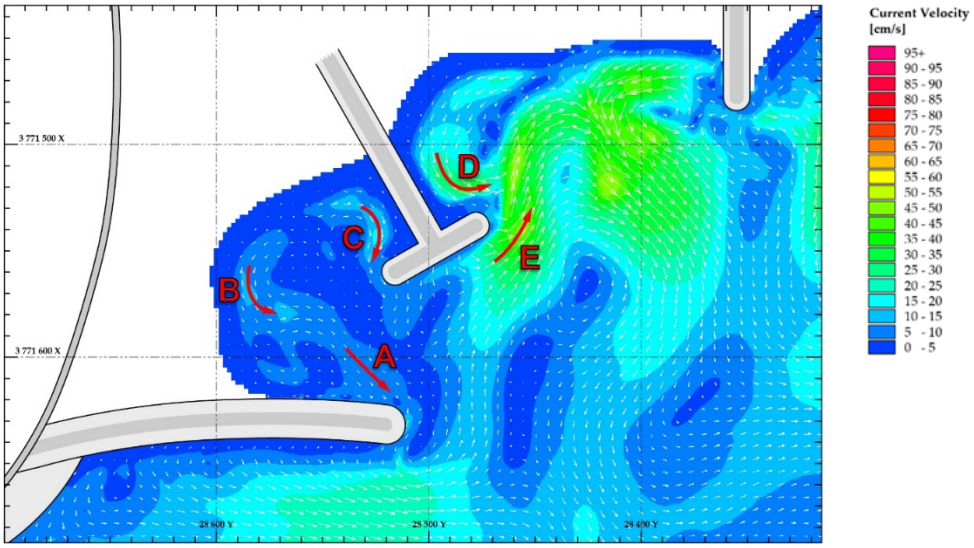

Figure 7-35: Typical circulation pattern and peak velocities occurrences for all the T-groyne simulations

7.3.6.1.1 Sheltered bay

The sheltered bay was notably calm with some weak flow currents evident in a few of the simulations. The strongest current usually occurred in the sheltered area behind the flanges of the T-groyne. The cause of this current could be explained by the current-groyne interaction as discussed in the literature study (§ 4.1.11.2.2). The incoming waves diffracted around the spur, allowing for limited wave action into the sheltered bay. The flanges of the T-groyne diffracted the waves again (Figure 7-36, left), causing a steep variation of wave setup close to the T-groyne, (Figure 7-36, middle), which resulted in a current along the T-groyne (red zone in Figure 7-36, right).

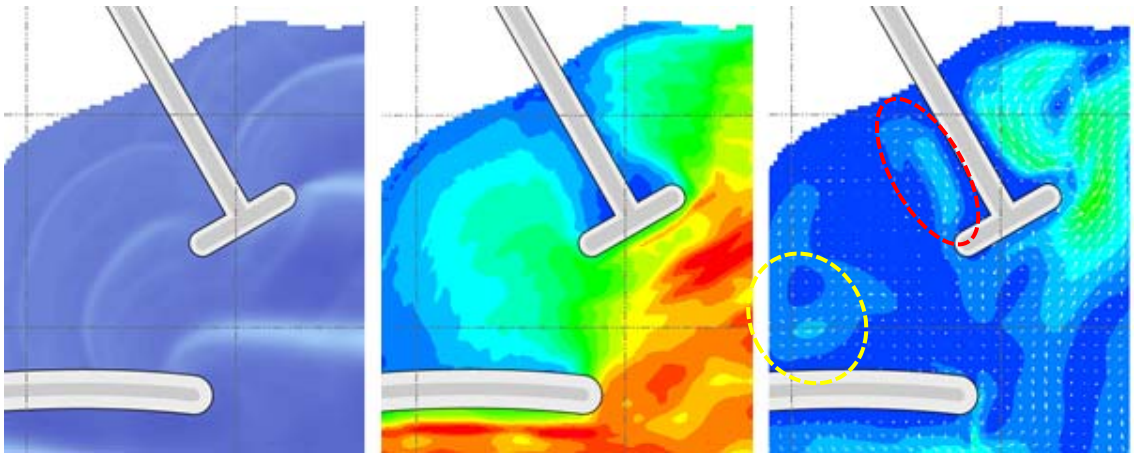

Figure 7-36: Instantaneous surface elevation illustrating diffraction processes (left), wave height distribution (middle) and current circulation pattern (right)
*(**MT017**: H_s = 1.4 m, T_p = 12 s, WL = +0.9 m MSL).*

The same process of diffraction wave setup gradient also caused other small velocity peaks in some models (yellow-zone in Figure 7-36, right). The wave setup gradient was not as concentrated in those areas, allowing for a wider and weak flow.

7.3.6.1.2 Exposed bay

The exposed bay was subject to a strong clockwise circulation pattern with two feeder currents from both sides of the T-groyne head. The southern feeder (Figure 7-35, Point E) was caused by the wave energy dissipation by breaking waves at the head of the T-groyne. The northern feeder (Figure 7-35, Point D) originated from the sheltered area behind the flange of the T-groyne, causing a current in a process similar to the sheltered bay.

It is interesting that this circulation is in an opposite direction than the circulation observed in Group A. The new bathymetry might have influenced the direction, but the most probable cause is the combination of the two feeder currents forcing the circulation in an opposite direction.

7.3.6.2 Statistical analysis

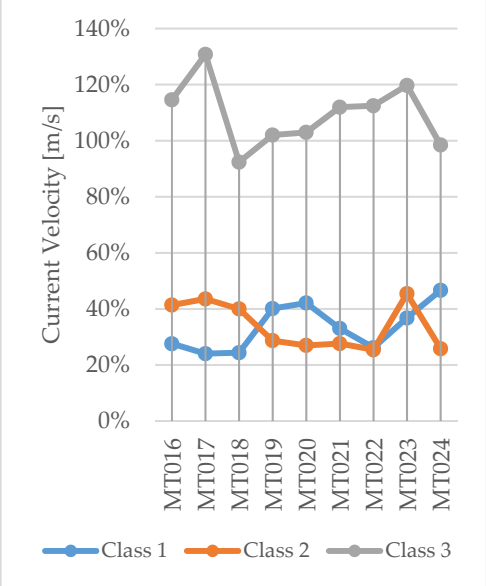

Figure 7-37: Baseline relative (U_r) velocities for Group F

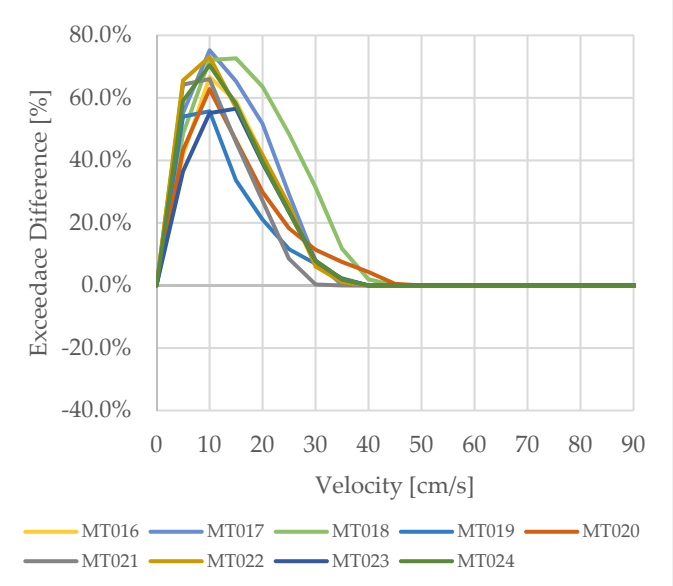

Figure 7-38: Designated swimming area exceedance difference curve for Group F

The T-groyne configurations showed a clear success in reducing the velocities within the sheltered bay for a variety of tide, wave and bathymetric conditions. The current along the spur (*Class 1*) were drastically reduced with an average relative baseline velocity of $\boldsymbol{U_{r(C1)} = 33\%}$. The secondary currents within the sheltered bay were equally reduced to an average relative baseline velocity of $\boldsymbol{U_{r(C2)} = 34\%}$. The designated swimming area was also noticeably safer relative to the baseline condition, evident by the positive exceedance difference curves. The wave-exposed bay (*Class 3*), however, saw an small increase of relative baseline average velocity: $\boldsymbol{U_{r(C3)} = 109\%}$.

7.3.6.3 Influence of environmental variables

A total of nine T-groyne configurations were tested with a variety of tide levels, wave heights, wave periods or beach profile configurations (refer to Table 7-8). Combinations could be paired from these nine configurations, where all the tested environmental conditions are the

same with the exception of one variable. The influence of the variable was studied by analysing the change of the peak current velocities and area velocity distribution. The four isolated variables are:

- Water level
- Wave height
- Wave period
- Beach configuration

The process is very similar to the baseline-variable study in § 7.2.3. With nine models and four variables, some combinations will only have a limited combination of two configurations to test the influence of the environmental variable. The conclusions that can be drawn from this analysis are therefore limited.

The T-groyne configurations and absolute velocity measurements (u) are listed in Table 7-9. Absolute velocities were used in this analysis without the velocity class system. The velocities $u_{(A)}$, $u_{(B)}$, $u_{(C)}$, $u_{(D)}$ and $u_{(E)}$ were consistently measured in the same vicinities as noted in Figure 7-35. It should be noted that the velocity distribution was limited to the designated swimming area only, and thus only reflected the velocity distribution of the sheltered area confined between the spur and T-groyne.

Table 7-9: Summary of T-groyne U_{PA30} velocities, measured at the consistent current peaks

ID	Setup Conditions			Velocity [cm/s]				
	WL [m MSL]	H_s [m]	T_p [s]	$u_{(A)}$	$u_{(B)}$	$u_{(C)}$	$u_{(D)}$	$u_{(E)}$
MT016	0.45	1.4	12	6.7	9.6	12.9	28.0	40.9
MT017	0.9	1.4	12	5.7	10.1	13.1	25.5	35.2
MT018	0.9	1.8	12	8.5	12.2	14.7	25.1	38.8
MT019	-0.1	1	12	6.1	5.6	7.5	14.7	39.0
MT020	-0.1	1.4	12	8.9	6.5	8.5	14.1	44.9
MT021	0.4	1.1	12	5.4	6.0	8.1	24.4	30.9
MT022	0.4	1.4	8	6.6	7.4	4.5	20.1	41.3
MT023*	0.4	1.4	12	8.1	11.3	14.7	27.6	44.6
MT024*	0.4	1.4	12	10.3	8.3	7.6	36.7	16.6

**Simulations with alternative beach configurations*

7.3.6.3.1 Influence of water/tide level

There were five configurations with H_s = 1.4 m, T_p = 12 s. Two of the five configurations included alternative beach configurations. The remaining three were used to study the effect of water level change on the velocities. Figure 7-39 and Figure 7-40 show the influence of the varying water levels on the velocity magnitude and area distribution respectively.

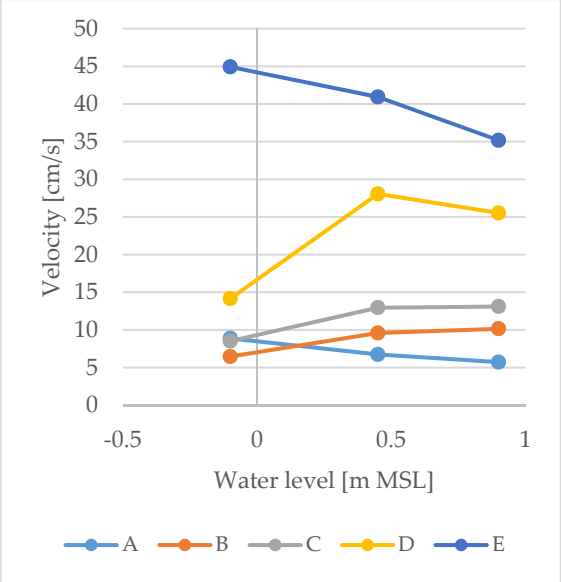

Figure 7-39: Influence of water/tide level on current velocities for a constant wave height of Hs =1.4 m

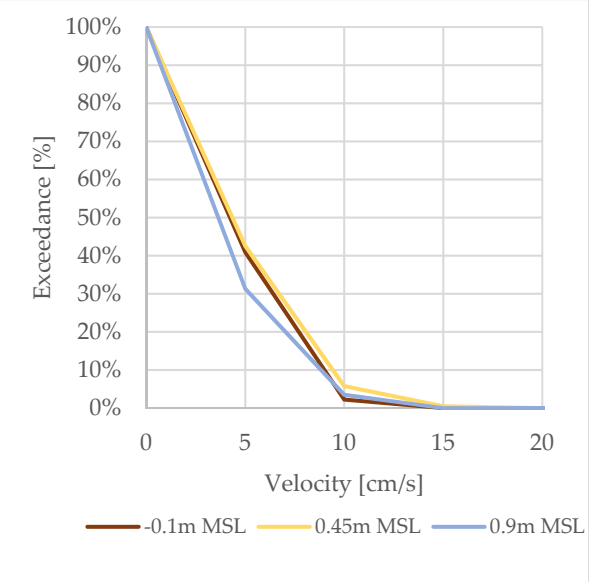

Figure 7-40: Influence of water/tide level on current velocity distribution for a constant wave height of Hs = 1.4 m

The individual velocity measurements (Figure 7-39) showed varying changes to the different tide levels. An increasing water level resulted in stronger currents in some areas and weaker currents in other areas. The overall area velocity distribution also did not show any clear trend, with relatively minimal deviation between the varying water levels.

The varying effect of the tide level could be explained by the indirect effects of varying water levels. Wave breaking is induced by depth limitation which is proportional to the changing water depth. The velocities are dependent on the combined effect of water level variation and the nearby topographic/bathymetric properties.

Some areas will react differently to tide level variations, based on their position. The specific wave height relative to the tide level will further influence the dynamics.

7.3.6.3.2 Influence of Wave Height

There were two pairs of setup configurations with similar setup conditions but varying wave heights. The water level differed for the two pairs, which meant that they had to be compared separately. Figure 7-41 and Figure 7-42 below show the influence of the varying wave heights on the velocity magnitude and area distribution respectively.

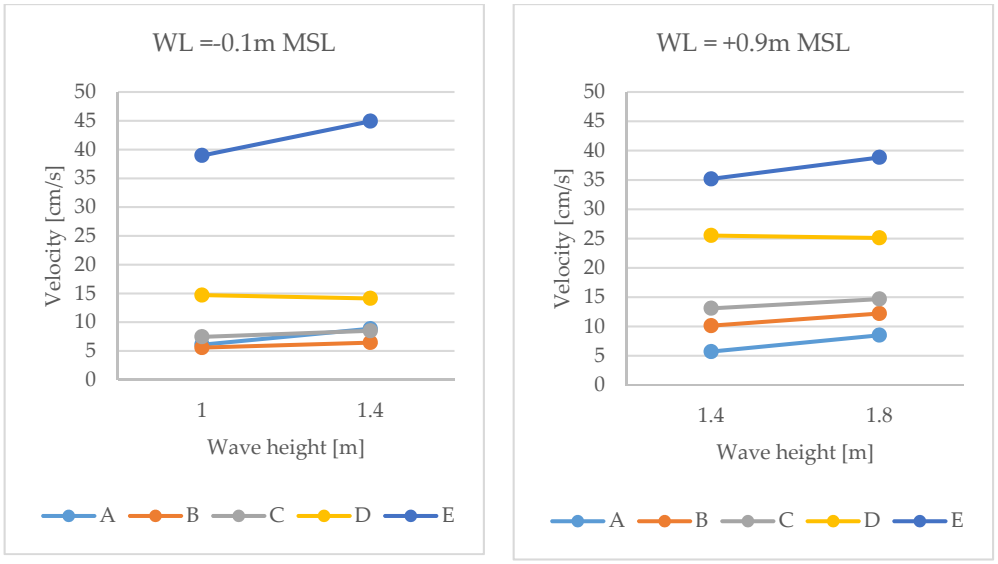

Figure 7-41: Influence of wave height on current velocities

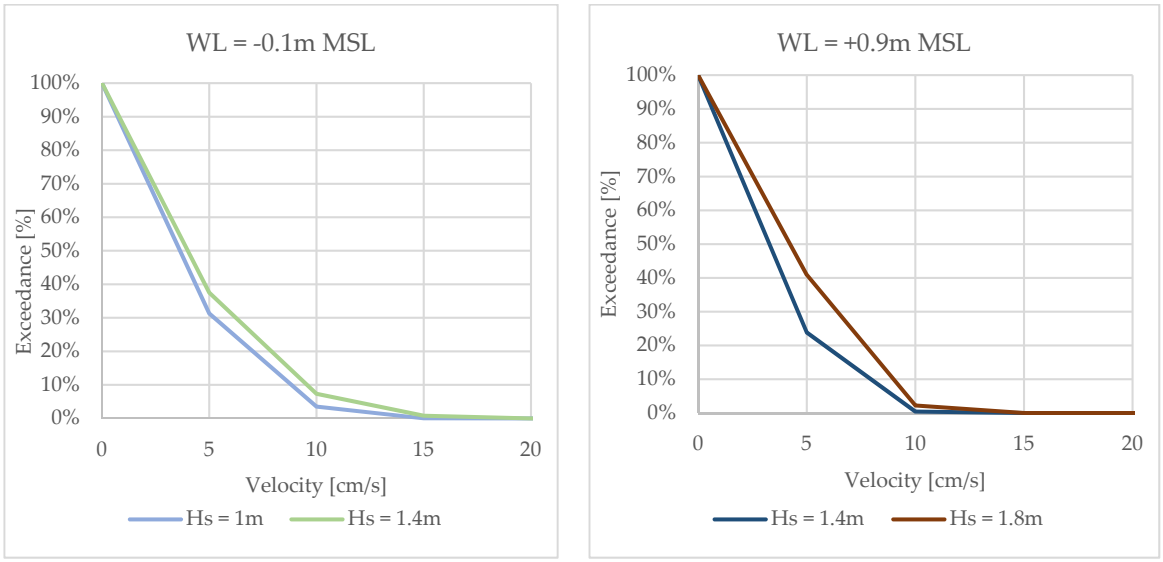

Figure 7-42: Influence of wave height on current velocity distribution

A similar trend was visible in both of the configuration pairs: all the velocities (with the exception of $\boldsymbol{u}_{(\boldsymbol{D})}$) increased with larger waves, as expected. The ratio of increase was not the same for all velocities, and was probably related to the position of the measuring-vector relative to the bathymetry and wave exposure. Interestingly, $\boldsymbol{u}_{(\boldsymbol{D})}$ showed a slight decrease in velocity. The change was very small, which made it difficult to hypothesise the cause for the decrease. One possibility was that the orientation of $\boldsymbol{u}_{(\boldsymbol{D})}$ against incoming waves could mean that the larger waves would slow down the current to an extent. The tests were too limited to make any definite conclusions.

The average increase of velocity was also very evident in the area velocity exceedance curves, with both curves illustrating the increase of the area velocity distribution proportional to an increase of wave height. This trend agrees well with the radiation stress theory which relates the momentum flux of a wave proportionally to the wave height.

7.3.6.3.3 Influence of wave period

Most of the T-groyne configurations used a 12-second wave period. An 8-second wave period was tested in only one of the T-groyne options, which meant that limited insight could be gained on the influence of wave period on current velocities.

Figure 7-43 and Figure 7-44 show the influence of the wave period on the velocity magnitude and area distribution respectively.

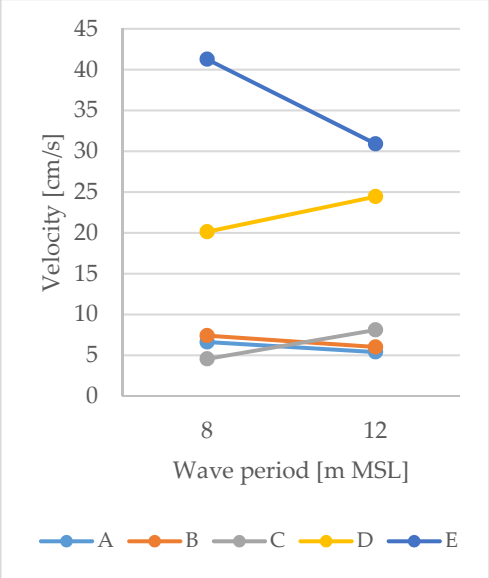

Figure 7-43: Influence of wave period on current velocities for a constant wave height of Hs =1.4 m and water level of +0.4 m MSL

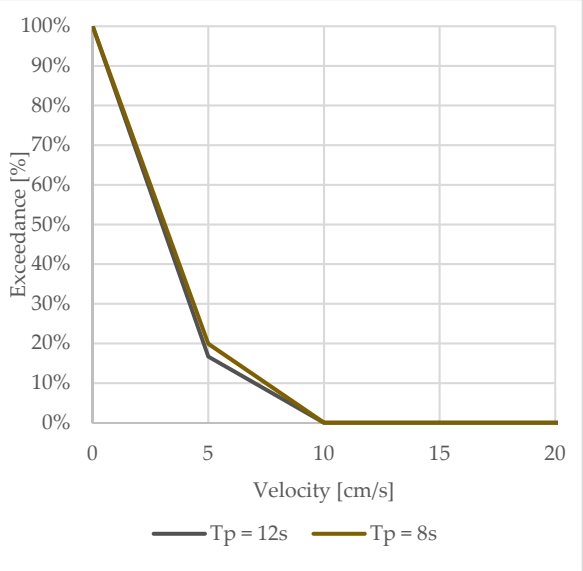

Figure 7-44: Influence of wave period on current velocity distribution for a constant wave height of Hs =1.4 m and water level of +0.4 m

There was no strong evidence for a specific trend in the U_{PA30} velocities (Figure 7-43). The effects were varying at the different measuring points. The sheltered area ($\boldsymbol{u}_{(A)}$,$\boldsymbol{u}_{(B)}$, and $\boldsymbol{u}_{(C)}$) was influenced less than the exposed area ($\boldsymbol{u}_{(D)}$ and $\boldsymbol{u}_{(E)}$). $\boldsymbol{u}_{(D)}$ and $\boldsymbol{u}_{(E)}$ were affected oppositely, with $\boldsymbol{u}_{(D)}$ slightly increasing and $\boldsymbol{u}_{(E)}$ showing a stronger decrease with longer wave periods. This trend is fairly similar to the observations from the decrease in wave height. The results suggest that the shorter waves result in stronger currents, perhaps due to the more frequent wave energy dissipation.

This is further evident in the exceedance curves (Figure 7-44) where shorter waves caused a slight increase in current energy. It should be reiterated the total range and amount of wave period-related simulations were too limited to make any substantial conclusions.

7.3.6.3.4 Influence of beach configuration

There were two models with different beach configurations and similar wave and tide conditions. The one model had a smaller, but longer beach (denuded) while the other had a larger, but shorter beach (built-up) in comparison to the rest of the T-groyne configurations. There was no "normal"-beach configuration T-groyne option with exactly same wave and tide conditions, but MT016 (see Table 7-10 below) was considered close enough, with only a tidal difference of 0.05 m.

Table 7-10: Tested conditions for the influence of the beach configuration

ID	Setup Conditions			
	Tide [m MSL]	H_s [m]	T_p [s]	Beach Configuration
MT016	0.45	1.4	12	Normal
MT023	0.4	1.4	12	Built-up
MT024	0.4	1.4	12	Denuded

Figure 7-45 and Figure 7-46 below show the influence of the different beach configurations on the velocity magnitude and area distribution respectively.

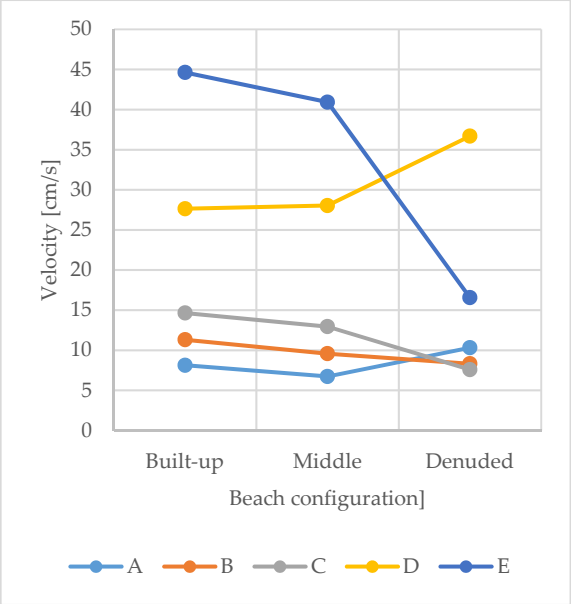

Figure 7-45: Influence of beach configuration on current velocities

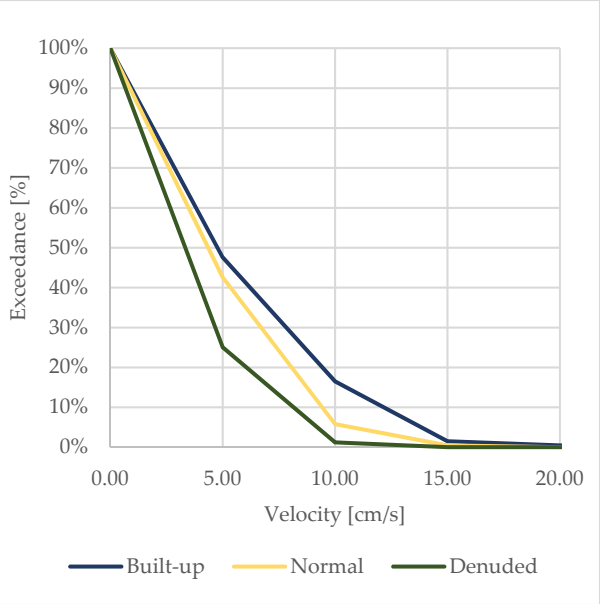

Figure 7-46: Influence of beach configuration on current velocity distribution

In the sheltered bay, the current velocities ($\boldsymbol{u}_{(A)}$, $\boldsymbol{u}_{(B)}$ and $\boldsymbol{u}_{(C)}$) decreased with for a smaller and longer beach. $\boldsymbol{u}_{(A)}$, however, deviated from the trend for the denuded beach configuration with a sudden increase in velocity. It is not very clear what caused this deviation. The general trend was also evident in the exceedance curves (Figure 7-46) which showed a decrease in current energy for smaller (denuded) beach configurations. By decreasing the beach size the length of the beach also increase. This allows the wave energy to disperse over a wider region, resulting in a lower concentration of currents.

In the exposed bay the velocities $\boldsymbol{u}_{(D)}$ and $\boldsymbol{u}_{(E)}$ reacted oppositely. $\boldsymbol{u}_{(D)}$ increased with a smaller and longer beach while $\boldsymbol{u}_{(E)}$ decreased conversely. The difference could be explained by their position relative to the breaking waves. The increased water depth associated with the denuded beach allowed more wave energy to enter and break closer to $\boldsymbol{u}_{(D)}$ in the wave-exposed area, consequently increasing the velocity for $\boldsymbol{u}_{(D)}$. The area in front of the T-groyne head was also slightly deepened with the denuding of the beach, which possibly caused more wave energy to be absorbed by the T-groyne, rather than dissipating energy on the bed-level.

The influence of the different beach configuration was therefore similar to the water level variation in the sense that the deviations are more spatially dependent. The current velocities changed differently depending on the combination and interaction of the surrounding bathymetry, wave-setup gradient and water level.

7.3.7 Overall performance comparison of all the proposed solutions

The relative velocity measurements and exceedance difference curves from the various tested group configurations can be summarised in a two graphs to compare the performance of all the proposed solutions.

7.3.7.1 Relative baseline velocities

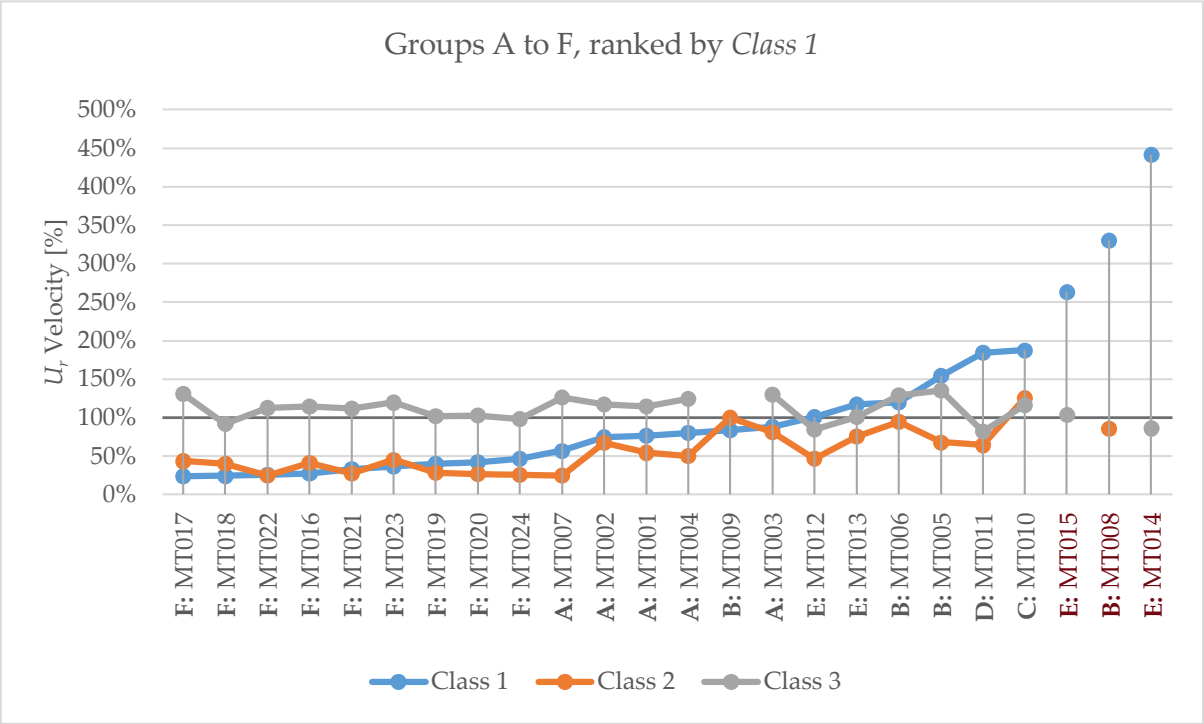

Figure 7-47: Relative baseline (U_r) velocities for all of the proposed solutions, ranked by Class 1 performance

Fifteen of the proposed solutions were successful in decreasing the velocity along the spur (*Class 1*). Interestingly, all of these solutions were related to the addition of a groyne, with the single exception of the *gap-through-spur* scenario (**MT009**). The T-groyne solutions were overall the most successful, with the maximum reduction of $\boldsymbol{U_{r(C1)} = 24\%}$**.** The secondary currents within the sheltered bay (Class 2) were reduced in almost all of the simulations, with the exception of the *gap-through-spur* scenario (**MT009**) and the *detached breakwater in bay* (**MT010**). In contrast, the currents velocities in the exposed bay (Class 3) were the least affected and were slightly increased for the majority of the simulations.

7.3.7.2 *Designated swimming area exceedance difference curve*

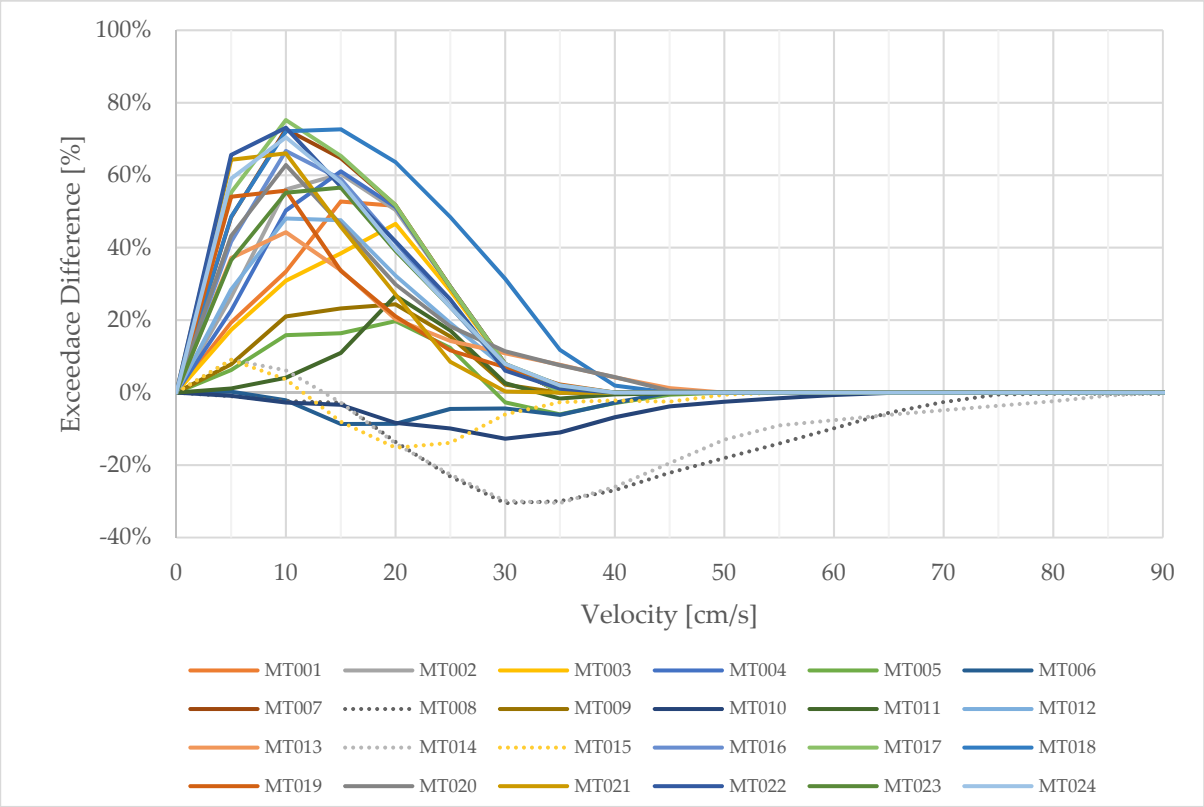

Figure 7-48: Designated swimming area exceedance difference curve for all of the proposed solutions. The dotted lines denote the unreliable results from the "overtopping" simulations.

In terms of the designated swimming area, most of the proposed solutions resulted in calmer and safer conditions, with the exception of the *seaward spur extension* (**MT006**) and *detached breakwater in bay* (**MT010**). The T-groyne configurations evidently resulted in the safest designated swimming areas compared to the rest of the proposed solutions.

It is important to note that four proposed solutions (**MT005**, **MT010**, **MT12** and **MT013**) resulted in a calmer designated swimming area, but had an increased exit (Class 1) velocity relative to the baseline conditions. These conditions are arguably more dangerous than before. The swimming area appears safer and more attractive, but the sudden increase in velocity near the spur could pull unsuspecting bathers into the dangerous current.

7.4 OVERALL PERFORMANCE INDICATOR: SWIMMING DANGER FACTOR

It would be useful to combine results of the proposed solutions into a single quantitative factor. Such a factor could be useful in providing an indication of the performance of the tested scenario, without having to analyse the hydrodynamics in depth. This section will therefore summarise the key results from the proposed solutions in relatively simple, albeit very indicative format. The formulation of the new quantitative factor is based on the exit velocity along the spur as well as the velocity distribution of the designated swimming area, and is discussed in the sub-sections that follow.

7.4.1 Area Velocity Distribution Weighted Average

The *Area Velocity Distribution Weighted Average*, or simply $\bar{u}_A$, summarises the designated swimming area velocity distribution by a simple weighted mean function:

$$\bar{u}_A = \frac{\sum_{i=1} u_{(i)} \cdot o_{(i)}}{\sum_{i=1} o_{(i)}} \tag{7.3}$$

where

- $\bar{u}_A$ = Area Velocity Distribution Weighted Average in cm/s
- $u_{(i)}$ = average absolute velocity for each i^{th} interval
- $o_{(i)}$ = number of velocity occurrences in the i^{th} interval
- i = occurrence interval number

The velocity distribution measurements were in 5 cm/s intervals, starting at 0cm/s to 5cm/s. With U_i was centred / average velocity for each interval such that:

$$u_{(i)} = 5i - 2.5$$

$$\therefore u_{(1)} = 2.5, u_{(2)} = 7.5, u_{(3)} = 12.5, \ldots$$

$$\therefore \bar{u}_A = \frac{2.5 \cdot o_{(1)} + 7.5 \cdot o_{(2)} + 12.5 \cdot o_{(3)} + \ldots}{o_{(1)} + o_{(2)} + o_{(3)} + \ldots}$$

For the upper limit $i \to \infty$, the area velocity distribution weighted average $\bar{u}_A$ will reach uniformity from the maximum velocity onwards. The maximum upper limit i is therefore undefined in the generalised context as the maximum velocities differ for each model.

The $\bar{u}_A$ velocity was calculated from the designated swimming area velocity distribution for all of the MBWS simulations (including baseline), and is shown below in Figure 7-49. The baseline simulations are indicated in green and the modified beach simulations in blue.

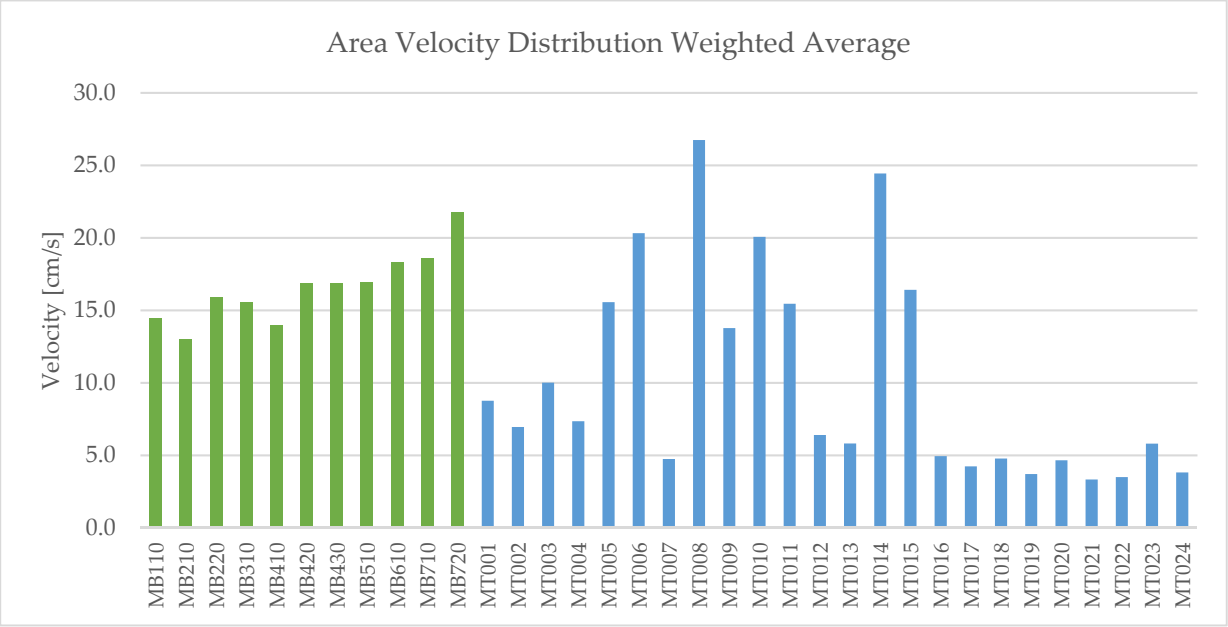

Figure 7-49: Area Velocity Distribution Weighted Average for all of the MBWS models. The green bars indicate the baseline simulations and the blue bars indicate the proposed structure scenarios

From Figure 7-49 it can be seen that the $\bar{u}_A$ velocities varied significantly for all of the proposed solution simulations (blue). The variation in the baseline models was somewhat less, as it was only influenced by the environmental conditions.

7.4.2 Area Velocity Improvement

The $\bar{u}_A$ velocity could thus far only be used to compare the models relative to each other. The complexity of defining a dangerous velocity and the uncertainty related to the reliability of the absolute velocities, make it difficult to define the danger or safety limits for $\bar{u}_A$. By factorising the $\bar{u}_A$ velocity to the baseline models, a reference for comparison is established:

$$\bar{U}_{Ar} = \bar{u}_{A(T)}/\bar{u}_{A(RB)} \tag{7.4}$$

where

- $\bar{U}_{Ar}$ = Relative Weighted Average Velocity
- $\bar{u}_{A(T)}$ = Area Velocity Distribution Weighted Average Velocity for the proposed solution
- $\bar{u}_{A(RB)}$ = Area Velocity Distribution Weighted Average for the relative baseline

Since the $\bar{u}_A$ velocity of each model is factorised to their relative baseline, the relative weighted average velocity $\bar{U}_{Ar}$ becomes a benchmark of improvement. It is therefore similar to the relationship between the absolute velocities (u) and the relative velocities ($\bar{U}_{Ar}$) as defined in § 7.1.2.2.1. In other words, the $\bar{U}_{Ar}$ velocity is an indication of how much safer the proposed *designated swimming area* is in comparison to the present beach configuration. Values below 100% ($\bar{U}_{Ar}$ < 100%) indicate improvement while values above 100% ($\bar{U}_{Ar}$ > 100%) indicate more dangerous conditions.

The $\bar{U}_{Ar}$ velocities are shown below in Figure 7-50, ranked by best overall improvement. All models that showed improvements to the existing situation ($\bar{U}_{Ar}$ < 100%) were highlighted in blue (with the T-groyne models in dark blue). The models that showed worsening of conditions ($\bar{U}_{Ar}$ > 100%) were highlighted in yellow (with the unreliable overtopping simulations in red). The relative velocities (U_r) along the spur (*Class 1*) were also plotted on the same graph for reference.

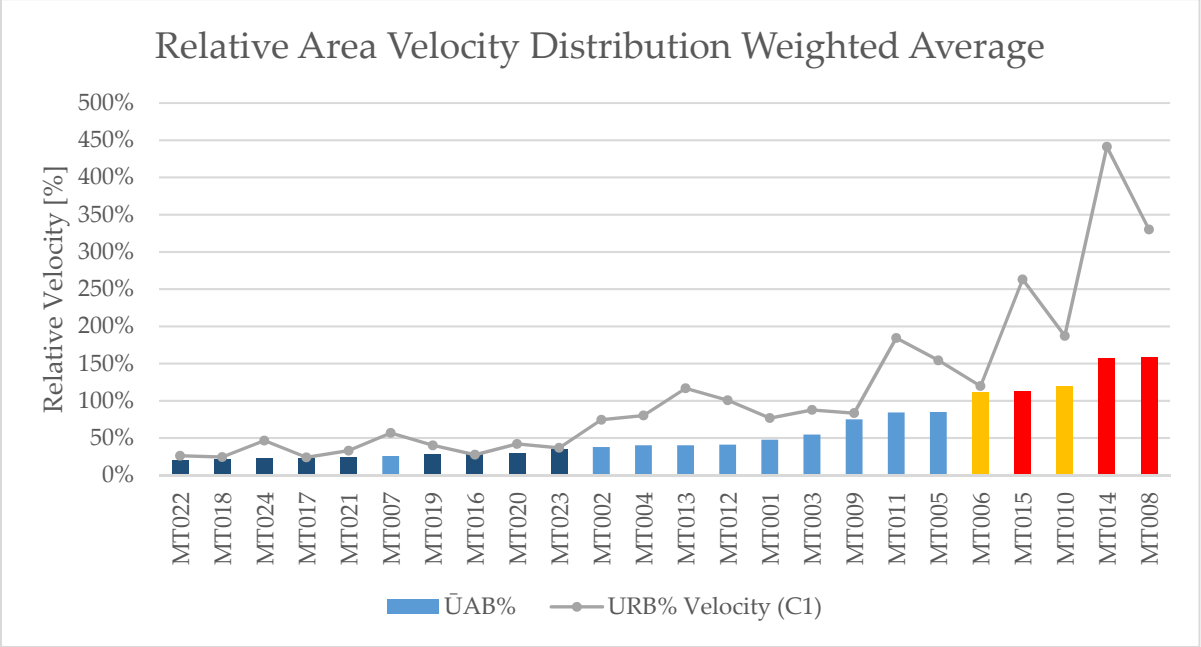

Figure 7-50: Relative Weighted Average Velocity compared to the relative baseline velocity along the spur (Class 1), for all of the MBWS scenarios.

7.4.3 Benchmark of danger: swimming danger factor

From Figure 7-50 it can be seen that there was a general trend between the baseline relative velocity along the spur and the relative weighted average velocity, but the deviations meant that the velocity along the spur did not necessarily change proportionally to the change of area velocities. Since both terms are considered important to the safety of the beach, they were combined to formulate the *Swimming Danger Factor*, $\mathcal{S}_{\mathrm{D}}$, to provide a single improvement factor of the proposed solutions:

$$\mathcal{S}_D = \frac{U_{r(C1)} + w \cdot \bar{U}_{Ar}}{1 + w} \tag{7.5}$$

where

- $\mathcal{S}_{\mathrm{D}}$ = Swimming danger factor
- $U_{r(C1)}$ = Relative baseline velocity along the spur (Class 1)
- w = Weighting factor, subjective to the importance of the velocity along the spur. For this study it was decided to keep an equal weight, thus w = 1

The swimming danger factor is therefore a danger (or safety) benchmark factor that indicates the performance of any proposed solution with regard to the velocity along the spur and the designated swimming area. Smaller values of $\mathcal{S}_{\mathrm{D}}$ indicates less of a danger relative to the present situation at Monwabisi. The swimming danger factor should therefore be interpreted as:

- $\mathcal{S}_{\mathrm{D}} > 100\%$: more dangerous swimming conditions
- $\mathcal{S}_{\mathrm{D}} < 100\%$: safer swimming conditions
- $\mathcal{S}_{\mathrm{D}} = 100\%$: no significant change to the dangerous currents

The swimming danger factor was calculated for all of the MBWS simulations. The results are shown below in Figure 7-51. The proposed solutions are ranked by their S_D value in ascending order. All models that showed improvements in the swimming conditions (S_D < 100%) were highlighted in blue (with the T-groyne scenarios in dark blue). The models that showed more dangerous swimming conditions (S_D > 100%) were highlighted in yellow (with the unsuccessful overtopping simulations in red).

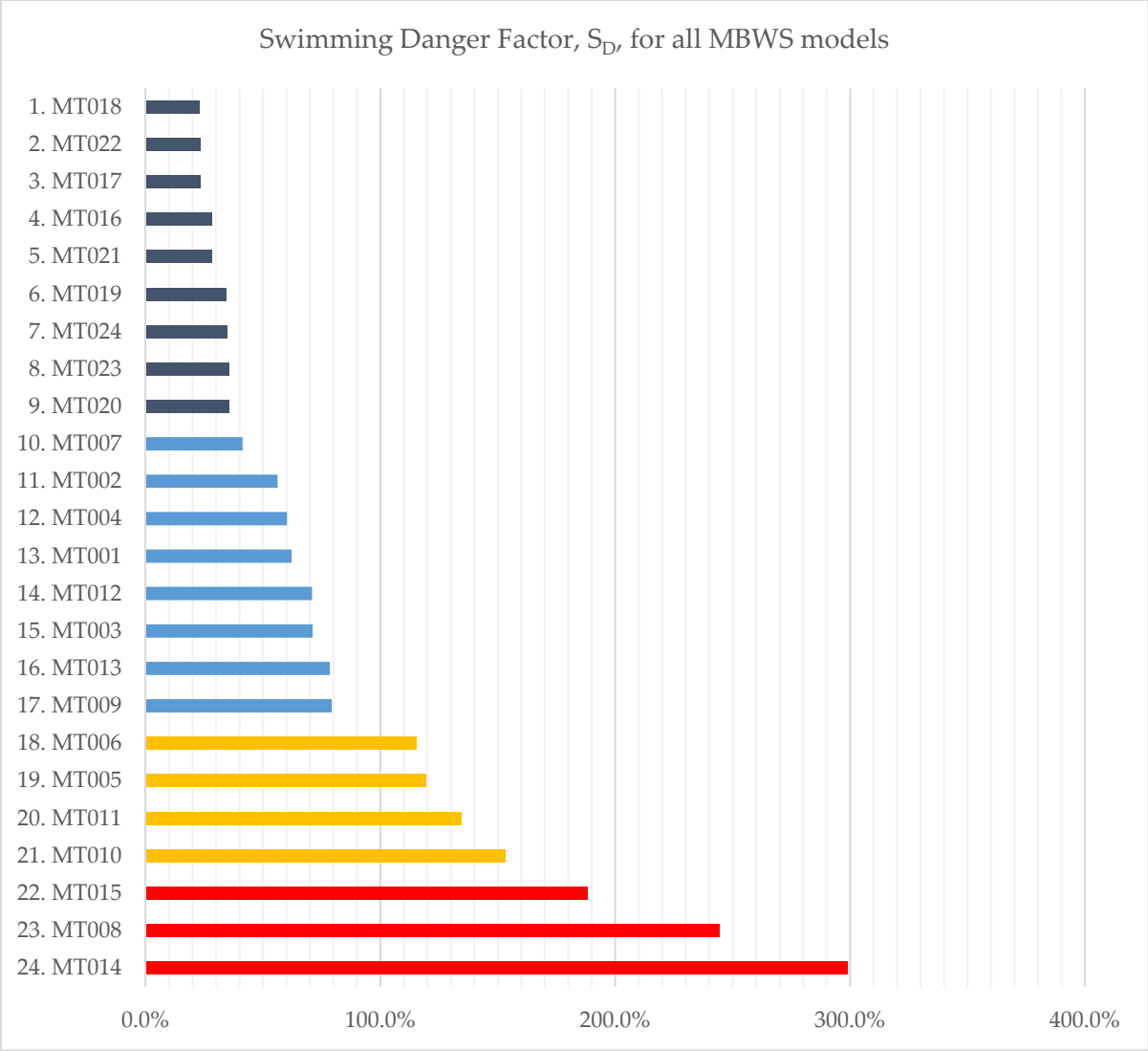

Figure 7-51: Swimming danger factor for all of the proposed solutions

From Figure 7-51 it is clear that no other proposed solution performed as well as any of the T-groyne options. The T-groyne simulation of **MT018** performed the best overall with a low swimming danger factor of $\boldsymbol{S_D = 23\%}$**. MT020** performed the worst of all the T-groyne simulations with $\boldsymbol{S_D = 36\%}$**.** The average swimming danger factor for all of the T-groyne simulations was $\boldsymbol{S_D = 30\%}$**.**

The *dog-legged spur off the beach* (**MT007)** was still ranked relatively high, but since the velocity along the spur was not improved as much as in the T-groyne simulations, it was ranked lower than all of the T-Groyne models. The swimming danger factor for **MT007** was still a relatively low $\boldsymbol{S_D = 41\%}$– not that much worse than the T-groyne simulations. The rest of the proposed

solutions did not show the same calibre of improvement. **MT007** was followed by one of the groyne scenarios, **MT002**, but it had a significantly higher danger factor of $\mathcal{S}_D = 56\%$.

By subjectively comparing the swimming danger factors, $\mathcal{S}_D$, to the detailed results from the MBWS simulations, it was concluded that the $\mathcal{S}_D$ factor summarised the performance of the proposed solutions, with regard to the beach safety, reasonably well. The swimming danger factor is therefore a very useful statistical measure to provide a quick measure of performance without the requiring reference to the detailed hydrodynamics.

7.5 SUMMARY OF THE MBWS MODEL STUDY

The success of the proposed solutions could only be determined by co-analysis of the visual and statistical aspects. With the *MIKE 21 Boussinesq Wave* model it was possible to analyse each proposed solution with as much detail as required.

7.5.1 Visual and Statistical analysis

The visual analysis mostly involved a qualitative investigation of the circulation pattern, surface elevation, average wave distribution, bathymetry and the structural features, as well as the interaction between all of these elements. This provided a more holistic understanding of why certain structures performed better than others.

The statistical analysis, on the other hand, was mostly quantitative, focusing primarily on the performance of the structures by examination of the current velocity statistics. The statistical comparison was rather complex in the sense that the spatially varying 2-dimensional parameters had to be simplified to 1-dimensional and 0-dimensional parameters for ease of assessment. This was made possible by using a *velocity class system* which categorized a velocity based on its location. The subjective velocity class system worked successfully, especially in benchmarking the velocity along the spur.

In addition, with the lack of prototype measurements there was no true reference point for comparison. This issue was solved by simulating both the structural modification, and a baseline scenario with similar tide level and wave conditions. These baseline scenarios, referred to as *relative baselines*, provided a reference to measure the performance of all of the MBWS models. The performance in this context was therefore an indication of improvement relative to the current situation.

The statistical analysis included both vector velocities (shorter, local current peaks) and area-velocities (velocity distribution for a defined area). The area-velocities were based on the *designated swimming area*, a safe and sheltered area which could be demarcated with a structure and confined to a depth range of 0 m to 2 m.

A *swimming danger factor*, $\mathcal{S}_D$, was also formulated as a function of the area velocity distribution and the vector velocity along the spur. The purpose of the $\mathcal{S}_D$ factor was to provide a quantitative indication of the danger of the swimming conditions, relative to the present situation. The $\mathcal{S}_D$ factor showed great potential in providing a concise model performance indicator in terms of beach safety. This factor could perhaps be used in future studies to investigate a greater number of proposed solutions where time constraints would not allow for in-depth analysis.

7.5.2 Success of proposed solutions

The majority of the wave-current energy originated from the northern-most part of the beach which was the most exposed to incoming wave energy. The rest of the bay was also exposed to limited wave energy diffracting around the spur. The breaking waves dispersed energy, thereby inducing currents along the beach. These currents, if uninterrupted, caused a strong circulation in the bay.

It was therefore no surprise to see that structures that interrupted this circulation allowed for local diffusion of the currents. The separation of the beach reduced the energy in two ways: cutting off the circulation feeder currents from the exposed bay and reducing incoming wave energy into the sheltered bay. Multiple configurations of groynes were tested with varying degrees of success, but all of them showed some benefits.

Other methods have also been tested, such as modifications to the spur, a detached breakwater, a wave-deflecting structure or combinations of groynes and modifications to the spur. The modifications to the spur included gaps, lowered sections or extensions to the spur. None of these tests were quite as successful as the standard groyne options. Some options were successful in reducing the average current energy in the swimming bay, but not the current velocity along the spur. This was considered a particularly dangerous situation, as the swimming area may attract more bathers, despite the presence of a danger current.

Due to the success of the groyne structures, the CSIR (1997) proposed the optimised solution of the T-groyne. The T-groyne reduced the circulation pattern with the same general process as the other groynes, but with more success. The T-shaped head of the groyne increased the distance between the entrances of the sheltered and exposed bay. This reduced the influence of the circulation of the exposed bay on the sheltered bay. By further enclosing the bay, less current-inducing wave energy could enter the sheltered bay.

The success of the T-groyne models relative to the other models was very evident in the statistical study. The T-groyne models did not only result in the most quiescent bays, but also reduced the strong velocity along the spur significantly ($\boldsymbol{U_{r(C1)} = 33\%}$ on average for all the T-groyne simulations).

By using the newly formulated *Swimming Danger Factor* (S_D), it was illustrated how much the T-groynes reduced the danger relative to the present situation – and in comparison to the other models. The average S_D factor for the T-groyne options was $\boldsymbol{S_D = 30\%}$ in comparison to the other models which ranged between $\boldsymbol{S_D = 41\%}$ and $\boldsymbol{S_D = 153\%}$.

7.5.3 Influence of environmental variables

In the baseline and the T-groyne configurations, a number of different environmental combinations were used on otherwise the same model configuration. This made it possible to examine the influence of environmental conditions on the current velocities.

The study quantitatively analysed the influence of wave heights, wave period, tide level and beach configuration (for the T-groyne simulations). The complexity associated with the 2D hydrodynamics was illustrated in the results, with mostly variable outcomes and very few trends. It should be noted that the number of tests was too limited for determining robust trends.

From the baseline and T-groyne models, it was seen that there is an intricate interaction between water level, bathymetry and wave conditions, which makes it difficult define a general rule for any of the environmental parameters. The peak velocities tended to change, depending on the location of the measurement. The wave height was the only environmental parameter that showed a strong trend of increasing velocities for a variation of (larger) wave heights. The beach configuration also had a rather large influences on all of the velocities, but was also dependent on the location of measurement.

This velocity-sensitivity to the beach configuration emphasises the need for conducting a more thorough beach configuration study for a final solution. The apparent influence of wave height also suggests the need for further studies to focus on more wave-height related aspects. Random (spectrum) waves and the influence of long waves could be useful in future research. Larger waves are not specifically required, as the danger is associated with smaller waves which create an illusion of safe conditions.

7.5.4 Conclusion on the MBWS-results analysis

The *MIKE 21 Boussinesq Wave* model showed great success in replicating the complex hydrodynamic system at Monwabisi for both the present situation and the proposed solutions. The ability of the model to resolve wave-induced currents and surface elevation proved to be especially useful for this study. The detailed results from the simulations made it possible to qualitatively and quantitatively, although uncalibrated, analyse the hydrodynamics in-depth. The results of the simulations clearly showed that a T-groyne placed on the beach can reduce the circulation and the current along the spur, resulting in a much safer beach.

8 COMPARISON TO THE CSIR PHYSICAL MODEL

8.1 INTRODUCTION

This chapter presents the comparison of the results of the physical model study by the CSIR (1997) and the results of the numerical model of the current study. The circulation pattern and the current velocities of the two models were compared by means of visual and statistical analysis. To fully comprehend the comparative study, it is necessary to be aware of how the two models were compared, and why it was chosen to do so. This chapter will therefore also provide an overview on some important aspects regarding the interpretation of the results.

8.1.1 Scope of the analysis

The visual analysis focuses mainly on the current-circulation patterns by examining the 2D-horizontal flow patterns of the MBWS numerical model and CSIR physical model. The purpose of the visual analysis is to compare the agreement of the two models in terms of circulation processes.

The statistical analysis will focus on the current velocities, by studying similar peak velocities occurrences between the MBWS numerical model and CSIR physical model. The purpose of the statistical analysis is to quantify the similarities between the two models

8.1.2 Model differences

There were a number of differences between the two models which had some influence on the means of comparison.

8.1.2.1 Velocity measurements

The CSIR measured the current velocities by means of adding floats to the water and measuring the distance travelled over time. The distance travelled was not specified in the CSIR report, but the author assumed it not to be excessively long (< 50m in prototype). This process was repeated a number of times to derive average and peak velocities. The average velocity was the mean velocity of the set of recordings, and the peak was the maximum recorded velocity of the set.

The MBWS model was only capable of producing a time-mean velocity for the whole duration of the simulation. The model was therefore not able to simulate cyclic current events. Only the CSIR average values were compared to the MBWS average values.

The MBWS model was simulated in a 2D domain over two horizontal axes, resulting in the simplification of any 3D effect to a depth-integrated value across the whole vertical axis. This meant that cross-section flow dynamics could not be modelled in the MBWS model, while this phenomenon was included in the CSIR's physical model.

8.1.2.2 Units of measurement

The CSIR did not provide absolute values for their velocity measurements. The reason being that their models were not calibrated to any on-site velocity measurements. They motivated that a relative measurement may therefore be more significant than an absolute velocity. The CSIR therefore simulated the present situation (**MB610**), and used the velocity of the current flow along the spur as a benchmark for the rest of the simulations. The "M" in Figure 8-1

marks the area of the measurement from **MB610**. All of the velocities from the CSIR's (1997) report were therefore expressed a ratio relative to the same velocity from **MB610**.

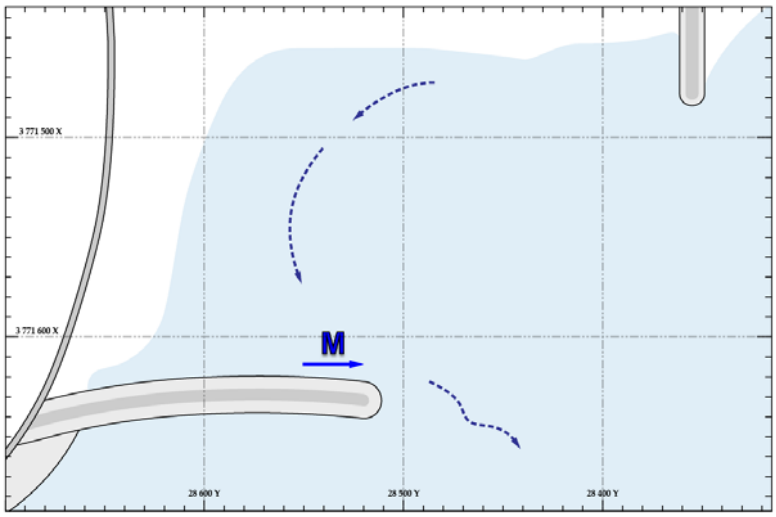

Figure 8-1: The present situation at Monwabisi, from the CSIR's physical model simulation. All velocities from the CSIR simulation were reported as a ratio relative to the velocity measured at "M".

The velocity output data of the MBWS model was processed as absolute measurements (metre per second). The MBWS absolute velocities could not be compared directly to the CSIR relative velocities. The data therefore needed to be processed first as discussed in § 8.1.4.

8.1.2.3 Circulation patterns

The CSIR (1997) report used diagrams to indicate the flow pattern of each simulation by means of simple directional arrows (see Figure 8-2). This simplified method provides a good visualization of the circulation process, but is limited to the information provided. It was not always clear if the lack of directional arrows meant no significant flow, or only that it was not recorded. The directional arrows were derived by observing the movement of the floats (as used in velocity measurements) in the physical model.

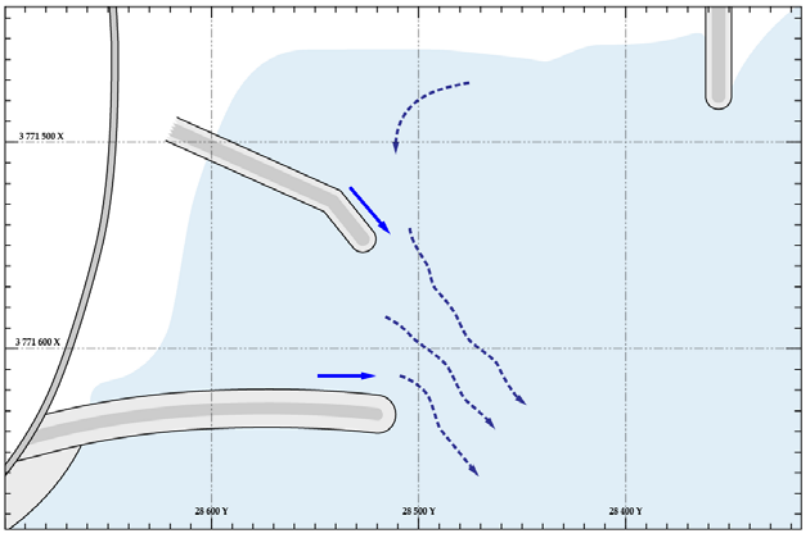

*Figure 8-2: Example of a simplified flow pattern for **MT007** as reported by the CSIR (1997). Solid arrows represent area of velocity measurement.*

The results from the MBWS model were much more detailed. At every 2 m x 2 m grid point, the average current flow was provided as a vector (magnitude and direction). This provided detailed current information wherever needed. The raw output format, as shown in Figure 8-3 below, did not visually compare well with the simplified format of the CSIR diagrams. This data therefore also required processing for the comparison to the CSIR results and is further discussed in § 8.1.3.

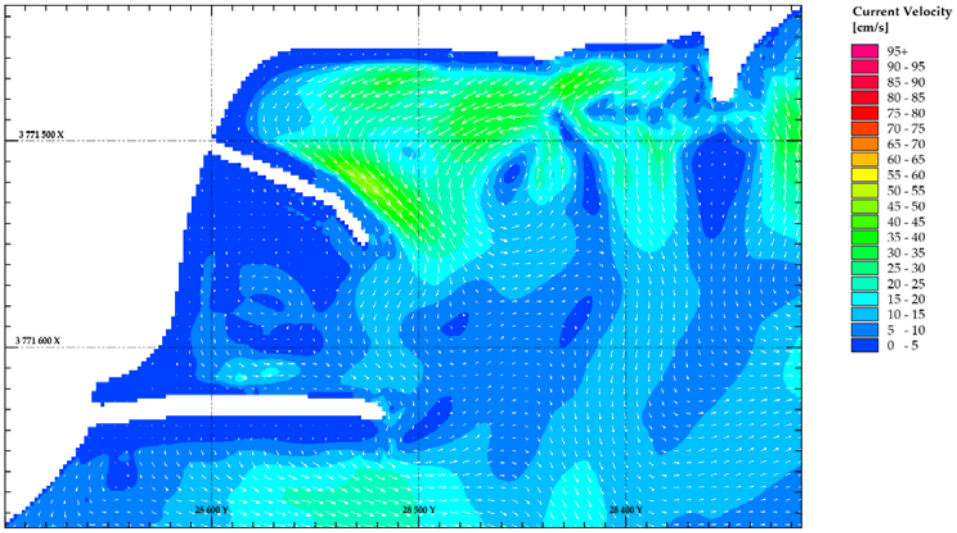

*Figure 8-3: Raw velocity current velocity distribution for **MT007** from the MBWS model.*

8.1.2.4 Limitations of comparison

The CSIR model included a number of simulations with wave-overtopping. *MIKE 21 Boussinesq Wave* is capable of modelling wave overtopping, but this is a relatively complex process which requires experience and extensive calibration data. Since no calibration data was available, the overtopping was ignored in less important situations, or resulted in unrealistic model results for the overtopping dependent cases.

A major advantage of the MBWS model is the capability to simulate the instantaneous surface elevation which is very useful in the analysis of wave action in the embayment. This was also possible in the CSIR's physical model but no material (photographic material or related data) were provided in their report.

8.1.3 Processing the circulation pattern for comparison

The *MIKE 21 Boussinesq Wave* model was not able to simulate particle tracing, i.e. visualising the circulation patterns as per the CSIR's diagrams. The vectors from the MBWS simulation results were traced by hand to provide more simplified current circulation patterns, enabling a simplified comparison to the CSIR's simulations as shown below:

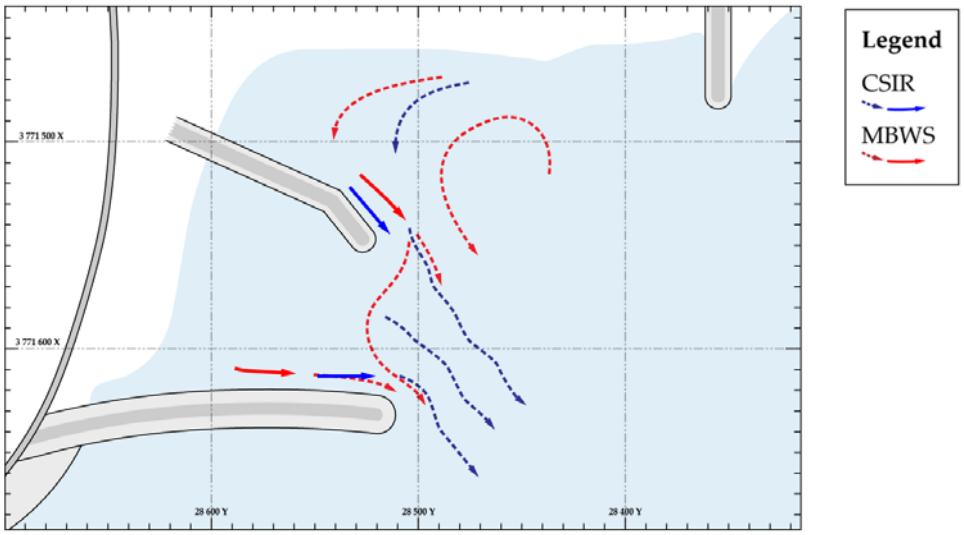

Figure 8-4: Comparison of simplified CSIR (blue) and MBWS (red) circulation patterns.

The CSIR and MBWS currents are presented as blue and red lines respectively. The dashed lines indicate the prominent observed or recorded flow patterns and the solid arrows indicate area of velocity measurement – or velocity vector. All of the MBWS simulations were simplified to the level of detail as per Figure 8-4 for comparison to the CSIR simulations.

8.1.4 Processing the velocities for comparison

For the comparative study, the MBWS velocity measurements were specifically measured to allow for direct comparison with the results from the CSIR simulations. The position of the measurements may therefore differ from MBWS analysis measurements, as they were based on the position of the CSIR's recordings.

8.1.4.1 Defining the velocity type

Two current vectors can be statistically compared if their location, direction and respective flow pattern show evidence of a reasonable match. The task quickly becomes more complex as the two circulations patterns start to deviate from each other. In such cases, a judgement call is required to decide if- and where a comparable velocity exists.

To generalise the process, a basic *circulation matching type* system was developed to establish whether the current vectors of the CSIR and MBWS models could be compared statistically, and to what extent. This system was dependent on a visual interpretation, and was therefore subjective. The classification process is defined as follows:

Type 1 (T1), Exact or close match: The two models show a definite agreement in flow pattern and peak velocities.

Type 2 (T2), Inexact match: The flow patterns of the models differ to some extent, but a *significant velocity* (a velocity of substantial importance) could be identified in the same vicinity. This is typical where both models have a dangerous or strong current in the same vicinity, but with some difference of the circulation pattern.

Type 3 (T3), No match: Flow patterns of the models differ completely and there are no *relevant velocities* in a close vicinity.

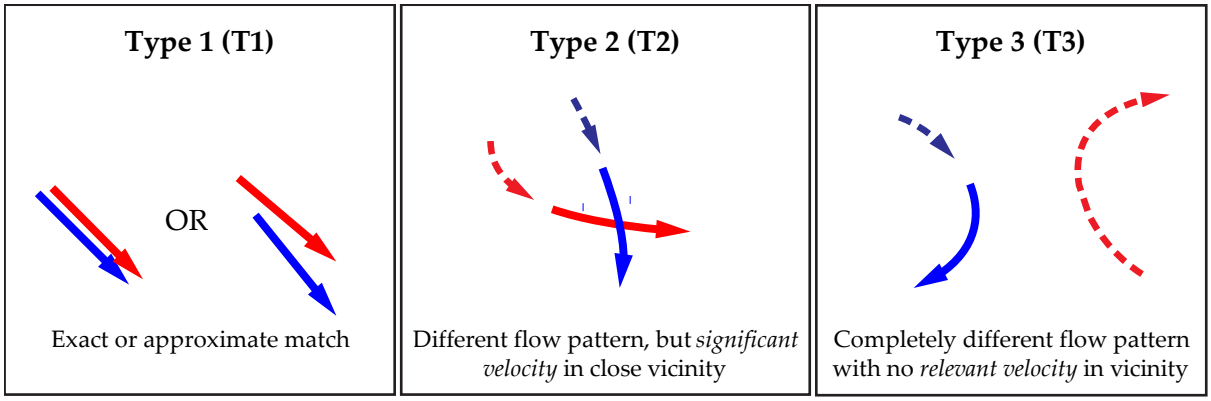

Figure 8-5: Visualisation of velocity type classification

8.1.4.2 Units of measurement

One of the complexities in the comparison process related to the CSIR's use of *relative velocity* (velocity as a percentage unit). Effectively, this factorised all of the CSIR's velocity measurements with a factor equal to the inverse of the original baseline current along the spur, v_{MB610}. The reported velocities from the CSIR's simulations could there be expressed as:

$$V_{f(i)} = v_{(i)} \cdot f_{CSIR} \tag{8.1}$$

$$f_{CSIR}{}^{-1} = v_{MB610} \tag{8.2}$$

where

- $V_{f(i)}$ = MB610-factorised velocity in the CSIR model at any given point *i* [%]
- $v_{(i)}$ = Absolute velocity in the CSIR model at any given point *i* [m/s]
- $v_{MB610(M)}$ = Absolute current velocity from the CSIR's MB610 simulation, measured along the spur [m/s]
- f_{CSIR} = CSIR-Conversion factor; the inverse of the velocity measured along the spur in the baseline test, [s/m]

In order to compare the MBWS results to the CSIR results, the velocities also need to be factorised so that:

$$U_{f(i)} = u_{(i)} \cdot f_{CSIR} \tag{8.3}$$

where

- $U_{f(i)}$ = MB610-factorised velocity in the MBWS model at any given point *i* [%]
- $u_{(i)}$ = Absolute velocity in the MBWS model at any given point *i* [m/s]

Neither the absolute CSIR velocities ($v_{(i)}$) nor the CSIR-conversion factor (f_{CSIR}) were known, which made it impossible to factorise the MBWS velocities using the same factor as was used for the CSIR velocities.

Therefore, the CSIR conversion factor, f_{CSIR}, has to be estimated for the MBWS model, and equation 8.3 becomes:

$$\therefore U_{f(i)} = u_{(i)} \cdot f_{MBWS} \qquad (8.4)$$
$$f_{CSIR} \cong f_{MBWS}$$

where

- f_{MBWS} = MBWS-Conversion factor; the inverse of the velocity measured along the spur in the baseline test, [s/m]

It cannot simply be assumed that the MBWS conversion factor, f_{MBWS}, should also be derived from the baseline-spur flow velocity of the MBWS model. A deviation might have occurred in the baseline test, which could potentially skew the comparison results. The CSIR and MBWS data sets should therefore be compared first, before deciding on the MBWS conversion factor. To establish the MBWS conversion factor, f_{MBWS}, it was decided to use only the *Type 1* measurements as they were the most reliable in terms of flow pattern comparability. As a starting point, f_{MBWS} was derived from the MBWS-baseline spur flow velocity as a first estimation (measured $u_{MB610(M)} = 0.252\ m/s$).

$$f_{MBWS}{}^{-1} = u_{MB610(M)}$$
$$\therefore f_{MBWS} = {}^{1}/_{0.252} = 3.97\ m^{-1} \cdot s$$

The graph below shows the comparison of all the CSIR and MBWS Type 1 velocities for $f_{MBWS} = 3.97\ m^{-1} \cdot s$. The yellow dot in the figure represents the baseline test. The solid line indicates a 1:1: ratio of comparison – or a perfect match. The dotted line is a function of linear regression for the Type 1-velocity data set.

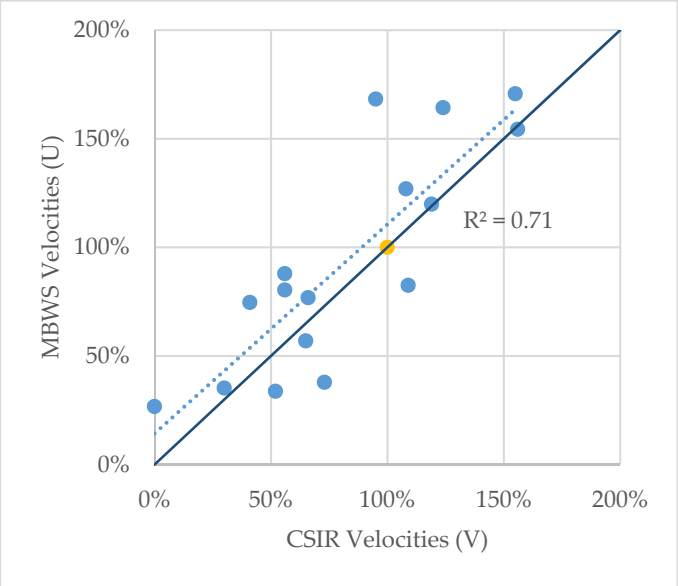

Figure 8-6: Type-1 velocity comparison of the MBWS numerical model and the CSIR physical model

Surprisingly for $f_{MBWS} = 3.97\ m^{-1} \cdot s$ the CSIR and MBWS models compared reasonably well. There were some deviations as expected, but the linear regression indicated a good statistical comparison between the two data sets with an a reasonably good statistical coefficient of determination of: $R^2 = 0.71$.

It was therefore decided to keep the MBWS conversion factor $f_{MBWS} = 3.97\ m^{-1} \cdot s$. This decision assumes that MBWS simulation for the baseline configuration (**MB610**) had the same results as CSIR-baseline simulation. All of the measured velocities in the MBWS model could now be expressed as:

$$\therefore U_{f(i)} = 3.97 \cdot u_{(i)} \tag{8.5}$$

The velocities from equation 8.5 are therefore considered acceptable for the comparison to the CSIR's relative velocities.

It is very important to note that this velocities are relative to one specific measurement (velocity along the spur for the **MB610**-baseline simulation). This means that the velocity ratios among the relative velocities are still the same as the ratios among the absolute velocities. This is different from relative baseline velocities (U_r) in Chapter 7 where the velocity-factorisation varied according to the position of measurement and wave and tide conditions.

8.2 Summary of Preliminary Tests

This section examines the similarities between the CSIR and MBWS models for the proposed solutions by visually and statistically analysing the results of the MBWS simulations. The simulation analysis will be discussed in their respective groups, as set out below.

A. Groynes extending from the beach
B. Modification to the spur
C. Detached breakwater
D. Current-reducing or reflecting structure
E. Combination of the above (A to D)
F. T-groyne off the beach

The full results of the comparative study are presented in Appendix E and Appendix F.2.

8.2.1 Baseline test

Table 8-1: Short summary of baseline test

ID	Short Description	Setup Conditions				Spur Velocity	
		WL [m MSL]	H_s [m]	T_p [s]	θ [deg]	CSIR V_f	MWBS U_f
MB610	*Baseline test*	0.7	1.5	12	8	(100%)	(100%)

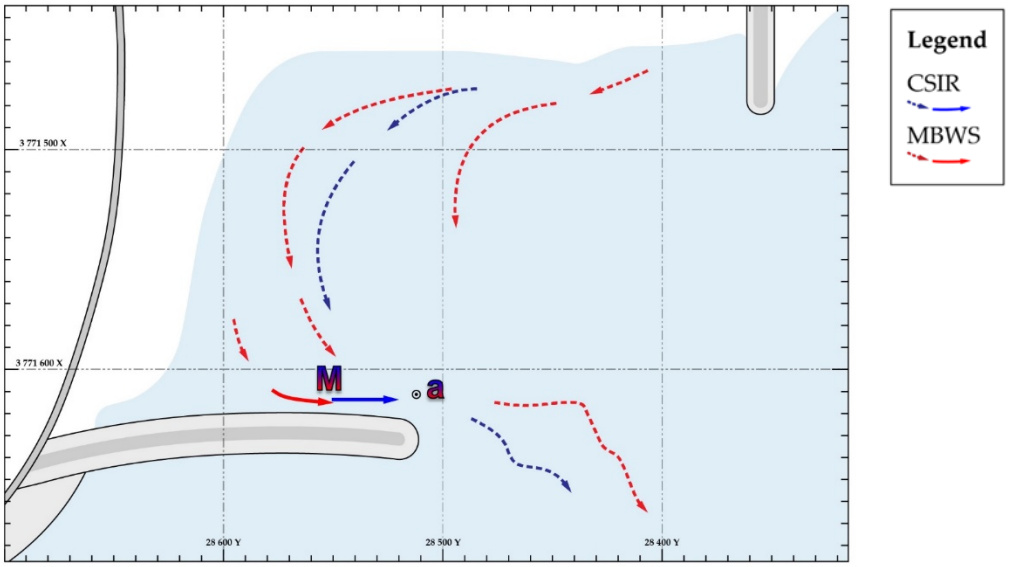

*Figure 8-7: The CSIR-MBWS Baseline comparison (**MB610**: H_s = 1.5 m, T_p = 12 s, WL = +0.7 m MSL)*

The CSIR- and MBWS-baseline tests showed a good agreement in terms of the circulation pattern. Since the baseline was used to measure the factorised velocity for all the modified beach test cases, and the CSIR did not provide any absolute velocity measurements, nothing meaningful could be said about the comparison of the velocity magnitudes.

8.2.2 Group A: groynes extending from the beach

Table 8-2: Short summary of Group A tests

ID	Short Description	Setup Conditions				Spur Velocity		Type
		WL [m MSL]	H_s [m]	T_p [s]	θ [deg]	CSIR V_f	MWBS U_f	
MT001	*Short groyne opposite spur head.*	0.7	1.5	12	8	66%	77%	T1
MT002	*Long groyne opposite spur head.*	0.7	1.5	12	8	41%	75%	T1
MT003	*Long groyne away from spur head*	0.7	1.5	12	8	56%	88%	T1
MT004	*Dog-legged groyne opposite spur head*	0.7	1.5	12	8	56%	80%	T1
MT007	*Dog-legged groyne off present beach*	0.7	1.5	12	8	65%	57%	T1

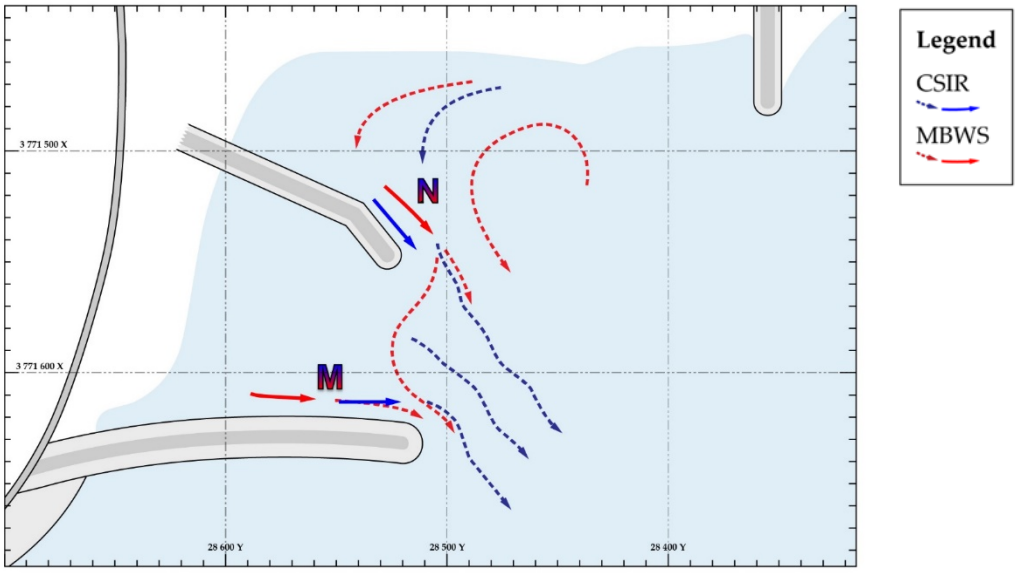

*Figure 8-8: Dog-legged groyne off the beach from Group A (**MT007**: H_s = 1.5 m, T_p = 12 s, WL = +0.7 m MSL)*

All the Group A options resulted in a decrease of the current velocity along the spur. Interestingly, the CSIR simulations resulted in stronger currents occurring away from the spur – usually about halfway between the spur and the new structure. In the MBWS simulations, the strongest exit current always occurred along the spur. This current magnitude were usually between the CSIR's spur-current and the CSIR's exit current in the middle of the bay. Figure 8-9, compares the relative current velocities between the two models.

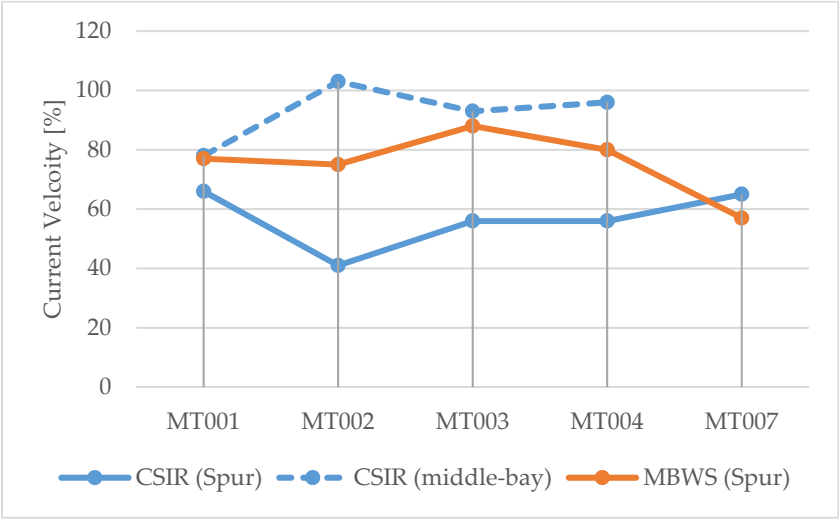

Figure 8-9: Exit current comparison for Group A

In the CSIR simulations, the shift of the current meant that the groynes effectively just migrated the problem away from the spur, as the currents in the middle of the bay were not significantly different from the original recording.

In all of the MBWS simulations a strong circulation pattern developed in the exposed bay (see Figure 8-10, Point D). The CSIR report only indicated similar circulation developments for **MT004** and **MT007**. It is unclear whether this circulation was present in the CSIR simulations,

or whether it was omitted in the report. The CSIR report did remark that this area is less likely to be used by bathers as it is visibly exposed to much higher wave energy.

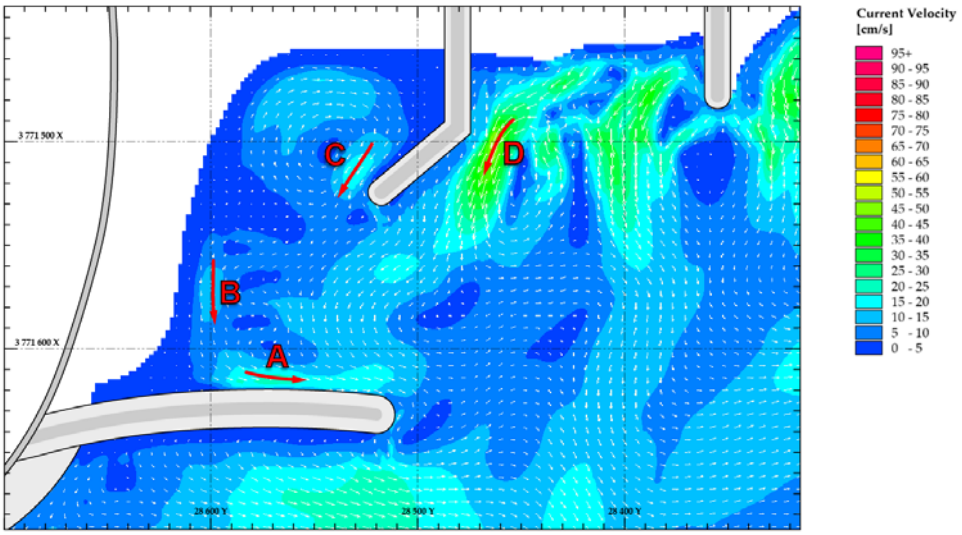

*Figure 8-10: **MT004** showing strong current along the dog-legged groyne in the sheltered area. (H_s = 1.5 m, T_p = 12 s, WL = +0.7 m MSL)*

In the MBWS model, there was evidence of a new adverse effect in terms of safety. In the majority of the groyne tests (with the exception of **MT007**) a relatively strong current was present on the sheltered side of the new groyne (See Figure 8-10, Point C). The velocity of this current measured on average $\boldsymbol{U_{f(C)} = 70\%}$ relative to the original recording along the spur. This is potentially dangerous as the relatively low wave action in this area can create a false illusion of a "safe area", similar to the present danger of the spur. The CSIR did not report any similar effects.

8.2.3 Group B: modification to the spur

Table 8-3: Short summary of Group B tests

ID	Short Description	Setup Conditions				Spur Velocity		Type
		WL [m MSL]	H_s [m]	T_p [s]	θ [deg]	CSIR V_f	MWBS U_f	
MT005	*Dog-legged spur off spur head (landward)*	0.7	1.5	12	8	156%	154%	T1
MT006	*Spur off spur head (seaward)*	0.7	1.5	12	8	119%	120%	T1
MT008	*Lowered end of spur*	0.4	1.4	12	8	101%	189%	T2
MT009	*Gap through spur (west section)*	0.7	1.5	12	8	73%	84%	T2

The *spur-extension* configurations (**MT005** and **MT006**) showed excellent agreement between the CSIR and MBWS models. In both cases the average velocity matched within a 2% difference. The overall results of the *spur-extensions*, however, indicated a worsening of the current situation.

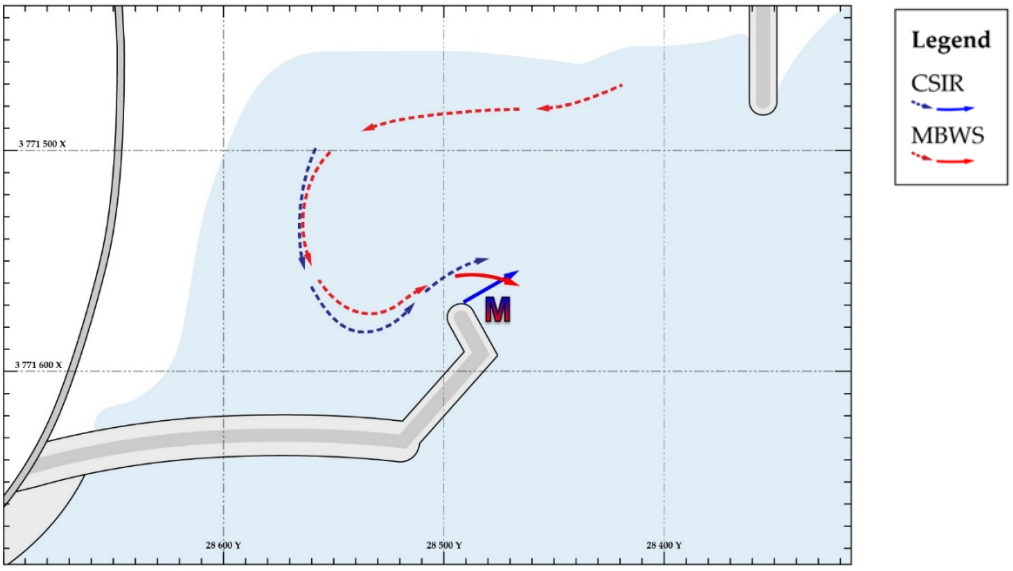

*Figure 8-11: Landward spur extension comparison from Group B (**MT005**: H_s = 1.5 m, T_p = 12 s, WL = +0.7 m MSL)*

The MBWS model did not handle wave-overtopping action well, which resulted in a major deviation between the two models for the *lowered spur crest* scenario (**MT008**). The extremes could have been reduced by artificially dampening the overtopping energy by means of a friction or porosity coefficient.

It has been mentioned that overtopping-modelling is a difficult task which relies on experience and extensive calibration data, and could very well be a study in itself. Furthermore, neither of the two models tested any of the additional scouring effects that would have been caused with the increased wave action. The results were therefore not comparable.

The two models showed some agreements in the *gap-in-the-spur* simulation (**MT009**), but the measured peaks occurred in different areas. In the CSIR simulation the velocity along the spur was reduced to $\boldsymbol{V_{f(M)} = 74\%}$ of the original recording. In the MBWS simulation there was no strong current along the spur, but a relatively strong exit current occurred at the gap in the spur with $\boldsymbol{U_{f(M)} = 84\%}$.

Some of the deviations may be due to bathymetric differences. The bathymetries were re-profiled in both models to adjust to the gap in the spur. The 0m-MSL contour was the same in the two models, but it is unclear how the CSIR adapted the rest of the contours. For both the MBWS and CSIR models this configuration generally did not show significant improvement to the present hazards.

8.2.4 Group C: detached breakwaters

Table 8-4: Short summary of Group C test

ID	Short Description	Setup Conditions				Spur Velocity		Type
		WL [m MSL]	H_s [m]	T_p [s]	θ [deg]	CSIR V_f	MWBS U_f	
MT010	*Detached breakwater in bay*	0.4	1.4	12	8	124%	164%	T1

There was a fair agreement between the CSIR and MBWS model simulations for the *detached breakwater* case (**MT010**). There were some differences in the current circulation pattern around the breakwater. In both of the models the current along the spur further increased in strength. The MBWS simulation had a more significant increase of velocity, $\boldsymbol{U_{f(M)} = 164\%}$, compared to the CSIR's measurement of $\boldsymbol{V_{f(M)} = 124\%}$.

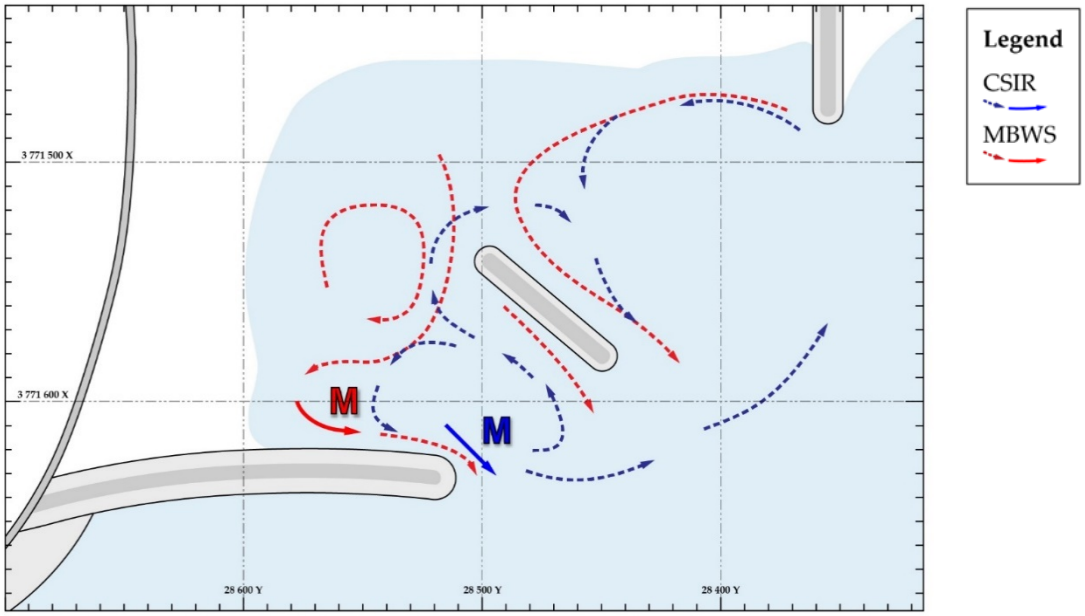

*Figure 8-12: CSIR-MBWS comparison for the detached breakwater in Group C (**MT010**: H_s = 1.4 m, T_p = 12 s, WL = +0.4 m MSL)*

The increased velocity was due to the increased wave action in the bay, caused by wave reflections off the spur. The wave-reflection action was reported by the CSIR, but no visual materials were provided. The MBWS model also showed wave reflection off the breakwater, but it is unclear how the reflection compared between the two models. The visible wave reflection is shown in Figure 8-13 on the next page.

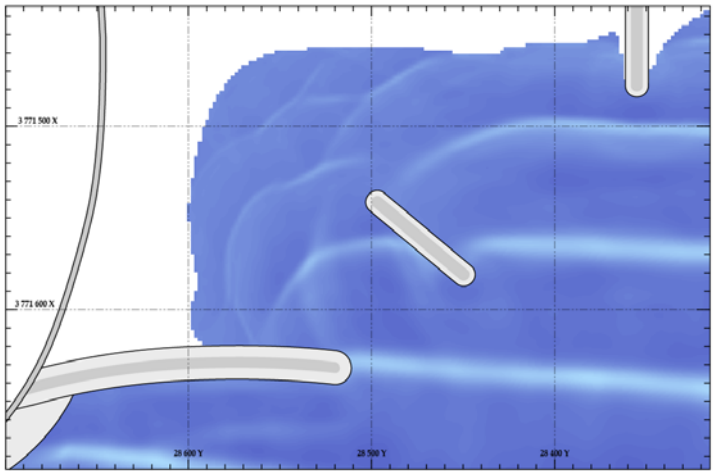

*Figure 8-13: Wave reflection action visible in the bay in the MBWS simulation (**MT010**: H_s = 1.4 m, T_p = 12 s, WL = +0.4 m MSL)*

8.2.5 Group D: current deflecting structures

Table 8-5: Short summary of Group D test

ID	Short Description	Setup Conditions				Spur Velocity		
		WL [m MSL]	H_s [m]	T_p [s]	θ [deg]	CSIR V_f	MWBS U_f	Type
MT011	*Raised bed level at spur head*	0.7	1.5	12	8	73%	184%	T2

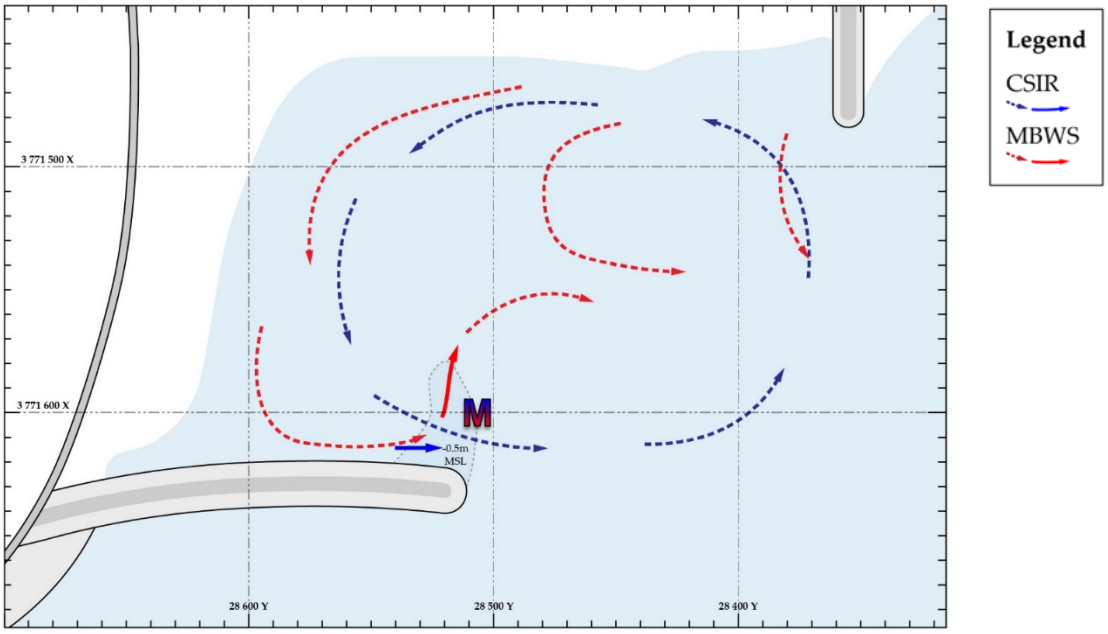

*Figure 8-14: CSIR-MBWS comparison for the raised bed level in Group D (**MT011**: H_s = 1.5 m, T_p = 12 s, WL = +0.7 m MSL)*

The raised bed level affected the MBWS simulation more than the CSIR simulation. In the CSIR simulation, the current still flowed over the raised bed section, but with slightly reduced

energy. In the MBWS model, the current appeared to be deflected by the elevated bed in a northerly direction. Upon further inspection, it was discovered that the diffraction around the spur head and refraction on the raised bed caused waves to break at the spur. The wave breaking caused a sudden increase of current velocity – almost double the strength of the original measurement ($\boldsymbol{U_{f(M)} = 184\%}$). The models did not account for any possible beach equilibrium changes due to the raised bed level.

8.2.6 Group E: combination A to D

Table 8-6: Short summary of Group E tests

ID	Short Description	Setup Conditions				Spur Velocity		Type
		WL [m MSL]	H_s [m]	T_p [s]	θ [deg]	CSIR V_f	MWBS U_f	
MT012	*Gap in spur section (west) & groyne off beach*	0.3	1.3	12	8	91%	74%	T2
MT013	*Gap in spur section (west) & groyne off beach*	-0.3	1.3	12	8	109%	82%	T1
MT014	*Lowered spur section (east) & groyne off beach*	0.3	1.3	12	8	104%	326%	T2
MT015	*Lowered spur section (east) & groyne off beach*	-0.3	1.3	12	8	88%	186%	T2

8.2.6.1 Gap in spur (west section) with groyne off beach

There was a fair agreement between the CSIR and MBWS models for the *hole-in-the spur and groyne* (**MT012** and **MT013**) scenarios. The circulation patterns showed similarities in some areas, but differed completely in other areas. The exit velocity at the spur differed between 17- and 27 percentage points and did not indicate any significant improvements relative to the present situation.

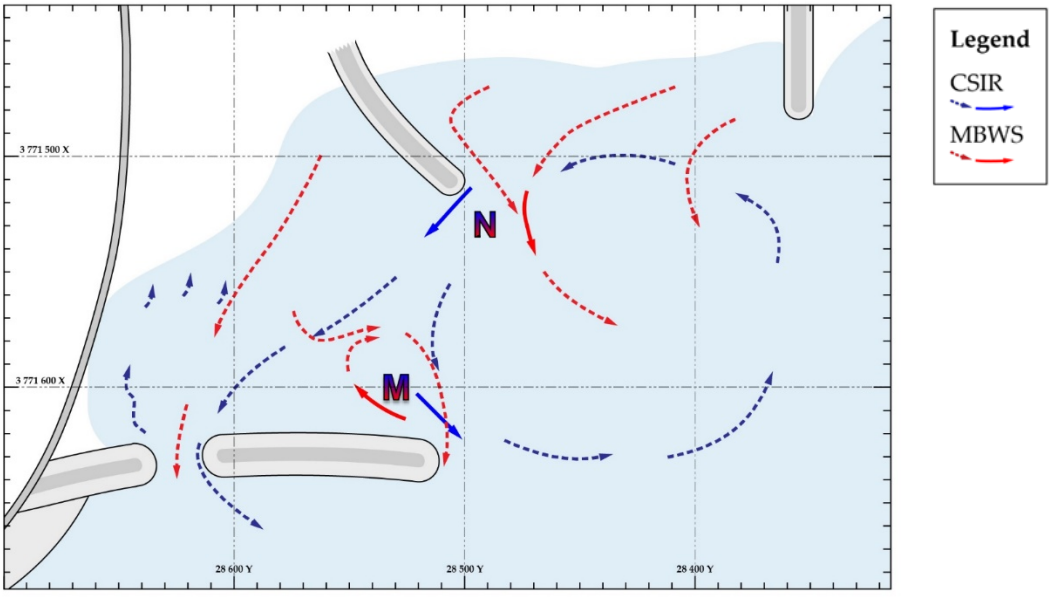

*Figure 8-15: CSIR-MBWS comparison of the gap-in-spur and groyne in Group B (**MT012**: H_s = 1.3, T_p = 12 sec, WL = +0.3m MSL)*

Both models responded similarly to the lowered tide-level. At lower water levels, the groyne had less of an obstructing influence, allowing for a stronger circulation to develop in the bay. This increased the current velocities off the spur head – relative to the higher tide – in both models. The CSIR reported that the current off the new groyne was non-existent at low tide (the circulation cell was too far from the groyne to measure).

Conversely, the MBWS simulation showed strong evidence of a current about 30 m from the groyne (see Figure 8-16). The CSIR did indicate a large circulation in that vicinity, but no measurements were reported.

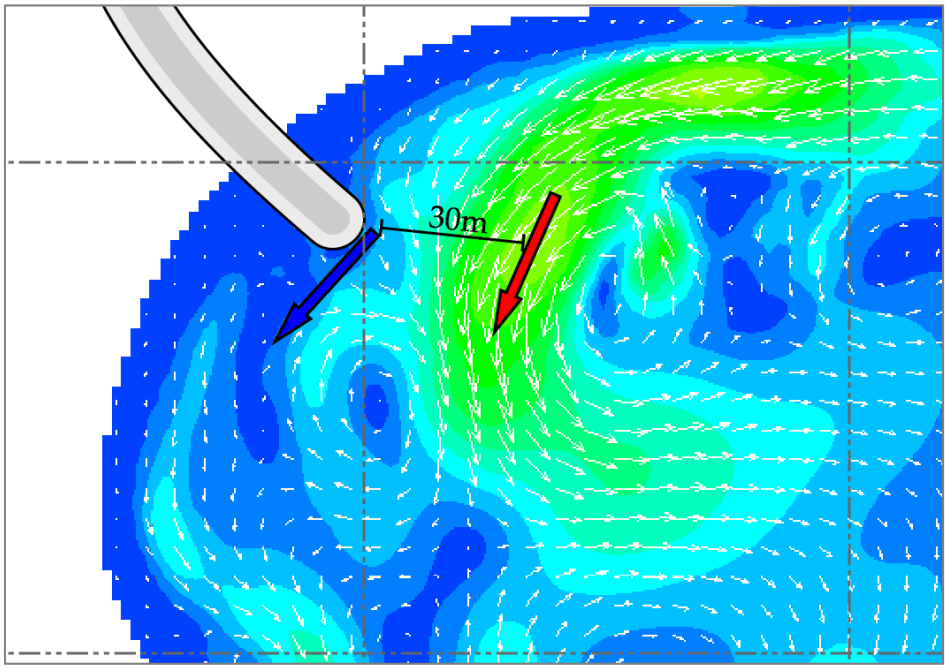

Figure 8-16: Comparison of measured vectors in the CSIR (blue) and MBWS (red) model. The colour-coded flow pattern is from the MBWS model.

8.2.6.2 Lowered section in spur (east section) with groyne off beach

Similar to the previous *lowered spur crest* scenario (**MT008**), the MBWS model did not simulate wave-overtopping action well, which resulted in a major deviation between the two models. Calibration of the overtopping action may have resulted in better agreement. The unreliable MBWS results for **MT014** and **MT015** made the comparison invalid. The CSIR's model did not show any significant improvements to the current circulation pattern.

8.2.7 Group F: T-groyne

Table 8-7: Short summary of T-groyne (Group F) tests. "N/M" denotes not measured.

ID	Short Description	Setup Conditions				Spur Velocity		Type
		WL [m MSL]	H_s [m]	T_p [s]	θ [deg]	CSIR V_f	MWBS U_f	
MT016	*T-groyne off beach*	0.45	1.4	12	8	≤ 37%	27%	T1
MT017	*T-groyne off beach*	0.9	1.4	12	8	N/M	23%	-
MT018	*T-groyne off beach*	0.9	1.8	12	8	52%	34%	T1
MT019	*T-groyne off beach*	-0.1	1	12	8	N/M	24%	-
MT020	*T-groyne off beach*	-0.1	1.4	12	8	30%	35%	T1
MT021	*T-groyne off beach*	0.4	1.1	12	8	N/M	21%	-
MT022	*T-groyne off beach*	0.4	1.4	8	8	N/M	26%	-
MT023	*T-groyne off beach (built-up beach)*	0.4	1.4	12	8	73%	38%	T1
MT024	*T-groyne off beach (denuded beach)*	0.4	1.4	12	8	≤16%	41%	T1

The CSIR and MBWS models showed good agreement in the T-groyne simulation results. Both models showed significant improvements by providing a well-sheltered bay between the new T-groyne and spur. Both models also agreed on the adverse circulation pattern developing between the T-groyne and the existing groyne, though there were more deviations in terms of current velocities.

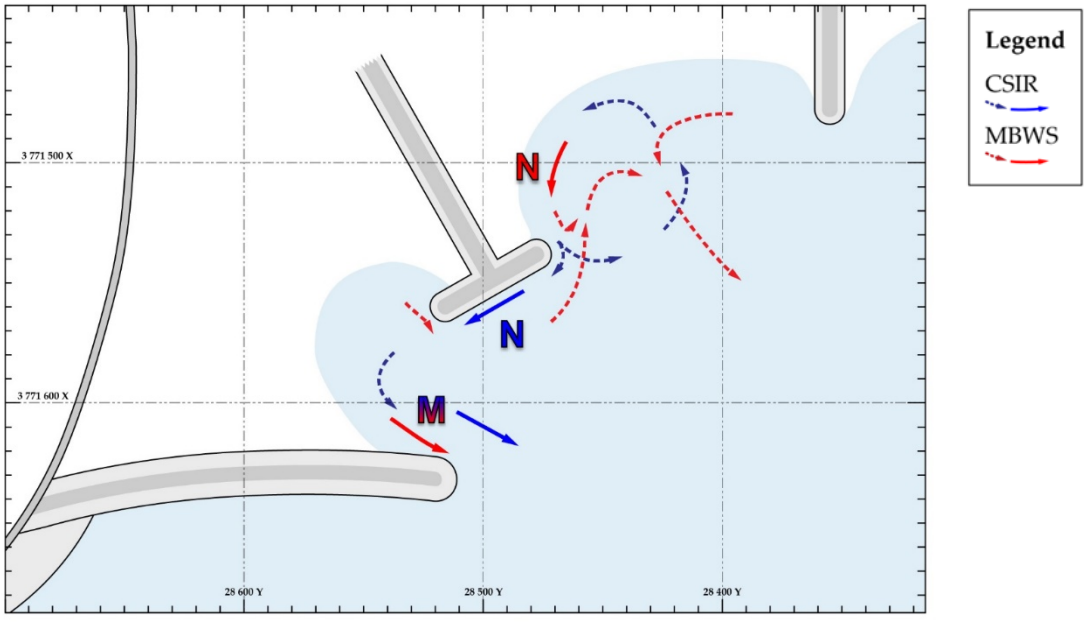

*Figure 8-17: Example CSIR-MBWS comparison for the T-groyne structures (**MT020**: H_s = 1.4 m, T_p = 12 s, WL = -0.1 m MSL)*

Some cyclic effects were reported in the CSIR model. Firstly, it was mentioned in § 8.1.2.1 that the MBWS model was not capable of simulating cyclic current effects. Secondly, the CSIR

noted that the cyclic effects may have been caused by long waves due to boundary effects, which suggests that the cyclic effects was a physical model-specific phenomenon, and not a representation of the prototype conditions.

8.2.7.1 Sheltered bay

Table 8-7 (above) showed the comparison of the exit current velocities along the spur for the CSIR and MBWS simulations. It can be seen that in four of the T-groyne scenarios the velocity along the spur was not measured (denoted "N/M"). The CSIR noted that in these cases the velocities were too low to be measured. The lack of measurements implied that the results were very positive in the CSIR simulations, but made the quantitative comparison somewhat difficult. The velocities are shown below for visual comparison.

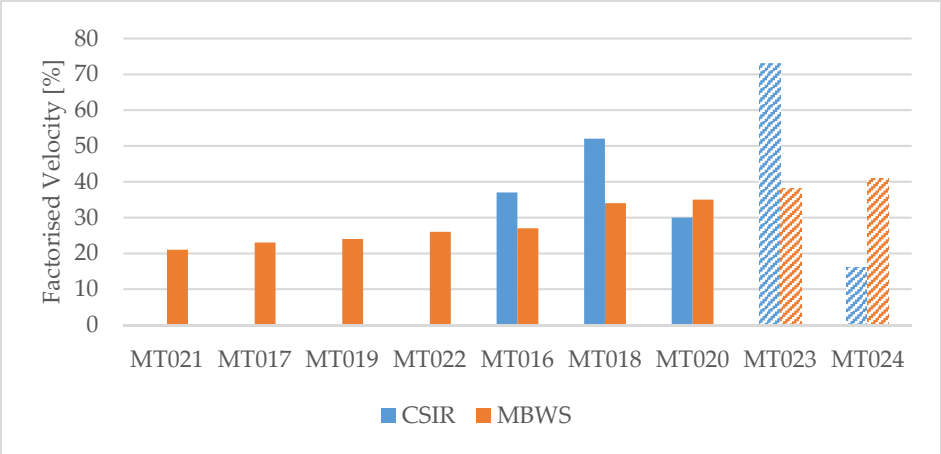

Figure 8-18: CSIR-MBWS comparison of sheltered-bay exit velocities along the spur, ranked by MBWS-velocity magnitude. The hatched bars indicate the scenarios with re-profiled beach configurations.

Two noteworthy occurrences are visible in Figure 8-18. Firstly, it can be seen that the CSIR's velocity measurements were subject to more variability, with a total range from insignificant velocities to $\boldsymbol{V_f = 73\%}$, whereas the velocity measurements of the MBWS simulations ranged only between $\boldsymbol{U_f = 21\%}$ and $\boldsymbol{U_f = 41\%}$. Secondly, where the CSIR simulations considered the exit velocities as negligible, the MBWS simulations also resulted in lowest velocities (**MT017**, **MT019**, **MT021** and **MT022**). This data was too limited to make any definite conclusions on possible trends.

In several cases the MBWS simulations showed evidence of current flows (with velocity ranging between $\boldsymbol{U_f = 18\%}$ to $\boldsymbol{U_f = 58\%}$) occurring in the sheltered area behind the flange of the T-groyne. This is a possible danger, as it may create a false illusion of safety due to the lack of wave action – similar to the present danger of the spur. This effect was not reported by the CSIR for their simulation.

The CSIR simulations included two high tide scenarios (**MT017** and **MT018**) which included wave overtopping on the spur. This caused strong but relatively short currents in shallow areas that quickly diffused in deeper water. Due to the relative complexity involved, overtopping was not simulated in the MBWS model.

8.2.7.2 *Wave-exposed area*

The graph below compares the velocities measured in the strong circulation in or near the exposed bay. Overall, the MBWS simulations showed significantly higher velocities than the CSIR model. **MT019** and **MT020** were omitted from this graph, because the CSIR velocities were measured along the head of the T-groyne and no similar current patterns were present in the corresponding MBWS simulations. For **MT023** the CSIR reported no significant current flow in the region of the exposed area. All of the MBWS velocities were simulated behind the T-flange in the exposed bay. This area was relatively sheltered against incoming waves. Similar to the situation on the opposite side of the T-groyne, this may present a zone of false security.

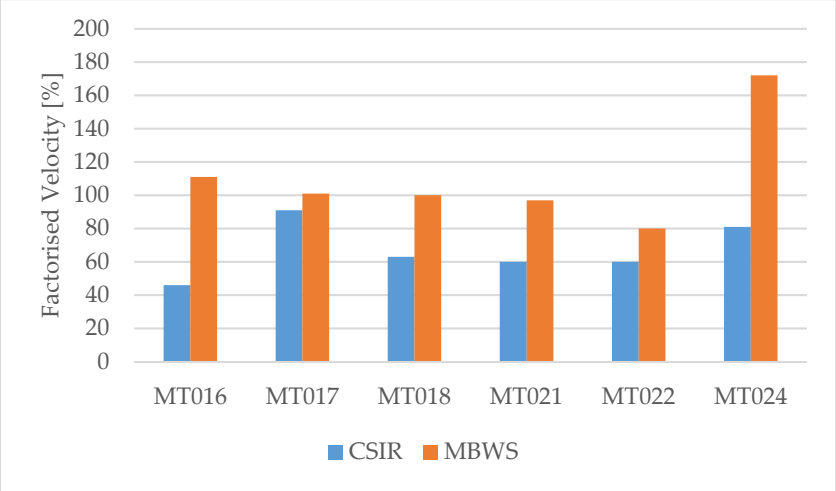

Figure 8-19: Comparison of velocities of the circulation pattern in the exposed bay

8.2.7.3 *Influence of beach configuration*

All T-groyne models of the CSIR and MBWS were re-profiled to account for the possible beach configuration response to the T-groyne. The re-profiled beach configuration was only an estimate which could not be validated. To test the influence of beach equilibrium configurations, a more built-up beach and a denuded beach were tested with similar wave and tide conditions.

Table 8-8 (below) compares the influence of the bathymetry on the current velocities for similar wave and tide conditions. **MT023** and **MT024** represent the built-up and denuded beaches respectively. **MT016** lies somewhere in the middle, with the water level 0.05 m higher than in **MT023** and **MT024**.

Table 8-8: CSIR-MBWS comparison of current trends for different re-profiled bathymetries

Section	Factorised Velocities: V_f & U_f [%]					
	Built-up beach		Normal beach*		Denuded beach	
	CSIR	MBWS	CSIR	MBWS	CSIR	MBWS
Spur	73%	38%	37%	27%	16%	41%
T-flange	-	58%	-	51%	-	30%
Circulation (north)	-	110%	46%	111%	81% - 117%	146%

**The normal beach (MT016) scenario was at water level 0.05m higher than the built-up beach and denuded beach*

By examining the CSIR's current velocities along the spur, it can be seen how the sheltered bay became more energetic for a more built up beach. In the MBWS model, the trend was not as clear from the velocities along the spur itself. It was, however, evident in the previous chapter that the sheltered bay was more energetic for built-up beaches in the MBWS simulations. From § 7.3.6.3.4, the current velocity distribution exceedance curve can be used to illustrate this trend:

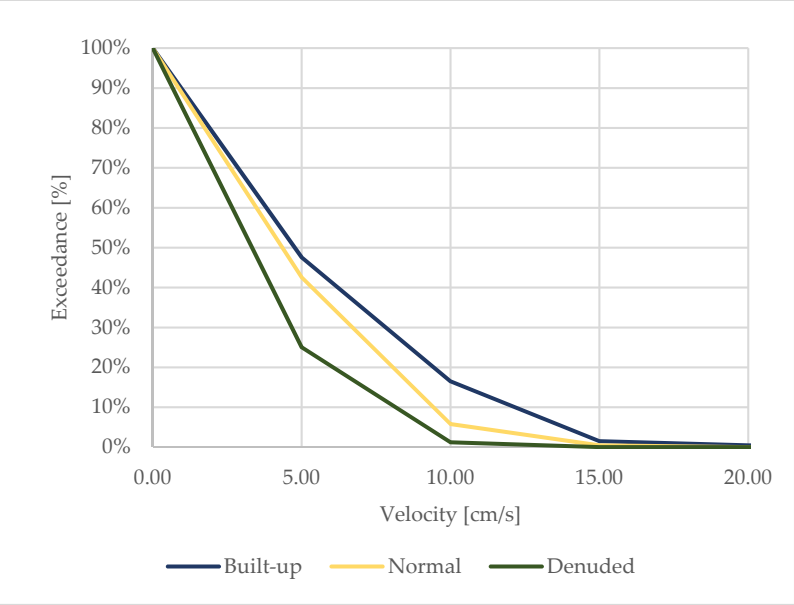

Figure 8-20: Influence of beach configuration on current velocity distribution for the MBWS T-groyne simulations.

Both models showed how the current velocities in the exposed area were reduced for more built-up beaches. The effect was more prominent in the CSIR simulations. In the MBWS simulations, the difference between the built-up beach profile (**MT023**) and normal beach profile (**MT016**) was relatively small. No area-statistics were measured for this area.

8.3 Simplified Rating System for both CSIR and MBWS Models:

Finally, a simplified rating system was used to categorise the performance of each simulation, for both the CSIR and MBWS models. This rating system evaluated the maximum exit-current velocity for each individual test.

The exit velocity in this case were defined as any strong current that could potentially pull bathers out of the sheltered bay. In most cases this was relatively close to the spur. The exit velocities therefore excluded any of the currents from the wave-exposed region which presented a more visible hazard. For each CSIR and MBWS simulation only the single and strongest exit velocity was chosen for the rating. The velocities between the MBWS and CSIR models did not necessarily have to occur in the same region. The figure below shows the rating system used to categorise the safety improvement for a specific layout option.

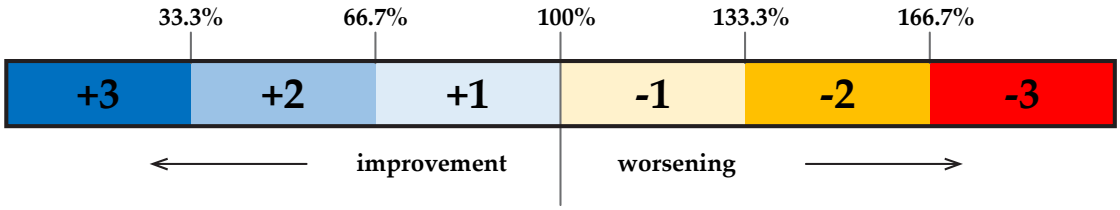

Figure 8-21: A simplified rating system to compare the performance of various tests

All velocities (U_f and V_f) below 33.3% of the original measured spur velocity were categorised as "+3", indicating excellent reduction in exit velocities. On the other hand, all velocities above 166.7% were categorised as "-3", indicating much more dangerous conditions. A comparison factor "$\mathcal{F}_C$" was introduced as a quantitative measurement of agreement between the CSIR and MBWS models. The comparison factor is simply the absolute difference of the performance rating of the two models.

Table 8-9: Simplified performance rating comparison for the CSIR and MBWS models

Model	CSIR	MBWS	$\mathcal{F}_C$
MT001	+1	+1	0
MT002	- 1	+1	2
MT003	+1	+1	0
MT004	- 1	+1	2
MT005	- 2	- 2	0
MT006	- 1	- 1	0
MT007	+ 2	+ 2	0
MT008	- 1	- 3	2
MT009	+1	+1	0
MT010	- 1	- 2	1
MT011	+1	- 3	2
MT012	+1	+1	0
MT013	- 1	+1	2
MT014	- 1	- 3	2
MT015	+1	- 3	4

Model	CSIR	MBWS	$\mathcal{F}_C$
MT016	+ 2	+ 3	1
MT017	+ 3	+ 3	0
MT018	+ 2	+ 2	0
MT019	+ 3	+ 3	0
MT020	+ 3	+ 2	1
MT021	+ 3	+ 3	0
MT022	+ 3	+ 3	0
MT023	+1	+ 2	1
MT024	+ 3	+ 2	0

The simplified rating system again shows how well the T-groyne scenarios (**MT016** through **MT024**) performed – both in terms of inter-model comparison and current-reduction performance. This rating system quickly points out that none of the preliminary tested models (**MT001** through **MT015**) showed promising results, except for the *dog-legged groyne off beach* (**MT007**). Both the CSIR and MBWS models also showed very good agreement for **MT007**. This option may be worth considering in future studies.

This test is generalised and no final conclusions can be made based on this rating system alone, but it provides a useful quick overview of the performance of the tests and how the CSIR and MBWS models compared.

8.4 CONCLUSION OF THE MBWS-CSIR MODEL COMPARATIVE STUDY

The MBWS model was set up as similar as possible to the CSIR model in order to compare the results. At best, the two models had almost exactly the same results, which made comparison between the two models straightforward. This, however, was rarely the case as some degree of difference between the models was mostly present. The general circulation pattern and the current velocities were the main focus of comparison.

8.4.1 Compatibility

The published results from the CSIR's 1997 study were very simplified and uncalibrated. The circulation patterns for each model were visualised by means of a line-illustrations and the velocities were expressed as relative values, since the model was not calibrated. The results from the MBWS model were simplified to a similar format for easier comparison. The drawback of the 1997 study was that only a fraction of the output of the physical simulation was reported, and it was not always clear whether a certain current was omitted due to insignificance or never existed in the physical model. This is understandable, as the recording instruments used in the physical model simply cannot provide the same level of detail as the output results from the MBWS model.

Another complexity associated with the comparative study was differences in circulation patterns. When the general circulation patterns differed between the two models, it becomes difficult to subjectively compare peak velocities within the currents. Therefore a velocity vector comparison classification system was designed to define the quantitative compatibility of two vectors between the CSIR and MBWS models. This system was used to identify *Type 1* velocities, which was the only type that could be compared directly due their similar match.

8.4.2 Comparison of simulation results

The models compared well with reasonably good agreement in terms of the current circulation patterns and velocity approximation. In the majority of the cases a similar (T1) exit velocity was present in both models, which made it possible to do a simple statistical performance comparison between the two models.

Generally the same circulation patterns were present, but there were a few cases were the direction of circulation was opposite or the circulation pattern was completely different. It was not always clear what the cause of the difference was, due to the limited amount of information available. The MBWS simulations consistently showed relatively strong circulation patterns developing in the northern-most (exposed) bay. In some of the CSIR models a similar circulation was reported, but not as often as in the MBWS model.

The MBWS simulations also showed evidence of a secondary current developing in the lee of the T-groyne flange, which posed a danger of false security, similar to the present current along the spur. Although the current was not as strong as the present current along the spur, it may present some degree of danger. The CSIR did not report any such findings.

The CSIR simulations sometimes included cyclic events of moving circulation patterns or occasional rip currents. In the MBWS model the wave-induced currents were resolved by phase-averaging, which meant that the currents and associated circulation patterns were a stable and uniform solution, and therefore did not indicate any cyclic events. The CSIR noted however, that the cyclic effects may have been caused by long waves due to boundary effects,

and without validation data it cannot be established whether these effects would indeed occur in prototype conditions.

The CSIR simulations also included overtopping effects in a few of the models. The MBWS model did not simulate the overtopping effects well. It was found that without available calibration data, the wave overtopping could not be resolved accurately. *MIKE 21 Boussinesq Wave* can simulate overtopping effects, but to do it accurately would require a comprehensive study. This unsuccessful modelling resulted in three cases with unreliable – and therefore – incomparable results.

In conclusion, a simplified rating was set up and used to rate and compare exit current performance of the MBWS and CSIR model side by side. This rating system attested to the good agreement of the models, as well as to the excellent performance of the T-groyne structures in reducing the current.

8.4.3 Conclusion on the numerical and physical model comparison

With a limited amount of results available from the physical model study of the CSIR (1997) it was not possible to conduct a very thorough comparison. The results were, however, sufficient to prove that good similarity between the physical model and Boussinesq wave model was achieved. Furthermore, both models specifically showed good results in reducing the hazardous current along the spur by means of using the proposed T-groyne structure. This modelling and performance agreement does not only demonstrate the potential of using a Boussinesq wave model, but perhaps, more importantly demonstrated the proven potential of a T-groyne structure in this situation.

9 CONCLUSIONS

9.1 BRIEF SUMMARY OF THE EXISTING SITUATION

A hazardous circulation cell exists at Monwabisi, which resulted from the addition of a spur adjacent to a tidal pool. This danger is made worse because the wave-sheltered area behind the spur creates an effect of false security. Closer to the spur, the beach is more sheltered against incoming waves. This creates a false perception of safe water as currents are not easily spotted by the untrained eye. Near the head of the spur the beach profile steepens. The sudden increase in depth and the presence of a strong current present a very hazardous combination. This strong current, often referred to as a rip current, has been linked to several rescues or drownings. Removal of the structure was not considered an option, as it protects the tidal pool against excessive wave overtopping and scouring. The spur also holds a beach, which would be eroded upon removal of the structure.

The primary objective of this study was to re-evaluate the proposed solutions of the CSIR by means of a numerical model. The secondary objective was to investigate whether this complex hydrodynamic system could be successfully simulated by means of a numerical 2D Boussinesq-type wave model. DHI's *MIKE 21 Boussinesq Wave* was used to set-up the *Monwabisi Boussinesq Wave Simulation* (MBWS) model. With the MBWS numerical model, the proposed solutions could be investigated by means of an in-depth visual and statistical analysis to better understand the processes that cause the currents, as well as how the proposed structures could successfully reduce these. The results could further be compared to the findings of the CSIR's report to assess similarities and differences between the physical and numerical models. Agreements in successful proposed solutions could further support the recommendation for structural mitigation of the hazardous circulation.

9.2 SUCCESSFUL REPLICATION OF HAZARDOUS CIRCULATION

An initial numerical model was set up to simulate the present situation at Monwabisi. The model showed excellent agreement to observed and reported physical processes, which included the wave effects of shoaling, breaking, refraction and diffraction – and most importantly – the hazardous counter-clockwise current circulation in the embayment. This was followed by the replication of the CSIR's proposed solutions, with similar structural, bathymetric, wave and tidal conditions as had been used in the physical model study. There were no calibration data available on the current velocities at Monwabisi, and most results were therefore interpreted as relative velocities instead of absolute velocities.

9.3 MONWABISI BOUSSINESQ WAVE SIMULATION IN-DEPTH ANALYSIS

The results of the MBWS numerical models were studied by means of visual and statistical analysis. The visual analysis was mostly qualitative, which provided insight into the holistic two-dimensional process of the circulation pattern, surface elevation, average wave distribution, bathymetry and the structural features, as well as the interaction between all of these elements. The statistical analysis was more concerned with the quantitative performance of the proposed structures and how they improved beach safety relative to the existing situation with regard to the current velocities. The statistical analysis therefore focussed

mostly on the velocity components by examining both peak velocities as well as velocity distributions over defined areas.

The majority of the proposed solutions showed successful results in reducing the hazardous circulation cell. The most successful options were found to be associated with groynes that could interrupt the circulation process and reduce the incoming wave energy simultaneously. This solution separated the bay into two distinct areas: a wave exposed area, subject to direct incoming waves and strong circulations, and a sheltered bay with reduced waves and currents relative to the present situation.

The option of a more refined T-groyne solution was investigated with a bigger variety of wave and tide conditions. By all accounts the T-groyne option showed excellent results in reducing the current along the spur, as well as allowing for a very quiescent, bather friendly bay to exist. With the use of a newly-formulated *Swimming Danger Factor*, $\mathcal{S}_{\mathrm{D}}$, it was conclusively illustrated that the T-groyne on average reduced the present danger of the bay to $\mathcal{S}_{\mathrm{D}} = 30\%$, in terms of the combined velocity along the spur and the average velocity along the swimming beach.

The Boussinesq wave model showed great potential for in-depth analysis of the current situation, but also qualitatively and quantitatively proved that a T-groyne placed on the beach can result in much safer bating conditions.

9.4 COMPARISON TO THE CSIR'S PHYSICAL MODEL STUDY

The results of the MBWS numerical models were directly compared to the data available from the CSIR's (1997) physical model results. This mostly included simplified illustrations of the circulation cell and velocity measurements at key areas. For ease of comparison, the results of the MBWS models were processed to be in a similar format as used by the CSIR. Both models lacked velocity calibration data, but the results still compared relatively well.

The majority of the simulations showed good agreement, both in terms of the measured velocities, as well as the general circulation patterns. Some of the disagreements could not be clarified, as the CSIR only reported on the key findings deemed necessary for the report. Some differences were also caused by the limitations of the numerical model, which will be discussed in the next sub-section. However, in general the MBWS model agreed with the CSIR model with regard to which options are the best.

Most importantly, the CSIR and MBWS models strongly agreed to the success of the T-groyne structure. The two models not only agreed well in terms of results-similarity, but also clearly indicated that the T-groyne is a very good solution, especially in terms of reducing the current along the spur.

9.5 ADVERSE EFFECTS

The proposed solutions illustrated that it was possible to establish a safer quiescent beach by means of a structure, but a strong circulation cell persistently remained present in the wave-exposed part of the beach. The various solutions mostly caused this circulation cell to decrease in size, but slightly increase in terms of velocity. It was argued that the sheltered beach could be demarcated as a *designated swimming beach*, while the hazardous exposed beach should be demarcated as off-limit.

In the MBWS T-groyne simulations, a secondary current developed in the sheltered area behind the flange of the T-groyne head. The magnitude of this current was comparable to the reduced current along the spur, but it presented a similar danger of false safety due to the visibly low exposure to incoming waves.

9.6 LIMITATIONS OF THE STUDY

The modelling limitations in this study were mostly associated with the Boussinesq wave model's capabilities and insufficient calibration data.

The wave-induced currents in the Boussinesq wave model are resolved by depth-integrated phase-averaged terms. This meant that the currents and associated circulation patterns were a stable and uniform solution, and therefore did not indicate any cyclic events. The CSIR reported a few cyclic events in their simulations, but it was noted to probably be the result of boundary effects specific to the physical model.

The CSIR physical model included wave overtopping effects in five of the models. The MBWS numerical model runs did not simulate the overtopping effects well and thereby significantly overestimated the wave-induced currents. It was concluded that the numerical model is capable of modelling overtopping effects, provided that extensive data could be used to calibrate the overtopping effects. Only three of the proposed solutions were fully dependent on overtopping effects and those scenarios were therefore declared as unreliable.

9.7 FINAL CONCLUSION

The two-dimensional Boussinesq wave model proved to be suitable for simulating the complex hydrodynamic system at Monwabisi. The present hazardous circulation cell, as well as the proposed solutions were simulated with reasonable success. The model is therefore an excellent tool for such hydrodynamic studies. By means of various forms of visual and statistical analysis, it was shown that a T-groyne placed on the beach can potentially reduce the hazardous circulation cell present at Monwabisi to a significant extent. The findings resonate the CSIR's same conclusion from a similar physical model, which emphasises the motivation of a structural solution to obtain a safer beach.

10 RECOMMENDATIONS FOR FURTHER STUDIES

10.1 REFINING THE EXISTING MODEL

Field tests could be conducted to measure the prototype velocities of the circulation system in Monwabisi, especially the current velocity along the spur. This could be of great use to the calibration of the model, as well as to provide a more definitive benchmark of improvement.

In the sensitivity analysis, it was shown how to analyse the stability of the model. Although the influence of the instabilities of the MBWS models were arguably minimal, it is recommended that an even more stable model is used for similar studies in the future.

More wave conditions could be tested in terms of wave period, incident wave angle and wave height. The MBWS model was limited to long-crested regular waves, which did not include long wave effects. Long waves contribute significantly to the longshore current system and may therefore also have a significant impact on the circulation cell at Monwabisi. With the use of spectrum-defined distribution of wave heights, long waves could be created by wave grouping.

Some of the proposed solutions included re-profiling of the bathymetry, but this was simply based on estimation. It was shown in this study that the beach configuration is an important part of the overall performance of the model and can significantly influence the hydrodynamics. A physical or numerical sediment transport model could be used to evaluate the beach configuration response to the inclusion of a structure.

10.2 ADDITIONAL TESTING POSSIBILITIES

The existing options, like the T-groyne, could possibly be optimized further by testing more variations. Alternatively, completely new structures and layouts could be designed and tested in the model, including more groyne options or larger offshore structures such as submerged breakwaters.

Alternative means of numerical modelling could also be used to be compared to the Boussinesq wave models. For example, the *MIKE 21 Flow Model HD FM* hydrodynamic flow model could be coupled with the *MIKE 21 Spectral Wave SW* model to simulate wave-induced currents from spectral waves. The advantage of such a model is the inclusion of particle tracing, which can be used to simulate swimmers caught in the current. In this way a social perspective could be included in the study to assess the swimming conditions based on structural changes. Another advantage of a coupled model is the ability to study longer periods of simulation, including tide level changes.

DHI released a relatively new development, *MIKE 21 Shoreline Morphology SM*. This model extends the coupled spectral wave and hydrodynamic flow by including two-dimensional shoreline morphology changes. This would allow for the simultaneous simulation of the hazardous currents as well as beach-configuration response to structural changes.

REFERENCES

Aagard, T. 2007. *Waves.* [Online]. Available: http://www.coastalwiki.org/wiki/Waves [29 July 2015]

Alfa Kinetic. 2008. *Stream indicator buoy.* [Online]. Available: http://www.alfakinetic.dk/ [30 July 2015]

Bailard, J.A. 1981. An Energetics Total Load Sediment Transport Model for a Plane Sloping Beach. *Journal of Geophysical Research: Oceans* 86(11): 10938-10954.

Bamford, H. 1999. Cape Town's Beach of Death. *Cape Argus,* 14 October 1999

Battjes, J.A., Sobey, R.J. & Stive, M.J.F. 1990. Nearshore Circulation. *The Sea-Volume 9: Ocean Engineering Science*: 467.

Bezuidenhout, V. 2011. *Separate Amenities; Topographics of Recreational Spaces in South Africa.* University of Cape Town, South Africa.

Bosman, D.E. & Scholtz, D.J.P. 1982. A Survey of Man-made Tidal Swimming Pools along the South African Coast. *Coastal Engineering Proceedings* 18: 2504-2513.

Brander, R.W., Bradstreet, A., Sherker, S. & MacMahan, J. 2011. Responses of Swimmers Caught in Rip Currents: Perspectives on Mitigating the Global Rip Current Hazard. *International Journal of Aquatic Research and Education* 5(4): 476-482.

Brighton, B., Sherker, S., Brander, R., Thompson, M. & Bradstreet, A. 2013. Rip Current Related Drowning Deaths and Rescues in Australia. *Natural Hazards and Earth System Sciences* 13(4): 1069-1075.

Burchard, H., Gräwe, U. & Umlauf, L. 2015. *Coastal Ocean Processes*. [pdf] Available at: http://www.io-warnemuende.de/tl_files/staff/burchard/pdf/coastal.pdf [12 August 2016]

Carey, W., Kirby, J. and Svendsen, I. 2005. *Rip Currents*. [pdf] Available at: http://nsgl.gso.uri.edu/delu/delug05006.pdf [30 July 2015]

Chow, V.T. 1959. *Open-channel hydraulics.* New York: McGraw-Hill

CoCT. 2015. *Monwabisi resort.* [Online]. Available: https://www.capetown.gov.za/en/SportRecreation/Pages/Monwabisiresort [4 August 2015]

CSIR. 1989. Site Visit of Macassar to Monwabisi Beach. [Photo]

CSIR. 1990. Historic Aerial photographs of Monwabisi Resort. [Photo]

CSIR. 1997. *Monwabisi Beach Safety Investigation*. ENV/S-C 97084. Pretoria: CSIR

Dalrymple, R.A. 1978. Rip Currents and their Causes. *Coastal Engineering Proceedings 1*(16): 1414-1427.

Dean, R.G. & Dalrymple, R.A. 2004. *Coastal processes with engineering applications.* Cambridge University Press

Dear, I.C.B. and Kemp, P. 2006. Lifesaving. In: *The Oxford Companion to Ships and the Sea*, 2nd ed. Oxford University Press.

DHI. 2007. *MIKE 21 Toolbox.* Hørsholm, Denmark: DHI.

DHI. 2014. *MIKE 21 Boussinesq Wave*. Hørsholm, Denmark: DHI.

DRDLR. 1945. Historic Aerial photographs of Swartklip. [Photo]

Engle, J., MacMahan, J., Thieke, R.J., Hanes, D.M. and Dean, R.G. 2002. Formulation of a Rip Current Predictive Index using Rescue Data. In: *Proceedings of the National Conference on Beach Preservation Technology*.

Fredsøe, J. & Deigaard, R. 1992. *Mechanics of coastal sediment transport.* Singapore; New Jersey: World Scientific

Gensini, V.A. & Ashley, W.S. 2010. An Examination of Rip Current Fatalities in the United States. *Natural Hazards* 54(1): 159-175.

GeoRepository. 2016. *Cape / Lo19.* [Online]. Available: http://georepository.com/crs_22279/Cape-Lo19.html [31 July 2016]

Ghani, A.A., Zakaria, N.A., Kiat, C.C., Ariffin, J., Hasan, Z.A. & Abdul Ghaffar, A.B. 2007. Revised Equations for Manning's Coefficient for Sand-Bed Rivers. *International Journal of River Basin Management* 5(4): 329-346.

Gourlay, M. 1982. *Nonuniform alongshore currents and sediment transport*. St. Lucia, Qld.: Dept. of Civil Engineering, University of Queensland.

Haller, M.C. & Dalrymple, R.A. 2001. Rip Current Instabilities. *Journal of Fluid Mechanics* 497: 225-234.

Haller, M.C. 1999. *Rip current dynamics and nearshore circulation.* Ph.D. University of Delaware.

Hansen, B. & Svendsen, I.A. 1984. A Theoretical and Experimental Study of Undertow. *Coastal Engineering Proceedings* 19: 2246-2262.

Hatfield, J., Williamson, A., Sherker, S., Brander, R. & Hayen, A. 2012. Development and Evaluation of an Intervention to Reduce Rip Current Related Beach Drowning. *Accident Analysis & Prevention* 46: 45-51.

Hur, D.S., Cho, W.C., Yoon, J.S., Kim, I.H. & Lee, W.D. 2014. Control Technologies in Reducing Rip Currents Around the Open Inlet between Two Submerged Breakwaters. *Journal of Coastal Research* 72(1): 75-85.

Komar, P.D. 1971. Nearshore Cell Circulation and the Formation of Giant Cusps. *Geological Society of America Bulletin* 82(9): 2643-2650.

Kraus, N.C. 1996. *History and heritage of coastal engineering*. New York: American Society of Civil Engineers.

Larsen, J. & Dancy, H. 1983. Open Boundaries in Short Wave Simulations — A New Approach. *Coastal Engineering* 7(3): 285-297.

Longuet-Higgens, M.S. & Stewart, R.W. 1964. Radiation Stresses in Water Waves: A Physical Discussion, with Applications. *Deep-Sea Research* 11: 529 - 562.

Longuet-Higgens, M.S. 1970. Longshore Currents Generated by Obliquely Incident Sea Waves, 2. *Journal of Geophysical Research: Oceans* 75(33): 6790–6801.

LSA. 2015a. *History of lifesaving South Africa.* [Online]. Available: http://lifesaving.co.za/background_mission_vision/ [7 August 2015]

LSA. 2015b. *Lifesaving South Africa: Drowning statistics 2011 - 2015*. [email]

Lushine, J.B. 1991. A Study of Rip Current Drownings and Related Weather Factors. *National Weather Digest* 16: 13-19.

MacMahan, J.H., Thornton, E.B. & Reniers, J.H.M. 2006. Rip Current Review. *Coastal Engineering* 53(2-3): 191 – 208.

MacMahan, J.H., Thornton, E.B., Stanton, T.P. & Reniers, J.H.M. 2005. RIPEX: Observations of a Rip Current System. *Marine Geology* 218(2): 113-134.

Madsen, P.A. & Sørensen, O.R. 1992. A New Form of the Boussinesq Equations with Improved Linear Dispersion Characteristics. Part 2. A Slowly-Varying Bathymetry. *Coastal Engineering* 18(3-4): 183-204.

Madsen, P.A. 1983. Wave Reflection from A Vertical Permeable Wave Absorber. *Coastal Engineering* 7(4): 381-396.

Madsen, P.A., Murray, R. & Sørensen, O.R. 1991. A New Form of the Boussinesq Equations with Improved Linear Dispersion Characteristics. *Coastal Engineering* 15(4): 371-388.

Madsen, P.A., Sørensen, O.R. & Schaffer, H.A. 1997. Surf Zone Dynamics Simulated by a Boussinesq Type Model. Part I. Model Description and Cross-Shore Motion of Regular Waves. *Coastal Engineering* 32(4): 255-287

McKenzie, P. 1958. Rip-Current Systems. *The Journal of Geology* 66(2): 103-113.

News24. 2014. *Boy, 5, drowns at cape resort.* [Online]. Available: http://www.news24.com/SouthAfrica/News/Boy-5-drowns-at-Cape-resort-20141231 [4 August 2015]

News24. 2012a. *False bay angler swept into sea missing.* [Online]. Available: http://www.news24.com/SouthAfrica/News/False-Bay-angler-swept-into-sea-missing-20120817 [4 August 2015]

News24. 2012b. *Man drowns in Western Cape.* [Online]. Available: http://www.news24.com/SouthAfrica/News/Man-drowns-in-Western-Cape-20120108 [4 August 2015]

NGI. 2013. *Datums and coordinate systems.* [Online]. Available: http://www.ngi.gov.za/index.php/technical-information/geodesy-and-gps/datum-s-and-coordinate-systems [25 August 2016]

NSRI. 2013. *1 missing and 6 rescued at Monwabisi.* [Online]. Available: http://www.nsri.org.za/2013/12/1-missing-and-6-rescued-at-monwabisi/ [31 July 2015]

NSRI. 2015a. *NSRI - Strandfontein station.* [Online]. Available: http://www.nsri.org.za/tag/strandfontein/ [31 July 2015]

NSRI. 2015b. *Sea rescue stats.* [Online]. Available: http://www.nsri.org.za/stats/ [31 July 2015]

NSRI. 2016. T*eenager drowns at Monwabisi.* [Online]. Available: http://www.nsri.org.za/2016/07/teenager-drowns-at-monwabisi/ [3 August 2016]

Prochazka, K. & Kruger, L. 2010. Trends in Beach Utilisation on the Cape Peninsula, South Africa, during and After Apartheid. *Transactions of the Royal Society of South Africa* 56(1): 25-40.

Reeve, D. 2009. *Risk and reliability: Coastal and hydraulic engineering.* London: Spon Press.

Reeve, D., Chadwick, A. & Fleming, C. 2004. *Coastal engineering*. London: Spon Press.

Rip Buoy. 2014. *Rip Buoy*. [Online]. Available: http://ripbuoy.com/ [8 August 2015]

RNLI. 2011. *RNLI Annual Operational Statistics Report.* [Online]. Available: http://rnli.org/ [4 August 2015]

SANHO. 2016. *Tidal levels for Simon's Town.* [Online]. Available: http://www.satides.co.za/common/scripts/today/?loc=rsa_sb [2 August 2016]

Schäffer, H.A., Madsen, P.A. & Deigaard, R. 1993. A Boussinesq model for waves breaking in shallow water. *Coastal Engineering* 20(3-4): 185-202

Shepard, F.P. & Inman, D.L. 1951. Nearshore Circulation. *Proceedings of First Conference on Coastal Engineering.* New York: ASCE. 50-59.

Shepard, F.P. 1950. Longshore Current Observations in Southern California. *DTIC Tech. Memorandum 13*

Shepard, F.P., Emery, K.O. & La Fond, E.C. 1941. Rip Currents: A Process of Geological Importance. *The Journal of Geology* 49(4): 337-369.

Short, A.D. & Hogan, C.L. 1994. Rip Currents and Beach Hazards: Their Impact on Public Safety and Implications for Coastal Management. *Journal of Coastal Research* 12: 197-209.

Sørensen, O.R., Schäffer, H.A. & Madsen, P.A. 1998. Surf Zone Dynamics Simulated by a Boussinesq Type Model. III. Wave-Induced Horizontal Nearshore Circulations. *Coastal Engineering* 33(2–3): 155-176.

Sørensen, O.R., Schäffer, H.A. & Sørensen, L.S. 2004. Boussinesq-Type Modelling using an Unstructured Finite Element Technique. *Coastal Engineering* 50(4): 181-198.

Tarbuck, E.J., Lutgens, F.K. & Tasa, D. 2011. *Earth: An introduction to physical geology.* Upper Saddle River, N.J.: Pearson Prentice Hall

Theron, A.K. & Schoonees, J.S. 2007. Sand Transport at and Shoreline Response to a Breakwater Attached to a Large Tidal Pool at Monwabisi, Cape Town. *Journal of the South African Institution of Civil Engineering* 49(2): 2-9

Thompson, E.F., Chen, H.S. & Hadley, L.L. 1996. Validation of Numerical Model for Wind Waves and Swell in Harbours. *Journal of Waterway, Port, Coastal, and Ocean Engineering* 122(5): 245-257.

Thompson, G. 2013. Riding the waves of change. *Cape Times,* 9 September 2013

U.S. Army Coastal Engineering Research Centre. 1984. *Shore protection manual, volume 1.* Washington, DC: U.S. Goverment Printing Office

University of Delaware. 2009. *Rip current research.* [Online]. Available: http://www.ceoe.udel.edu/ripcurrents/Research/index.html [30 July 2015]

USLA. 2014. *United States Lifesaving Association Statistics.* [Online]. Available: http://arc.usla.org/Statistics/current.asp?Statistics=5 [4 August 2015]

Weaver, T. 1999. The Real Reasons for Drownings. *Cape Argus,* 18 October 1999: 15

Woodward, E.M., Beaumont, E., Russell, P.E., Wooler, A. & Macleod, R. 2013. Analysis of Rip Current Incidents and Victim Demographics in the UK. *Journal of Coastal Research* 65(1): 850-855

Zyserman, J., Fredsoe, J. & Deigaard, R. 1990. Prediction of the Dimensions of a Rip Current System on a Coast with Bars. *Coastal Engineering Proceedings 1*(22): 959-972

Appendix: A

High-resolution imagery

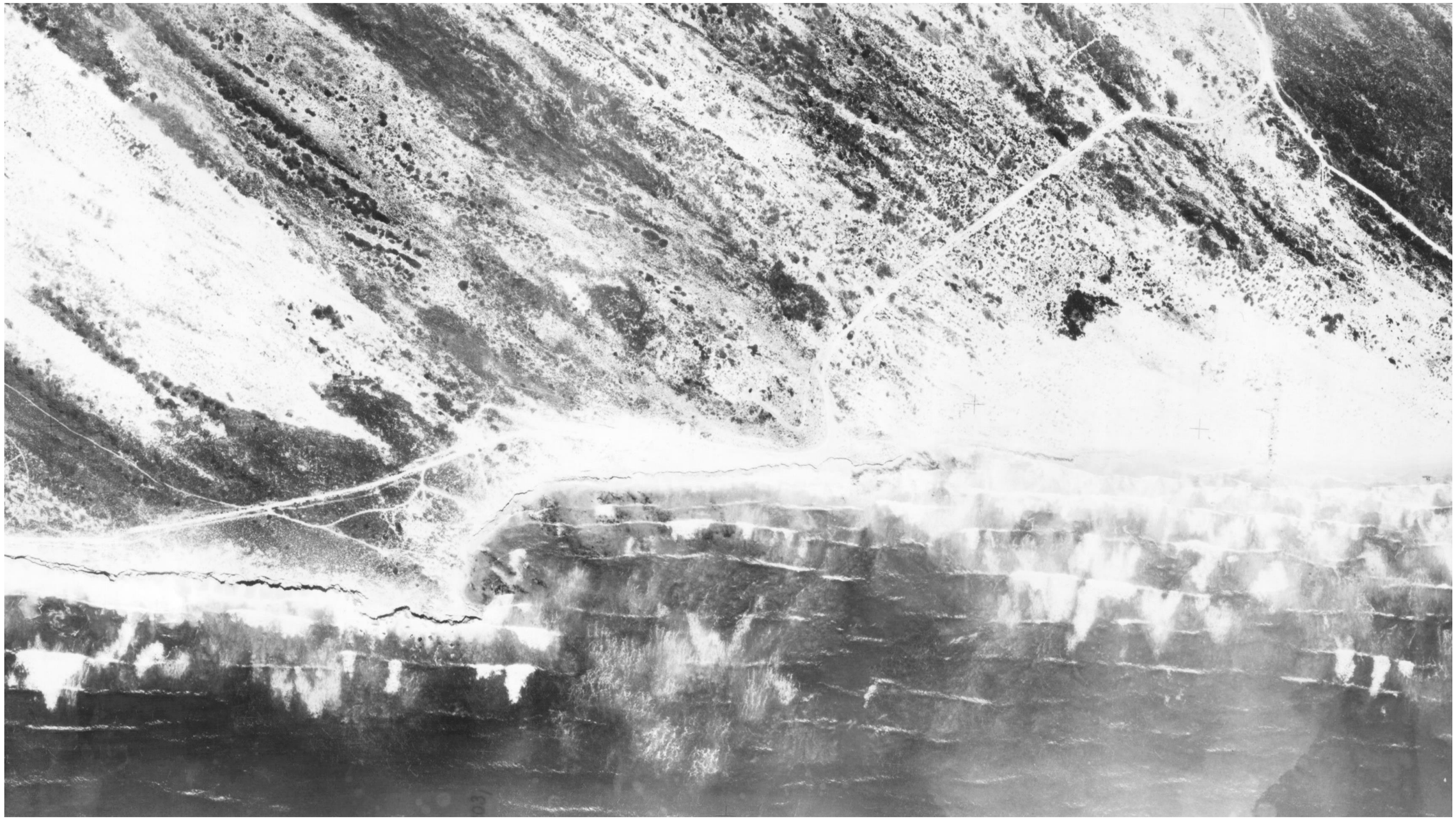

Figure A-1: DRDLR (1945)

Figure A-2: DRDLR (1983)

Figure A-3: CSIR (1990)

Figure A-4: Google Earth (2014)

Appendix: B

Structurally modified beach configurations and layouts

B.0 BASELINE SETUP

Layout & Bathymetry

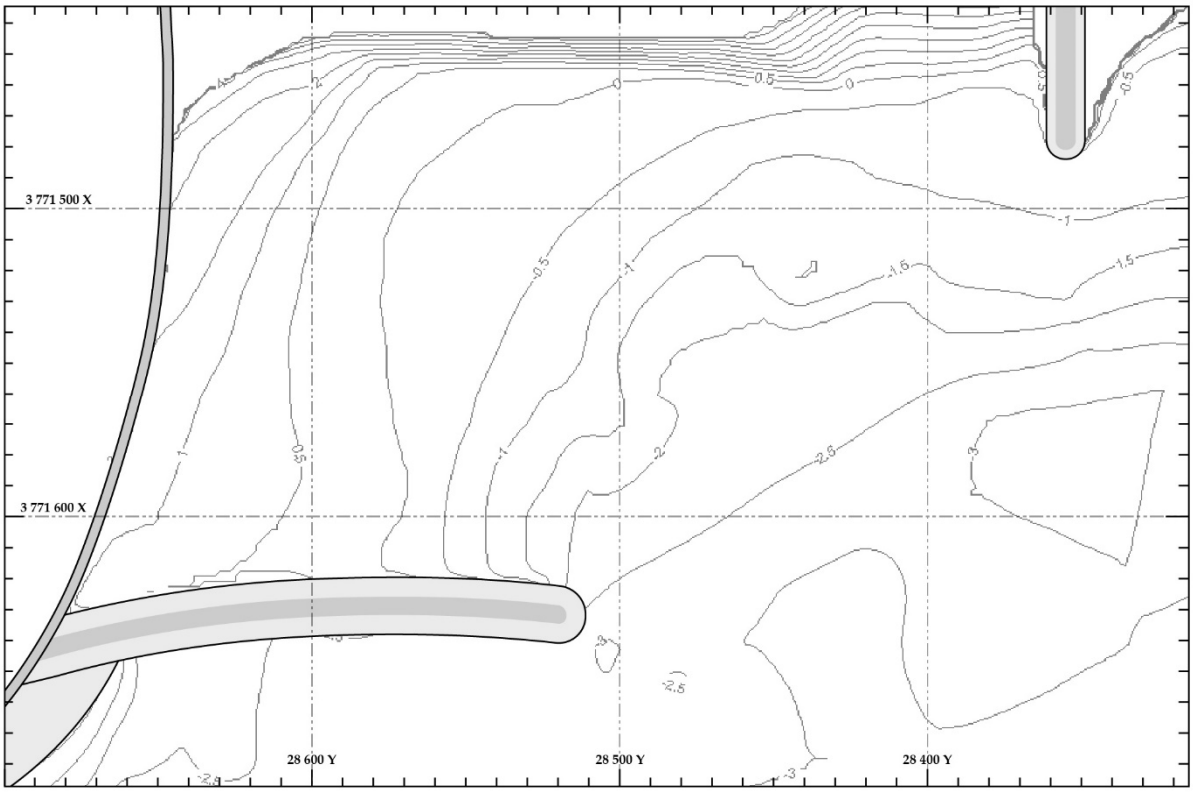

Used in Test(s):

Test	Tide Level	Wave Height	Wave Period	Wave Angle
MB110	-0.3 m MSL	1.3 m	12 s	+ 8°
MB210	-0.1 m MSL	1.0 m	12 s	+ 8°
MB220	-0.1 m MSL	1.4 m	12 s	+ 8°
MB310	+0.3 m MSL	1.3 m	12 s	+ 8°
MB410	+0.4 m MSL	1.1 m	12 s	+ 8°
MB420	+0.4 m MSL	1.4 m	12 s	+ 8°
MB430	+0.4 m MSL	1.1 m	8 s	+ 8°
MB510	+0.45 m MSL	1.4 m	12 s	+ 8°
MB610	+0.7 m MSL	1.5 m	12 s	+ 8°
MB710	+0.9 m MSL	1.4 m	12 s	+ 8°
MB720	+0.9 m MSL	1.8 m	12 s	+ 8°

B.A GROYNES EXTENDING FROM THE SHORELINE

B.A.1 Short groyne away from the spur

B.A.1.1 Layout & Bathymetry

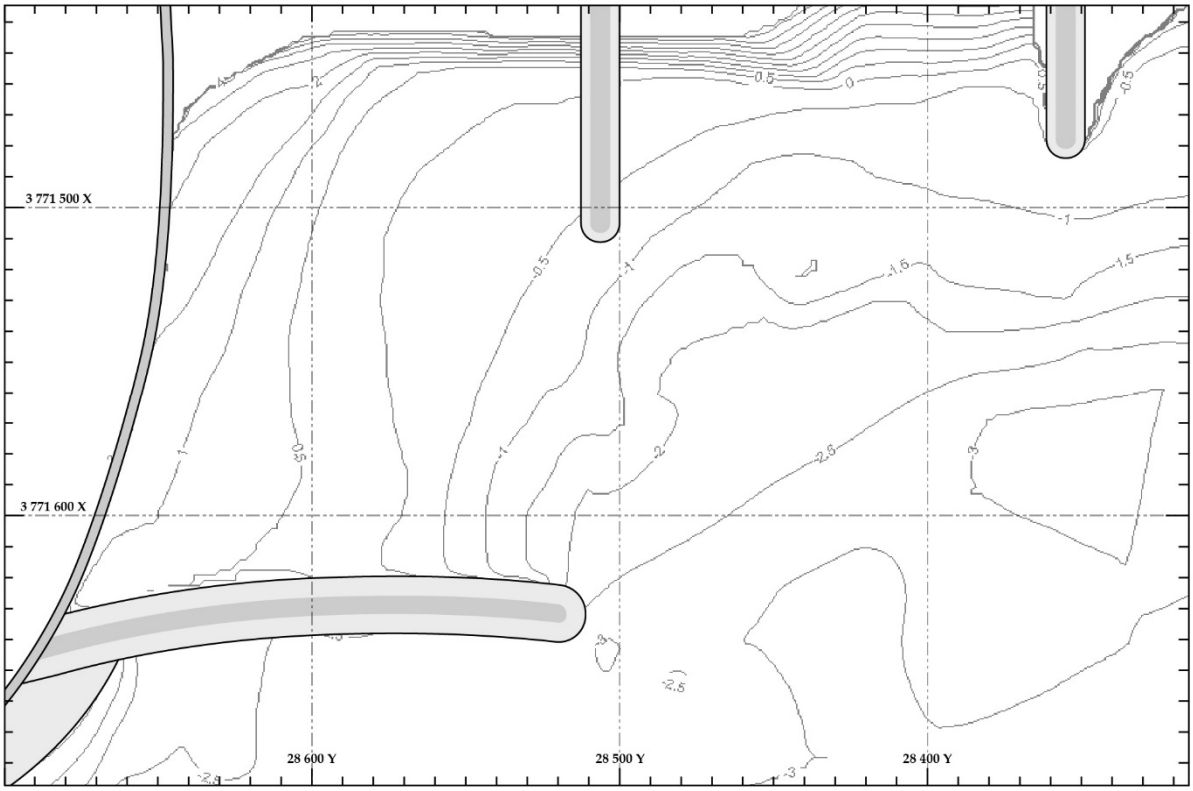

B.A.1.2 Used in Test(s):

Test	Tide Level	Wave Height	Wave Period	Wave Angle
MT001	+0.7m MSL	1.5 m	12 s	+ 8°

B.A.2 Long groyne opposite spur head

B.A.2.1 Layout

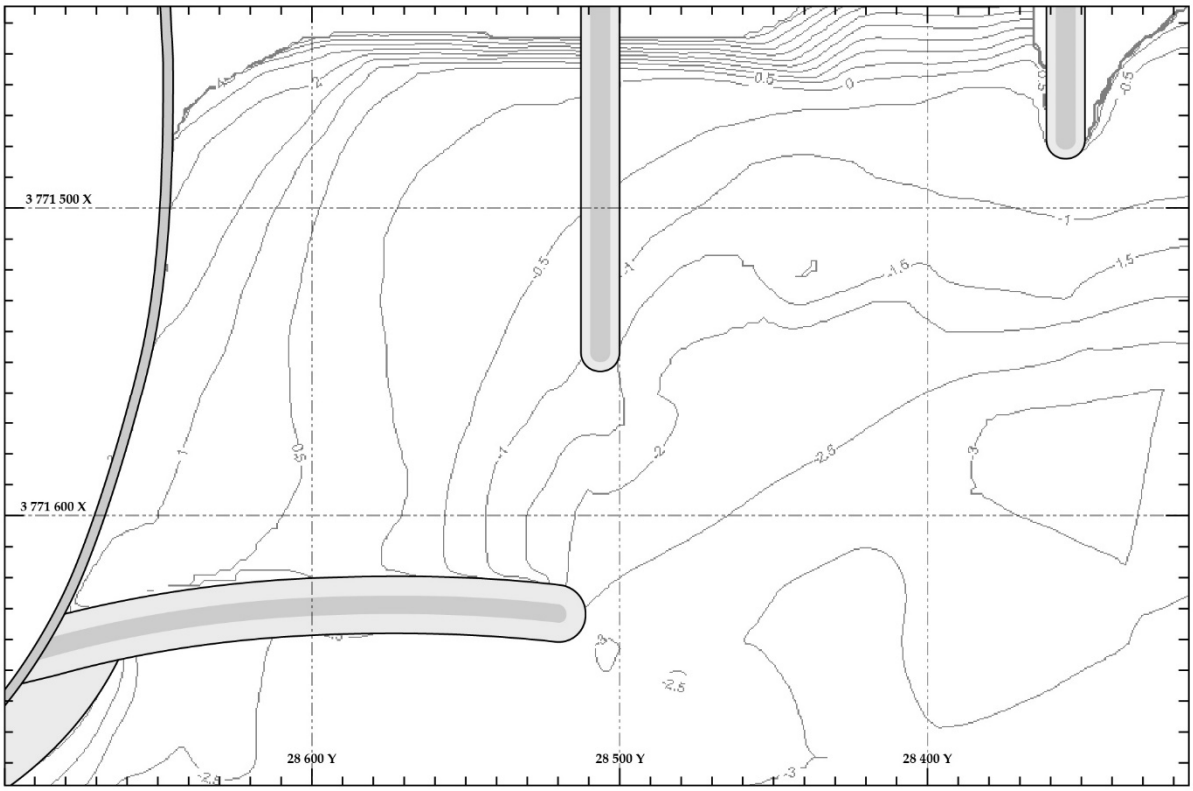

B.A.2.2 Used in Setups:

Test	Tide Level	Wave Height	Wave Period	Wave Angle
MT002	+0.7m MSL	1.5 m	12 s	+ 8°

B.A.3 Long groyne away from spur head

B.A.3.1 Layout

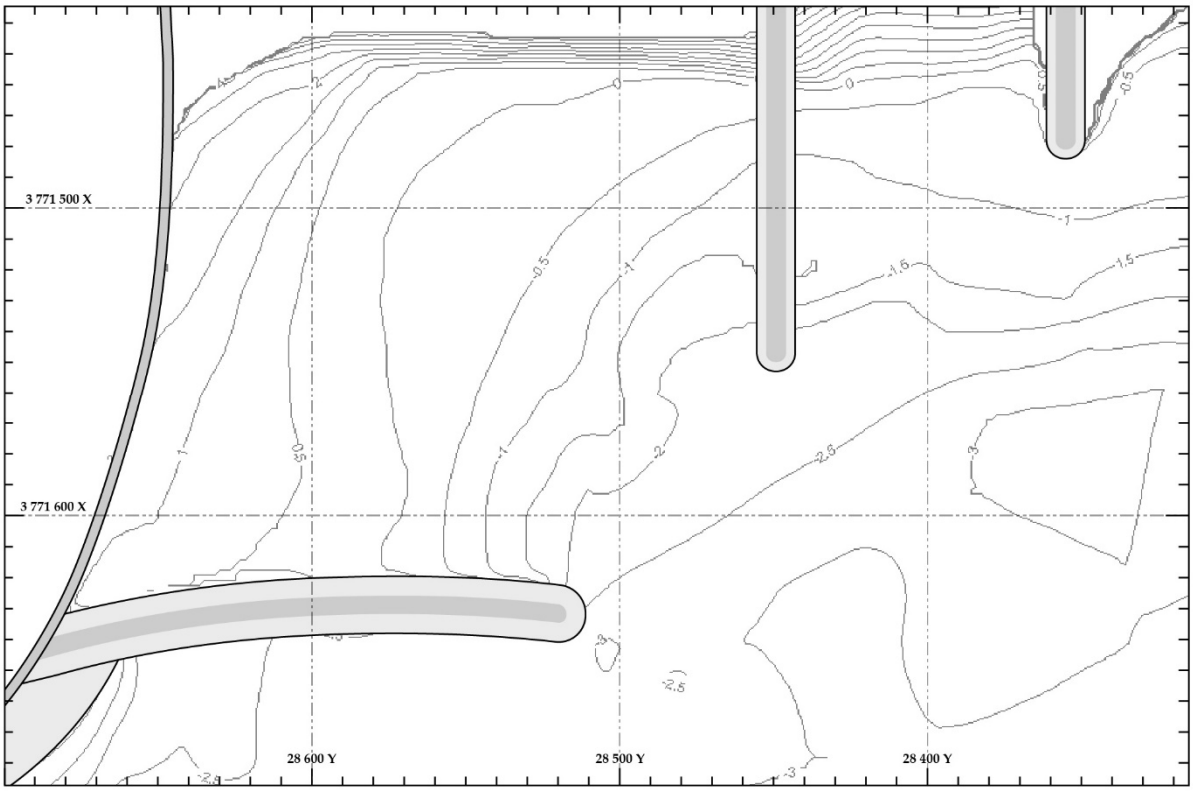

B.A.3.2 Used in Setups:

Test	Tide Level	Wave Height	Wave Period	Wave Angle
MT003	+0.7m MSL	1.5 m	12 s	+ 8°

B.A.4 Dog-legged groyne opposite spur head

B.A.4.1 Layout

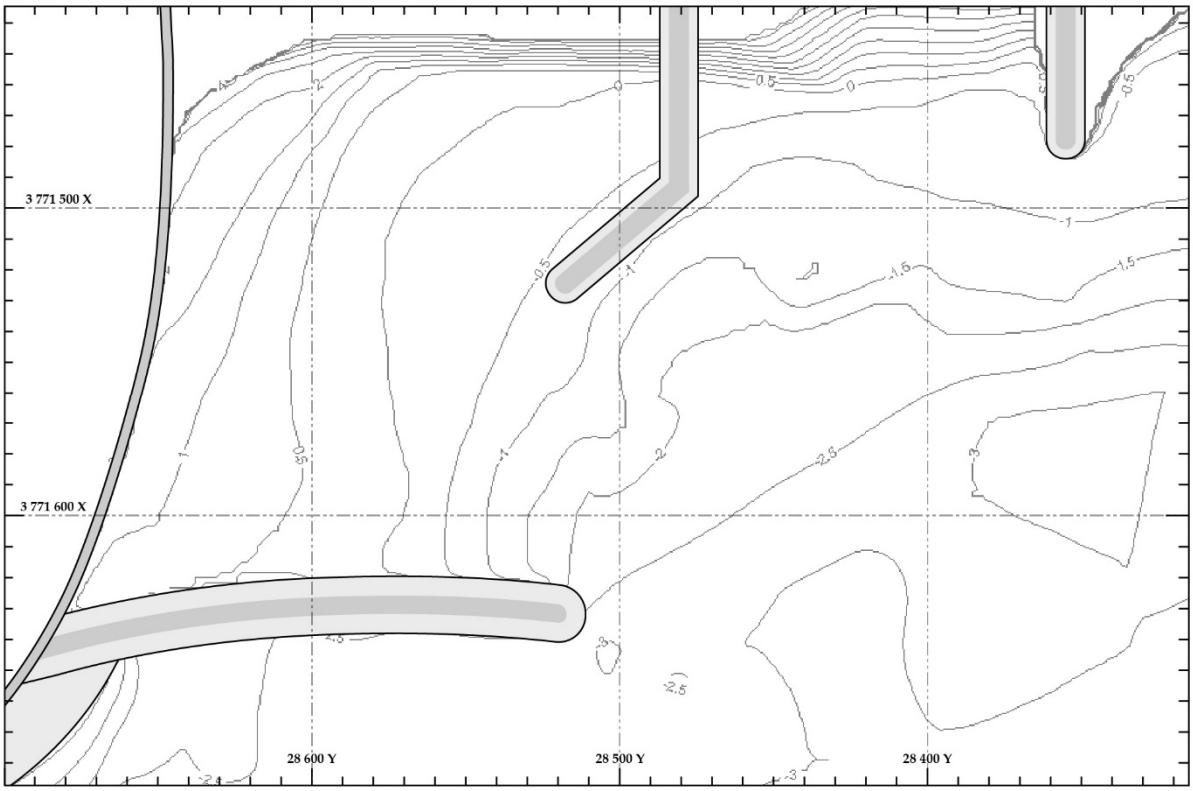

B.A.4.2 Used in Setups:

Test	Tide Level	Wave Height	Wave Period	Wave Angle
MT004	+0.7m MSL	1.5 m	12 s	+ 8°

B.A.5 Dog-legged Groyne off present beach

B.A.5.1 Layout

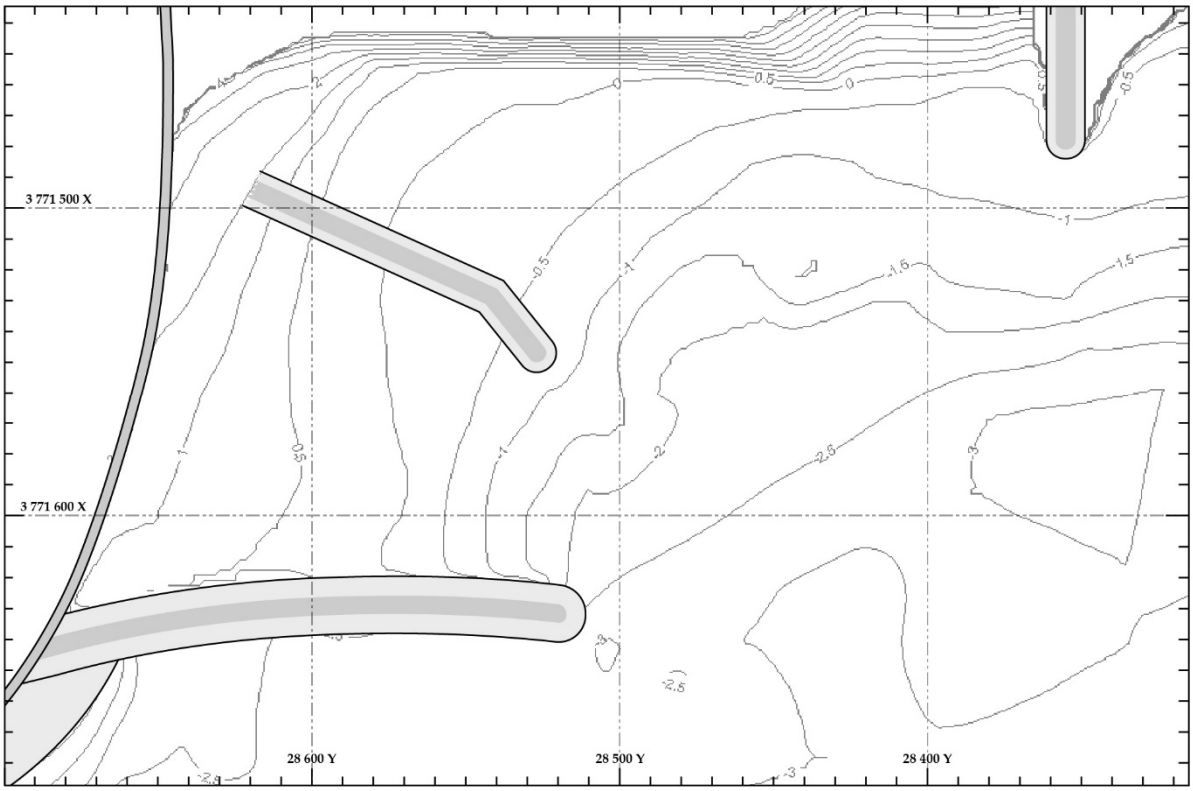

B.A.5.2 Used in Setups:

Test	Tide Level	Wave Height	Wave Period	Wave Angle
MT007	+0.7m MSL	1.5 m	12 s	+ 8°

B.B MODIFICATIONS TO THE SPUR

B.B.1 Dog-legged Spur off spur head (Landward)

B.B.1.1 Layout

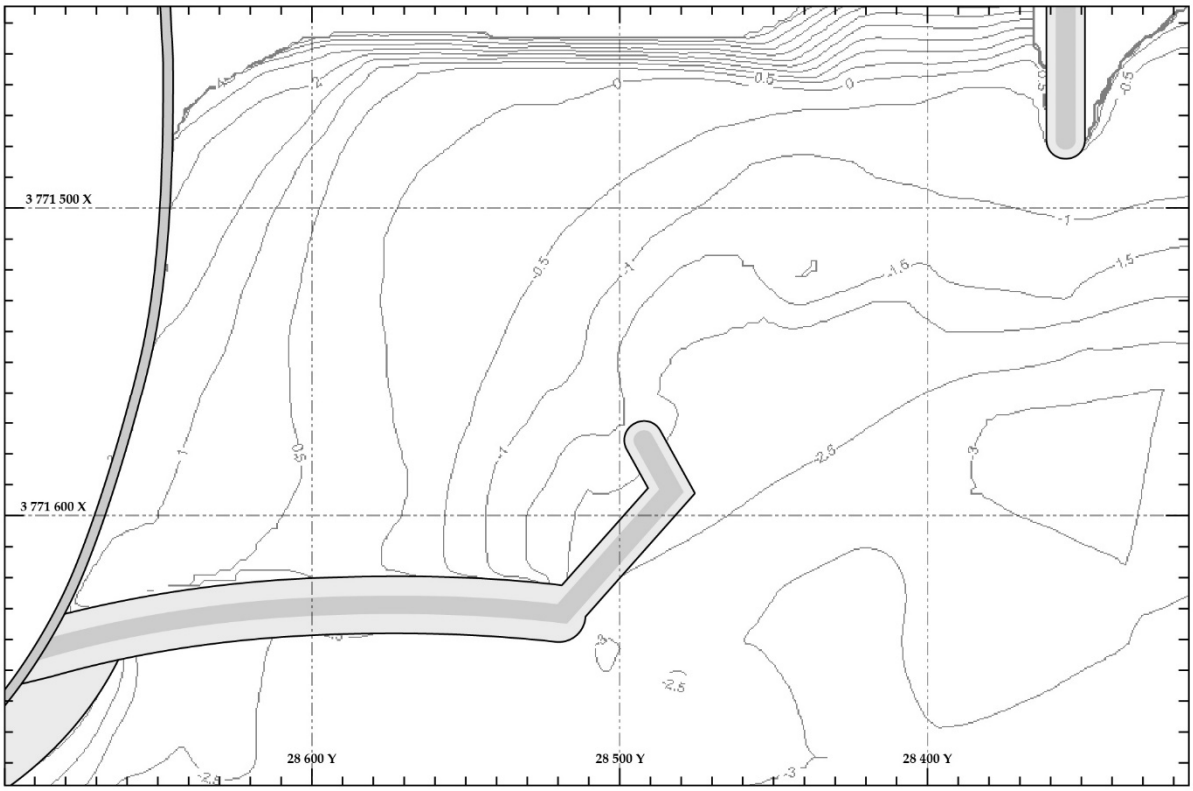

B.B.1.2 Used in Setups:

Test	Tide Level	Wave Height	Wave Period	Wave Angle
MT006	+0.7m MSL	1.5 m	12 s	+ 8°

B.B.2 Spur off spur head (seaward)

B.B.2.1 Layout

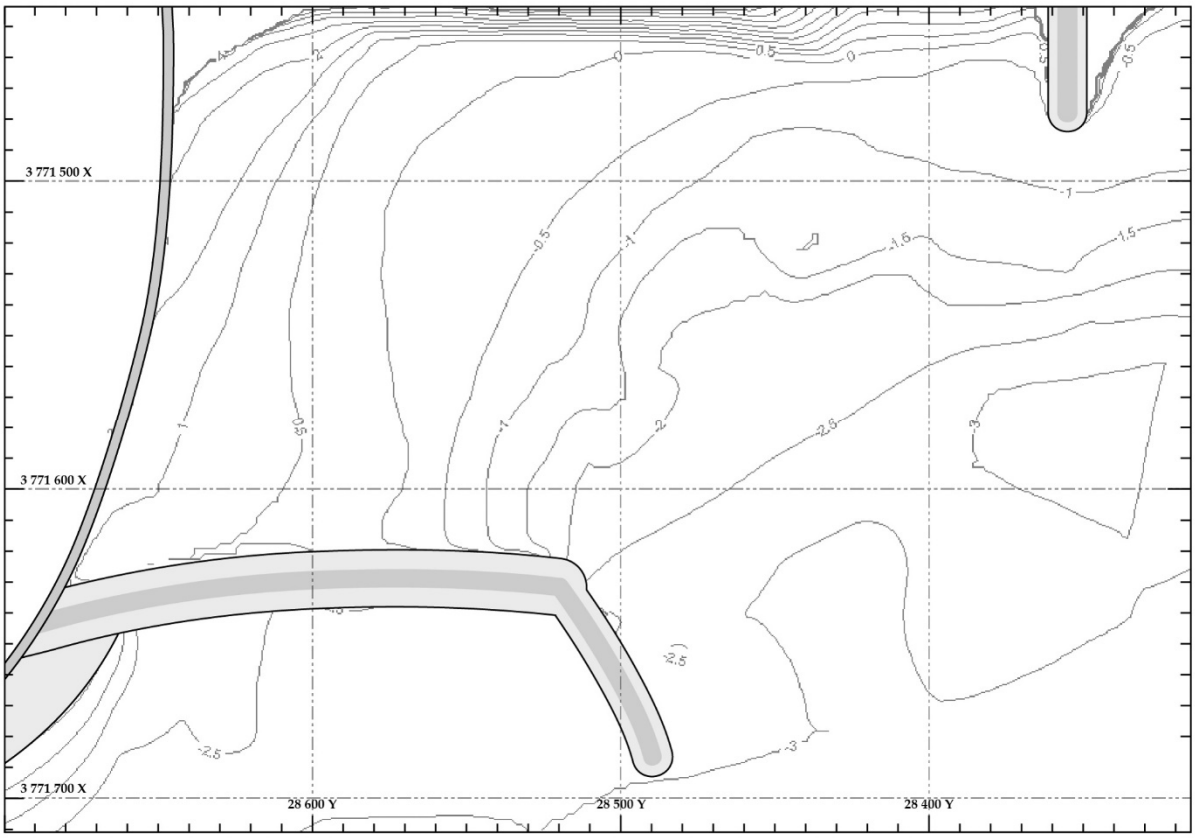

B.B.2.2 Used in Setups:

Test	Tide Level	Wave Height	Wave Period	Wave Angle
MT007	+0.7m MSL	1.5 m	12 s	+ 8°

B.B.3 Lowered end of spur

B.B.3.1 Layout

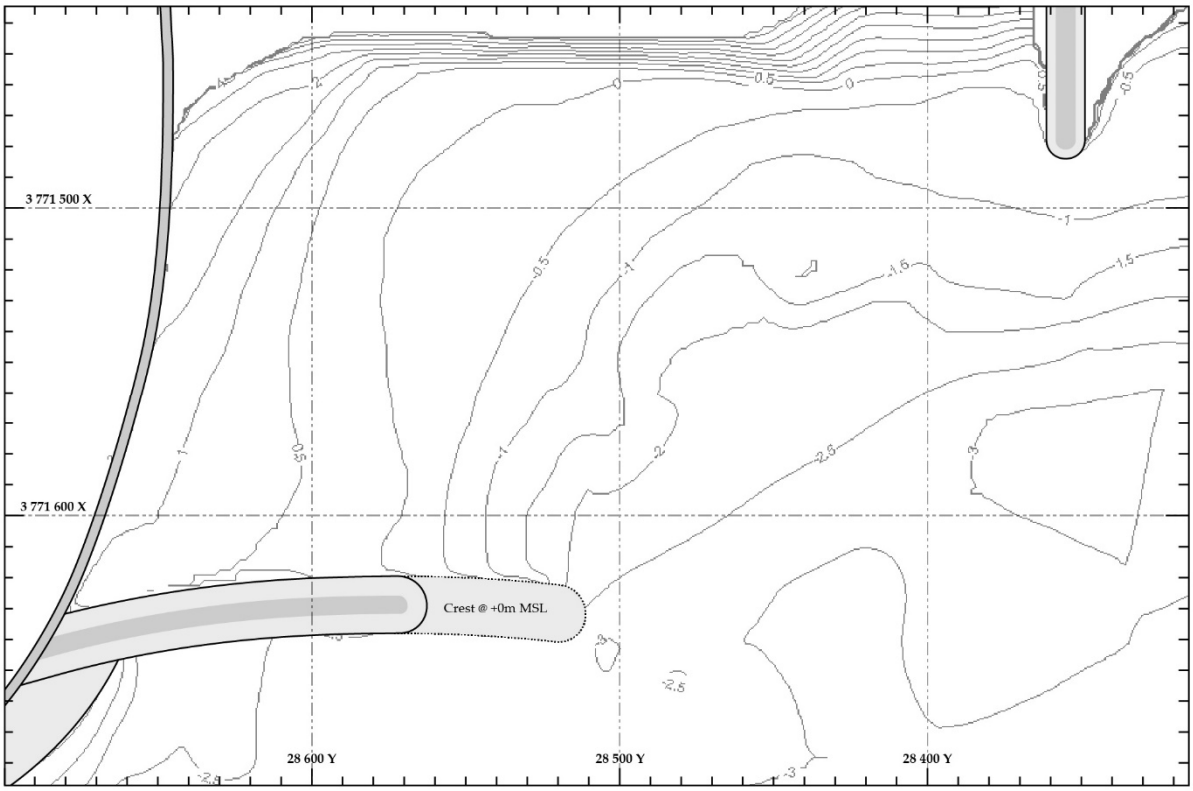

B.B.3.2 Used in Setups:

Test	Tide Level	Wave Height	Wave Period	Wave Angle
MT008	+0.4m MSL	1.4 m	12 s	+ 8°

B.B.4 Gap through spur (west stion)

B.B.4.1 Layout

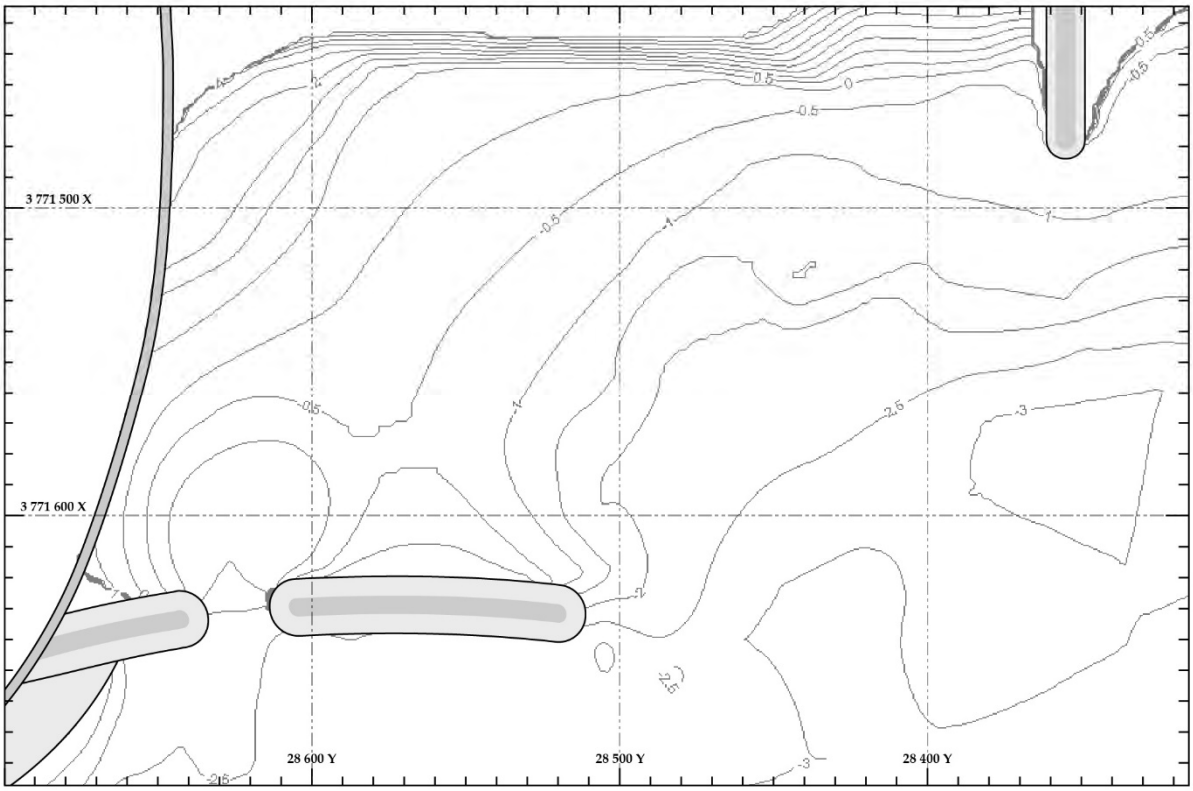

B.B.4.2 Used in Setups:

Test	Tide Level	Wave Height	Wave Period	Wave Angle
MT009	+0.7m MSL	1.5 m	12 s	+ 8°

B.C DETACHED BREAKWATERS

B.C.1 Detached breakwater in bay

B.C.1.1 Layout

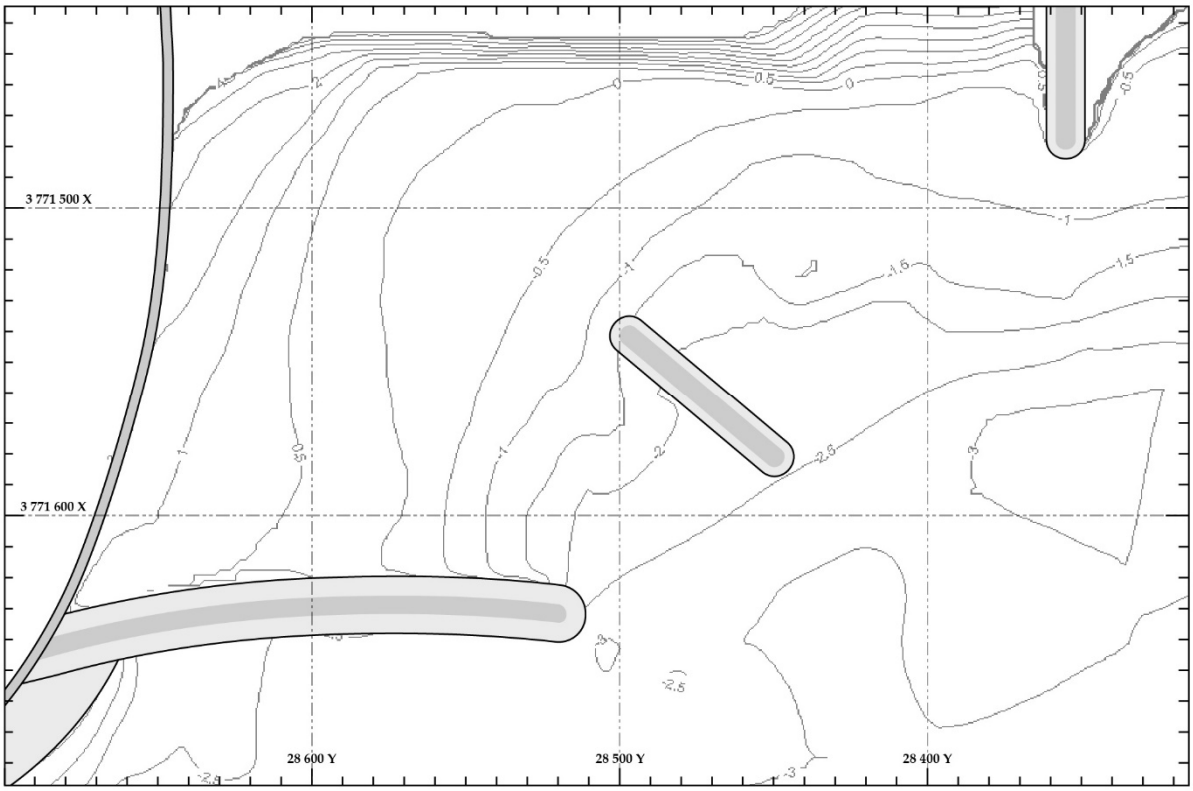

B.C.1.2 Used in Setups:

Test	Tide Level	Wave Height	Wave Period	Wave Angle
MT010	+0.4m MSL	1.4 m	12 s	+ 8°

B.D CURRENT DEFLECTING STRUCTURES

B.D.1 Raised bed level at spur head

B.D.1.1 Layout

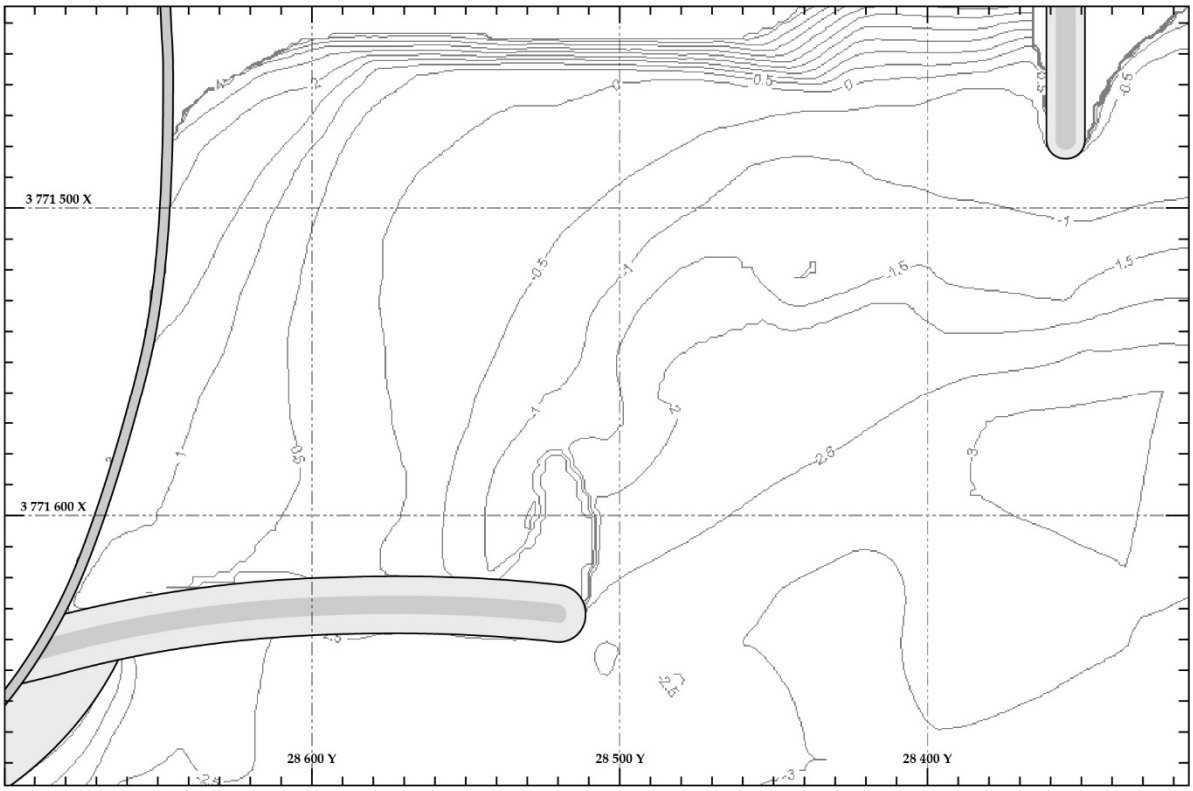

B.D.1.2 Used in Setups:

Test	Tide Level	Wave Height	Wave Period	Wave Angle
MT011	+0.7m MSL	1.5 m	12 s	+ 8°

B.E COMBINATION OF ELEMENTS (A TO D)

B.E.1 Gap through spur (west stion) with groyne off beach

B.E.1.1 Layout

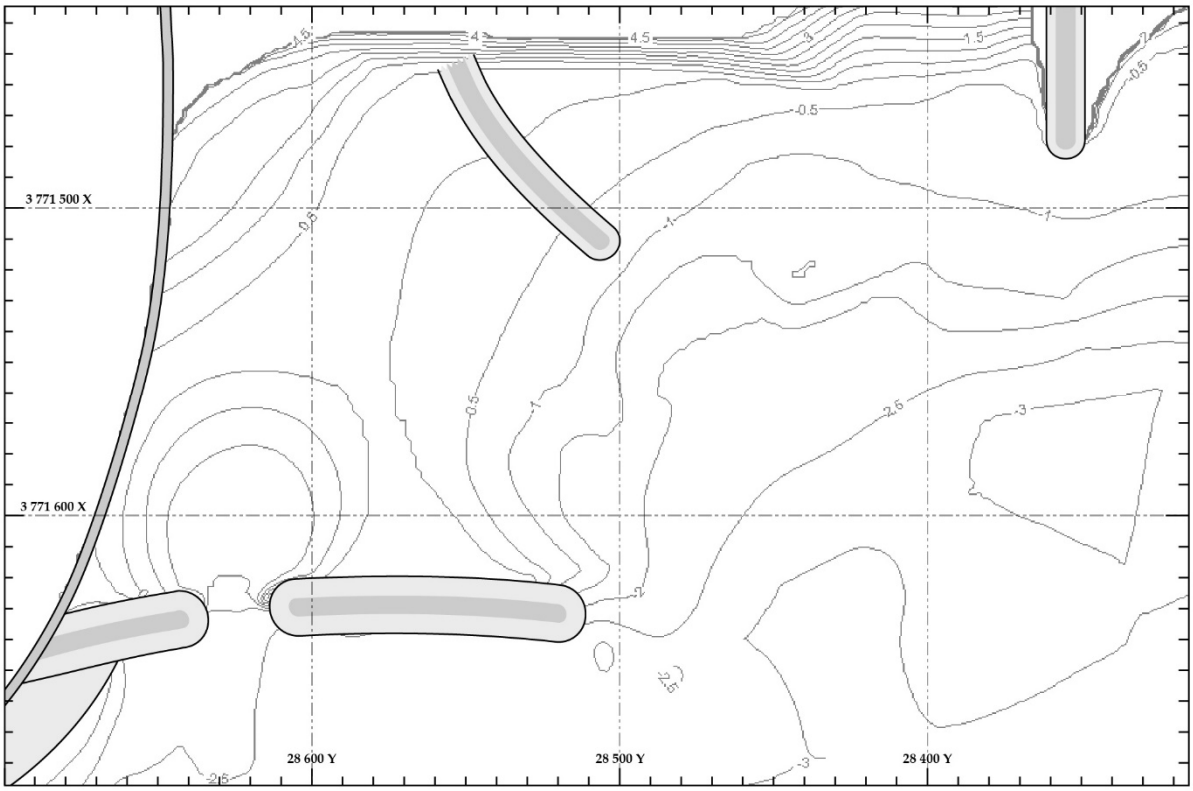

B.E.1.2 Used in Setups:

Test	Tide Level	Wave Height	Wave Period	Wave Angle
MT012	+0.3m MSL	1.3 m	12 s	+ 8°
MT013	-0.3m MSL	1.3 m	12 s	+ 8°

B.E.2 Lowered stion in spur (east) with groyne off beach

B.E.2.1 Layout

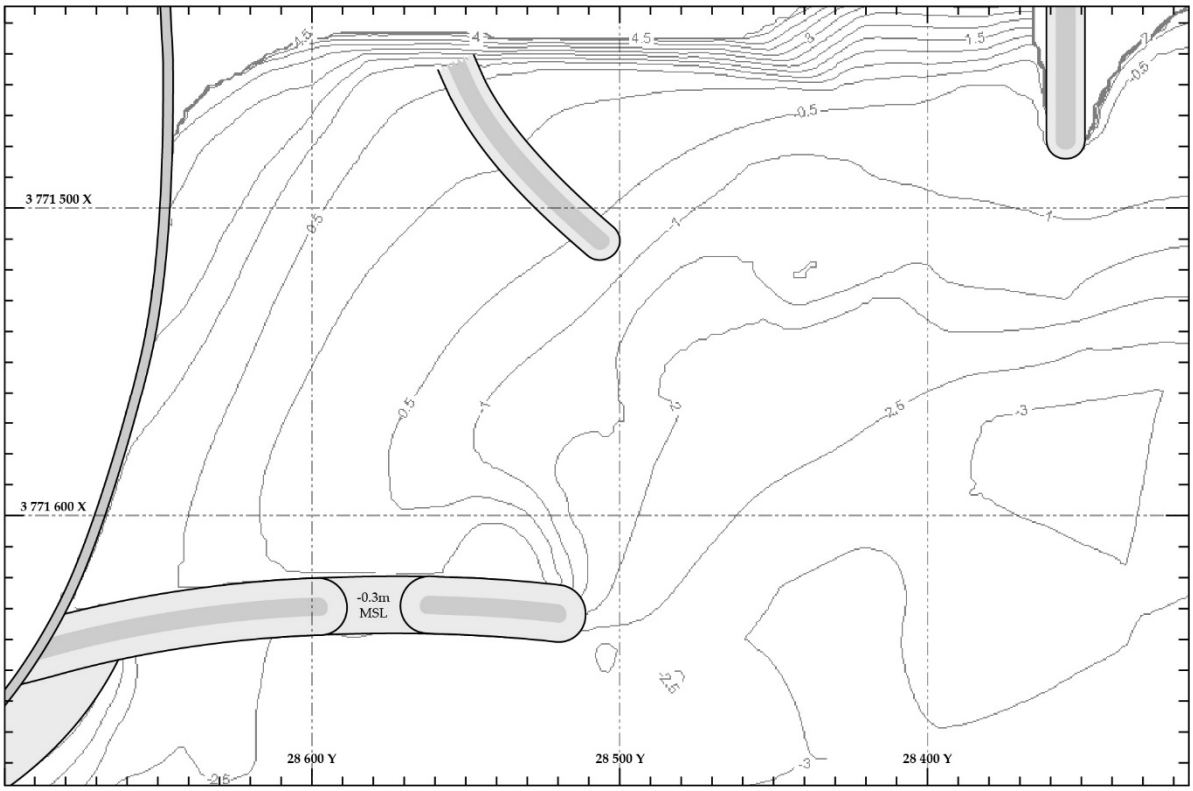

B.E.2.2 Used in Setups:

Test	Tide Level	Wave Height	Wave Period	Wave Angle
MT014	+0.3m MSL	1.3 m	12 s	+ 8°
MT015	-0.3m MSL	1.3 m	12 s	+ 8°

B.F OPTIMAL STRUCTURE: T-GROYNE

B.F.1 Standard T-groyne Setup

B.F.1.1 Layout

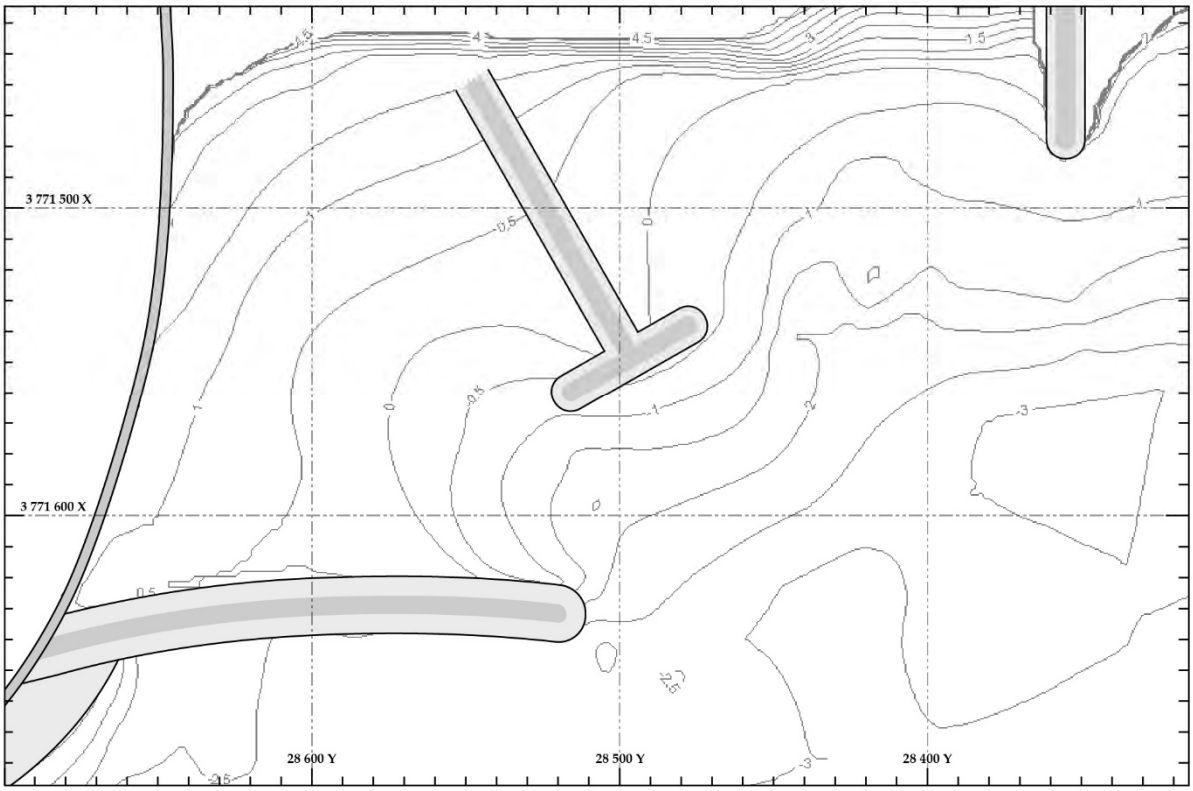

B.F.1.2 Used in Setups:

Test	Tide Level	Wave Height	Wave Period	Wave Angle
MT016	+0.45m MSL	1.5 m	12 s	+ 8°
MT017	+0.9m MSL	1.4 m	12 s	+ 8°
MT018	+0.9m MSL	1.8 m	12 s	+ 8°
MT019	-0.1m MSL	1.0 m	12 s	+ 8°
MT020	-0.1m MSL	1.4 m	12 s	+ 8°
MT021	+0.4m MSL	1.1 m	12 s	+ 8°
MT022	+0.4m MSL	1.1 m	8 s	+ 8°

B.F.2 Built-up beach

B.F.2.1 Layout

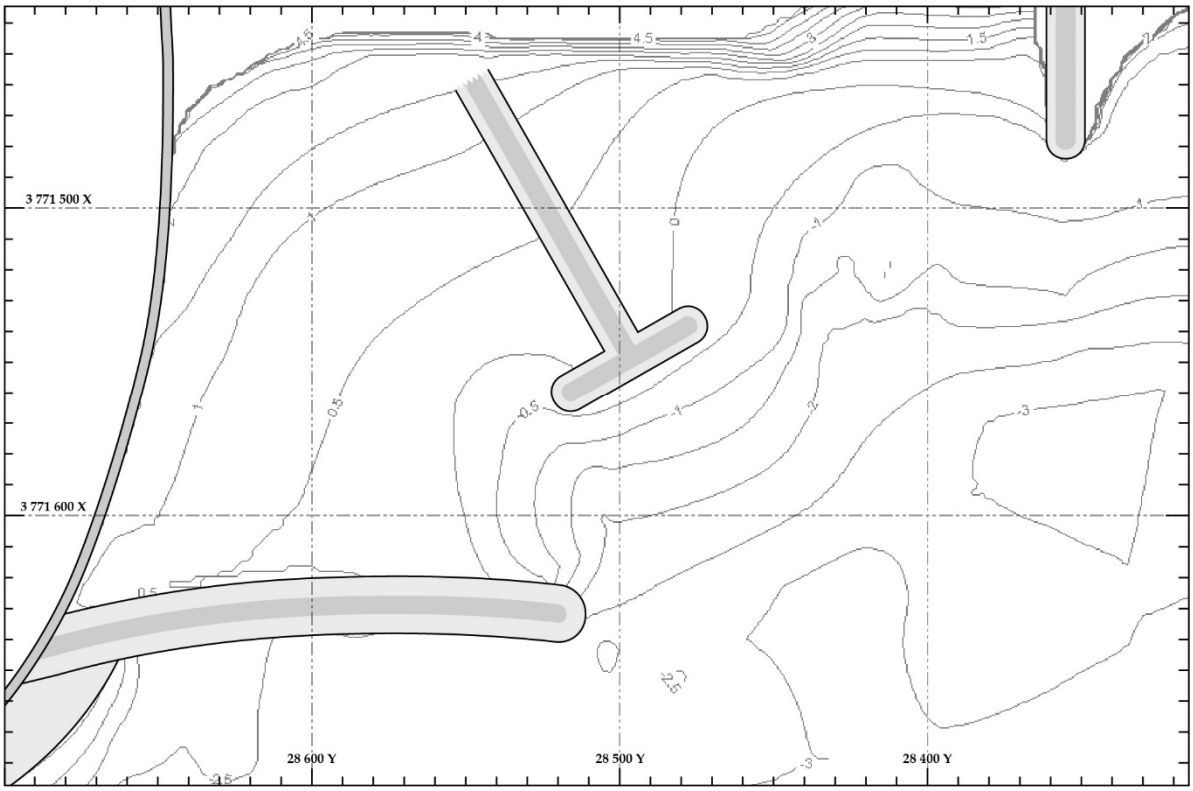

B.F.2.2 Used in Setups:

Test	Tide Level	Wave Height	Wave Period	Wave Angle
MT023	+0.4m MSL	1.4 m	12 s	+ 8°

B.F.3 Denuded beach

B.F.3.1 Layout

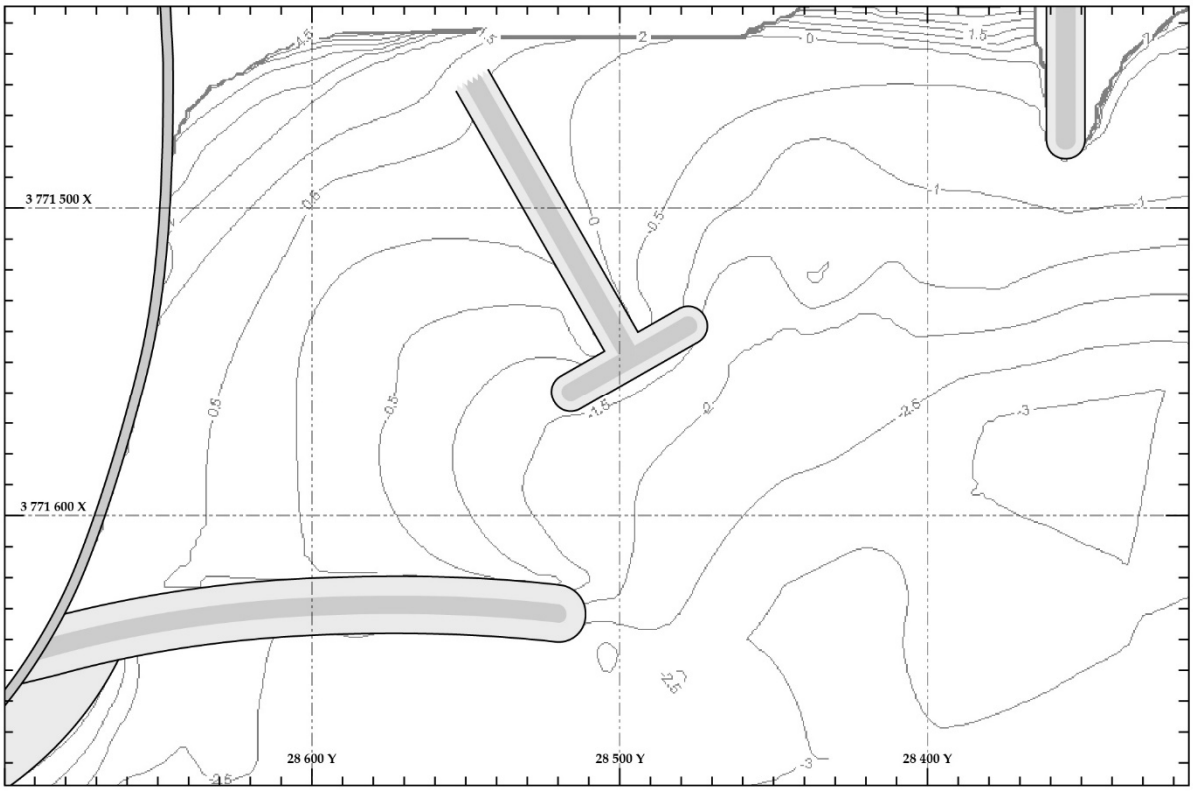

B.F.3.2 Used in Setups:

Test	Tide Level	Wave Height	Wave Period	Wave Angle
MT024	+0.4m MSL	1.4 m	12 s	+ 8°

Appendix C:

Additional detail to the Monwabisi Boussinesq Wave Simulation Model

C.1 DETAILED BATHYMETRY SETUP

This section provides additional detail on the bathymetry setup as discussed in § 6.3.1.2. A hybrid bathymetric map was set up similar to the CSIR's physical model as explained in § 5.3.2.1. This process required converting bathymetric survey data (hard copies) to a final *MIKE21 BW*-ready bathymetry file. This process arguably was the most important part of the setup as it defined the physical domain for the simulation, as well as any structural elements. The process was also the most time consuming, with a relatively long process from input to output.

C.1.1 Available survey data

The majority of the bathymetry-input data was based on old survey data predating and including the year 1997. The survey data were available from the CSIR's (1997) report, as well as supplementary material made available by the CSIR as used for the 1997 report. The readily available survey data from the CSIR was a convenience and also meant that the bathymetry would be consistent between the MBWS and CSIR models. The survey data was representative of the beach equilibrium profile, and thus any newer surveys would only reflect seasonal variability as no major physical modifications have been made to the beach since 1997.

The level of detail and coverage of the available survey data varied quite significantly. It was therefore necessary to construct a hybrid map by using a combination of the various survey data. *Google Earth* imagery was also used in combination with the survey data to establish a more detailed shoreline (where the survey data was lacking) and also to aid the spatial calibration of the survey data in the conversion between different coordinate systems. Table C-1 below lists the survey data as used in the MBWS model.

Table C-1: Collection of various survey data as used in the MBWS model

Source	Survey Date	Description
CSIR	22/8/1994	Detailed depth on offshore side of spur
CSIR	8/4/1997	Detailed bathymetry of the embayment
CSIR	11/1983 - 12/1983	Depth readings outside of embayment
CSIR	14/01/1997	Elevation measurements along the spur
CSIR	25/04/1994	Topographic data of the beach stretch outside of embayment.
Google Earth	*Varied*	

It should be noted that the survey data from the 1997 CSIR report was recorded in the Cape / Lo19 projection format. This projection format is specific to South Africa, applicable to longitudes between 18°E and 20°E. The Cape / Lo19 projection format uses a Cartesian coordinate system, plotting the coordinates along an X and Y axis with the distance units in meters (1:1 scale). The Lo19 refers to the longitude origin of 19°E – the X-axis - with the longitude spanning positively in a western direction along the Y-axis, and the latitude spanning positively along in a southern direction along the X-axis (Figure C-1) (GeoRepository, 2015; NGI, 2013).

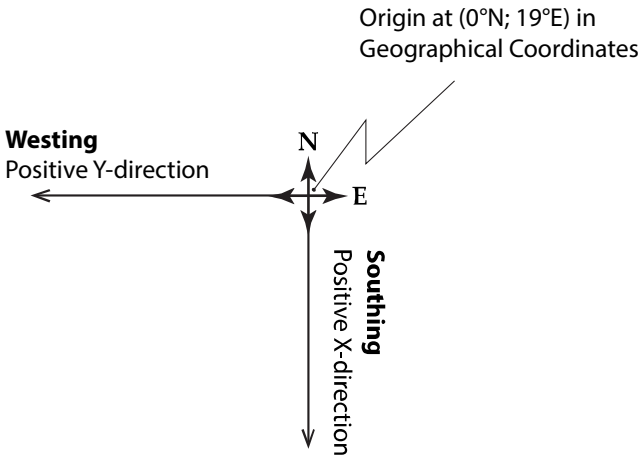

Figure C-1: Cartesian convention of the Cape / Lo19 coordinate system

With the survey data already in Cartesian-distance format, no conversion of coordinate system was necessary. Cape / Lo19 projection format has also been used for reference in this thesis.

C.1.2 Process from survey data to bathymetric file

The survey data were only available as hard copies from the reports. The contour and point-depth surveys were scanned to a common digital image format. Once in a digital format it was possible to manually convert the image data to tabulated coordinates through a digitization process. This involved assigning coordinate metadata to the images, manually tracing depth readings, and assigning the respective values to the readings. The result was a tabulated format of coordinates with their respective depth readings. The tabular format was then imported into the *MIKE Bathymetry Editor* from where the coordinate data were selected to create a hybrid map.

Note at this point the bathymetry consists of loose coordinates with assigned depth values, as shown in Figure C-2 below. The blank space in-between needs to be estimated by an interpolation process before it can be used as an input file.

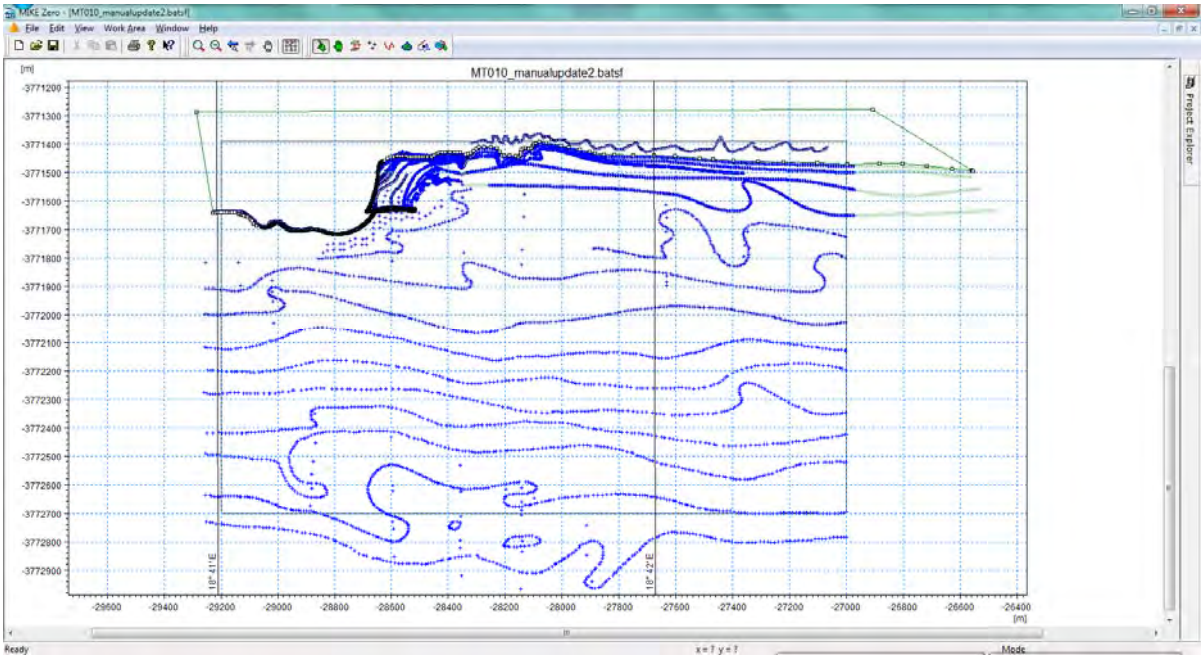

Figure C-2: Example of imported coordinate data from the surveys, as in the MIKE Bathymetry Editor

C.1.3 Land & water in *MIKE 21 Boussinesq Wave*

The MIKE21 Boussinesq Wave model distinguishes between water and land areas and identifies them as two separate entities. The *water areas* includes any grid-cell in the spatial domain that is to be included in the Boussinesq equations. In some special cases this may extend to some of the dry land sections, for example in the inclusion of wave run-up effects by means of a moving shoreline. Conversely, the *land area* is thus the specified area of the spatial domain which is excluded from any of the numerical calculations, and therefore considered to be "permanently dry". If wave run-up effects are excluded, the transition between land and water is a sudden change over the mean water level boundary as illustrated in Figure C-3.

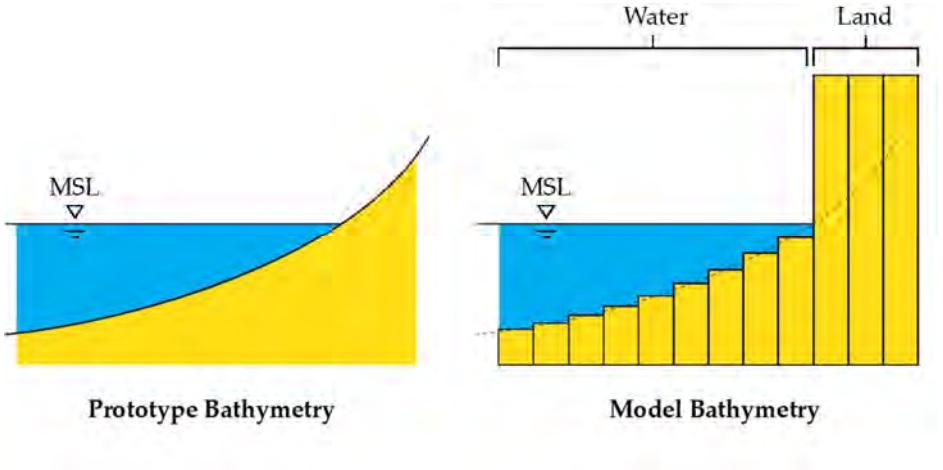

Figure C-3: Illustration of water & land representation between prototype and Boussinesq wave models (wave run-up / moving shoreline excluded)

For this study run-up effects were excluded. For each test, the *land-water* boundary was based on the mean sea level. A total of seven different tide levels were tested, which therefore required seven unique land-water boundary levels by changing the water-land boundaries for each case, as illustrated below in Figure C-4.

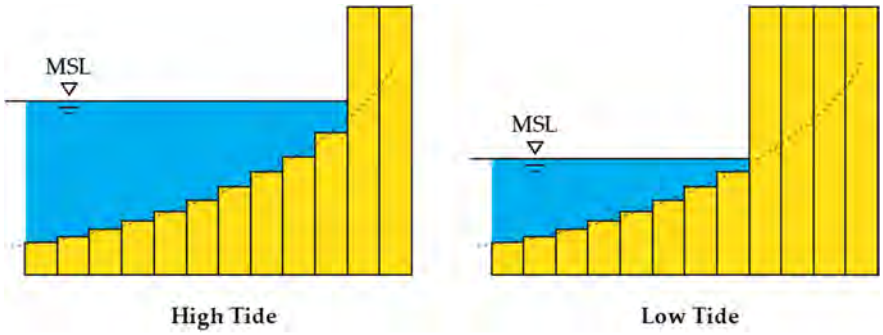

Figure C-4: Illustration of tidal differences in the Boussinesq Wave model

C.1.4 Specifying the domain of interest

The spatial domain of the model's bathymetry is confined to a finite area between the simulation boundaries. Logically this should include the area of interest (the embayment in this case), but also sufficient surrounding coverage to account for any potential hydrodynamic interaction between the areas. Too little additional coverage may lead to unrealistic results, but too much coverage can lead to very long simulation time.

Another influencing factor is the wave generation line. The available wave data for this study was recorded approximately at the -10m MSL contour. To keep the wave generation accurate, the waves had to be generated from the recorded position. The CSIR also generated the waves from the same area, which was another motivation for this decision with regard to comparability. The angle of the incident waves combined with the travelling distance should also be considered as they will define the width of the domain.

In addition to the simulation boundaries, a layer of absorption boundaries was also required. These layers absorb the waves propagating out of the model area which would otherwise just reflect against the boundaries. These layers add an extra width to the computational domain and are therefore important to the planning process.

Sometimes it is required to rotate the grid of the spatial domain to suit the output needs better or to coincide with the wave propagation. There were no such requirements for this study as the beach of interest was already roughly aligned east-to-west and the wave-direction was also roughly aligned to the grid. For this specific domain and the Cape / Lo19 projection system the deviation from true north was less than 0.2°.

C.1.5 Grid cell size

For ease-of-processing purposes it was decided to keep the cell size as an integer value. It was decided that the optimal grid cell size was 2 m x 2 m as it was large enough to keep simulation time to a minimum, while sufficiently small enough to ensure model stability

and it provided a level of resolution that was sufficiently detailed for presentation and data extraction purposes.

C.1.6 Minimum water depth

A very important aspect was the realistic representation of the embayment. For stability reasons, the numerical model could only resolve waves up to a minimum water depth. This meant that all depths that preceded this minimum depth had to be "flattened" to the level of the specified minimum depth (see Figure C-5). Since the embayment included relatively shallow depths, the minimum depth had to be an optimum value that would allow for the most realistic representation, while allowing for a stable numerical model.

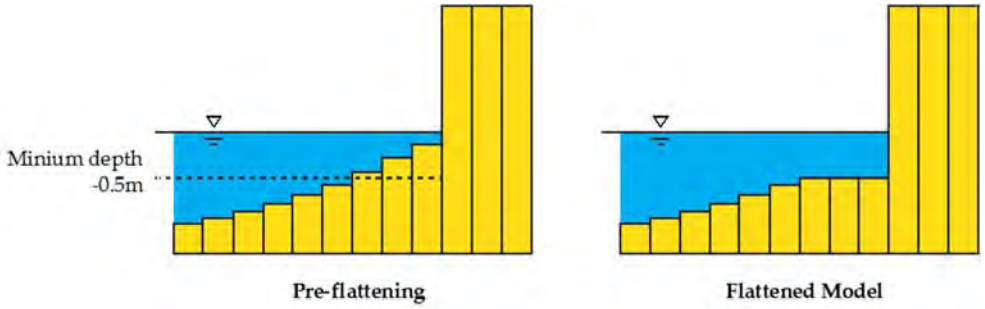

Figure C-5: Illustration of model flattening to required depth of 0.5m

The decision-making process was heuristically executed in parallel with the decision on spatial resolution and time-step specification. A combination of theoretical background and trial-and-error simulation runs were used to settle on a minimum depth of 0.5m. This decision was further supported by theoretical background from Madsen & Sørensen (1992).

Madsen & Sørensen (1992) recommended a minimum spatial resolution 8-10 grid per wave length to avoid artificial dissipation of the wave energy. A spatial resolution of 2m was used. For a chosen depth of 0.5 m, the transitional wave length equation could be used to estimate the transitional wave length:

$$L = \frac{g \cdot T^2}{2 \cdot \pi} \cdot \tanh\left(\frac{2 \cdot \pi \cdot d}{L}\right) \qquad \text{(C.1)}$$

Where

- L = the transitional wave length
- g = gravitational acceleration constant ($g = 9.81\ m/s^2$)
- T = transitional wave period
- d = water depth

With a depth of $d = 0.5$ m and a wave period of $T = 12$ s, the equation could be solved for $L = 26.51$ m. Thus with a spatial resolution of 2 m, there would be about 13 grid points per wave length – which just exceeds the recommendation of Madsen & Sørensen (1992). A minimum water depth of 0.5 m was deemed sufficient for the simulation.

C.1.7 Definition of structures

MIKE 21 Boussinesq Wave makes it possible to model structural features by simplifying the characteristics of the structure to a two-dimensional footprint with reflective properties. Any structural features to be used in the MBWS model should therefore also be integrated in the bathymetry file by specifying the footprint of the structure on the grid. The reflective properties of the structure are defined by a porosity coefficient.

MIKE 21 Boussinesq Wave allows for two types of structures: permeable or impermeable. For this study all of the structures were assumed to be impermeable, as permeable structures are much more difficult to calibrate.

Since the structures are defined in a two-dimensional domain, the height of the structure was irrelevant and zero-overtopping was assumed. The slope of the structure was somewhat accounted for by the definition of the porosity coefficient.

C.1.8 Summary of grid specification

Once the survey data had been prepared and the grid dimensions had been determined, the data were ready for interpolation. The *MIKE Bathymetry Editor* has a built-in interpolation tool to produce a *MIKE 21 Boussinesq Wave* compatible bathymetry grid file. However, it was found that the variable spacing of the survey data (due to multiple bathymetry survey sources) did not produce satisfactory results post-interpolation (Figure C-6).

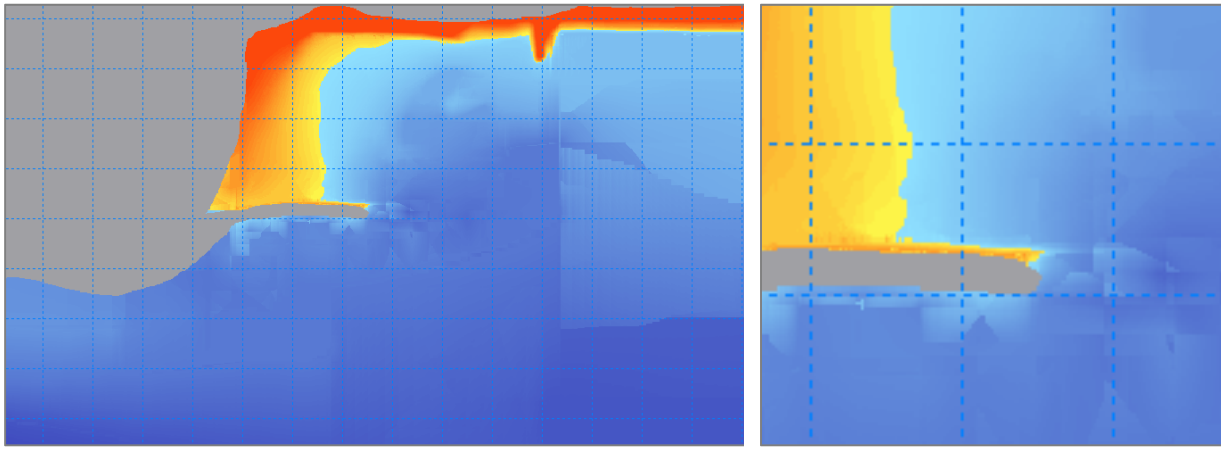

Figure C-6: The MIKE 21-interpolated bathymetry. A lot of interpolation errors are visible due to the variable data density.

Golden Software's Surfer was subsequently used for the interpolation process. The natural neighbour method was used for the interpolation as it was suitable for generating contours with data sets with varying densities – which was optimal for the variable spacing of the *hybrid* dataset. The natural neighbour method also does not extrapolate Z (depth) values beyond the data range (resulting in depths beyond what was recorded), which makes the interpolation more reliable.

The *MIKE 21* suite conveniently included a tool to convert *Surfer's* interpolated output to a *MIKE 21 Boussinesq Wave* compatible grid file. After the interpolation, the bathymetry grid file was near-ready for modelling use. Some additional features, such as the bathymetry flattening, and specification of model boundaries (Sponge) and structural boundaries

(Porosity layers) were added post-interpolation. Figure C-7 below shows the bathymetry file as used for the **MB610** baseline test.

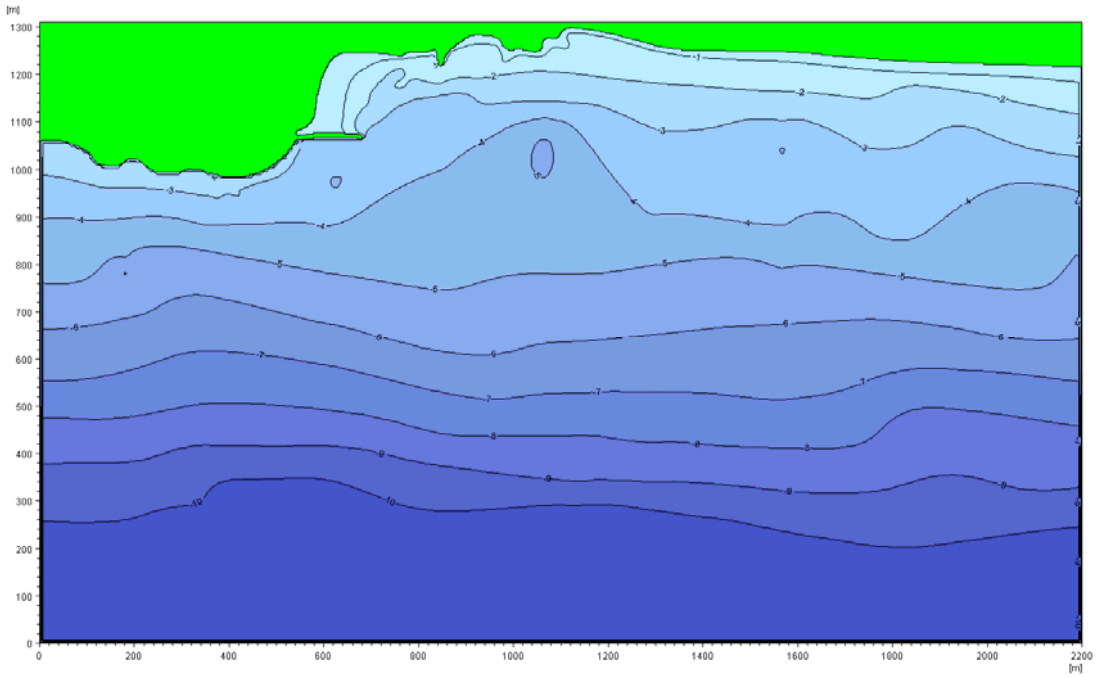

Figure C-7: Visualisation of final bathymetry file as used for the MB610 baseline test (+0.7m MSL). The green area indicates the land.

C.1.9 Special modifications of the bathymetry

For the majority of the models, the same bathymetry was used, including the embayment. For a couple of models the bathymetry required special modifications. These modifications included extra bathymetric adjustments (re-profiling) or structural modifications to the existing spur. Table C-2 below lists the special modifications required. These modifications can be found in Appendix B as referenced in the table.

Table C-2: Special modifications to tests

Appendix Reference	Description	Special Modifications
App. B.B.3	*Lowered end of spur*	• Structural modification
App. B.B.4	*Hole through spur (west section)*	• Bathymetry re-profiling
App. B.D.1	*Raised bed level at spur head.*	• Bathymetry re-profiling
App. B.E.1	*Hole in spur section (west) & groyne off beach*	• Bathymetry re-profiling
App. B.E.3	*Lowered spur section (east) & groyne off beach*	• Bathymetry re-profiling • Structural modification
App. B.F.1	*T-Groyne (standard)*	• Bathymetry re-profiling
App. B.F.2	*T-Groyne (built-up beach)*	• Bathymetry re-profiling
App. B.F.3	*T-Groyne (denuded beach)*	• Bathymetry re-profiling

C.1.9.1 Bathymetry re-profiling

Sediment transport was not accounted for in the MBWS model. For most of the cases the structural modifications were applied to the same static bathymetry, thus ignoring any potential changes to the beach profile due to the addition of the structure. There were, however, some cases where the beach profile had to be adapted. The re-profiling of the bathymetries was based the *type* of structural modifications present and the *importance* of the test case.

Four of the seven bathymetries were re-profiled due to their structural *type*: The first three of the structural setups included a gap or lowered section in the spur. These modifications introduced a whole new wave action entry point that could only be adequately simulated if the bathymetry was adapted accordingly. The fourth case, the raised bed level at the spur head, required a section of the bathymetry to be elevated and the surrounding beach slope had to be adapted accordingly.

The remaining three cases were the T-Groyne simulations. Their bathymetries were adjusted due to their *importance*. The T-Groyne structure was considered by the CSIR to be the optimal solution for a safer beach at Monwabisi. It was therefore decided that a re-profiled bathymetry could provide an even more realistic simulation. The beach-configuration was re-profiled accordingly - including two extreme cases of a built-up and denuded beach.

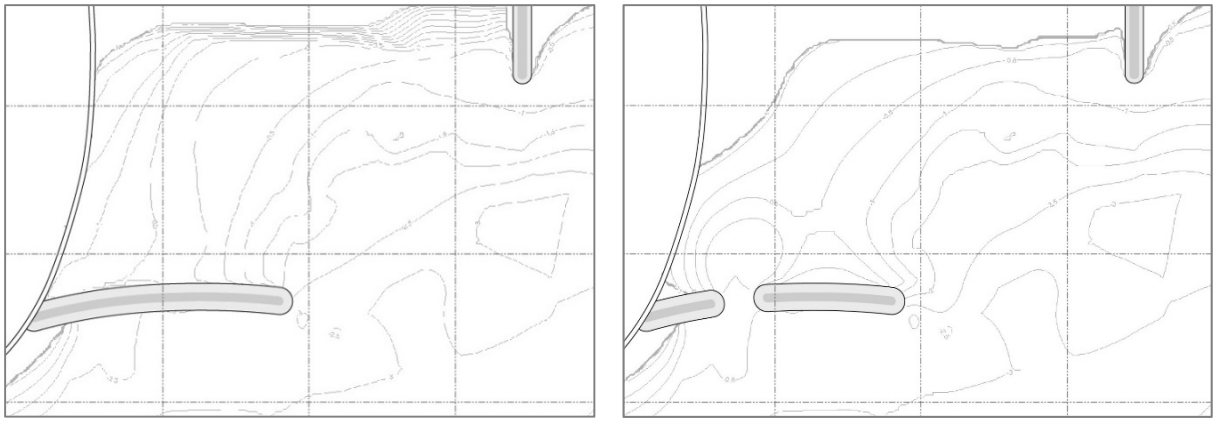

Figure C-8: Side-by-side comparison of the baseline bathymetry (left) with the re-profiled bathymetry for hole-in-the-spur test (right) (0m MSL).

The re-profiling was done in accordance with the CSIR's (1997) test cases; the re-profiled bathymetries for the MBWS model corresponded to the re-profiled bathymetries of the CSIR report. The CSIR only provided the new still water line (0 MSL) for the re-profiled bathymetries, which was used a basis for the MBWS modified bathymetries.

C.1.9.2 Structural modifications

Two of the proposed beach modifications included "special" changes to the existing spur. Both of these cases were related to a lowered crest elevation of the spur (but not a complete gap). These cases differ from the other structural modifications in their relative complexity required to model adequately.

The lowered sections in the spurs effectively meant that the overtopping effect of the structures had to be tested. To allow wave energy to pass over the spur in the MBWS model, the lowered section of the solid "land" structure (spur) had to be changed to a "water" component. It should be noted that overtopping also occurred in the CSIR's simulations of **MT017** and **MT018**, but the effects were only secondary to incoming waves through the bay entrance. A normal solid structure without any special modifications was therefore used in the MBWS simulations for **MT017** and **MT018**.

C.1.9.3 Bathymetry "flattening" along wave generation line

The wave energy flux is a depth-dependant parameter. It is therefore necessary to have a uniform and flat bathymetric bottom along the wave generation line. For this reason, the bathymetry had to be flattened to a uniform depth along the wave generation line section. The *flattening* was executed by identifying the shallowest point along the line. All depths greater than the shallowest point were then equalised to this value to ensure than the bathymetry was flat along the wave generation line. The wave generation line is roughly parallel to the depth contours, meaning that the *flattening* processes did not influence the bathymetry far beyond the wave generation line, as illustrated in Figure C-9.

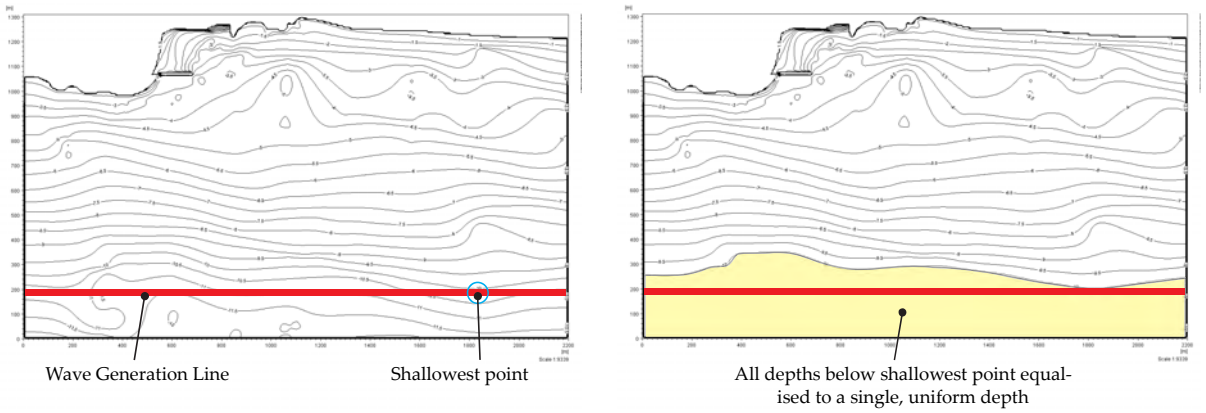

Figure C-9: Illustration of Bathymetry flattening for the wave generation line

C.2 DETAILED POROSITY LAYER SETUP

This section provides additional detail on the porosity layer setup as discussed in § 6.3.1.15. Porosity layers are used to simulate the wave-land or wave-structure interaction. Without porosity layers, waves will simply reflect off the land. Porosity layers provide a form of wave absorption to prevent this reflection. They differ from sponge layers as they allow for a definite amount of partial wave reflection. This feature is used to simulate the partial reflection properties of various structures and sloping beaches. The porosity maps could potentially be adjusted to specification to allow for realistic simulation of wave-land or wave-structure interaction.

C.2.1 Partial reflection theory

The porosity-formulations are based on Madsen's (1983) *Vertical wall absorption* theory. Linear waves reflect a defined amount off a vertical-faced wall with a homogenous porous structure. The reflection amount is quantified by a reflection coefficient, ranging between 0 (full absorption) and 1 (full reflection). This theory assumes a horizontal bed level with incident waves propagating normal to the structure face. This theory does not include the effects of wave breaking.

The calculation of the reflection coefficient, α_r, is lengthy and complicated process which is detailed Madsen's *Wave Reflection From A Vertical Permeable Wave Absorber* (1983). The dependant variables are:

1. The porosity coefficient, α_P,
2. Width of the absorber (usually a function of the wave length)
3. Diameter of stones or grains of permeable layer (recommended to keep constant)
4. Water depth in front of structure
5. Wave period
6. Incoming wave height

The *MIKE 21* suite includes a tool which uses the variables listed above to calculate the reflection coefficient as a function of the porosity coefficient. The input data are based on wave parameters and porosity layer parameters. The wave parameters are defined by the wave height, wave period and water depth for the specific structure (the specification of these values are discussed below). The porosity layer parameters are defined by the width of the layer, diameter of stones, laminar particle resistance coefficient and turbulent particle resistance coefficient. The latter three variables are kept constant, as defined by Madsen (1983). The width of the porosity layer should be at least 25% of the incoming wave length (Madsen, 1983)

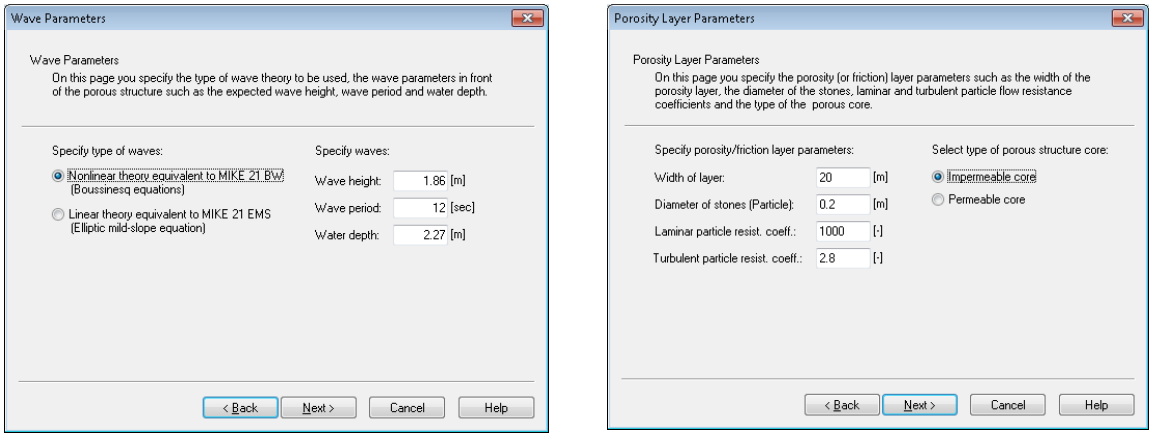

Figure C-10: Input specifications for porosity-reflection curve generation, as in the MIKE 21 environment

Once the parameters have been set, the MIKE21 wave reflection tool produces a reflection-porosity curve (Figure C-11, below). Note that for increasing porosity values the reflection-coefficient becomes more absorptive until it reaches a peak of maximum (but not full-) absorption. After the peak, the reflection coefficient becomes fully reflective. ($\alpha_r = 1 = \alpha_P$)

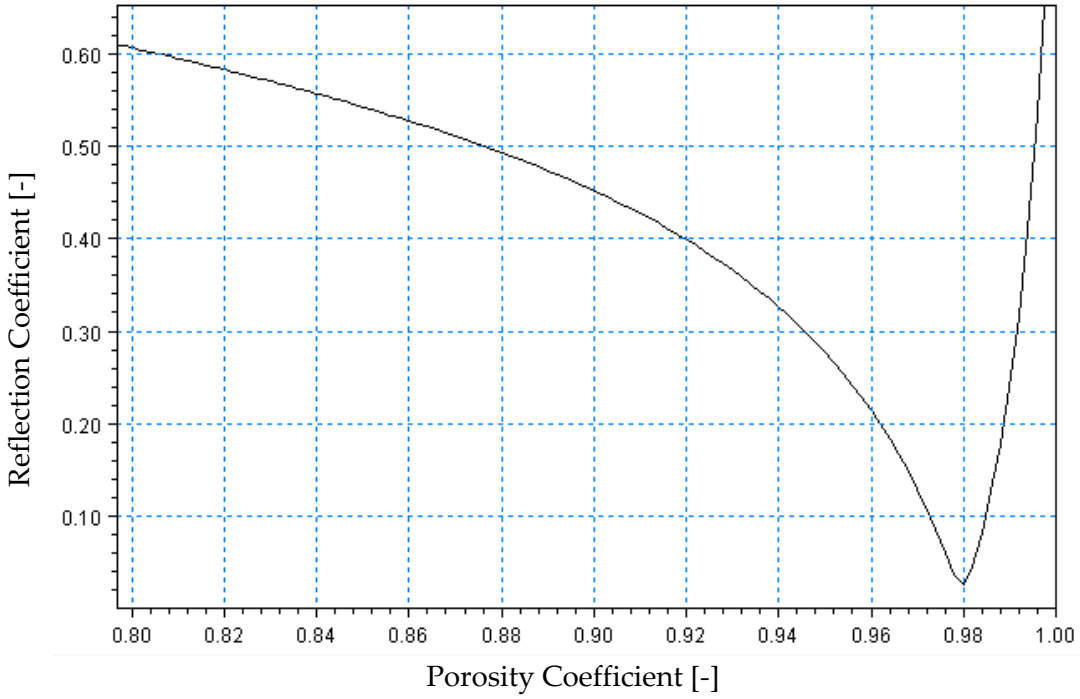

Figure C-11: Theorised reflection-porosity coefficient ratio for 2 m wave height, 12 s wave period, 2 m depth, 16 m layer width

The reflection-porosity coefficient curve is used to manually select a porosity coefficient that would result in the required amount of reflection. The desired reflection coefficient for a specific structure can be found for a generalised value from literature, or preferably from site-specific data. Since the latter was not available, the former had to be used, as discussed in the next section.

C.2.2 Theoretical reflective coefficients

Thomson *et al.* (1996) defined the typical reflection coefficient ranges for short-period waves. This was used as a guideline to establish the reflective properties of the structures in the MBWS model.

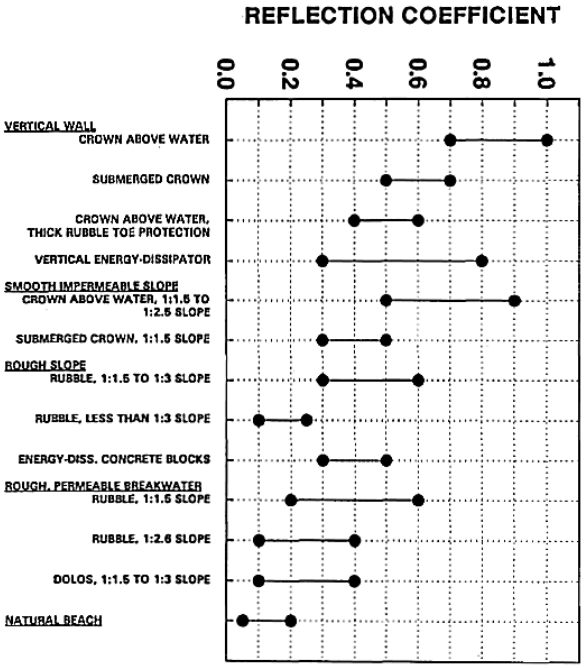

Figure C-12: Reflective properties of structures for short period waves (Thomson et al. *1996)*

A list of the different structural sections was compiled - as a guideline to specify the porosity coefficients of the structures - with the use of the theoretical reflective properties from Thompson *et al.* (1996). Table C-3 below describes the different sections in the MBWS models with the reflection coefficient range from Thompson *et al.* (1996).

Table C-3: Estimated reflection coefficient ranges for different identified sections

Section	Description	Reflection Coefficient (from Figure C-12)
A	Existing spur	0.1 – 0.25
B	Existing groyne	0.1 – 0.25
C	Beach within embayment	0.05 – 0.2
D	Rocky section protecting the tidal pool	0.1 – 0.25
E	Eastern stretch (the rocky beach section east of the existing groyne)	0.1 – 0.25
F	Western stretch (the rocky beach section west of the tidal pool)	0.1 – 0.25
G	additional structures / beach modifications	0.05 – 0.25

Since the actual performance was unknown, the reflection coefficients were usually chosen to be the least reflective (lowest reflection coefficient) within the specified range. For each of these sections the incoming wave height and water depth wave varied along the structure. In theory, this would require a varying porosity layer along the specific entity. Each of these sections would therefore require multiple reflection-porosity curves to establish the required varying porosity coefficients for the unique wave, bathymetry and structural combinations. Furthermore, eleven different water-level and wave conditions were to be tested, which would require the whole exercise to be repeated for all of the eleven cases. This can quickly lead to an unrealistically long and tedious exercise which only results in a *theoretical* reflection coefficient.

From early simulation results it was found that the reflection energy of the porosity layers was significantly higher than the theoretical reflection coefficients. The excessive reflection is shown in Figure C-13. These discrepancies were expected due to varying bed levels in front of the structures, waves propagating oblique to the grid and wave breaking.

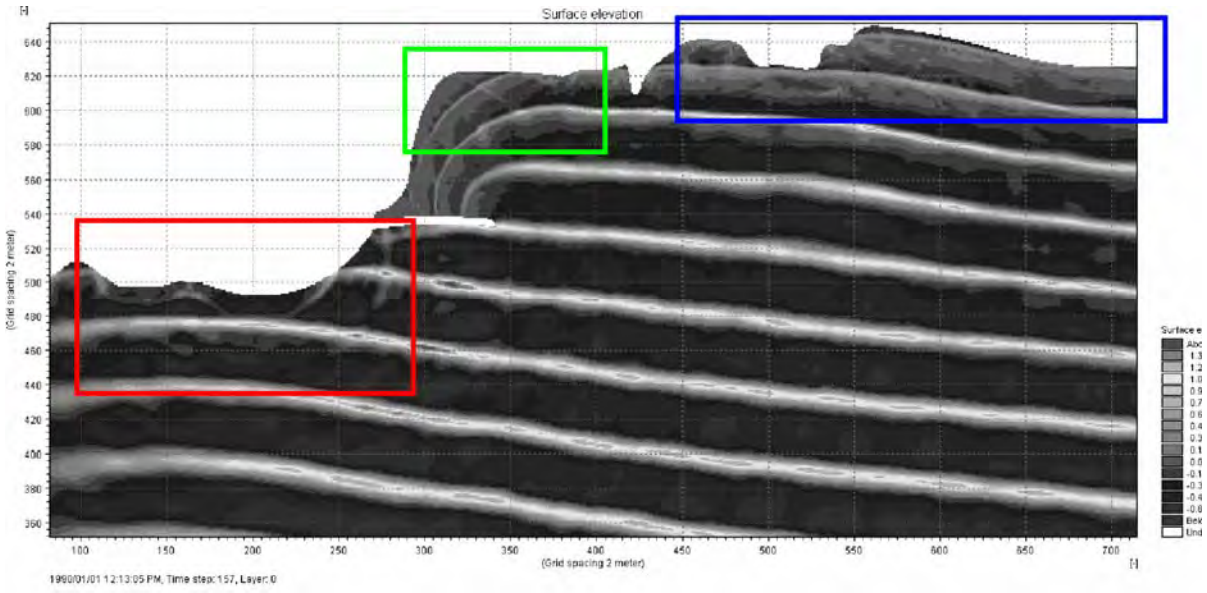

Figure C-13: Early simulation results showing excessive wave reflection at sections D and F (red section) and also from the beach at section C (green section)

Ultimately, it was decided to reconsider the priority of the wave reflection coefficient definition in the MBWS setup: the focus of the study remained the wave-current interaction. Wave reflection within the embayment (from the beach or any structure) does have an influence on the wave-induced currents. The extent of this influence was not clear as no real-world data – aside from satellite imagery - were available with regard to the wave reflection at Monwabisi. It was consequently decided to define a simplified porosity scheme which would be used uniformly across all testing conditions.

For time-constraint and priority reasons, four unique groups of porosity coefficients were used, with constant parameters (coefficient and layer width) throughout all of the simulations. The parameters are set out below in Table C-4.

Table C-4: Summary of Reflection coefficients used in MBWS model

Description	From Table C-3	Porosity Coefficient	Layer Width [m]
West of Spur	D+F	0.925	12
Spur	A	0.925	16
Beach, groyne and eastern shore	C+B+E	0.940	8
Additional structure in bay	G	0.930	10

The aim of this porosity scheme was to keep reflection low (0.05 to 0.1). These values were accepted to be realistic in accordance with the study by Thomson *et al.* (1996). The influence of the porosity layer is further discussed in the Sensitivity Analysis section.

C.3 DETERMINISTIC AND PHASE-AVERAGED OUTPUT

This section provides additional detail on the determinist and phase-average output terms as referred to in § 6.4. The MIKE21 Boussinesq Wave suite provided two main types of output data: deterministic- and phase-averaged parameters.

Deterministic parameters are instantaneous output data available for each specified time step. *Phase-averaged* results are temporal averaged values for a specified time interval. *Phase-averaged* output is especially important in functions where $\Delta t \to 0$ would result in null values, such as the first order momentum equations. Both the *deterministic* and *phase-averaged* results are presented as a function of time-steps, and can therefore be formulised by generalised equations:

C.3.1 Deterministic:

The instantaneous results could be formulated with by a generalised continuous function:

$$R_D = f(t) \tag{C.2}$$

Where

- R_D = output (or results) parameter of interest as a function of time
- t = time

The numerical model only solves R as a discontinues function at specified time intervals "i", such that the deterministic output, R_D, is formulated as a discontinuous function for the time-step "s":

$$R_D = f(s) \tag{C.3}$$

$$s = s_c \cdot t \tag{C.4}$$

Where

- s = time-step
- s_c = time-step interval constant

C.3.2 Phase-averaged

The phase averaging in MIKE21 is a two-step process involving *sub-series* and *cumulative series* averaging. The first process of *sub-series* calculations involves solving of temporal-averaging integrals of the continuity function $R = f(t)$ over a given time interval m so that

$$R_{P(Sub)} = g(t) = g(f(t))$$

$$R_{P(Sub)} = \frac{1}{m}\int_{t_i}^{t_{i+m}} f(t) \cdot dt \tag{C.5}$$

Where

- $R_{P(Sub)}$ = phase-averaged sub-series parameter of interest
- m =defined time interval for sub-series averaging
- t_i = time at ith interval, where i = 0, m, $2m$, $3m$ ...

The numerical expresses sub-series results as a function of time-steps. From equation C.4, $R_{P(Sub)}$can be expressed as a function of time steps:

$$R_{P(Sub)} = g(s) = \frac{1}{n}\int_{s_j}^{s_j+n} f(s) \cdot ds \tag{C.6}$$

$$n = s_c \cdot m \tag{C.7}$$

Where

- n =defined time-step interval for sub-series averaging
- s_j = time-step at jth interval, where j = 0, n, $2n$, $3n$ ...

The *cumulative series* follows as the temporal-averaging of the sub-series function. The cumulative series is therefore discontinuous, corresponding to the intervals of the *sub-series*:

$$R_{P(Cum)} = q(t) = \frac{1}{t}\sum_{t=0}^{t} g(t)$$

$$R_{P(Cum)} = \frac{1}{t} \cdot \frac{1}{m}\sum_{t=0}^{t}\left(\int_{t_i}^{t_{i+m}} f(t) \cdot dt\right) \tag{C.8}$$

Where

- $R_{P(Cum)}$ = phase-averaged cumulative-series parameter of interest
- $t = 0, m, 2m, 3m$ ...

Similar to the sub-series, the cumulative series can be expressed as a function of time steps:

$$R_{P(Cum)} = q(s) = \frac{1}{s}\sum_{s=0}^{s} g(s)$$

$$R_{P(Cum)} = \frac{1}{s}\cdot\frac{1}{n}\sum_{s=0}^{s}\left(\int_{s_j}^{s_j+n} f(s)\cdot ds\right) \quad \text{(C.9)}$$

Where

- $R_{P(Cum)}$ = phase-averaged cumulative-series parameter of interest
- $s = 0, n, 2n, 3n$ ...

Thus, from equation C.9 it arises that for a defined range of fluctuations in the *sub-series* $R_{P(Sub)}$, the cumulative series $R_{P(Cum)}$ function will eventually approach uniformity. The time required to approach uniformity is proportional to the limits of the fluctuations. This concept is of importance to the stability of the model. A uniform sub-series function with zero fluctuations will therefore be equal to the cumulative series function at each time step.

C.3.3 Application to the MIKE 21 Boussinesq model

In terms of the MIKE Boussinesq Model, the output results are specified as

- Deterministic, $R_D = f(s)$
- Phase-averaged sub series, $R_{P(Sub)} = g(s)$ OR
- Phase-averaged cumulative series, $R_{P(Cum)} = q(s)$

Note that phase-averaged results are calculated either *as sub-series* or *as cumulative. In the event where both are required, two simulation runs will be required.*

C.3.3.1 Phase-averaged results & model stability

The wave-induced currents – a key parameter to the MBWS model – can only be resolved by means of a phase-averaged function. The phase-averaging is also sensitive to model instabilities, and recording of the phase-averaging values should therefore only start once the model has reached stability. The cumulative series is the best indicator of velocity, as the sub-series may be subject to periodic fluctuations. Fluctuations may arise due to boundary effects, long-waves, or where the sub-series interval is not synchronised with the wave period ($m \neq T_p$).

It was shown that the MBWS model reached reasonable stability from the 12 000th time step. For this reason it was decided to record the cumulative phase-averaged output between time steps 12 000 and 20 000, so that the calculations started at time step 12 000 and ended at time step 20 000, with wave period-asynchronous intervals of 97 time steps. The sample output, as function of time steps is shown below:

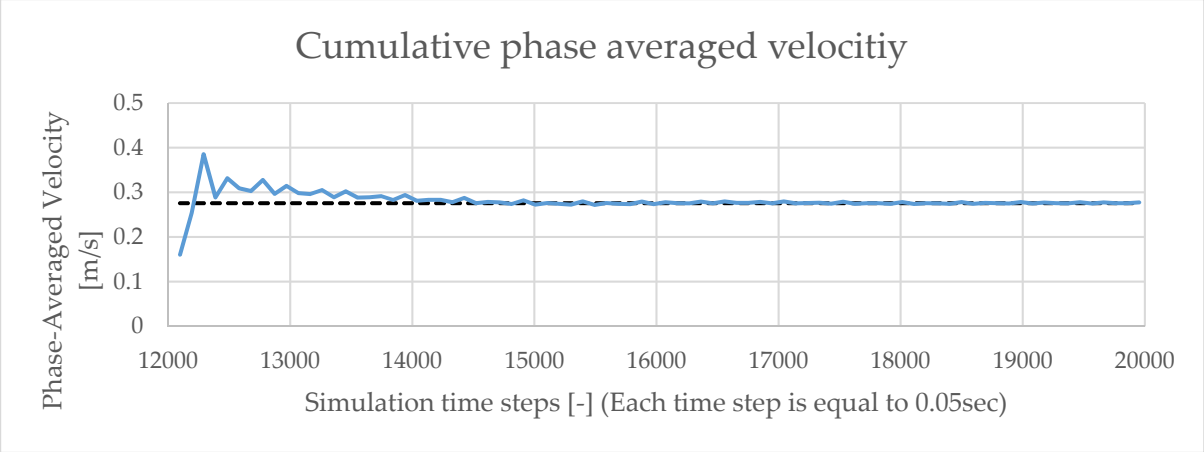

Figure C-14: Cumulative phase-averaged velocity as a function of time steps, measured at a single cell

The cumulative-series phase-averaged velocity is shown as a function of time steps. There are fluctuations evident between time steps 12 000 and 14 500, but the velocity function appears to have reached uniformity thereafter. It was therefore decided that the model was sufficiently stable from time step 12 000 and onwards. The phase-averaged recordings were therefore recorded between time steps 12 000 and 20 000, as above, and the average velocities were extracted at the last interval of the phase-averaged recording.

C.3.3.2 Wave heights

MIKE 21 Boussinesq Wave can provide wave data in both deterministic and phase-averaged output formats. The deterministic wave output is in the form of a surface elevation time-series recording. The phase-averaged output provides the maximum- or statistically significant wave height for a specified duration of recording. It is important to consider how each parameter is calculated before accepting the result as a final value.

C.3.3.2.1 Significant wave height

Significant wave height is determined by the relationship between surface elevation and the Rayleigh distribution of wave heights:

$$H_{m0} = 4 \cdot \sigma \qquad \text{(C.10)}$$

Where

- H_{m0} = is the significant wave height as defined by the Rayleigh distribution
- σ = is the standard deviation of the surface elevation

The standard deviation, σ, is obtained by a Fourier analysis of wave elevation series. The average amplitudes of the series are summarised as a root mean square value of the wave amplitudes, defined η_{RMS} or σ, and calculated as below:

$$\eta_{RMS} = \sigma = \sqrt{\frac{1}{N} \cdot \sum_{i=1}^{N} {\eta_i}^2} \tag{C.11}$$

Where

- η = amplitude of an individual wave
- η_{RMS} = root mean square value of the wave amplitudes
- N = Infinitesimally small segments along the wave series.

For a regular wave series the relationship between the root mean square wave amplitude η_{RMS} and absolute wave amplitude η is:

$$\eta_{RMS} = \eta \cdot \frac{1}{\sqrt{2}} \tag{C.12}$$

…and the for regular wave height:

$$H_S = 2 \cdot \eta \tag{C.13}$$

Where

- H_s = wave height of a regular wave series

By substituting η_{RMS} for η in equation C.13 from equation C.12

$$\therefore H_s = 2 \cdot \sqrt{2} \cdot \eta_{RMS} \tag{C.14}$$

Comparing the regular wave height from equation C.14 to the Rayleigh distribution's definition of significant wave heights in equation 6.12:

$$H_{m0} = 4 \cdot \sigma = 4 \cdot \eta_{RMS}$$

$$\therefore {H_{m0}}/{H_s} = \frac{4 \cdot \eta_{RMS}}{2 \cdot \sqrt{2} \cdot \eta_{RMS}}$$

$$\therefore {H_{m0}}/{H_s} = \sqrt{2} \tag{C.15}$$

Therefore, from equation C.15 it can be seen that in the case of regular waves, significant wave height based on the standard deviation, σ, will overestimate the wave height by a factor of $\sqrt{2} \approx 1.4$.

MIKE 21 Boussinesq Wave estimates the significant wave height with the phase-averaged standard deviation of the surface-elevation. The same calculation is used across all types of waves (regular or random waves), and thus for regular waves the phase-averaged significant wave height output should be reduced by ≈ 1.4 to get an estimate of the average regular wave height. This reduction factor is only accurate where the surface elevation follows a single regular wave pattern. Reflection effects causing wave super positioning, as in the example below, will influence the standard deviation of the surface elevation by an unknown extent. The phase-averaged significant wave height is therefore not very reliable for regular waves.

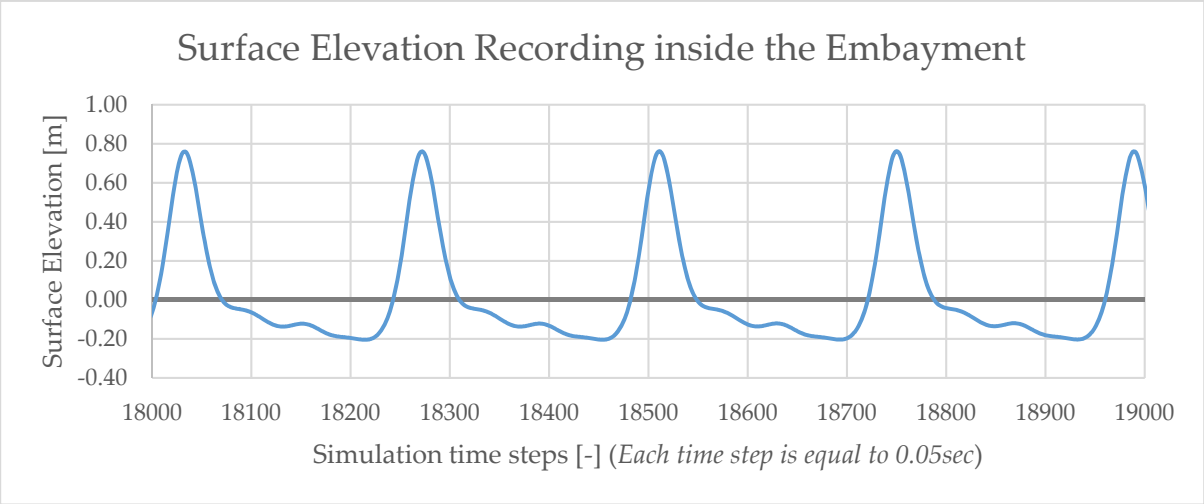

Figure C-15: Wave time series showing super positioning effects due to wave reflection.

C.3.3.2.2 Maximum wave height

Maximum wave heights are defined by the maximum zero-crossing wave height for a specified time period. *MIKE21BW* can produce the maximum wave height distribution by means of phase-average calculations.

Theoretically, for regular waves the maximum wave height should be equal to any wave height in a regular wave series. The maximum wave height distribution should therefore be a better indicator of the wave height distribution than the phase-averaged significant wave height. Any irregularities or instabilities may temporarily cause abnormal wave heights which could in turn influence the wave height recordings. It is therefore very important to verify the model's stability before the maximum wave height distribution can be accepted.

C.3.3.3 Alternative solution: manual time series elevation

Perhaps the safest way to calculate the wave height is by measuring the wave heights from the deterministic surface elevation time-series output by means of the zero-crossing method. This method does not rely on statistical estimation and the wave form could be studied for instabilities or abnormalities, thus eliminating the problems associated with the phase averaged significant wave heights and maximum wave heights respectively. The limitation to the zero crossing method is that the output file should use relatively small time steps to resolve the peak and troughs of the surface elevation.

This method should provide the most accurate results for wave heights, but through its manual operation it is limited to singular, zero-dimensional measurements.

C.3.3.3.1 Hybrid calculation of wave height

Depending on the final use, a hybrid recording of the deterministic and phase-averaged wave heights can be used in the MBWS model. The phase-averaged maximum wave heights is useful for wave-distribution purposes, but may not provide the most accurate results. The deterministic surface-elevation output provides the most accurate wave heights, but is limited to single point measurements. Thus, for the most accurate results, the deterministic surface-elevation should be used for single wave height measurements and the phase-averaged maximum wave heights should be used for wave height distribution only.

C.4 SENSITIVITY ANALYSIS: PARAMETERS

This section provides detail on the sensitivity analysis parameters as used in § 6.7.

C.4.1 Influence on Velocities

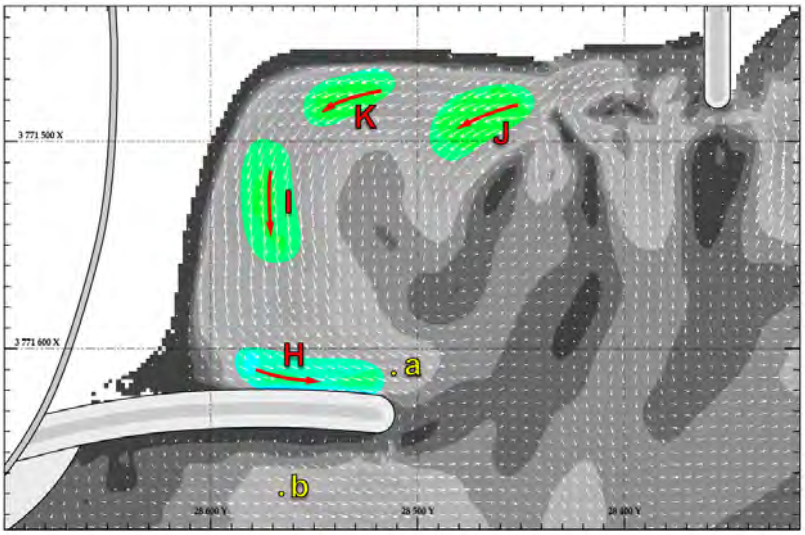

Figure C-16: Key velocity areas and wave height measuring points.

The change in velocity was simply calculated as the difference between the velocity of the sensitivity model and the MB610 baseline model:

$$\Delta u_i = \frac{u_{i(S)} - u_{i(B)}}{u_{i(B)}} \times 100\% \qquad \text{(C.16)}$$

Where

- Δu_i = velocity change relative to the **MB610** baseline model at point i
- $u_{i(S)}$ = UPA30 velocity measured in the sensitivity model at point i
- $u_{i(B)}$ = UPA30 velocity measured in the **MB610** baseline model at point i
- point $i = \{\text{H, I, J, K}\}$

Average absolute velocity change ($\bar{u}'_S$) denotes the average change of the *absolute* velocities relative to the measurements of the baseline velocities. The use of absolute velocities was necessary, due to simultaneous increase and decrease of velocities within a single simulation. $\bar{u}'_S$ can be expressed as:

$$\bar{u}'_S = \frac{|\Delta u_H| + |\Delta u_I| + |\Delta u_J| + |\Delta u_K|}{4} \qquad \text{(C.17)}$$

Where

- $\bar{u}'_S$ = average absolute velocity change [%]
- $\{u_H, u_I, u_J, u_K\}$ = velocities measured at the respective areas
- The vertical brackets | | denote absolute (positive) values

C.4.2 Influence on wave heights

The influence of the sensitivity parameters on the wave heights was also quantitatively studied by measuring and tabulating the wave heights at the fixed points "a" and "b" in Figure C-16.

The wave change of wave heights could be formulated similarly to equation 6.4 and 6.5 so that:

$$\Delta H_j = \frac{H_{j(S)} - H_{j(B)}}{H_{j(B)}} \times 100\% \tag{C.18}$$

$$\bar{H}'_S = \frac{|\Delta H_a| + |\Delta H_b|}{2} \tag{C.19}$$

- ΔH_j = wave height change relative to the **MB610** baseline model at point j
- $H_{j(S)}$ = Wave height measured in the sensitivity model at point j
- $H_{j(B)}$ = Wave height measured in the **MB610** baseline model at point j
- $\bar{H}'_S$ = average absolute wave height change [%]
- point $j = \{a, b\}$

Appendix D

Monwabisi Boussinesq Wave Simulation detailed results

D.1 PROPOSED SOLUTION SIMULATIONS

D.1.1 MT001

D.1.1.1 Setup

D.1.1.1.1 Description

Short groyne opposite spur head.

D.1.1.1.2 Wave Conditions

Water / Tide Level	+0.7m MSL	**Wave Period (T_p)**	12 s
Wave Height (H_s)	1.5m	**Wave Angle**	+ 8°

D.1.1.2 Results

D.1.1.2.1 Current Velocity and Direction Map

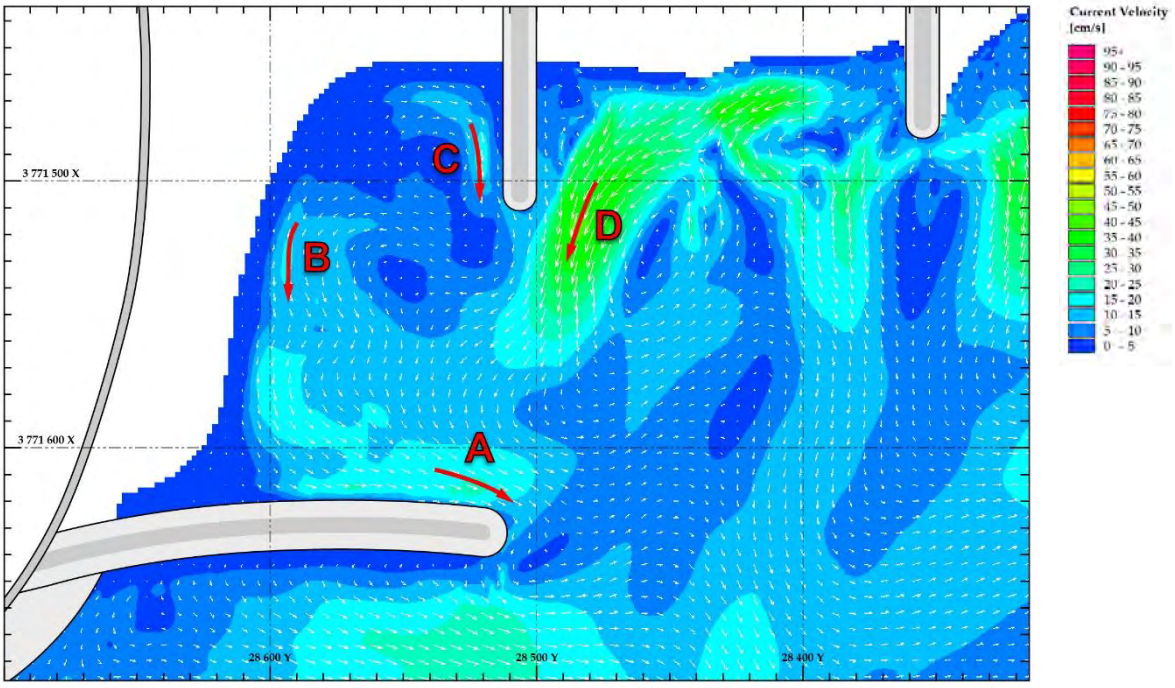

D.1.1.2.2 Measured Peak Flow Velocities

Vector	Class	30m Peak Average Velocities		
		u (absolute)	U_r (relative) (§ 7)	U_f (factorised) (§ 8)
A	1	19.4 cm/s	77%	77%
B	2	17.4 cm/s	54%	69%
C	2	14.3 cm/s	45%	57%
D	3	39.1 cm/s	115%	155%

D.1.1.2.3 Area-Velocity: Designated Swimming Area

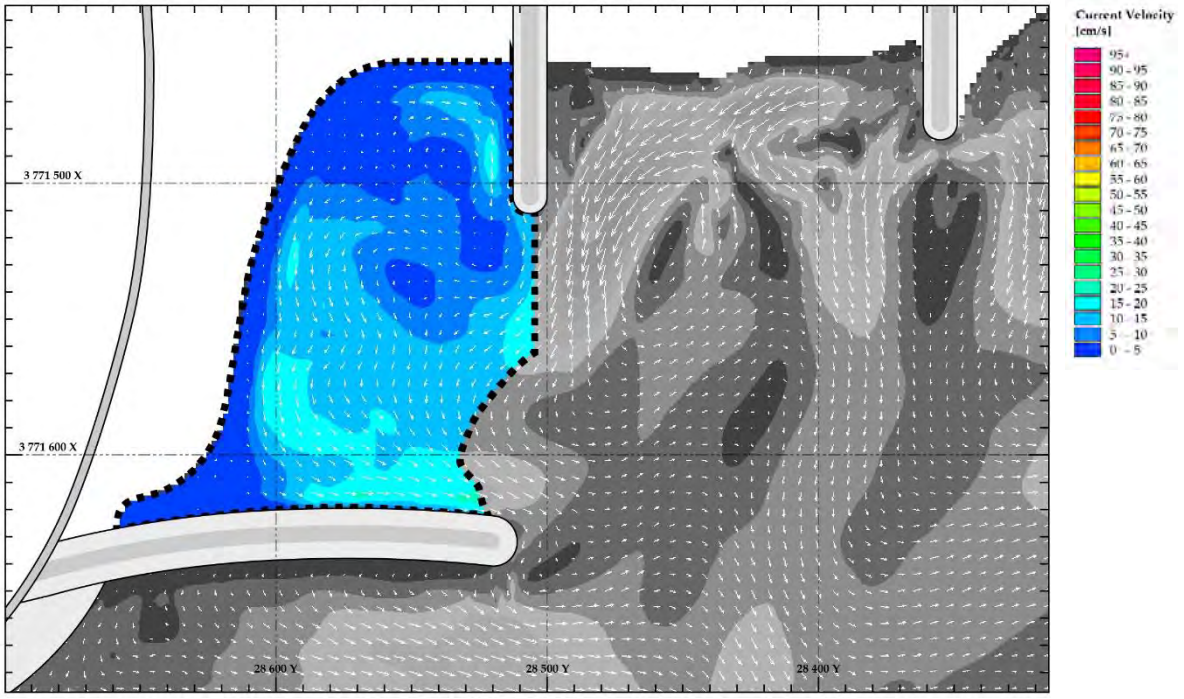

D.1.1.2.4 Velocity Exceedance: Designated Swimming Area

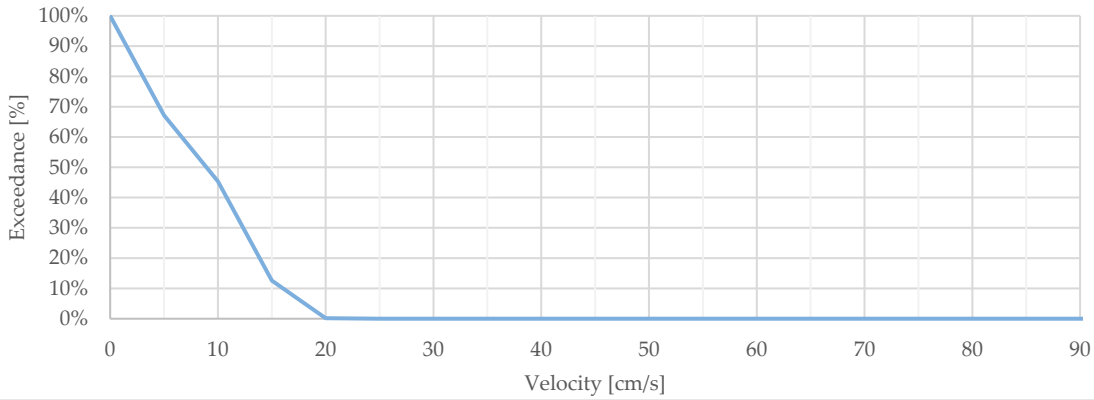

D.1.1.2.5 Velocity Baseline Exceedance Difference: Designated Swimming Area

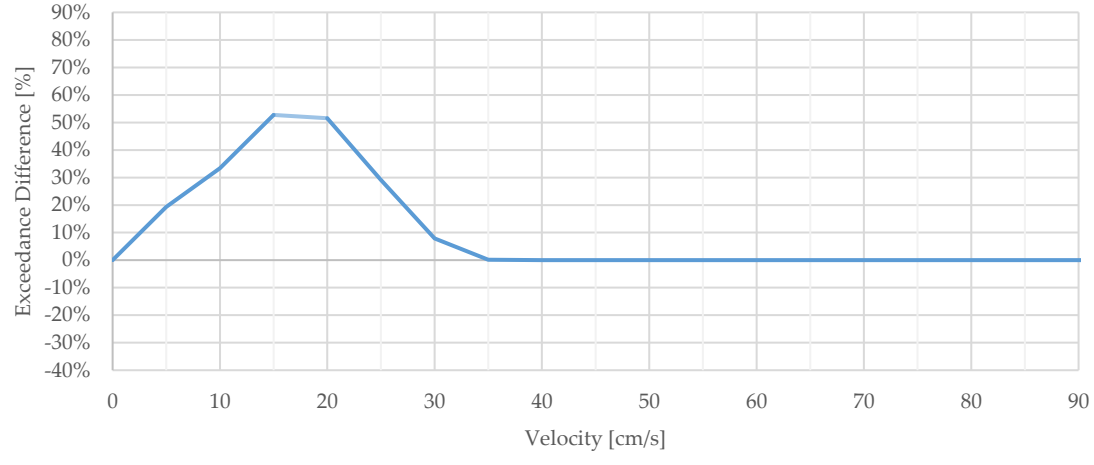

D.1.2 MT002

D.1.2.1 Setup

D.1.2.1.1 Description

Long Groyne Opposite Spur Head

D.1.2.1.2 Wave Conditions

Water / Tide Level	+0.7m MSL	**Wave Period (T_p)**	12 s
Wave Height (H_s)	1.5m	**Wave Angle**	+ 8°

D.1.2.2 Results

D.1.2.2.1 Current Velocity and Direction Map

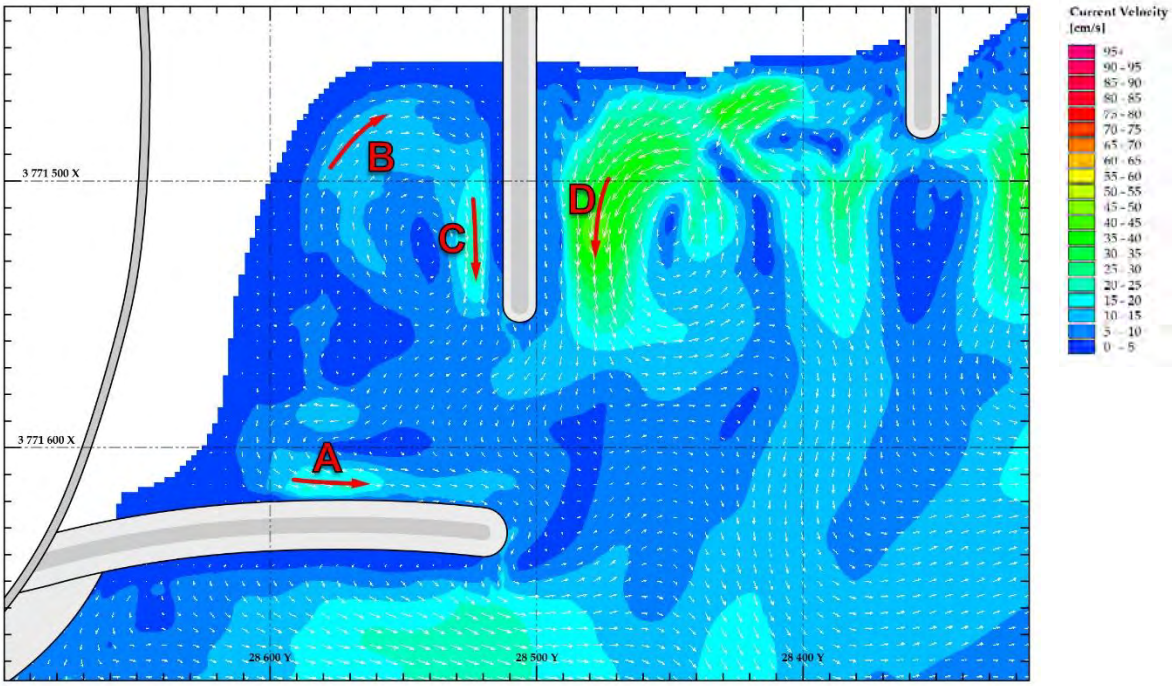

D.1.2.2.2 Measured Peak Flow Velocities

Vector	Class	30m Peak Average Velocities		
		u (absolute)	U_r (relative) (§ 7)	U_f (factorised) (§ 8)
A	1	18.8 cm/s	75%	75%
B	2	11.2 cm/s	35%	45%
C	2	21.7 cm/s	68%	86%
D	3	39.9 cm/s	117%	158%

D.1.2.2.3 Area-Velocity: Designated Swimming Area

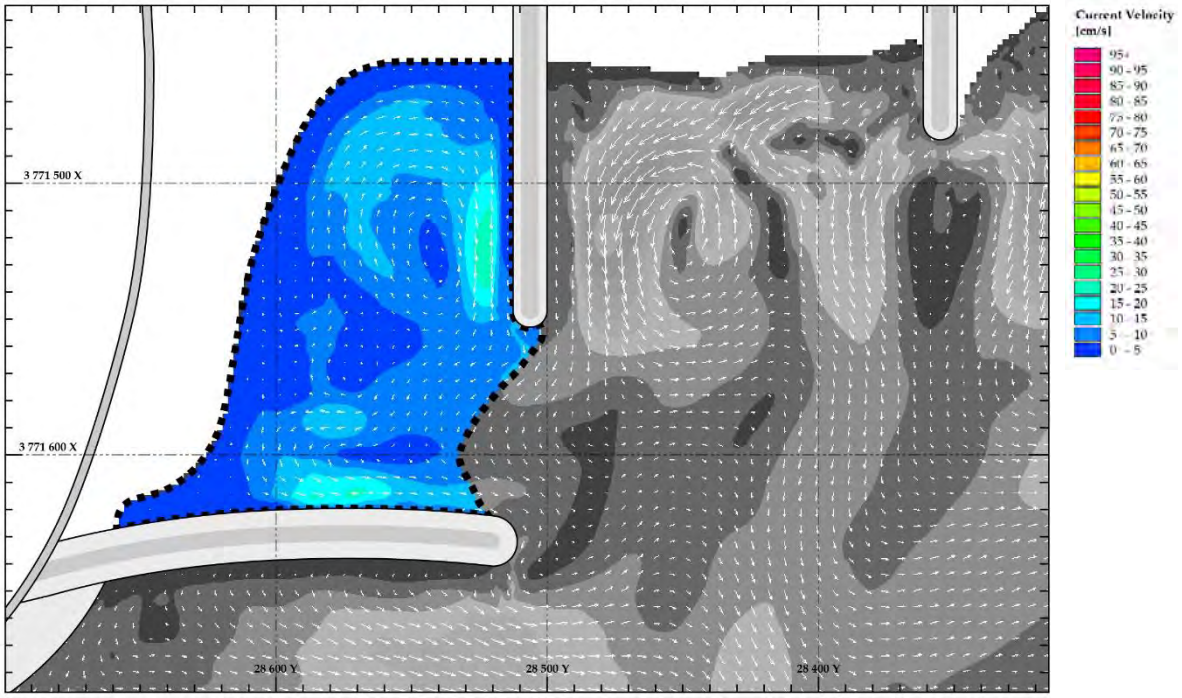

D.1.2.2.4 Velocity Exceedance: Designated Swimming Area

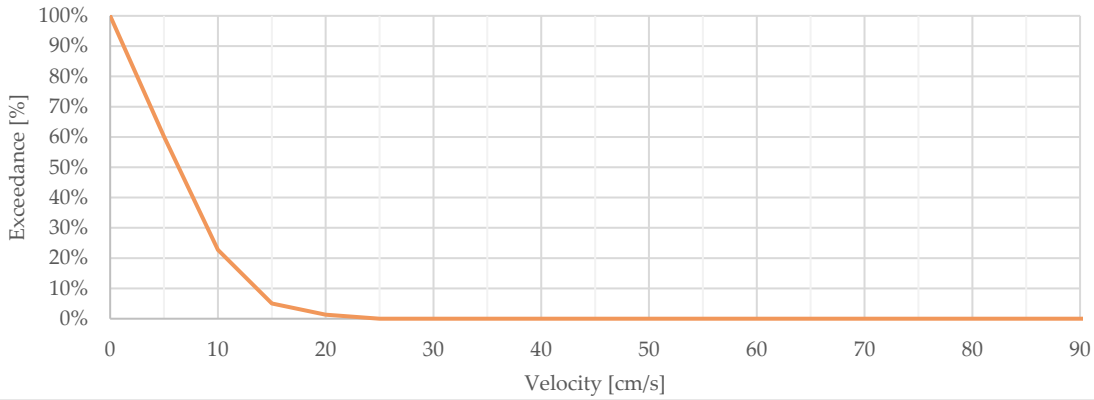

D.1.2.2.5 Velocity Baseline Exceedance Difference: Designated Swimming Area

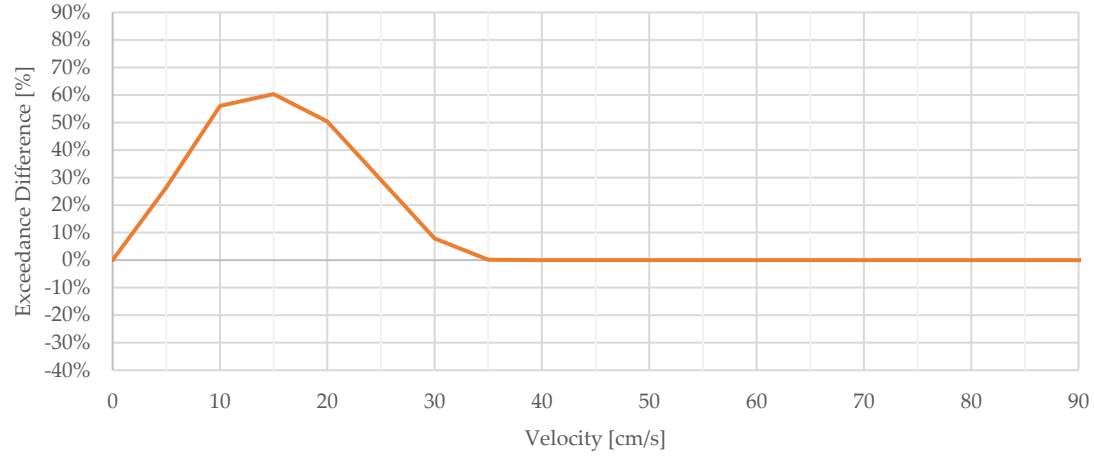

D.1.3 MT003

D.1.3.1 Setup

D.1.3.1.1 Description

Long groyne away from spur head.

D.1.3.1.2 Wave Conditions

Water / Tide Level	+0.7m MSL	**Wave Period (T_p)**	12 s
Wave Height (H_s)	1.5m	**Wave Angle**	+ 8°

D.1.3.2 Results

D.1.3.2.1 Current Velocity and Direction Map

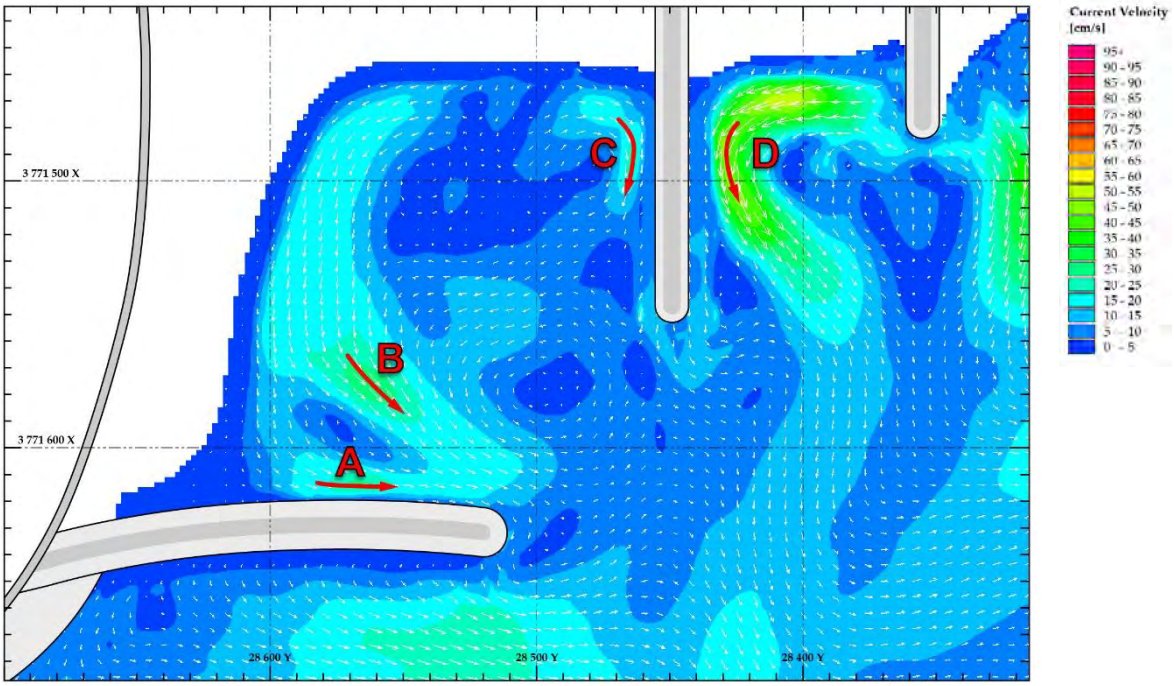

D.1.3.2.2 Measured Peak Flow Velocities

Vector	Class	30m Peak Average Velocities		
		***u* (absolute)**	**U_r (relative)** (§ 7)	**U_f (factorised)** (§ 8)
A	1	22.2 cm/s	88%	88%
B	2	26.1 cm/s	81%	103%
C	2	18.2 cm/s	57%	72%
D	3	44.4 cm/s	130%	176%

D.1.3.2.3 Area-Velocity: Designated Swimming Area

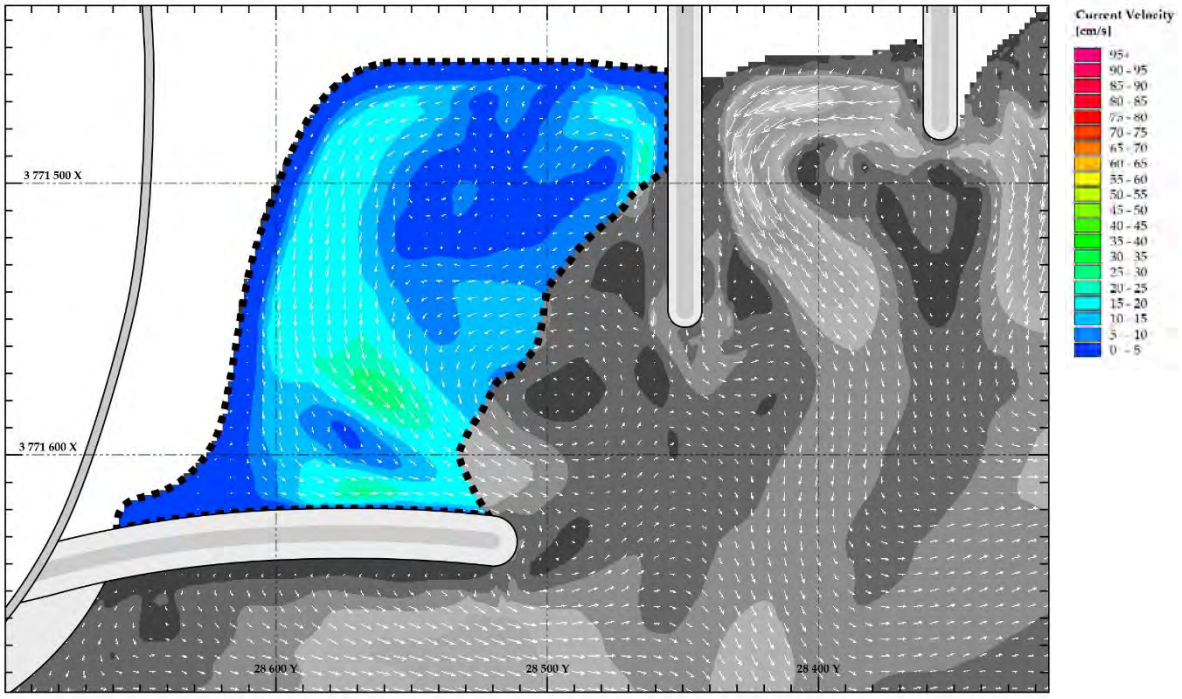

D.1.3.2.4 Velocity Exceedance: Designated Swimming Area

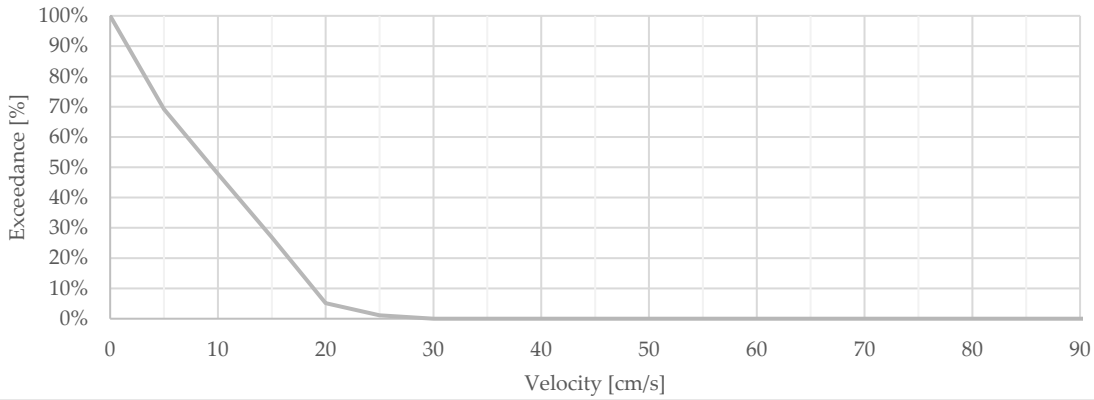

D.1.3.2.5 Velocity Baseline Exceedance Difference: Designated Swimming Area

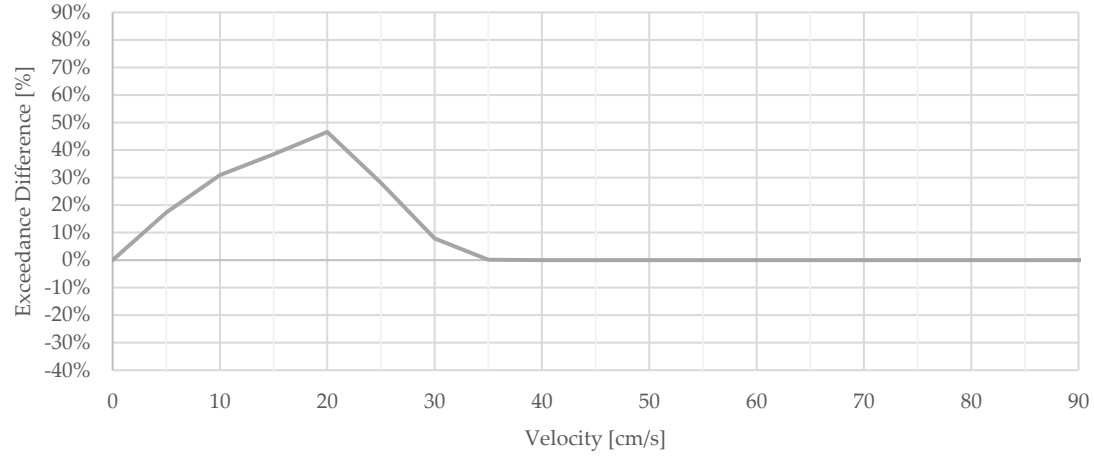

D.1.4 MT004

D.1.4.1 Setup

D.1.4.1.1 Description

Dog-legged groyne opposite spur head

D.1.4.1.2 Wave Conditions

Water / Tide Level	+0.7m MSL	**Wave Period (T_p)**	12 s
Wave Height (H_s)	1.5m	**Wave Angle**	+ 8°

D.1.4.2 Results

D.1.4.2.1 Current Velocity and Direction Map

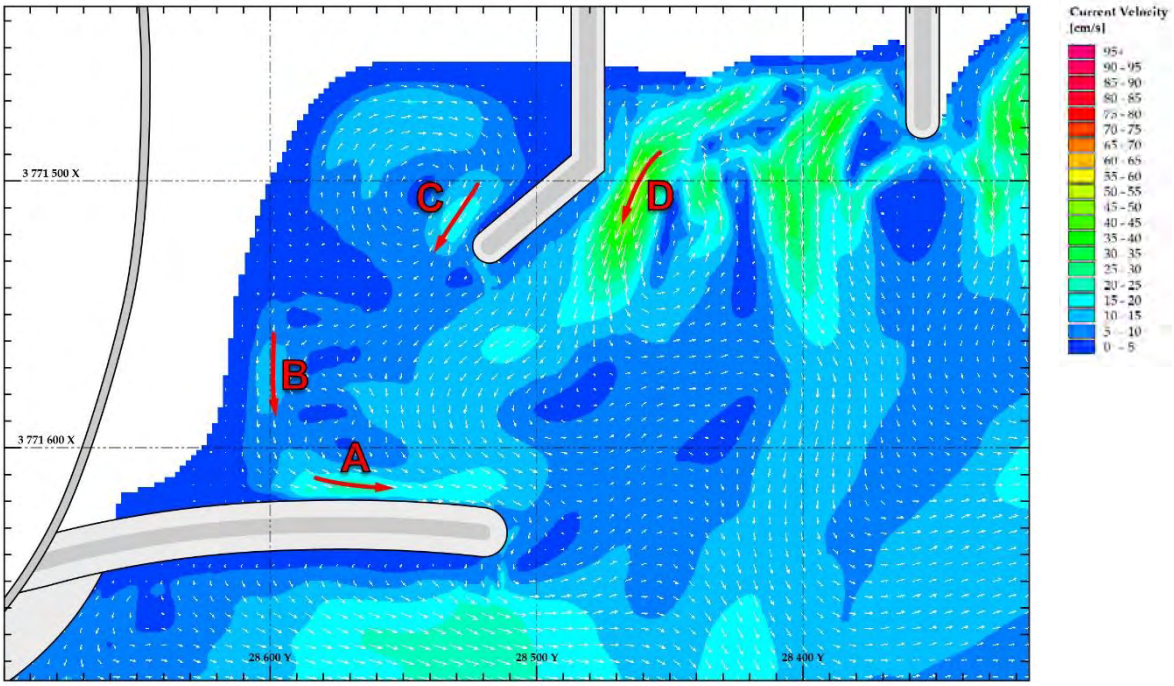

D.1.4.2.2 Measured Peak Flow Velocities

Vector	Class	30m Peak Average Velocities		
		***u* (absolute)**	**U_r (relative)** (§ 7)	**U_f (factorised)** (§ 8)
A	1	20.3 cm/s	80%	80%
B	2	11.3 cm/s	35%	45%
C	2	16.0 cm/s	50%	63%
D	3	42.4 cm/s	124%	168%

D.1.4.2.3 Area-Velocity: Designated Swimming Area

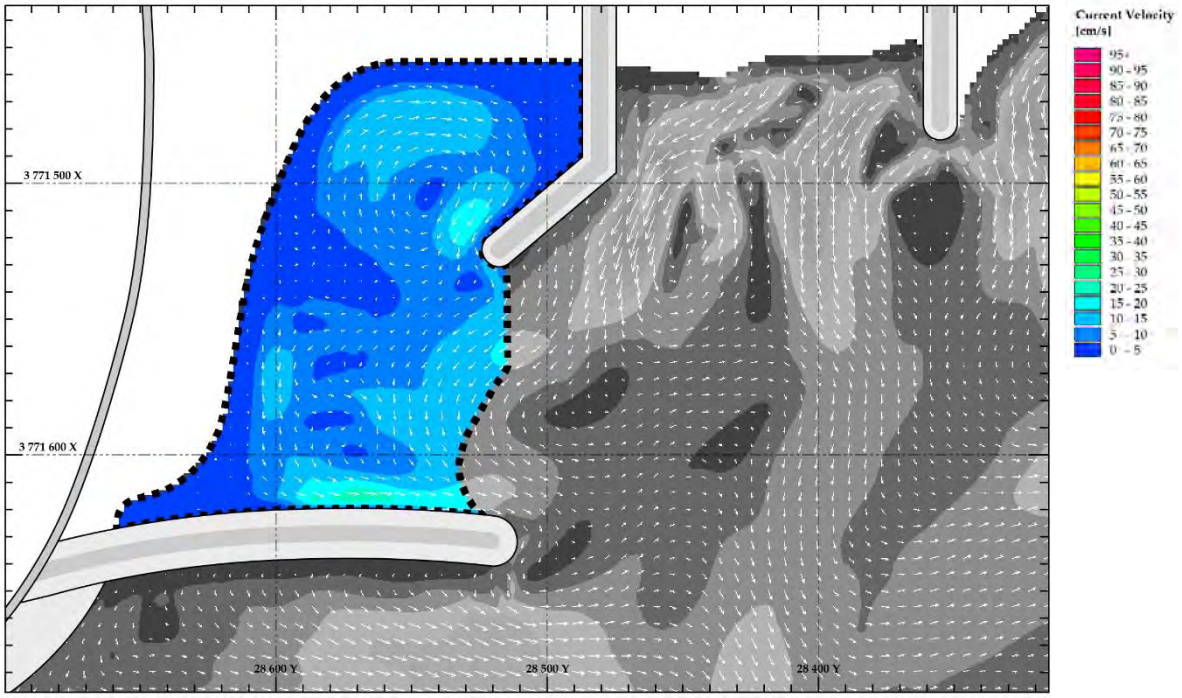

D.1.4.2.4 Velocity Exceedance: Designated Swimming Area

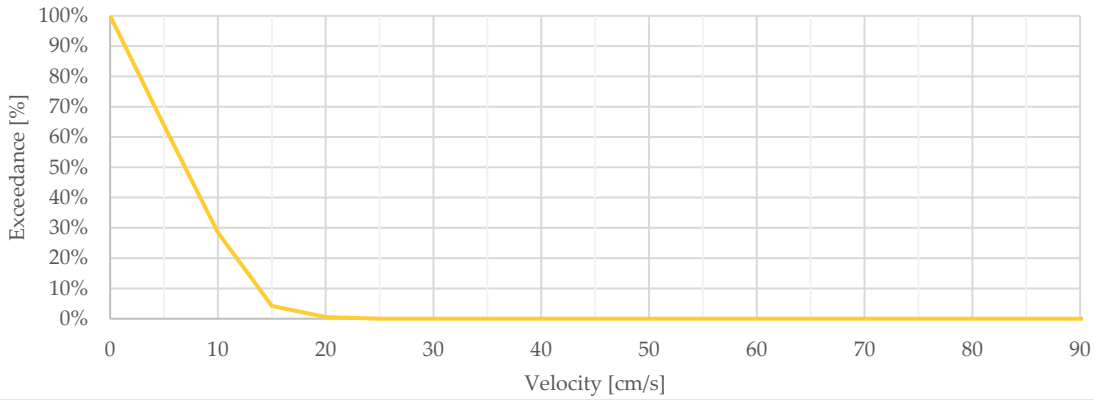

D.1.4.2.5 Velocity Baseline Exceedance Difference: Designated Swimming Area

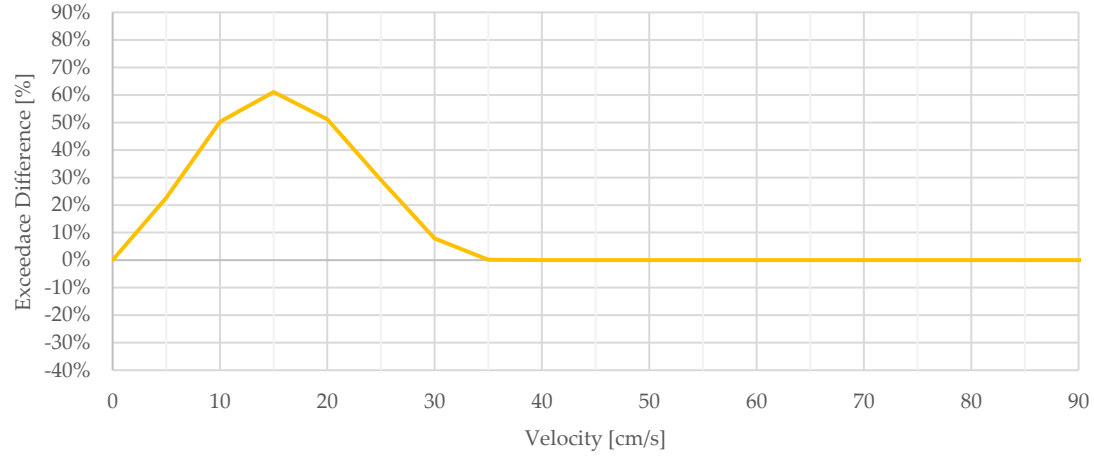

D.1.5 MT005

D.1.5.1 Setup

D.1.5.2 Description

Dog-legged spur off spur head (landward)

D.1.5.2.1 Wave Conditions

Water / Tide Level	+0.7m MSL	**Wave Period (T_p)**	12 s
Wave Height (H_s)	1.5m	**Wave Angle**	+ 8°

D.1.5.3 Results

D.1.5.3.1 Current Velocity and Direction Map

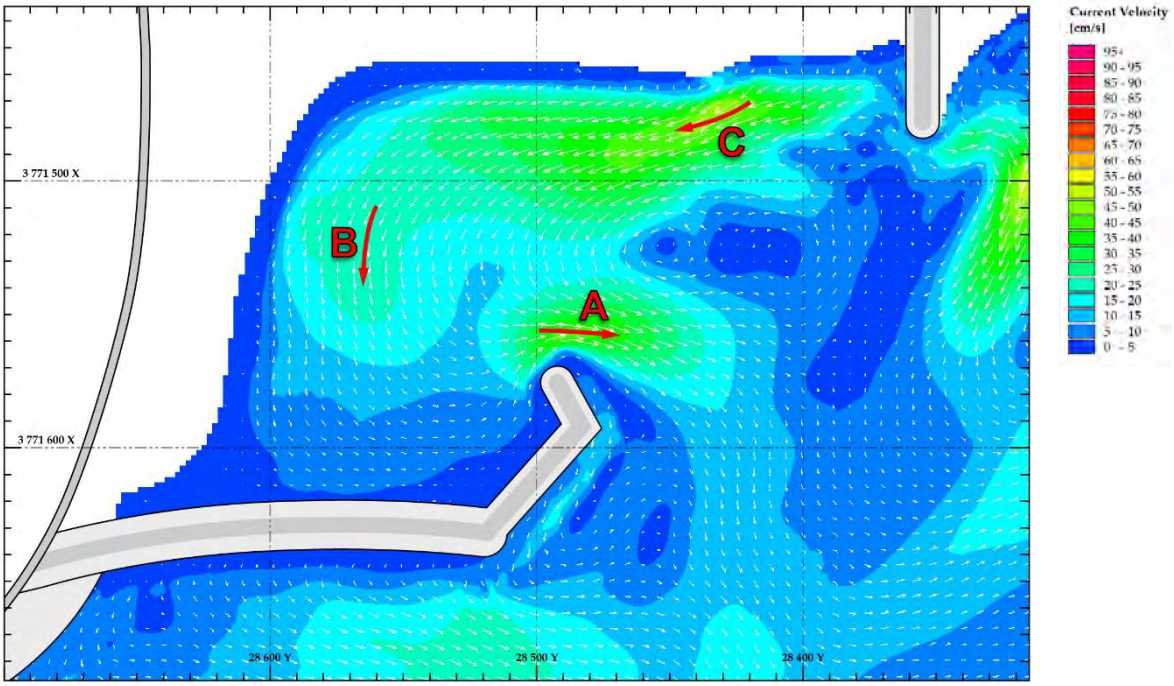

D.1.5.3.2 Measured Peak Flow Velocities

Vector	Class	30m Peak Average Velocities		
		u (absolute)	U_r (relative) (§ 7)	U_f (factorised) (§ 8)
A	1	38.9 cm/s	154%	154%
B	2	21.8 cm/s	68%	86%
C	2	46.1 cm/s	135%	183%

D.1.5.3.3 Area-Velocity: Designated Swimming Area

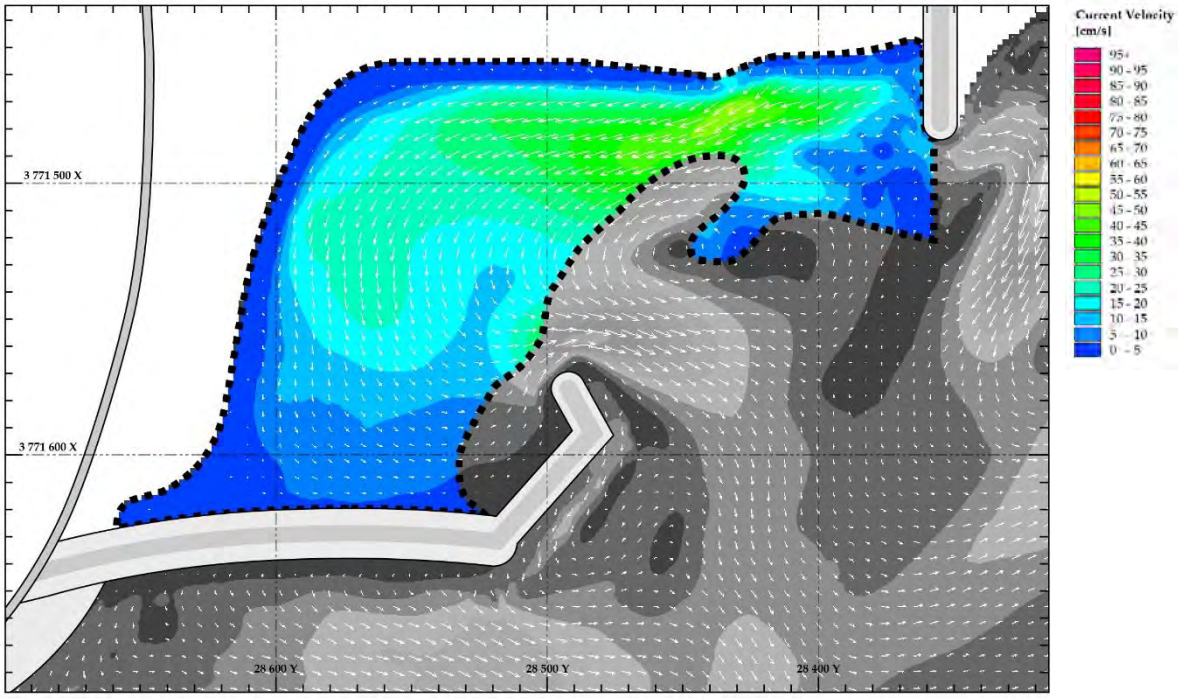

D.1.5.3.4 Velocity Exceedance: Designated Swimming Area

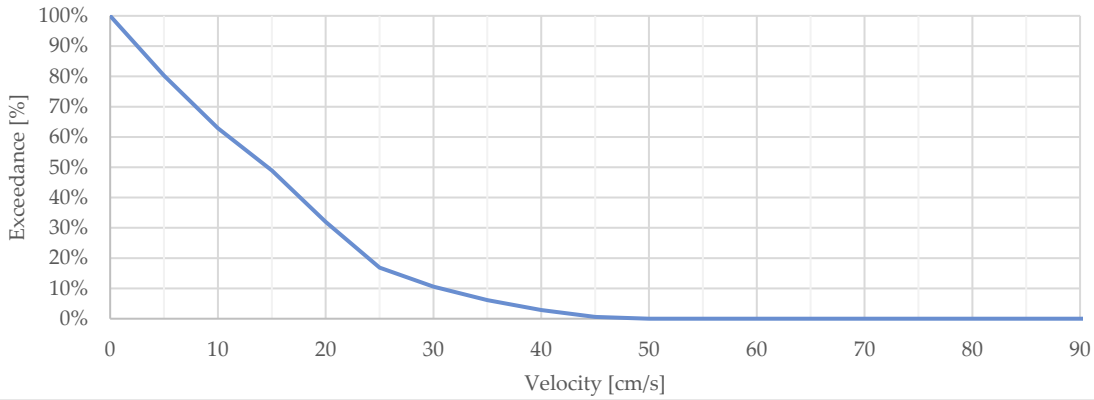

D.1.5.3.5 Velocity Baseline Exceedance Difference: Designated Swimming Area

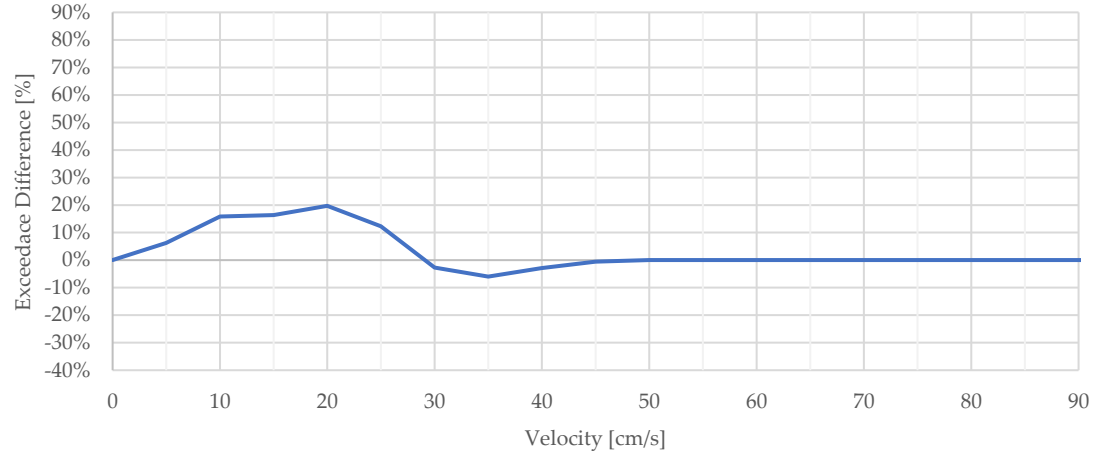

D.1.6 MT006

D.1.6.1 Setup

D.1.6.1.1 Description

Spur off spur head (seaward)

D.1.6.1.2 Wave Conditions

Water / Tide Level	+0.7m MSL	**Wave Period (T_p)**	12 s
Wave Height (H_s)	1.5m	**Wave Angle**	+ 8°

D.1.6.2 Results

D.1.6.2.1 Current Velocity and Direction Map

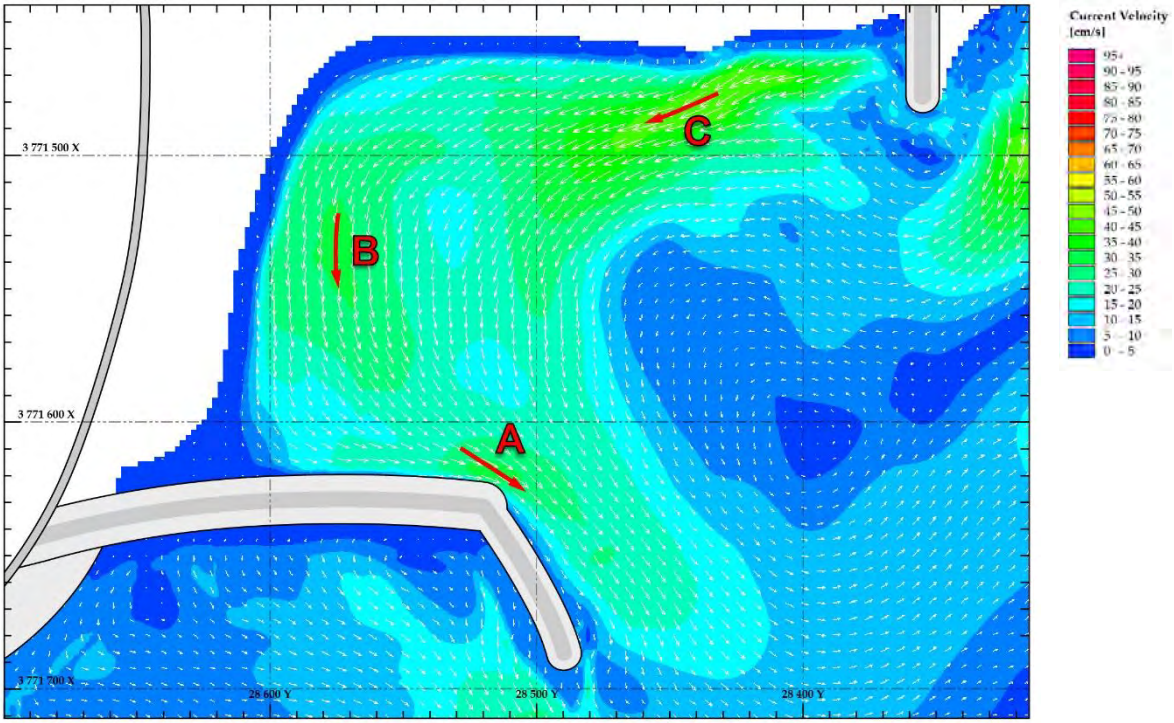

D.1.6.2.2 Measured Peak Flow Velocities

Vector	Class	30m Peak Average Velocities		
		u (absolute)	U_r (relative) (§ 7)	U_f (factorised) (§ 8)
A	1	30.2 cm/s	120%	120%
B	2	30.4 cm/s	95%	121%
C	3	44.1 cm/s	129%	175%

D.1.6.2.3 Area-Velocity: Designated Swimming Area

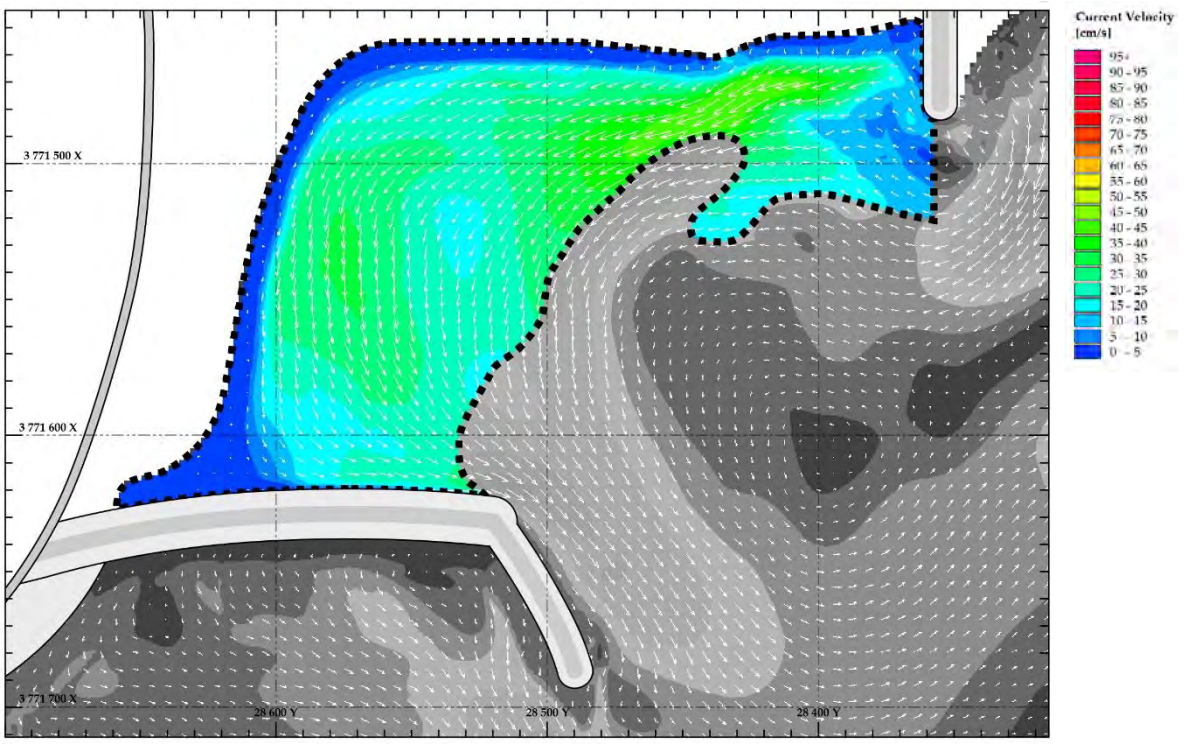

D.1.6.2.4 Velocity Exceedance: Designated Swimming Area

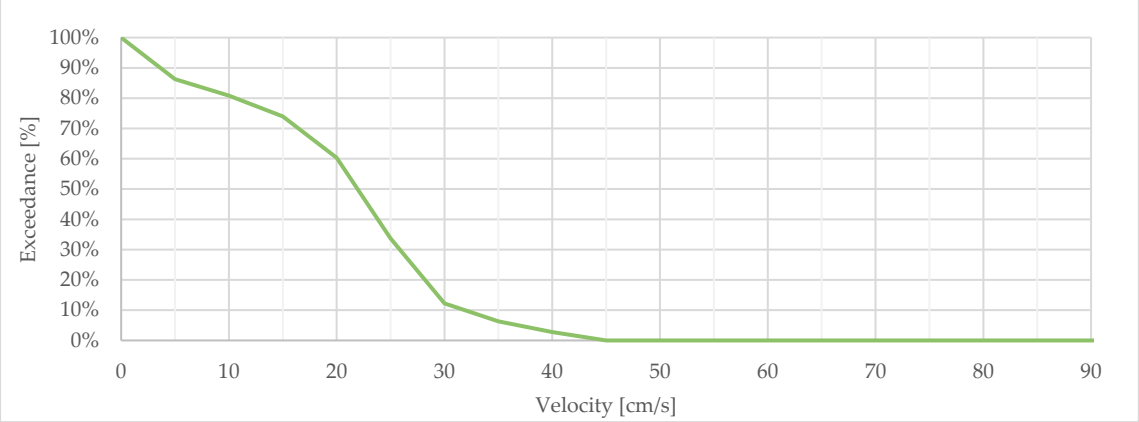

D.1.6.2.5 Velocity Baseline Exceedance Difference: Designated Swimming Area

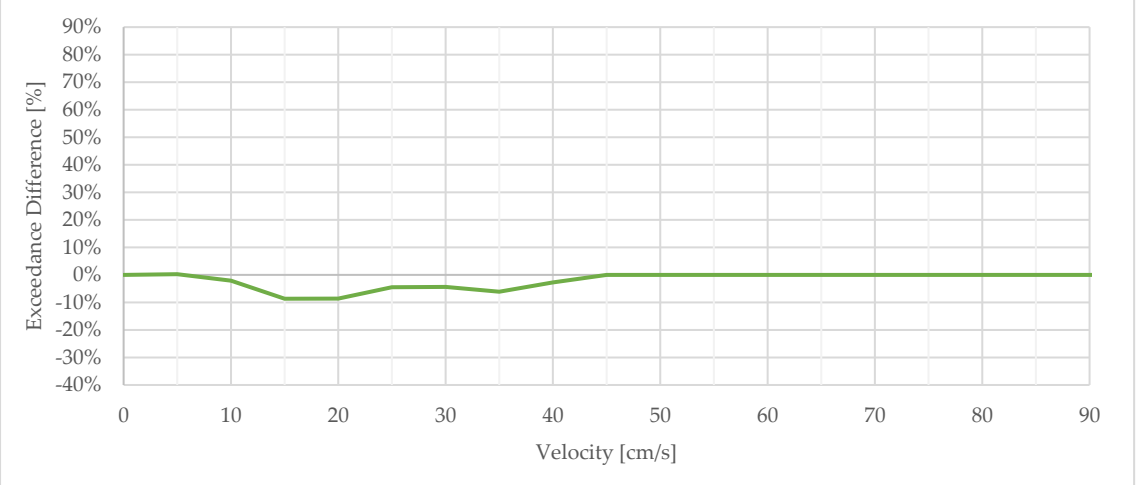

D.1.7 MT007

D.1.7.1 Setup

D.1.7.1.1 Description

Dog-legged Groyne off present beach

D.1.7.1.2 Wave Conditions

Water / Tide Level	+0.7m MSL	**Wave Period (T_p)**	12 s
Wave Height (H_s)	1.5m	**Wave Angle**	+ 8°

D.1.7.2 cm/s Results

D.1.7.2.1 Current Velocity and Direction Map

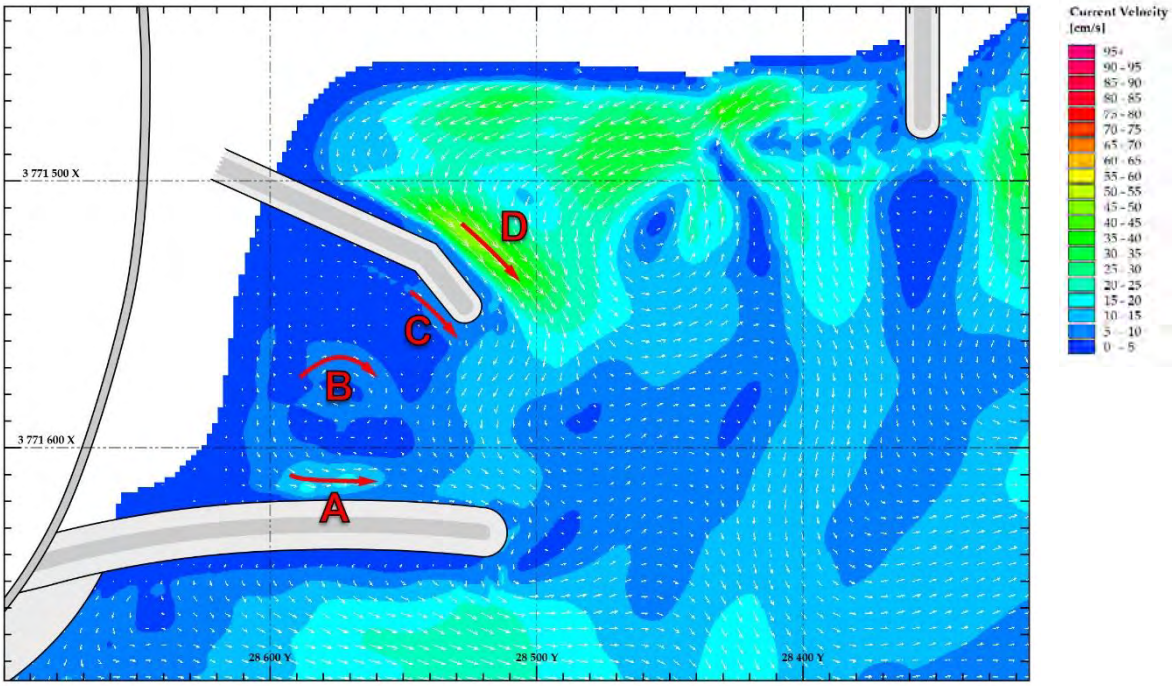

D.1.7.2.2 Measured Peak Flow Velocities

Vector	Class	30m Peak Average Velocities		
		u (absolute)	U_r (relative) (§ 7)	U_f (factorised) (§ 8)
A	1	14.3 cm/s	57%	57%
B	2	8.0 cm/s	25%	32%
C	2	8.0 cm/s	25%	32%
D	3	43.0 cm/s	126%	171%

D.1.7.2.3 Area-Velocity: Designated Swimming Area

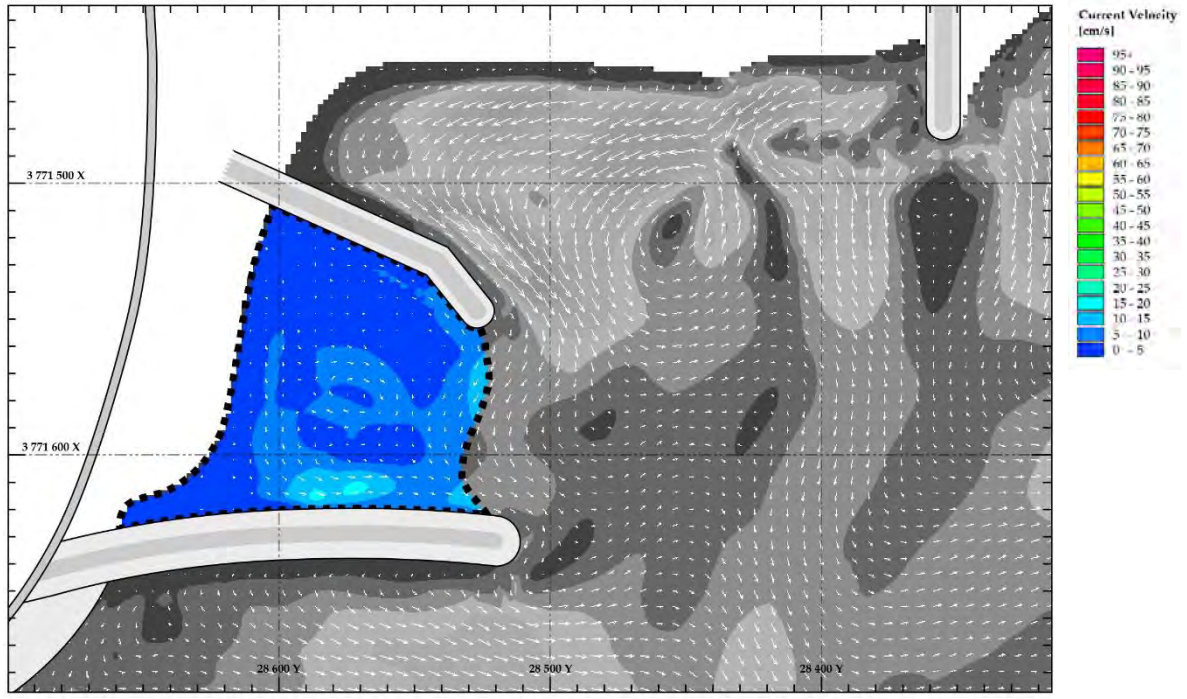

D.1.7.2.4 Velocity Exceedance: Designated Swimming Area

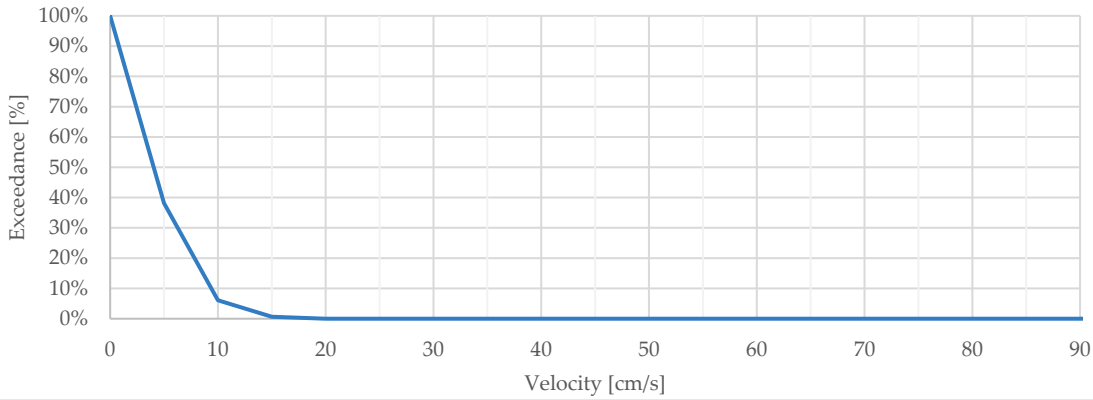

D.1.7.2.5 Velocity Baseline Exceedance Difference: Designated Swimming Area

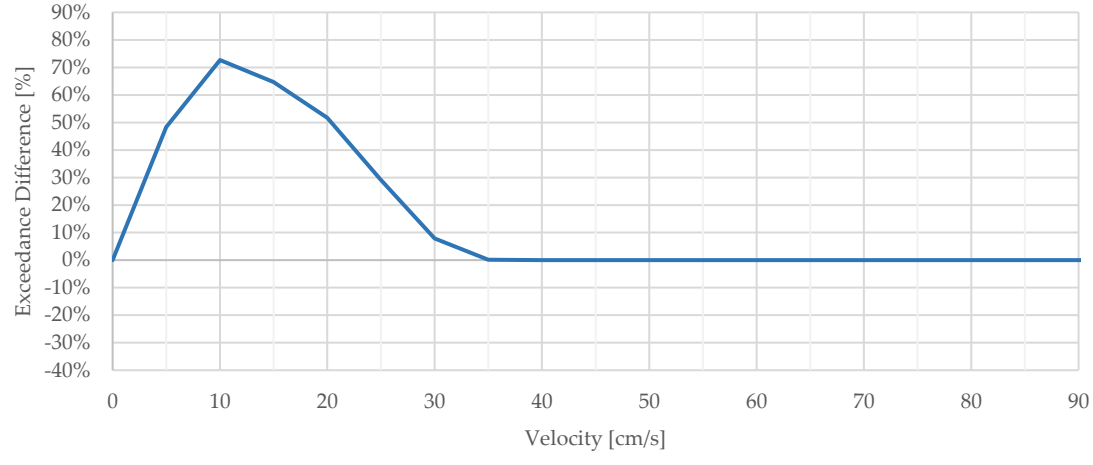

D.1.8 MT008

Note: The results are unreliable due to the unsuccessful modelling of wave overtopping action

D.1.8.1 Setup

D.1.8.1.1 Description

Lowered end of Spur

D.1.8.1.2 Wave Conditions

Water / Tide Level	+0.4m MSL	**Wave Period (T_p)**	12 s
Wave Height (H_s)	1.4m	**Wave Angle**	+ 8°

D.1.8.2 Results

D.1.8.2.1 Current Velocity and Direction Map

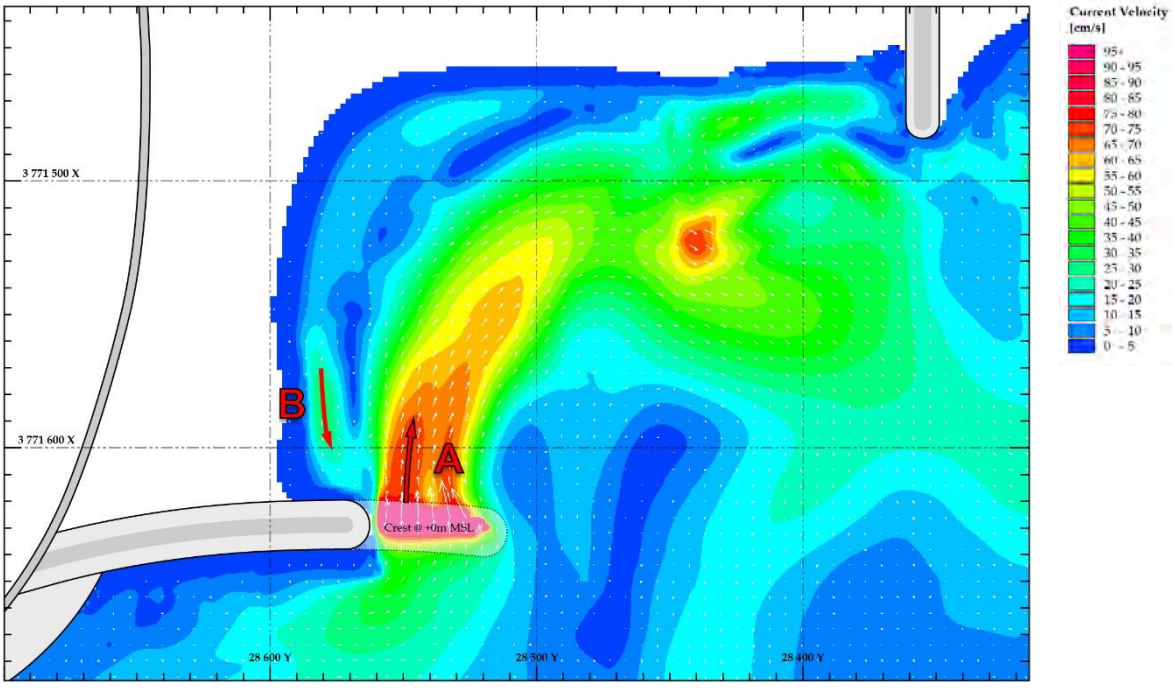

D.1.8.2.2 Measured Peak Flow Velocities

Vector	Class	30m Peak Average Velocities		
		u (absolute)	U_r (relative) (§ 7)	U_f (factorised) (§ 8)
A	1	73.0 cm/s	330%	290%
B	2	27.6 cm/s	86%	110%

D.1.8.2.3 Area-Velocity: Designated Swimming Area

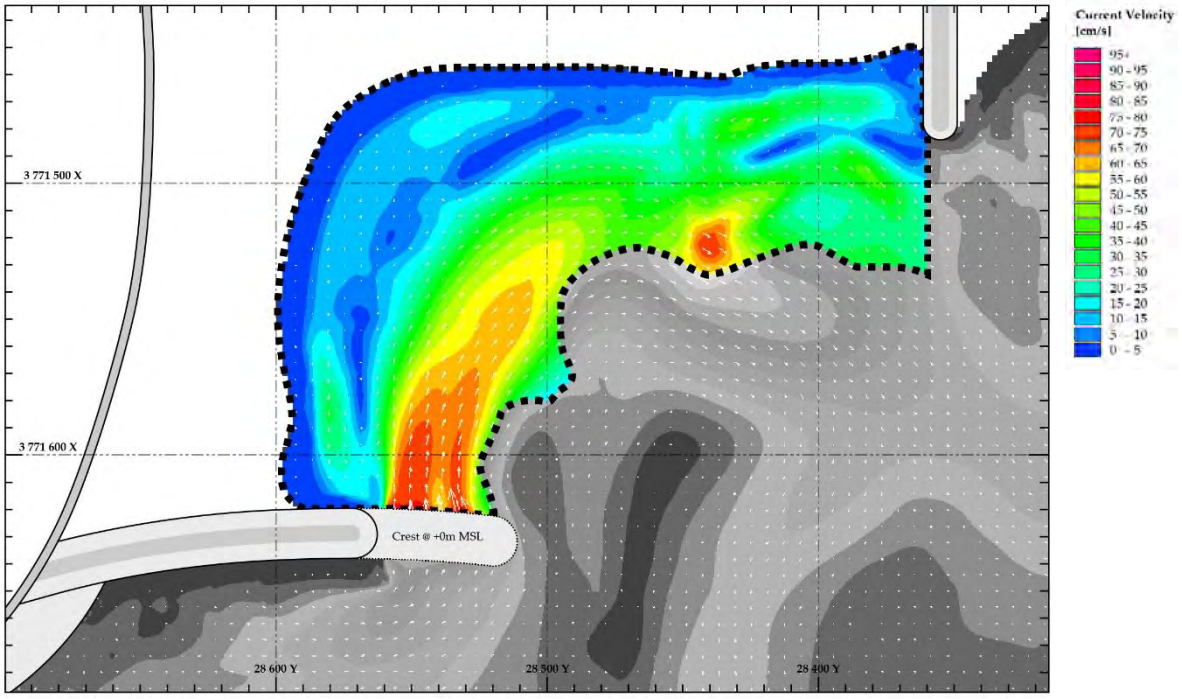

D.1.8.2.4 Velocity Exceedance: Designated Swimming Area

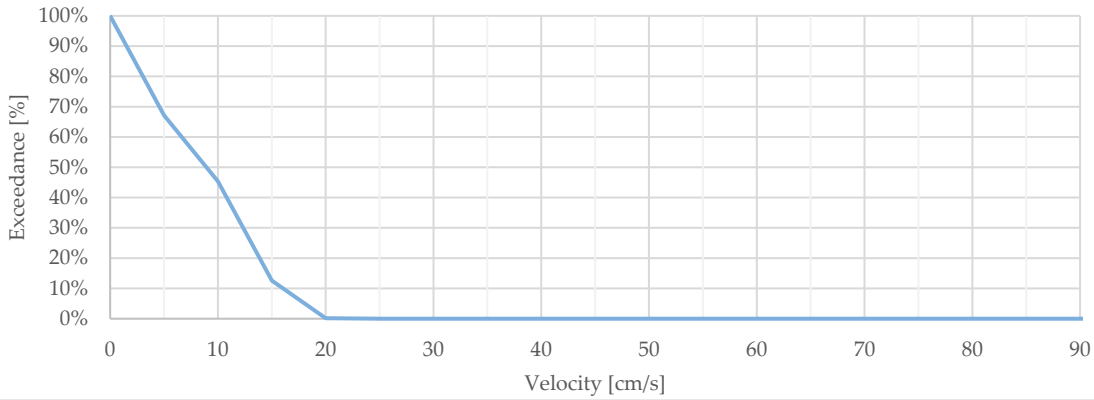

D.1.8.2.5 Velocity Baseline Exceedance Difference: Designated Swimming Area

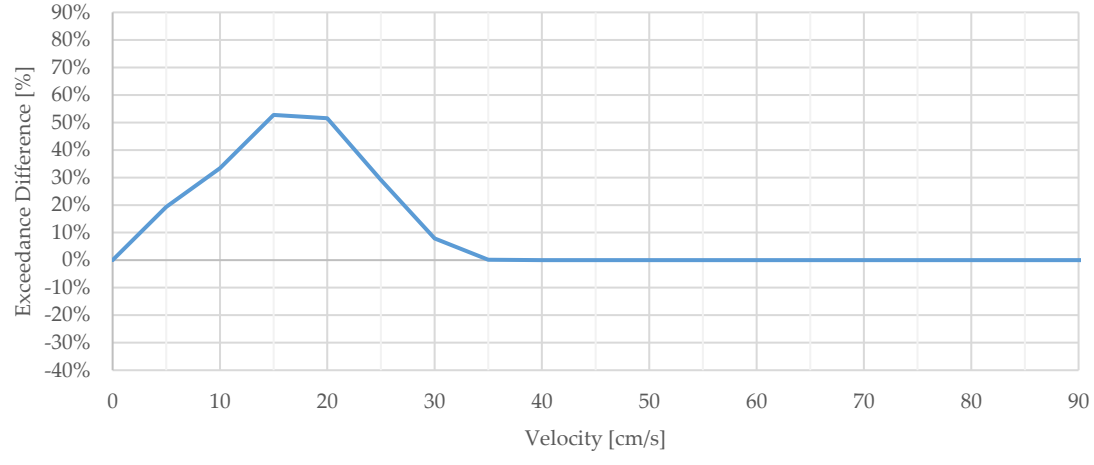

D.1.9 MT009

D.1.9.1 Setup

D.1.9.1.1 Description

Gap through spur (west stion)

D.1.9.1.2 Wave Conditions

Water / Tide Level	+0.7m MSL	**Wave Period (T_p)**	12 s
Wave Height (H_s)	1.5m	**Wave Angle**	+ 8°

D.1.9.2 Results

D.1.9.2.1 Current Velocity and Direction Map

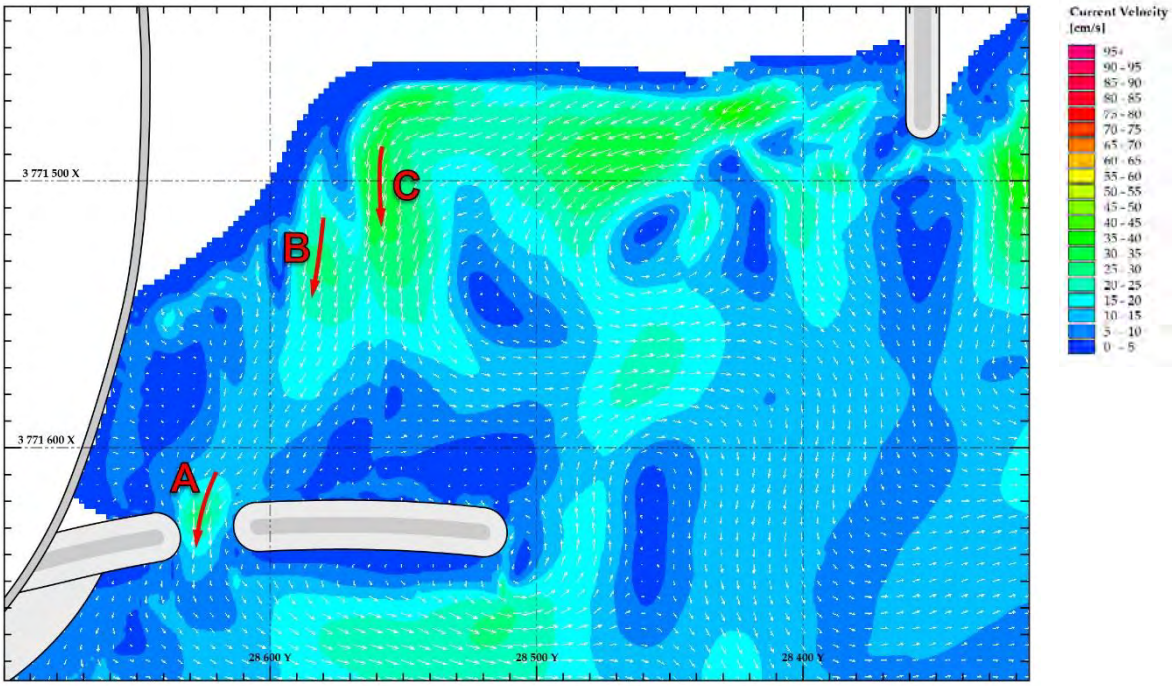

D.1.9.2.2 Measured Peak Flow Velocities

Vector	Class	30m Peak Average Velocities		
		u (absolute)	U_r (relative) (§ 7)	U_f (factorised) (§ 8)
A	1	21.1 cm/s	84%	84%
B	2	24.5 cm/s	77%	97%
C	2	32.0 cm/s	100%	127%

D.1.9.2.3 Area-Velocity: Designated Swimming Area

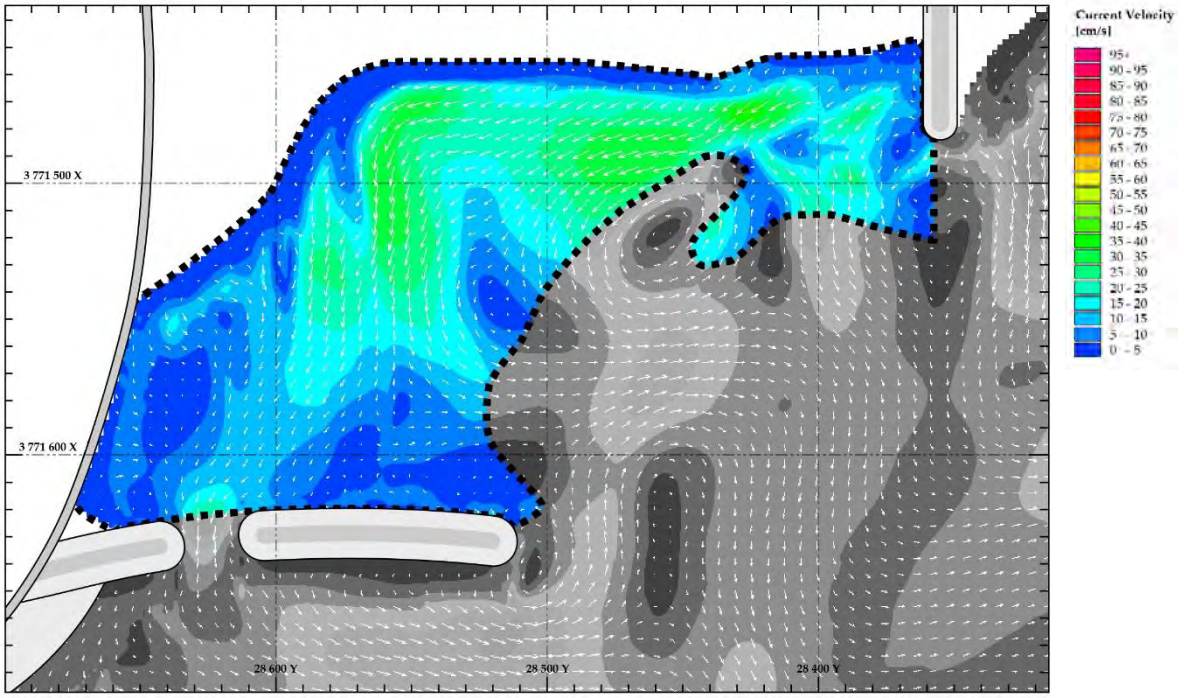

D.1.9.2.4 Velocity Exceedance: Designated Swimming Area

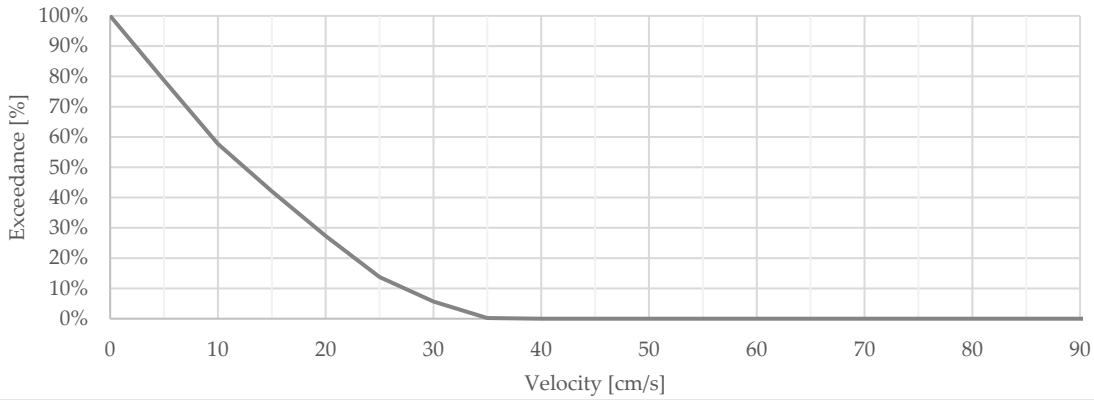

D.1.9.2.5 Velocity Baseline Exceedance Difference: Designated Swimming Area

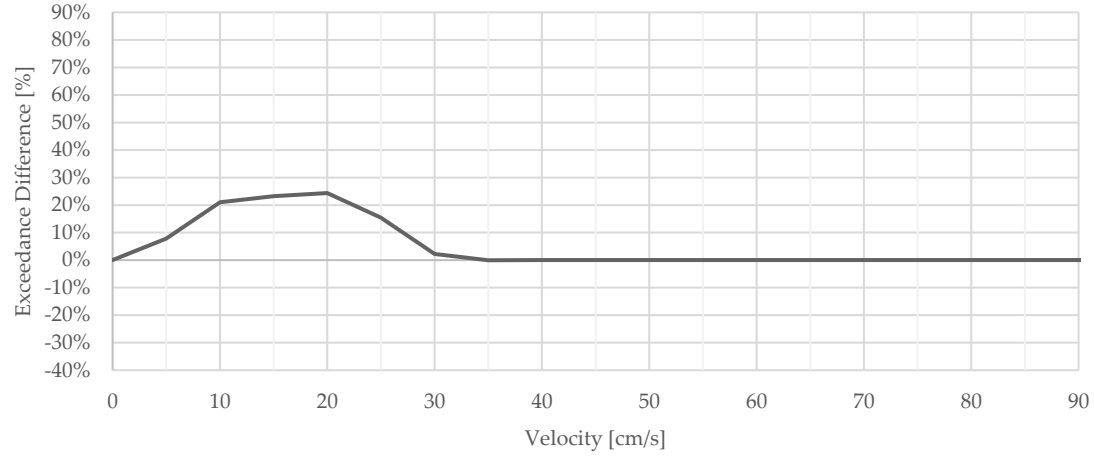

D.1.10 MT010

D.1.10.1 Setup

D.1.10.1.1 Description

Detached breakwater in bay

D.1.10.1.2 Wave Conditions

Water / Tide Level	+0.4m MSL	**Wave Period (T_p)**	12 s
Wave Height (H_s)	1.4m	**Wave Angle**	+ 8°

D.1.10.2 Results

D.1.10.2.1 Current Velocity and Direction Map

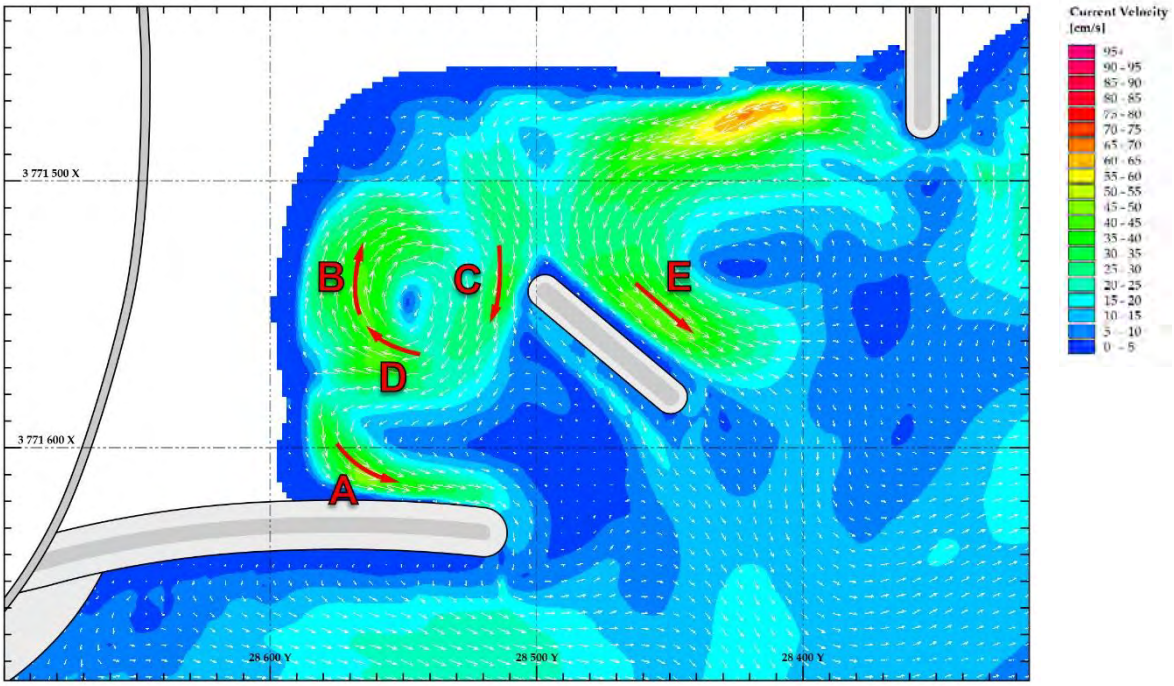

D.1.10.2.2 Measured Peak Flow Velocities

Vector	Class	30m Peak Average Velocities		
		u (absolute)	U_r (relative) (§ 7)	U_f (factorised) (§ 8)
A	1	41.4 cm/s	187%	164%
B	2	40.4 cm/s	125%	160%
C	2	33.1 cm/s	103%	131%
D	2	37.1 cm/s	115%	147%
E	3	43.2 cm/s	116%	171%

D.1.10.2.3 Area-Velocity: Designated Swimming Area

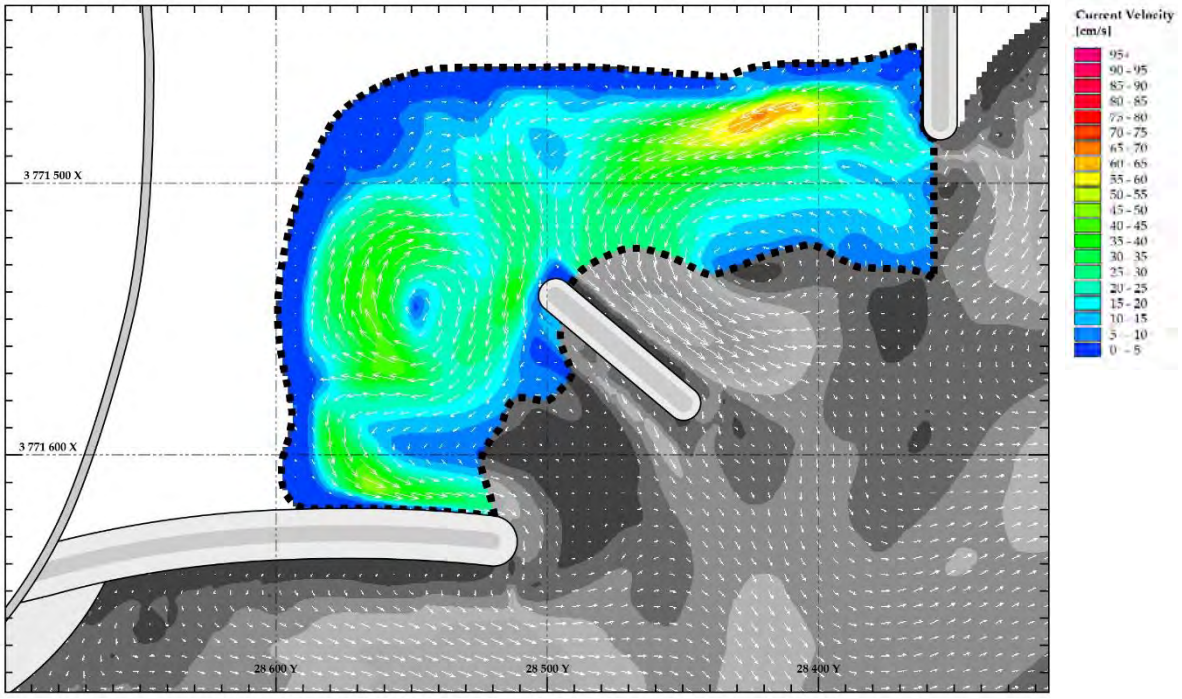

D.1.10.2.4 Velocity Exceedance: Designated Swimming Area

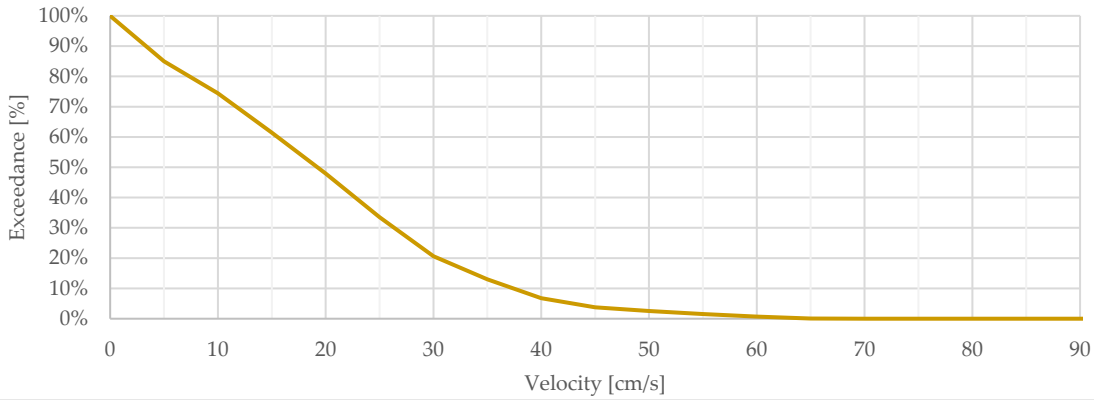

D.1.10.2.5 Velocity Baseline Exceedance Difference: Designated Swimming Area

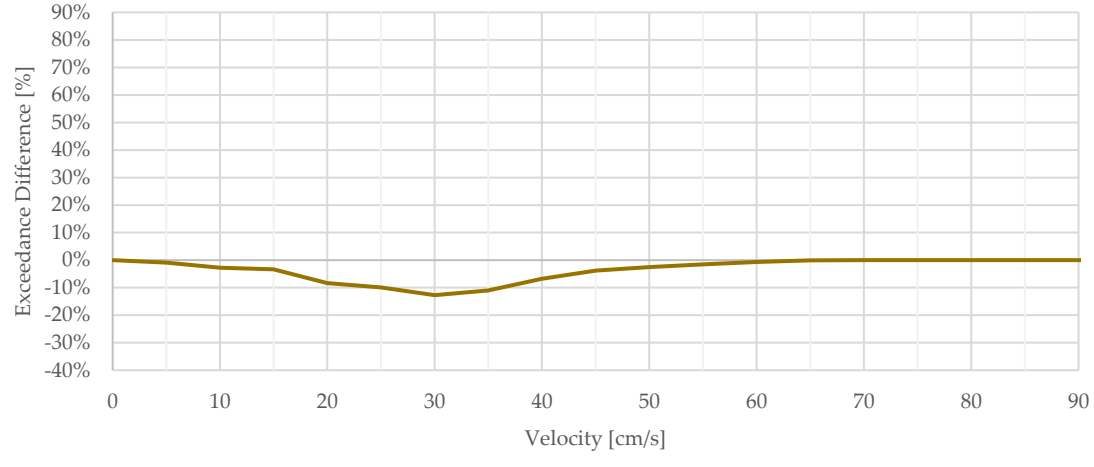

D.1.11 MT011

D.1.11.1 Setup

D.1.11.1.1 Description

Raised bed level at spur head

D.1.11.1.2 Wave Conditions

Water / Tide Level	+0.7m MSL	**Wave Period (T_p)**	12 s
Wave Height (H_s)	1.5m	**Wave Angle**	+ 8°

D.1.11.2 Results

D.1.11.2.1 Current Velocity and Direction Map

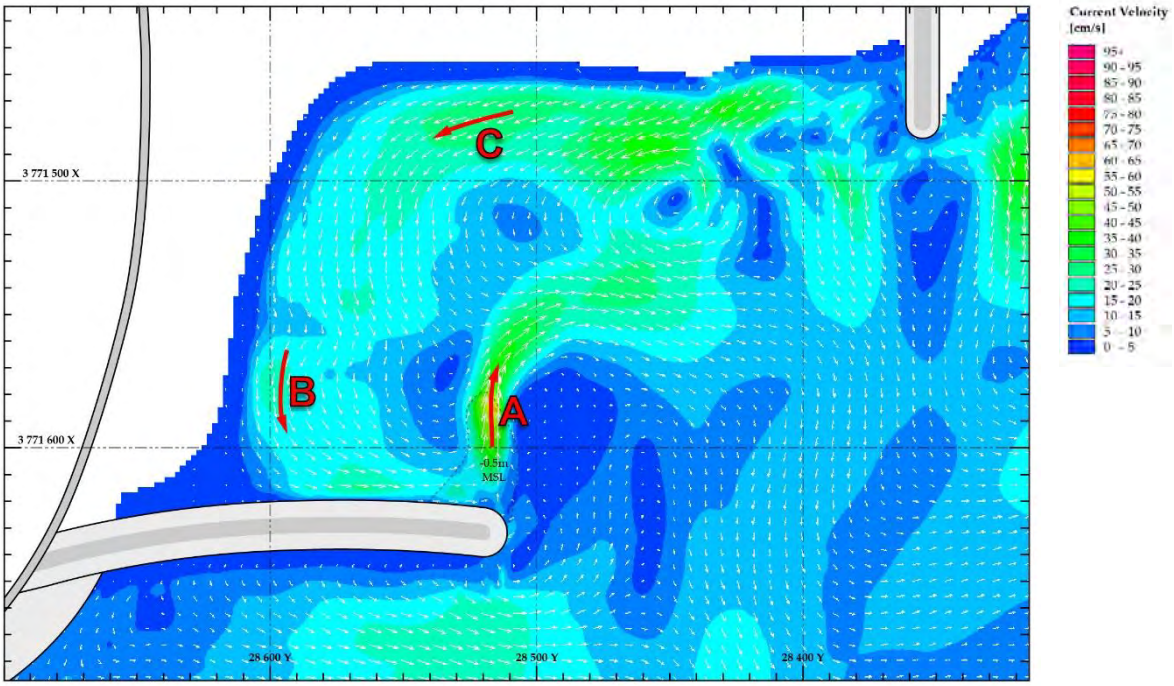

D.1.11.2.2 Measured Peak Flow Velocities

Vector	Class	30m Peak Average Velocities		
		u (absolute)	U_r (relative) (§ 7)	U_f (factorised) (§ 8)
A	1	46.5 cm/s	184%	184%
B	2	20.6 cm/s	64%	82%
C	2	28.1 cm/s	82%	111%

D.1.11.2.3 Area-Velocity: Designated Swimming Area

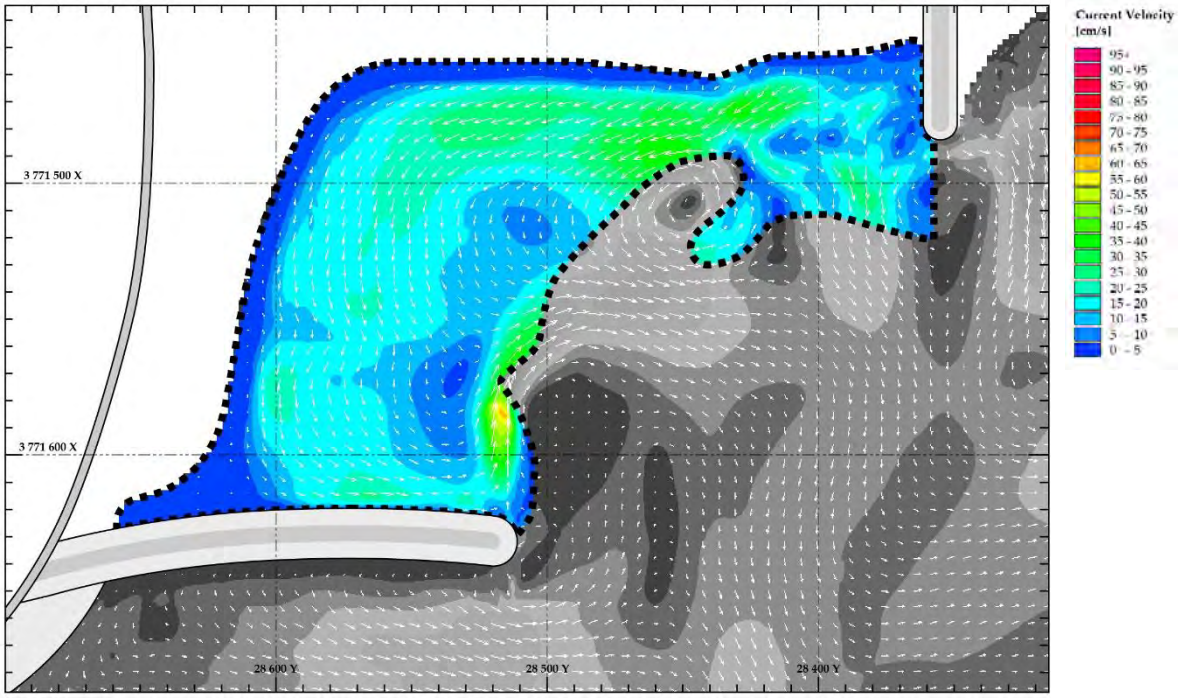

D.1.11.2.4 Velocity Exceedance: Designated Swimming Area

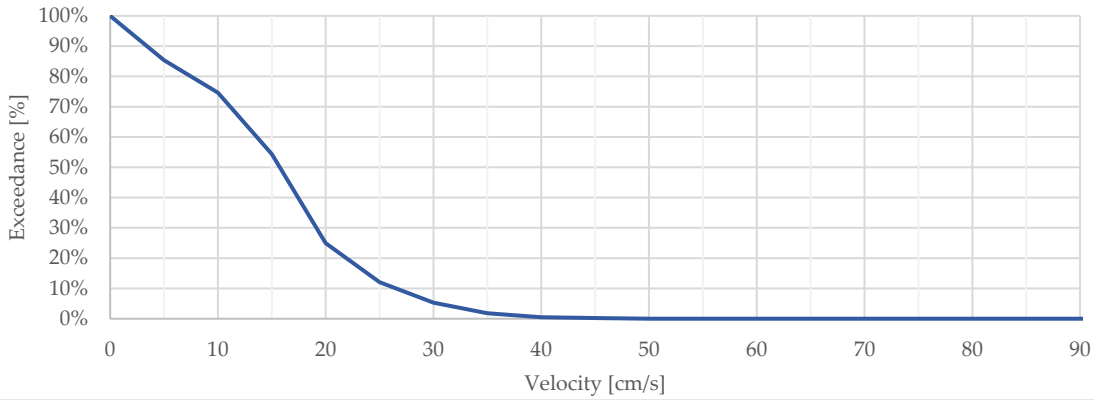

D.1.11.2.5 Velocity Baseline Exceedance Difference: Designated Swimming Area

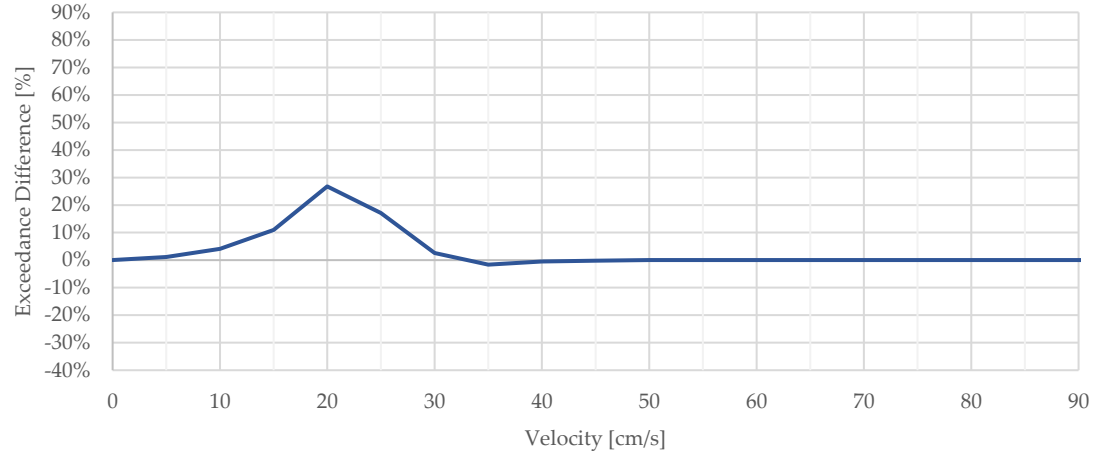

D.1.12 MT012

D.1.12.1 Setup

D.1.12.1.1 Description

Gap through spur (West Stion) with Groyne off beach [high water]

D.1.12.1.2 Wave Conditions

Water / Tide Level	+0.3m MSL	**Wave Period (T_p)**	12 s
Wave Height (H_s)	1.3m	**Wave Angle**	+ 8°

D.1.12.2 Results

D.1.12.2.1 Current Velocity and Direction Map

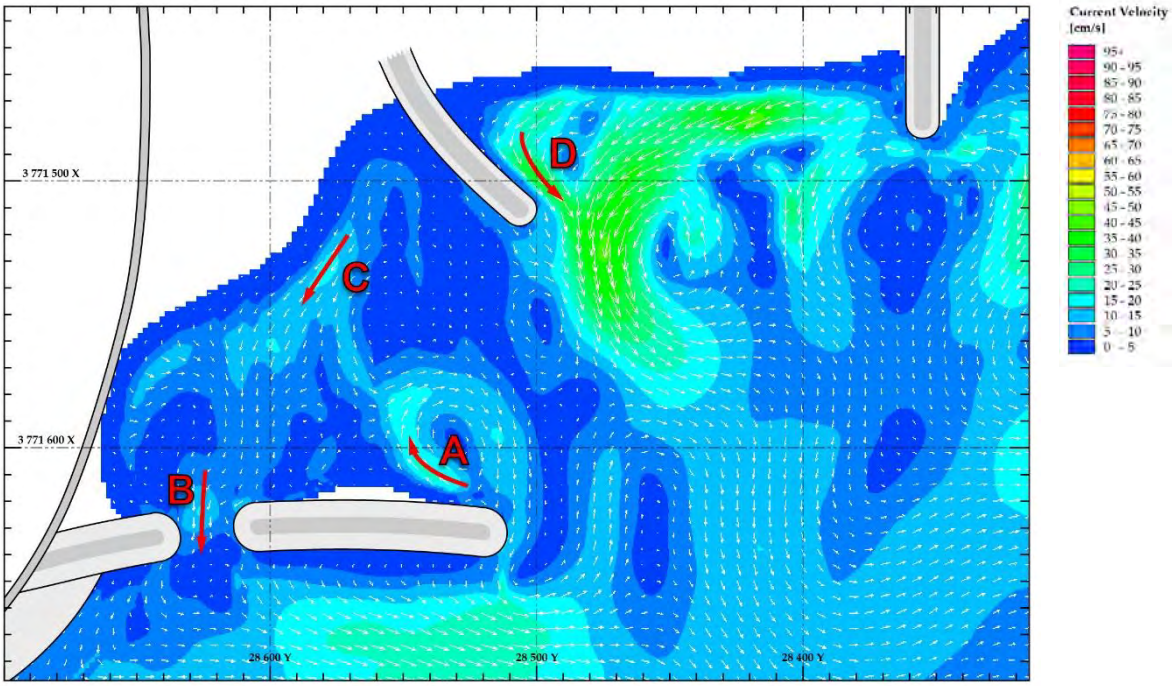

D.1.12.2.2 Measured Peak Flow Velocities

Vector	Class	30m Peak Average Velocities		
		u (absolute)	U_r (relative) (§ 7)	U_f (factorised) (§ 8)
A	1	18.8 cm/s	101%	74%
B	1	10.4 cm/s	56%	41%
C	2	14.8 cm/s	47%	59%
D	3	30.0 cm/s	84%	119%

D.1.12.2.3 Area-Velocity: Designated Swimming Area

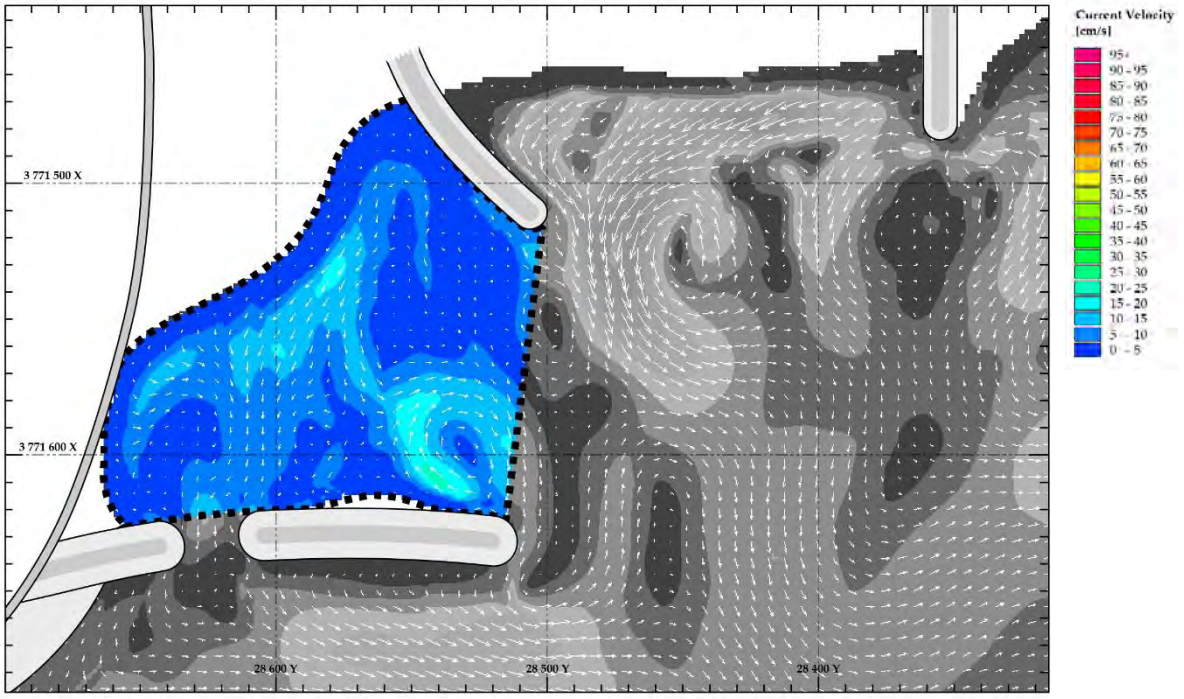

D.1.12.2.4 Velocity Exceedance: Designated Swimming Area

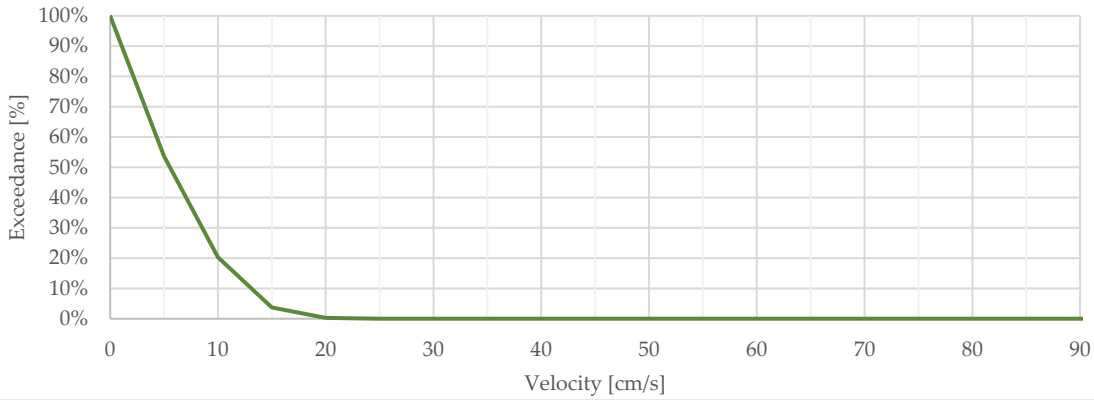

D.1.12.2.5 Velocity Baseline Exceedance Difference: Designated Swimming Area

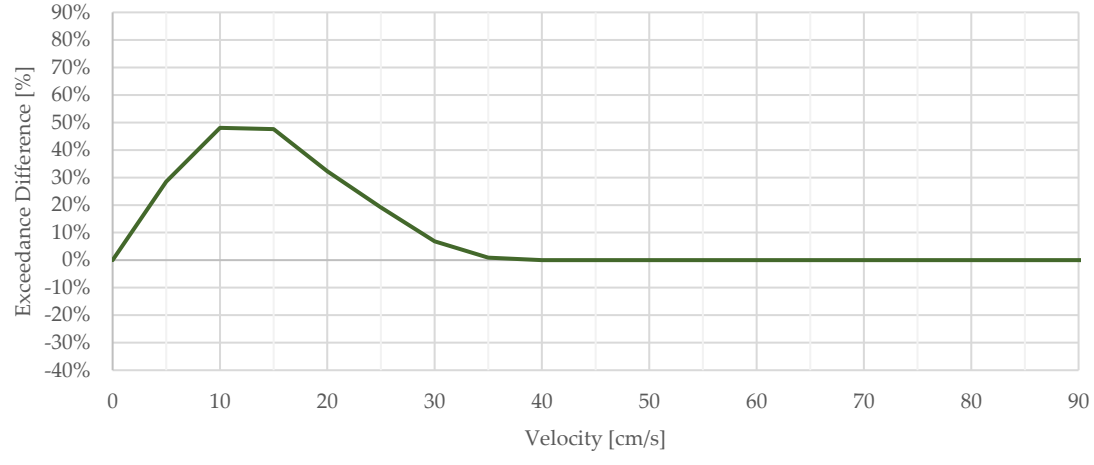

D.1.13 MT013

D.1.13.1 Setup

D.1.13.1.1 Description

Gap through spur (West Stion) with Groyne off beach [low water]

D.1.13.1.2 Wave Conditions

Water / Tide Level	-0.3m MSL	**Wave Period (T_p)**	12 s
Wave Height (H_s)	1.3m	**Wave Angle**	+ 8°

D.1.13.2 Results

D.1.13.2.1 Current Velocity and Direction Map

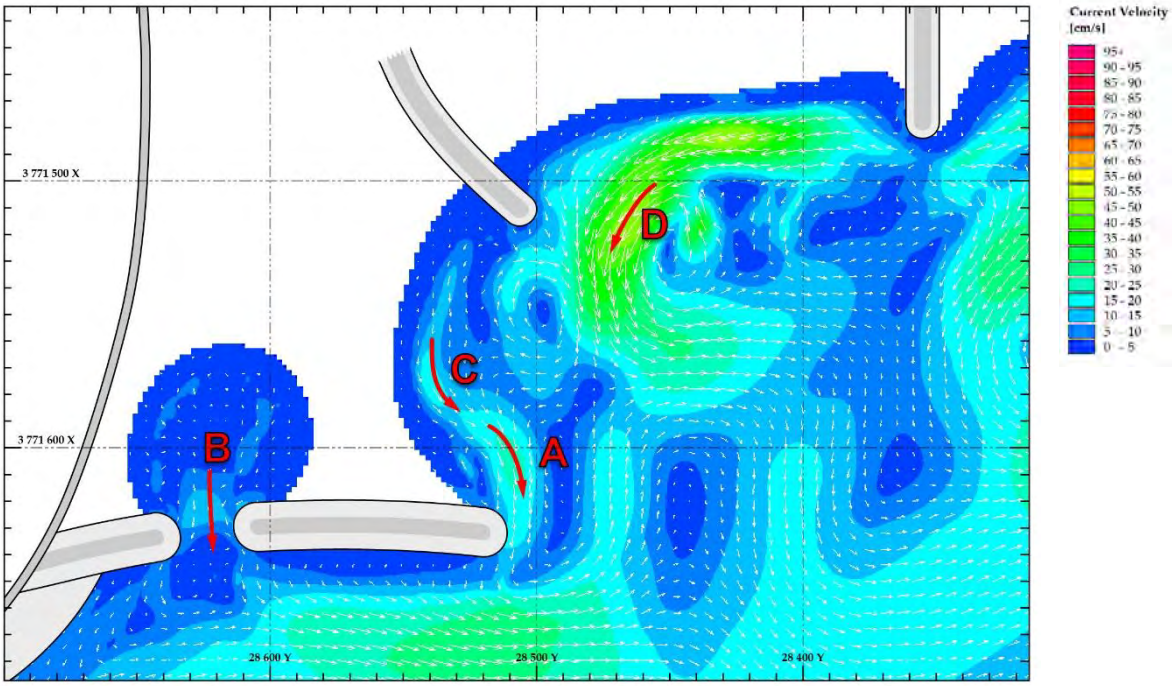

D.1.13.2.2 Measured Peak Flow Velocities

Vector	Class	30m Peak Average Velocities		
		u (absolute)	U_r (relative) (§ 7)	U_f (factorised) (§ 8)
A	1	20.8 cm/s	117%	82%
B	1	8.5 cm/s	48%	34%
C	2	16.1 cm/s	76%	64%
D	3	46.2 cm/s	101%	183%

D.1.13.2.3 Area-Velocity: Designated Swimming Area

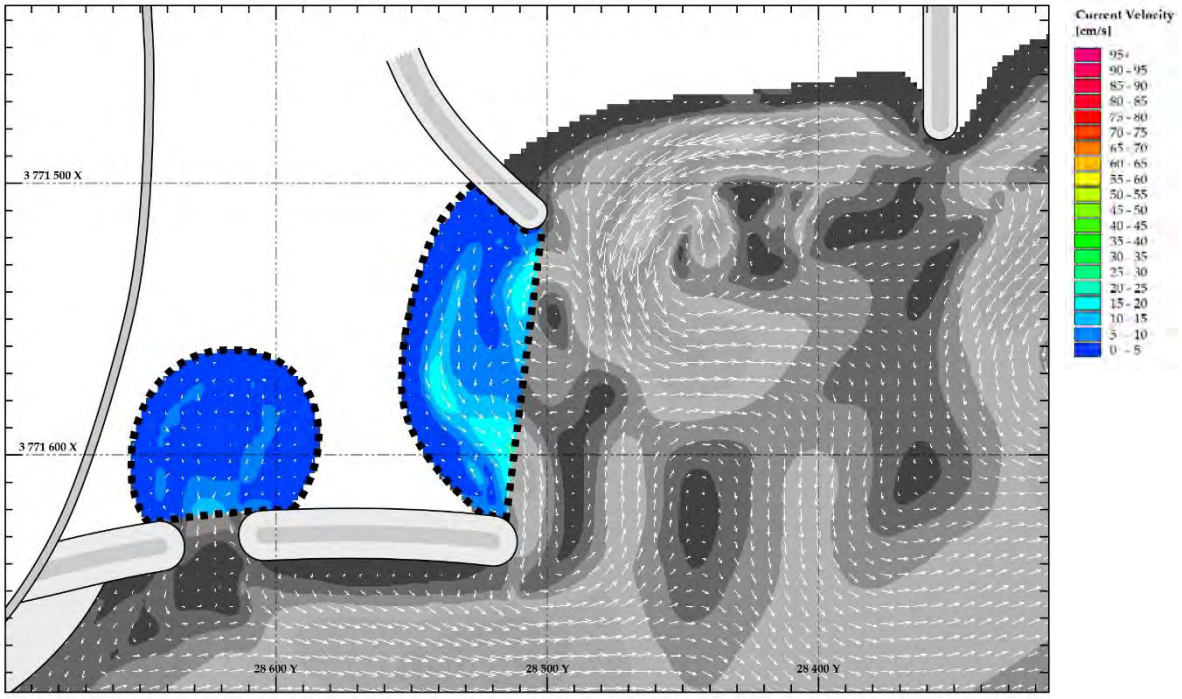

D.1.13.2.4 Velocity Exceedance: Designated Swimming Area

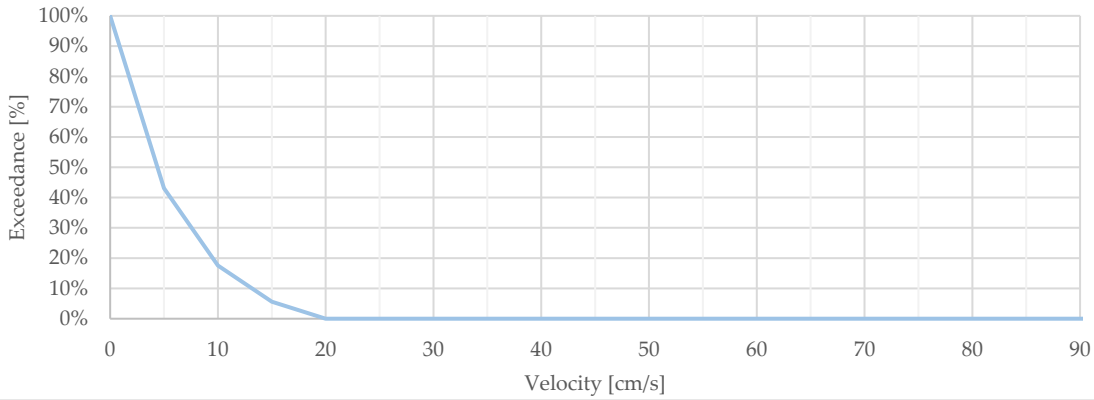

D.1.13.2.5 Velocity Baseline Exceedance Difference: Designated Swimming Area

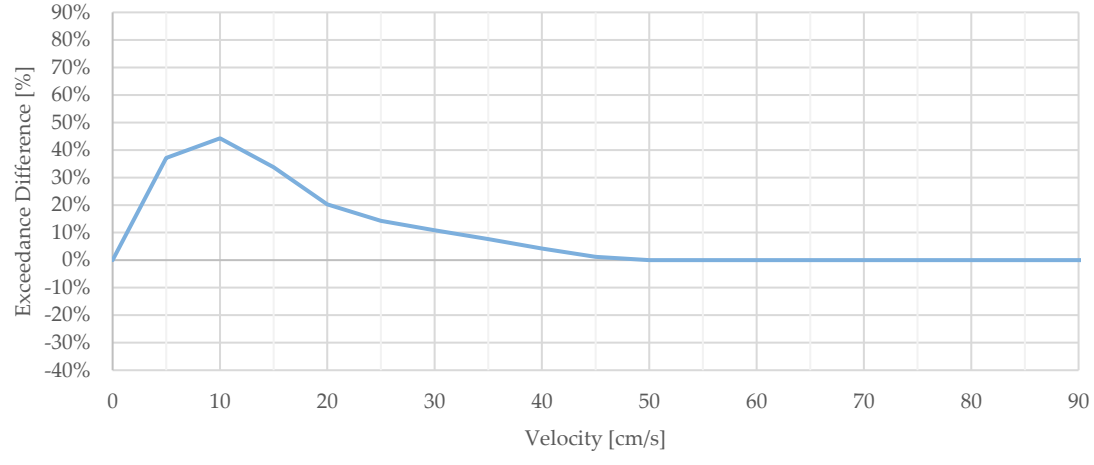

D.1.14 MT014

Note: The results are unreliable due to the unsuccessful modelling of wave overtopping action

D.1.14.1 Setup

D.1.14.1.1 Description

Lowered stion in spur (east) with groyne off beach [high water]

D.1.14.1.2 Wave Conditions

Water / Tide Level	+0.3m MSL	**Wave Period (T_p)**	12 s
Wave Height (H_s)	1.3m	**Wave Angle**	+ 8°

D.1.14.2 Results

D.1.14.2.1 Current Velocity and Direction Map

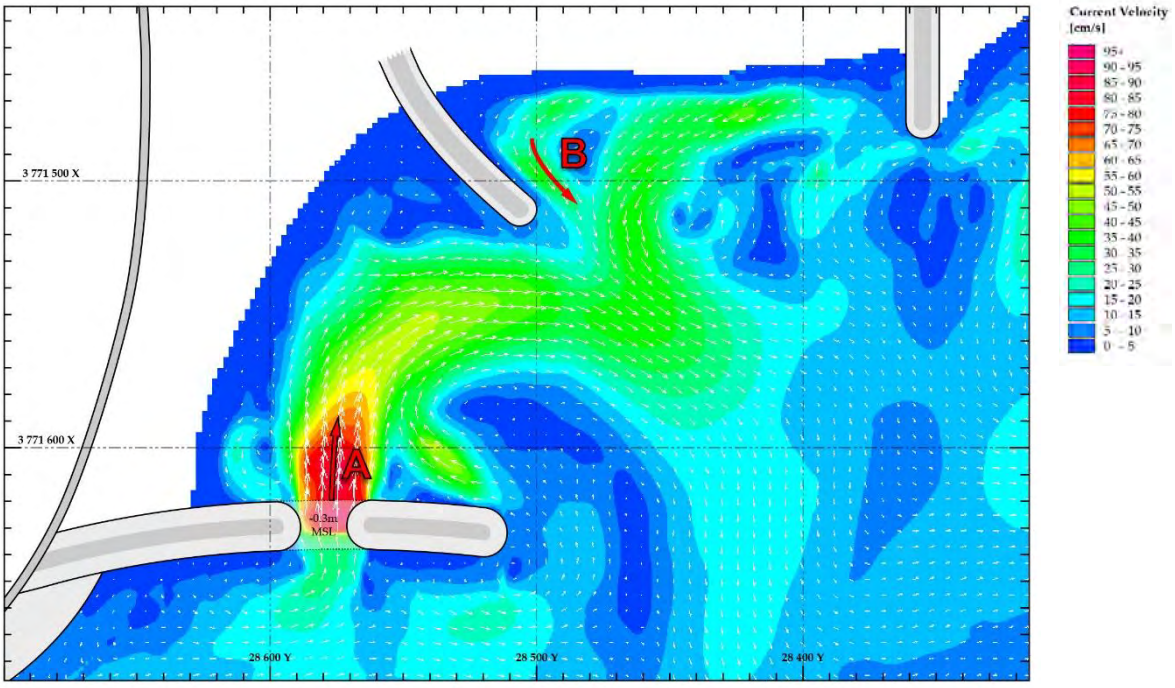

D.1.14.2.2 Measured Peak Flow Velocities

Vector	Class	30m Peak Average Velocities		
		u (absolute)	U_r (relative) (§ 7)	U_f (factorised) (§ 8)
A	1	82.3 cm/s	441%	326%
B	3	30.7 cm/s	86%	122%

D.1.14.2.3 Area-Velocity: Designated Swimming Area

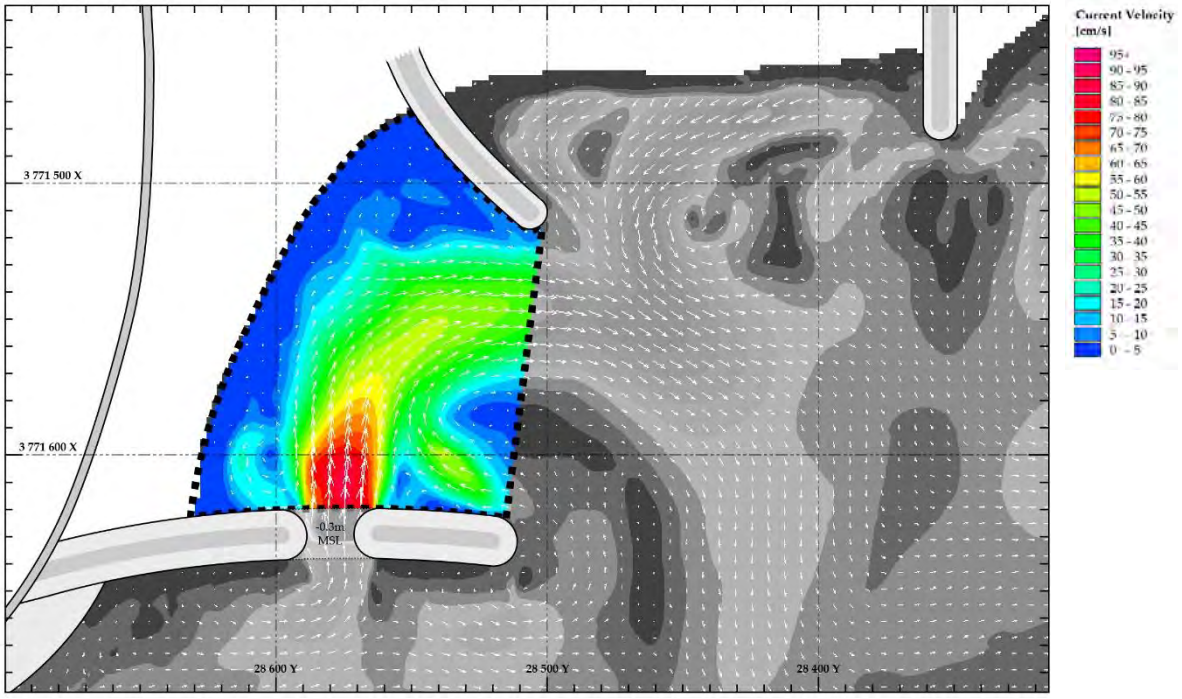

D.1.14.2.4 Velocity Exceedance: Designated Swimming Area

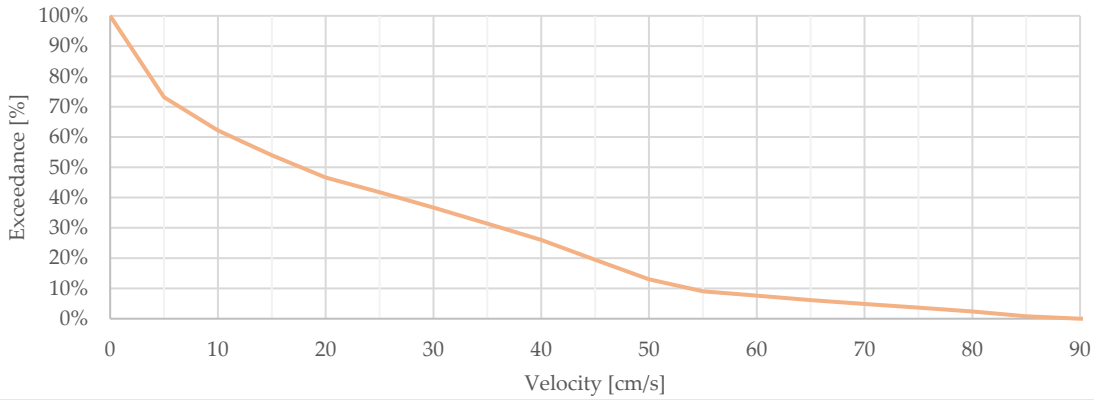

D.1.14.2.5 Velocity Baseline Exceedance Difference: Designated Swimming Area

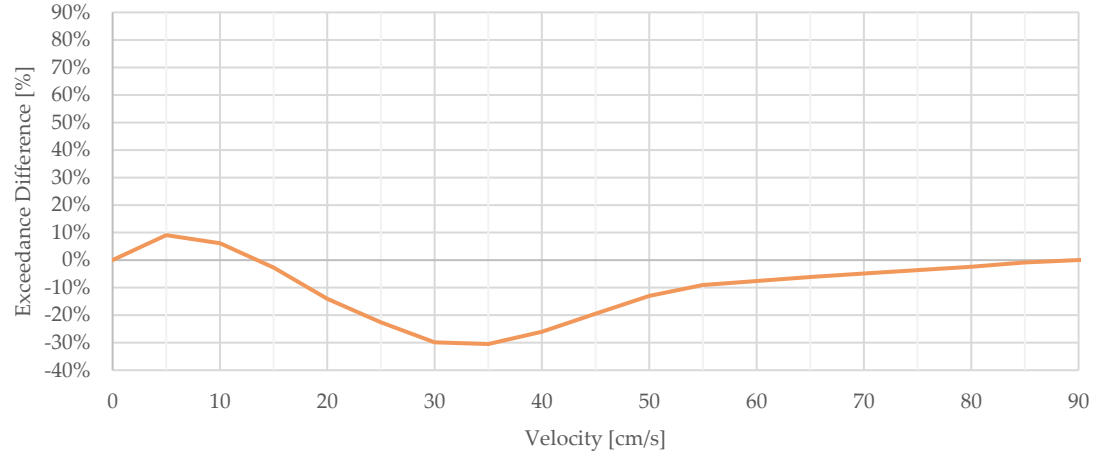

D.1.15 MT015

Note: The results are unreliable due to the unsuccessful modelling of wave overtopping action

D.1.15.1 Setup

D.1.15.1.1 Description

Lowered stion in spur (east) with groyne off beach [low water]

D.1.15.1.2 Wave Conditions

Water / Tide Level	-0.3m MSL	**Wave Period (T_p)**	12 s
Wave Height (H_s)	1.3m	**Wave Angle**	+ 8°

D.1.15.2 Results

D.1.15.2.1 Current Velocity and Direction Map

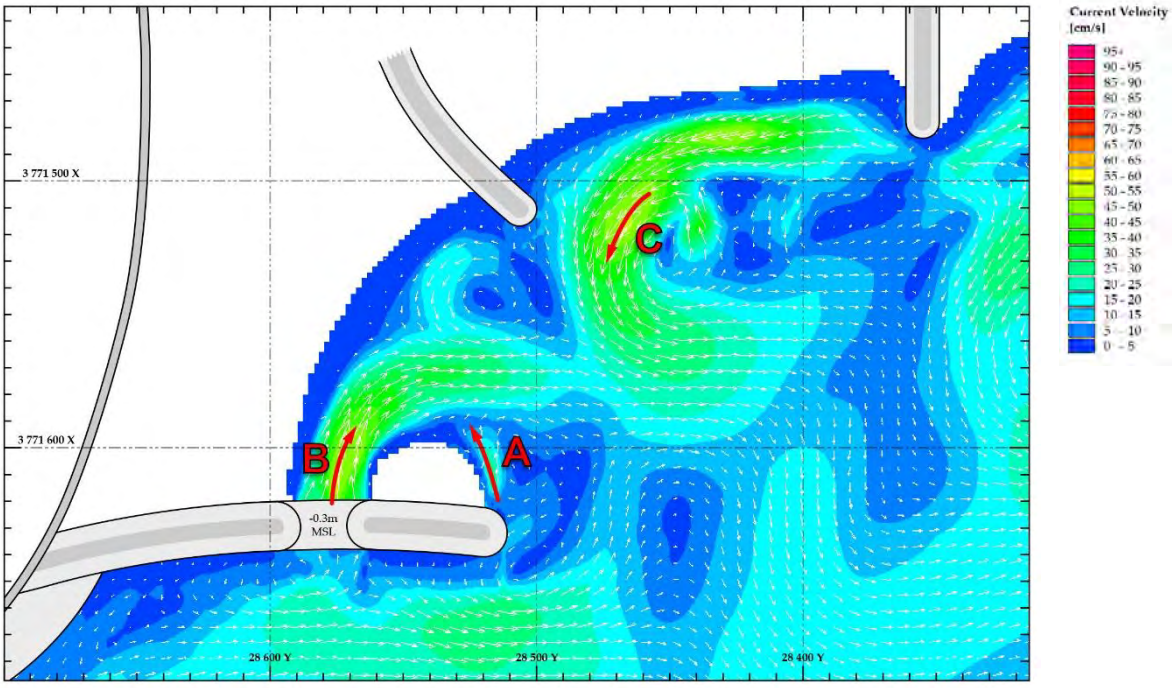

D.1.15.2.2 Measured Peak Flow Velocities

Vector	Class	30m Peak Average Velocities		
		u (absolute)	U_r (relative) (§ 7)	U_f (factorised) (§ 8)
A	1	17.8 cm/s	100%	71%
B	1	46.8 cm/s	263%	186%
C	3	47.5 cm/s	104%	188%

D.1.15.2.3 Area-Velocity: Designated Swimming Area

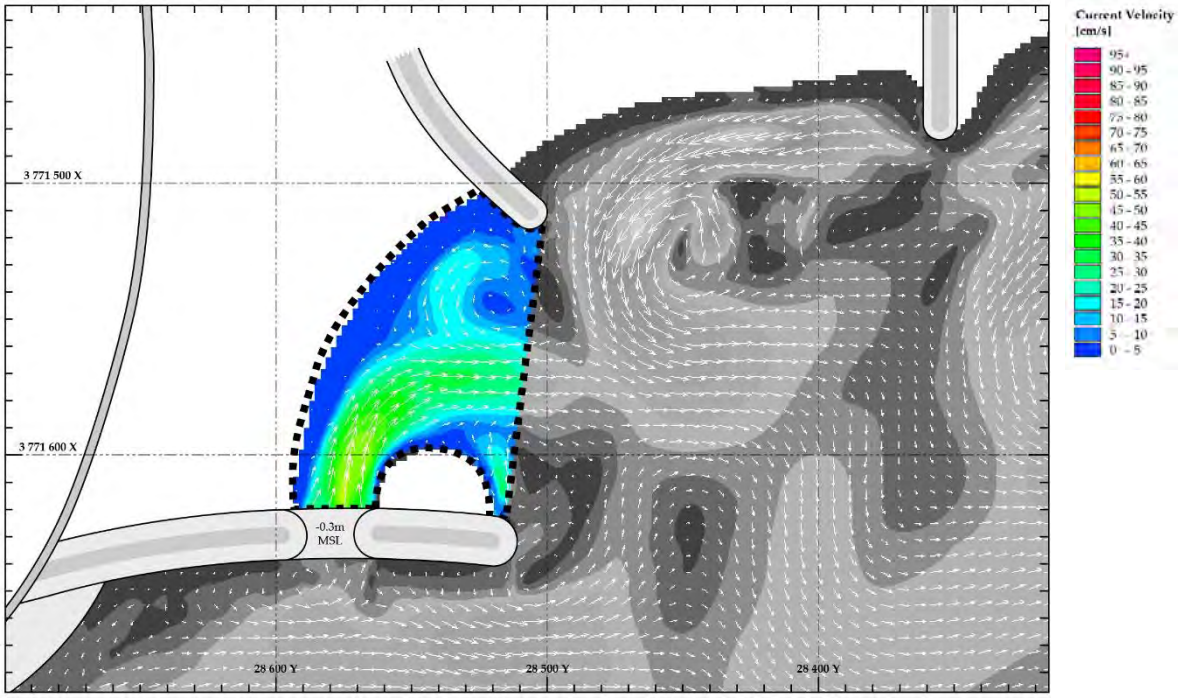

D.1.15.2.4 Velocity Exceedance: Designated Swimming Area

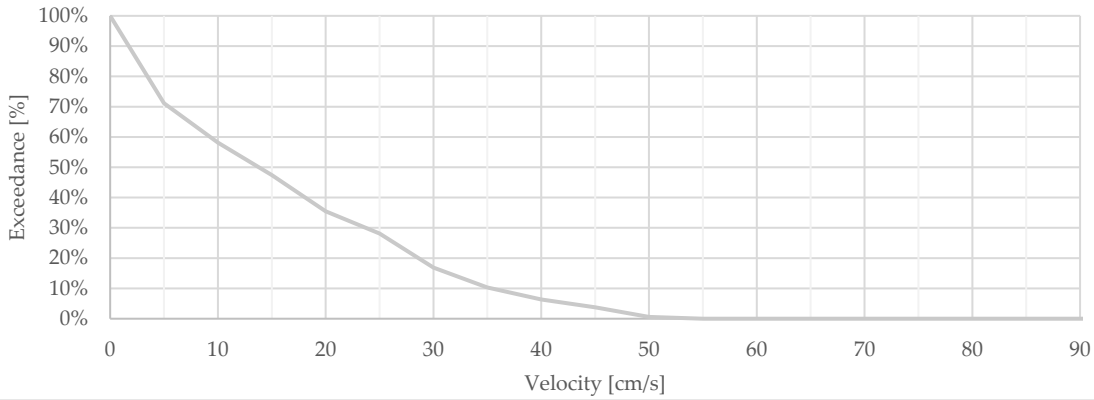

D.1.15.2.5 Velocity Baseline Exceedance Difference: Designated Swimming Area

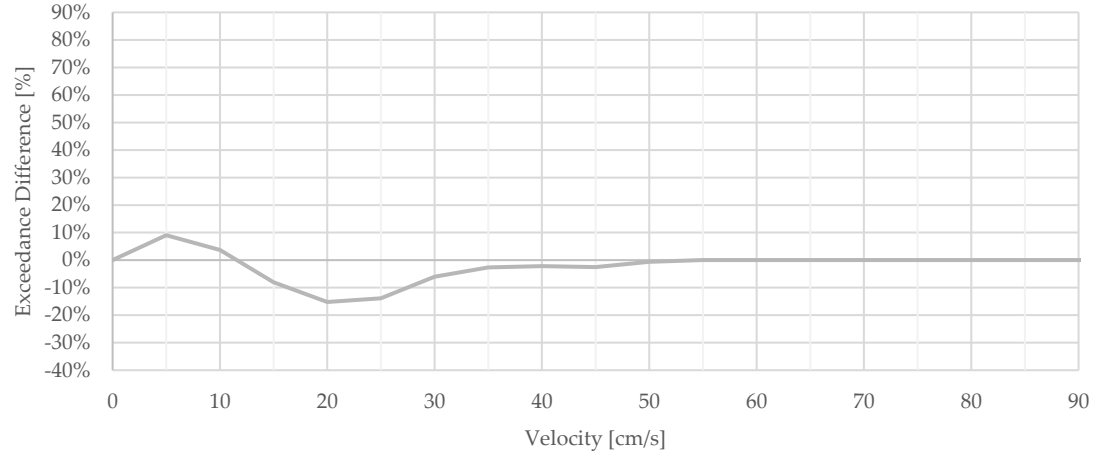

D.1.16 MT016

D.1.16.1 Setup

D.1.16.1.1 Description

T-Groyne off beach

D.1.16.1.2 Wave Conditions

Water / Tide Level	+0.45m MSL	**Wave Period (T_p)**	12 s
Wave Height (H_s)	1.4m	**Wave Angle**	+ 8°

D.1.16.2 Results

D.1.16.2.1 Current Velocity and Direction Map

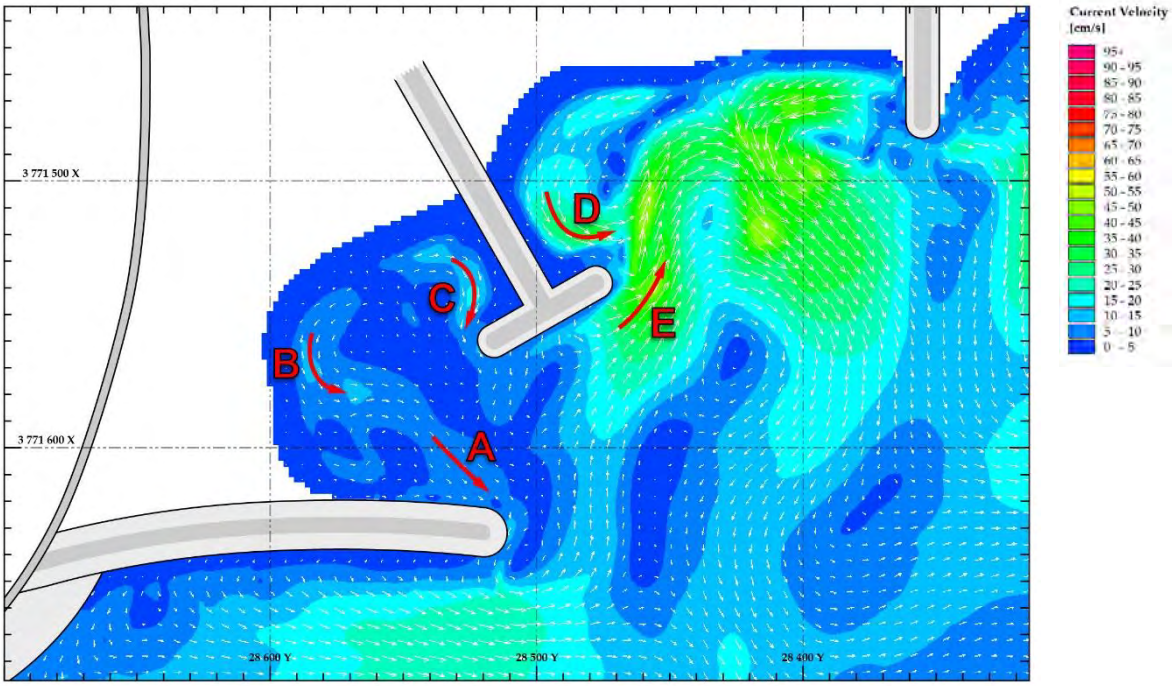

D.1.16.2.2 Measured Peak Flow Velocities

Vector	Class	30m Peak Average Velocities		
		u (absolute)	U_r (relative) (§ 7)	U_f (factorised) (§ 8)
A	1	6.7 cm/s	28%	27%
B	2	9.6 cm/s	31%	38%
C	2	12.9 cm/s	41%	51%
D	3	28.0 cm/s	79%	111%
E	3	40.9 cm/s	115%	162%

D.1.16.2.3 Area-Velocity: Designated Swimming Area

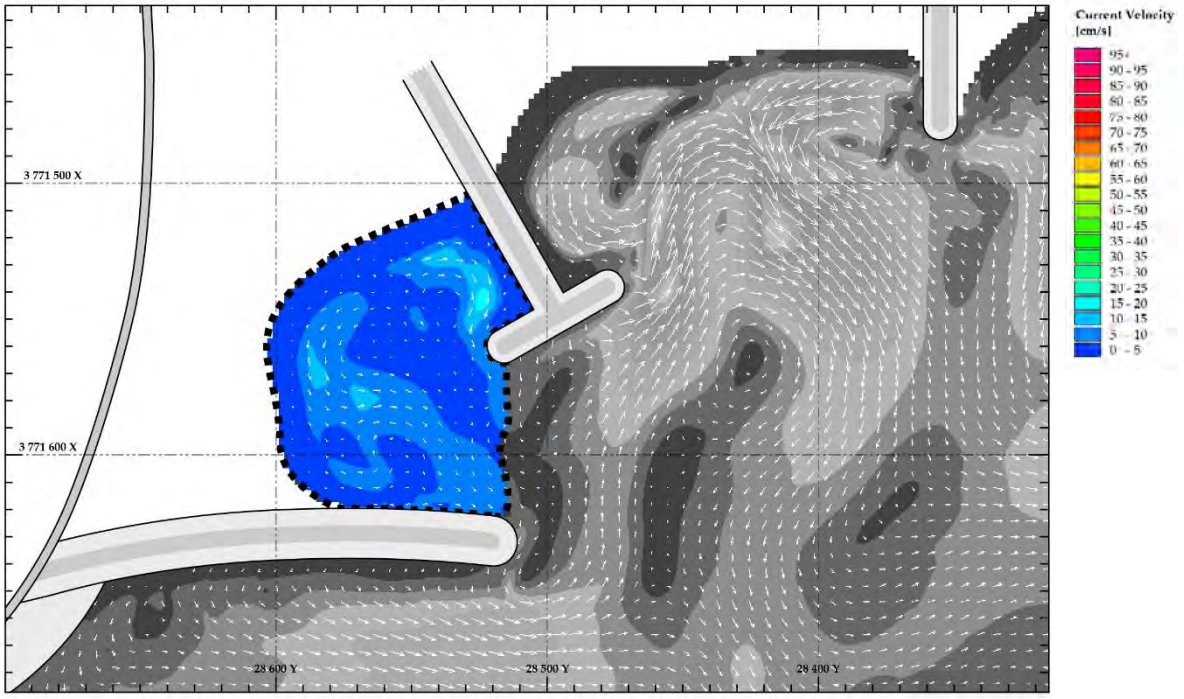

D.1.16.2.4 Velocity Exceedance: Designated Swimming Area

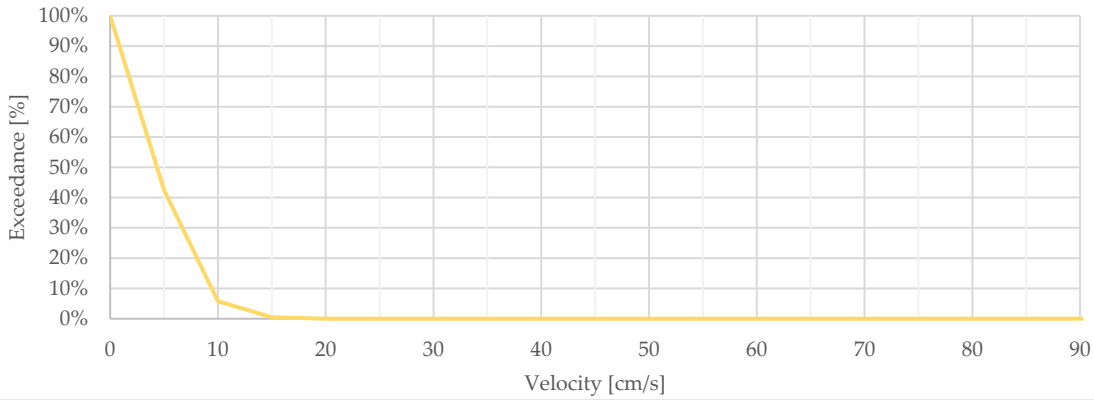

D.1.16.2.5 Velocity Baseline Exceedance Difference: Designated Swimming Area

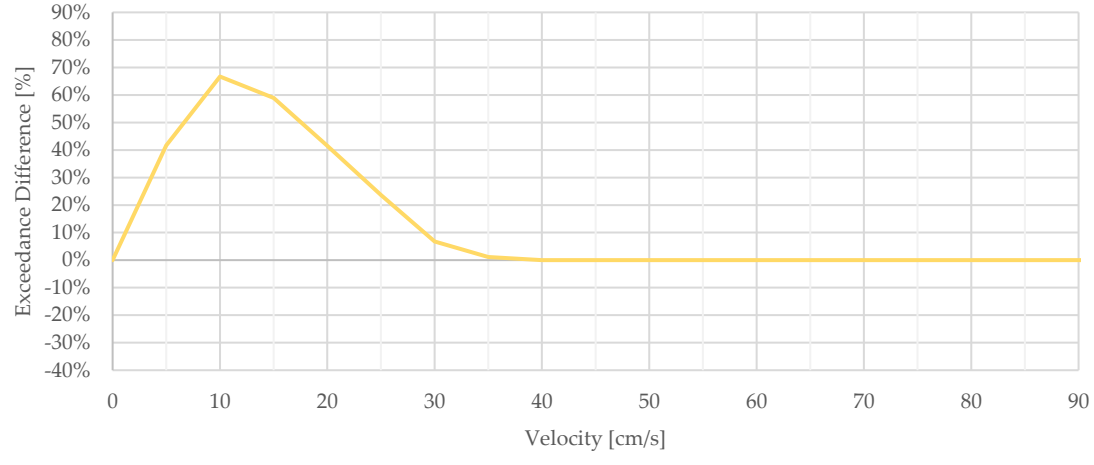

D.1.17 MT017

D.1.17.1 Setup

D.1.17.1.1 Description

T-Groyne off beach

D.1.17.1.2 Wave Conditions

Water / Tide Level	+0.9m MSL	**Wave Period (T_p)**	12 s
Wave Height (H_s)	1.4m	**Wave Angle**	+ 8°

D.1.17.2 Results

D.1.17.2.1 Current Velocity and Direction Map

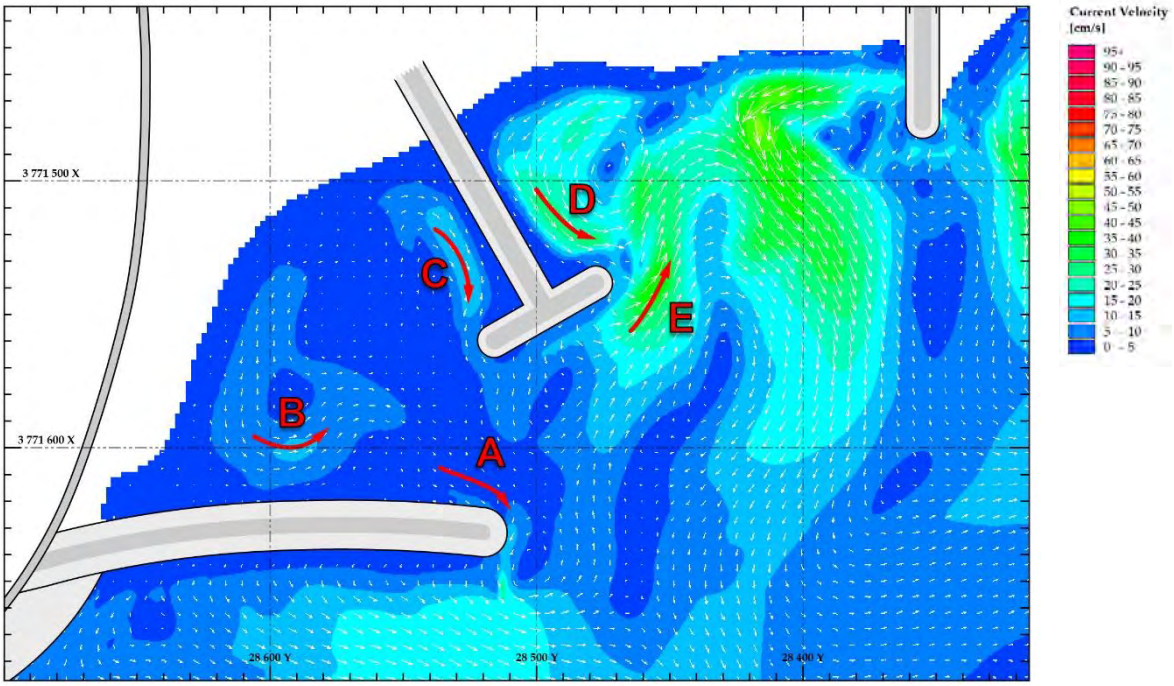

D.1.17.2.2 Measured Peak Flow Velocities

Vector	Class	30m Peak Average Velocities		
		u (absolute)	U_r (relative) (§ 7)	U_f (factorised) (§ 8)
A	1	5.7 cm/s	24%	23%
B	2	10.1 cm/s	34%	40%
C	2	13.1 cm/s	44%	52%
D	3	25.5 cm/s	95%	101%
E	3	35.2 cm/s	131%	139%

D.1.17.2.3 Area-Velocity: Designated Swimming Area

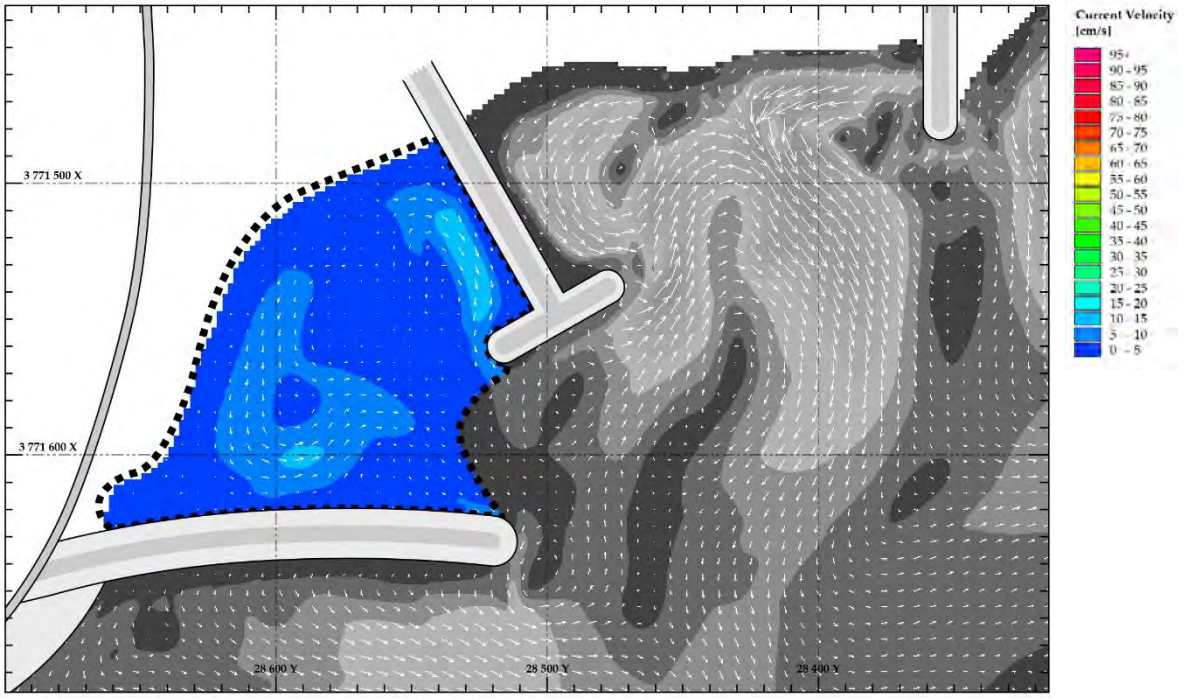

D.1.17.2.4 Velocity Exceedance: Designated Swimming Area

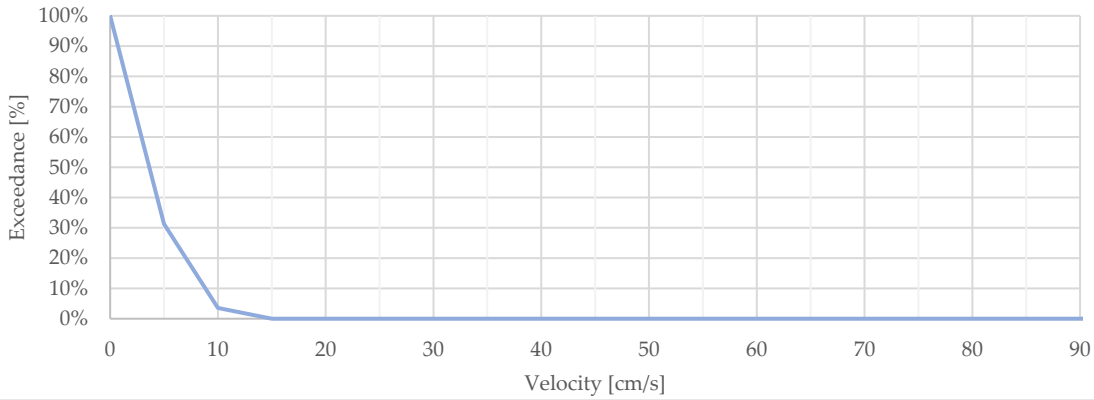

D.1.17.2.5 Velocity Baseline Exceedance Difference: Designated Swimming Area

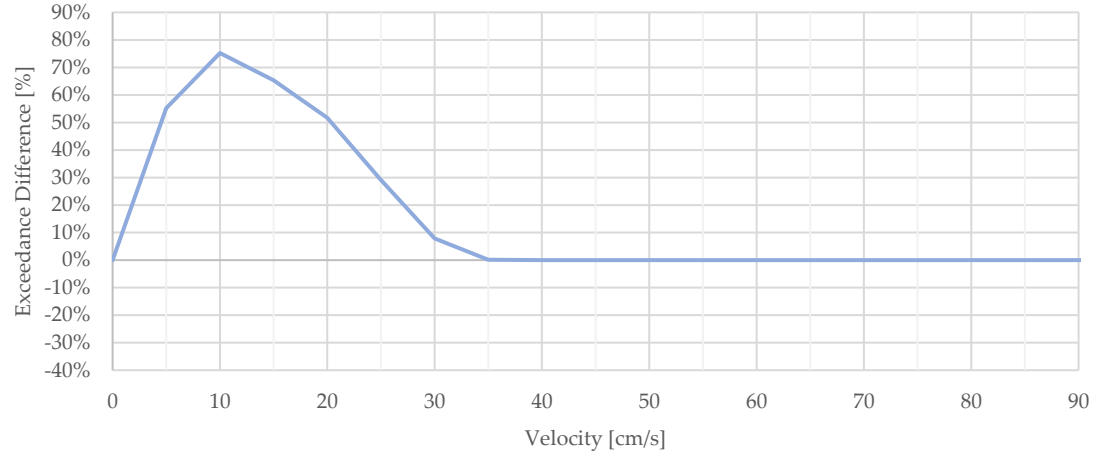

D.1.18 MT018

D.1.18.1 Setup

D.1.18.1.1 Description

T-Groyne off beach

D.1.18.1.2 Wave Conditions

Water / Tide Level	+0.9m MSL	**Wave Period (T_p)**	12 s
Wave Height (H_s)	1.8m	**Wave Angle**	+ 8°

D.1.18.2 Results

D.1.18.2.1 Current Velocity and Direction Map

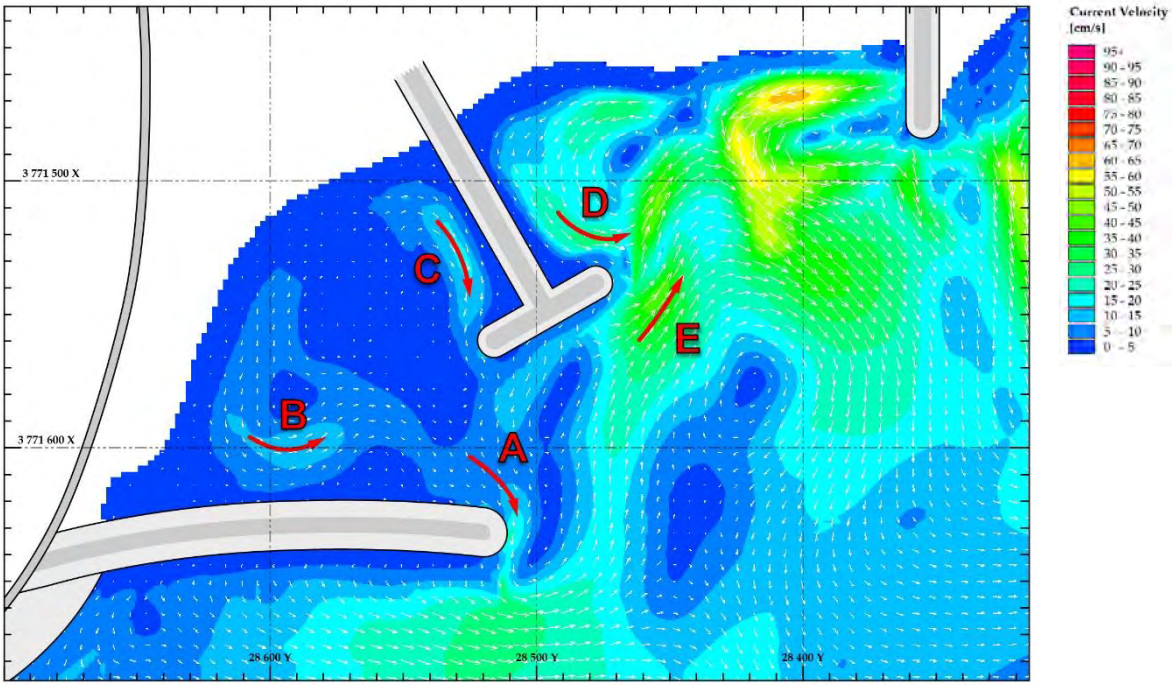

D.1.18.2.2 Measured Peak Flow Velocities

Vector	Class	30m Peak Average Velocities		
		u (absolute)	U_r (relative) (§ 7)	U_f (factorised) (§ 8)
A	1	8.5 cm/s	24%	34%
B	2	12.2 cm/s	33%	48%
C	2	14.7 cm/s	40%	58%
D	3	25.1 cm/s	60%	100%
E	3	38.8 cm/s	92%	154%

D.1.18.2.3 Area-Velocity: Designated Swimming Area

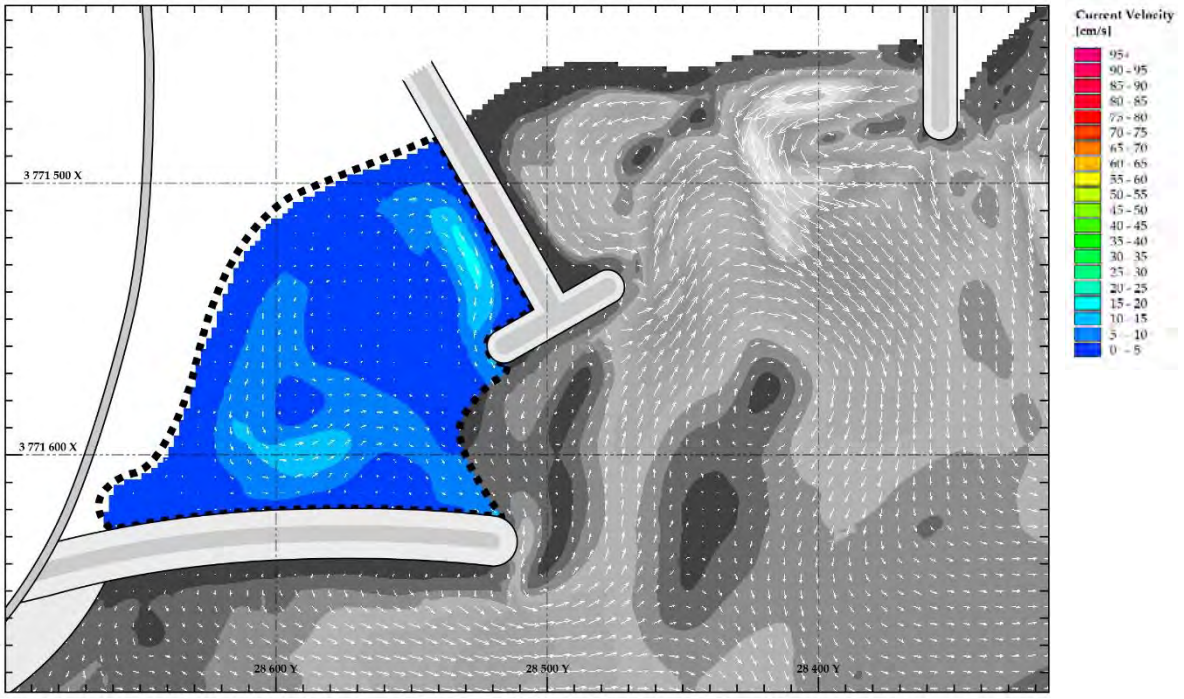

D.1.18.2.4 Velocity Exceedance: Designated Swimming Area

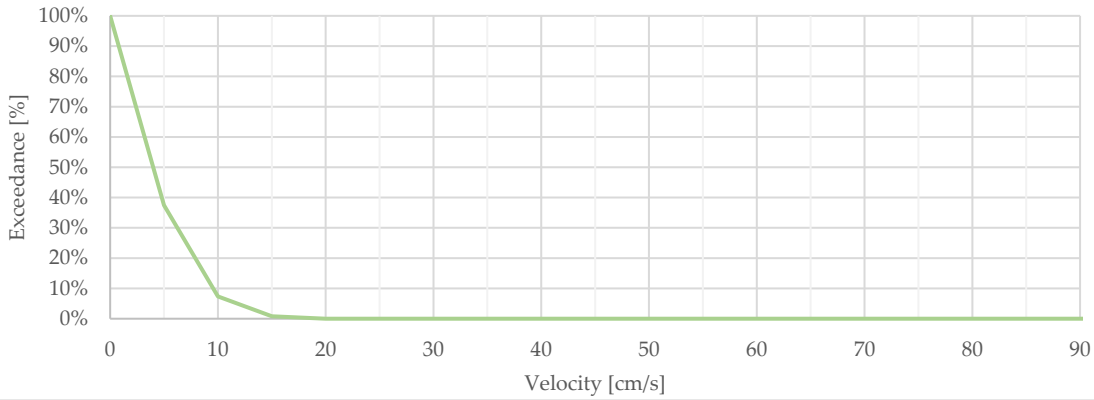

D.1.18.2.5 Velocity Baseline Exceedance Difference: Designated Swimming Area

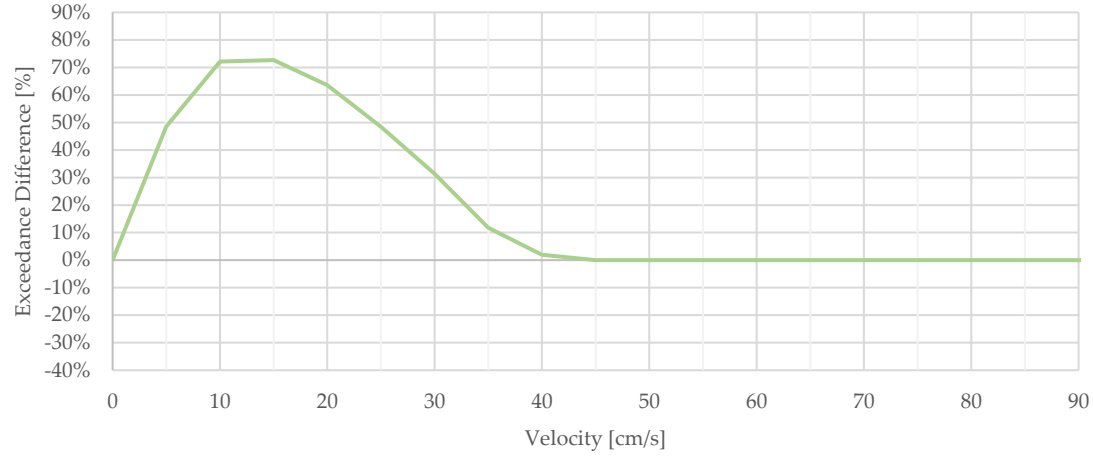

D.1.19 MT019

D.1.19.1 Setup

D.1.19.1.1 Description

T-Groyne off beach

D.1.19.1.2 Wave Conditions

Water / Tide Level	-0.1m MSL	**Wave Period (T_p)**	12 s
Wave Height (H_s)	1.0m	**Wave Angle**	+ 8°

D.1.19.2 Results

D.1.19.2.1 Current Velocity and Direction Map

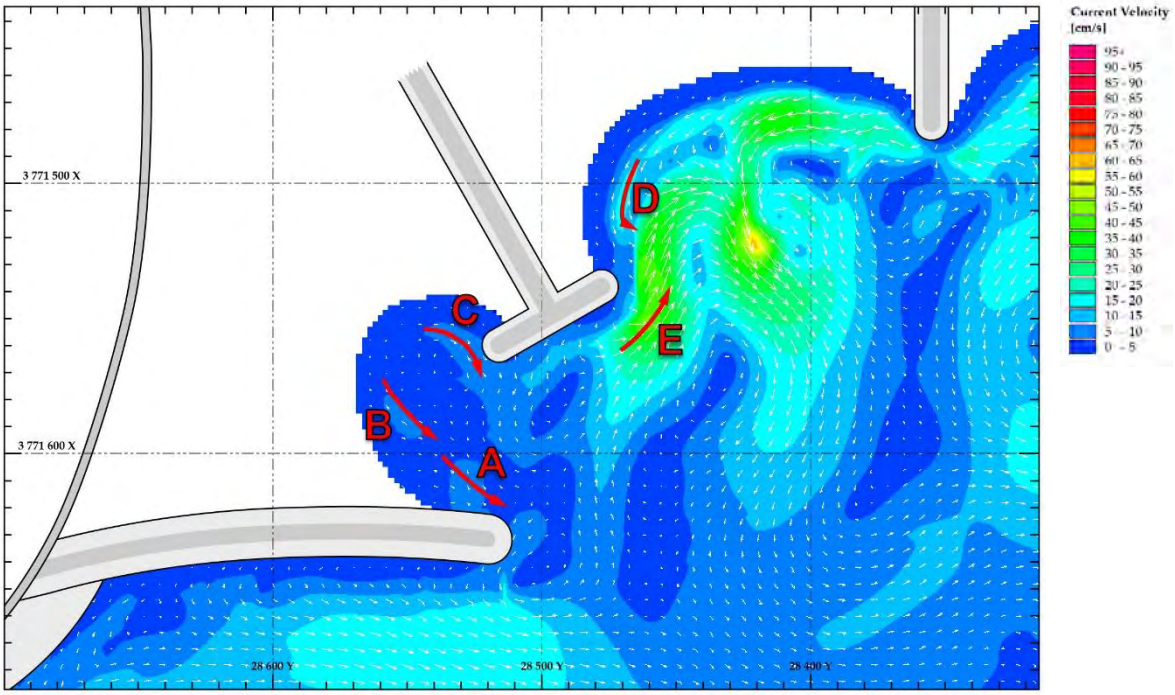

D.1.19.2.2 Measured Peak Flow Velocities

Vector	Class	30m Peak Average Velocities		
		u (absolute)	U_r (relative) (§ 7)	U_f (factorised) (§ 8)
A	1	6.1 cm/s	40%	24%
B	2	5.6 cm/s	21%	22%
C	2	7.5 cm/s	29%	30%
D	3	14.7 cm/s	38%	58%
E	3	39.0 cm/s	102%	155%

D.1.19.2.3 Area-Velocity: Designated Swimming Area

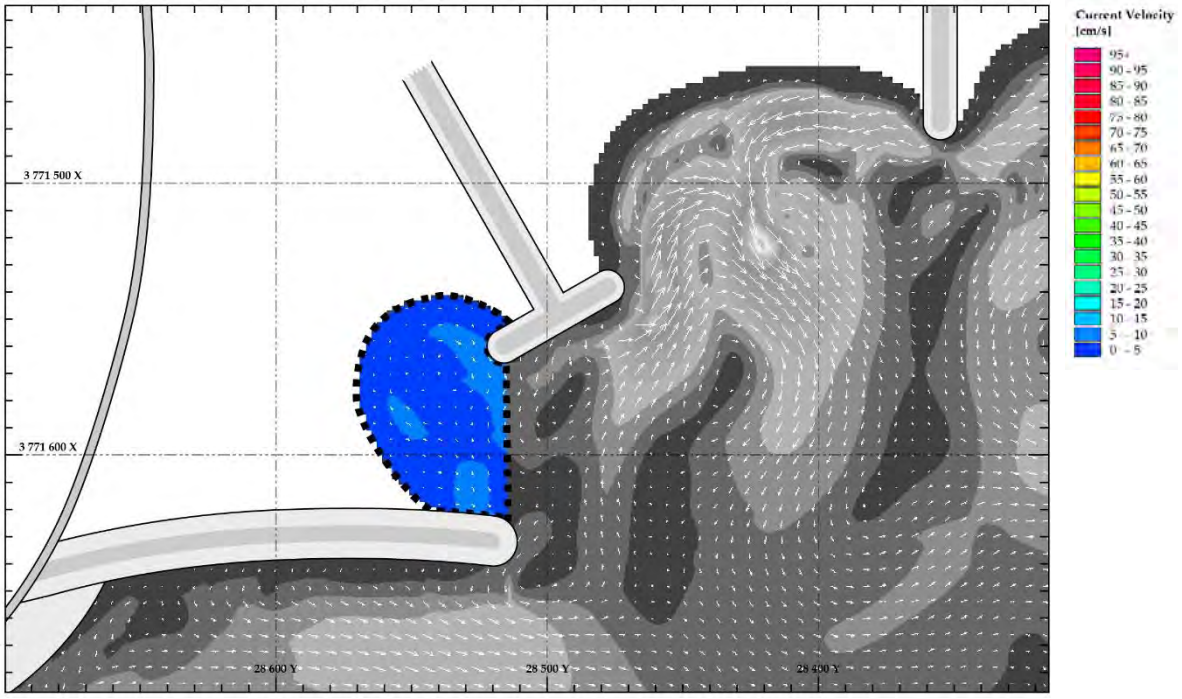

D.1.19.2.4 Velocity Exceedance: Designated Swimming Area

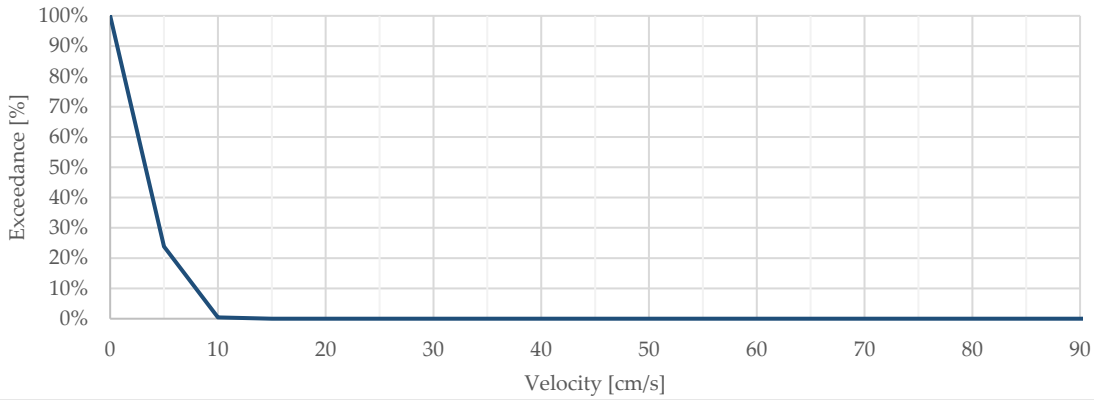

D.1.19.2.5 Velocity Baseline Exceedance Difference: Designated Swimming Area

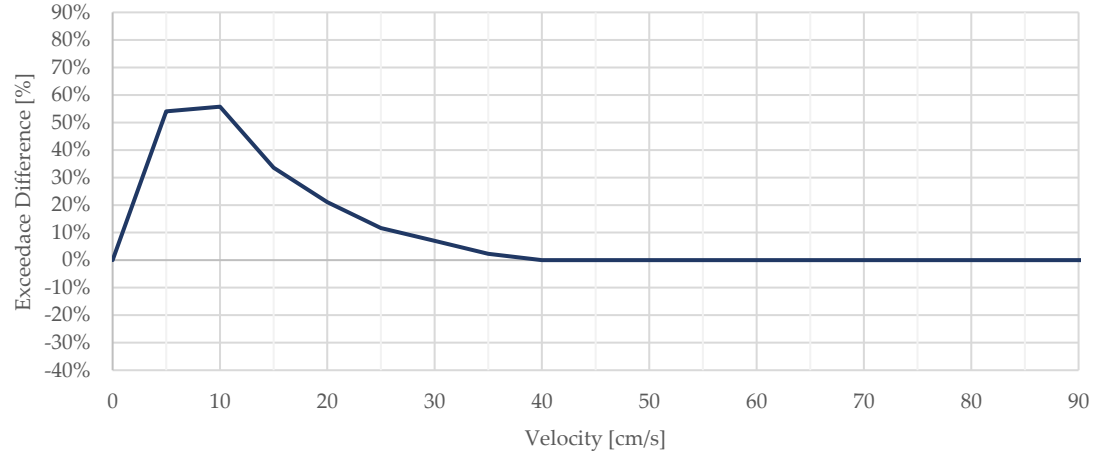

D.1.20 MT020

D.1.20.1 Setup

D.1.20.1.1 Description

T-Groyne off beach

D.1.20.1.2 Wave Conditions

Water / Tide Level	-0.1 MSL	**Wave Period (T_p)**	12 s
Wave Height (H_s)	1.4m	**Wave Angle**	+ 8°

D.1.20.2 Results

D.1.20.2.1 Current Velocity and Direction Map

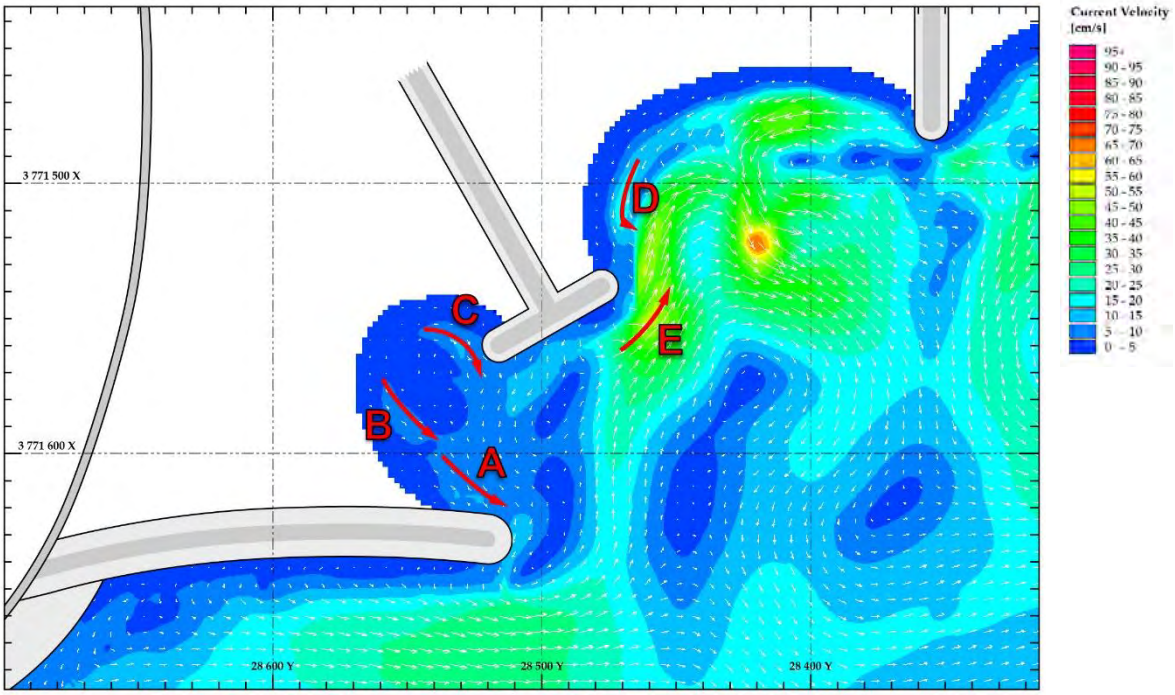

D.1.20.2.2 Measured Peak Flow Velocities

Vector	Class	30m Peak Average Velocities		
		u (absolute)	U_r (relative) (§ 7)	U_f (factorised) (§ 8)
A	1	8.9 cm/s	42%	35%
B	2	6.5 cm/s	20%	26%
C	2	8.5 cm/s	27%	34%
D	3	14.1 cm/s	32%	56%
E	3	44.9 cm/s	103%	178%

D.1.20.2.3 Area-Velocity: Designated Swimming Area

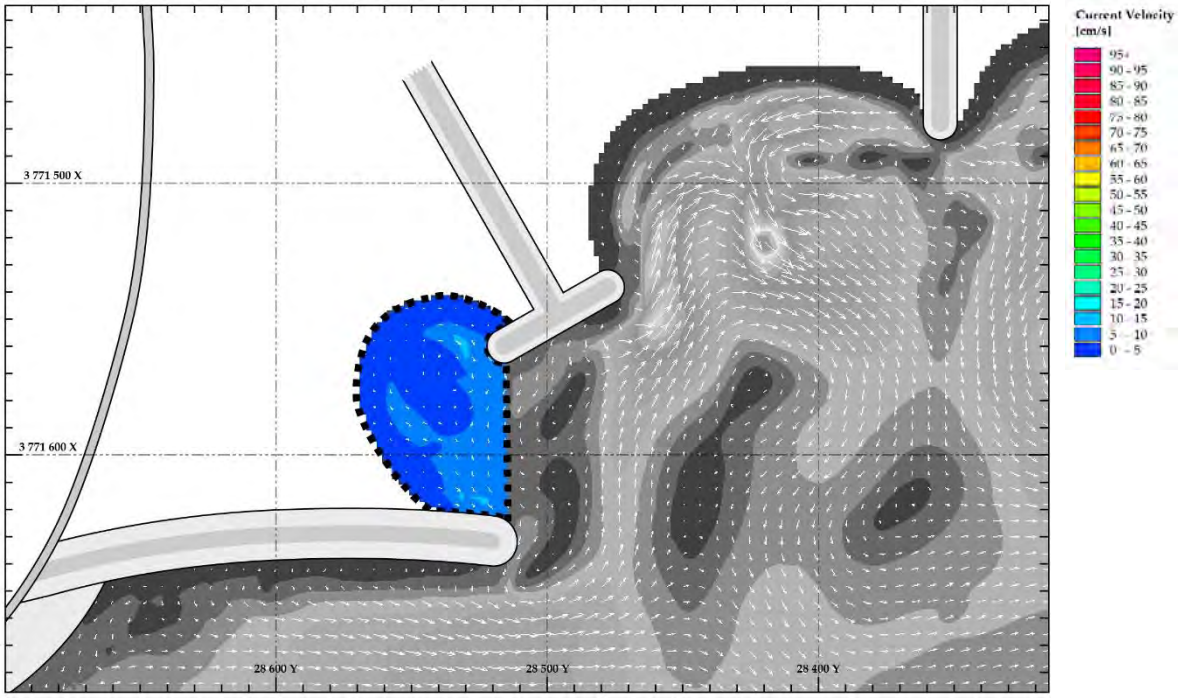

D.1.20.2.4 Velocity Exceedance: Designated Swimming Area

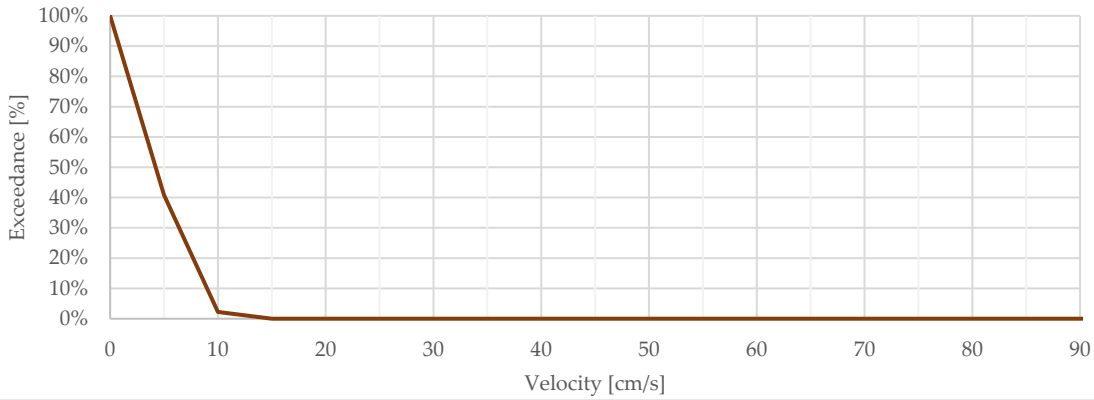

D.1.20.2.5 Velocity Baseline Exceedance Difference: Designated Swimming Area

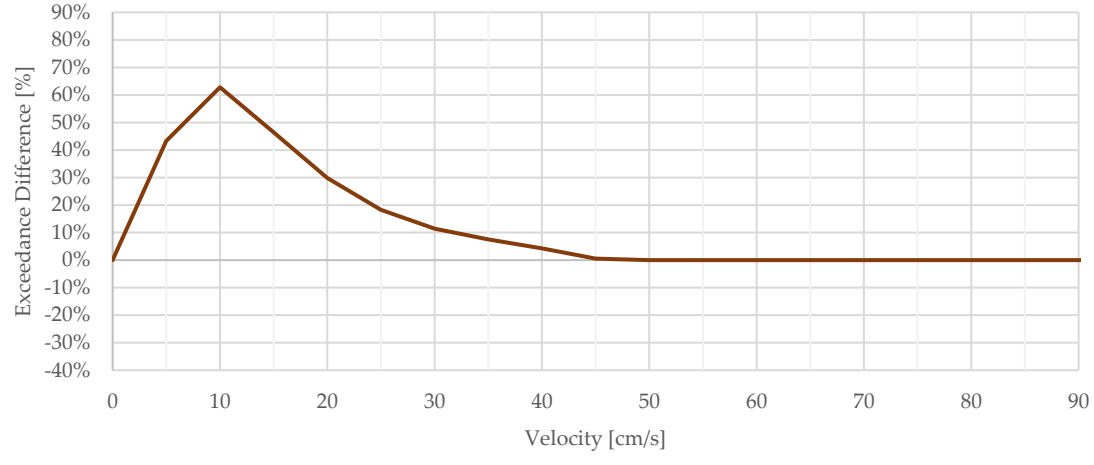

D.1.21 MT021

D.1.21.1 Setup

D.1.21.1.1 Description

T-Groyne off beach

D.1.21.1.2 Wave Conditions

Water / Tide Level	+0.4m MSL	**Wave Period (T_p)**	12 s
Wave Height (H_s)	1.1m	**Wave Angle**	+ 8°

D.1.21.2 Results

D.1.21.2.1 Current Velocity and Direction Map

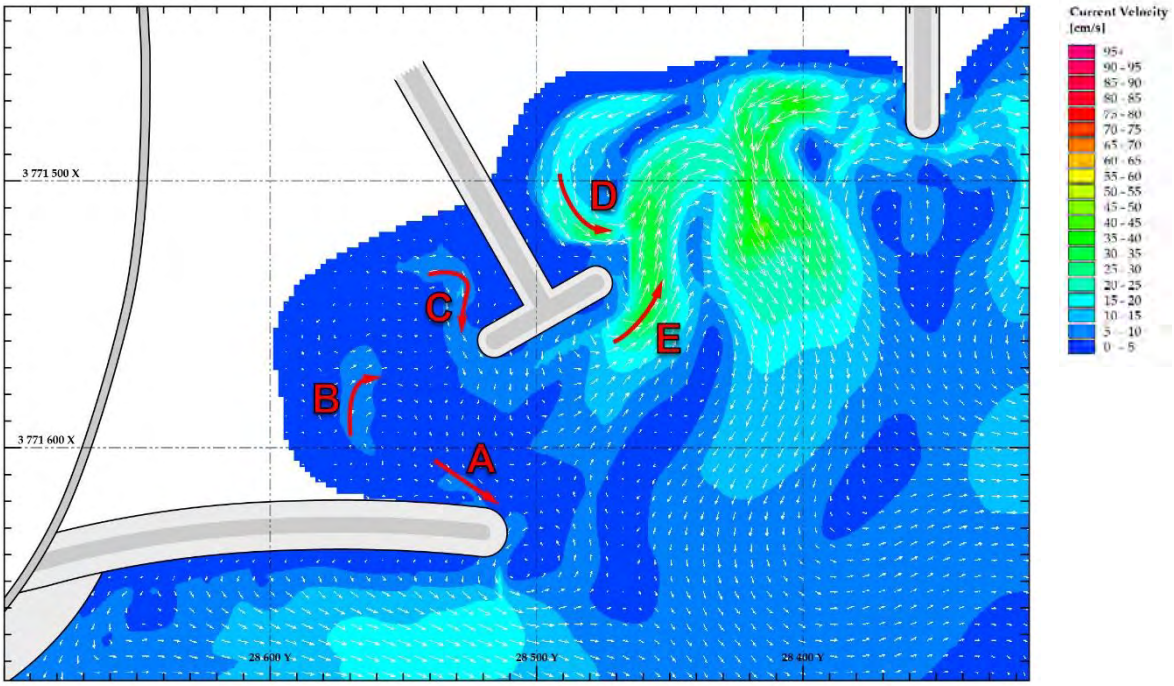

D.1.21.2.2 Measured Peak Flow Velocities

Vector	Class	30m Peak Average Velocities		
		u (absolute)	U_r (relative) (§ 7)	U_f (factorised) (§ 8)
A	1	5.4 cm/s	33%	21%
B	2	6.0 cm/s	20%	24%
C	2	8.1 cm/s	28%	32%
D	3	24.4 cm/s	89%	97%
E	3	30.9 cm/s	112%	123%

D.1.21.2.3 Area-Velocity: Designated Swimming Area

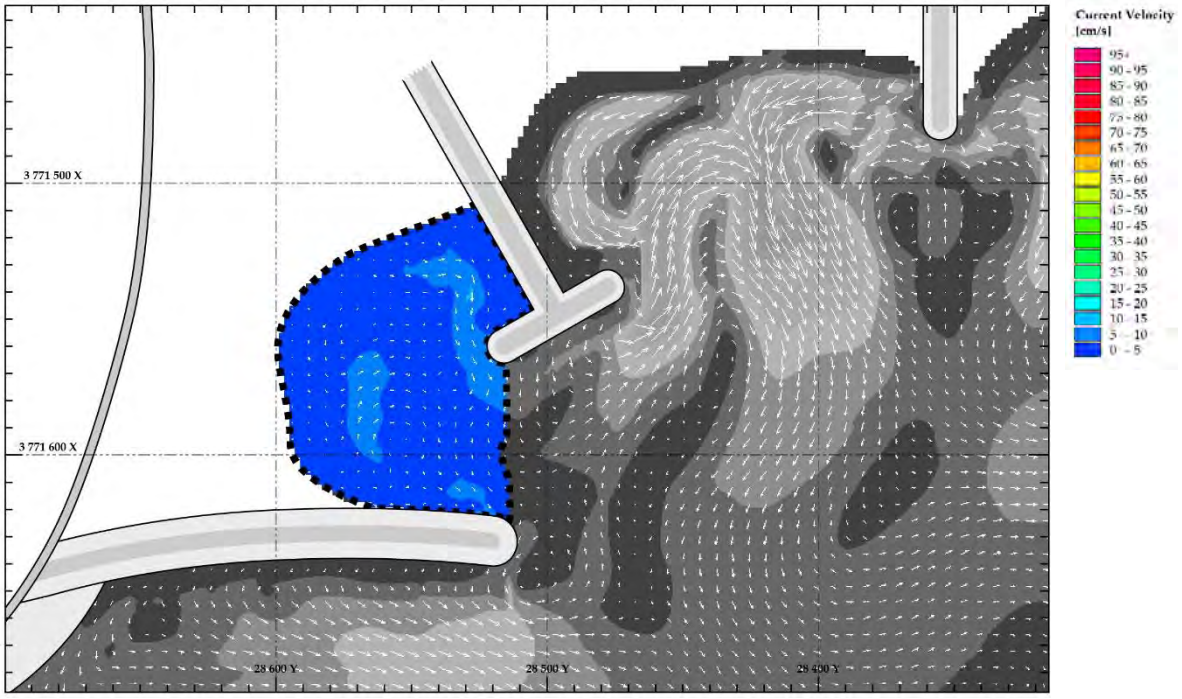

D.1.21.2.4 Velocity Exceedance: Designated Swimming Area

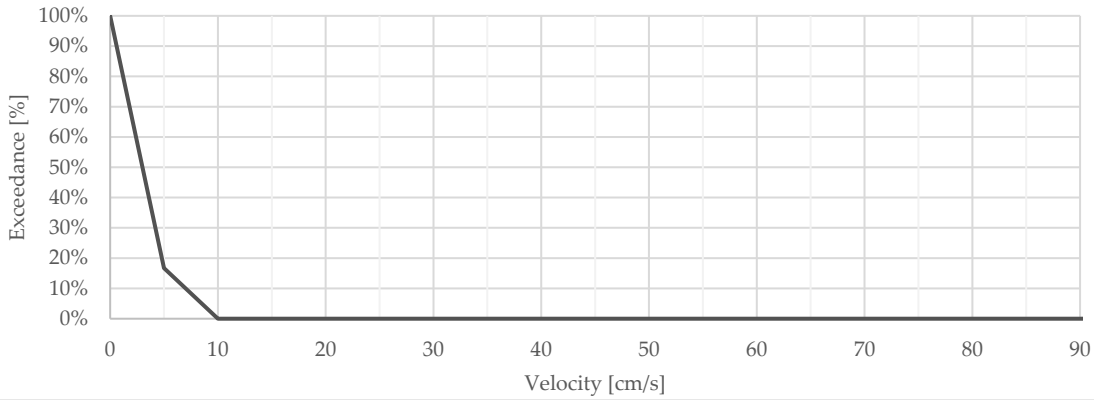

D.1.21.2.5 Velocity Baseline Exceedance Difference: Designated Swimming Area

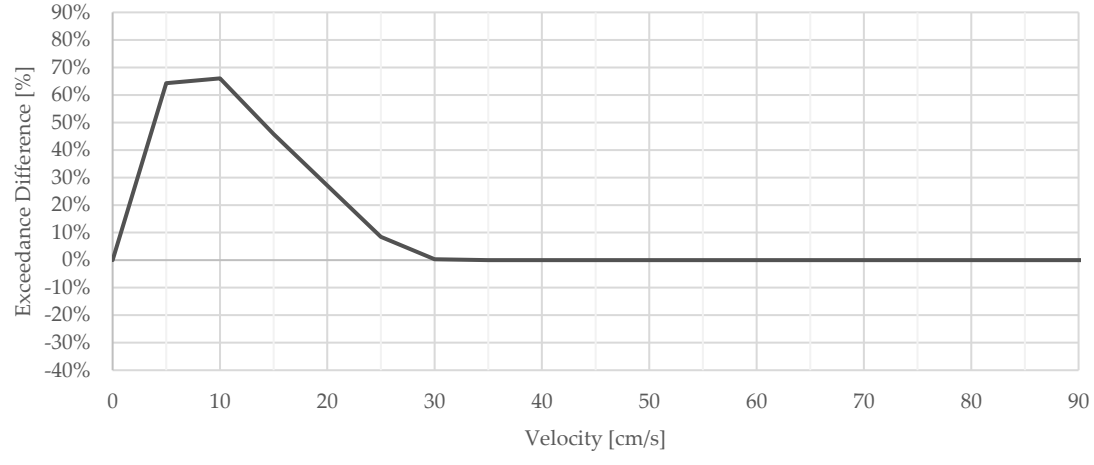

D.1.22 MT022

D.1.22.1 Setup

D.1.22.1.1 Description

T-Groyne off beach

D.1.22.1.2 Wave Conditions

Water / Tide Level	+0.4m MSL	**Wave Period (T_p)**	8 s
Wave Height (H_s)	1.1m	**Wave Angle**	+ 8°

D.1.22.2 Results

D.1.22.2.1 Current Velocity and Direction Map

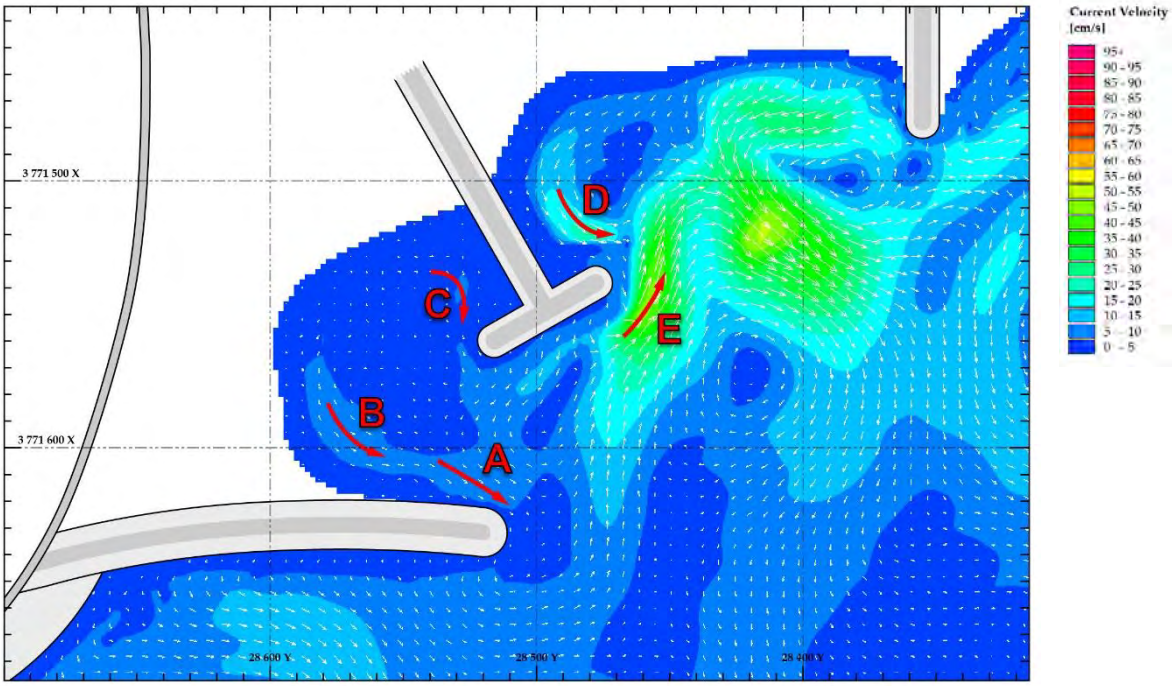

D.1.22.2.2 Measured Peak Flow Velocities

Vector	Class	30m Peak Average Velocities		
		u (absolute)	U_r (relative) (§ 7)	U_f (factorised) (§ 8)
A	1	6.6 cm/s	26%	26%
B	2	7.4 cm/s	25%	29%
C	2	4.5 cm/s	16%	18%
D	3	20.1 cm/s	55%	80%
E	3	41.3 cm/s	112%	164%

D.1.22.2.3 Area-Velocity: Designated Swimming Area

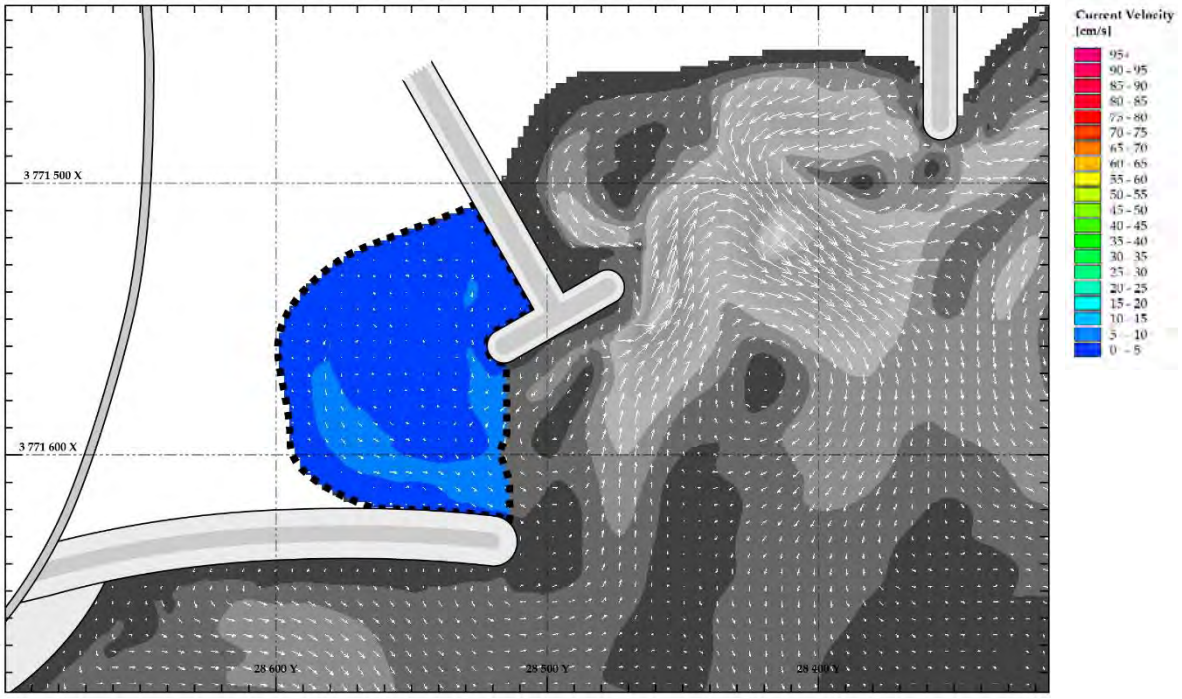

D.1.22.2.4 Velocity Exceedance: Designated Swimming Area

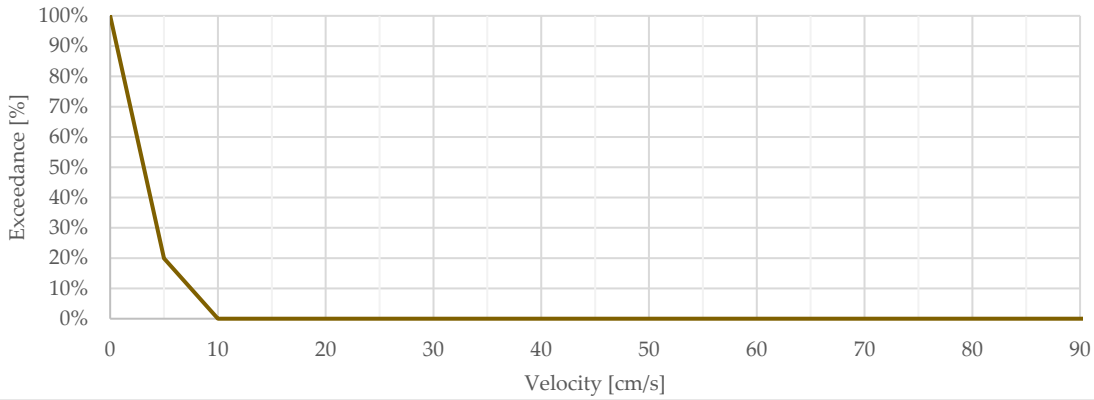

D.1.22.2.5 Velocity Baseline Exceedance Difference: Designated Swimming Area

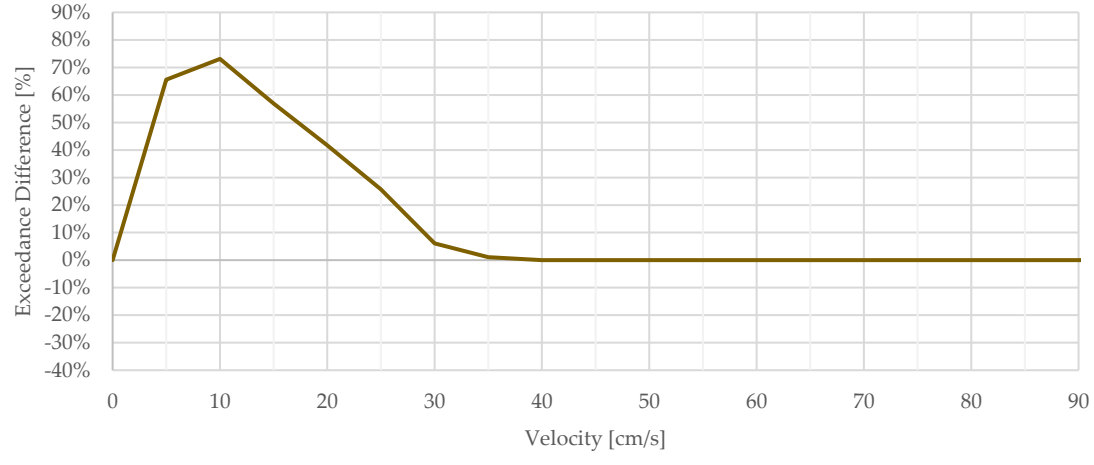

D.1.23 MT023

D.1.23.1 Setup

D.1.23.1.1 Description

T-Groyne off (built-up) beach

D.1.23.1.2 Wave Conditions

Water / Tide Level	+0.4m MSL	**Wave Period (T_p)**	12 s
Wave Height (H_s)	1.1m	**Wave Angle**	+ 8°

D.1.23.2 Results

D.1.23.2.1 Current Velocity and Direction Map

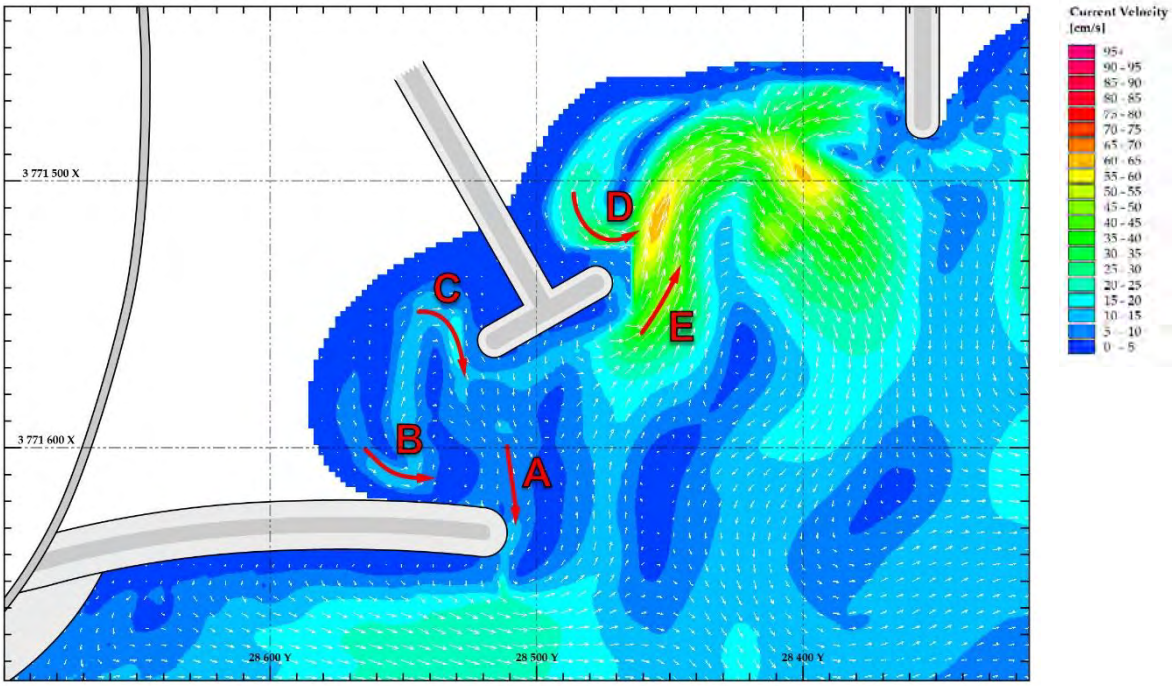

D.1.23.2.2 Measured Peak Flow Velocities

Vector	Class	30m Peak Average Velocities		
		u (absolute)	U_r (relative) (§ 7)	U_f (factorised) (§ 8)
A	1	8.1 cm/s	37%	32%
B	2	11.3 cm/s	35%	45%
C	2	14.7 cm/s	45%	58%
D	3	27.6 cm/s	74%	110%
E	3	44.6 cm/s	120%	177%

D.1.23.2.3 Area-Velocity: Designated Swimming Area

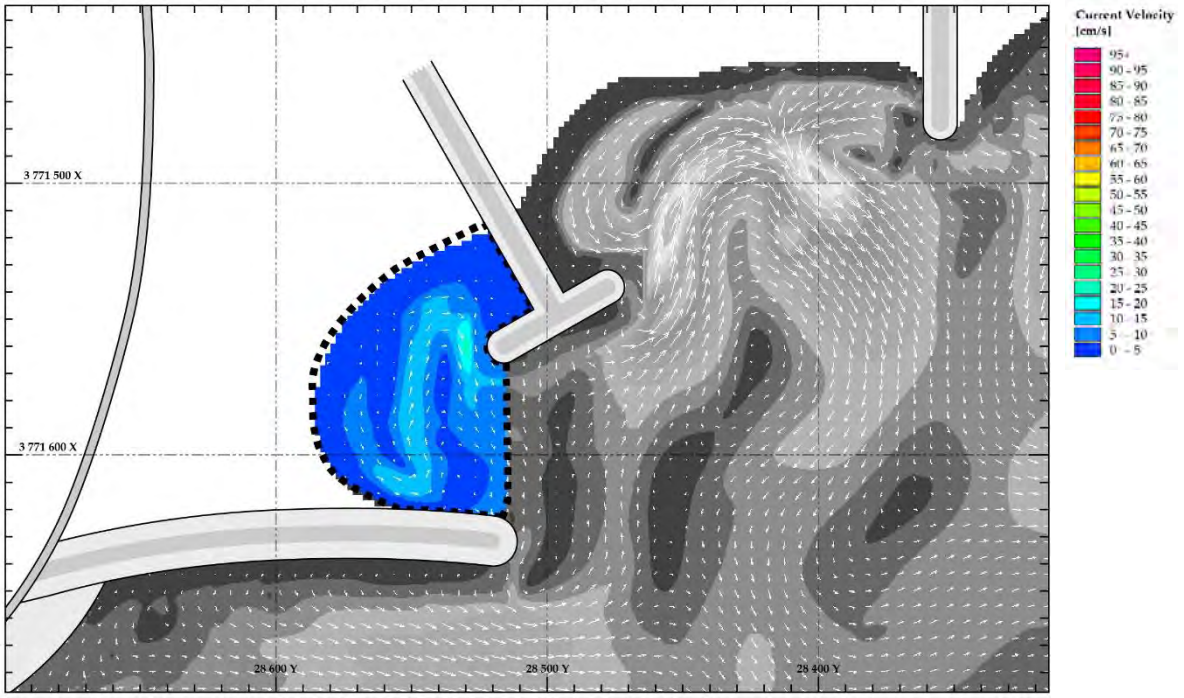

D.1.23.2.4 Velocity Exceedance: Designated Swimming Area

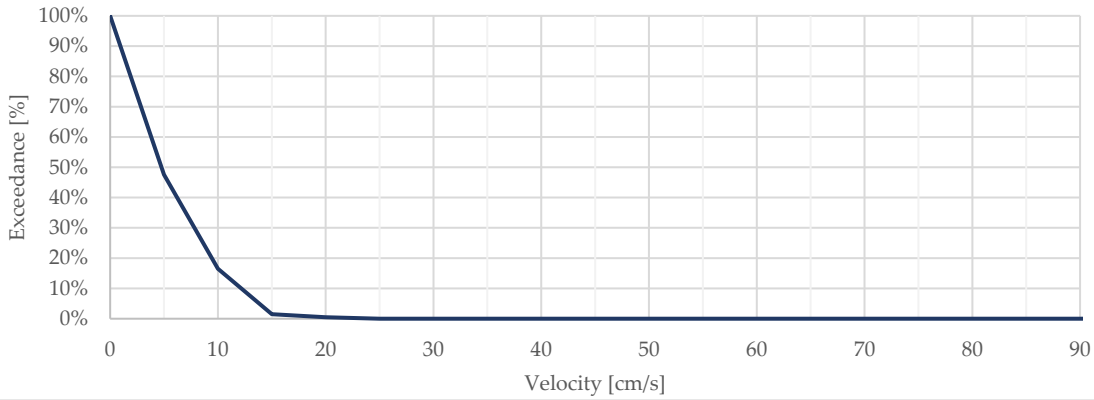

D.1.23.2.5 Velocity Baseline Exceedance Difference: Designated Swimming Area

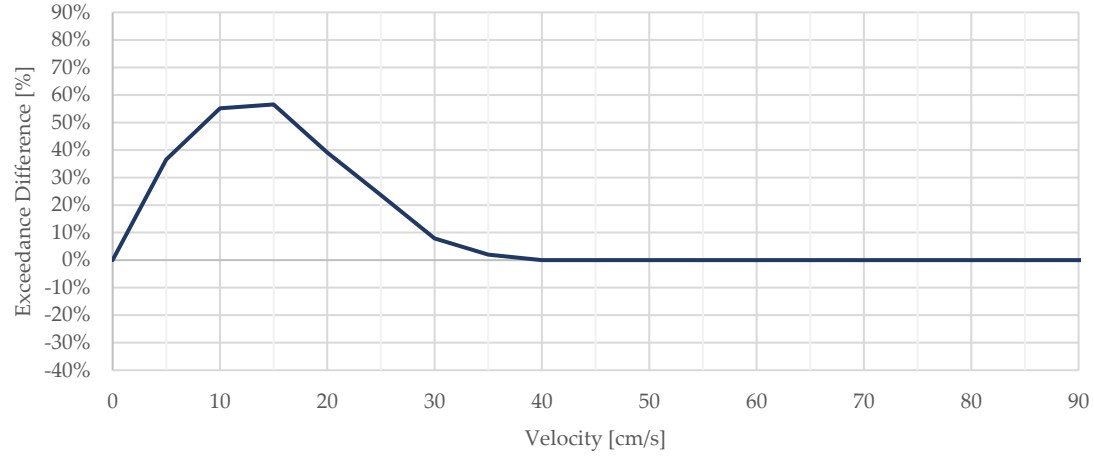

D.1.24 MT024

D.1.24.1 Setup

D.1.24.1.1 Description

T-Groyne off (denuded) beach

D.1.24.2 Wave Conditions

Water / Tide Level	+0.4m MSL	**Wave Period (T_p)**	12 s
Wave Height (H_s)	1.1m	**Wave Angle**	+ 8°

D.1.24.3 Results

D.1.24.3.1 Current Velocity and Direction Map

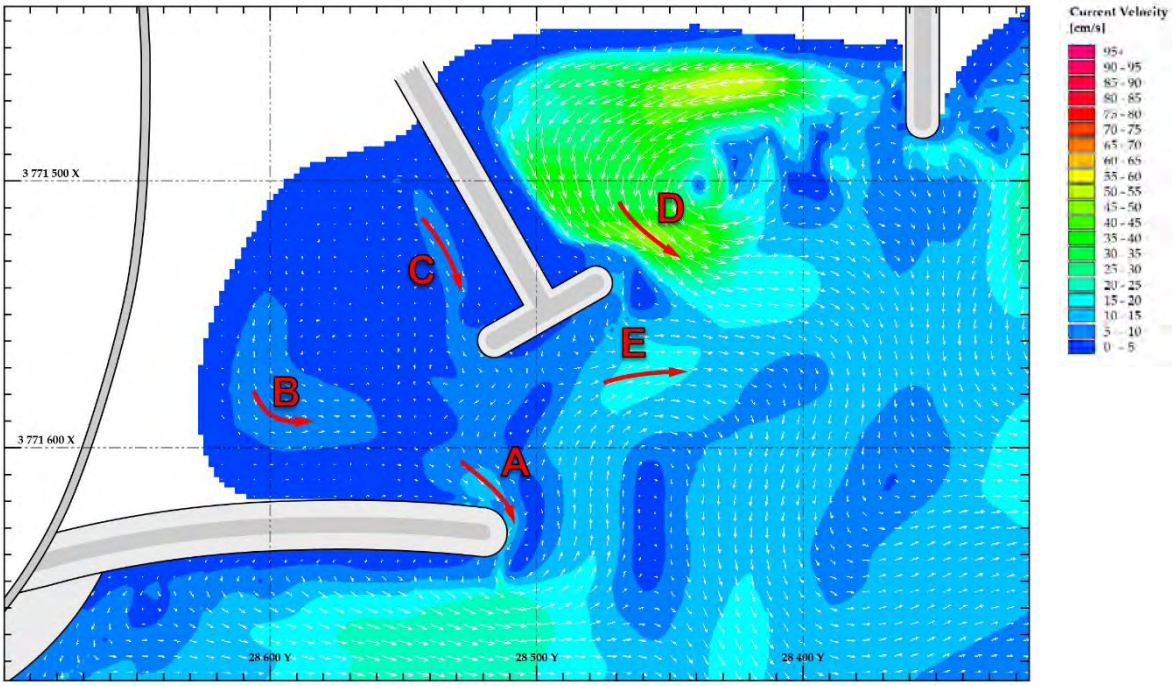

D.1.24.3.2 Measured Peak Flow Velocities

Vector	Class	30m Peak Average Velocities		
		u (absolute)	U_r (relative) (§ 7)	U_f (factorised) (§ 8)
A	1	10.3 cm/s	47%	41%
B	2	8.3 cm/s	26%	33%
C	2	7.6 cm/s	24%	30%
D	3	36.7 cm/s	98%	146%
E	3	16.6 cm/s	44%	66%

D.1.24.3.3 Area-Velocity: Designated Swimming Area

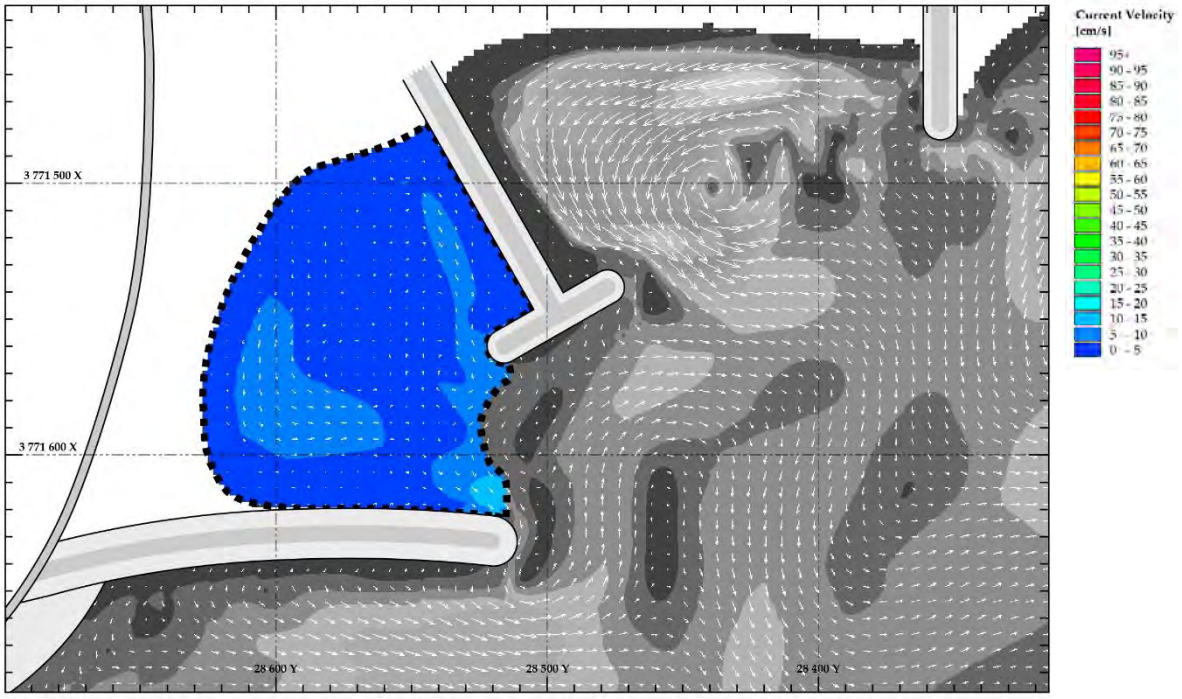

D.1.24.3.4 Velocity Exceedance: Designated Swimming Area

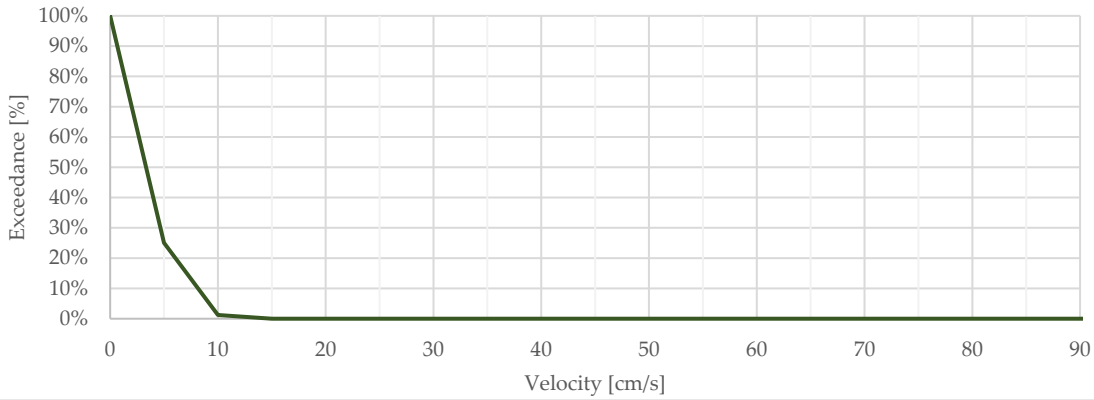

D.1.24.3.5 Velocity Baseline Exceedance Difference: Designated Swimming Area

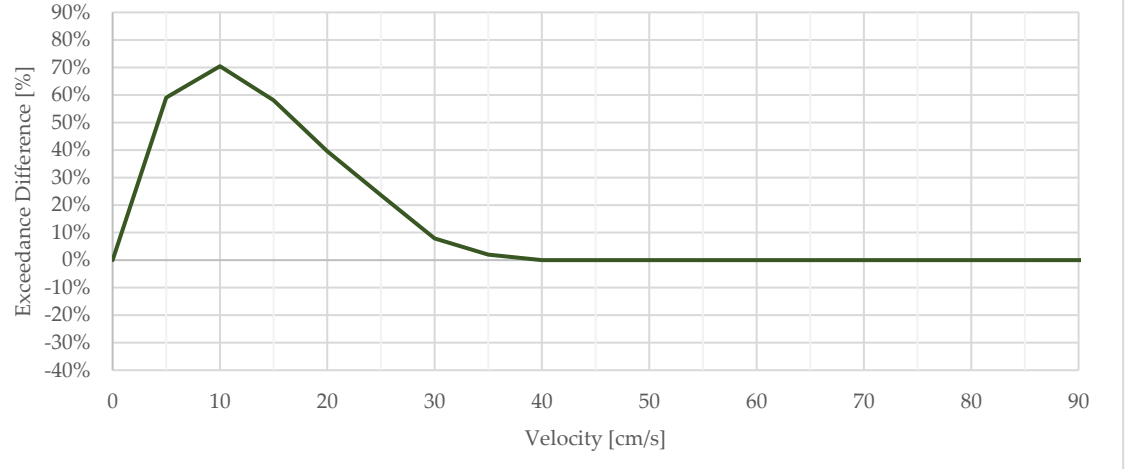

D.2 BASELINE SIMULATIONS

D.2.1 MB110

D.2.1.1 Setup

D.2.1.1.1 Wave Conditions

Water / Tide Level	-0.3m MSL	**Wave Period (T_p)**	12 s
Wave Height (H_s)	1.3m	**Wave Angle**	+ 8°

D.2.1.2 Results

D.2.1.2.1 Current Velocity and Direction Map

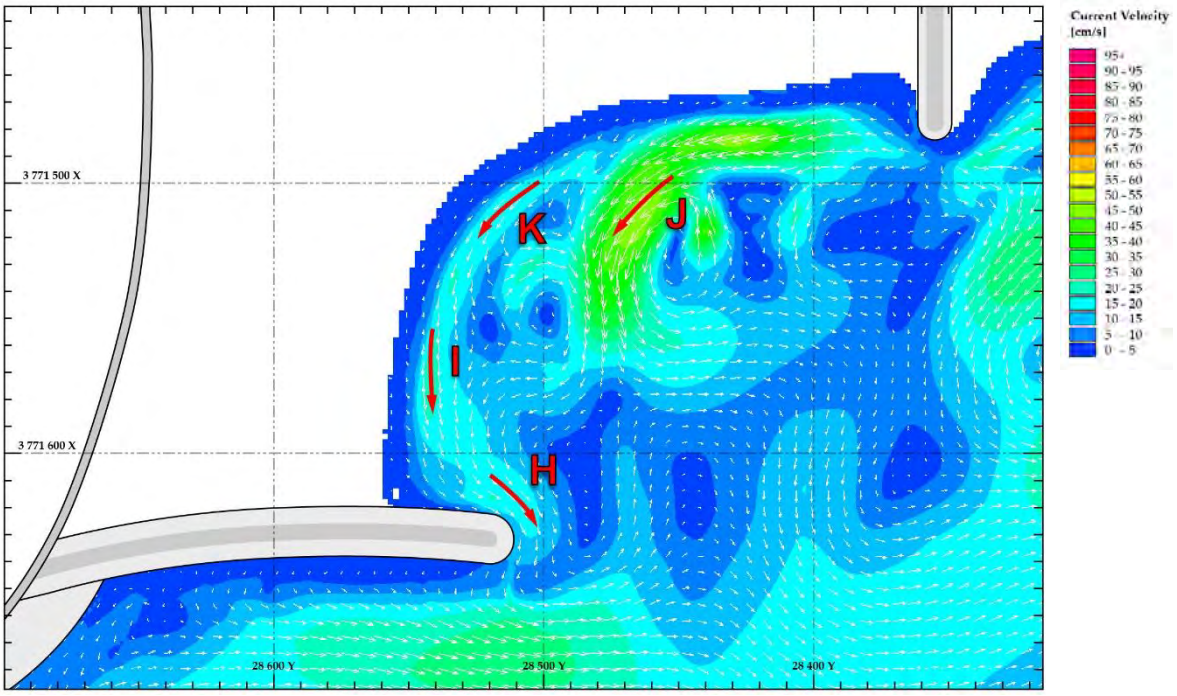

D.2.1.2.2 Measured Peak Flow Velocities

Vector	Class	30m Peak Average Velocities
		***u* (absolute)**
H	1	17.8 cm/s
I	2	21.2 cm/s
J	3	45.9 cm/s
K	2	18.6 cm/s

D.2.1.2.3 Area-Velocity: Designated Swimming Area

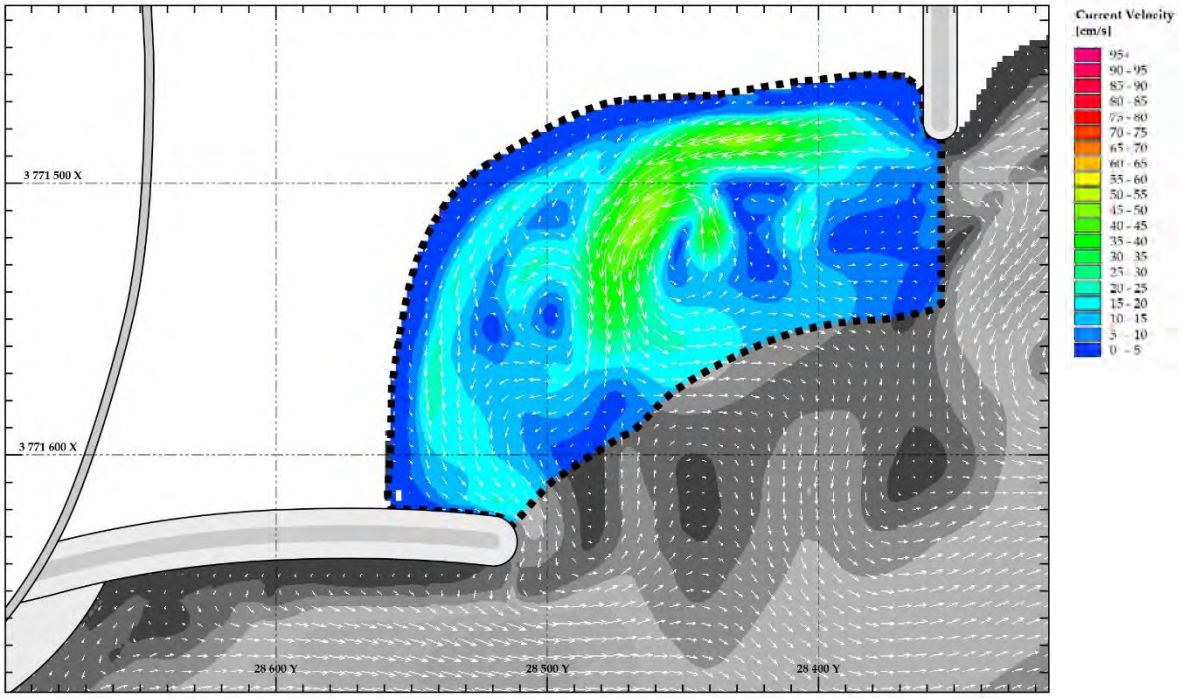

D.2.1.2.4 Velocity Exceedance: Designated Swimming Area

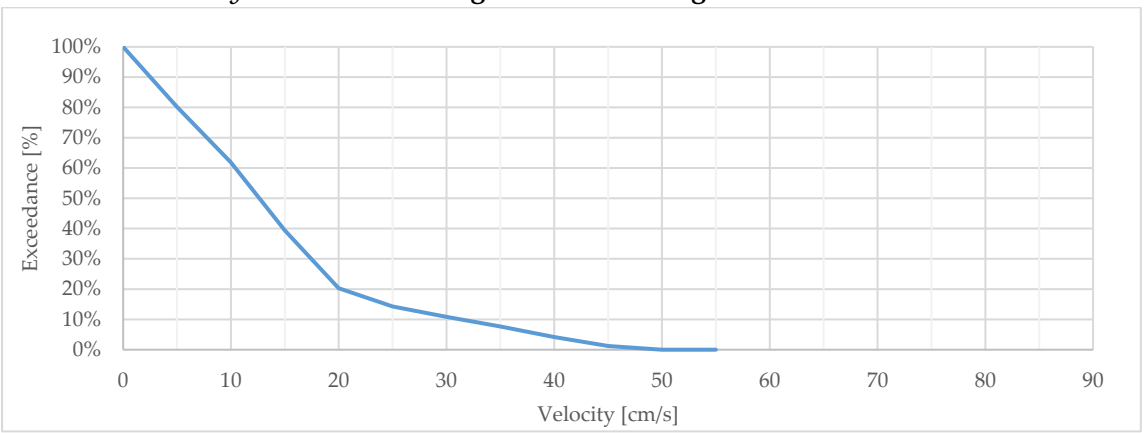

D.2.2 MB210

D.2.2.1 Setup

D.2.2.1.1 Wave Conditions

Water / Tide Level	-0.1m MSL	**Wave Period (T_p)**	12 s
Wave Height (H_s)	1m	**Wave Angle**	+ 8°

D.2.2.2 Results

D.2.2.2.1 Current Velocity and Direction Map

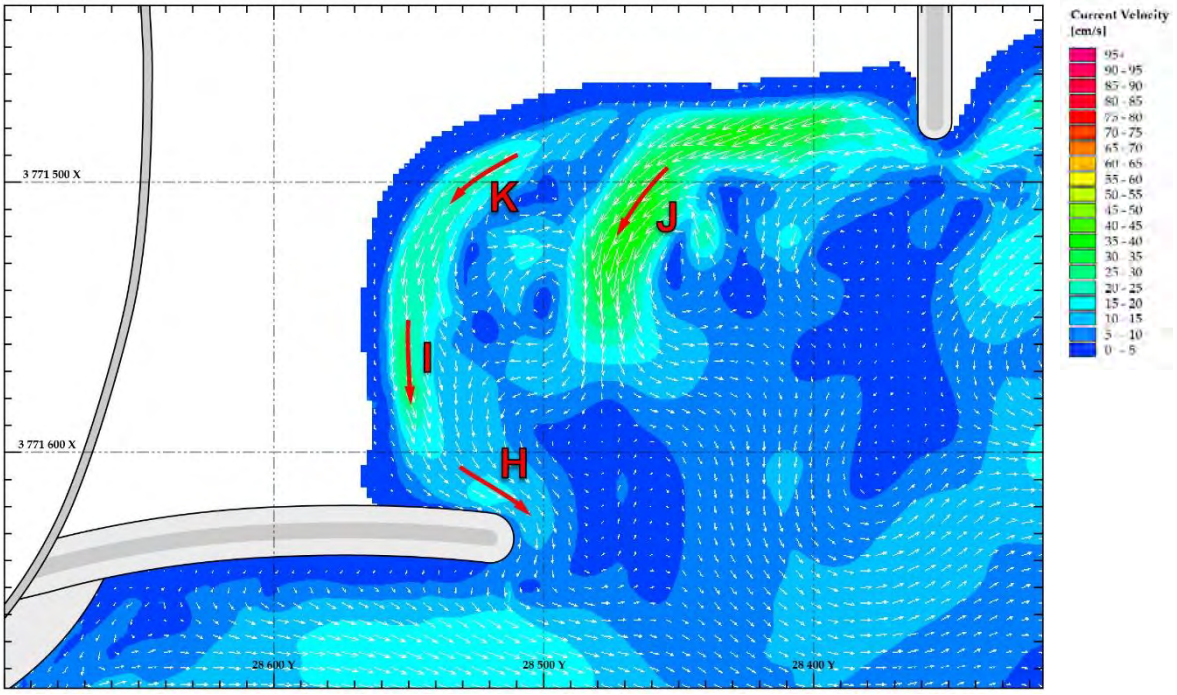

D.2.2.2.2 Measured Peak Flow Velocities

Vector	Class	30m Peak Average Velocities
		u **(absolute)**
H	1	15.2 cm/s
I	2	26.0 cm/s
J	3	38.2 cm/s
K	2	21.9 cm/s

D.2.2.2.3 Area-Velocity: Designated Swimming Area

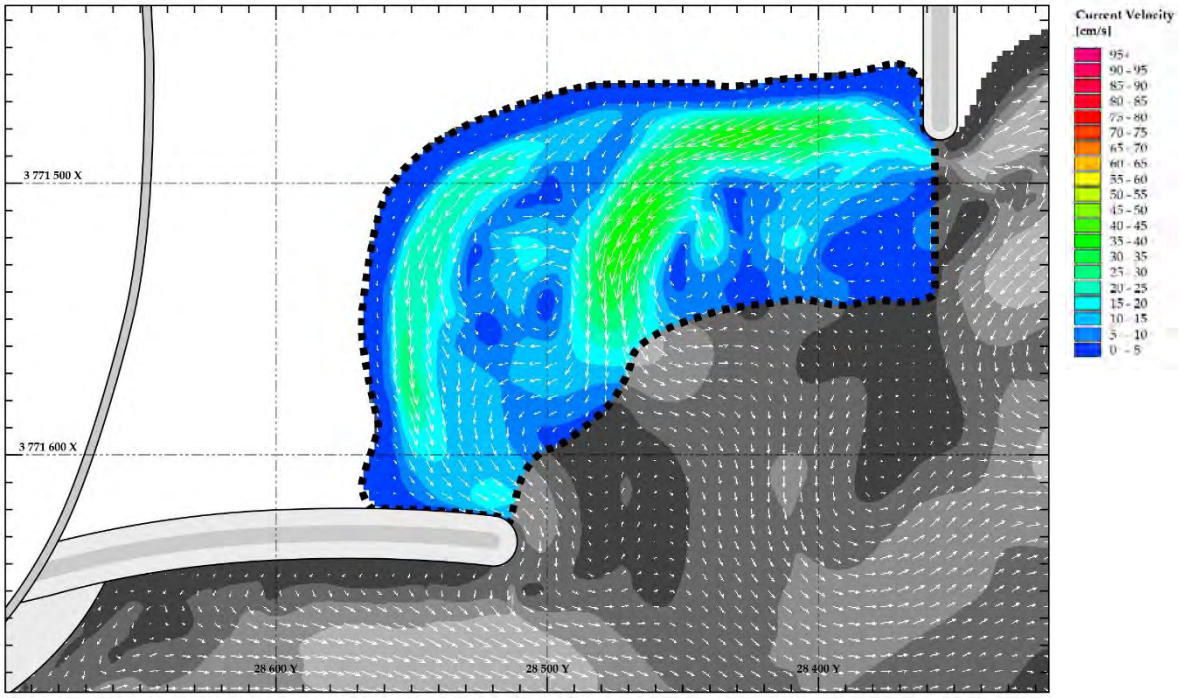

D.2.2.2.4 Velocity Exceedance: Designated Swimming Area

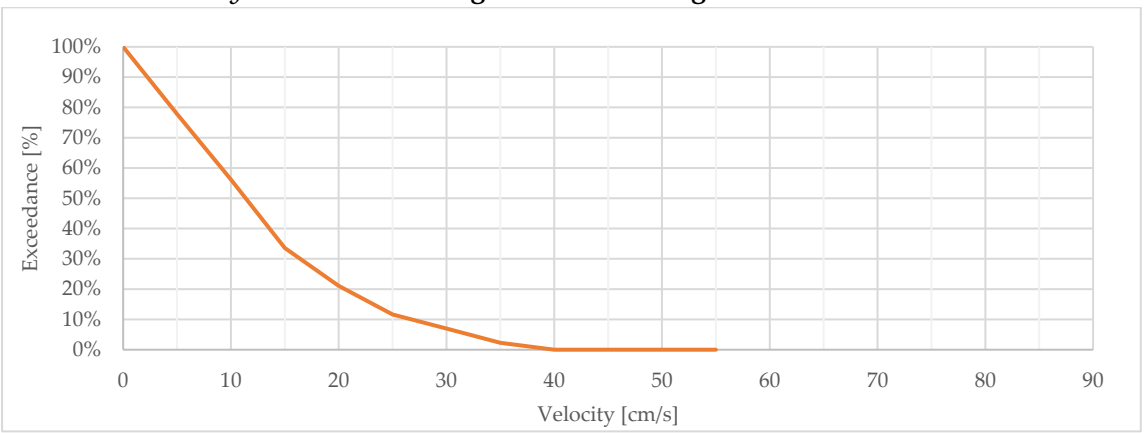

D.2.3 MB220

D.2.3.1 Setup

D.2.3.1.1 Wave Conditions

Water / Tide Level	-0.1m MSL	**Wave Period (T_p)**	12 s
Wave Height (H_s)	1.4m	**Wave Angle**	+ 8°

D.2.3.2 Results

D.2.3.2.1 Current Velocity and Direction Map

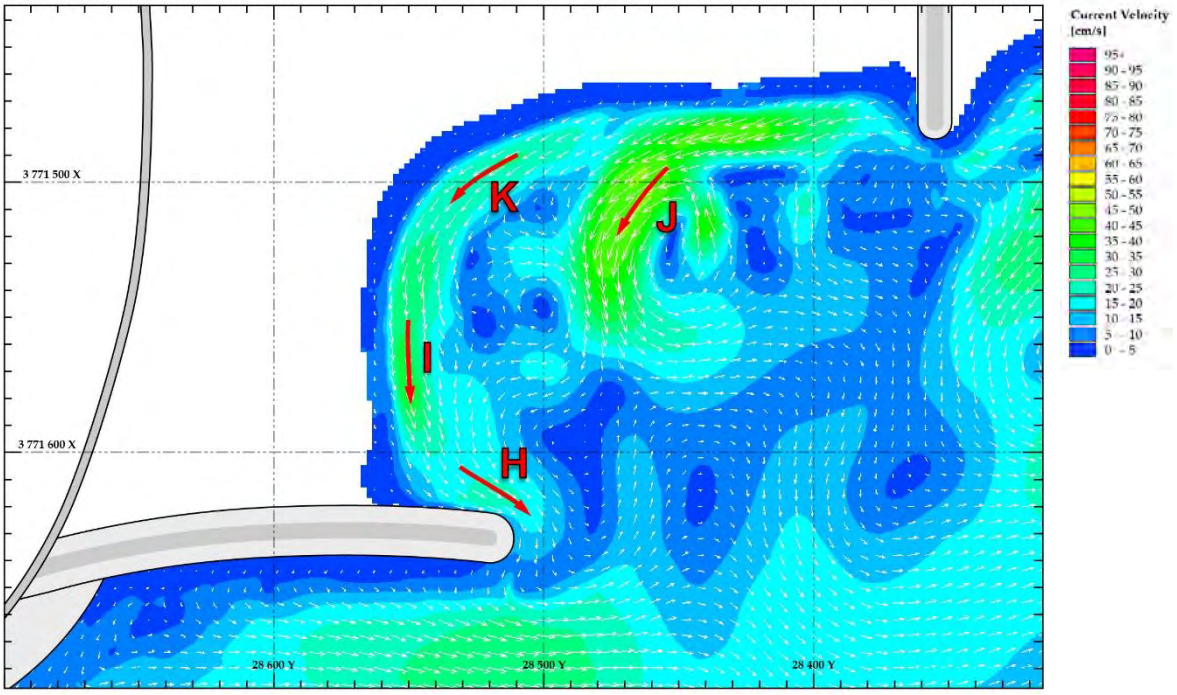

D.2.3.2.2 Measured Peak Flow Velocities

Vector	Class	30m Peak Average Velocities
		u **(absolute)**
H	1	21.1 cm/s
I	2	31.5 cm/s
J	3	43.6 cm/s
K	2	24.7 cm/s

D.2.3.2.3 Area-Velocity: Designated Swimming Area

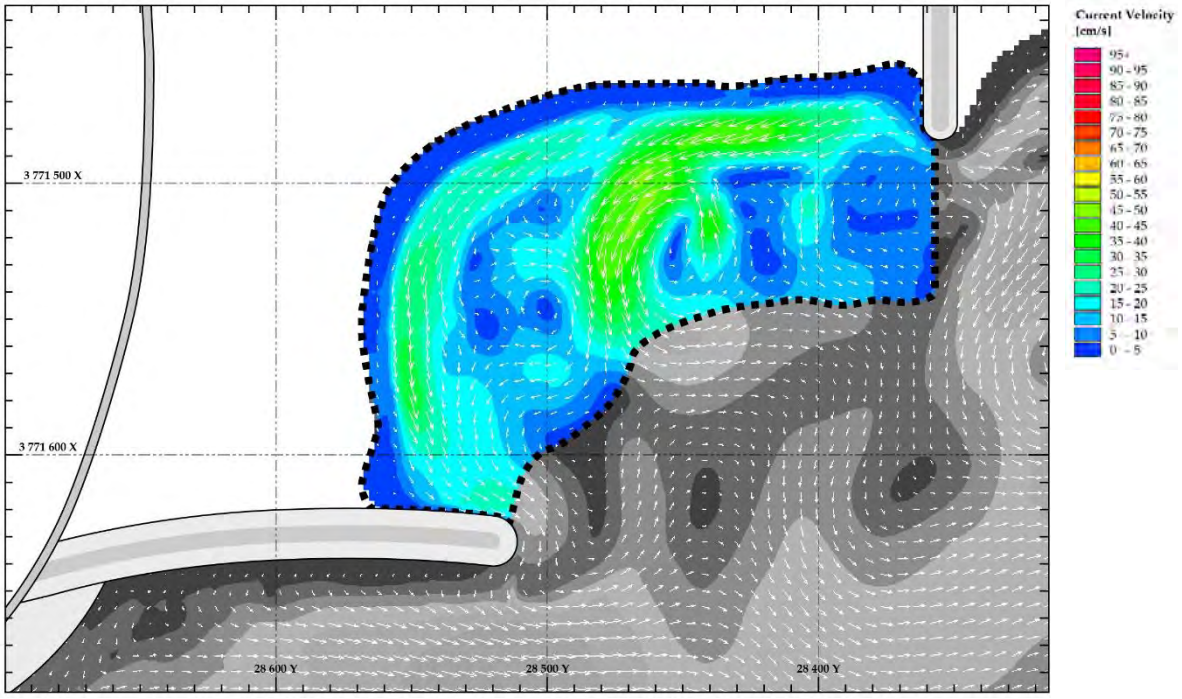

D.2.3.2.4 Velocity Exceedance: Designated Swimming Area

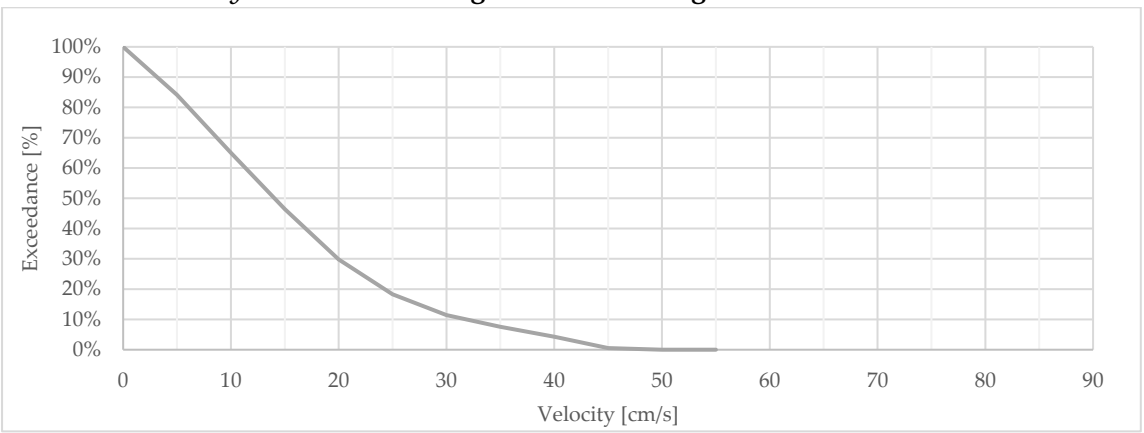

D.2.4 MB310

D.2.4.1 Setup

D.2.4.1.1 Wave Conditions

Water / Tide Level	+0.3m MSL	**Wave Period (T_p)**	12 s
Wave Height (H_s)	1.3m	**Wave Angle**	+ 8°

D.2.4.2 Results

D.2.4.2.1 Current Velocity and Direction Map

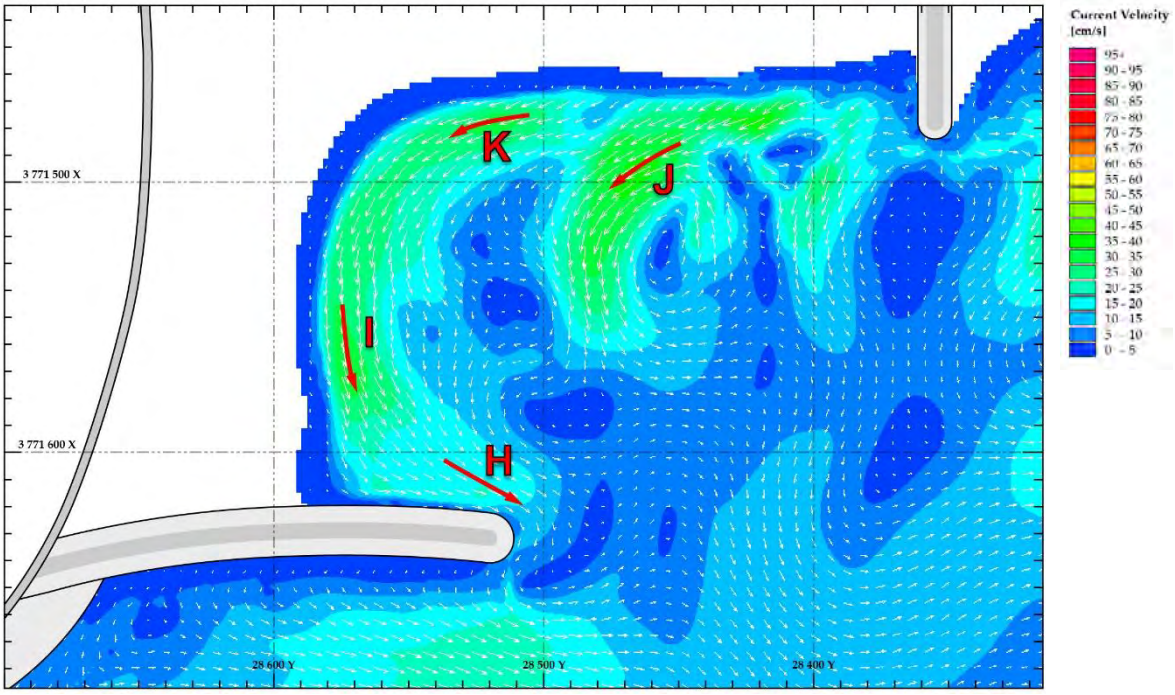

D.2.4.2.2 Measured Peak Flow Velocities

Vector	Class	30m Peak Average Velocities
		u **(absolute)**
H	1	18.7 cm/s
I	2	31.4 cm/s
J	3	35.7 cm/s
K	2	30.1 cm/s

D.2.4.2.3 Area-Velocity: Designated Swimming Area

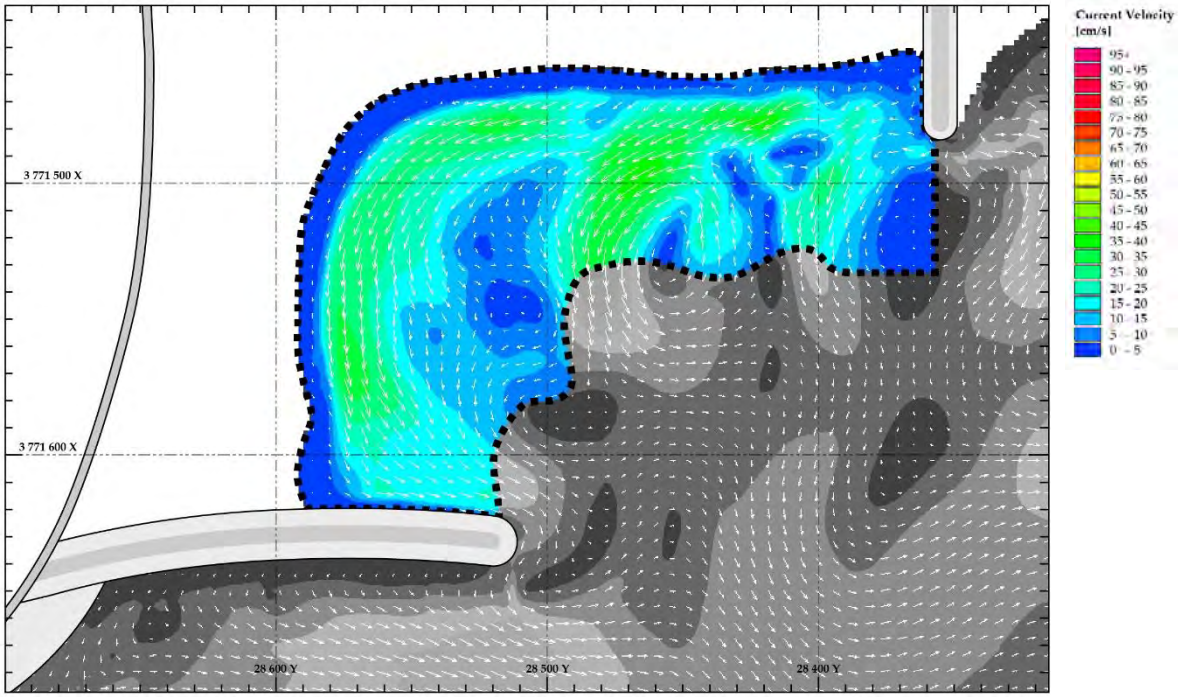

D.2.4.2.4 Velocity Exceedance: Designated Swimming Area

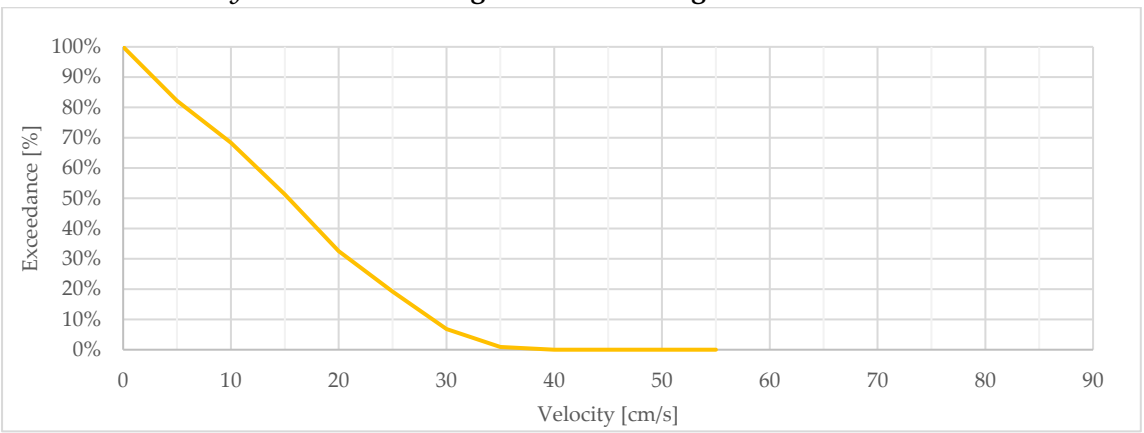

D.2.5 MB410

D.2.5.1 Setup

D.2.5.1.1 Wave Conditions

Water / Tide Level	+0.4m MSL	**Wave Period (T_p)**	12 s
Wave Height (H_s)	1.1m	**Wave Angle**	+ 8°

D.2.5.2 Results

D.2.5.2.1 Current Velocity and Direction Map

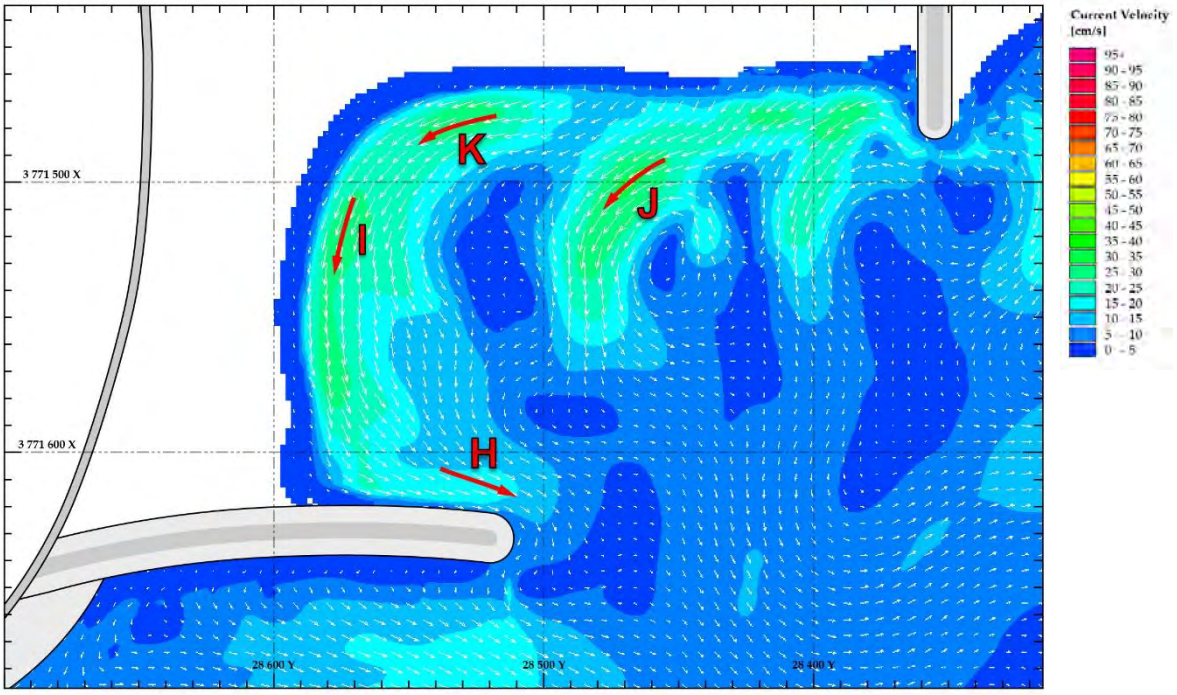

D.2.5.2.2 Measured Peak Flow Velocities

Vector	Class	30m Peak Average Velocities
		***u* (absolute)**
H	1	16.3 cm/s
I	2	26.5 cm/s
J	3	27.6 cm/s
K	2	29.3 cm/s

D.2.5.2.3 Area-Velocity: Designated Swimming Area

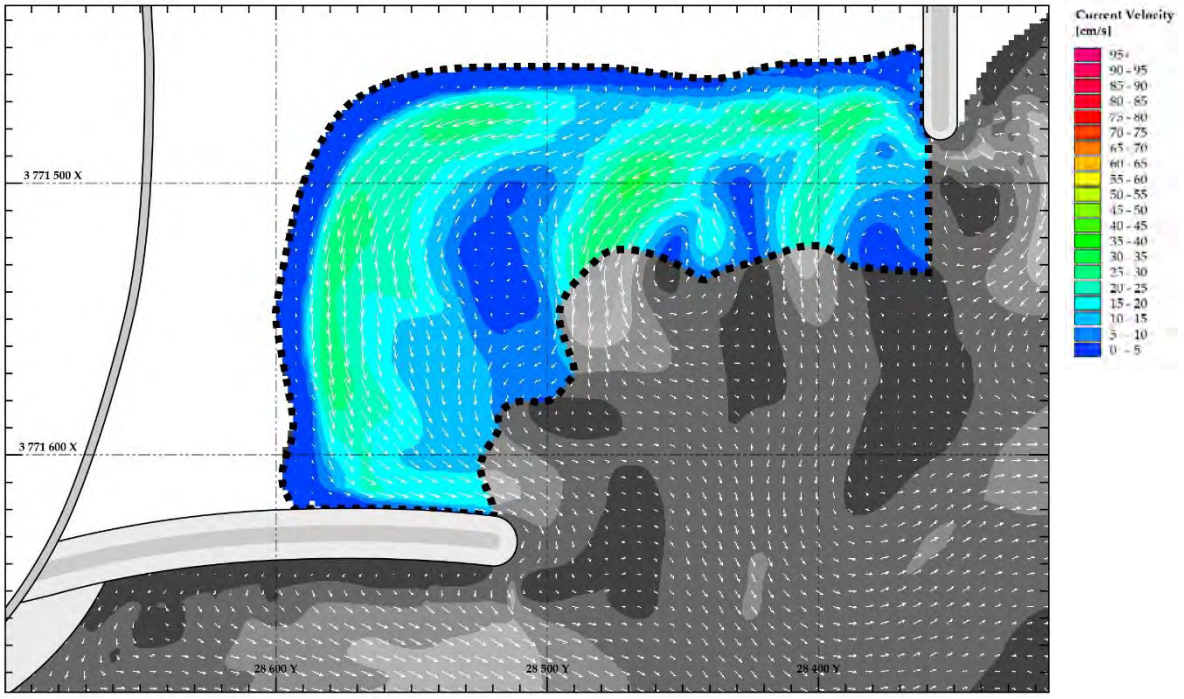

D.2.5.2.4 Velocity Exceedance: Designated Swimming Area

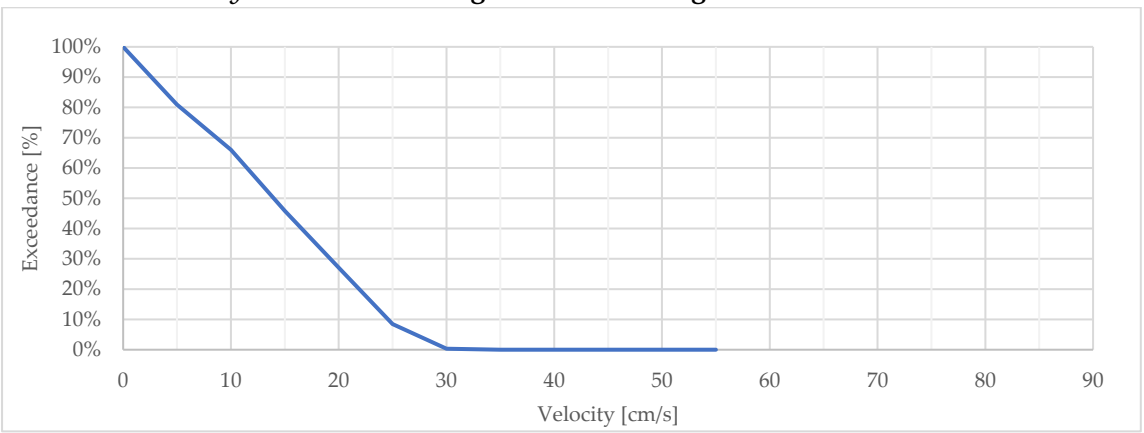

D.2.6 MB420

D.2.6.1 Setup

D.2.6.1.1 Wave Conditions

Water / Tide Level	+0.4m MSL	**Wave Period (T_p)**	12 s
Wave Height (H_s)	1.4m	**Wave Angle**	+ 8°

D.2.6.2 Results

D.2.6.2.1 Current Velocity and Direction Map

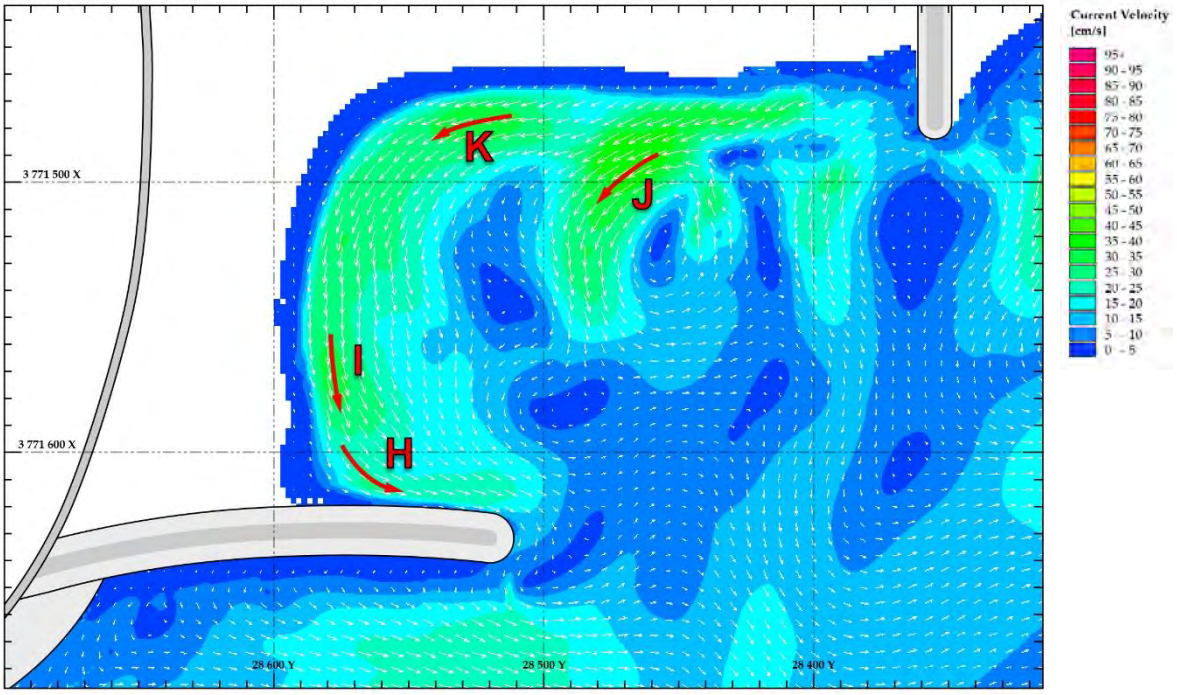

D.2.6.2.2 Measured Peak Flow Velocities

Vector	Class	30m Peak Average Velocities
		u **(absolute)**
H	1	22.1 cm/s
I	2	30.9 cm/s
J	3	37.3 cm/s
K	2	32.2 cm/s

D.2.6.2.3 Area-Velocity: Designated Swimming Area

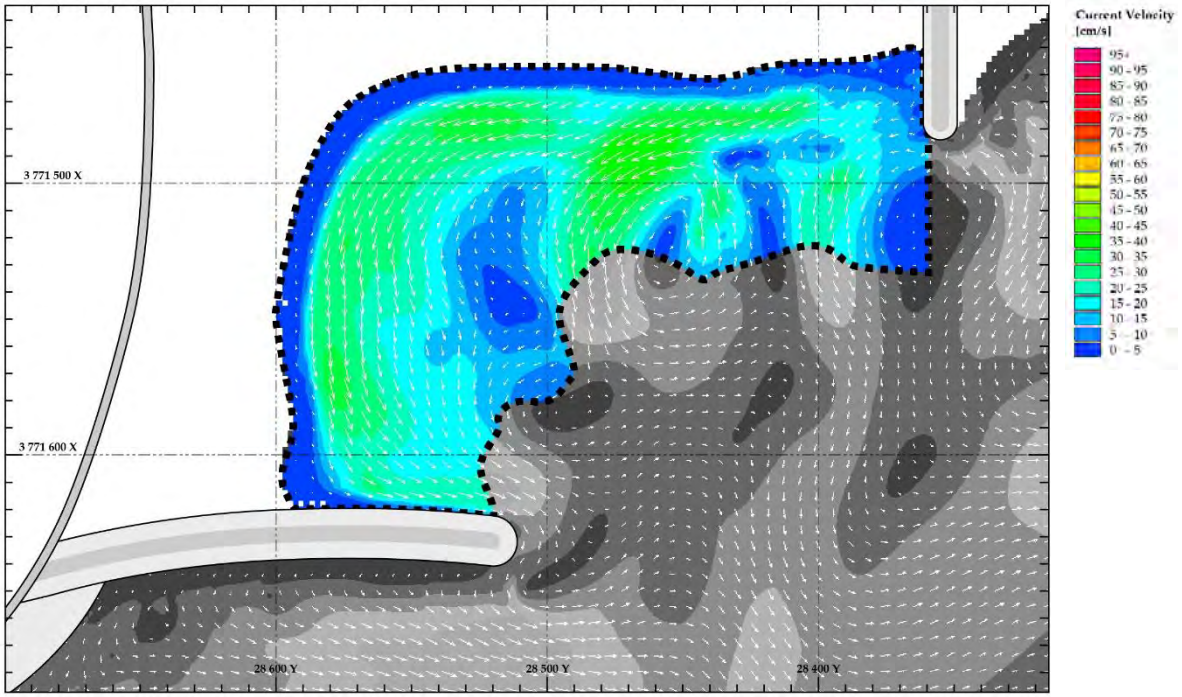

D.2.6.2.4 Velocity Exceedance: Designated Swimming Area

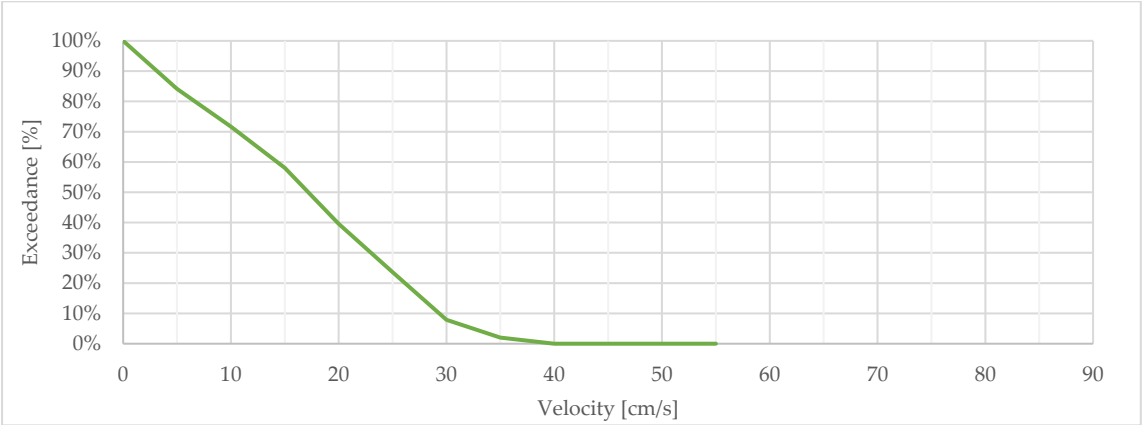

D.2.7 MB430

D.2.7.1 Setup

D.2.7.1.1 Wave Conditions

Water / Tide Level	+0.4m MSL	**Wave Period (T_p)**	8 s
Wave Height (H_s)	1.1m	**Wave Angle**	+ 8°

D.2.7.2 Results

D.2.7.2.1 Current Velocity and Direction Map

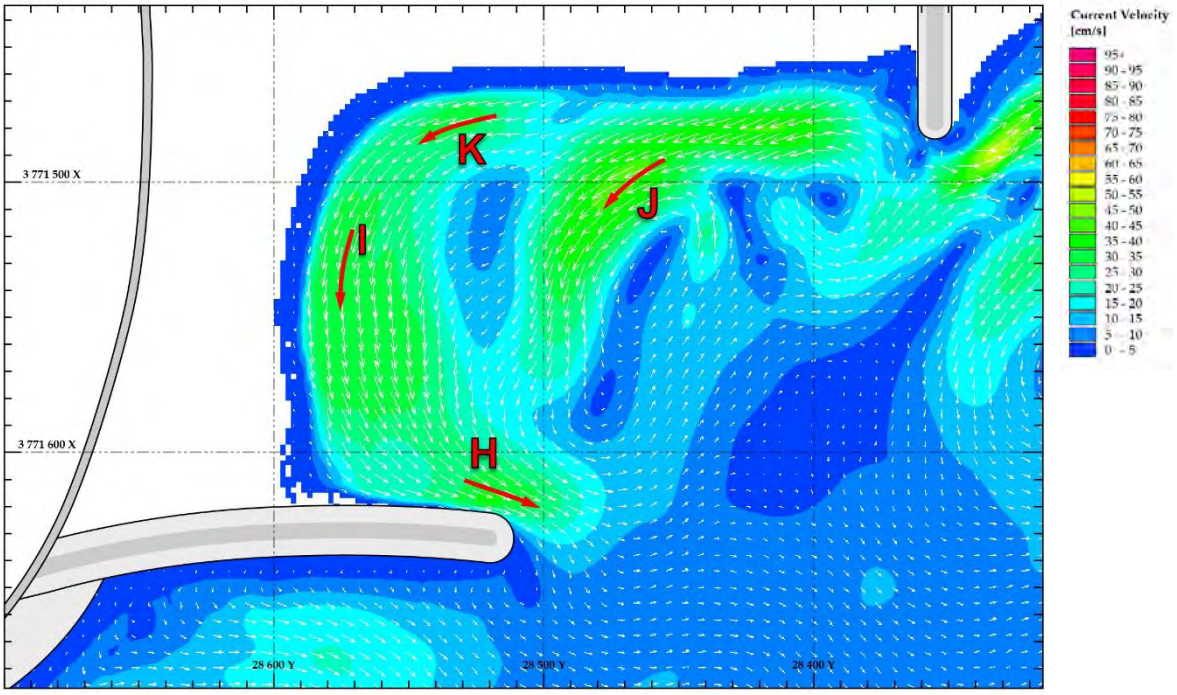

D.2.7.2.2 Measured Peak Flow Velocities

Vector	Class	30m Peak Average Velocities
		u **(absolute)**
H	1	25.3 cm/s
I	2	28.8 cm/s
J	3	36.7 cm/s
K	2	29.1 cm/s

D.2.7.2.3 Area-Velocity: Designated Swimming Area

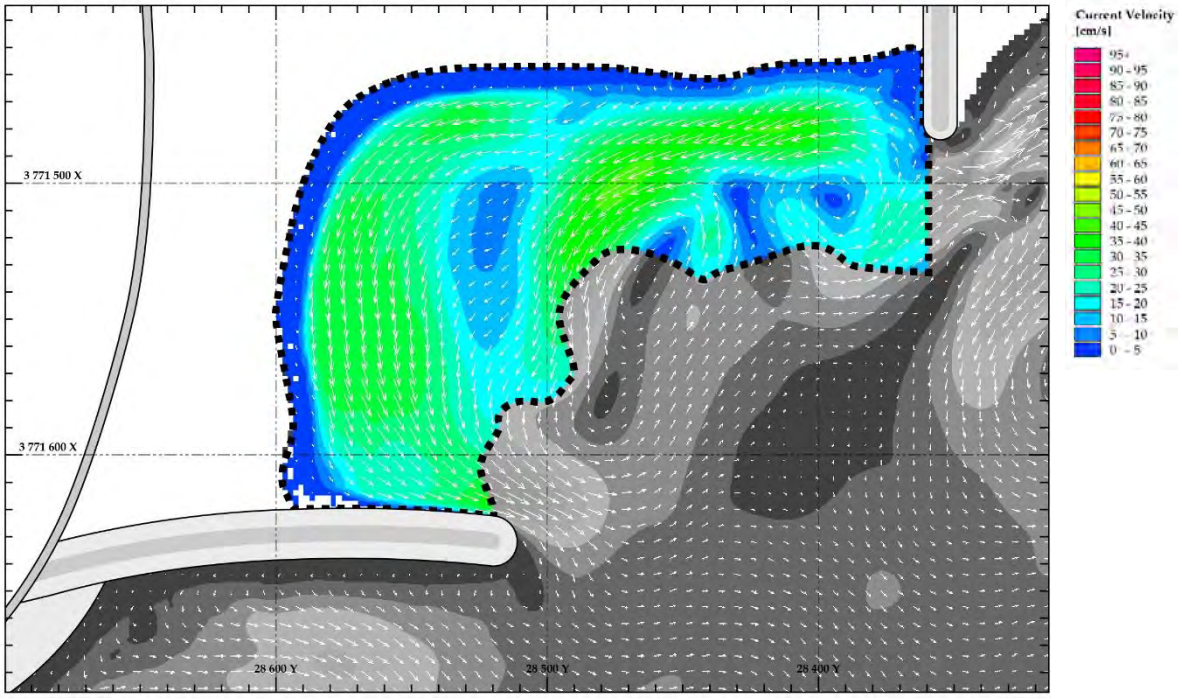

D.2.7.2.4 Velocity Exceedance: Designated Swimming Area

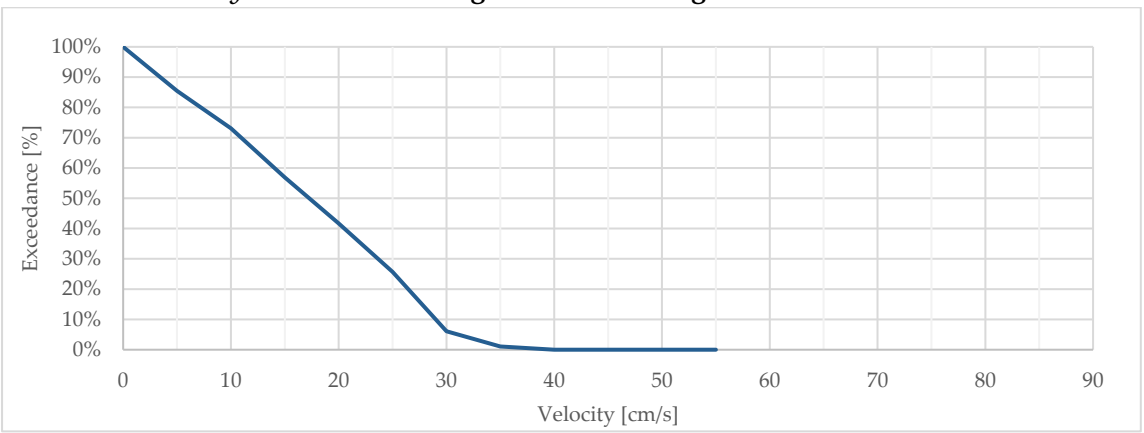

D.2.8 MB510

D.2.8.1 Setup

D.2.8.1.1 Wave Conditions

Water / Tide Level	+0.45m MSL	**Wave Period (T_p)**	12 s
Wave Height (H_s)	1.1m	**Wave Angle**	+ 8°

D.2.8.2 Results

D.2.8.2.1 Current Velocity and Direction Map

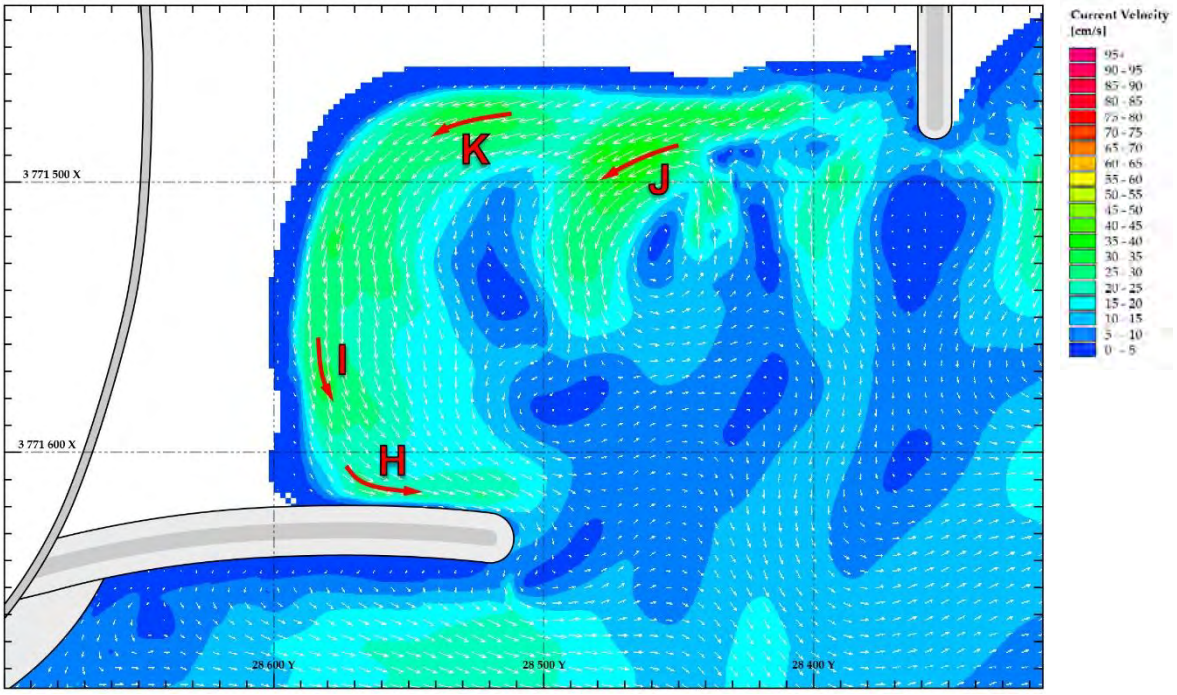

D.2.8.2.2 Measured Peak Flow Velocities

Vector	Class	30m Peak Average Velocities
		u **(absolute)**
H	1	24.4 cm/s
I	2	30.2 cm/s
J	3	35.7 cm/s
K	2	31.3 cm/s

D.2.8.2.3 Area-Velocity: Designated Swimming Area

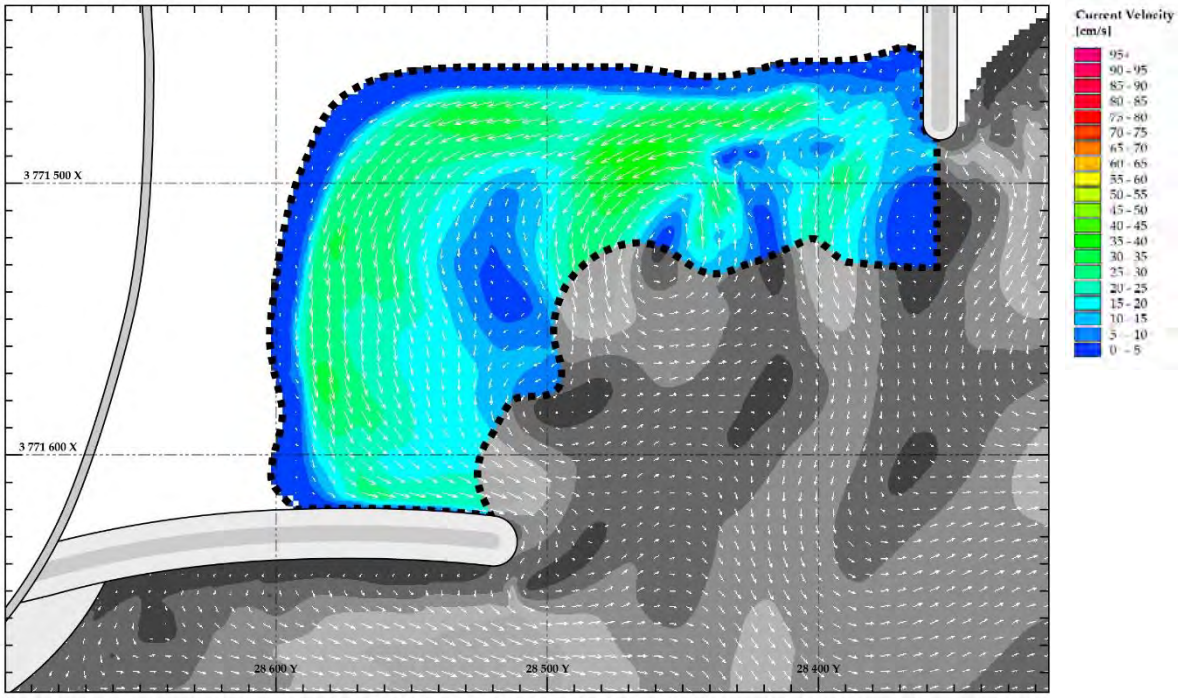

D.2.8.2.4 Velocity Exceedance: Designated Swimming Area

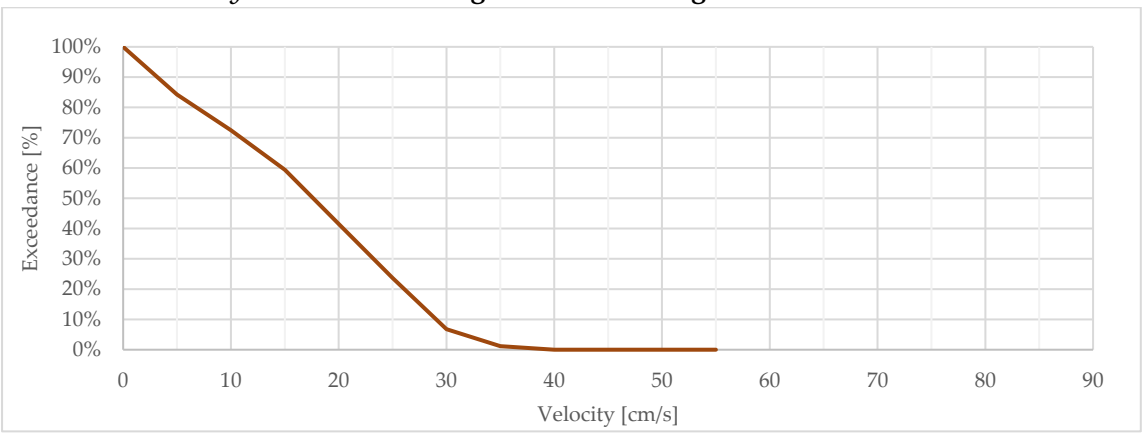

D.2.9 MB610

D.2.9.1 Setup

D.2.9.1.1 Wave Conditions

Water / Tide Level	+0.7m MSL	**Wave Period (T_p)**	12 s
Wave Height (H_s)	1.5m	**Wave Angle**	+ 8°

D.2.9.2 Results

D.2.9.2.1 Current Velocity and Direction Map

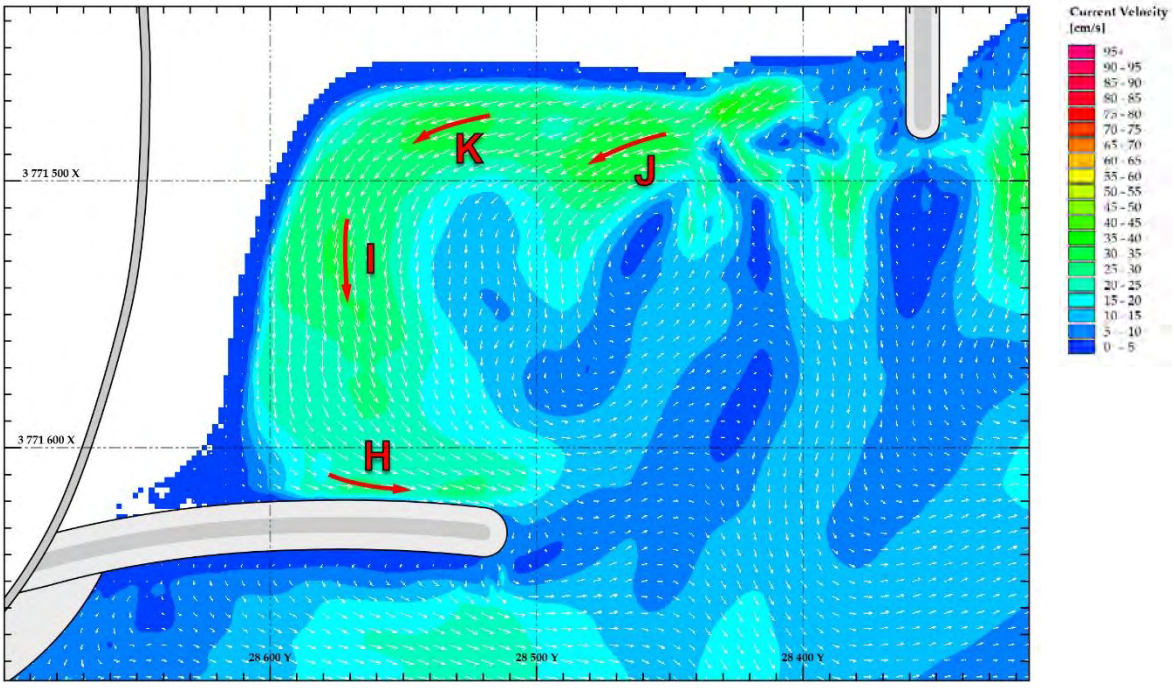

D.2.9.2.2 Measured Peak Flow Velocities

Vector	Class	30m Peak Average Velocities
		u **(absolute)**
H	1	25.2 cm/s
I	2	30.4 cm/s
J	3	34.1 cm/s
K	2	32.1 cm/s

D.2.9.2.3 Area-Velocity: Designated Swimming Area

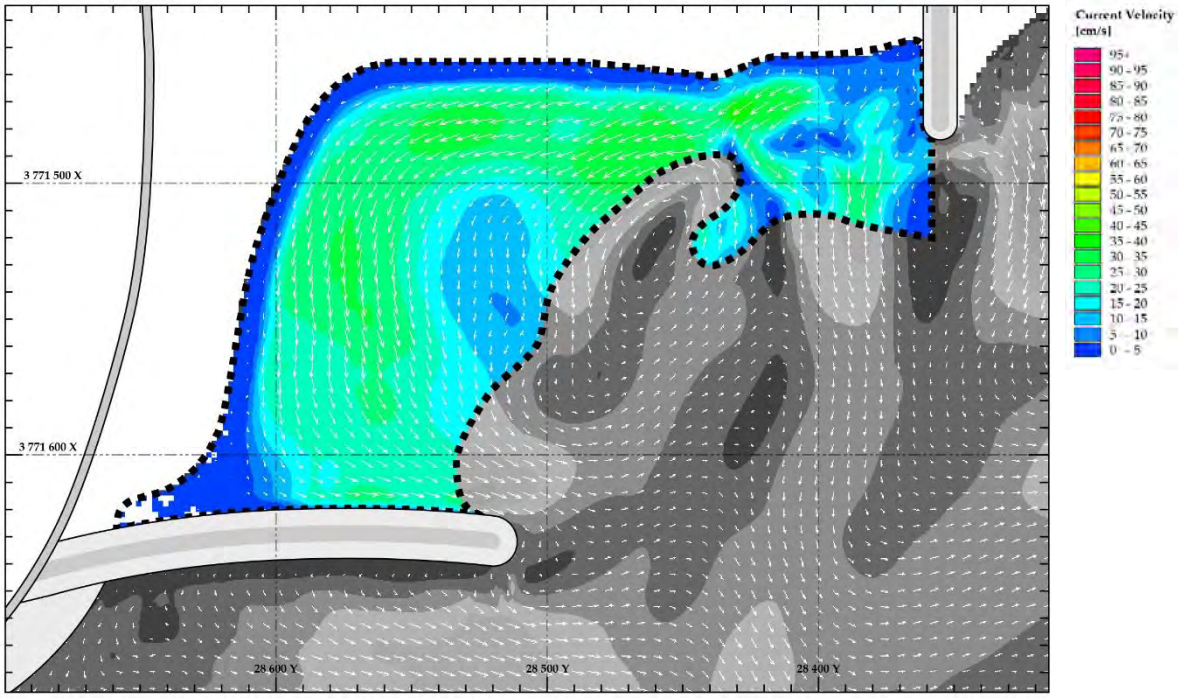

D.2.9.2.4 Velocity Exceedance: Designated Swimming Area

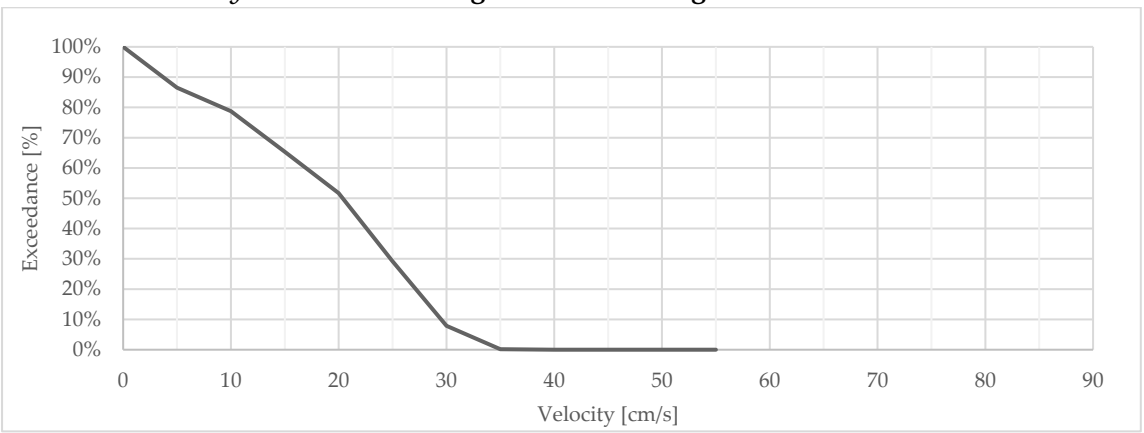

D.2.10 MB710

D.2.10.1 Setup

D.2.10.1.1 Wave Conditions

Water / Tide Level	+0.9m MSL	**Wave Period (T_p)**	12 s
Wave Height (H_s)	1.4m	**Wave Angle**	+ 8°

D.2.10.2 Results

D.2.10.2.1 Current Velocity and Direction Map

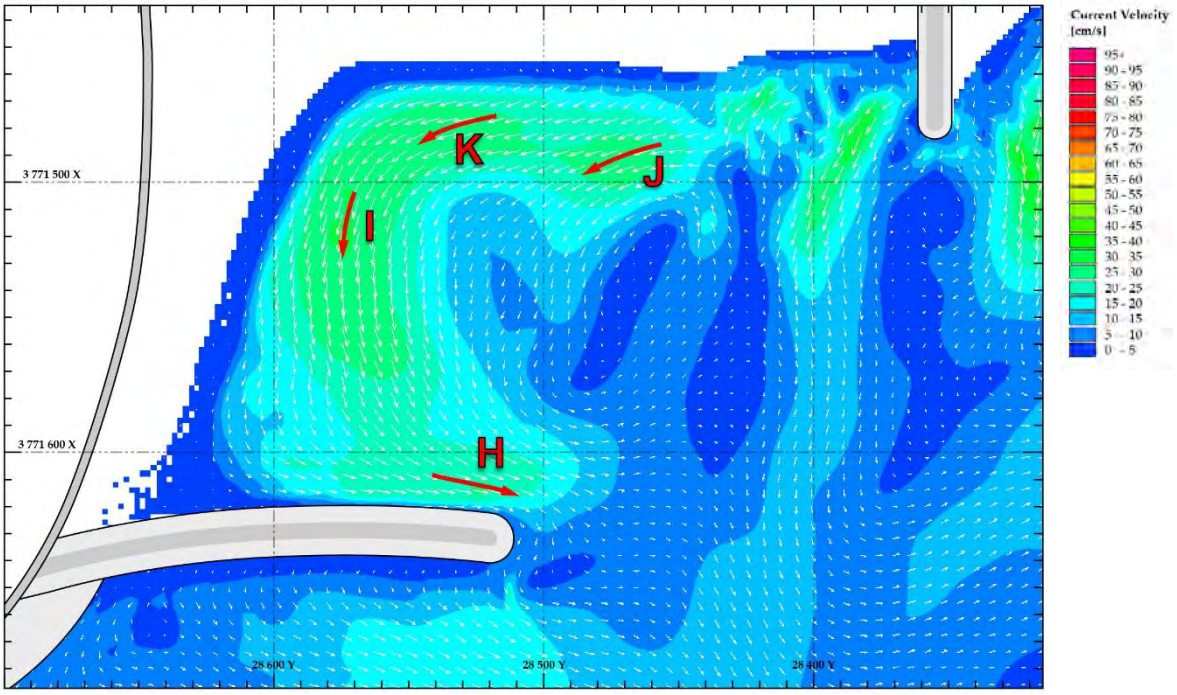

D.2.10.2.2 Measured Peak Flow Velocities

Vector	Class	30m Peak Average Velocities
		u **(absolute)**
H	1	23.7 cm/s
I	2	30.0 cm/s
J	3	26.9 cm/s
K	2	29.2 cm/s

D.2.10.2.3 Area-Velocity: Designated Swimming Area

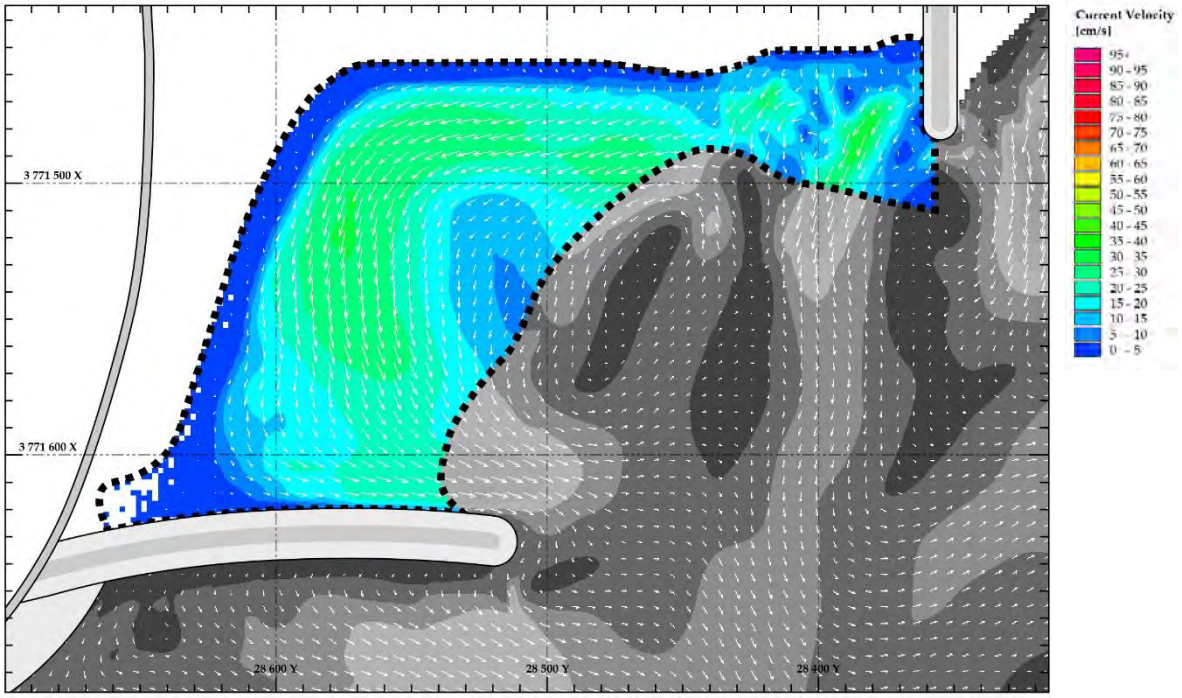

D.2.10.2.4 Velocity Exceedance: Designated Swimming Area

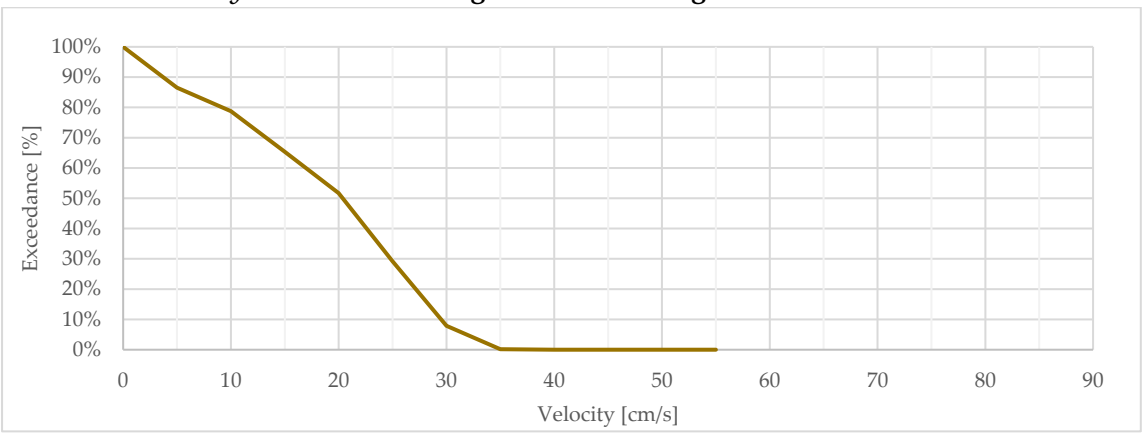

D.2.11 MB720

D.2.11.1 Setup

D.2.11.2 Wave Conditions

Water / Tide Level	+0.9m MSL	**Wave Period (T_p)**	12 s
Wave Height (H_s)	1.8m	**Wave Angle**	+ 8°

D.2.12 Results

D.2.12.1 Current Velocity and Direction Map

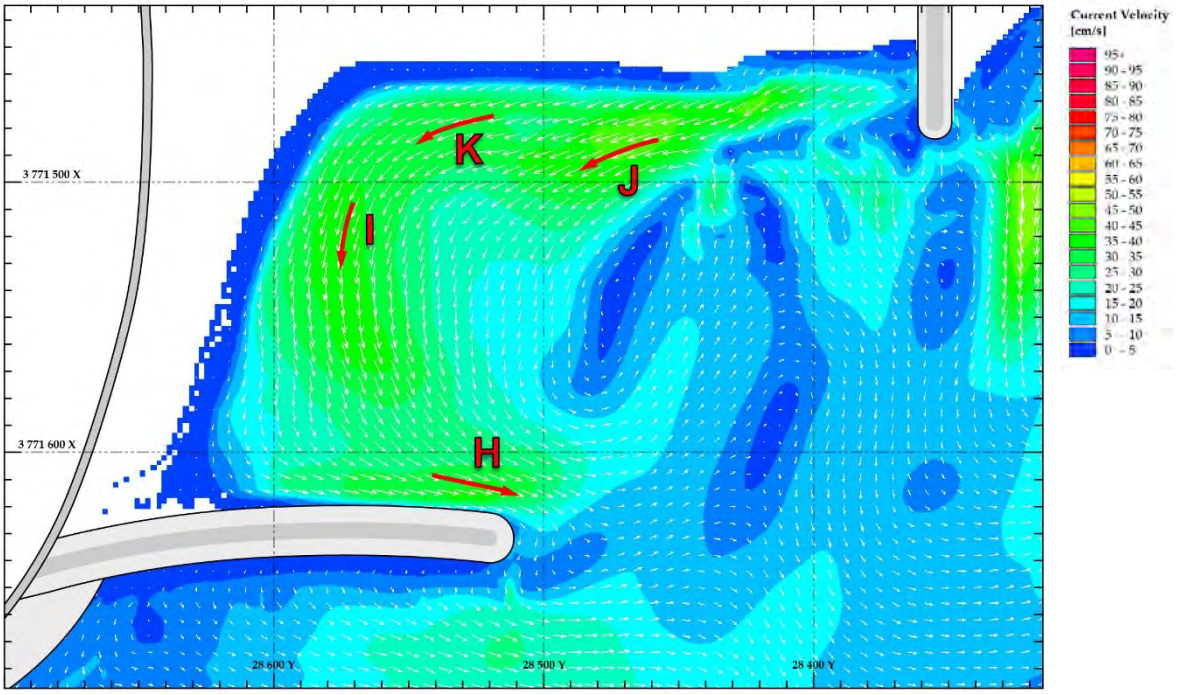

D.2.12.2 Measured Peak Flow Velocities

Vector	Class	30m Peak Average Velocities
		u **(absolute)**
H	1	34.9 cm/s
I	2	36.7 cm/s
J	3	42.0 cm/s
K	2	34.3 cm/s

D.2.12.2.1 Area-Velocity: Designated Swimming Area

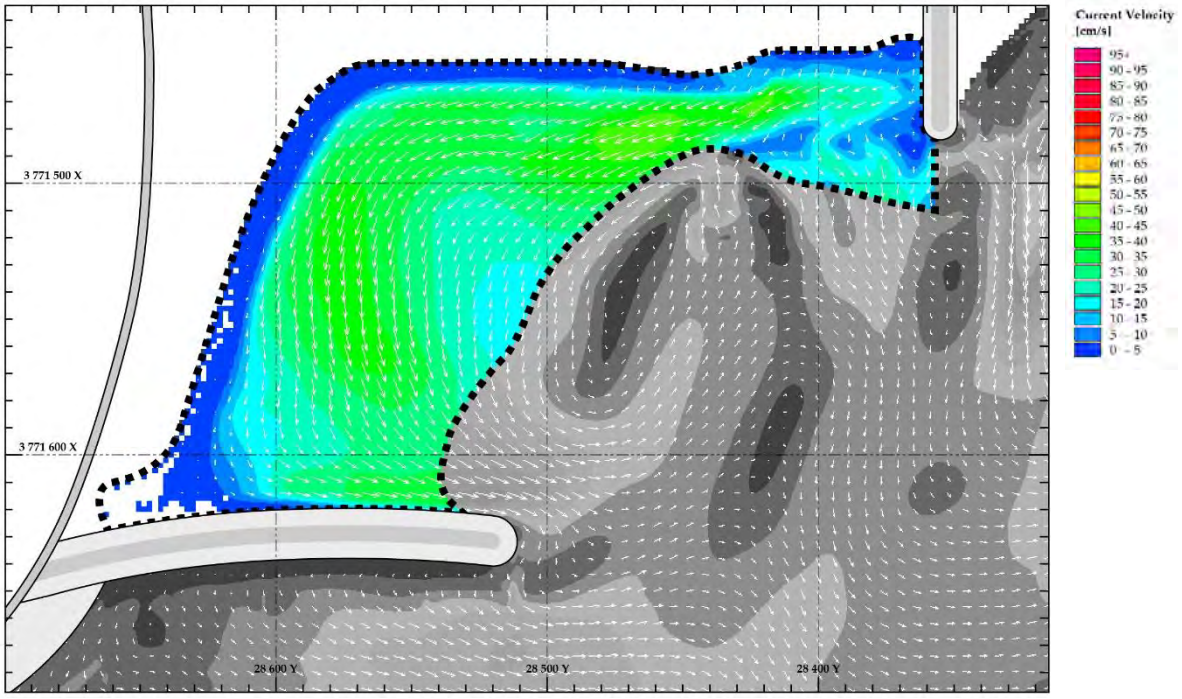

D.2.12.2.2 Velocity Exceedance: Designated Swimming Area

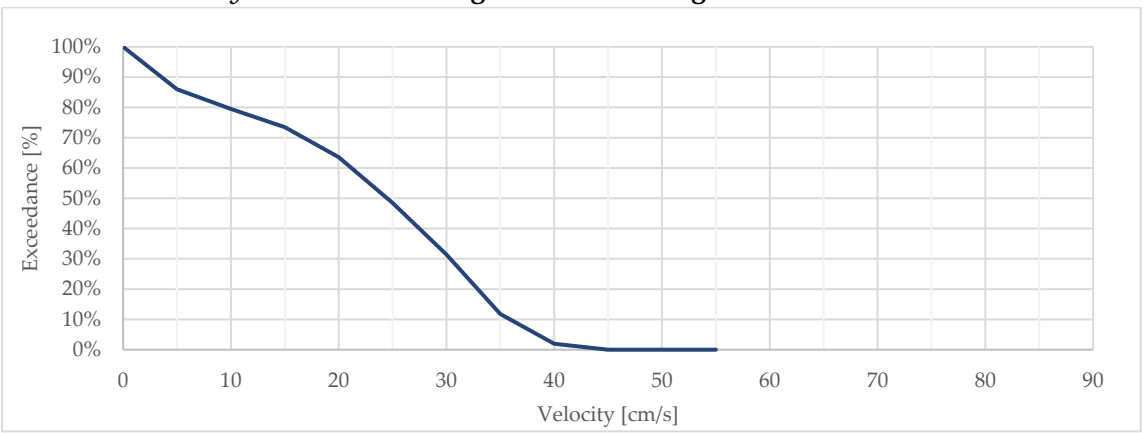

Appendix: E

MBWS-CSIR Results Comparison

E.0 MB610

E.0.1 Setup

E.0.1.1 Description

Baseline test / present situation at Monwabisi

E.0.1.2 Wave Conditions

Water / Tide Level	+0.7m MSL	**Wave Period (T_p)**	12 s
Wave Height (H_s)	1.5m	**Wave Angle**	+ 8°

E.0.2 Results

E.0.2.1 Current Velocity and Vector Map

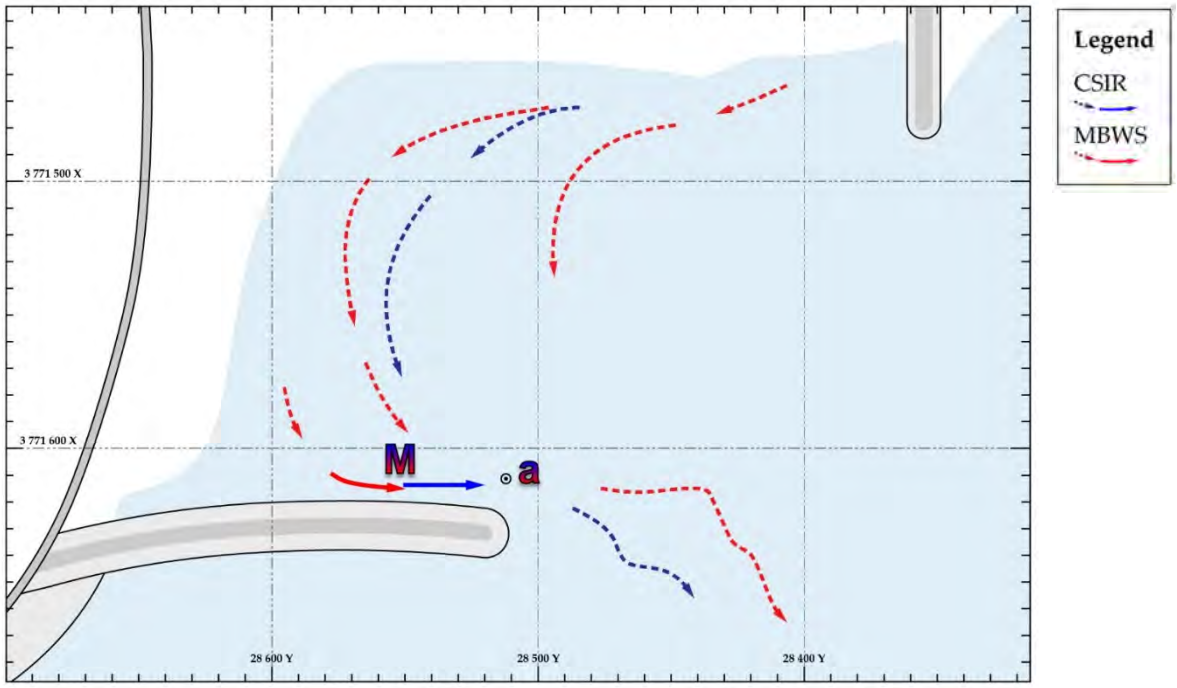

E.0.2.2 Measured Peak Flow Velocities

Vector	CSIR	MBWS		Comparison	
	V_f	u	U_f	Difference	Type
M	100%	25.2 cm/s	100%	-	T1

E.0.2.3 Wave Height & depth

Component	CSIR		MBWS		Difference	
	H_s	d	H_s	d	H_s	d
a	1.2m	2.7m-	0.96m	2.82m	-20%	+4%

E.1 MT001

E.1.1 Setup

E.1.1.1 Description

Short groyne opposite spur head.

E.1.1.2 Wave Conditions

Water / Tide Level	+0.7m MSL	**Wave Period (T_p)**	12 s
Wave Height (H_s)	1.5m	**Wave Angle**	+ 8°

E.1.2 Results

E.1.2.1 Current Velocity and Direction Map

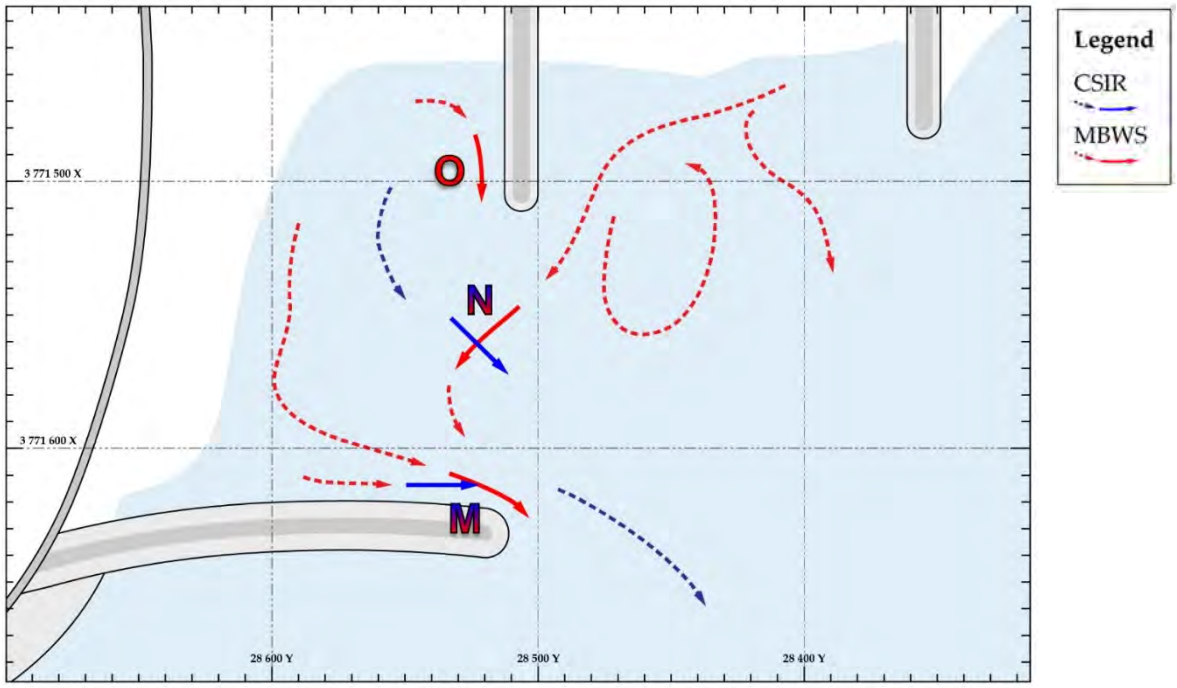

E.1.2.2 Measured Peak Flow Velocities

Vector	CSIR	MBWS		Comparison	
	V_f	u	U_f	Difference	Type
M	66%	19.4 cm/s	77%	+ 11%	T1
N	78%	14.6 cm/s	58%	N/A	T3
O	-	14.3 cm/s	57%	N/A	T3

E.2 MT002

E.2.1 Setup

E.2.1.1 Description

Long Groyne Opposite Spur Head.

E.2.1.2 Wave Conditions

Water / Tide Level	+0.7m MSL	**Wave Period (T_p)**	12 s
Wave Height (H_s)	1.5m	**Wave Angle**	+ 8°

E.2.2 Results

E.2.2.1 Current Velocity and Direction Map

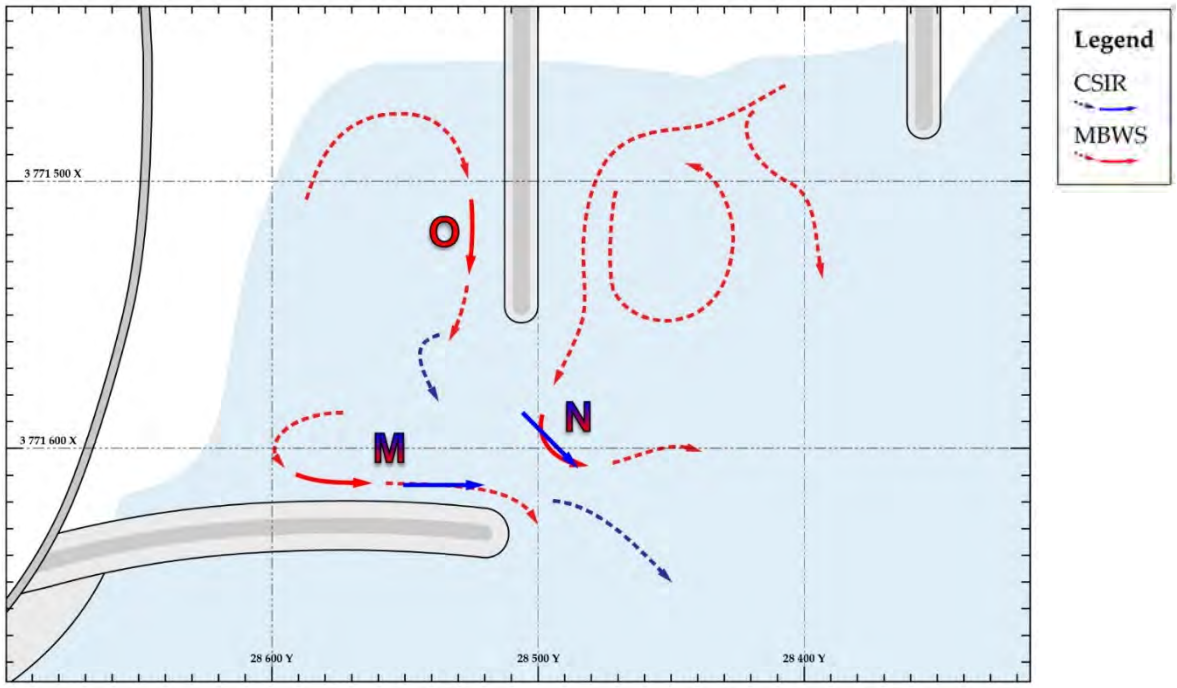

E.2.2.2 Measured Peak Flow Velocities

Vector	CSIR	MBWS		Comparison	
	V_f	u	U_f	Difference	Type
M	41%	18.8 cm/s	75%	34%	T1
N	103%	5.6 cm/s	22%	N/A	T3
O	-	21.7 cm/s	86%	N/A	T3

E.3 MT003

E.3.1 Setup

E.3.1.1 Description

Long groyne away from spur head.

E.3.1.2 Wave Conditions

Water / Tide Level	+0.7m MSL	**Wave Period (T_p)**	12 s
Wave Height (H_s)	1.5m	**Wave Angle**	+ 8°

E.3.2 Results

E.3.2.1 Current Velocity and Direction Map

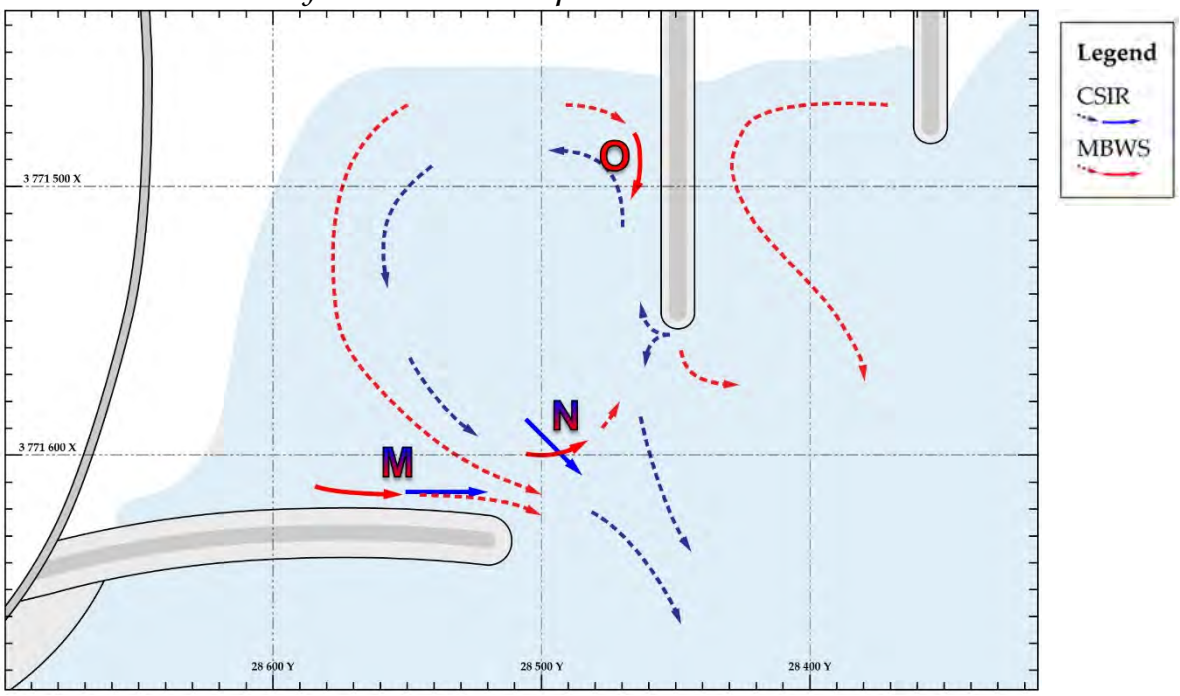

E.3.2.2 Measured Peak Flow Velocities

Vector	CSIR	MBWS		Comparison	
	V_f	u	U_f	Difference	Type
M	56%	22.2 cm/s	88%	32%	T1
N	93%	11.1 cm/s	44%	N/A	T3
O	-	18.2 cm/s	72%	N/A	T3

E.4 MT004

E.4.1 Setup

E.4.1.1 Description

Dog-legged groyne opposite spur head

E.4.1.2 Wave Conditions

Water / Tide Level	+0.7m MSL	**Wave Period (T_p)**	12 s
Wave Height (H_s)	1.5m	**Wave Angle**	+ 8°

E.4.2 Results

E.4.2.1 Current Velocity and Direction Map

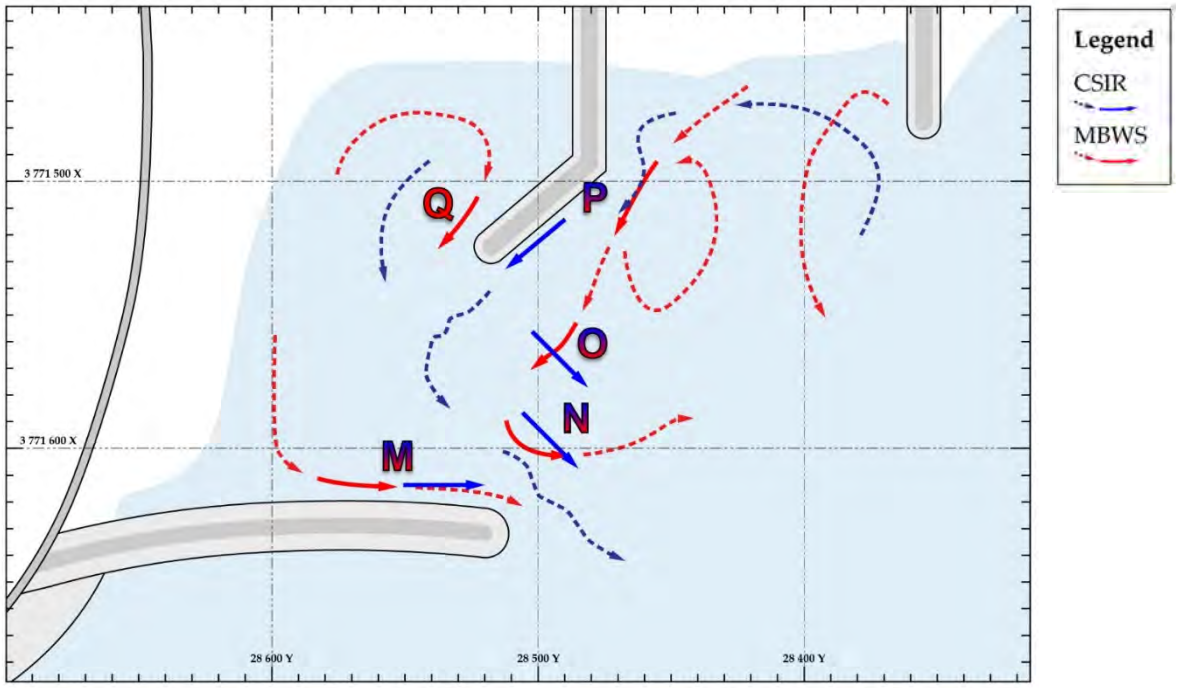

E.4.2.2 Measured Peak Flow Velocities

Vector	CSIR	MBWS		Comparison	
	V_f	u	U_f	Difference	Type
M	56%	20.3 cm/s	80%	24%	T1
N	62%	6.7 cm/s	27%	N/A	T3
O	96%	10.5 cm/s	42%	N/A	T3
P	95%	42.4 cm/s	168%	73%	T2
Q	-	16.0 cm/s	63%	N/A	T3

E.5 MT005

E.5.1 Setup

E.5.1.1 Description

Dog-legged spur off spur head (landward)

E.5.1.2 Wave Conditions

Water / Tide Level	+0.7m MSL	**Wave Period (T_p)**	12 s
Wave Height (H_s)	1.5m	**Wave Angle**	+ 8°

E.5.2 Results

E.5.2.1 Current Velocity and Direction Map

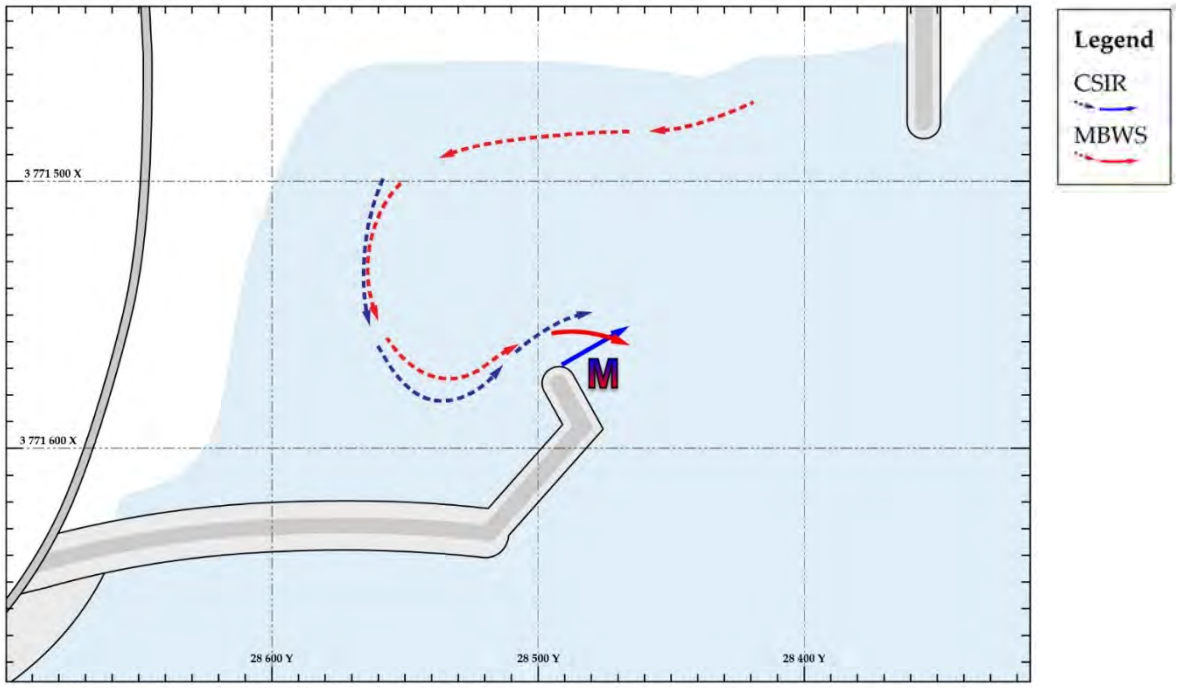

E.5.2.2 Measured Peak Flow Velocities

Vector	CSIR	MBWS		Comparison	
	V_f	u	U_f	Difference	Type
M	156%	38.9 cm/s	154%	-2%	T1

E.6 MT006

E.6.1 Setup

E.6.1.1 Description

Spur off spur head (seaward)

E.6.1.2 Wave Conditions

Water / Tide Level	+0.7m MSL	**Wave Period (T_p)**	12 s
Wave Height (H_s)	1.5m	**Wave Angle**	+ 8°

E.6.2 Results

E.6.2.1 Current Velocity and Direction Map

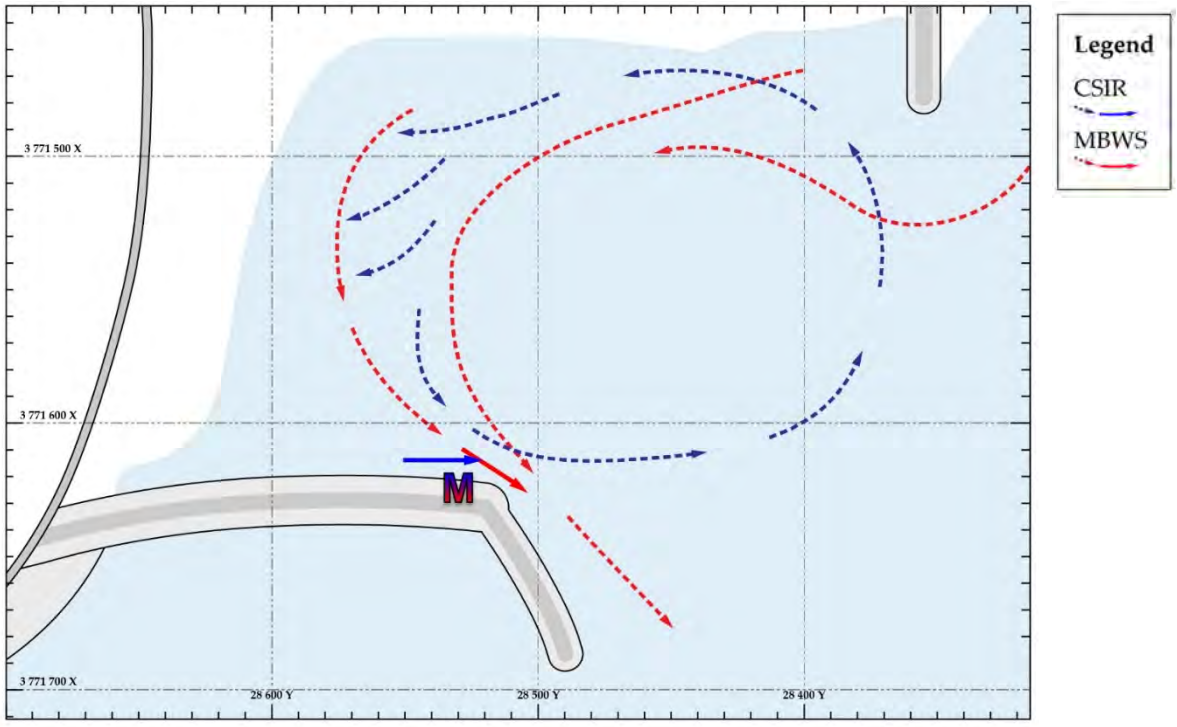

E.6.2.2 Measured Peak Flow Velocities

Vector	CSIR	MBWS		Comparison	
	V_f	u	U_f	Difference	Type
M	119%	30.2 cm/s	120%	1%	T1

E.7 MT007

E.7.1 Setup

E.7.1.1 Description

Dog-legged Groyne off present beach

E.7.1.2 Wave Conditions

Water / Tide Level	+0.7m MSL	**Wave Period (T_p)**	12 s
Wave Height (H_s)	1.5m	**Wave Angle**	+ 8°

E.7.2 Results

E.7.2.1 Current Velocity and Direction Map

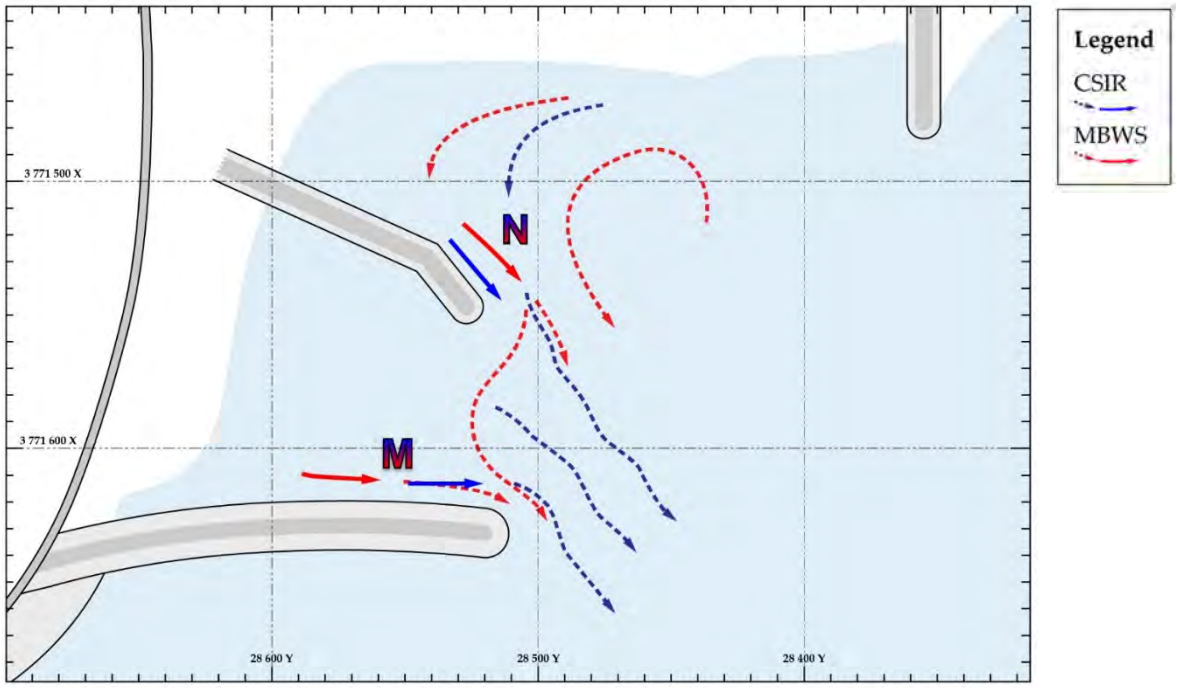

E.7.2.2 Measured Peak Flow Velocities

Vector	CSIR	MBWS		Comparison	
	V_f	u	U_f	Difference	Type
M	65%	14.3 cm/s	57%	-8%	T1
N	155%	43.0 cm/s	171%	16%	T1

E.8 MT008

Note: The MBWS results are unreliable due to the unsuccessful modelling of wave overtopping action.

E.8.1 Setup

E.8.1.1 Description

Lowered end of Spur

E.8.1.2 Wave Conditions

Water / Tide Level	+0.4m MSL	**Wave Period (T_p)**	12 s
Wave Height (H_s)	1.4m	**Wave Angle**	+ 8°

E.8.2 Results

E.8.2.1 Current Velocity and Direction Map

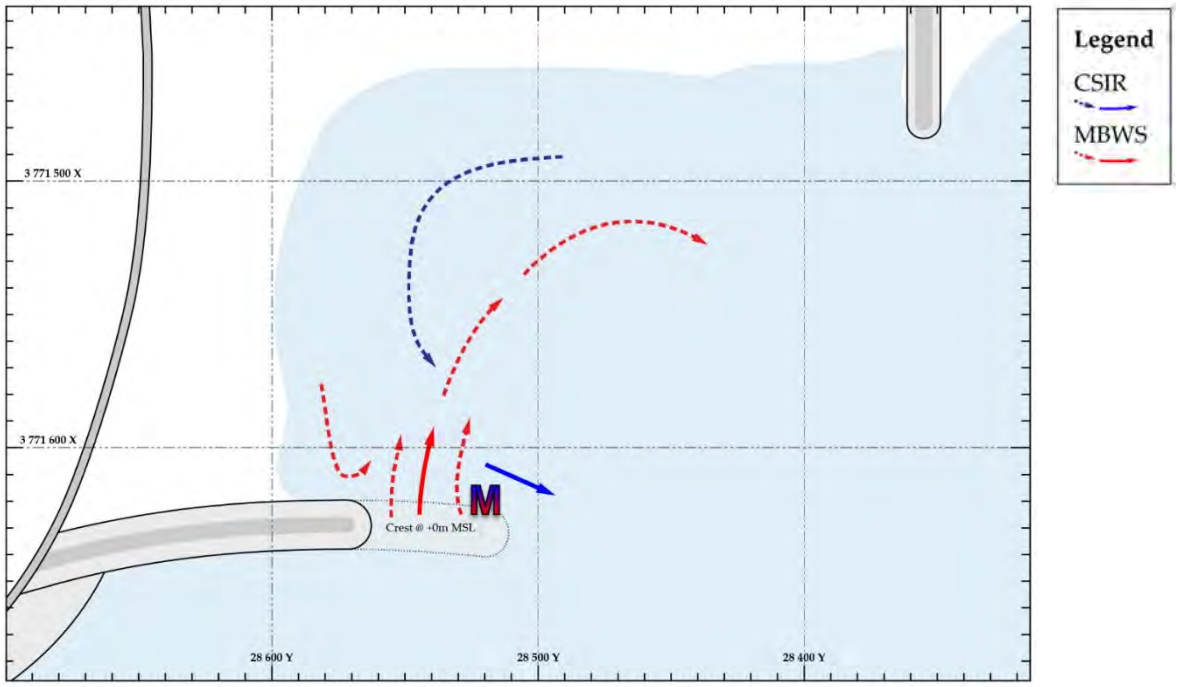

E.8.2.2 Measured Peak Flow Velocities

Vector	CSIR	MBWS*		Comparison	
	V_f	u	U_f	Difference	Type
M	101%	73.0 cm/s	290%	189%	T2

**Unsuccessful simulation of wave overtopping renders the MBWS results unreliable*

E.9 MT009

E.9.1 Setup

E.9.1.1 Description

Hole through spur (west stion)

E.9.1.2 Wave Conditions

Water / Tide Level	+0.7m MSL	**Wave Period (T_p)**	12 s
Wave Height (H_s)	1.5m	**Wave Angle**	+ 8°

E.9.2 Results

E.9.2.1 Current Velocity and Direction Map

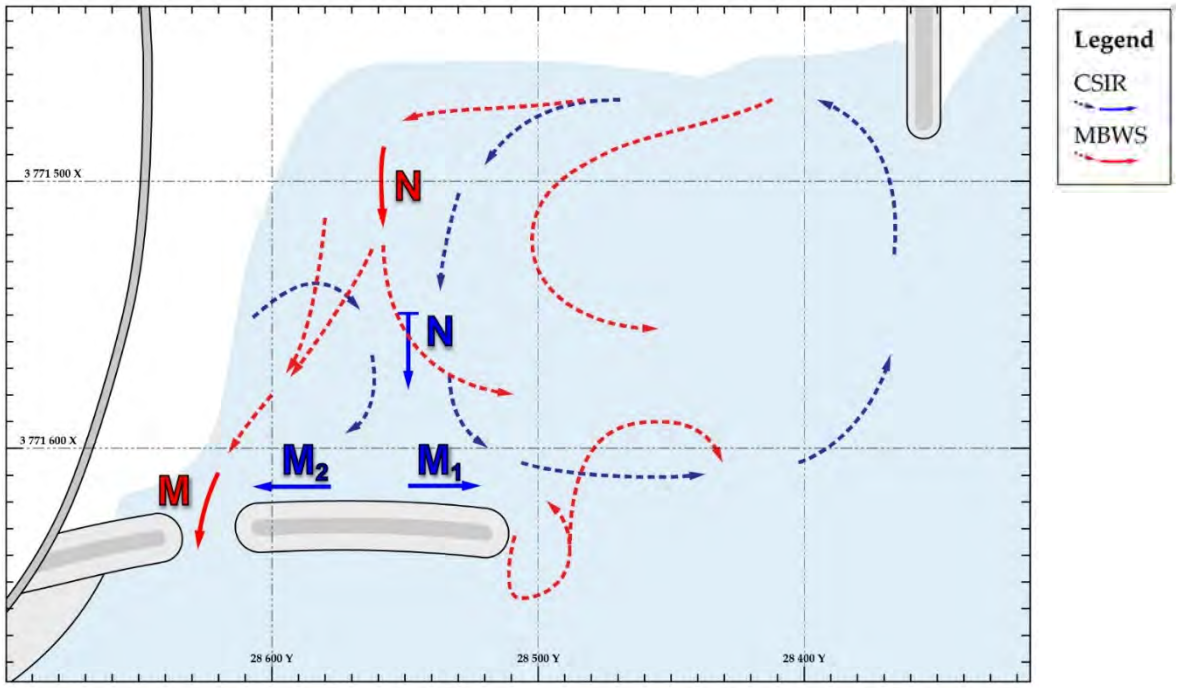

E.9.2.2 Measured Peak Flow Velocities

Vector	CSIR	MBWS		Comparison	
	V_f	u	U_f	Difference	Type
M1	73%	21.1 cm/s	84%	N/A	T3
M2	51%			33%	T2
N	108%	32.0 cm/s	127%	19%	T1

E.10 MT010

E.10.1 Setup

E.10.1.1 Description

Detached breakwater in bay

E.10.1.2 Wave Conditions

Water / Tide Level	+0.4m MSL	**Wave Period (T_p)**	12 s
Wave Height (H_s)	1.4m	**Wave Angle**	+ 8°

E.10.2 Results

E.10.2.1 Current Velocity and Direction Map

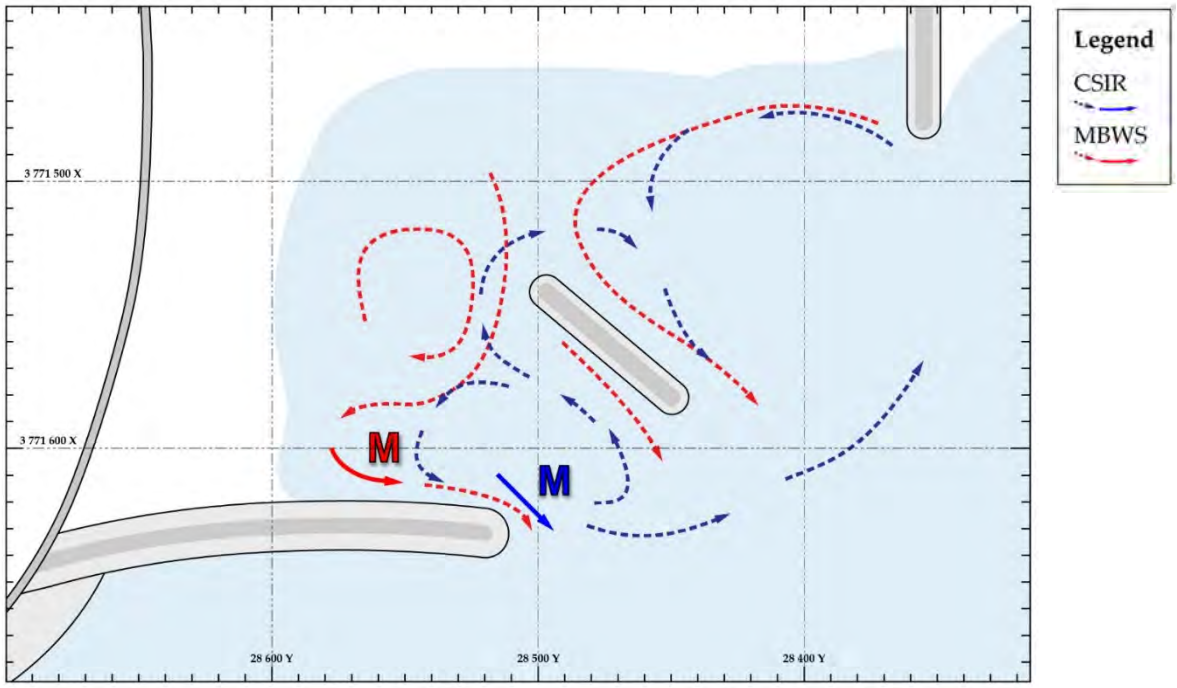

E.10.2.2 Measured Peak Flow Velocities

Vector	CSIR	MBWS		Comparison	
	V_f	u	U_f	Difference	Type
M	124%	41.4 cm/s	164%	40%	T1

E.11 MT011

E.11.1 Setup

E.11.1.1 Descriptio

Raised bed level at spur head

E.11.1.2 Wave Conditions

Water / Tide Level	+0.7m MSL	**Wave Period (T_p)**	12 s
Wave Height (H_s)	1.5m	**Wave Angle**	+ 8°

E.11.2 Results

E.11.2.1 Current Velocity and Direction Map

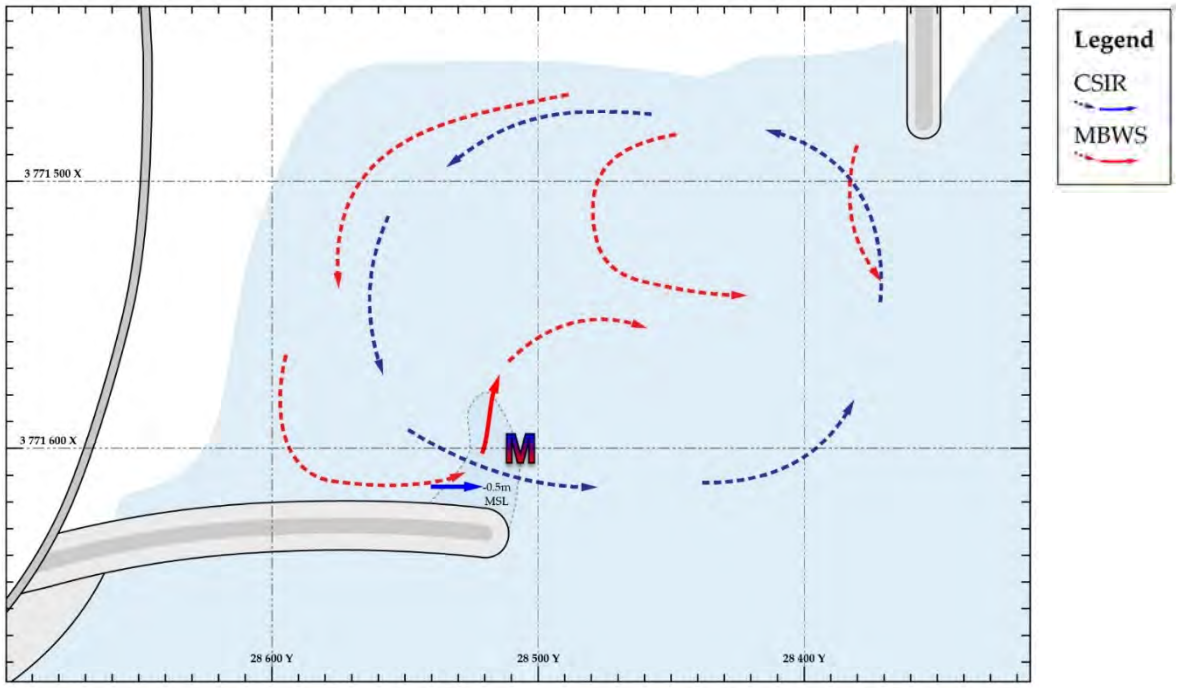

E.11.2.2 Measured Peak Flow Velocities

Vector	CSIR	MBWS		Comparison	
	V_f	u	U_f	Difference	Type
M	73%	46.5 cm/s	184%	111%	T2

E.12 MT012

E.12.1 Setup

E.12.1.1 Description

Hole through spur (West Stion) with Groyne off beach [high water].

E.12.1.2 Wave Conditions

Water / Tide Level	+0.3m MSL	**Wave Period (T_p)**	12 s
Wave Height (H_s)	1.3m	**Wave Angle**	+ 8°

E.12.2 Results

E.12.2.1 Current Velocity and Direction Map

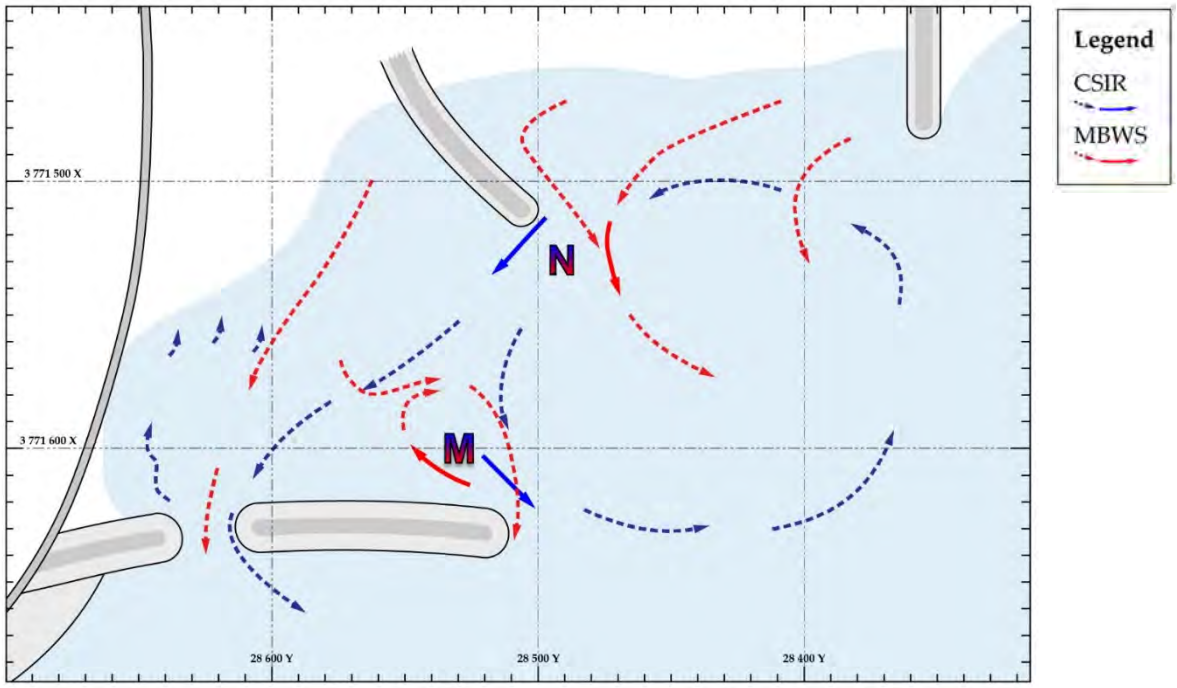

E.12.2.2 Measured Peak Flow Velocities

Vector	CSIR	MBWS		Comparison	
	V_f	u	U_f	Difference	Type
M	91%	18.8 cm/s	74%	-17%	T2
N	107%	39.2 cm/s	156%	49%	T2

E.13 MT013

E.13.1 Setup

E.13.1.1 Description

Hole through spur (West Stion) with Groyne off beach [low water].

E.13.1.2 Wave Conditions

Water / Tide Level	-0.3m MSL	**Wave Period (T_p)**	12 s
Wave Height (H_s)	1.3m	**Wave Angle**	+ 8°

E.13.2 Results

E.13.2.1 Current Velocity and Direction Map

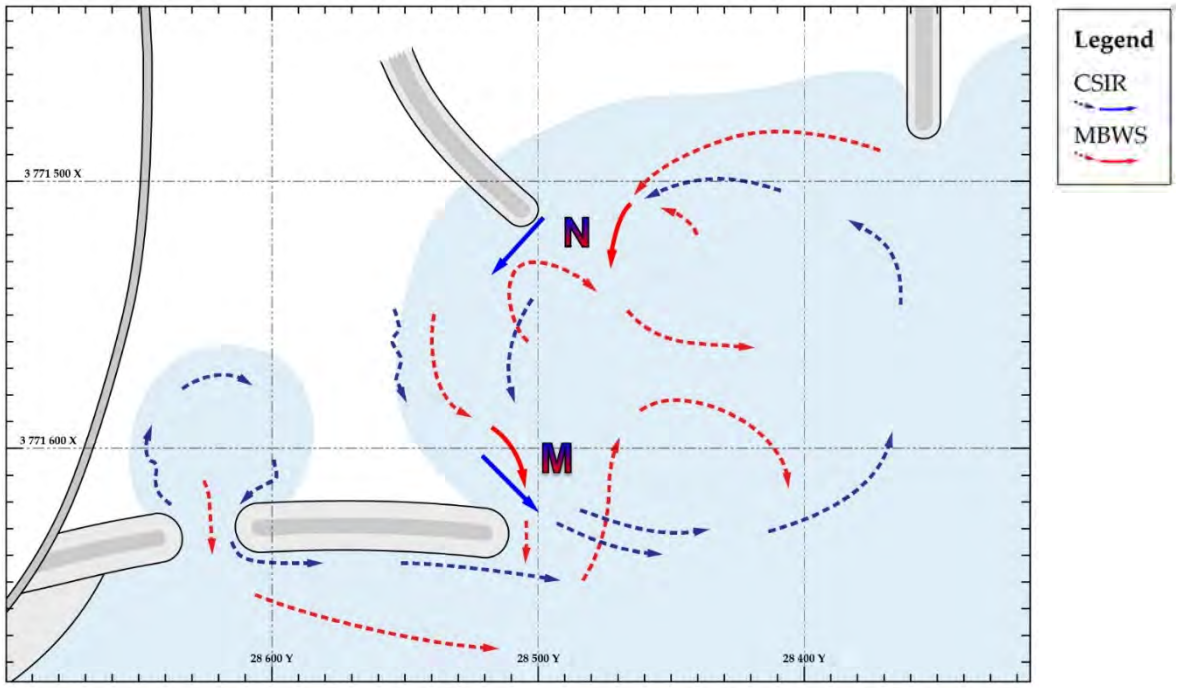

E.13.2.2 Measured Peak Flow Velocities

Vector	CSIR	MBWS		Comparison	
	V_f	u	U_f	Difference	Type
M	109%	20.8 cm/s	82%	-27%	T1
N	0%	46.4 cm/s	184%	184%	T2

E.14 MT014

Note: The MBWS results are unreliable due to the unsuccessful modelling of wave overtopping action.

E.14.1 Setup

E.14.1.1 Description

Lowered stion in spur (east) with groyne off beach [high water]

E.14.1.2 Wave Conditions

Water / Tide Level	+0.3m MSL	**Wave Period (T_P)**	12 s
Wave Height (H_s)	1.3m	**Wave Angle**	+ 8°

E.14.2 Results

E.14.2.1 Current Velocity and Direction Map

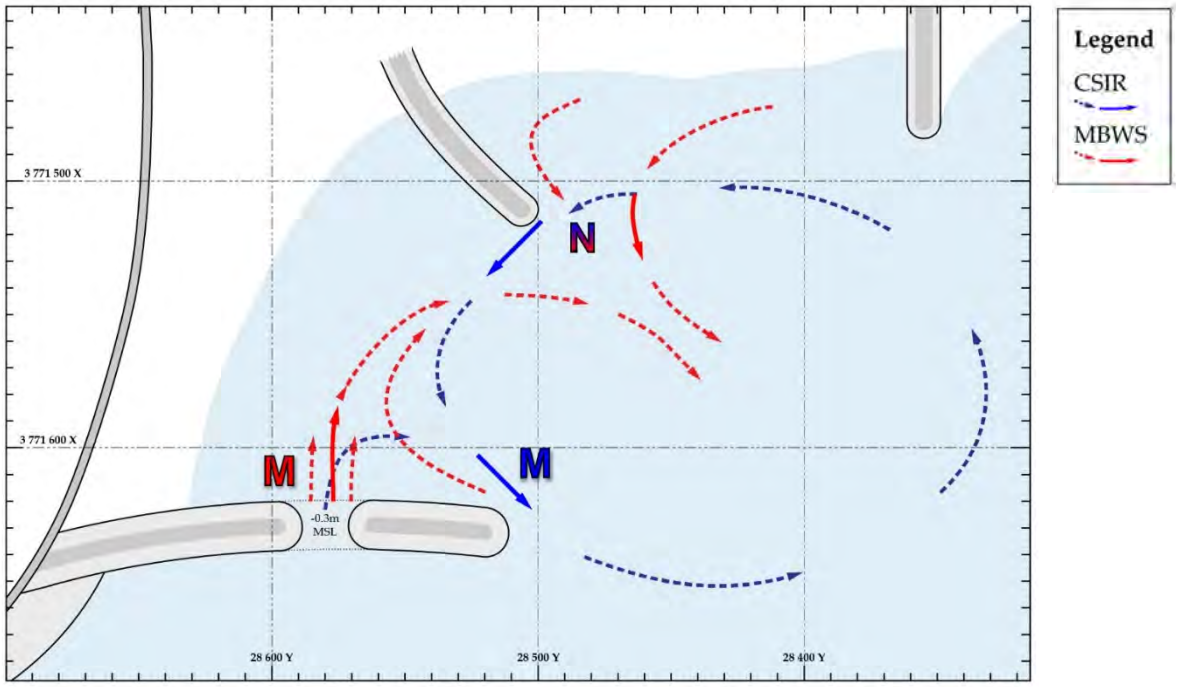

E.14.2.2 Measured Peak Flow Velocities

Vector	CSIR	MBWS*		Comparison	
	V_f	u	U_f	Difference	Type
M	104%	82.3 cm/s	326%	222%	T2
N	91%	37.6 cm/s	149%	58%	T2

**Unsuccessful simulation of wave overtopping renders the MBWS results unreliable*

E.15 MT015

Note: The MBWS results are unreliable due to the unsuccessful modelling of wave overtopping action.

E.15.1 Setup

E.15.1.1 Description

Lowered stion in spur (east) with groyne off beach [low water]

E.15.1.2 Wave Conditions

Water / Tide Level	-0.3m MSL	**Wave Period (T_P)**	12 s
Wave Height (H_s)	1.3m	**Wave Angle**	+ 8°

E.15.2 Results

E.15.2.1 Current Velocity and Direction Map

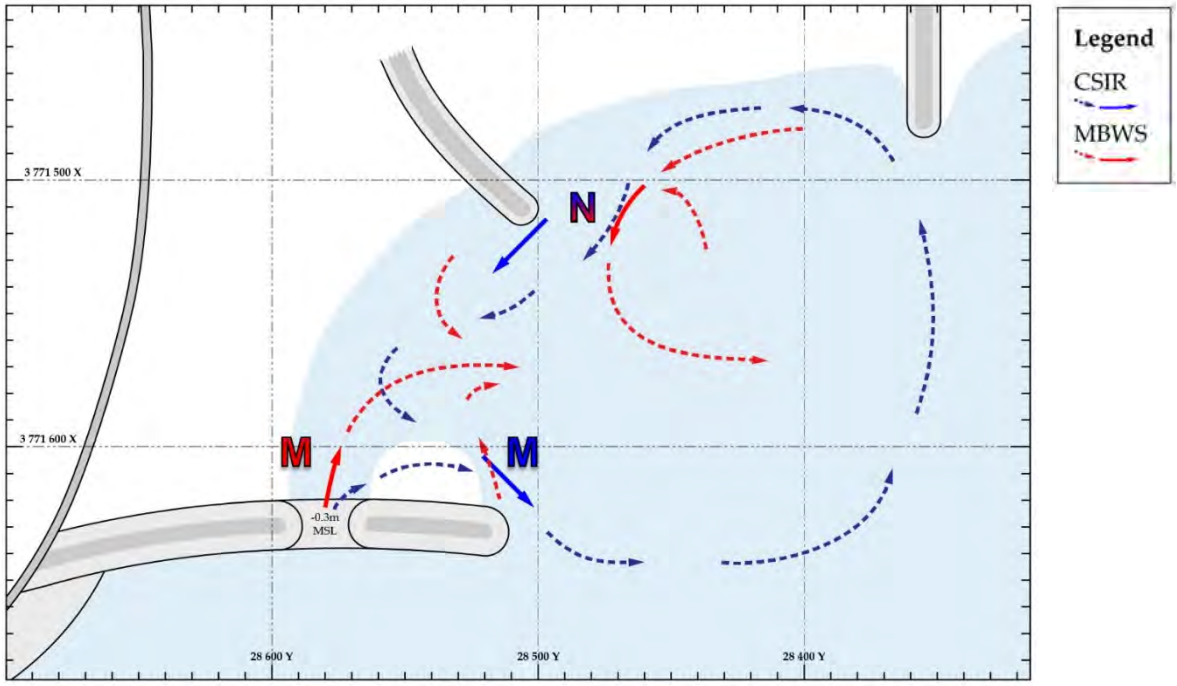

E.15.2.2 Measured Peak Flow Velocities

Vector	CSIR	MBWS*		Comparison	
	V_f	u	U_f	Difference	Type
M	88%	46.5 cm/s	186%	91%	T2
N	0%	47.9 cm/s	190%	190%	T2

**Unsuccessful simulation of wave overtopping renders the MBWS results unreliable*

E.16 MT016

E.16.1 Setup

E.16.1.1 Description

T-Groyne off beach

E.16.1.2 Wave Conditions

Water / Tide Level	+0.45m MSL	**Wave Period (T_p)**	12 s
Wave Height (H_s)	1.4m	**Wave Angle**	+ 8°

E.16.2 Results

E.16.2.1 Current Velocity and Direction Map

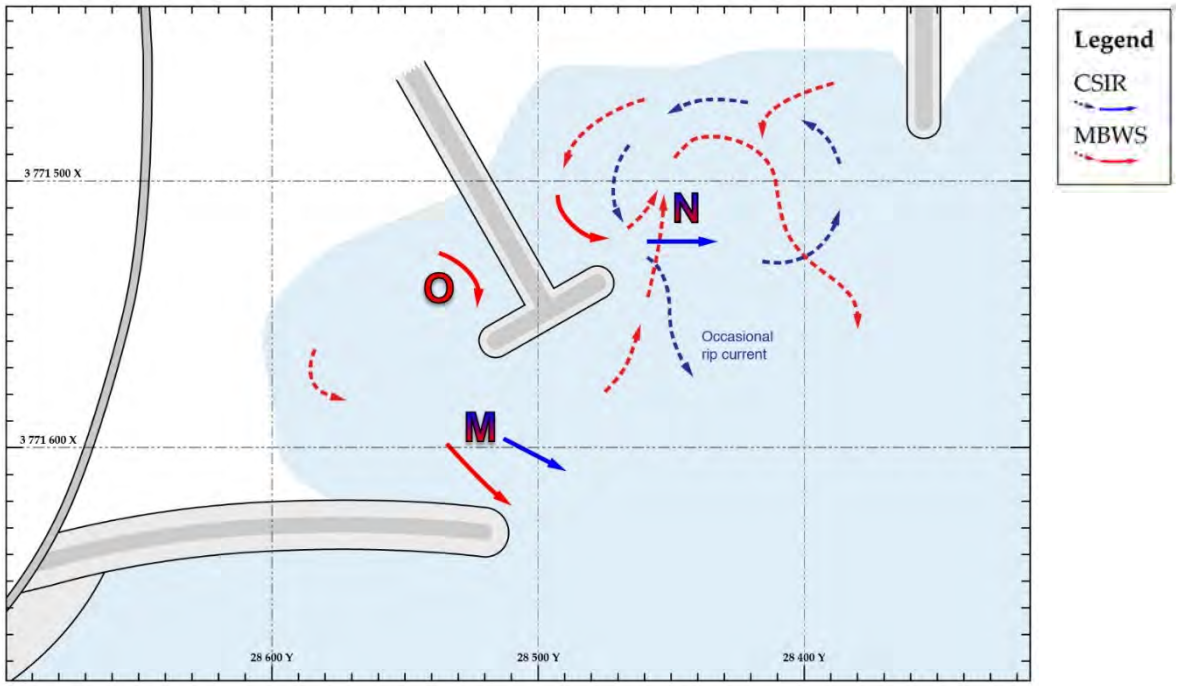

E.16.2.2 Measured Peak Flow Velocities

Vector	CSIR	MBWS*		Comparison	
	V_f	u	U_f	Difference	Type
M	≤ 37%	6.7 cm/s	27%	27%	T1
N	≤ 46%	28.0 cm/s	111%	≥ 65%	T2
O	-	12.9 cm/s	51%	N/A	T3

E.17 MT017

E.17.1 Setup

E.17.1.1 Description

T-Groyne off beach

E.17.1.2 Wave Conditions

Water / Tide Level	+0.9m MSL	**Wave Period (T_p)**	12 s
Wave Height (H_s)	1.4m	**Wave Angle**	+ 8°

E.17.2 Results

E.17.2.1 Current Velocity and Direction Map

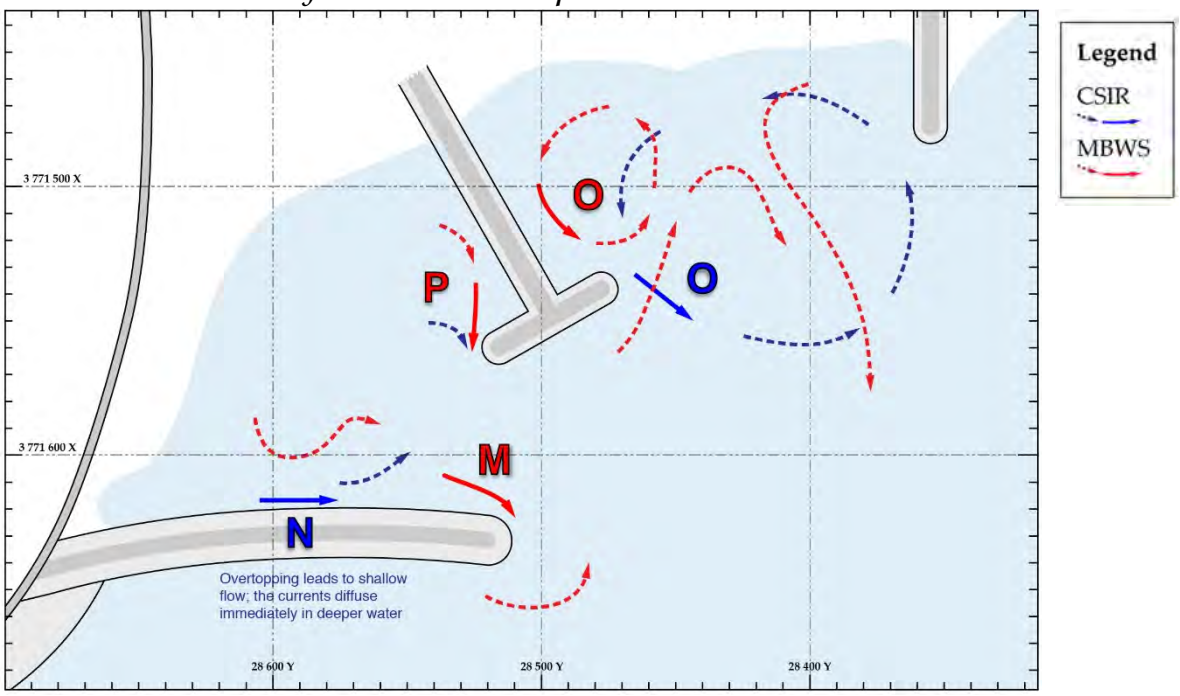

E.17.2.2 Measured Peak Flow Velocities

Vector	CSIR	MBWS*		Comparison	
	V_f	u	U_f	Difference	Type
M	-	5.7 cm/s	23%	N/A	T3
N	84%	*	-	-	-
O	91%	25.5 cm/s	101%	10%	T2
P	-	13.1 cm/s	44%	N/A	T3

**Crest overtopping not simulated in MBWS model*

E.18 MT018

E.18.1 Setup

E.18.1.1 Description

T-Groyne off beach

E.18.1.2 Wave Conditions

Water / Tide Level	+0.9m MSL	**Wave Period (T_p)**	12 s
Wave Height (H_s)	1.8m	**Wave Angle**	+ 8°

E.18.2 Results

E.18.2.1 Current Velocity and Direction Map

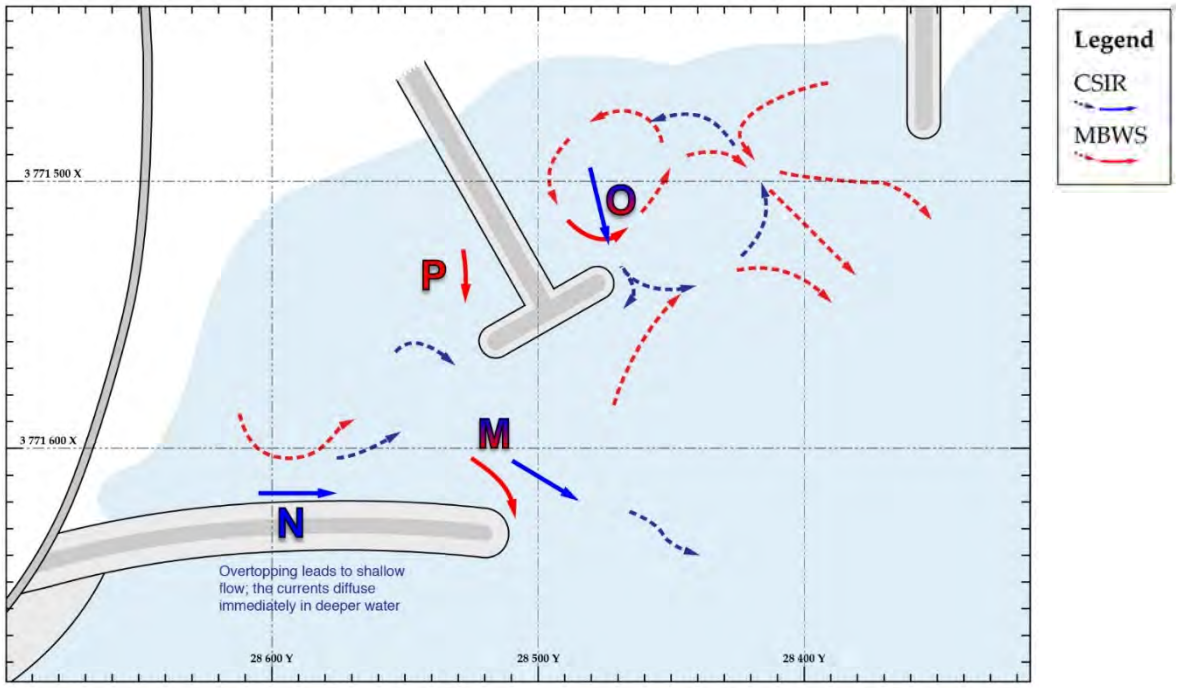

E.18.2.2 Measured Peak Flow Velocities

Vector	CSIR	MBWS*		Comparison	
	V_f	u	U_f	Difference	Type
M	52%	8.5 cm/s	34%	-18%	T1
N	114%	*	-	-	-
O	63%	25.1 cm/s	100%	37%	T2
P		14.7 cm/s	40%	N/A	T3

**Crest overtopping not simulated in MBWS model*

E.19 MT019

E.19.1 Setup

E.19.1.1 Description

T-Groyne off beach

E.19.1.2 Wave Conditions

Water / Tide Level	-0.1m MSL	**Wave Period (T_p)**	12 s
Wave Height (H_s)	1.0m	**Wave Angle**	+ 8°

E.19.2 Results

E.19.2.1 Current Velocity and Direction Map

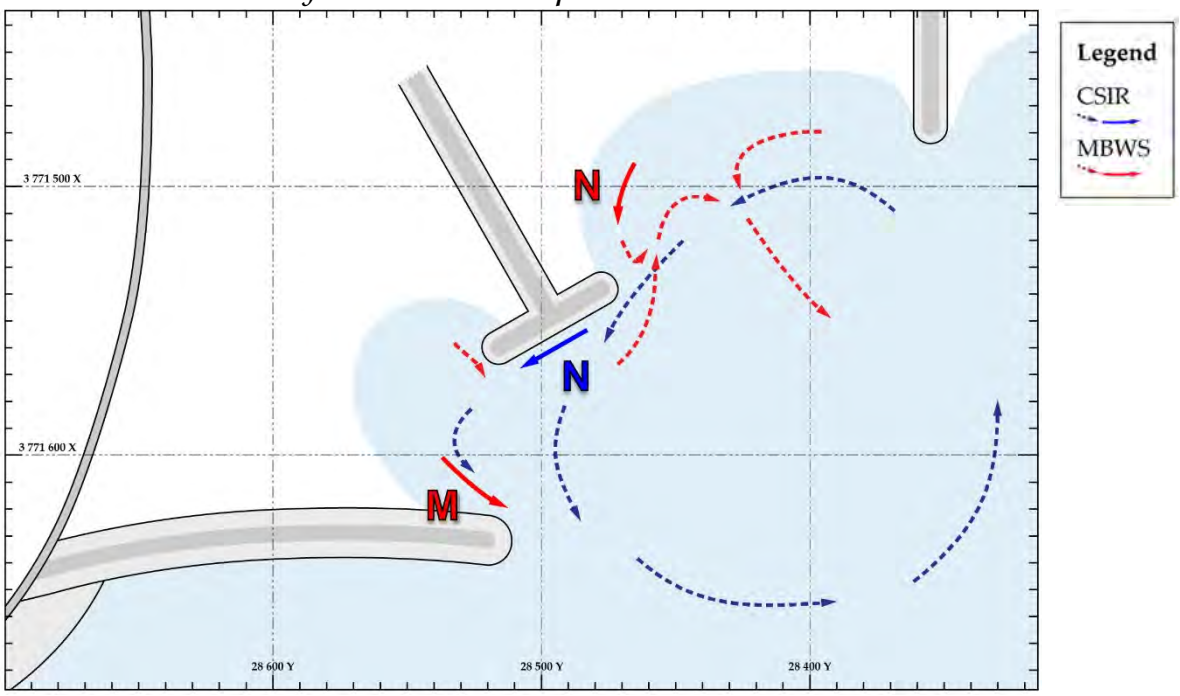

E.19.2.2 Measured Peak Flow Velocities

Vector	CSIR	MBWS*		Comparison	
	V_f	u	U_f	Difference	Type
M		6.1 cm/s	34%	N/A	T3
N	*	39.0 cm/s	155%	N/A	T3

**Very inconsistent flow, no average velocity measured*

E.20 MT020

E.20.1 Setup

E.20.1.1 Description

T-Groyne off beach

E.20.1.2 Wave Conditions

Water / Tide Level	-0.1m MSL	**Wave Period (T_p)**	12 s
Wave Height (H_s)	1.4m	**Wave Angle**	+ 8°

E.20.2 Results

E.20.2.1 Current Velocity and Direction Map

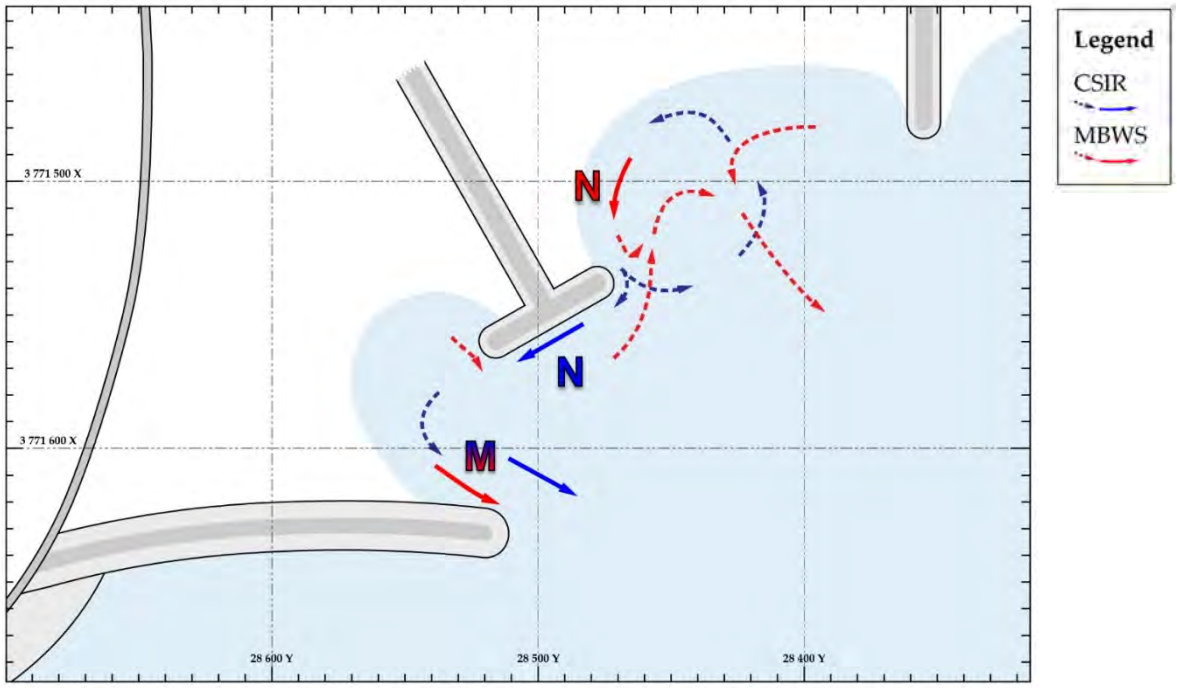

E.20.2.2 Measured Peak Flow Velocities

Vector	CSIR	MBWS*		Comparison	
	V_f	u	U_f	Difference	Type
M	30%	8.9 cm/s	35%	5%	T1
N	29%	44.9 cm/s	178%	149%	T2

E.21 MT021

E.21.1 Setup

E.21.1.1 Description

T-Groyne off beach

E.21.1.2 Wave Conditions

Water / Tide Level	+0.4m MSL	**Wave Period (T_p)**	12 s
Wave Height (H_s)	1.1m	**Wave Angle**	+ 8°

E.21.2 Results

E.21.2.1 Current Velocity and Direction Map

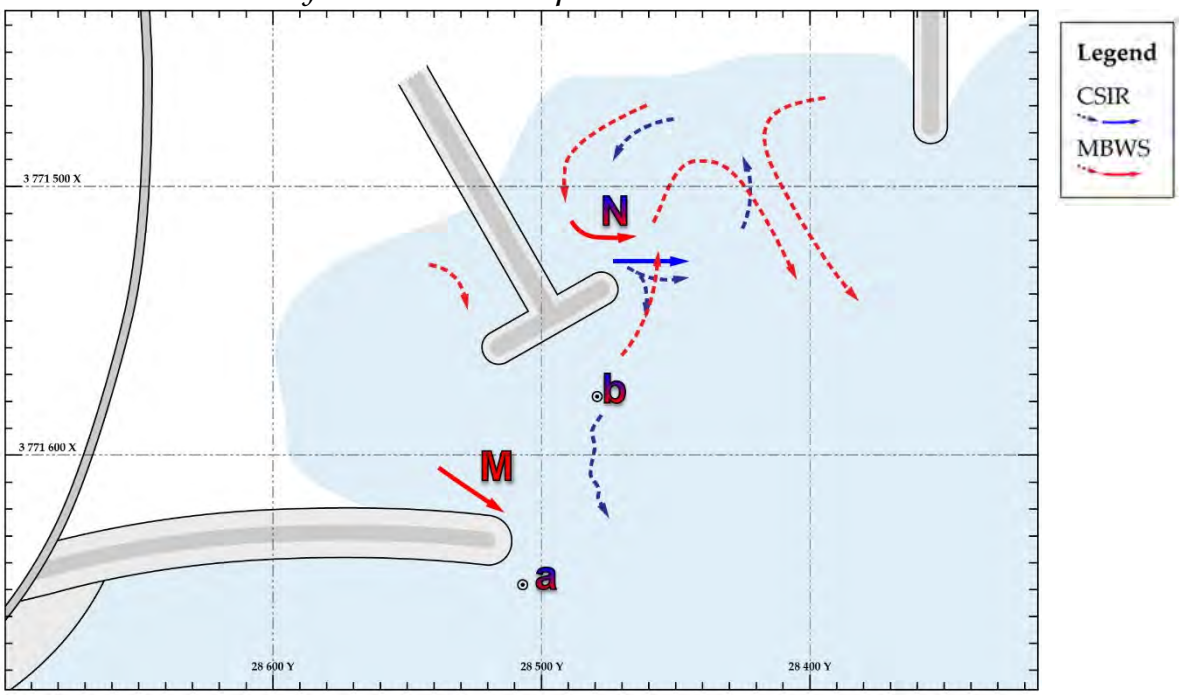

E.21.2.2 Measured Peak Flow Velocities

Vector	CSIR	MBWS*		Comparison	
	V_f	u	U_f	Difference	Type
M		5.4 cm/s	21%		T3
N	60%	24.4 cm/s	97%	37%	T2

E.21.2.3 Wave Height

Component	CSIR H_s	MWBWS H_s	Difference
a	1.1m	1.08	-2%
b	1.4m	1.01	-28%

E.22 MT022

E.22.1 Setup

E.22.1.1 Description

T-Groyne off beach

E.22.1.2 Wave Conditions

Water / Tide Level	+0.4m MSL	**Wave Period (T_p)**	8 s
Wave Height (H_s)	1.1m	**Wave Angle**	+ 8°

E.22.2 Results

E.22.2.1 Current Velocity and Direction Map

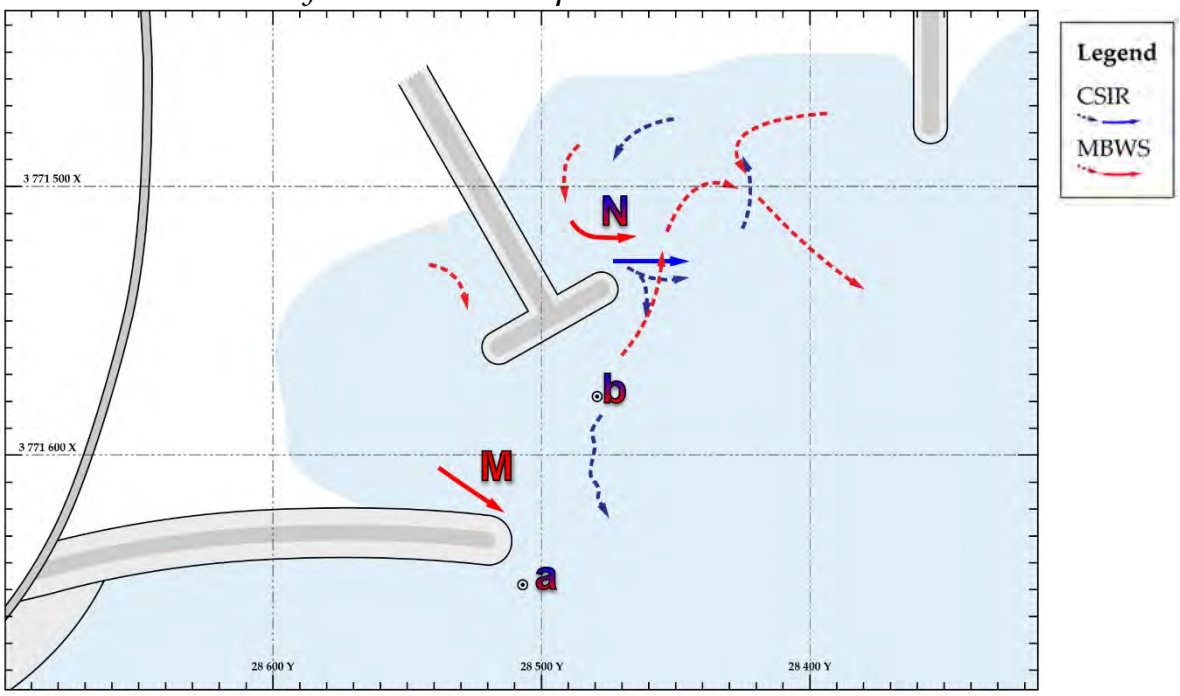

E.22.2.2 Measured Peak Flow Velocities

Vector	CSIR	MBWS*		Comparison	
	V_f	u	U_f	Difference	Type
M		6.6 cm/s	26%		T3
N	60%	20.1 cm/s	80%	20%	T2

E.22.2.3 Wave Height

Component	CSIR H	MWBWS H	Difference
a	1.4m	0.82	-41%
b	1.3m	0.99	-24%

E.23 MT023

E.23.1 Setup

E.23.1.1 Description

T-Groyne off (built-up) beach

E.23.1.2 Wave Conditions

Water / Tide Level	+0.4m MSL	**Wave Period (T_p)**	12 s
Wave Height (H_s)	1.4m	**Wave Angle**	+ 8°

E.23.2 Results

E.23.2.1 Current Velocity and Direction Map

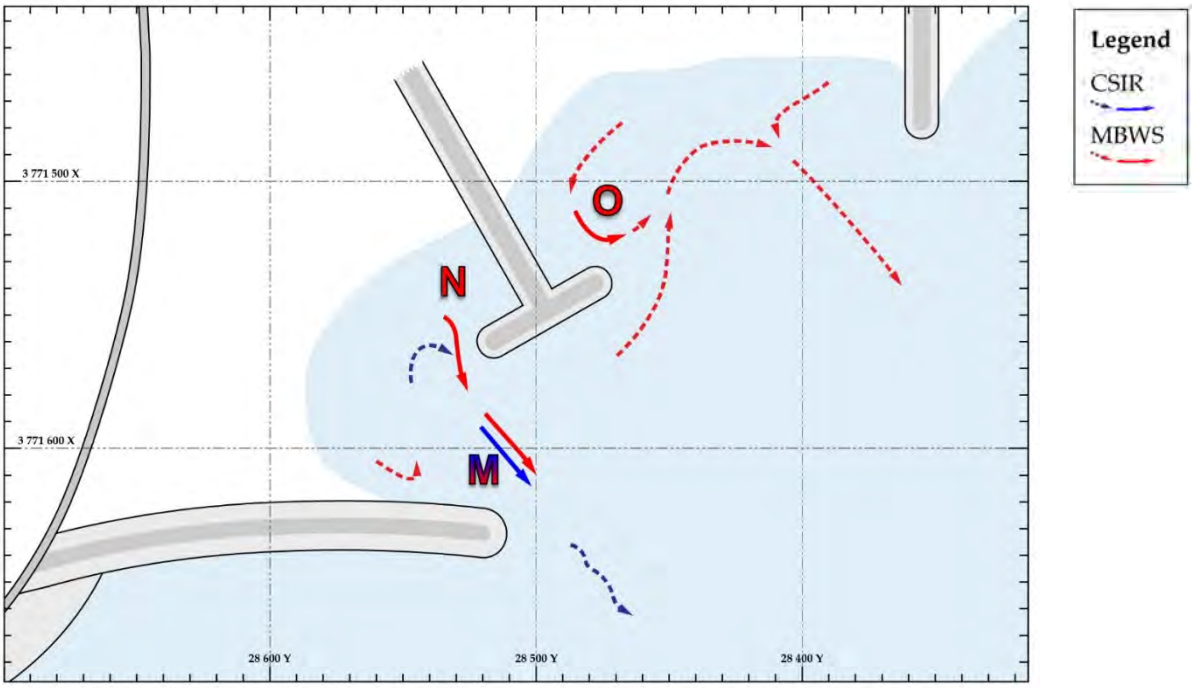

E.23.2.2 Measured Peak Flow Velocities

Vector	CSIR	MBWS*		Comparison	
	V_f	u	U_f	Difference	Type
M	73%	9.5 cm/s	38%	-35%	T1
N	-	14.7 cm/s	45%	N/A	T3
O		27.6 cm/s	110%	N/A	T3

E.24 MT024

E.24.1 Setup

E.24.1.1 Description

T-Groyne off (denuded) beach

E.24.1.2 Wave Conditions

Water / Tide Level	+0.4m MSL	**Wave Period (T_p)**	12 s
Wave Height (H_s)	1.4m	**Wave Angle**	+ 8°

E.24.2 Results

E.24.2.1 Current Velocity and Direction Map

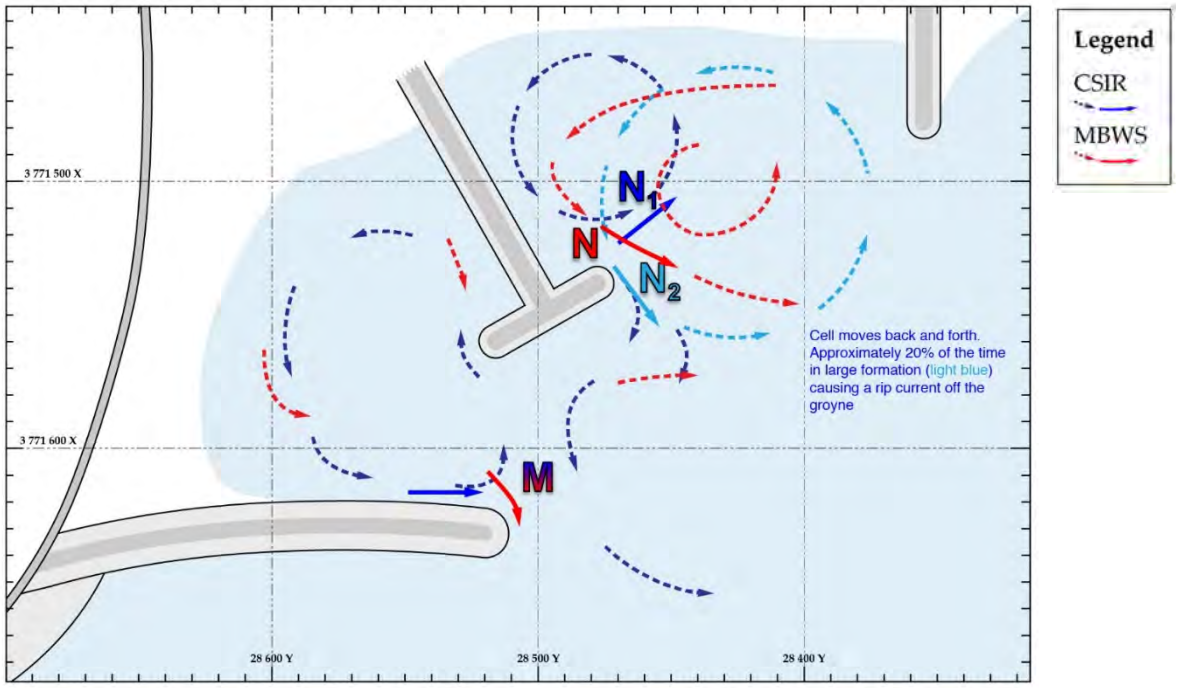

E.24.2.2 Measured Peak Flow Velocities

Vector	CSIR	MBWS*		Comparison	
	V_f	u	U_f	Difference	Type
M	≤ 16%	10.3 cm/s	41%	≥ 25%	T1
N_1	81%	43.5 cm/s*	172%	91%	T2
N_2	117%			55%	T2

**CSIR simulation had a moving circulation cell. The phase averaged measurements of the MBWS simulation did not record any cyclic event, thus a single measurement was used for the comparison*

Appendix: F

Summary of Results: Tables & Figures

F.1 MBWS Analysis

F.1.1 Summary of velocity measurements, by class velocity

Proposed Solutions									Relative Baseline				Relative Change			
ID	Group	Short Description	WL (m MSL)	H_s (m)	T_p (s)	u [cm/s]			ID	u [cm/s]			U_r [%]			
						C1	C2	C3		C1	C2	C3	C1	C2	C3	
MT001	A	*Short groyne opposite spur head.*	0.7	1.5	12	19.4	17.4	39.1	**MB610**	25.2	32.1	34.1	**77%**	**54%**	**115%**	
MT002	A	*Long Groyne Opposite Spur Head.*	0.7	1.5	12	18.8	21.7	39.9	**MB610**	25.2	32.1	34.1	**75%**	**68%**	**117%**	
MT003	A	*Long groyne away from spur head*	0.7	1.5	12	22.2	26.1	44.4	**MB610**	25.2	32.1	34.1	**88%**	**81%**	**130%**	
MT004	A	*Dog-legged groyne opposite spur head*	0.7	1.5	12	20.3	16.0	42.4	**MB610**	25.2	32.1	34.1	**80%**	**50%**	**124%**	
MT005	B	*Dog-legged spur off spur head (landward)*	0.7	1.5	12	38.9	21.8	46.1	**MB610**	25.2	32.1	34.1	**154%**	**68%**	**135%**	
MT006	B	*Spur off spur head (seaward)*	0.7	1.5	12	30.2	30.4	44.1	**MB610**	25.2	32.1	34.1	**120%**	**95%**	**129%**	
MT007	A	*Dog-legged Groyne off present beach*	0.7	1.5	12	14.3	8.0	43.0	**MB610**	25.2	32.1	34.1	**57%**	**25%**	**126%**	
MT008	B	*Lowered end of Spur*	0.4	1.4	12	73.0	27.6	-	**MB420**	22.1	32.2	37.3	**330%**	**86%**	**-**	
MT009	B	*Hole through spur (west section)*	0.7	1.5	12	21.1	32.0	-	**MB610**	25.2	32.1	34.1	**84%**	**100%**	**-**	
MT010	C	*Detached breakwater in bay*	0.4	1.4	12	41.4	40.4	43.2	**MB420**	22.1	32.2	37.3	**187%**	**125%**	**116%**	
MT011	D	*Raised bed level at spur head*	0.7	1.5	12	46.5	20.6	28.1	**MB610**	25.2	32.1	34.1	**184%**	**64%**	**82%**	
MT012	E	*Hole in spur section (West) & groyne off beach*	0.3	1.3	12	18.8	14.8	30.0	**MB310**	18.7	31.4	35.7	**101%**	**47%**	**84%**	
MT013	E	*Hole in spur section (West) & groyne off beach*	-0.3	1.3	12	20.8	16.1	46.2	**MB110**	17.8	21.2	45.9	**117%**	**76%**	**101%**	
MT014	E	*Lowered spur section (East) & groyne off beach*	0.3	1.3	12	82.3	-	30.7	**MB310**	18.7	31.4	35.7	**441%**	**-**	**86%**	
MT015	E	*Lowered spur section (East) & groyne off beach*	-0.3	1.3	12	46.8	-	47.5	**MB110**	17.8	21.2	45.9	**263%**	**-**	**104%**	
MT016	F	*T-Groyne off beach*	0.45	1.4	12	6.7	12.9	40.9	**MB510**	24.4	31.3	35.7	**28%**	**41%**	**115%**	
MT017	F	*T-Groyne off beach*	0.9	1.4	12	5.7	13.1	35.2	**MB710**	23.7	30.0	26.9	**24%**	**44%**	**131%**	
MT018	F	*T-Groyne off beach*	0.9	1.8	12	8.5	14.7	38.8	**MB720**	34.9	36.7	42.0	**24%**	**40%**	**92%**	
MT019	F	*T-Groyne off beach*	-0.1	1	12	6.1	7.5	39.0	**MB210**	15.2	26.0	38.2	**40%**	**29%**	**102%**	
MT020	F	*T-Groyne off beach*	-0.1	1.4	12	8.9	8.5	44.9	**MB220**	21.1	31.5	43.6	**42%**	**27%**	**103%**	
MT021	F	*T-Groyne off beach*	0.4	1.1	12	5.4	8.1	30.9	**MB410**	16.3	29.3	27.6	**33%**	**28%**	**112%**	
MT022	F	*T-Groyne off beach*	0.4	1.4	8	6.6	7.4	41.3	**MB430**	25.3	29.1	36.7	**26%**	**25%**	**112%**	
MT023	F	*T-Groyne off beach (built-up beach)*	0.4	1.4	12	8.1	14.7	44.6	**MB420**	22.1	32.2	37.3	**37%**	**45%**	**120%**	
MT024	F	*T-Groyne off beach (denuded beach)*	0.4	1.4	12	10.3	8.3	36.7	**MB420**	22.1	32.2	37.3	**47%**	**26%**	**98%**	

C1 = Class 1 / C2 = Class 2 / C3 = Class 3. Red highlighted values denote the unreliable overtopping results

F.1.2 Absolute (*u*) velocities for all proposed solutions

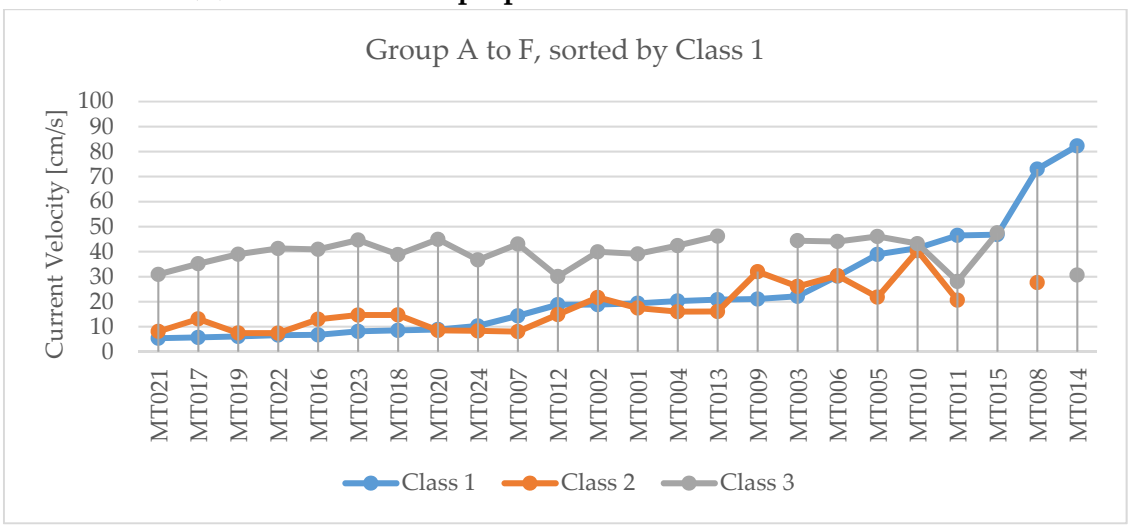

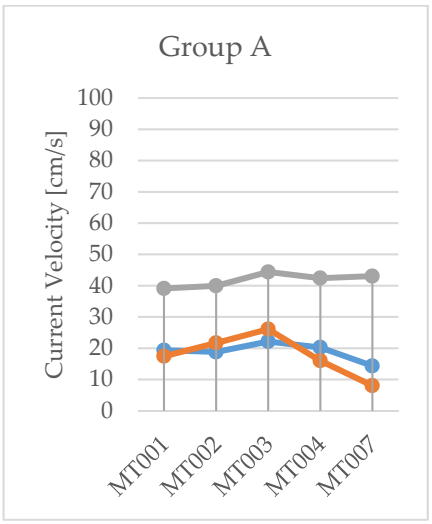

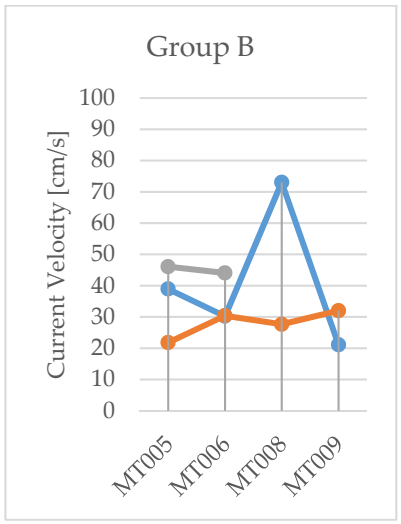

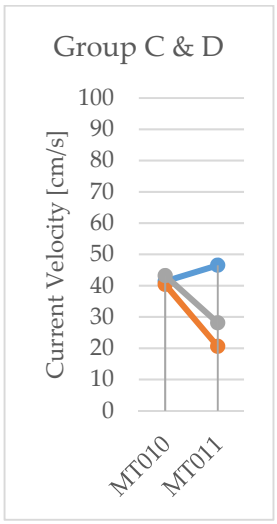

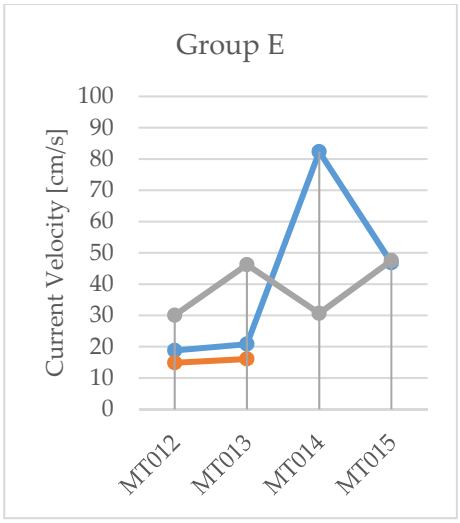

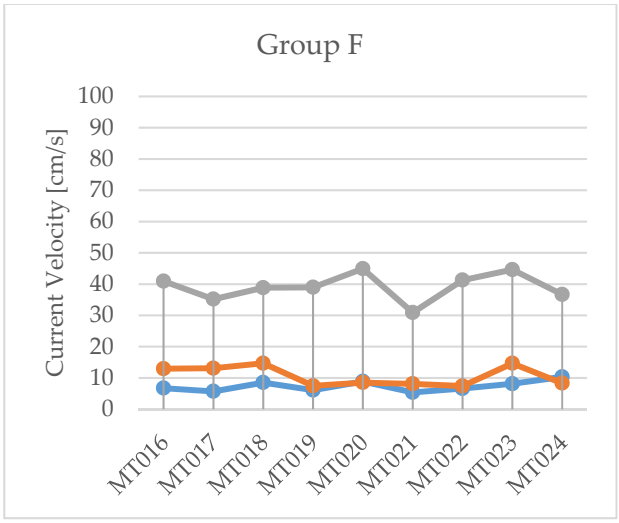

F.1.3 Baseline relative (U_r) velocities, for all proposed solutions

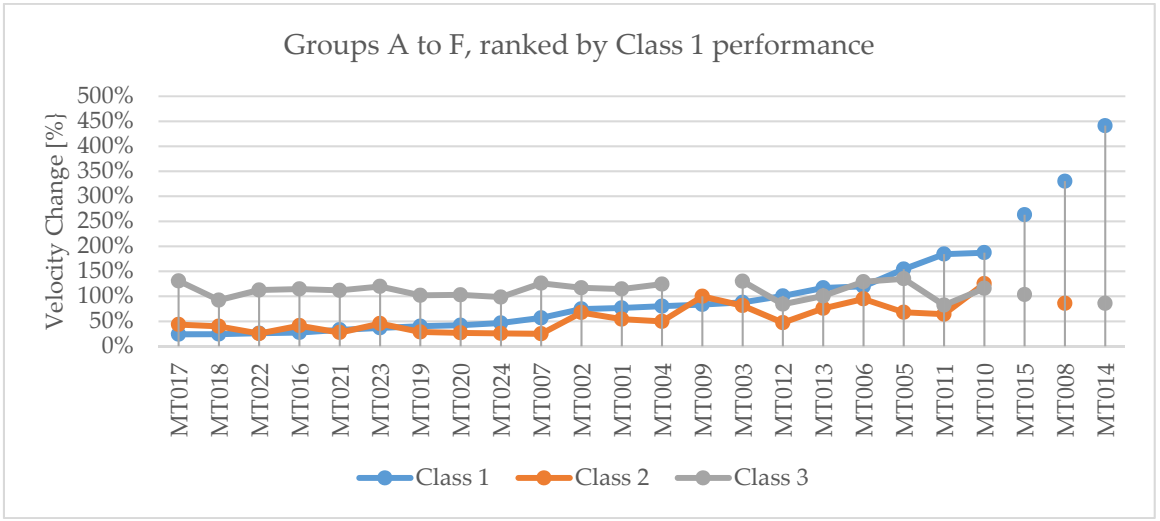

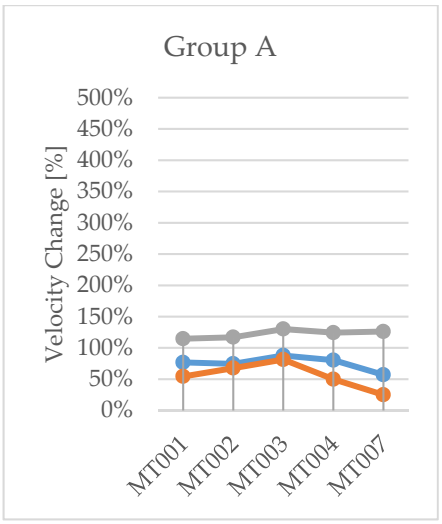

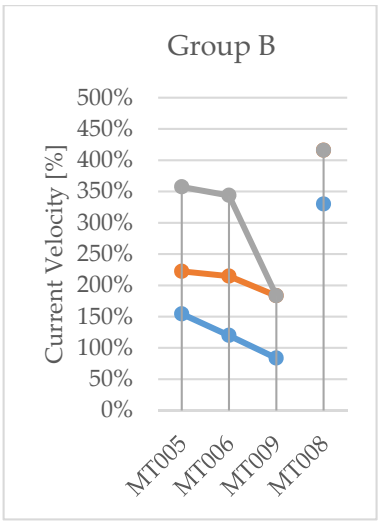

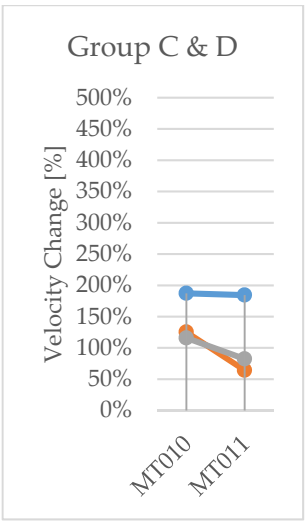

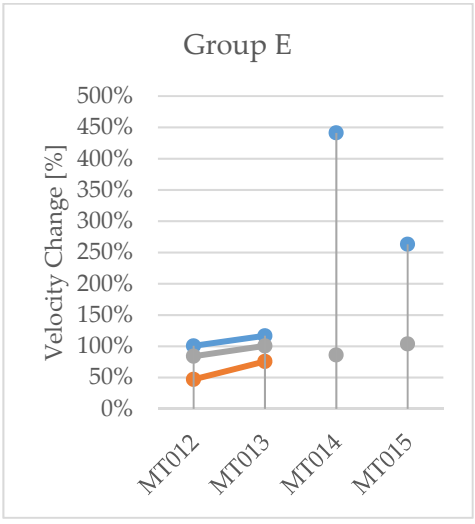

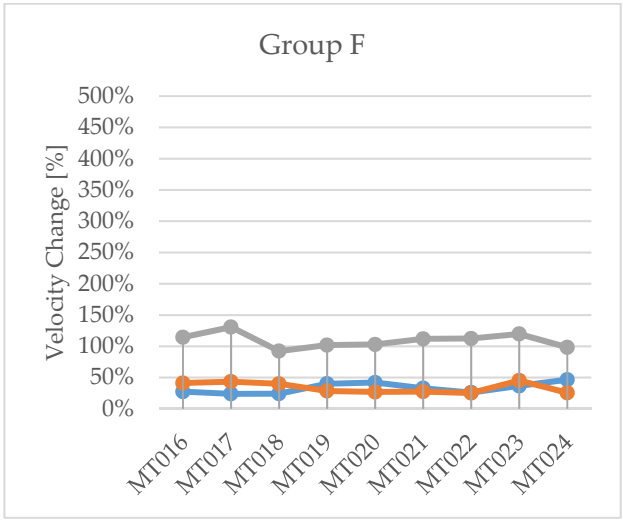

F.1.4 Designated swimming area: Exceedance curves for all proposed solutions

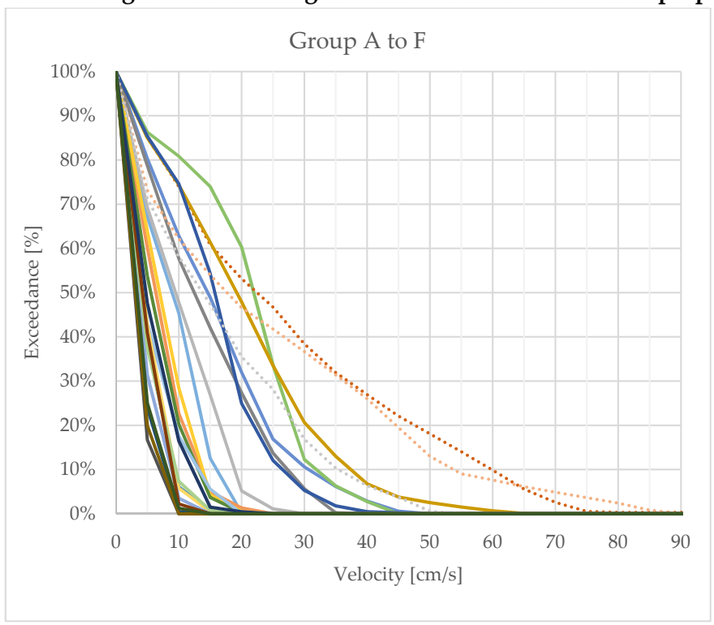

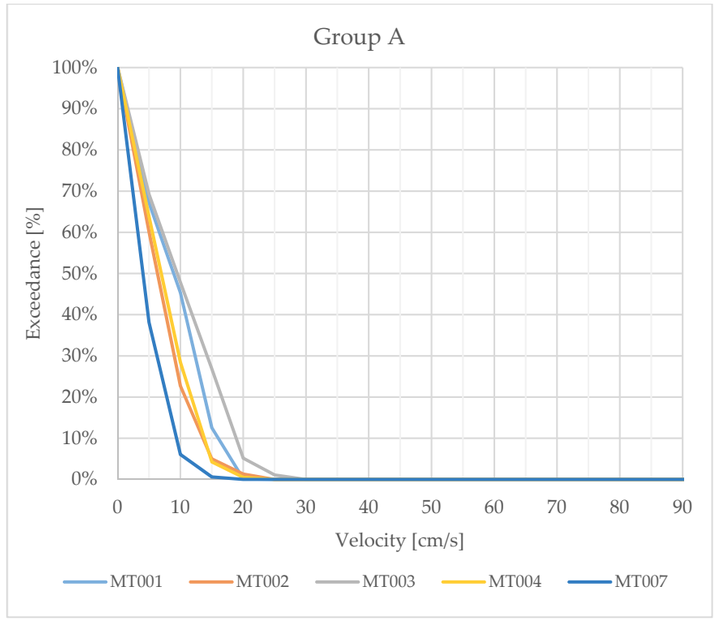

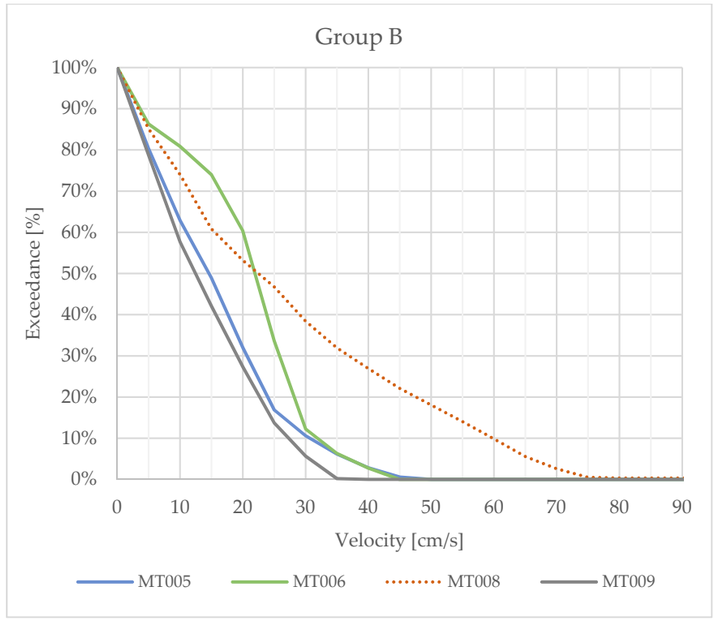

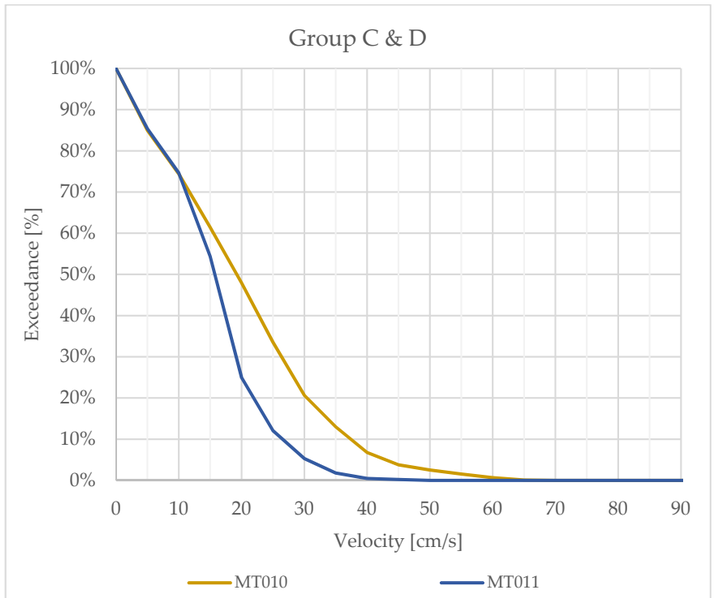

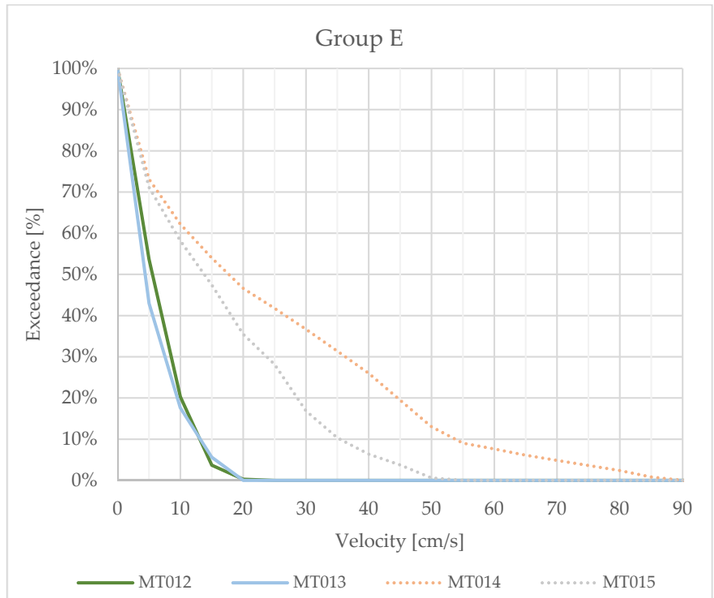

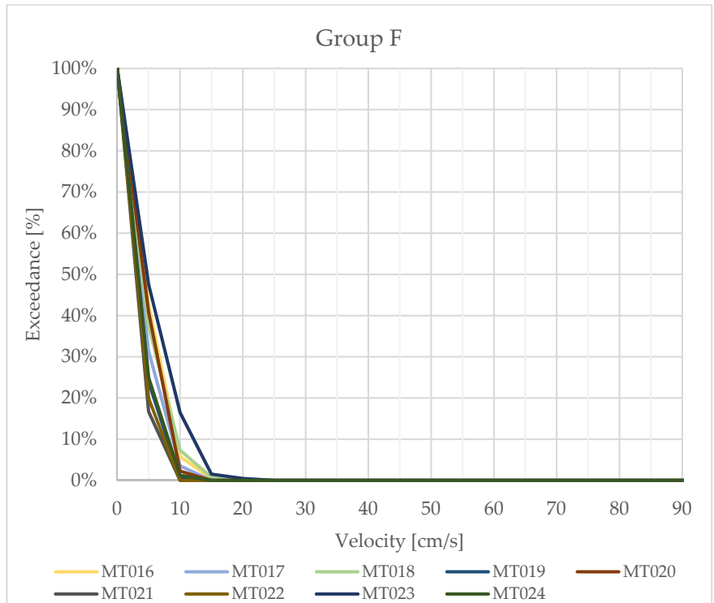

F.1.5 Designated swimming area: Exceedance-difference (relative baseline) curves for all proposed solutions

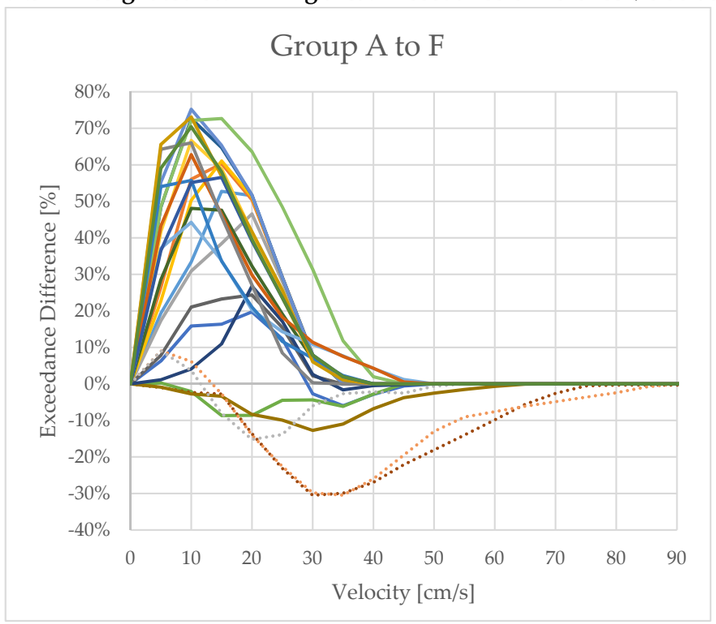

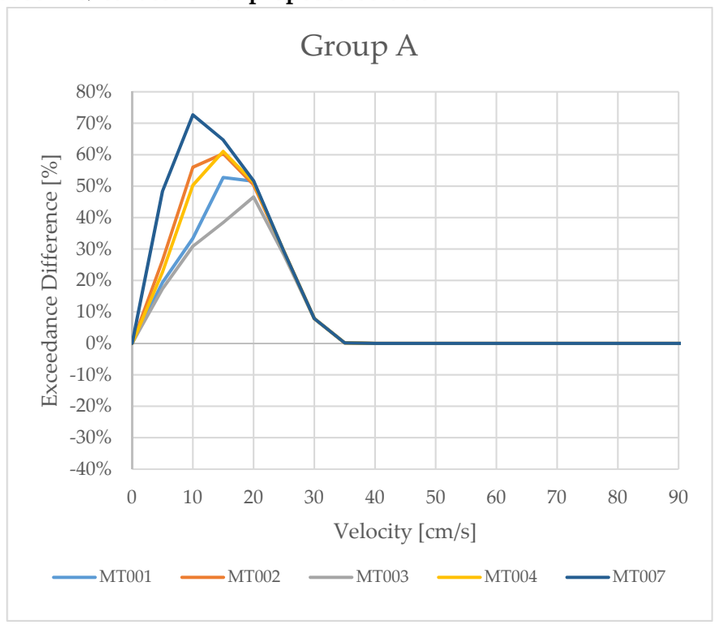

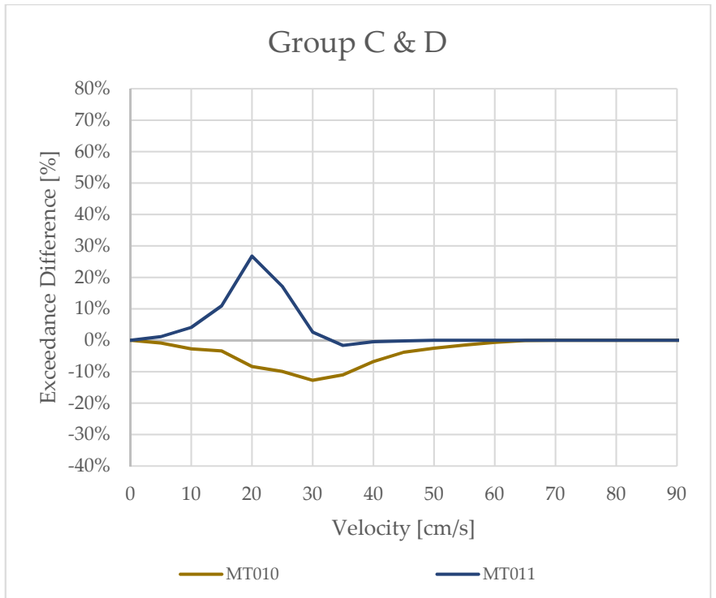

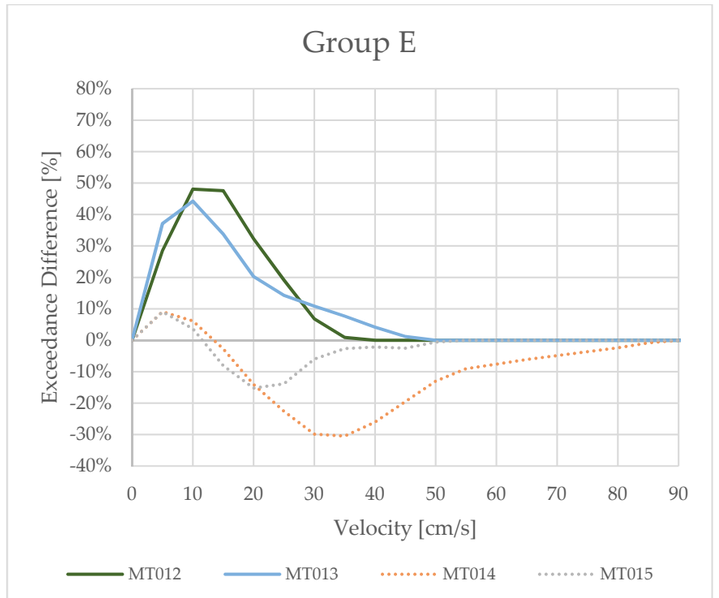

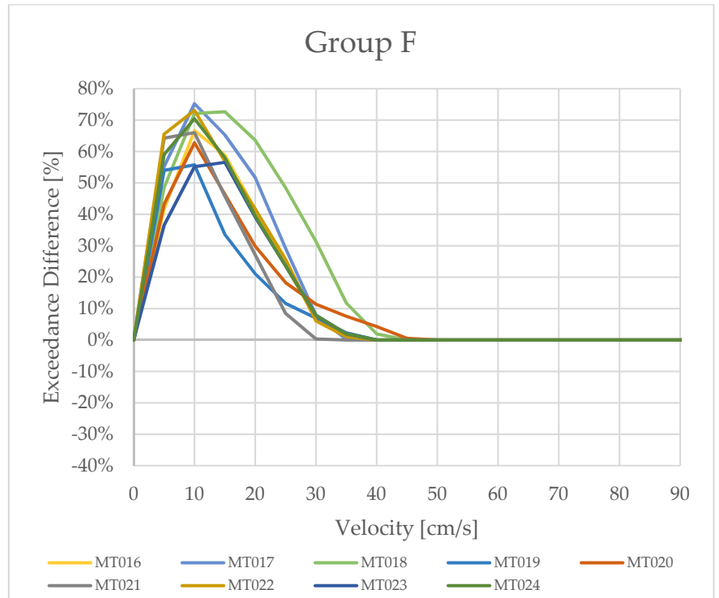

F.2 CSIR-MBWS COMPARISON

F.2.1 Summary of velocity measurements

ID	Group	Short Description	WL (m MSL)	H_s (m)	T_p (s)	Factorised Velocities														
						Vector M			Vector N			Vector O			Vector P			Vector Q		
						V_f	U_f	TYPE	V_f	U_f	TYPE	V_f	U_f	TYPE	V_f	U_f	TYPE	V_f	U_f	TYPE
MT001	A	*Short groyne opposite spur head.*	0.7	1.5	12	**66%**	**77%**	**T1**	78%	58%	T3	N/M	57%	T3						
MT002	A	*Long Groyne Opposite Spur Head.*	0.7	1.5	12	**41%**	**75%**	**T1**	103%	22%	T3	N/M	86%	T3						
MT003	A	*Long groyne away from spur head*	0.7	1.5	12	**56%**	**88%**	**T1**	93%	44%	T3	N/M	72%	T3						
MT004	A	*Dog-legged groyne opposite spur head*	0.7	1.5	12	**56%**	**80%**	**T1**	62%	27%	T3	96%	42%	T3	95%	168%	T3	N/M	63%	T3
MT005	B	*Dog-legged spur off spur head (landward)*	0.7	1.5	12	**156%**	**154%**	**T1**												
MT006	B	*Spur off spur head (seaward)*	0.7	1.5	12	**119%**	**120%**	**T1**												
MT007	A	*Dog-legged Groyne off present beach*	0.7	1.5	12	**65%**	**57%**	**T1**	**155%**	**171%**	**T1**									
MT008	B	*Lowered end of Spur*	0.4	1.4	12	101%	290%	T2												
MT009	B	*Hole through spur (west section)*	0.7	1.5	12	73%	84%	T3	51%	84%	T2	108%	127%	T1						
MT010	C	*Detached breakwater in bay*	0.4	1.4	12	**124%**	**164%**	**T1**												
MT011	D	*Raised bed level at spur head*	0.7	1.5	12	73%	184%	T2												
MT012	E	*Hole in spur section (West) & groyne off beach*	0.3	1.3	12	91%	74%	T2	107%	156%	T2									
MT013	E	*Hole in spur section (West) & groyne off beach*	-0.3	1.3	12	**109%**	**82%**	**T1**	0%	184%	T2									
MT014	E	*Lowered spur section (East) & groyne off beach*	0.3	1.3	12	104%	326%	T2	91%	149%	T2									
MT015	E	*Lowered spur section (East) & groyne off beach*	-0.3	1.3	12	88%	186%	T2	0%	190%	T2									
MT016	F	*T-Groyne off beach*	0.45	1.4	12	**≤ 37%**	**27%**	**T1**	≤ 46%	111%	T2									
MT017	F	*T-Groyne off beach*	0.9	1.4	12	N/M	23%	T3	94%	N/M*	N/M	91%	101%	T2	N/M	44%	T3			
MT018	F	*T-Groyne off beach*	0.9	1.8	12	**52%**	**34%**	**T1**	114%	N/M*	N/M	63%	100%	T2	N/M	40%	T3			
MT019	F	*T-Groyne off beach*	-0.1	1	12	N/M	34%	T3	N/M	155%	T3									
MT020	F	*T-Groyne off beach*	-0.1	1.4	12	**30%**	**35%**	**T1**	29%	178%	T2									
MT021	F	*T-Groyne off beach*	0.4	1.1	12	N/M	21%	T3	60%	97%	T2									
MT022	F	*T-Groyne off beach*	0.4	1.4	8	N/M	26%	T3	60%	80%	T2									
MT023	F	*T-Groyne off beach (built-up beach)*	0.4	1.4	12	**73%**	**38%**	**T1**	N/M	45%	T3	-	110%	T3						
MT024	F	*T-Groyne off beach (denuded beach)*	0.4	1.4	12	**≤ 16%**	**41%**	**T1**	81%	172%	T2	117%	172%	T2						

All Type 1 (exact or close match) velocities are highlighted in bold. (N/M denotes "Not measured". Red highlighted values denote the unreliable overtopping results / V_f = CSIR factorised velocity / U_f = MBWS factorised velocity

**Crest overtopping not simulated in MBWS model*

F.3 SENSITIVITY ANALYSIS

F.3.1 Friction Coefficient (MS01)

ID	Test #	Adjustment	Velocity Sensitivity									Wave Height Sensitivity				
			Measurements [cm/s]				Change [%]					Measurement [m]		Change [%]		
			u_H	u_I	u_J	u_K	Δu_H	Δu_I	Δu_J	Δu_K	$\bar{u}'_S$	H_a	H_b	ΔH_a	ΔH_b	$\bar{H}'_S$
MB610	Original	*M = 32*	25.2	30.4	34.1	32.1	-	-	-	-	-	0.96	1.56	-	-	-
MS01	1	*M = 38.4*	32.6	37.7	39.1	36.9	29%	24%	15%	15%	**21%**	0.98	1.58	1.3%	1.0%	**1.2%**
MS01	2	*M = 25.6*	17.6	22.3	28.0	25.5	-30%	-27%	-18%	-20%	**24%**	0.94	1.55	-2.9%	-1.1%	**2.0%**
MS01	3	*M = 64*	59.2	58.2	48.6	46.7	135%	91%	42%	46%	**79%**	0.96	1.59	-0.8%	1.9%	**1.4%**
MS01	4	*C = 32*	25.2	28.8	28.5	30.3	0%	-5%	-16%	-5%	**7%**	0.93	1.54	-3.8%	-1.4%	**2.6%**

F.3.2 Wave Breaking: Half-time cut off roller (MS02)

ID	Test #	Adjustment	u_H	u_I	u_J	u_K	Δu_H	Δu_I	Δu_J	Δu_K	$\bar{u}'_S$	H_a	H_b	ΔH_a	ΔH_b	$\bar{H}'_S$
MB610	Original	HTCR = 0.4s	25.2	30.4	34.1	32.1	0%	0%	0%	0%	**0%**					
MS02	1	HTCR = 1.2s	25.7	30.8	34.7	31.4	2%	1%	2%	-2%	**2%**	0.96	1.57	0.0%	0.1%	**0.1%**
MS02	2	HTCR = 1.2s	25.7	31.0	36.0	31.7	2%	2%	5%	-1%	**3%**	0.97	1.57	0.1%	0.4%	**0.2%**

F.3.3 Porosity Coefficient (MS03)

ID	Test #	Adjustment	u_H	u_I	u_J	u_K	Δu_H	Δu_I	Δu_J	Δu_K	$\bar{u}'_S$	H_a	H_b	ΔH_a	ΔH_b	$\bar{H}'_S$
MB610	Original	$\propto_p$ = 100%	25.2	30.4	34.1	32.1	0%	0%	0%	0%	**0%**					
MS03	1	$\propto_p$ = 102%	25.6	29.9	33.5	31.5	2%	-2%	-2%	-2%	**2%**	0.98	1.57	1.3%	0.2%	**0.8%**
MS03	2	$\propto_p$ = 98%	25.0	30.6	34.2	32.0	-1%	1%	0%	0%	**0%**	0.96	1.56	-0.8%	0.0%	**0.4%**
MS03	3	$\propto_p$ = 96%	25.0	30.7	34.2	32.0	-1%	1%	0%	0%	**1%**	0.95	1.57	-1.3%	0.3%	**0.8%**

F.3.4 Simulation duration: recording time (MS04)

ID	Test #	Adjustment	u_H	u_I	u_J	u_K	Δu_H	Δu_I	Δu_J	Δu_K	$\bar{u}'_S$	H_a	H_b	ΔH_a	ΔH_b	$\bar{H}'_S$
MB610	Original	Time steps: 12 000 to 20 000	25.2	30.4	34.1	32.1	0%	0%	0%	0%	**0%**					
MS04	1	Time steps: 20 000 to 40 000	25.2	30.3	34.2	31.7	0%	0%	0%	-1%	**0%**	0.96	1.56	-0.5%	-0.5%	**0.5%**

F.3.5 Velocity measurement rigidity (MS05)

ID	Test #	Adjustment	u_H	u_I	u_J	u_K	Δu_H	Δu_I	Δu_J	Δu_K	$\bar{u}'_S$
MB610	Original	N/A	25.2	30.4	34.1	32.1	0%	0%	0%	0%	**0%**
MS05	1	N/A	24.7	30.4	34.2	32.0	-2%	0%	0%	0%	**1%**
MS05	2	N/A	24.7	30.4	34.2	32.0	-2%	0%	0%	0%	**1%**
MS05	3	N/A	24.7	30.4	34.2	32.1	-2%	0%	0%	0%	**1%**

Appendix G

Summary of Simulations and Tested Wave and Tide Conditions

ID	Grouping	Short Description	WL (m MSL)	H_s (m)	T_p (s)	θ (deg)
MB110	N/A	*Baseline test*	-0.3	1.3	12	8
MB210	N/A	*Baseline test*	-0.1	1	12	8
MB220	N/A	*Baseline test*	-0.1	1.4	12	8
MB310	N/A	*Baseline test*	0.3	1.3	12	8
MB410	N/A	*Baseline test*	0.4	1.1	12	8
MB420	N/A	*Baseline test*	0.4	1.4	12	8
MB430	N/A	*Baseline test*	0.4	1.1	8	8
MB510	N/A	*Baseline test*	0.45	1.4	12	8
MB610	N/A	*Baseline test*	0.7	1.5	12	8
MB710	N/A	*Baseline test*	0.9	1.4	12	8
MB720	N/A	*Baseline test*	0.9	1.8	12	8
MT001	A.1	*Short groyne opposite spur head.*	0.7	1.5	12	8
MT002	A.2	*Long groyne opposite spur head.*	0.7	1.5	12	8
MT003	A.3	*Long groyne away from spur head*	0.7	1.5	12	8
MT004	A.4	*Dog-legged groyne opposite spur head*	0.7	1.5	12	8
MT005	B.1	*Dog-legged spur off spur head (landward)*	0.7	1.5	12	8
MT006	B.2	*Spur off spur head (seaward)*	0.7	1.5	12	8
MT007	A.5	*Dog-legged Groyne off present beach*	0.7	1.5	12	8
MT008	B.3	*Lowered end of Spur*	0.4	1.4	12	8
MT009	B.4	*Hole through spur (west section)*	0.7	1.5	12	8
MT010	C.1	*Detached breakwater in bay*	0.4	1.4	12	8
MT011	D.1	*Raised bed level at spur head*	0.7	1.5	12	8
MT012	E.1	*Hole in spur section (West) & groyne off beach*	0.3	1.3	12	8
MT013	E.1	*Hole in spur section (West) & groyne off beach*	-0.3	1.3	12	8
MT014	E.2	*Lowered spur section (East) & groyne off beach*	0.3	1.3	12	8
MT015	E.2	*Lowered spur section (East) & groyne off beach*	-0.3	1.3	12	8
MT016	F.1	*T-Groyne off beach*	0.45	1.4	12	8
MT017	F.1	*T-Groyne off beach*	0.9	1.4	12	8
MT018	F.1	*T-Groyne off beach*	0.9	1.8	12	8
MT019	F.1	*T-Groyne off beach*	-0.1	1	12	8
MT020	F.1	*T-Groyne off beach*	-0.1	1.4	12	8
MT021	F.1	*T-Groyne off beach*	0.4	1.1	12	8
MT022	F.1	*T-Groyne off beach*	0.4	1.4	8	8
MT023	F.2	*T-Groyne off beach (built-up beach)*	0.4	1.4	12	8
MT024	F.3	*T-Groyne off beach (denuded beach)*	0.4	1.4	12	8

WL = Water Level relative to MSL / H_s = Regular Wave Height / T_p = Wave Period / θ = Angle of wave propagation clockwise from North